UNIVERSIDAD DE BURGOS
Facultad de Ciencias

Functional naphthalimide luminogens: from aggregation-induced emission and self-assembly to biological activity and nanomaterials applications

---

Luminógenos funcionales de naftalimida: desde la emisión inducida por agregación y el autoensamblaje hasta la actividad biológica y aplicaciones en ciencia de los nanomateriales

PhD THESIS

CARLA HERNANDO MUÑOZ

Supervisor:

Tomás Torroba Pérez

Burgos, September 2025

“It always seems impossible until it's done”.

“Todo parece imposible hasta que se hace”.

Nelson Mandela.

AGRADECIMIENTOS

Los comienzos siempre asustan. Cuatro años parecen un camino eterno, pero a mitad de trayecto, cuando uno mira atrás, se da cuenta de que el tiempo ha volado. Y al llegar al destino, solo queda respirar hondo, sonreír y pensar: “lo logré”.

Desde muy pequeña sentí fascinación por la química y, en especial, por sus aplicaciones en la medicina, quizá condicionada por mis propias patologías, que me acompañan desde la infancia. Siempre soñé con contribuir, de alguna manera, a encontrar soluciones para mejorar la vida de las personas y, en especial, para la diabetes con la que convivo. La unión de química y medicina es, en muchos sentidos, parte de mi identidad.

Fue antes de comenzar con mi Trabajo Fin de Máster cuando mi director de tesis, Tomás Torroba, confió en mí y me brindó la oportunidad de adentrarme en la investigación biomédica, abriendo para mí una nueva línea de trabajo dentro de su laboratorio, hasta entonces centrado en la detección de explosivos. A él le debo no solo la oportunidad de trabajar en lo que realmente me apasiona, sino también su confianza, que en aquel momento fue mayor incluso que la que yo tenía en mí misma. Gracias, Tomás, por permitirme jugar con la química orgánica para abordar nuevos retos y por creer en mi capacidad de hacerlo, siempre aceptando las nuevas ideas que se me ocurrían.

En mis primeros pasos fue esencial el apoyo de la entonces doctoranda, hoy Dra. Andrea Revilla, quien me enseñó con paciencia el manejo de los instrumentos, las dinámicas del laboratorio y todo lo necesario para desenvolverme. Fuera del ambiente de trabajo también hemos compartido cafés y risas, gracias a nuestro grupo de amigos de la carrera “Los Alquimistas”, que ha sido un pilar imprescindible para desahogarme y entender que solo quienes hemos vivido la orgánica sabemos cuán compleja puede llegar a ser.

Volviendo a los compañeros de laboratorio, no puedo olvidar al Dr. Mateo Martín y la Dra. Patricia Calvo, que me guiaron en mis inicios con la química de aminoácidos.

Como compañera fundamental que me ha acompañado durante todos estos años, he de agradecer a Irene Abajo todo su trabajo, las medidas interminables y su dedicación desde el minuto cero. Puedo afirmar, que es una de las personas más perseverantes, trabajadoras y perfectas en su trabajo que he conocido. Nada se la escapa, nada puede quedar mal, así que todo termina quedando brillante.

También quiero mencionar a Cristian Almeida, siempre dispuesto a ayudar sin importar lo larga que fuese ya su lista de tareas. Desde mover bidones imposibles hasta solucionar cualquier contratiempo del laboratorio, siempre haciéndolo sin esperar nada a cambio.

A los técnicos que han pasado por el laboratorio, mi más sincera gratitud. En especial a la Dra. María Medrano, por alegrarnos cada mañana con tu sonrisa y por llenar de arte y color nuestro entorno, y a Miguel Rodríguez, por tu paciencia infinita tanto con mis elecciones musicales de la radio (sé que no eres fan del pop) como con las columnas interminables del depsipéptido.

No menos importantes son los distintos alumnos de trabajo de fin de grado que he conocido durante estos años, donde Valeria Alonso, Karl Tilmann Schuppe y Alejandro Elam García dejaron sus primeras huellas. Luego siguieron Andrés Jesús Saiz, Jon Daniel Cacho y Carolina Martínez. Como alumno de fin de máster, no puedo olvidarme de Yeray Moreno, una persona que desde el minuto cero supimos que era prometedora y brillante. No puedo estar más agradecida con él por sus ideas siempre tan resolutivas, su gran imaginación y dotes artísticas que rompen con la monotonía.

A otros compañeros de laboratorio con quienes he compartido horas y consejos: Andrea Sancho, Javier Gómez, Daniel Alonso, Laura Gangoso, Rosana Ruiz y la última incorporación, Virginia Arnaiz, cuya compañía y conversaciones han sido de gran apoyo.

Una persona que ha sido fundamental en todo este camino es la Dra. Pilar Castroviejo, técnico de Parque científico Tecnológico de la UBU, sin la cual esta tesis no habría sido posible ya que es quien me ha enseñado a manejar el microscopio electrónico de barrido (no son pocas las imágenes adquiridas en este trabajo). Gracias por confiar en mí, y por convertirte en una amiga de las de verdad: siempre apoyándome, no solo con mi investigación, sino también en mis momentos más duros y luchas personales que he atravesado durante estos años.

Por último, y probablemente los más importantes en todo este proceso, son mis padres Rocío y Juan Carlos, y mi hermana mayor, Sandra. Mi familia, que desde el primer momento confiaron en mí, me dijeron no abandones, me transmitieron seguridad incluso cuando yo creía que no podía más. Me hicisteis sentir que era capaz de hacer una tesis doctoral y me disteis el coraje suficiente para conseguirlo. Gracias por enseñarme a ver el mundo como una adulta, pero también por cuidarme como a vuestra niña. Gracias por no dejarme caer en los momentos en los que la salud me puso a prueba, que no han sido pocos a lo largo de este camino. Ahora, vuestra niña, por fin acaba el proyecto que empezó hace cuatro años, y sin vosotros no habría sido posible.

Finalmente, gracias a mis amigo/as ajenos al mundo de la química, que me escucharon, me acompañaron y trataron de comprenderme incluso cuando lo que contaba no tenía mucho sentido para ellos. Vuestra presencia ha sido un refugio.

A todos, de corazón: gracias.

Financiación: quiero expresar mi agradecimiento al Ministerio de Ciencia, Innovación y Universidades por la beca recibida a través de la convocatoria de 2021 de las Ayudas para la Formación de Profesorado Universitario (FPU21/01473), sin la cual la realización de esta Tesis Doctoral no habría sido posible.

INDEX OF ABBREVIATIONS

SOLVENTS

DCM: Dichloromethane.

DMF: *N,N*-Dimethylformamide.

DMSO: Dimethyl sulfoxide.

EtOAc: Ethyl acetate.

EtOH: Ethanol.

Et_2O: Diethylether.

Hex: Hexane.

MCH: Methylcyclohexane.

MeCN: Acetonitrile.

CD_3OD: Deuterated methanol.

MeOH: Methanol.

THF: Tetrahydrofuran.

Tol: Toluene.

REAGENTS

DIPEA: *N,N*-Diisopropylethylamine.

HOBt: Hydroxybenzotriazole.

PyBOP: Benzotriazol-1-yl-oxytripyrrolidinophosphonium hexafluorophosphate.

TECHNIQUES

^{1}H NMR: Proton Nuclear Magnetic Resonance.

^{13}C NMR: Carbon Nuclear Magnetic Resonance.

AFM: Atomic Force Microscopy.

BSEs: Backscattered electrons.

CD: Circular Dichroism.

CPL: Circular Polarized Luminiscence.

CLSM: Confocal Laser Microsocopy.

DEPT: Distortionless Enhancement by Polarization Transfer. (13C-NMR analysis).

DLS: Dynamic Light Scattering.

EDX: Energy Dispersive X-Ray spectroscopy.

ESI: Electrospray Ionization.

FESEM: Field emission Scanning Electron Microscopy.

HRMS: High Resolution Mass Spectrometry.

MALDI: Matrix-Assisted Laser Desorption/Ionization.

MD: Molecular Dynamics.

SEM: Scanning Electron Microscopy.

STED: Stimulated Emission Depletion.

TAS: Transient Absorption Spectroscopy.

TEM: Transmission Electron Microscopy.

TLC: Thin Layer Chromatography.

OTHER ABBREVIATIONS

A2780: Ovarian carcinoma cell line.

A2780cis: Cisplatin-resistant ovarian carcinoma cell line.

A549: Lung carcinoma cell line.

ACQ: Aggregation Caused Quenching.

AIE: Aggregation-Induced Emission.

AIEgens: Aggregation-Induced Emission luminogens.

AR: Androgen Receptor.

AgNPs: Silver nanoparticles.

AuNPs: Gold nanoparticles.

BSA: Bovine Serum Albumin (cell cultures).

C_{Ar}: Aromatic Carbon.

CDDP: Cis-diamminedichloroplatinum (II).

C_q: Cuaternary Carbon BSEs: Backscattered electrons.

CPK: Corey-Pauling-Koltun (representation model).

CT: Computed Tomography.

DNA: Deoxyribonucleic acid.

DMEM: Dulbecco's Modified Eagle Medium (cell cultures).

EADS: Evolution-Associated Difference Spectra.

ER: Endoplasmic Reticulum.

ESA: Excited State Absorption.

ESPIT: Excited-State Intramolecular Proton Transfer

EWG: Electron Withdrawing Group.

FBS: Fetal Bovine Serum.

g_{lum}: Dissymmetry factor.

GSB: Ground State Bleach.

H_{Ar}: Aromatic Proton.

HEK-293: Human embryonic kidney cells.

HR: High Resolution.

ICT: Intramolecular Charge Transfer.

ISC: Intersystem Crossing.

IR: Infrared.

LNCaP: Prostate cancer cell line (androgen sensitive).

LSPR: Localized Surface Plasmon Resonance.

MLCT: Metal to Ligand Charge Transfer.

MRI: Magnetic Resonance Imaging.

mRNA: Messenger ribonucleic acid.

MTT: 3-(4,5- dimetylthiazol-2-yl)-2,5-diphenyl tetrazolium bromide.

NDI: Naphthalenediimide.

NMI: Naphthalenemonoimide.

NPs: Nanoparticles.

NIR: Near Infrared Spectroscopy.

OFETs: Organic Field-Effect Transistors.

OLED: Organic Light-Emitting Diode.

OFEWs: Optical Field- Effect Waveguides.

PC-3: Prostate cancer cell line (no androgen sensitive).

PCC: Pearson's correlation coefficient.

PDI: Perylenediimide.

PDT: Photodynamic Therapy.

PET: Photoinduced Electron Transfer.

PIF: Preimplantation Factor.

PPP: Pentaphenylpyrrole.

PS: Photosensitizer.

REF: Reference.

RIM: Restriction of Intramolecular Motion.

RIV: Restriction of Intramolecular Vibration.

ROS: Reactive oxygen species.

SD: Standard Deviation.

SE: Stimulated Emission.

SE: Standard Error ($\frac{SD}{\sqrt{n}}$).

SPR: Surface Plasmon Resonance.

TATP: Triacetone Triperoxide.

TICT: Twisted Intramolecular Charge Transfer.

TNT: Trinitrotoluene.

ΔA: Change in optical density.

$^1\Delta_g$ O_2: Singlet oxygen.

Φ_Δ: Singlet oxygen quantum yield.

GENERAL INDEX

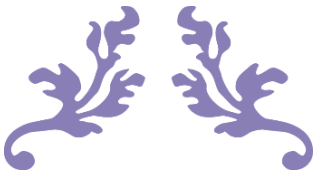

CONTEXTO GENERAL DE LA TESIS

1. PLANIFICACIÓN GENERAL DEL TRABAJO Y RESUMEN

Durante los últimos años, el grupo de investigación se ha centrado en la síntesis de derivados de naftalenomonoimida (naftalimida, NMI) con diferentes intereses y aplicaciones, todos ellos partiendo de una estructura base común ya descrita en tesis anteriores del mismo grupo. Así, mediante la incorporación de distintas unidades estructurales al colorante inicial, en esta tesis se ha logrado obtener una amplia variedad de compuestos con elevado potencial en diversos campos, que abarcan desde la biomedicina hasta la química quiral. Todos los compuestos sintetizados presentan un eje común: la formación de agregados en mezclas de disolventes orgánicos con alto contenido en agua. Los compuestos descritos en los capítulos del uno al cuatro manifiestan el fenómeno de emisión inducida por agregación (AIE, por sus siglas en inglés) en dichas mezclas. De esta forma, establecer una relación entre el fenómeno AIE y la nanoestructura de los agregados constituye uno de los objetivos principales de esta tesis.

En los comienzos de esta investigación, se nos concedió el proyecto nacional titulado “Depsipéptidos autoensamblados en luminógenos de emisión inducida por agregación para crear nanovesículas programables, nanoportadores y nanomateriales funcionales sostenibles” (FLUONANOVESICLE), financiado por el Ministerio de Ciencia e Innovación. Diversas secciones y objetivos de dicho proyecto se desarrollan en detalle a lo largo de esta tesis doctoral.

En primer lugar, el campo de la biomedicina resultó especialmente atractivo, por lo que se sintetizaron derivados depsipeptídicos de naftalimida y se estudiaron sus propiedades luminiscentes. Posteriormente, se relacionó la aparición del efecto AIE con la formación de nanovesículas. Estas nanovesículas fueron estudiadas en el interior de células, demostrando que es posible modular la citotoxicidad de los compuestos en función del número de ramas depsipeptídicas unidas al colorante inicial. Asimismo, se investigó el uso de estos compuestos como nanotransportadores de péptidos activos naturales. Todo ello se desarrolla en el **Capítulo 1.**

Los estudios de simulación mediante dinámica molecular realizados en el capítulo anterior revelaron que las nanovesículas se forman debido a que el apilamiento de los anillos de naftaleno del colorante central adquiere cierta curvatura cuando se acumulan muchas unidades. La presencia de las cadenas depsipeptídicas, además de favorecer el autoensamblaje, confiere flexibilidad a la estructura, dando lugar a estructuras huecas. En base a estos resultados, el **Capítulo 2A** estudia cual ha de ser la longitud mínima y la naturaleza de las cadenas de aminoácidos para que tenga lugar la formación de vesículas. De esta forma, se analizó cómo varía la nanoestructura en función del número y naturaleza de los aminoácidos unidos al núcleo de naftalimida. Por otro lado, se observó que los derivados de NMI que contienen aminoácidos con cadenas alifáticas son susceptibles de interactuar y reducir metales como el oro o la plata, promoviendo la formación de nanopartículas metálicas, como nanodendritas de oro en mezclas específicas de agua y disolvente orgánico. Además, se comprobó que las nanoestructuras de oro presentan actividad catalítica en reacciones de acoplamiento carbono-carbono, concretamente la reacción de Suzuki-Miyaura. Todos estos hallazgos, así como las condiciones y naturaleza de la formación de nanoestructuras metálicas, se detallan en el **Capítulo 2B.**

Los resultados obtenidos en el Capítulo 1 motivaron un estudio más profundo de derivados con emisión inducida por agregación en aplicaciones médicas. Asimismo, se corroboró que la formación de nanovesículas está relacionada con el apilamiento curvado de los anillos de naftaleno, lo cual se ve favorecido por la unión de estructuras que aportan flexibilidad al sistema. De este modo surge el **Capítulo 3**, en el cual se enlaza una testosterona modificada a los derivados depsipeptídicos del Capítulo 1, así como a los colorantes originales no modificados. Así se obtiene una amplia serie de compuestos que también presentan el efecto AIE y forman nanovesículas en mezclas de disolventes orgánicos y agua. Esta sección tiene como objetivo explorar el potencial anticancerígeno de esta serie

de compuestos en líneas celulares de cáncer de próstata PC-3 (no sensibles a andrógenos) y LNCaP (sensibles a andrógenos) y determinar el destino celular de los compuestos mediante microscopía confocal.

Por otra parte, los NMI iniciales fueron enlazados a ureas quirales, lo que da origen al **Capítulo 4.** Aquí se observó que la aparición del efecto AIE en mezclas con alto contenido de agua está relacionada con la formación de nanofibras helicoidales. En este caso, el apilamiento entre los anillos de naftaleno difiere del observado en los capítulos previos. El Capítulo 4 se centra en el papel que juega la quiralidad interna de las moléculas en el signo de las señales de dicroísmo circular, así como en la influencia de la formación de estructuras supramoleculares sobre las señales de luminiscencia circularmente polarizada. Además, estas hélices orgánicas quirales pueden recubrirse de forma selectiva de nanopartículas de plata, cuya naturaleza se describe en profundidad en este capítulo.

Finalmente, en el **Capítulo 5,** las NMI de partida se unieron a complejos organometálicos de rutenio e iridio. Se observaron procesos de transferencia electrónica entre los distintos centros fluorescentes, bien dentro de la misma molécula o entre moléculas agregadas. Ensayos de absorción transitoria ultrarrápida revelaron la formación de estados excitados intermedios en mezclas de disolventes orgánicos con alta proporción de agua. Posteriormente, dichos estados intermedios evolucionan hacia un estado triplete estable que interacciona con el oxígeno, generando oxígeno singlete. Estos compuestos también fueron estudiados en células de cáncer de riñón (HEK 293) por su potencial aplicación en terapia fotodinámica. El oxígeno singlete formado tras la excitación es una especie altamente reactiva, capaz de inducir daño oxidativo en componentes celulares esenciales, lo que puede conducir finalmente a la muerte celular. Además, su estabilidad estructural y su absorción dentro de la ventana terapéutica los convierten en candidatos idóneos para ejercer actividad citotóxica inducida por luz.

Finalmente, además de los resultados de los distintos capítulos de esta tesis, se incluyen dos secciones adicionales. El Anexo proporciona información detallada sobre los reactivos, materiales y especificaciones técnicas de los equipos utilizados, así como un resumen de las publicaciones y congresos en los que se ha presentado este trabajo. Por otra parte, para una mayor claridad, la Información Suplementaria (seis anexos en formato digital) contiene todos los esquemas de reacción, caracterización estructural completa, imágenes de microscopía y experimentos adicionales, organizados por capítulos.

2. ESQUEMA DE OBJETIVOS

Cada capítulo de esta tesis presenta sus propios objetivos específicos, los cuales se desarrollan en detalle a lo largo del trabajo. Sin embargo, el siguiente esquema proporciona una visión general, clara y concisa de los aspectos clave y de los objetivos generales abordados en cada uno de los capítulos.

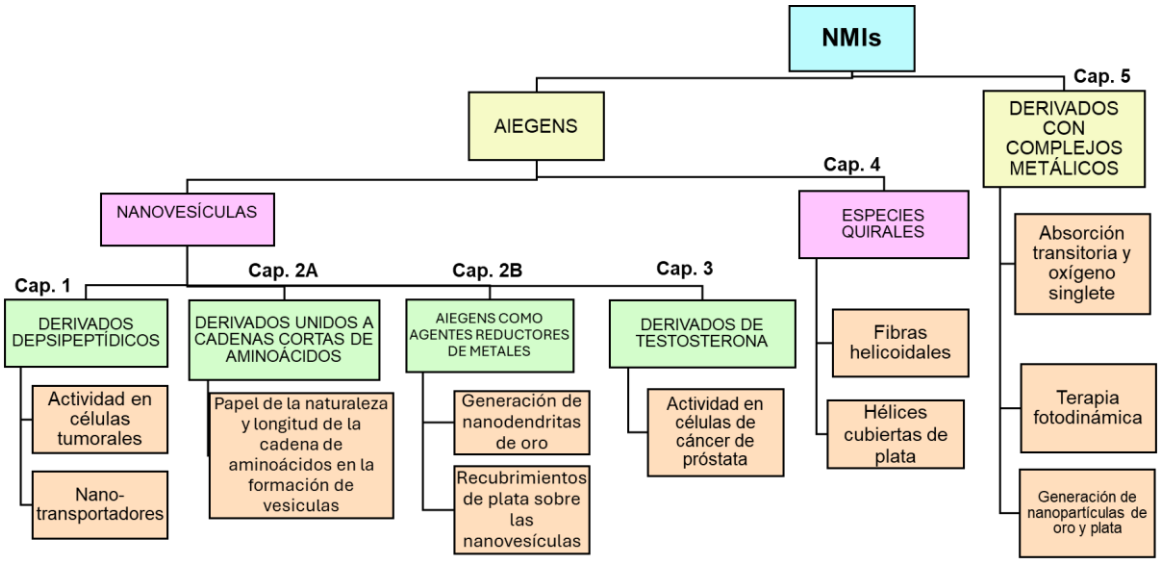

Figura 1. *Diagrama de los aspectos clave de los distintos capítulos de la tesis.*

3. COLABORACIONES

Esta tesis comprende un amplio conjunto de experimentos y ensayos realizados con una gran variedad de equipos. Algunos de estos estudios se llevaron a cabo en colaboración con otros grupos de investigación. En esta sección se describen las colaboraciones que han contribuido al desarrollo del trabajo presentado en los distintos capítulos.

Capítulo 1. Depsipéptidos autoensamblables unidos a emisores de luz inducida por agregación.

Las medidas de luminiscencia circularmente polarizada (CPL) fueron realizadas por Robert Pal y Dominic Black, del Departamento de Química de la Universidad de Durham (Reino Unido).

Los espectros de dicroísmo circular fueron obtenidos por José García Calvo, del Departamento de Química Orgánica de la Universidad Autónoma de Madrid, España.

Los cálculos de simulación por dinámica molecular fueron llevados a cabo por Giampaolo Barone y Angello Spinello, del Departamento STEBICEF (Scienze e Tecnologie Biologiche Chimiche e Farmaceutiche) de la Universidad de Palermo (Sicilia), Italia.

Los ensayos celulares fueron realizados por Natalia Busto y Camilla Andreini, del Departamento de Ciencias de la Salud de la Universidad de Burgos, España.

Capítulo 3. Testosterona modificada en emisores de luz inducida por agregación.

La testosterona modificada fue generosamente donada por Gervais Bérubé, del Departamento de Química de Université du Québec à Trois-Rivières, Canadá.

Los estudios en cultivos celulares fueron llevados a cabo por Silvia Albillos y David Palacios, del Departamento de Biotecnología de la Universidad de Burgos, España.

Capítulo 4. Unidades de urea quirales en emisores de luz inducida por agregación.

Las medidas de luminiscencia circularmente polarizada (CPL) fueron realizadas por Robert Pal y Dominic Black, del Departamento de Química de la Universidad de Durham (Reino Unido).

Los espectros de dicroísmo circular fueron obtenidos por José García Calvo, del Departamento de Química Orgánica de la Universidad Autónoma de Madrid, España.

Las simulaciones de dinámica molecular fueron realizadas por Giampaolo Barone, Angello Spinello y Salvatore Muscarella, del Departamento STEBICEF (Scienze e Tecnologie Biologiche Chimiche e Farmaceutiche) de la Universidad de Palermo (Sicilia), Italia.

Capítulo 5. Complejos de rutenio e iridio en 1,8-naftalimidas: fotofísica, nanoestructura y aplicaciones.

Los espectros de absorción transitoria fueron obtenidos por Mariangela Di Donato y Greta Sambucari en el Laboratorio Europeo de Espectroscopía No Lineal (LENS), Florencia, Italia.

Las medidas de oxígeno singlete fueron realizadas por Luca Conti, Gina Elena Giacomazzo y Claudia Giorgi, del Departamento de Química Inorgánica “Ugo Schiff” de la Universidad de Florencia, Italia.

Los ensayos celulares y los estudios de terapia fotodinámica fueron llevados a cabo por Lucía Gardini y Chiara Caldini en el Laboratorio Europeo de Espectroscopía No Lineal (LENS), Florencia, Italia.

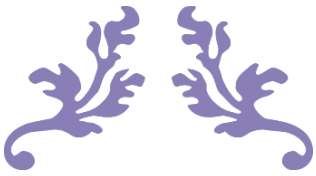

GENERAL CONTEXT OF THE THESIS

1. GENERAL WORK PLANNING AND SUMMARY

Over the last years the research group has focused on making naphthalenemonoimide (NMI) derivatives with different interests and applications, all of them starting from a common dye structure already described in a former thesis of the research group. In this research, by joining different moieties to the starting dye, a wide variety of chemical compounds with strong potential applications in different fields have been obtained, ranging from biomedicine to chiral chemistry. All synthetized compounds have a common feature: they form aggregates in mixtures of organic solvents with high water content. The compounds described from Chapter 1 to 4 show the aggregation-induced emission effect (AIE) in those mixtures. To stablish a relation between the AIE and the nanostructure of aggregates is one of the aims of the thesis.

At the beginning of this research, the group was involved in the project entitled "Self-assembling depsipeptides on aggregation-induced emission luminogens as a new way to create programmable nanovesicles, soft nanocarriers and green functional nanomaterials", FLUONANOVESICLE, granted by the Science and Innovation Ministry. Several sections and objectives of this project are meticulously developed in this doctoral thesis.

First, the biomedicine field was the most attractive, so depsipeptidic naphthalenemonoimide derivatives were synthesized and their luminescent properties were studied. Thereafter, the appearance of AIE was related to the formation of nanovesicles. The nanovesicles were then studied inside cells, showing that it is possible to modulate the cytotoxicity of the compounds depending on the number of depsipeptide branches attached to the initial dye. The compounds were also studied as soft nanocarriers of naturally active peptides. All these aspects will be developed in **Chapter 1.**

The molecular dynamics simulation studies performed within the previous chapter revealed that nanovesicles are formed because the stacking of the naphthalene rings of the core dye acquired certain degree of curvature when the number of units was high. The presence of the depsipeptide chains, in addition to promoting self-assembly, confers flexibility to the structure, giving rise to hollow nanostructures. Considering these results, **Chapter 2A** studies the length and nature of the amino acids chain required for vesicle formation. We therefore studied how the nanostructure changes depending on the number and nature of amino acids bonded to the naphthalimide core. NMI derivatives containing amino acids with aliphatic chains are susceptible to interact with metals such as silver or gold and promote the formation of metal nanoparticles and nanodendrites in specific water-solvent mixtures. In addition, the gold nanostructures were found to exhibit catalytic activity in Suzuki-coupling reactions. All these findings, as well as the nature and conditions for metallic nanostructure formation are described in **Chapter 2B.**

The results obtained in Chapter 1 motivated further study of fluorescent derivatives with medical applications. Additionally, it was shown that nanovesicle formation is linked to the curved stacking of the naphthalene rings, favoured by the attachment to moieties that confer flexibility to the structure. This is how **Chapter 3** emerges, where a modified testosterone is linked to the depsipeptide derivatives from Chapter 1, as well as to the original intact dyes, giving rise to a wide variety of compounds that also exhibit AIE and form nanovesicles in organic solvent-water mixtures. This section aims to discover the anticancer potential of this series of compounds in PC-3 (non-androgen sensitive) and LNCaP (androgen sensitive) prostate cancer cell lines. In addition, the target organelle of the studied compounds will be determined by using confocal microscopy.

On the other hand, the starting NMIs were linked to chiral ureas, giving rise to **Chapter 4.** In this case, it was seen that the appearance of AIE in mixtures of high-water percentages was linked to the formation of helicoidal nanofibers. Here, the stacking between the naphthalene rings is no longer the same as that seen in previous chapters. Chapter 4 is focused on the role of the molecule's internal chirality in the sign of circular dichroism

signals, as well as the role of the supramolecular structure in circularly polarized luminescence signals. Furthermore, these chiral organic helices can be selectively coated with silver nanoparticles, and its nature is fully described in this chapter.

Finally, in **Chapter 5** the starting NMIs were bonded to organometallic complexes of ruthenium and iridium. Energy transfer processes between the different fluorescent centres were observed, occurring either within the same molecule or between different stacked molecules. Ultrafast transient absorption assays were performed and revealed the formation of intermediate states in mixtures of organic solvent with high water ratios. Then, these intermediate states evolve to the formation of a stable triplet state which interacts with oxygen, giving rise to singlet oxygen. These compounds were also studied in cells (HEK 293) for their potential application in photodynamic therapy. The singlet oxygen, generated upon excitation, is a highly reactive species capable of inducing oxidative damage to cellular components and ultimately leading to cell death. Additionally, their structural stability and absorption in the therapeutic window make them ideal candidates for light-induced cytotoxic activity in biomedical applications.

Lastly, in addition to the findings discussed throughout the various chapters of this thesis, two supplementary sections are provided. The Annex offers detailed information on the reagents, materials, and technical specifications of the equipment used, along with a summary of the publications and conferences where this work was presented. Additionally, to provide further clarification, the Supporting Information (six annexes in digital format) contains all reaction schemes, full structural characterization, microscopy images and additional experiments depending on the chapter.

2. OUTLINE OF OBJECTIVES

Within each chapter of this thesis a set of specific objectives is included. However, this diagram offers a highly visual overview of the key points and general objectives to be developed and addressed in each chapter.

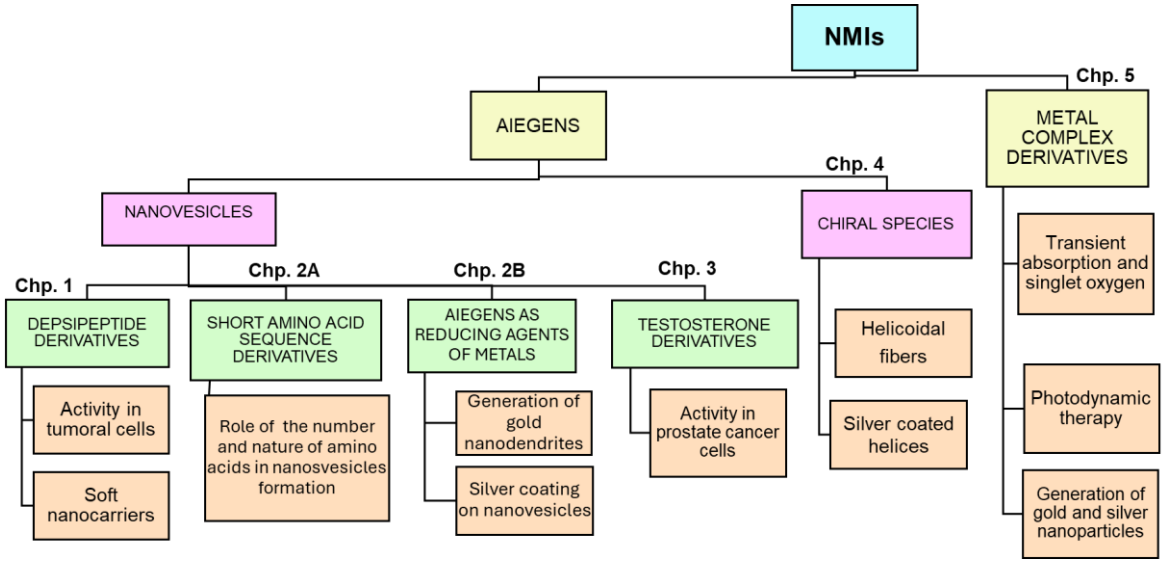

Figure 1. *Diagram of the key points of the different chapters of the thesis.*

3. COLLABORATIONS

This thesis includes a large number of experiments and tests carried out by using a wide variety of equipment. Some of these experiments were carried out in collaboration with other research groups. Accordingly, this section outlines the collaborations that supported the research presented in some chapters.

Chapter 1. Self-Assembling depsipeptides on Aggregation-Induced Emission Luminogens.

Circularly polarized luminescence (CPL) measurements were conducted by Robert Pal and Dominic Black from the Chemistry Department at Durham University (UK).

Circular dichroism spectra were acquired by Jose Garcia Calvo from the Organic Chemistry Department at the Universidad Autónoma of Madrid, Spain.

The molecular dynamics simulation calculations were carried out by Giampaolo Barone and Angello Spinello, from the STEBICEF (Scienze e Tecnologie Biologiche Chimiche e Farmaceutiche) Department at the University of Palermo, (Sicilia), Italy.

Cellular assays were carried out by Natalia Busto and Camilla Andreini from the Department of Health Science, at the University of Burgos, Spain.

Chapter 3. Modified testosterone on Aggregation-Induced Emission Luminogens.

Cell culture studies were carried out by Silvia Albillos and David Palacios from the Biotechnology Department at the University of Burgos, Spain.

Chapter 4. Chiral urea moieties on Aggregation-Induced Emission Luminogens.

Circularly polarized luminescence (CPL) measurements were conducted by Robert Pal and Dominic Black from the Chemistry Department at Durham University (UK).

Circular dichroism spectra were acquired by Jose Garcia Calvo from the Organic Chemistry Department at the Universidad Autónoma of Madrid.

The molecular dynamics simulation calculations were carried out in Italy by Giampaolo Barone, Angello Spinello and Salvatore Muscarella from the STEBICEF (Scienze e Tecnologie Biologiche Chimiche e Farmaceutiche) Department at the University of Palermo, (Sicilia), Italy.

Chapter 5. Ruthenium and iridium complexes on 1,8-naphthalimides: Photophysics, nanostructure and applications.

Transient absorption spectra were acquired by Mariangela Di Donato and Greta Sambucari at the European Laboratory for Non-Linear Spectroscopy (LENS) in Florence, Italy.

The singlet oxygen measurements were acquired by Luca Conti, Gina Elena Giacomazzo and Claudia Giorgi, from the inorganic Chemistry Department “Ugo Schiff” at the University of Florence, Italy.

Cellular assays and photodynamic therapy studies were conducted by Lucia Gardini and Chiara Caldini at the European Laboratory for Non-Linear Spectroscopy (LENS) in Florence, Italy.

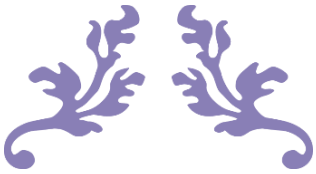

GENERAL INTRODUCTION

1. INSIGHT INTO PHOTOLUMINISCENCE

1.1. BACKGROUND OF LUMINISCENCE

Luminescence was discovered by humans centuries ago. The presence of materials that emitted light caught the attention of our ancestors. The term "phosphorus" originates from ancient Greek, referring to the planet Venus as the morning star which shone in the sky at the sunrise. In the Middle Ages, "phosphor" described materials that glow in the dark, such as the Bolognian phosphorus (impure barium sulphate). The element phosphorus, discovered in 1677, emits light through chemiluminescence.[1]

In 1565, Nicolás Monardes documented the fluorescence of *Lignum nephriticum*, a wood used for medicinal purposes. Its blue fluorescence was later identified as matlaline.[2] The 19th century saw further studies of fluorescence, including Edward D. Clarke's observations of the dichroic nature of certain fluorite crystals *(Figure 1)*[1] and Sir David Brewster's research on the red glow coming from chlorophyll solutions.

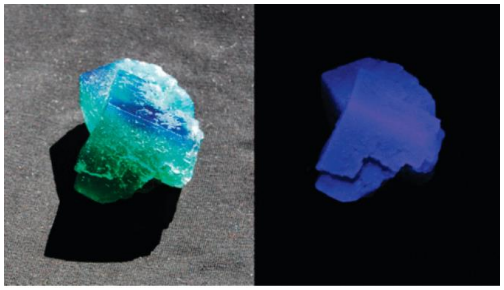

Figure 1. *Crystals of green fluorite illuminated with sunlight (left) and a UV light (right). Although pure fluorite is colourless, natural fluorites usually contain rare-earth elements that give these properties to the mineral.*

Sir John Herschel, in 1845, described "epipolic dispersion" in quinine sulphate solutions, incorrectly attributing fluorescence to surface effects.[3] Brewster later refuted this, proposing "internal dispersion," though he misunderstood the phenomenon. These studies contributed to the eventual understanding of fluorescence.

In 1852, Sir George Gabriel Stokes published *On the Refrangibility of Light*, where he described fluorescence and formulated Stokes's Law: fluorescent light always has a longer wavelength than the incident light. His key experiment showed that quinine solution glows blue under ultraviolet light, coining to that emission the term *fluorescence* because it reminded him to the colour of fluorspar crystals.[4]

Independently to Stokes' experiments, ten years earlier, Edmond Becquerel had observed a similar effect in calcium sulphide, leading to a priority dispute. While Stokes saw fluorescence as instantaneous light scattering, Becquerel viewed it as a short-lived form of phosphorescence.[5] Both made significant contributions to the actual concepts of fluorescence and phosphorescence, though their theoretical interpretations were years later refined.

1.2. FLUORESCENCE FEATURES

There are two main forms of photoluminescence of organic compounds: fluorescence and phosphorescence. The first one is observed when certain substances absorb energy from a radiation source and use it to excite electrons to a singlet excited state. Then, the electrons return to the ground state emitting the energy excess in the form of light. This transition ($S^* \rightarrow S_0$) is spin allowed because there is no change in multiplicity. It must be added that the time between absorption and light emission is around 10^{-8} seconds.[6] By contrast, when

[1] B. Valeur, M. N. Berberan-Santos, *J. Chem. Educ.* **2011,** *88,* 6, 731–738.
[2] A. Acuña, F. Amat-Guerri, *Early History of Solution Fluorescence: The Lignum nephriticum of Nicolás Monardes.* In M.N. Berberan-Santos, *Fluorescence of Supermolecules, Polymers and Nanosystems*. Springer Series on Fluorescence, Vol. 4, Berlin, **2008,** pp 3−20.
[3] J. F. W. Herschel, *Philos. Trans.* **1845**, 143−145, 147–153.
[4] G. G. Stokes, *Philos. Trans.* **1853**, *143*, 385–396.
[5] E. Becquerel, *Ann. Chim. Phys.* **1842**, *9,* 257–322.
[6] J. R. Lakowicz, *Principles of Fluorescence Spectroscopy.* Third edition, Springer Science + Business Media, Singapore, **2006,** chapter 1, pp. 1−26.

the phosphorescence phenomenon takes place (usually by the presence of heavy atoms in the structure), an intersystem crossing from singlet to triplet excited states (*Figure 2)*[7] is produced before the electronic transition. Since the spin states of the initial and final energy levels are different ($T^* \rightarrow S_0$), this process involves a change of multiplicity. Consequently, phosphorescence lifetimes are longer than fluorescence's, requiring between 10^{-3} and 1 s.

It should be added that the energy of the absorbed photon is always larger than the energy of the emitted one. As a result, the emission wavelength is longer than the excitation one. This difference between the positions of both bands' maximum is called the Stokes Shift.[8] This loss of energy is caused by non-radiant decay processes which compete with photoluminescence. The most frequent ones are described below:

- *Vibrational relaxation:* some energy is transferred to the medium because of electronic transitions between two vibrational levels of the same electronic state. This causes a slight increase in the surrounding medium temperature.
- *Internal Conversion:* the electronic relaxation involves two different electronic states with the same multiplicity, meaning singlet-to-singlet or triplet-to-triplet transitions. The internal conversion is more efficient when two electronic energy levels are close enough that two vibrational energy levels are overlapped. This phenomenon is much faster than fluorescence so that light emission is not observed.
- *Intersystem Crossing:* this is an energy deactivation process that occurs between two excited electronic states with different spin multiplicities. Although transitions between states with different spin multiplicities are generally not allowed, they can still happen due to a mechanism called spin-orbit coupling.
- *Bimolecular Deactivation or Quenching:* This is a non-radiative process where an excited species loses energy by interacting with another molecule, known as a quencher or fluorescence inhibitor, which prevents the emission of light.

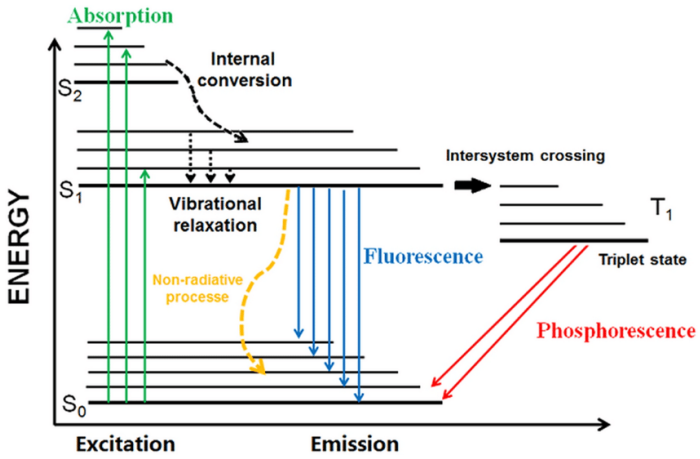

Figure 2. *Jablonski diagram.*

Photoluminescence features are highly related to the molecular structure. Hence, fluorescence is usually observed in aromatic and rigid species in which non-radiant decay processes are impeded. Solvent polarity and local environment interactions, such as proton transfer, also have profound effects on the quantum yield of luminescence.[6]

[7] T. Schweizer, H. Kubach, T. Koch, *Automot. Engine. Technol*. **2021;** *6,* 275−287.

[8] J. Zhang, K. Hoshino, *Molecular Sensors and Nanodevices: Principles, Designs and Applications in Biomedical Engineering;* Second Edition, **2018,** chapter 5.

2. NAPHTHALENEIMIDES

The general structure of naphthaleneimides consists of a naphthalene ring system *(Figure 3a)*, which is a fused bicyclic aromatic hydrocarbon. When the naphthalene core is functionalised with an N-imide group at the positions 1 and 8, a naphthalenemonoimide is obtained (NMI) *(Figure 3b)*. If the positions 4 and 5 are also functionalised, a naphthalenediimide (NDI) is formed *(Figure 3c)*. This work is focused on 1,8-naphthalimides or NMIs.

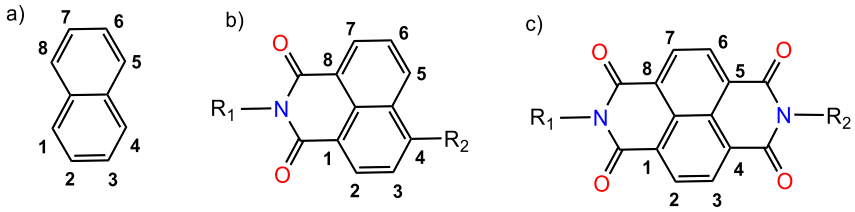

Figure 3. *Structure and positions of a) Naphthalene b) NMI c) NDI core.*

NMIs are a group of polycyclic π-electron deficient planar systems which have recently emerged as an important class of organic fluorophores whose configuration endows the molecules with strong electron-accepting properties and the ability to participate in charge transfer interactions. In addition, they show extraordinary thermal and chemical stability with high fluorescence quantum yields;[9] thus, they find a wide field of applications. Some examples are highlighted below:

1. **Fluorescent sensors and probes:** Naphthalenemonoimides are commonly used in the development of fluorescent sensors, particularly for detecting metal ions such as mercury or methylmercury,[10] anions, reactive oxygen species (ROS) and explosives such as trinitrotoluene (TNT)[11] or triacetone triperoxide (TATP).[12] Their fluorescence properties (normally intensity and colour of the emitted light) can change in the presence of specific analytes, making them useful for chemical sensing applications.[13]
2. **Photoinduced Electron Transfer (PET)**: They also feature in the design of materials for organic electronics and photovoltaic devices. For instance, NMIs can be incorporated into donor-acceptor systems where the imide group serves as an electron-deficient moiety, facilitating charge transfer when they are paired with suitable donor materials.[14] It has been demonstrated that incorporating NMIs into conjugated systems improve charge separation efficiency and device performance such as organic solar cells.[15]
3. **Charge transport in organic semiconductors:** NMIs are used in the fabrication of organic semiconductors due to their high charge transport capabilities. They contribute to the performance of organic field-effect transistors (OFETs) and optical waveguides (OFEWs) by improving charge mobility and stability in hybrid photonic-electronic

[9] P. Gopikrishna, N. Meher, P. K. Iyer, *ACS Appl. Mater. Interfaces* **2018,** *10 (15),* 12081-12111.
[10] A. Revilla, I. Abajo, L. Quadrini, S. Failli, A. Rodríguez, J. V. Cuevas, C. Hernando, J. García, T. Torroba, *Sens. Actuators B Chem.* **2024,** *421,* 136492.
[11] A. Revilla, I. Abajo, M. Medrano, M. Salgado, G. Pecori, T. Rodríguez, C. Hernando, J. García, J. Arcos, T. Torroba, *J. Photochem. Photobiol. A: Chem*, **2023,** *444,* 114911.
[12] A. Revilla, I. Abajo, M. Medrano, M. M. Salgado, M. Avella, M. T. Rodríguez, J. García, T. Torroba, *ACS Appl. Mater. Interfaces* **2023,** *15* (26), 32024−32036.
[13] H. Q. Dong, T. B. Wei, X. Q. Ma, Q.Y. Yang, Y. F. Zhang, Y.J. Sun, B. Shi, H. Yao, Y. M. Zhang, Q. Lin, *J. Mater. Chem. C.* **2020,** *8,* 13501−13529.
[14] A. Manna, S. Chakravorti, *J. Photochem. Photobiol.* **2010,** *86,* 47−54.
[15] F. Jilani, J. Iqbal, I. Shahid, M. Yaseen, M. S. Mahr, M. Khalid, K. Ayube, *Comput. Theor. Chem*. **2020,** *1187*, 112916.

devices.[16] Some NMIs which emit in their solid have been successfully used as an active light-emitting layer in organic light emitting diodes (OLEDs).[17]

4. **Polymers and materials science**: NMIs can also be incorporated into larger macromolecules to be used in materials science. Highly fluorescent polymers with NMI moieties have been developed since fluorescence properties of these fluorophores are preserved in the polymerized state, making them suitable for optoelectronic applications.[18] Moreover, they are incorporated into polymers because of their exceptional thermal stability and ability to undergo reversible photo-chemical reactions. These properties are beneficial in polymers with improved durability and performance for high-performance applications.[19] The use of 1,8-naphthalimide derivatives as dyes for textile polymeric materials as polyester or polyamides has been also described.[20]
5. **Biomedical applications:** NMIs have also been investigated in the context of biological imaging and molecular probes. Their ability to undergo fluorescence quenching or emission enhancement in response to specific biological environments makes them potential candidates for cellular imaging and diagnostics *(Figure 4)*.[21] They are used for selective imaging of cancer cells. The probes usually exhibit significant fluorescence changes upon interaction with the altered pH environments characteristic of cancerous tissues. They are also employed as anticancer agents because NMIs are π-electron-deficient planar systems, which facilitate effective π-π stacking interactions. This characteristic enables them to intercalate into DNA structures, disrupting essential biological processes in cancer cells.[22] Moreover, NMIs are employed in the design of biocompatible nanomaterials. It is reported the self-assembly behaviour of some NMI-containing amphiphiles in aqueous media, leading to the formation of micelles. These micelles have potential applications in drug delivery systems, offering a platform for the transport of therapeutic agents.[23]

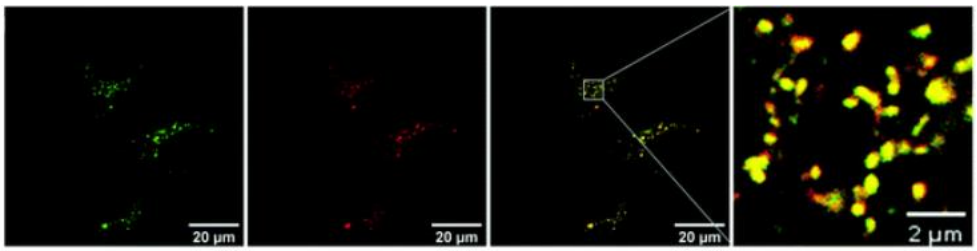

Figure 4. *Colocalization of an NMI (green) and specific lysosomes dye (red) in HeLa cells.*

6. **Catalysis:** Recent studies have highlighted the catalytic potential of NMIs in organic synthesis. Under photochemical conditions, NMIs can act as powerful reductants, facilitating dehydrogenation reactions. This property has been utilized in the synthesis of quinazolinones from o-aminoaryl nitriles and alcohols at room temperature, offering a sustainable alternative to traditional transition metal-catalysed methods.[24] It must be added that some NMI's derivatives have been also used as versatile photoinitiators of free radical polymerization under near UV and visible lights.[25]

[16] I. Torres-Moya, J. R. Carrillo , M. V. Gómez, A. H. Velders, B. Donoso, A. M. Rodríguez, Á. D. Ortiz, J. T. López, R. P. Ortiz, P. Prieto, *Dyes Pigm.* **2021,** 191, 109358.
[17] T. T. Do, S. Chavhan, J. Subbiah T. H. Ou, S. Manzhos, D. Jones, J. M. Bell, J. H. Jou, P. Sonar, *New J. Chem.* **2019,** *43,* 9243−9254.
[18] G. Tu, C. Mei, Q. Zhou, Y. X. Cheng, Y. H. Geng, L. X. Wang, D. G. Ma, X. B. Jing, F. S. Wang, *Adv. Funct. Mater*. **2006,** *16,* 101−106.
[19] S. Rehman, P. Li, H. Zhou, X. Zhao, G. Dang, C. Chen, *Polym. Degrad. Stab.* **2012,** *97* (9), 1581−1588.
[20] M. Dodangeh, I. Grabchev, D. Staneva, K. Gharanjig, *Fibers Polym*. **2021,** *22,* 2368–2379.
[21] A. Tannert, J. Garcia, N. Petkov, *J. Mater. Chem. B.* **2021,** *9,* 112−124.
[22] M. F. Brana, A. Ramos*, Curr. Med. Chem.* **2001,** *1* (3), 237−255.
[23] S. Ghosh, B. Pramanik, D. Das, *ChemNanoMat*. **2018,** *4*(8), 867−873.
[24] X. Yang, Y. Zhou, *Green Chem.*, **2023,** *25*(10), 1234–1243.
[25] J. Yang, C. Xu, Y. Xiong, X. Wang, Y. Xie, Z. Li, H. Tang, *Macromol. Chem. Phys.* **2018,** *219,* 1800256.

NMIs, as well as other aromatic and planar structures, show strong affinity to pack closely through intermolecular *π-π* interactions which result in the formation of nanoaggregates.[26] It is known that luminescence of a molecule in an aggregation state is highly influenced by concentration, temperature and the polarity of the surrounding environment.[27] In general, NMIs undergo strong intramolecular charge transfer (ICT) processes arising from their planar architecture combined with the electron-withdrawing ability of the imide core. Consequently, fluorescence quenching is observed in their solid or aggregated state.[28] However, recent studies reveal that NMIs' nanoaggregates can also show the aggregation-induced emission phenomenon,[29] which is deeper explained in the next section.

It must be added that optical and photophysical properties of 1,8-naphthaleneimides are very sensitive to the insertion of substituents in the aromatic ring structure.[30] For example, the derivatives with an halogen atom or alkoxy groups at the fourth position are colourless and exhibit blue fluorescence,[31, 32] while the amino-substituted 1,8-NMIs are yellow and exhibit green fluorescence.[33] Additionally, functionalizing the fluorophore is an effective tool to modulate the *π-π* interactions between naphthaleneimide cores and to restrain intramolecular rotation of substituents. In this way, their luminescence can be controlled.

3. AGGREGATION EFFECTS ON FLUORESCENCE PROPERTIES

Over the past decades, fluorescence phenomena have been commonly studied in dilute solutions. However, in practice, fluorescent materials are often used in condensed state, such as thin films in organic light emitting diodes, or nanoaggregates in aqueous media for sensing and imaging.[34] Consequently, precise design of fluorescent molecules with desired properties has enabled the rapid development of many research fields ranging from nanotechnology to biology.

Fluorescence is generally observed in conjugated polycyclic aromatic molecules such as rhodamines, BODIPYs and cyanine derivatives.[35] However, these conventional dyes share some inherent problems: they have low absorption coefficients and weak signals that reduce the sensitivity of the applications.[36] Moreover, due to the *π-π* stacking interactions between the aromatic planes *(Figure 5),* the mainstream fluorophores show the aggregation-caused quenching (ACQ) effect,[37] by which molecules have a bright fluorescence emission in diluted solutions but it decreases when the aromatic species agglomerate and form intermolecular non-covalent *π-π* stacks in polar environments, such as aqueous solutions or the intracellular space.[38] To overcome the ACQ effect, branched chains or bulky cyclic molecules can be covalently attached to the fluorophores, thus suppressing the formation of aggregates.

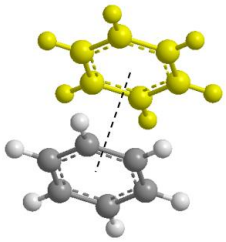

Figure 5. *π–π stacking interactions between two aromatic planes.*

By contrast, some aromatic molecules that are almost non-fluorescent in solution become highly emissive after aggregation.

[26] Y. Yin, Z. Chen, C. Fan, G. Liu, S. Pu, *ACS Omega.* **2019,** *4* (10), 14324–14332.
[27] X. Yu, X. Ge, H. Lan, L. Yajuan, G. Lijun, Z. Xiaoli, T. Yi, *ACS Appl. Mater. Interfaces* **2015,** *7*, 24312−24321.
[28] S. Mukherjee, P. Thilagar, *Chem. Eur. J.* **2014,** *20*, 8012−8023.
[29] D. Ding, *Aggregation-Induced Emission Luminogens for Biomedical Applications*. In: Y Tang., B. Z. Tang, *Principles and Applications of Aggregation-Induced Emission***.** Springer Nature, Switzerland, **2019,** chapter 19.
[30] G. Saito, D. Velluto, M. Resmini, *R. Soc. Open Sci.* **2018,** *5*, 1721−1737.
[31] L. Bekere, D. Gachet, V. Lokshin, W. Marine, V. Khodorkovsky, *Beilstein J. Org. Chem.* **2013,** *9,* 1311−1318.
[32] I. Grabchev, C. Petkov, V. Bojinov, *Macromol. Mater. Eng.* **2002,** 287 (12), 904–908.
[33] I. Grabchev, T. Konstantinova, *Dyes Pigm.* **1997,** *33* (3), 197–203.
[34] S. Xu, Y. Duan, B.Liu**,** *Adv. Mater.* **2020,** *132*, 9952−9970.
[35] N. Boens, V. Leen, W. Dehaen, *Chem. Soc. Rev.* **2012,** *751*, 1130–1172.
[36] M. J. Ruedas-Rama, J. D. Walters, A. Orte, E. A. H. Hall, *Anal. Chim. Acta.* **2012,** *751*, 1−23.
[37] N. Meher, P. K. Iyer*, Nanoscale* **2017,** *9*, 7674−7685.
[38] Y. Hong, J. W. Y. Lam, B. Z. Tang, *Chem. Commun.* **2009,** 4332−4353.

This singular behaviour is known as aggregation-induced-emission (AIE).[29] This phenomenon is deeper outlined in the next sub-section.
For the organic π-conjugated materials, the luminescent properties in their solid state can be highly influenced by the molecular stacking models *(Figure 6)*.[39] The aggregates formed directly affect the monomers' energy levels and its fluorescence quantum yields.[40] Thus, according to the Kasha model there are three principal types of aggregates:

- *H-aggregates (54.7º < θ < 90º):* these ones exhibit a cofacial, parallel molecular arrangement with a slip angle greater than 54.7°. In these aggregates, molecular transition dipoles are aligned "side-by-side," leading to an energy level splitting due to dipole interactions.[41] The lower of these two excited states is optically forbidden, whereas the higher state is allowed. This arrangement influences optical properties in two key ways: (a) the primary absorption peak experiences a blue shift (with "H" referring to hypsochromic shift) relative to the solution phase, corresponding to the optically allowed higher excited state; (b) H-aggregates typically exhibit a low radiative decay rate and weak fluorescence due to the optically forbidden nature of the lower excited state, which serves as the emitting state.[42]
- *J-aggregates (0º < θ < 54.7º):* By decreasing the slip angle within the cofacial stacking, the system can transition from H-aggregates to J-aggregates ("J" named after their discoverer Jelley).[43] In J-aggregates, molecules interact in a "head-to-tail" fashion, also leading to excited-state energy splitting. However, in this case, the lower excited state is optically allowed, while the higher one is forbidden. This molecular arrangement affects photophysical properties in two ways: (a) J-aggregates usually cause a red or bathochromic shift in the absorption (and emission) spectrum; (b) since the optically allowed lower excited state serves as the emitting state, J-aggregates generally exhibit high radiative decay rates and strong fluorescence efficiency.[44]

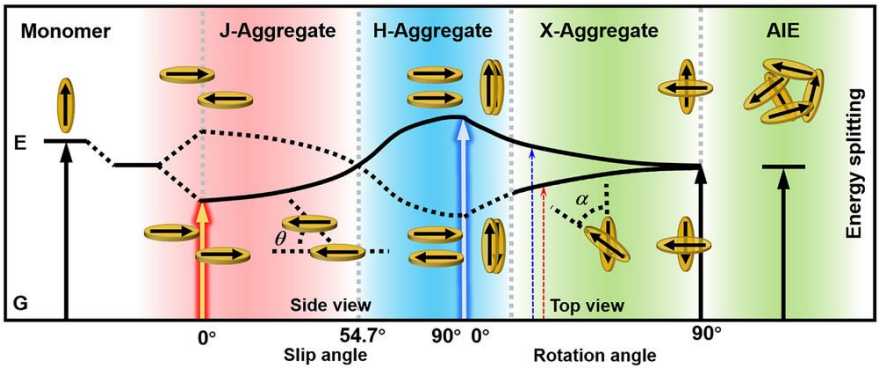

Figure 6. *Energy splitting diagram of excited states for J-aggregate, H-aggregate, X-aggregate, and AIE configurations.*

- *X-aggregates:* By rotating the molecules to create a specific angle between their long axes, X-aggregates (also known as cross-dipole stacking) can be formed with weaker exciton interactions due to the lower π-π interactions between molecular transition dipoles. Despite having a cofacial stacking arrangement, X-aggregates can still display intense fluorescence.[45]

[39] E. Sebastian, A. M. Philip, A. Benny, M. Hariharan, *Angew. Chem. Int. Ed.* **2018,** *57,* 15696.
[40] M. Kasha, H. R. Rawls, M. A. Bayoumi, *Pure Appl. Chem*. **1965,** *11,* 371.
[41] J. Zhou, W. Zhang, X.-F. Jiang, C. Wang, X. Zhou, B. Xu, L. Liu, Z. Xie, Y. Ma, *J. Phys. Chem. Lett.* **2018,** *9,* 596–600.
[42] F. C. Spano, *Acc. Chem. Res.* **2010,** *43,* 429.
[43] E. E. Jelley, *Nature* **1936,** *138,* 1009.
[44] N. J. Hestand, F. C. Spano, *Chem. Rev.* **2018,** *118*, 7069.
[45] S. Ma, Y. Liu, J. Zhang, B. Xu, W.Tian, *J. Phys. Chem. Lett.* **2020,** *11* (24), 10504−10510.

The aggregates can exhibit an emission wavelength similar to the monomer when the correct angle between molecules is achieved (θ = 54.7º). However, the Kasha model is not the only form to classify π-π interactions. Hunter and Sanders in 1990 classified these interactions into the next groups [46] *(Figure 7)* [47]:

- *π-π face-to-face stacking:* it takes place in a plane parallel to the molecules. The alignment between them is rarely perfect. Usually, one molecule is offset from another. Substituted and large multiring aromatic compounds prefer parallel displaced geometry. This geometry is also favoured when the stacked units are electron-poor, because of the presence of electron withdrawing groups.

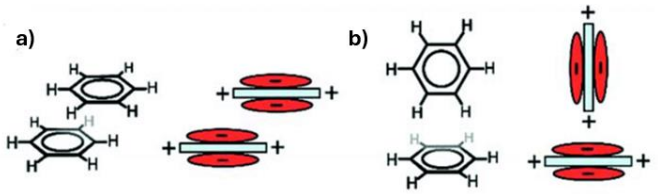

Figure 7. *a) π-π face-to-face offset stacking. b) T-shaped stacking.*

- *π-π edge-to-face or "T-shaped"* stacking: it occurs when molecules are in a perpendicular plane between them. The small, aromatic compounds prefer this geometry. The most common interactions between aromatic rings of amino acid residues in proteins are staggered stacks in a perpendicular orientation.[48]

Regardless of the model employed to classify the aggregates, it is known that the solvent polarity has a major role in their formation, as well as the presence of water in the medium. When interactions between solvent molecules are stronger than those between the solvent and aromatic molecules, the aromatic surfaces are excluded from the solvent and tend to cluster together. This effect, known as surface minimization, is particularly significant in highly polar solvents, where strong attractions between solvent molecules dominate.[49] It must be added that molecules can be stacked in a parallel or antiparallel form (head-to-head or head to tail) *(Figure 8).*

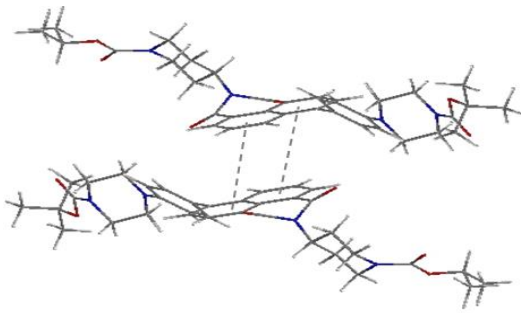

Figure 8. *Two naphthalenemonoimides with face-to-face antiparallel stacking.*

3.1. AGGREGATION-INDUCED EMISSION (AIE)

Lately, aggregation-induced emission luminogens (AIEgens) have become the state of the art in sensing chemistry due to their advantages over other methods, such as low detection limits, very high selectivity, non-invasiveness, fast response, notable photostability and good biocompatibility.[50]

However, the concept of aggregation-induced emission is not a recent discovery. In 1853, Sir George Gabriel Stokes described a similar phenomenon while examining the luminescent properties of certain inorganic salts.[51] However, for many years, this observation received little attention, and its potential for practical applications remained unexplored. It wasn't until 2001 that Tang and co-workers revisited this effect while studying

[46] C. A. Hunter, J. K. M. Sanders *J. Am. Chem. Soc.* **1990,** *112* (14), 5525−5534.
[47] I. Hamza, A. Abusaediyah, *World Wide J. Multidiscip. Res. Dev*. **2017,** *3(8)*, 265−268.
[48] G. B. McGaughey, M. Gagné, A. K. Rappé, *J. Biol. Chem.* **1998,** *273* (25), 15458–63.
[49] E. A. Meyer, R. K. Castellano, F. Diederich, *Angew. Chem., Int. Ed.* **2003,** *42,* 1210–1250.
[50] J. Sun, H. Li, X. Gu, B. Z. Tang, *Adv. Healthcare Mater.* **2021,** *10,* 2101177.
[51] G. G. Stokes, *Philos. Trans. R. Soc. Lond*. **1852,** *142,* 463–562.

the luminescence behaviour of rotor-rich methylpentaphenylsilole. They rediscovered the phenomenon and formally introduced the concept of AIE. [52]

Through a systematic investigation of AIE across different systems, they found in 2003 that the active intramolecular motion of AIE luminogens in their excited state likely accelerates the non-radiative decay of excitons, causing emission quenching in solution. However, in the aggregated state, this intramolecular rotation is restricted, reducing non-radiative decay and enhancing luminescence.

Extensive research was conducted to understand the working principle of AIE, leading to the proposal of various potential mechanisms, including J or H aggregation, conformational planarization, E/Z isomerization, twisted intramolecular charge transfer (TICT), and excited-state intramolecular proton transfer (ESIPT). However, most of these mechanisms were only applicable to specific AIE systems.[53]

Based on these findings, Tang and co-workers proposed that the restriction of intramolecular rotation (RIR) serves as the primary mechanism behind AIE.[54] To explain certain AIE systems that have not rotors in their structure, they later introduced the restriction of intramolecular vibration (RIV) as a complementary mechanism, as intramolecular vibrations can also contribute to non-radiative decay.[55] Together, RIR and RIV were unified under the broader concept of restriction of intramolecular motion (RIM) *(Figure 9)*.

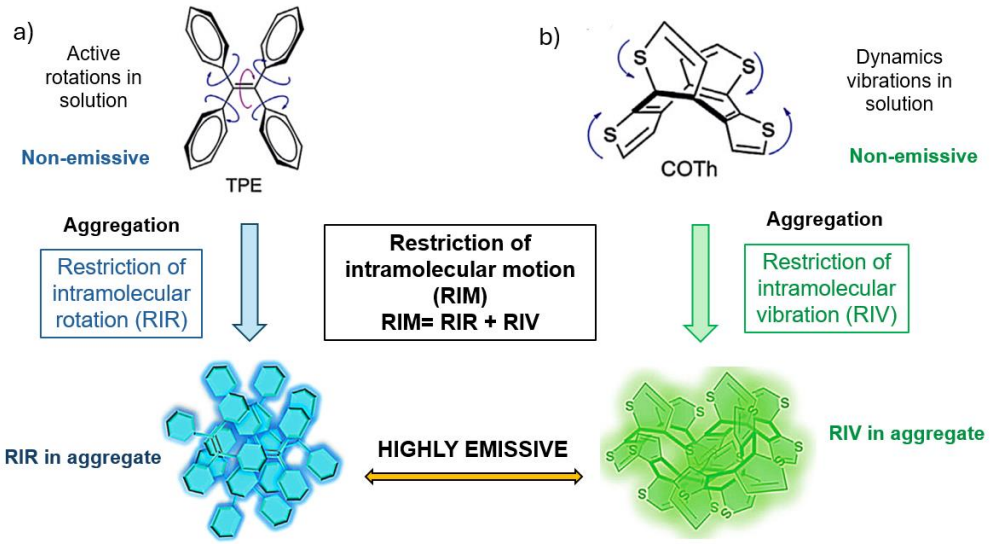

***Figure 9**. (a) Tetraphenylethene is non-emissive in solution but becomes emissive when it aggregates due to the restriction of intramolecular rotations. (b) Cyclooctatetrathiophene shows AIE effect due to the restriction of intramolecular vibration in the aggregated state.*

Today, the RIM mechanism is widely accepted as the explanation for AIE. In simple terms, in solution or a dispersed state, active intramolecular motion (such as rotation and vibration) facilitates non-radiative decay pathways, including conical intersections or dark decay processes, leading to emission quenching. However, in the aggregated state, these decay

[52] J. Luo, Z. Xie, J. W. Y. Lam, L. Cheng, H. Chen, C. Qiu, H. S. Kwok, X. Zhan, Y. Liu, D. Zhu, B. Z. Tang, *Chem. Commun.* **2001,** 1740–1741.
[53] P. Hana, J. Wanga, A. Qina, B. Z. Tang, Fundamental Principles of AIE in *Aggregation-Induced Emission (AIE), A Practical Guide*. J. Xu, M. H. Chua, B. Z. Tang. Eds.; Elsevier; Amsterdam, Netherlands, **2022,** chapter 1, pp 1−22.
[54] J. Chen, C. C. W. Law, J. W. Y. Lam, Y. Dong, S. M. F. Lo, I. D. Williams, D. Zhu, B. Z. Tang, *Chem. Mater.* **2003,** *15*, 1535–1546.
[55] Z. Zhao, X. Zheng, L. Du, Y. Xiong, W. He, X. Gao, C. Li, Y. Liu, B. Xu, J. Zhang, F. Song, Y. Yu, X. Zhao, Y. Cai, X. He, R. T. K. Kwok, J. W. Y. Lam X. Huang, D. L. Phillips, H. Wang, B. Z. Tang, *Nat. Commun.* **2019,** *10,* 2952.

pathways are blocked due to restricted intramolecular motion, resulting in enhanced emission.[56] Theoretically, any method capable of triggering the RIM process can be applied to create systems with several applications *(Figure 10).* [57]

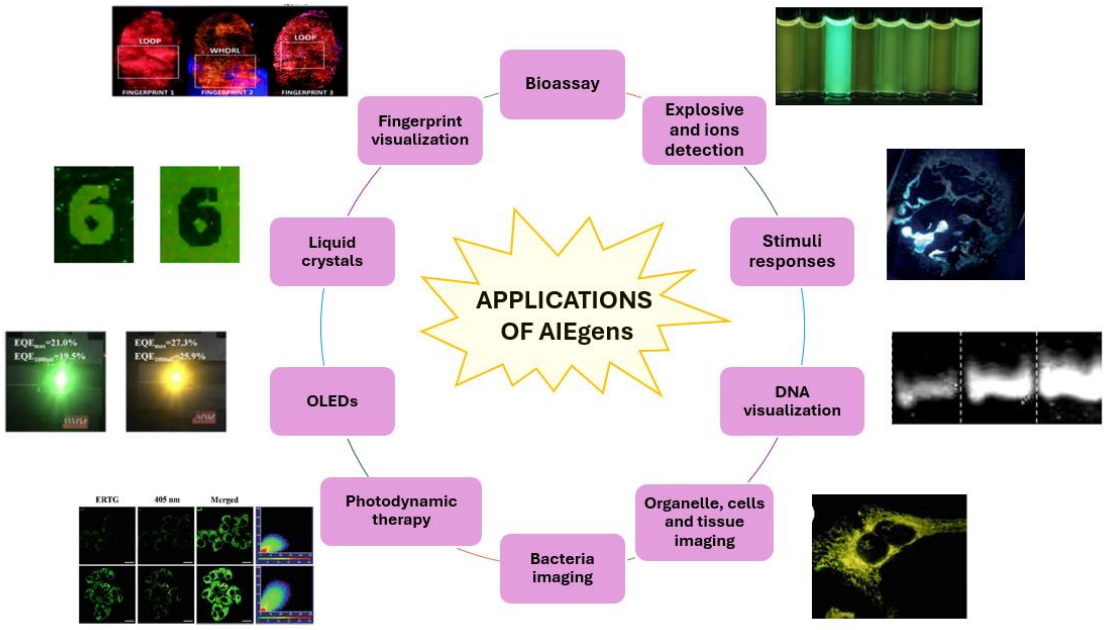

Figure 10. *Some applications of AIEgens.*[57]

AIEgens have been effectively utilized as fluorescence "turn-on" or "light-up" biosensors, DNA visualizers, and probes for biological events like protein fibrillation.[58] The AIE effect has facilitated targeted imaging of organelles, microorganisms, cells and tissues at molecular, cellular, and tissue scales.[59, 60] Highly luminescent nanostructures, such as AIE dots, are now making significant advancements in the field of bioimaging. Furthermore, multifunctional systems built using AIEgens have been designed for biomedical imaging, diagnostics, and therapeutic applications.[61]

A variety of AIE-based chemosensors have been developed to detect numerous analytes, including ions,[62] explosives,[63] and fingerprints,[64] which play essential roles in environmental protection, water quality monitoring, national security, and forensic science. Additionally, AIEgens have been integrated into various optoelectronic systems, as their AIE properties effectively eliminate the problematic ACQ effect that commonly affects traditional luminophores in solid states. Leveraging this beneficial AIE effect, researchers have

[56] Z. Zhao, H. Zhang, J. W. Y. Lam, B. Z. Tang, *Angew. Chem. Int. Ed*. **2020,** *59*, 888 – 9907.
[57] a) H. Singh, R. Sharma, G. Bhargava, S. Kumar, P. Singh, *New J. Chem.*, **2018,** *42*, 12900-12907. b) D. Zhao, F. Fan, V. G. Chigrinov, H. S. Kwok, B. Z. Tang, *J. Soc. Inf. Disp.* **2015,** *23,* 218-222. c) Z. Xu, J. Gu, X. Qiao, A. Qin, B. Z. Tang, *ACS Photonics* **2019,** *6*, 767–78. d) B. Yuan, J. Liu, R. Guan, C. Jin, L. Ji, H. Chao, *Dalton Trans.* **2019,** *48*, 6408–6415. e) W. Zhang, R. T. K. Kwok, Y. Chen, S. Chen, E. Zhao, C. Y. Y. Yu, J. W. Y. Lam, Q. Zheng, B. Z. Tang, *Chem Commun*. **2015,** *51*, 9022–9025. f) Y. Hong, M. Häußler, J. Lam, Z. Li, K. Sin, Y. Dong, H. Tong, J. Liu, A. Qin, R. Renneberg, B. Z. Tang, *Chem. Eur. J.* **2008,** *14,* 6428-6437.
[58] M.Wang, G. Zhang, D. Zhang, D. Zhu, B. Z. Tang, J. *Mater. Chem*. **2010,** *20*, 1858–1867.
[59] J. Mei, Y. Hong, J. W. Y. Lam, A.Y. Qin, Y. Tang, B. Z. Tang, *Adv. Mater*. **2014**, *26*, 5429–5479.
[60] D. Ding, C. C. Goh, G. Feng, Z. Zhao, J. Liu, R. Liu, N. Tomczak, J. Geng, B. Z. Tang, *Adv. Mater*. **2013**, *25*, 6083–6088.
[61] R. T. K. Kwok, C. W.T. Leung, J. W. Y. Lam, B. Z. Tang, *Chem. Soc. Rev*. **2015**, *44*, 4228–4238.
[62] N. Zhao, N, J. W. Y. Lam, H. H. Y. Sung, H. M. Su, I. D. Williams, K. S. Wong, B. Z. Tang, *Chem. Eur. J.* **2014**, *20*, 133–138.
[63] W. Dong, T. Fei, A. Palma-Cando, U. Scherf *Polym. Chem.*, **2014,** *5*, 4048-4053.
[64] Y. Li, L. Xu, B. Su, *Chem. Commun*. **2012**, *48*, 4109–4111.

successfully designed OLED devices,[65] circularly polarized luminescence (CPL) systems,[66] optical waveguides [67] and liquid crystal displays [68] with high-efficiency solid-state emissions. A wide range of AIEgens has been studied and transformed into advanced smart materials, which respond to external stimuli such as mechanical forces, temperature fluctuations, pH changes, toxic vapours, and photonic irradiation.[69] Several AIE-active smart materials exhibiting multiple stimuli-responsive behaviours, including thermo-,[70] mechano-,[71] vapo-,[72] and photochromism,[73] have been designed and synthesized. Consequently, thanks to its fundamental significance and practical applications, AIE research has captivated numerous scientists from diverse academic and technological fields, drawing us into this exciting and innovative world.

3.1.2. Self-assembling moieties, a way to design AIEgens

According to the RIM mechanism, any approach that limits the intramolecular motion of AIEgens can theoretically lead to stronger luminescence.[74] Based on this, it is attractive to find forms to enhance AIE effect by restraining intramolecular motions, and one method is bonding certain side chains to the chromophore. It is known that changing the end group of the side chains is an alternative way to tune the emission of the fluorophore, so it is possible to design AIE-active and fluorescent solid materials.[75] It has been discovered that chains with self-assembling properties such as peptides sequences, enhance AIE effect because they alter the stacking, favouring weak intermolecular dipole interactions, driven by a combination of noncovalent forces, including: electrostatic, hydrophobic, van de Waals, hydrogen bonds and π–π interactions.[76]

The spontaneous self-assembly of macromolecular entities is a fundamental process in living systems, essential for biological functions and the formation of diverse dynamic supramolecular structures across multiple length scales.[77] In this context, peptides stand out as ideal candidates due to their adaptable self-assembly properties and broad applications in advanced materials, including drug delivery, antimicrobial coatings, tissue engineering and bioinspired nanotechnology (such as hybrid materials for optoelectronics, nanocatalysis, and biosensing).[78]

Peptides also offer numerous advantages, including high biocompatibility, biodegradability, structural tunability, ease of biofunctionalization, natural biological origin, cost-effective synthesis, and remarkable sensitivity to environmental factors.[79] Their unique self-assembly characteristics, along with their ability to form various nanostructures (such as fibrils,

[65] P. Palanisamy, M. Rabiei, M. Hosseinnezhad, A. Palevicius, G. Janusas, P. B. Managutti, S. Mohamed, L. E. de Sousa, L. de Thieulloy, P. de Silva, A. Vilkauskas, S. Nasiri, J-M. Nunzi, V. Nutalapati, *ACS Appl. Opt. Mater.* **2024,** *2* (1), 76-87.
[66] J. Liu, H. Su, L. Meng, Y. Zhao, C. Deng, J. C. Y. Ng, P. Lu, M. Faisal, J. W. Y. Lam, X. Huang, H. Wu, K. S. Wong, B. Z. Tang, *Chem. Sci.* **2012**, *3*, 2737– 2747.
[67] N. Zhao, M. Li, Y. Yan, J. W. Y. Lam, Y. L. Zhang, Y. S. Zhao, K. S. Wong, B. Z. Tang, *J. Mater. Chem.* **2013,** *1,* 4640–4646.
[68] D. Zhao, F. Fan, J. Cheng, Y. Zhang, K.S. Wong, V. G. Chigrinov, H. S. Kwok, L. Guo, B. Z. Tang, *Adv. Opt. Mater*. **2015,** *3*, 199– 202.
[69] W. Z. Yuan, Y. Tan, Y. Gong, P. Lu, J. W. Y. Lam, X. Y. Shen, C. Feng, H. H-Y. Sung, Y. Lu, I. D. Williams, J. Z. Sun, Y. Zhang, B. Z. Tang, *Adv. Mater.* **2013,** *25,* 2837– 2843.
[70] M. Wang, D. Q. Zhang, G. X. Zhang, D. B. Zhu, *Chem. Phys. Lett.* **2009;** *475*, 64–67.
[71] Z. Chi, X. Zhang, B. Xu, X. Zhou, C. Ma, Y. Zhang, S. Liu, J. Xu, *Chem. Soc. Rev*. **2012,** *41*, 3878– 3896.
[72] P. Alam, M. Karanam, D. Bandyopadhyay, A. R. Choudhury, I. R. Laskar, *Eur. J. Inorg. Chem.* **2014**, 3710–3719.
[73] C. Yu, R. T. K. Kwok, J. Mei, Y. Hong, S. Chen, J. W. Y. Lam, B. Z. Tang, *Chem. Commun*. **2014,** *50*, 8134–8136.
[74] Z. He, P. Liu, S. Zhang, J. Yan, M. Wang, Z. Cai, J. Wang, Y. Dong, *Angew. Chem. Int. Ed.* **2019,** *58 (12)*, 3834–3837.
[75] X. Luo, Y. Qu, Y. Zhang, Y. Wu, W. Yuan, L. Wan, *Chem. Eng. J.*, **2021,** *415*, 129095.
[76] K. Liu, R. Zhang, Y. Li, T. Jiao, D. Ding, X. Yan, *Adv. Mater. Interfaces* **2017,** *4*, 1600183.
[77] A. M. Brizard, J. H. van Esch, *Soft Matter* **2009**, *5*, 1320–1327.
[78] L. Adler- Abramovich, E. Gazit, *Chem. Soc. Rev.* **2014,** *43*, 6881–6893.
[79] F. Qiu, Y. Chen, C. Tang, X. Zhao, *Int. J. Nanomed*. **2018**, *13*, 5003–5022.

vesicles, micelles, nanosheets, ribbons, and nanotubes) and adopt secondary structures like, α-helices, β-sheets, or coiled coils, make them highly valuable in supramolecular chemistry.[80]

The peptide-directed assembly of AIE molecules not only enhances the general understanding of emission tunability in these species but also facilitates the design of novel nanoarchitectures and materials with adjustable optical properties, thus making them highly valuable for various biomedical applications (an important topic in this thesis).

When aggregates are formed and the AIE phenomenon appears, the species forms different nanostructures that can be imaged by several techniques such as filed scanning electron microscopy (SEM), atomic force microscopy (AFM) or transmission electron microscopy (TEM). The morphology of the formed nanoparticles when the AIE effect appears has a major role in this work.

Attaching different self-assembling chains to the fluorophore, the AIE effect can be enhanced. Therefore, depsipeptide chains, modified hormones, chiral units or any other structures that favour aggregation are interesting to modulate the emission intensity of the aggregates and their morphology. Concretely, nanovesicles and nanofibers are exceptional soft nanostructures that can be formed by AIEgens,[81] and both morphologies are quite attractive in today's chemistry research.

[80] N. Habibi, N. Kamaly, A. Memic, H. Shafiee, *Nano Today* **2016**, 11, 41–60.
[81] M. H. Chua, K. L. Osmund Chin, X. J. Loh, Q. Zhu, J. Xu, *ACS Nano* **2023,** *17* (3), 1845–1878.

CHAPTER 1

Self-assembling depsipeptides on Aggregation-Induced Emission Luminogens

ABSTRACT

In this chapter it is demonstrated how aggregation-induced emission can be modulated depending on the side chains attached to the chromophore. Specifically, 1,8-naphthalenemonoimide AIEgens have been synthesized by bonding self-assembling depsipeptide sequences to the fluorophores. It has been shown that the nanostructures responsible of the AIE effect are hollow nanovesicles stable in mixtures of water and organic solvents. The newly formed nanovesicles are robust enough to be used to carry large molecules such as physiological peptides without losing their structural characteristics. In addition, they act as programmable nanocarrier systems within living cells as Trojan horses, constituting a new approach to active transport and nanoencapsulation. The Supporting Information associated with this chapter includes a multitude of structural and fluorescence characterization tests, microscopy images of the nanostructures formed as well as biological assays.

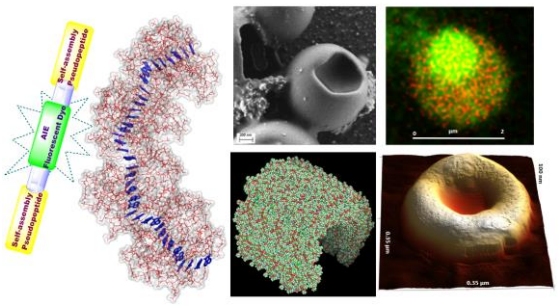

***Figure 1**. Images of depsipeptidic AIEgens and their structure.*

It must be added that one of the main objectives of the research is to publish the results, and in this case, the content of this chapter was published in the paper *"Self-Assembling Depsipeptides on Aggregation-Induced Emission Luminogens: A New Way to Create Programmable Nanovesicles and Soft Nanocarriers."* (DOI: 10.1021/acsami.4c19123).

1. INTRODUCTION

Nanotechnological methods is an increasingly important demand in our society. Classic metal and semiconductor nanocrystals[1] are well suited for established applications such as photonics, catalysis, sensing, energy harvesting and conversion, or bio-imaging, and newcomers such as perovskite quantum dots[2] have been applied to solar cells, photocatalysis, light emitting devices and displays, but all of them have issues as toxicity, environmental concerns and sustainability.[3] As an alternative, soft, organic nanoparticles are much more sustainable and suitable for many applications that are not covered by their metal-containing counterparts. Most of research of soft nanoparticles is intended for lipidic nanoparticles, mainly covered by vesicles formed by amphiphiles that mimic biological vesicles.[4] An important application was the development of lipid nanoparticle-based mRNA vaccines that pointed to self-assembled lipid nanostructures as good delivery vehicles for therapeutic nucleic acids during COVID19 pandemics.[5] Some limitations of the lipidic nanoparticles, such as stability in the long-term, have expanded the field to other amphiphiles in drug delivery, opening large avenues to polymeric[6] or multicomponent nanoparticles.[7] Important goals of artificial vesicles are: drug/nucleic acid delivery, reaction promoters and regulators, photodynamic therapy, mimic enzyme catalysis (metallo-nanozyme or photo-responsive catalyst) as well as fluorescence imaging, cancer monitoring

[1] J. Zhao, O. Chen, J. He, S. Zou, *Front. Chem.* **2019,** *7*, 310.
[2] J. Ma, H. Wang, D. Li, *Adv. Mater.* **2021**, *33*, 2008785.
[3] L. Pokrajac, A. Abbas, W. Chrzanowski, G. M. Dias, B. J. Eggleton, S. Maguire, E. Maine, T. Malloy, J. Nathwani, L. Nazar, A. Sips, J. Sone, A. van den Berg, P. S. Weiss, S. Mitra, *ACS Nano* **2021,** *15 (12),* 18608−18623.
[4] R. Pattipeiluhu, G. Arias-Alpizar, G. Basha, K. Y. T. Chan, J. Bussmann, T. H. Sharp, M.-A. Moradi, N. Sommerdijk, E. N. Harris, P. R. Cullis, A. Kros, D. Witzigmann, F. Campbell, *Adv. Mater.*, **2022**, *34*, 2201095.
[5] R. Das, P. Kanjilal, J. Medeiros. *Bioconjugate Chem.* **2022**, *23*, 1996–2007.
[6] Z. Wang, C. Sun, R. Wang, *Bioconjugate Chem.* **2022**, *33*, 2254–2261.
[7] M. J. Mitchell, M. M. Billingsley, R. M. Haley, M. E. Wechsler, N. A. Peppas, R. Langer, *Nat. Rev. Drug Discovery* **2020**, *21*, 101–124.

or diagnosis. Peptides are best suited for their intrinsic self-assembly characteristics and biocompatibility for some of the mentioned uses[8] but the formation of vesicles has been mainly related to peptide amphiphiles[9] and pseudopeptides.[10] The formation of vesicles from some macrocycles has been studied as well as their assembly mechanism on the way to functional materials.[11] Therefore, there is an urgent need of new stable artificial vesicles that may fulfil the society requirements such as cancer therapy.[12] A large interest in peptide-based supramolecular systems chemistry has been devoted to access complex functions that emerge when multiple reactions and interactions are coordinated and integrated.[13] These peptide-based systems are also studied as versatile platforms for biomedical applications, enzyme mimics[14] or enzyme regulators.[15] The improvement for precision medicines and how these can be addressed is largely mediated by innovative drug delivery systems *(Figure 2)*.[16]

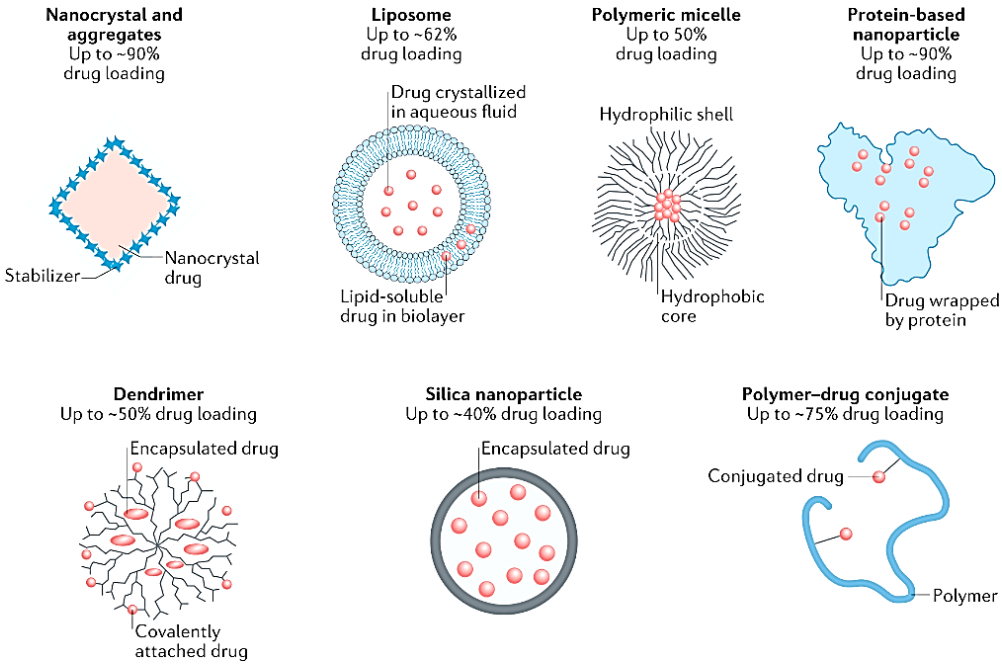

Figure 2. *Different existing drug vehicles*.

It must be added that the development of new diagnostic and therapeutic techniques has become a central issue in biomedical research. Currently, the mature techniques used for medical diagnostics are ultrasonic scanning, computed tomography (CT), X-ray and magnetic resonance imaging (MRI). However, these imaging modalities suffer from some drawbacks; for example, both X-ray and CT can have damage effects on human body due to the associated ionizing radiation. In addition, MRI is not well suited for solid tissues with bloodstreams. Ultrasonic scanning shows a relatively low resolution, and all of them feature

[8] Y. Huo, J. Hu, Y. Yin, P. Liu, K. Cai, W. Ji, *ChemBiochem.* **2023**, *24*, e202202.
[9] R. Qiu, I. R. Sasselli, Z. Álvarez, H. Sai, W. Ji, L. C. Palmer, S. I. Stupp, *J. Am. Chem. Soc*. **2022,** *144,* 5562–5574.
[10] V. Haridas, *Acc. Chem. Res.* **2021**, *54*, 1934–1949.
[11] A. Levin, T. A. Hakala, L. Schnaider, G. J. L. Bernardes, E. Gazit, T. P. J. Knowles, *Nat. Rev. Chem*. **2020**, *4,* 615–634.
[12] I. Khan, I. Hossain, K. Hossain, H. K. Rubel, K. M. Hossain, A. M. U. B. Mahfuz, M. I. Ani, *ACS Appl. Bio Mater.* **2022,** *5* (3), 971–1012.
[13] F. Sheehan, D. Sementa, A. Jain, M. Kumar, M. Tayarani-Najjaran, D. Kroiss, R. V. Ulijndoi, *Chem. Rev*. **2021**, *121* (22), 13869–13914.
[14] A. Chatterjee, A. Reja, S. Pal, D. Das, *Chem. Soc. Rev.* **2022**, *51*, 3047–307.
[15] Y. Song, M. Li, N. Song, X. Liu, G. Wu, H. Zhou, J. Long, L. Shi, Z. Yu, Z, *J. Am. Chem. Soc*. **2022,** *144,* 6907–6917.
[16] M. T. Manzari, Y. Shamay, H. Kiguchi, N. Rosen, M. Scaltriti, D. A. Heller, *Nat. Rev. Mater*. **2021**, *6*, 351–370.

limited sensitivity, which is extremely unfavourable for accurate diagnosis.[17] Consequently, new imaging techniques with less harmful effects, high resolution, fast and real-time responsiveness, wide applicability, and significant reliability are in increased demand.[18] Thus, the high resolution of AIE-gens fluorescence confers them a great solution for these problems.[19] It is known that AIEgens have expanded the field of aggregation-based nanomaterials[20] and are also useful for phototheranostics, super-resolution imaging, or smart aggregates in clinical diagnosis.[21] The combination of peptides and AIE-gens has opened new avenues in biomedicine,[22] drug delivery,[23] or encapsulation of anticancer drugs.[24] Peptides are easily recognized by the degradation systems inside cells, therefore their lifetime is very limited in living systems. However, depsipeptides are non-ribosomal peptide derivatives in which some amide groups have been replaced by ester groups,[25] which gives more flexibility to depsipeptide structures, as well as higher resistance to proteolysis by enzymes. Despite this, their self-assembly has been much less studied and very few examples of nanomaterials are known, so they constitute a rich source of new structural possibilities in nanomaterials construction. It is known that self-assembling depsipeptides form β-sheet nanofibers and gels[26] or biodegradable hydrogels[27] but there are no reports on the availability of depsipeptides in the formation of vesicles or other nanoaggregates. Therefore, the combination of depsipeptides and AIEgens could give a solution to the disadvantages posed by previous methodologies. Naphthalimides are known as AIEgens[28] and may form nanoribbons[29] or metallogels[30] and their self-assembly can be monitored by super-resolution imaging;[31] therefore, in combination to depsipeptides are perfect candidates for the creation of vesicles based on supramolecular self-assembly and molecular recognition between structural counterparts. These systems could contribute to solve important current problems associated to the cell transport of drugs and essential physiological peptides. Recent discoveries in the research group have highlighted that certain enzymes found in insect saliva can degrade polyethylene, emphasizing the great potential of nanoencapsulated catalysts.[32] Recognizing this gap in research, we have carefully refined the development of stable, hollow soft nanovesicles that meet all essential criteria for active cellular transport with a simple preparation process and great versatility.

---

[17] J. MeI, Y. Hong, J. W. Y. Lam, A. Qin, Y. Tang, B. Z. Tang, *Adv. Mater.* **2014,** *26(31),* 5429–5479.
[18] C. Zhu, R. T. K. Kwok, J. W. Y. Lam, B. Z. Tang, *ACS Appl. Biol. Mater.* **2018**, *1, (6),* 1768–1876.
[19] X. Yu, X. Ge, H. Lan, L. Yajuan, G. Lijun, Z. Xiaoli, T. Yi, *ACS Appl. Mater. Interfaces* **2015,** *7*, 24312-24321.
[20] Z. Zhao, W. He, B. Z. Tang, *Acc. Mater. Res*. **2021**, *2*, 1251–1260.
[21] a) P. Xiao, W. Xie, J. Zhang, Q. Wu, Z. Shen, C. Guo, Y. Wu, F. Wang, B. Z. Tang, D. Wang, *J. Am. Chem. Soc.* **2023,** *145*, 334–344. b) W. Li, G.S. K. Schierle, B. Lei,Y. Liu, C. F. Kaminski, *Chem. Rev.* **2022**; *122* (15), 12495– 12543. c) F. Sun, W. Zhao, H. Shen, N. Fan, J. Zhang, Q. Liu, C. Xu, J. Luo, M. Zhao, Y. Chen, K. W. K. Lam, X. Yang, R.T. K. Kwok, J. W. Y. Lam, J. Sun, H. Zhang, B. Z. Tang, *Adv. Mater.* **2022**; *34*, 220767.
[22] Y. Liu, L. Teng, B. Yin, H. Meng, X. Yin, S. Huan, G. Song, X. B. Zhang, *Chem. Rev*. **2022,** *122,* 6850–6918.
[23] J. Yang, X. Yu, J. I. Song, Q. Song, S. C. L. Hall, G. Yu, S. Perrier, *Angew. Chem. Int. Ed*. **2022,** *61*, e202115208.
[24] Y. Marciano, V. D. Solar, N. Nayeem, D. Dave, J. Son, M. Contel, R. V. Ulijn, *J. Am. Chem. Soc.* **2023,** *145* (1), 234-246
[25] M. Spinck, C. Piedrafita, W. E. Robertson, T. S. Elliott, D. Cervettini, D.Torre, J. W. Chin, *Nat. Chem.* **2023,** *15* (1), 61–69.
[26] Y. F. Tian, G. A. Hudalla, H. Hana, J. H. Collier, *Biomater. Sci.* **2013,** *1,* 1037–1045.
[27] K. M. Eckes, K. Baek, L. J. Suggs, *ACS Omega*. **2018,** *3*, 1635–1644.
[28] P. Gopikrishna, N. Meher, P. K. Iyer, ACS *Appl. Mater. Interfaces* **2018,** *10*, 12081–12111.
[29] H. Lin, J. Wang, J. Zhao, Y. Zhuang, B. Liu, Y. Zhu, H. Jia, K. Wu, J. Shen, X. Fu, X. Zhang, J. Long, *Angew. Chem. Int. Ed.* **2022,** *61*, e202117645.
[30] J. I. Lovitt, T. Gorai, E. Cappello, J. M. Delente, S. T. Barwich, M. E. Möbius, T. Gunnlaugsson, C. S. Hawes, *Mater. Chem. Front.* **2021,** *5,* 3458–3469.
[31] Q. Qiao, W. Liu, Y. Zhang, J. Chen, G. Wang, Y. Tao, L. Miao, W. Jiang, K. An, Z. Xu, *Angew. Chem. Int. Ed.* **2022,** *61,* e202208678.
[32] A. Sanluis-Verdes, P. Colomer-Vidal, F. Rodriguez-Ventura, M. Bello-Villarino, M. Spinola-Amilibia, E. Ruiz-Lopez, R. Illanes-Vicioso, P. Castroviejo, R. Aiese Cigliano, M. Montoya, P. Falabella, C. Pesquera, L. Gonzalez-Legarreta, E. Arias-Palomo, M. Solà, T. Torroba, C. F. Arias, F. Bertocchini*, Nat. Commun.* **2022,** *13*, 5568.

2. OBJECTIVES

The primary focus of this chapter is to design and develop cellular nanocarriers based on the combination of aggregation-induced emission

dyes with self-assembling depsipeptides. These species form fluorescent nanovesicles that can be used both as biomarkers and as time-programmed carriers for biologically active molecules. The chapter covers the study of their structure, morphology, and function, including their ability to carry drugs and their potential cytotoxic effects for cancer therapy. To achieve this, the following objectives have been established:

- To design and synthesize organic hybrids based on the self-assembly of depsipeptide-chains and the fluorescence properties of the naphthalimide cores.
- To perform solvatochromism studies to investigate the solvent-dependent optical properties of the synthesized compounds.
- To conduct fluorescence studies in mixtures of organic solvent (THF) and water in order to determine the required water content at which the aggregation-induced emission phenomenon occurs.
- To determine the nature of the aggregates formed when AIE takes place. Advanced imaging techniques such as atomic force microscopy (AFM), field emission scanning electron microscopy (FESEM) and transmission electron microscopy (TEM) will be used and reveal that the compounds undergo spontaneous self-assembly into hollow nanovesicles.
- To carry out molecular dynamics simulations to predict the intermolecular π-π stacking of the naphthalimide cores and to evaluate the role of the depsipeptide sequence in vesicle formation.
- To investigate the optical activity of the compounds through circularly polarized luminescence (CPL) and circular dichroism (CD) spectroscopy, considering the chiral nature of the amino acid sequences.
- To assess cellular uptake of the nanostructures in human cancer cell lines, including A549 (lung carcinoma), A2780 (ovarian carcinoma), and A2780cis (cisplatin-resistant ovarian carcinoma). Then confocal microscopy will be employed to determine the intracellular localization and target organelle of the compounds.
- To perform cytotoxicity assays to distinguish biocompatible compounds with potential as drug carriers, from highly cytotoxic species useful in anticancer therapies.
- To incorporate the biologically active preimplantation factor into the nanocarriers and study its impact on the cytotoxicity and functionality of the compounds, with particular attention to their ability to induce time-dependent programmed cell death.
- To modify the dye geometry from para-substituted to meta-substituted derivatives and evaluate the ability of these new hybrids to form nanovesicles in organic solvent-water mixtures.

3. PREVIOUS RESULTS AND STARTING MATERIALS

The research group has a long experience in developing new fluorogenic chemical sensors by carbon-carbon coupling chemistry; hence, many fluorogenic probes, that were tested for several types of analytes, were synthesized by using Suzuki and Sonogashira reactions.[33] From them, the aminoprotected NMIs *(Figure 3a)* displayed an increase of the fluorescence

[33] A. Revilla, I. Abajo, M. Medrano, M. M. Salgado, M. Avella, M. T. Rodríguez, J. García, T. Torroba, *ACS Appl. Mater. Interfaces* **2023**, *15*, 32024–32036.

intensity in mixtures of organic solvents with large amounts of water, i.e., they showed aggregation-induced emission (AIE) effect, and it disappeared when the terminal amines were partially or completely deprotected *(Figure 3b).* Therefore, it was demonstrated that the AIEgen fluorescence emission mechanism could be tuned with optimal performance through structural modification.[34]

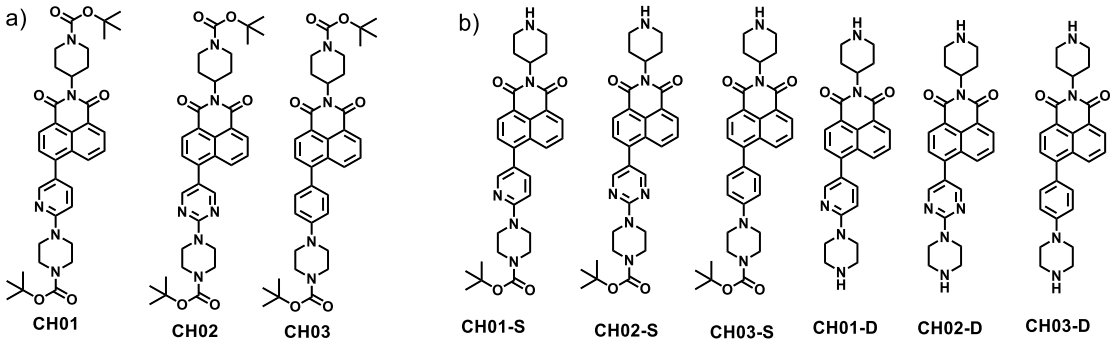

Figure 3. *Starting compounds: a) Boc amino-protected NMIs b) Semi and completely deprotected NMIs.*

On the other hand, the research group had interest in the artificial transformation of natural products on the way to hybrid synthetic-natural structures for the manipulation of physiological processes. It was shown that cyclic depsipeptides *(Figure 4)*, that are selective K^+ membrane ionophores, have implications in glucose-stimulated insulin secretion in ß-cells, and can be used as useful biomarkers for the visualization of chemical processes in live INS1E cells, when they are bonded to a fluorescent dye.[35] Additionally, the naturally occurring peptide, preimplantation factor (PIF), has been shown to enhance glucose-stimulated insulin secretion and could be useful in the type II diabetes treatment.[36]

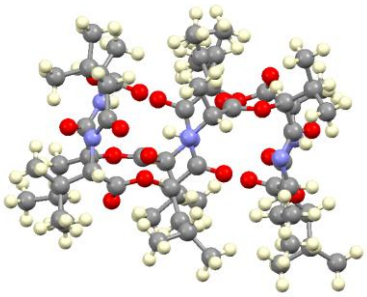

Figure 4*. Crystalline structure of the natural cyclic depsipeptide: cereulide.*

Then, we noticed that one of the synthetic intermediates of the above mentioned cyclic depsipeptide, shows self-association by hydrogen bonds. So, taking advantage of this natural association and the self-assembly capacity of AIEgens, we combined a short sequence (eight units) of the stated natural depsipeptide and the AIEgen naphthalimides to obtain new AIEgen-depsipeptide hybrids that were found to be highly fluorescent and solvatochromic while maintaining the AIEgen characteristics intact.

The preparation of the natural cyclic depsipeptide was described in detail in a previous thesis of the research group.[37] However, in this work we have employed an intermediate, and the steps we have followed to obtain the eight-unit depsipeptide are shown in the scheme below (*Figure 5)*. The sequence of amino acids is as follows: Boc-(L-Val-D-O-Leu-D-Ala-L-O-Val-L-Val-D-O-Leu-D-Ala-L-O-Val)-OH.

[34] A. Revilla, I. Abajo, M. Medrano, M. M. Salgado, G. Pecori, T. Rodríguez, C. Hernando, J. García J. Arcos, T. Torroba, *J. Photochem. Photobiol*. **2023,** *444*, 114911.
[35] J. García-Calvo, T. Torroba, V. Brañas-Fresnillo, G. Perdomo, I. Cózar-Castellano, Y. H. Li, Y. M. Legrand, M. Barboiu, *Chem. Eur. J.* **2019***, 25*, 9287–9294.
[36] A. Sanz-González, I. Cózar-Castellano, C. Broca, J. Sabatier, G. A. Acosta, M. Royo, C. Hernando-Muñoz, T. Torroba, G. Perdomo, B. Merino, *Diabetes Obes. Metab.* **2023,** *25*, 3268–3278.
[37] J. Garcia-Calvo *Fluorescent probes and nanostructured materials for the detection of environmental toxins and catalysts development*. Doctoral Thesis. University of Burgos, **2018.**

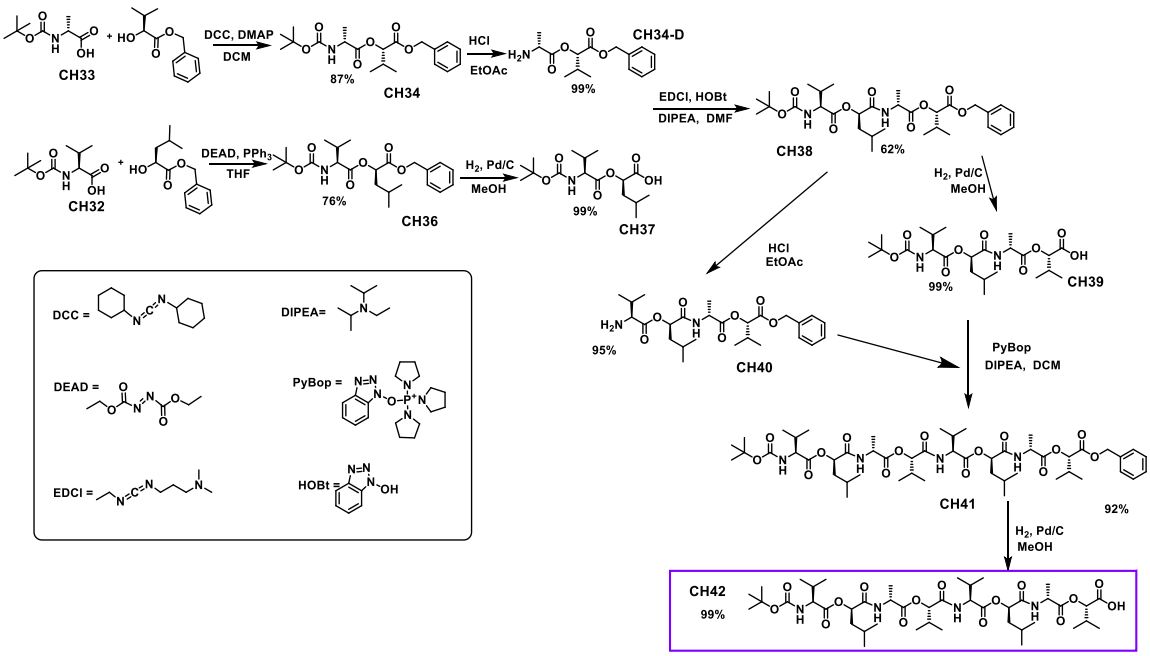

Figure 5. *Followed steps to obtain the eight-unit depsipeptide (CH42).*

4. SYNTHESIS OF AIE-GEN-DEPSIPEPTIDE HYBRIDS

The hybrid products are divided in two families: (a) products containing two depsipeptide chains and (b) products with only one chain of amino acids *(Figures 6a, 6b).*

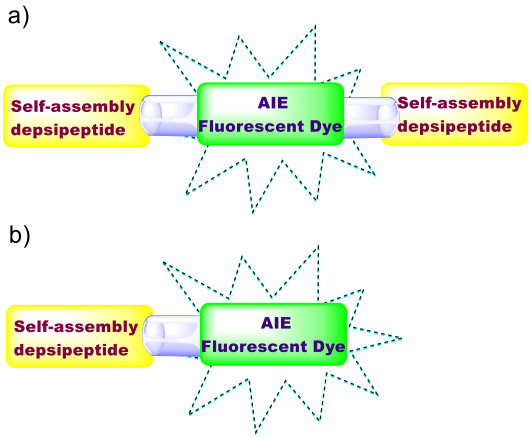

Figure 6. *Schematic structure of new hybrid of AIEgens and depsipeptide chains.*

All compounds described in this section have the same synthetic reaction mechanism which consists in the nucleophilic attack of the free amine group present in the piperazine and/or piperidine of the NMI to the depsipeptide's final carboxylic acid group. Hence, two amide bonds are formed when a deprotected NMI is functionalized *(Figure 7a)*, but only one amide bond is created when the depsipeptide is joined to a semi-protected structure *(Figure 7b).*

Due to the similarity between the six synthetic reactions herein studied, their experimental conditions and steps to be followed are similar. Only the nature of starting NMIs and the amount of the other reagents change, and they are described in full in the Supporting Information section, as well as their rigorous structural characterization. The common methodology is summarised below and showed in *Figure* 7.

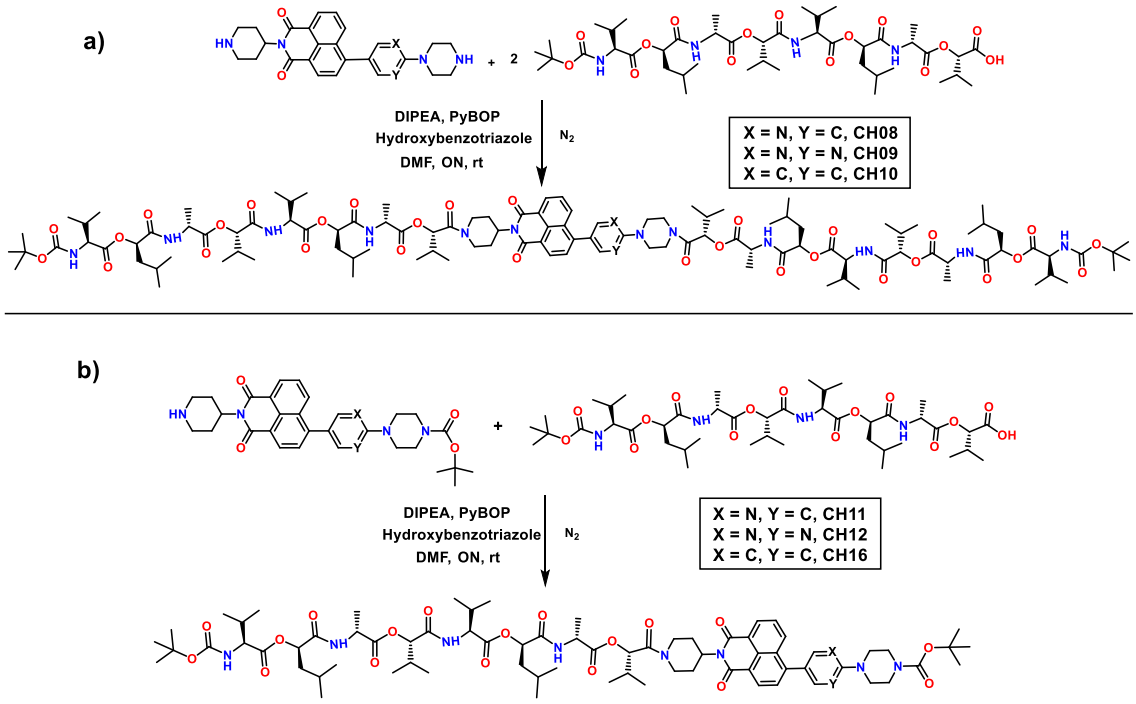

Figure 7. *Synthetic route to obtain a) Two-depsipeptide-AIEgen hybrids b) One-depsipeptide-AIEgen hybrids.*

In a 25 ml flask, provided with a magnetic stirrer, the unfunctionalized NMI (1 eq.), the depsipeptide sequence Boc-(L-Val-D-O-Leu-D-Ala-L-O-Val-L-Val-D-O-Leu-D-Ala-L-O-Val)-OH (1 or 2 eq.), the necessary milligrams of hydroxybenzotriazole monohydrate (2 eq.), benzotriazol-1-yloxytripyrrolidinophosphonium hexafluorophosphate (PyBOP) (2 eq.) and *N*,*N*-diisopropylethylamine (4 eq.) are dissolved under nitrogen atmosphere in 2.5 ml of anhydrous DMF. Keeping the inert atmosphere, the reaction mixture is stirred overnight at room temperature.

Once the reaction has finalized, 15 ml of ethyl acetate is added to the crude reaction mixture and then poured into a separatory funnel. Next, small amounts of water (5x10 ml) are added to drag out the DMF. After that, the ethyl acetate is removed under reduced pressure. The product is purified by column chromatography (SiO_2) employing a DCM-MeOH mixture, gradually increasing the MeOH content from 0% to 2%. Finally, the pure products are obtained with yields ranging from 40 to 70 per cent depending on the nature of the starting compounds.

5. FLUORESCENCE PROPERTIES OF SYNTHESIZED HYBRIDS

5.1. SOLVATOCHROMISM ASSAYS

Herein, the solvent polarity effect on the position and intensity of the absorption and emission bands is studied. In *Table 1*, the employed solvents are ordered from highest to lowest polarity, according to the Snyder polarity index.

Table 1. *Employed solvents in solvatochromism assays*

1. H_2O	4. DMF	7. EtOAc	10. THF	13. Hexane
2. MeOH	5. MeCN	8. THF	11. Toluene	14. MCH
3. DMSO	6. Acetone	9. $CHCl_3$	12. EtO_2	

Then, the 14 different solutions of each compound (10^{-5} M) were photographed under UV light of 366 nm *(Table 2)*.

***Table 2**. Solvatochromism assays under UV light (366 nm)*

Structure	Solvents (1-14)
CH08 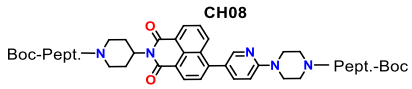	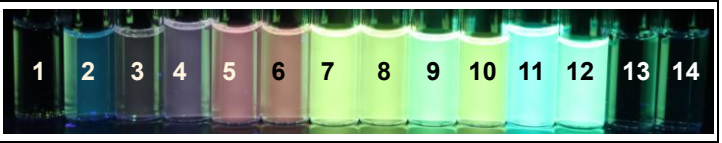
CH09 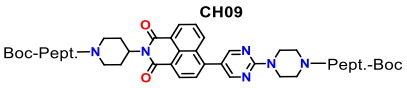	
CH10 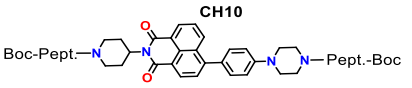	
CH11 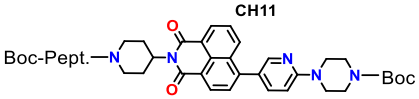	
CH12 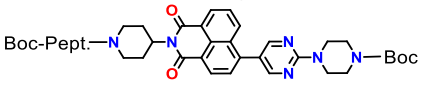	
CH16 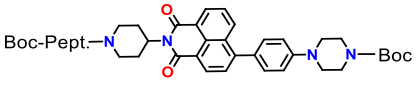	

It is observed that the fluorescence intensity of all NMIs increases as the solvent polarity decreases. This phenomenon is observed because the interactions between NMIs and the solvent are different in each medium. In high polarity solvents, the species tend to establish interactions between their aromatic cores and to aggregate. Consequently, fluorescence emission is quenched by the ACQ effect described in the general introduction. Otherwise, at lower polarities, the aliphatic regions (piperidine, piperazine and tert-butoxycarbonyl group) of the NMIs interact strongly with the solvent and aggregates are not formed, showing therefore a bright fluorescence. However, this behaviour is somewhat different between bi- and monofunctionalized species.

On the one hand, CH08, CH09, and CH10 are scarcely fluorescent in the less polar solvents as hexane and methylcyclohexane, and that's because they are less soluble in these media. These NMIs have two peptide chains with amide polar groups which hind the interactions between their aliphatic regions and the solvent when the environment polarity is too low. These statements are evidenced in their normalized absorption spectra, where neither hexane nor cyclohexane curves appear *(Table 3, Fig.a)*.

On the other hand, CH11, CH12, and CH16 are fluorescent both in hexane and MCH; in this case, there is a single peptide chain on the structure so the piperazine and the tert-butoxycarbonyl group can better interact with nonpolar solvents, making these compounds quite soluble (CH11, CH16) or slightly soluble (CH12). Consequently, in *Table 3, Fig.b*, MCH and hexane appear. As CH09 and CH11 show a representative behaviour of each type of compounds, their normalized absorption spectra are included in this report *(Table 3)*. It must be added that to simplify the hybrid structures, in the next figures the tert-butoxycarbonyl group and the depsipeptide sequence appear as "Boc" and "pept" abbreviations respectively.

***Table 3**. Normalized absorption spectra of (a) CH09 and (b) CH11*

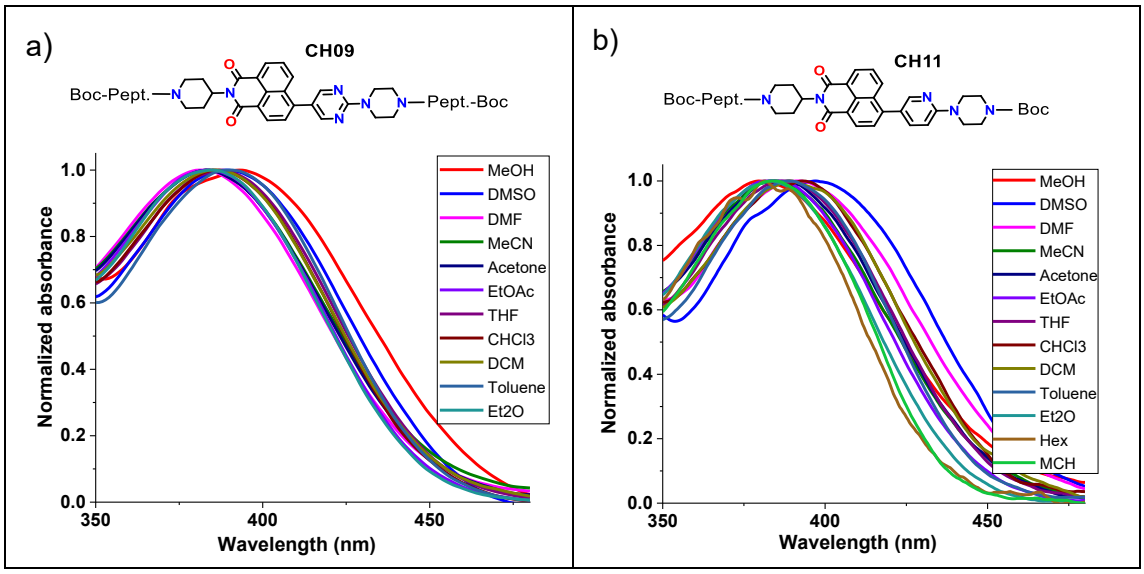

It can be noticed that the water signal does not appear in none of both spectra and that is because of the NMIs absence of absorption in this solvent. The photographs of *Table 2* showed that CH16 has a different behaviour regarding to the other monofunctionalized NMIs, since it shows high fluorescence both in non-polar and organic polar solvents. This is probably observed because while in the other monofunctionalized species the naphthalene core is bonded to pyridine (CH11) or pyrimidine (CH12) structures, CH16 has a phenyl group with no nitrogen atoms, so a different behaviour could be expected. The most likely explanation is that CH16 does not experience the ACQ effect in any of the studied solvents.

The fluorescence properties of these NMIs can be studied in more detail by the interpretation of their emission spectra. Once again, due to the representative behaviour of CH09 and CH11, their emission spectra have been selected to be analysed *(Table 4).*

***Table 4.** Emission spectra of (a) CH09 λ_{exc} = 380 nm and (b) CH11 λ_{exc} = 390 nm*

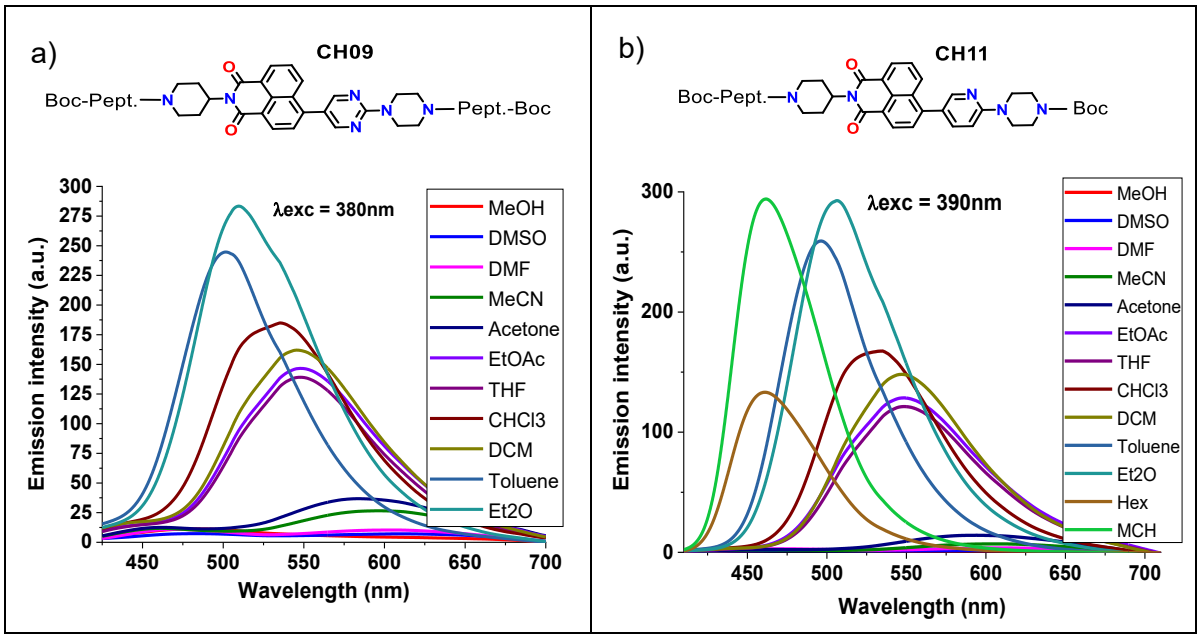

In both spectra the curves corresponding to the most polar media such as MeOH, DMSO and DMF are not distinguished because they are on the baseline. This fact bears out the absence of fluorescence observed in the previous qualitative analysis. In contrast, signal in water is not detected due to the mentioned NMIs' absence of emission (compounds are not soluble). The spectra also corroborate the increase of the emission intensity as the polarity is reduced. CH09 reaches its highest emission intensities in EtO_2 and toluene since they are the lowest polarity solvents where CH09 is fairly soluble, whereas CH11 shows the brightest fluorescence in MCH.

Moreover, absorption and emission spectra allow to select the most appropriate solvent for further analysis. Absorption ones are used to determine the solvents in which the species are best studied. Among those solvents, the selected one must be miscible with water and the fluorescence emission of the NMIs in that medium must not be too high. This way, THF is chosen since it complies with the requirements.

To analyse the effect of the solvent polarity on the position of the bands, normalized emission spectra of CH09 and CH11 have been obtained *(Table 5).*

***Table 5**. Normalized emission spectra of (a) CH09 λ_{exc} = 380 nm and (b) CH11 λ_{exc} = 390*

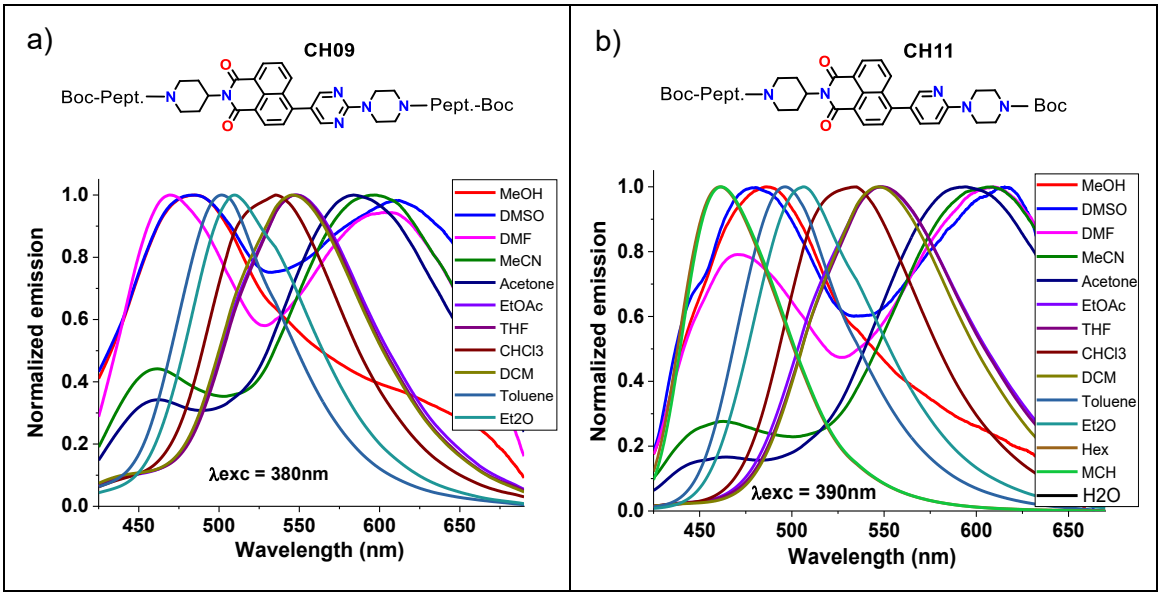

Notice that in most polar solvents like DMSO or THF, the fluorophores show two emission bands, however, to make possible the following analysis, only those of the largest wavelength have been considered. Both CH09 and CH11 spectra show how the maximum peaks are shifted towards longer wavelengths as the solvent polarity is increased. This displacement is called bathochromic shift, and it can be measured subtracting the peak wavelengths of the most and least polar solvents. Thus, in CH09 spectrum, the distance between DMSO (613 nm) and EtO_2 (509 nm) emission maxima is 104 nm. Moreover, the bathochromic shift for CH11 has a value of 154 nm, according to the difference between DMSO (615 nm) and MCH (461 nm) peaks. These results agree with bibliography which proves that if the NMIs' electron acceptor core is functionalized with donor units such as amine or hydroxyl groups, the emission spectrum shows a red-shifted intramolecular charge transfer (ICT) band with accused solvatochromic effect.[38] It must be added that the NMIs emission in MeOH does not fit this tendency, due to the formation of hydrogen bonds between the solvent and the depsipeptide's amide groups.

[38] P. Gopikrishna, N. Meher, P. K. Iyer, *ACS App. Mater. Interfaces* **2018,** *10 (15),* 12081−12111.

5.2. SOLVENT SENSITIVITY OF FLUOROPHORES: LIPPERT-MATAGA PLOTS

The observed bathochromic shifts can also be explained in terms of molecular energy levels. When a molecule is excited to its first singlet state, it has an excess of vibrational energy which is quickly dissipated into the medium. Moreover, the fluorophore dipole moment is usually larger in its excited state than in the ground state, therefore, when the fluorophore is excited, it interacts stronger with the solvent and experiments a stabilization to lower energy levels. This stabilization becomes larger as solvent polarity increases, resulting in an emission at lower energies or longer wavelengths.[39] Some recent studies have demonstrated this stabilization is also higher when the NMI core is bonded to aliphatic chains as peptide sequences and the tert-butoxycarbonyl group.[40, 41] Once a qualitative analysis has been made, the solvent polarity influence on the energy levels of the fluorophores can be quantitatively analysed.

The general solvent effects theory provides an appropriate framework to explain the already mentioned spectral shifts. This model considers the fluorophore as a dipole in a uniform dielectric constant medium.[42] Furthermore, this theory does not take into account any chemical interaction, so it cannot be used to explain some intermolecular interactions as hydrogen bonding, which are typically detected as deviations from this general theory.[43]

The interactions between the solvent and fluorophore affect the energy difference between the ground and excited states. The solvent sensitivity of a fluorophore can be estimated by the Lippert-Mataga equation (Eq.1) which describes the mentioned shifts in terms of the dipole moment changes upon excitation and the different energies a dipole acquires depending on the relative dielectric constant (ε) and the refractive index (*n*) of the medium.

$$\nu_{A-}\nu_F = \frac{2}{hc}\left(\frac{\varepsilon-1}{2\varepsilon+1}-\frac{n^2-1}{2n^2+1}\right)\frac{(\mu_E-\mu_G)^2}{a^3}+K \qquad \text{Eq. 1}$$

Where, ν_A and ν_F are the absorption and emission wavenumbers (cm^{-1}), *c (= 2.9979 × 10^{10} cm/s)* is the speed of light, *h (= 6.6256 × 10^{-27} erg·s)* is the Planck's constant, K is a constant, μ_E - μ_G is the dipole moment difference between the excited and ground states and the term Δ_f is the orientation polarizability, [43] which is the combined impact of electron mobility in the solvent and the solvent's dipole moment.

$$\left(\frac{\varepsilon-1}{2\varepsilon+1}-\frac{n^2-1}{2n^2+1}\right) \qquad \text{Eq. 2}$$

Hence, a quantitative analysis can be made by representing the Stokes Shift ($\nu_A - \nu_F$) versus Δ_f, obtaining the Lippert-Mataga plots of the different NMIs. The refraction index[44] and relative dielectric constants[45] of the employed solvents are collected in *Table 6.*

---

[39] C. Le Droumaguet, A. Sourdon, E. Genin, O. Mongin, M. Blanchard-Desce, *Chem. Asian J.* **2013,** *8*, 2984−3001.
[40] J. R. Lakowicz, *Principles of Fluorescence Spectroscopy,* Springer Science + Business Media, Singapore, third edition, **2006**, chapter 6, pp. 208−212.
[41] N. Meher, P. K. Iyer*, Nanoscale.* **2019**, *11*, 13233−13242.
[42] U. Subuddhi, S. Haldar, S. Sankararaman, A. K. Mishra, *Photochem. Photobiol. Sci.* **2006**, *5,* 459–466.
[43] B. Diaz de Greñu. *Detection and discrimination of organic contaminants of high environmental impact by means of fluorogenic probes.* Doctoral Thesis. University of Burgos. **2014.**
[44] J. E. Sounders, C. Sanders, H. Chen, H. P. Loock, *Appl. Opt.* **2016,** *55(4),* 947−953.
[45] *Dielectric constant of common solvents.* University of Washington website. Available at https://depts.washington.edu/eooptic/linkfiles/dielectric_chart%5B1%5D.pdf Consulted on 17/03/2025.

Table 6. *Refraction index (n) and relative dielectric constant (ε_r) of different solvents at 25 ºC*

	DMSO	DMF	MeCN	Acetone	EtOAc	THF	$CHCl_3$	DCM	Tol	Et_2O	Hex	MCH
ε_r	46.70	36.70	37.50	20.70	16.02	7.58	4.81	8.93	2.38	4.33	1.90	2.02
n	1.48	1.43	1.34	1.36	1.37	1.40	1.45	1.42	1.49	1.35	1.37	1.42

Here below, CH08 and CH11 plots are shown as models of a typical Lippert-Mataga representation in which the different solvents are labelled *(Table 7).* The slope is directly proportional to the change in dipole moment upon excitation.

Table 7. *Lippert-Mataga plot of CH08 and CH11: Stokes shift vs orientation polarizability*

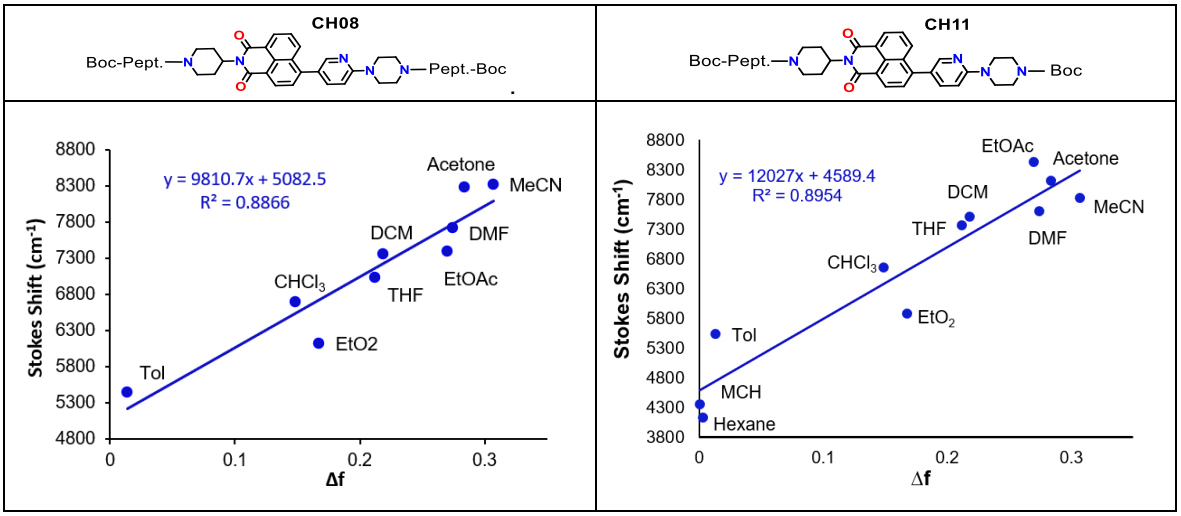

Notice that as the polarity of the medium increases, the solvent influence on the energy levels of the NMI increases too. This result agrees with the recent qualitative analysis, where it could be seen that the higher solvent polarities, the larger wavelength of the absorbed light. So, if the dipole moment of the fluorophore changes greatly upon excitation, a considerable reduction of the energy difference between the excited and ground states is detected. These measurements can therefore be used to estimate the polarity of the medium surrounding the fluorophore in different environments (proteins, cells…).[46]

It must be mentioned that methanol is not included in the graphic, that's because this protic solvent interacts with the NMIs by hydrogen bonds causing a deviation from the linear trend. The general theory of solvent effects is often insufficient for explaining many environments, as fluorophores tend to interact with their immediate surroundings, including the solvent itself. These interactions, known as specific solvent effects, involve phenomena such as hydrogen bonding, complex formation, or the creation of charge transfer states. The presence of these specific fluorophore-solvent interactions is typically reflected in alterations to the shape of emission spectra.[46]

Lippert-Mataga plots are also useful to determine which fluorophore is the most sensitive to the surrounding environment. Those NMIs with a larger slope are the most affected species by the solvent polarity. Then, comparative charts have been separately obtained for mono and biofunctionalized compounds *(Table 8).*

[46] N. Nagarajan, G. Vanitha, D. A. Ananth, A. Rameshkumar, T. Sivasudha, R. Renganathan, *J. Photochem. Photobiol. B* **2013**, *127*, 212–222.

Table 8. *Lippert-Mataga plots: comparison of different NMIs*

Bifunctionalized NMIs (CH08, CH09, CH10)	Monofunctionalized NMIs (CH11, CH12, CH16)
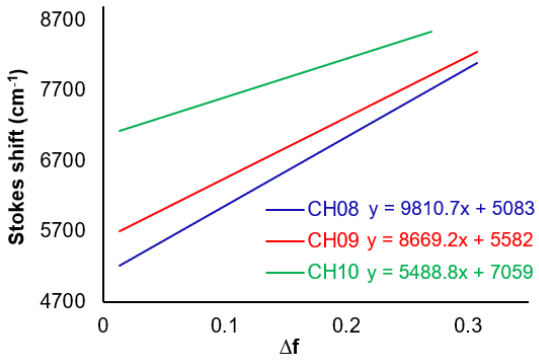	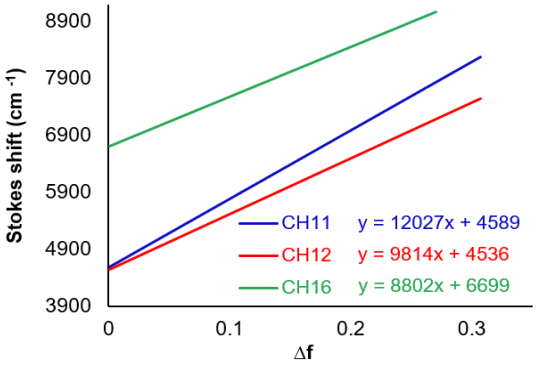

Both types of NMIs show the same behaviour. NMIs which contain a pyridine structure (CH08 and CH11, blue line) have the largest slope meaning they are the most sensitive species to the solvent polarity. This result matches with some published studies which prove that the change in dipole moment is bigger when the aromatic cores have nitrogen atoms in their structure.[42] In addition, the largest dipole moment gain of CH08 and CH11 demonstrates that their excited states are the most polar ones of each NMI type.[49]

It must be added that the obtained slopes for monofunctionalized species are higher than those for bifunctionalized NMIs. That also means that the excited states of the species with a single depsipeptide sequence are more polar than bifunctionalized ones. This result agrees with the bathochromic shifts observed in the previous section, where it was shown that the displacement of CH11 was 154 nm while the CH09 one was 104 nm, meaning the larger influence of the solvent polarity on monofunctionalized species.

5.3. WATER-ORGANIC SOLVENT RATIO ASSAYS

It has been shown that these NMIs tend to aggregate in polar solvents. It is also known that the AIE effect usually appears when the suitable compounds are solved in increasing polar environments.[47] In this case, the medium is gradually polarized mixing an organic solvent with increasing amounts of water. According to solvatochromism tests, THF has been selected as the best organic solvent for this study. So, a 0.1 mM stock solution of the NMI is prepared in THF. Then, eleven dilutions are made by mixing increasing amounts of water (0-90%) and the necessary amount of the stock solution, to get a final concentration of 10 μM in 500 μl. Finally, the mixtures have been photographed under UV light of 366 nm to determine if these NMIs exhibit the aggregation-induced emission phenomenon *(Table 9)*.

Table 9*. Water-solvent ratio assays of different NMIs using UV light (366 nm)*

Structure	THF-H_2O mixtures
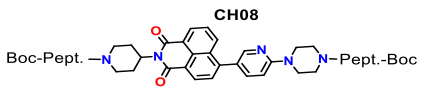	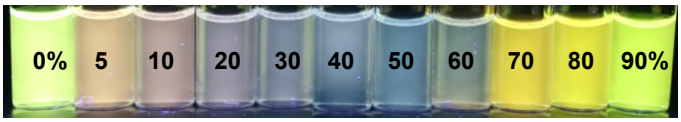
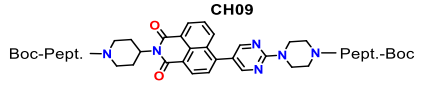	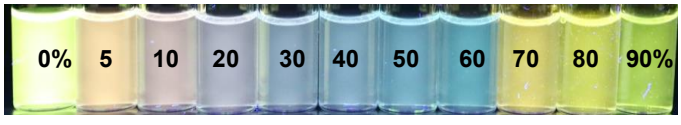

[47] B. R. Gao, H. Y. Wang, Y. W. Hao, L. M. Fu, H. H. Fang, Y. Jiang, L. Wang, Q. D. Chen, H. Xia, L. Y. Pan, Y. G. Ma, H. B. Sun, *J. Phys. Chem. B* **2010,** *114* (1), 128−134.

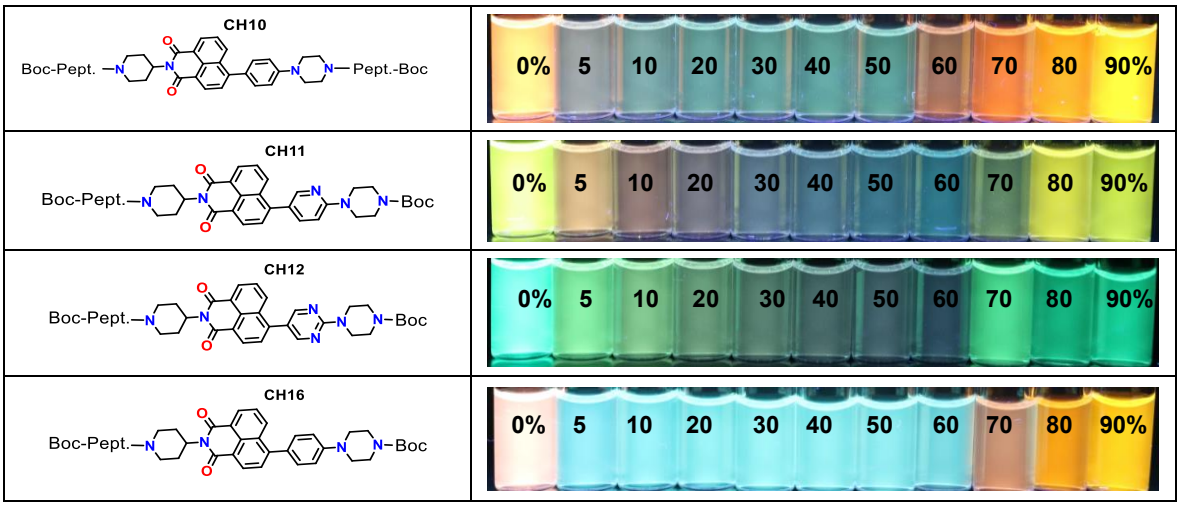

In accordance with the preceding section, it is observed that all NMIs emit light of larger wavelengths as the water percentage increases, and that is because the solvent polarity rises and molecules experience an energy stabilization resulting in emission at lower energies or longer wavelengths. This also matches with the formation of J-aggregates in polar environments, since as explained in the introduction, when J-aggregates are formed absorption and emission lights typically experience a red shift.

But the most important feature observed in these assays is the change of the emission intensity as the water ratio is modified. In mixtures with low water percentages (below 60 %) the fluorescence emission is very weak due to the ACQ effect (it is not observed in CH16 solutions). However, at higher water ratio (above 70 %), the species experience a sudden enhancement of fluorescence emission due to the higher agglomeration and the bigger nanoparticles formation. Therefore, this study confirms that at high water ratios these fluorophores form nanoaggregates large enough to exhibit the already described AIE effect, by which non-radiant decay processes are restricted due to the structural rigidity of nanoaggregates.

Nevertheless, it must be pointed that CH16 does not fit with those statements. Since this compound shows bright fluorescence even in low water percentages, it is suggested that ACQ effect does not appear. At high water percentages aggregates are formed since there is a change in the colour of the emitted light (it turns from blue to orange). However, there is no change in the emission intensity.

This qualitative analysis can be quantified with the emission spectra of the different mixtures. CH08 and CH11 have been selected as representative examples of each group of compounds. In *Table 10, Fig.a* and *Table 11, Fig.a* it is observed that the highest emission intensity takes place at 90% w.r. (AIE effect) and the lowest one at 20% w.r. (ACQ effect). In *Table 10, Fig.b* and *Table 11, Fig.b,* it can be noticed how the emission intensity (grey curve) suddenly decreases at intermediate water percentages, and above 60% w.r. it increases again. The shift of the emitted light to longer wavelengths when the aggregates are formed is also verified in *Table 10, Fig.b* and *Table* 11, Fig.*b.* The blue curve suddenly increases above 60-70% w.r.

Table 10. *(a) Emission intensity of CH08 at different w.r. λ_{exc}=390 nm. (b) Emission intensity (grey) and λ_{max} emission (blue) at same conditions, (THF-water mixtures)*

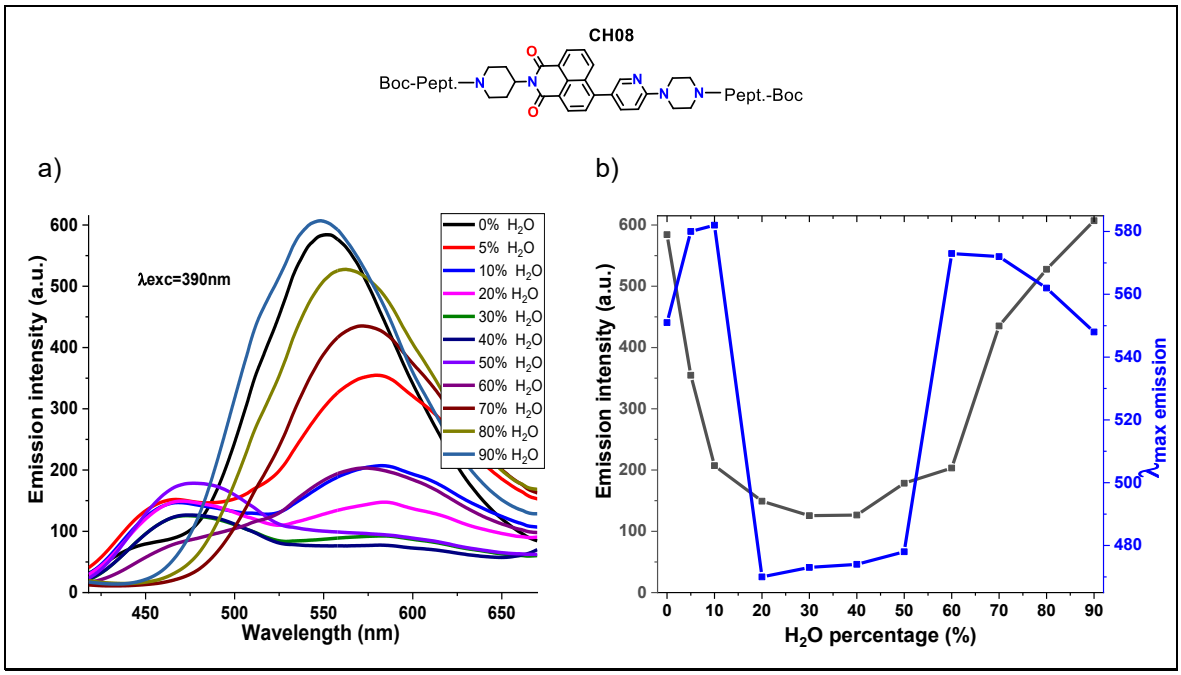

Table 11. *(a) Emission intensity of CH11 at different w.r. λ_{exc}=390 nm. (b) Emission intensity (grey) and λ_{max} emission (blue) at same conditions, (THF-water mixtures)*

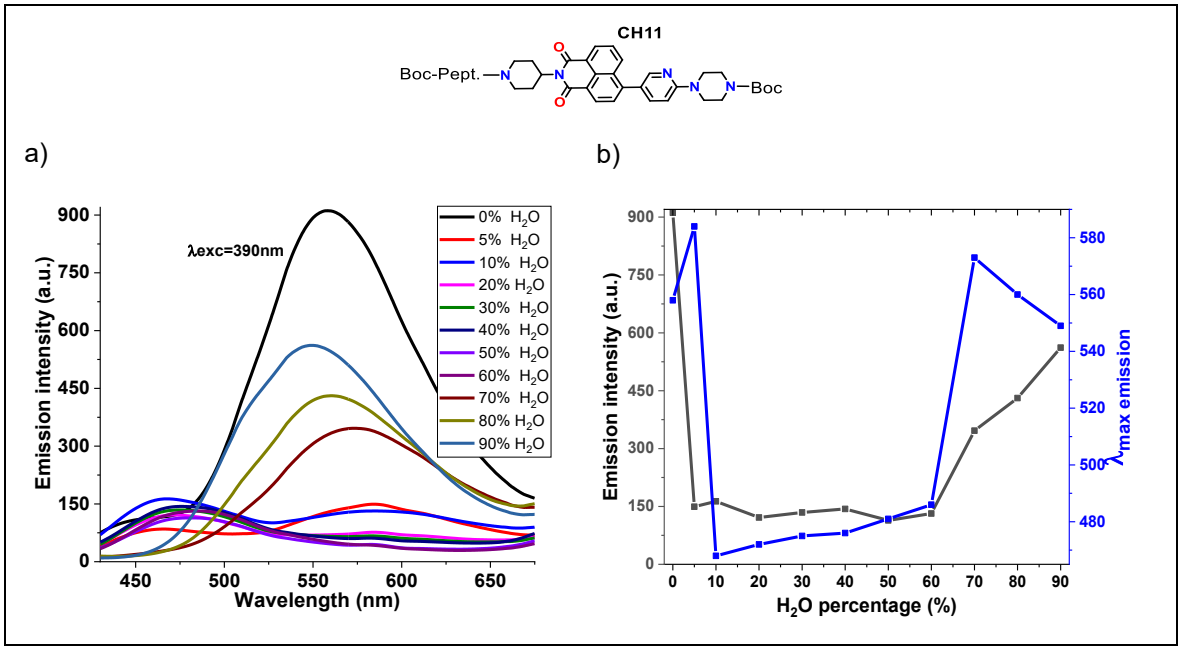

Once it is known these compounds show the AIE effect at high water ratios, we want to determine how the morphology of the suggested aggregates changes as the water ratio increases. So, microscopy techniques are employed to support it.

6. NANOPARTICLES MORPHOLOGY AND SIZE

This section includes several pictures obtained in different research centers: I+D+I/CIBA center (UBU), Instrumental Techniques Laboratory (UVa) and IMDEA Materials Institute (Madrid). Some images have been obtained by atomic force microscopy to verify if the nanoparticles heights grow as the water ratio increases. In addition, scanning electron microscopy has been used to determine the morphology of the aggregates when AIE phenomenon takes place (it is known AIEgens can form spheres, fibers, rods, cubes …).[48] And transmission electron microscopy has been used to confirm the existence of the nanostructures found by other techniques. Herein, a comparative analysis has been made for these NMIs showing how the nanoparticles' morphology changes depending on the water amount of the solvent mixture.

6.1. BIFUNCTIONALIZED NMIS IMAGES

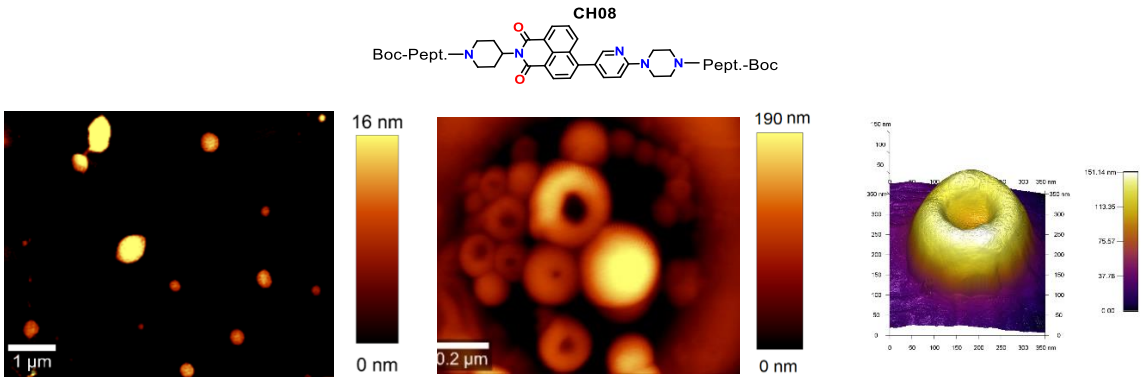

Figure 8. *AFM images of CH08 (THF-H_2O). Low resolution: (left) 20% w.r. (centre) 80 % w.r. High resolution: (right) 80% w.r.*

As it was expected, the nanoparticles are bigger at high water percentage mixtures. The images of *Figure 8* show that the nanoparticles formed at 20% water ratio (w.r.) reach a maximum height of 16 nm, whereas 190 -250 nm are reached at 80 % w.r. But the most interesting characteristic of aggregates formed by CH08 at 80 % of water content, is that some nanoparticles have a central hollow *(Figure 8, centre and right)*.

These results can be compared with SEM images, which verify that CH08 forms hollow structures. It was also observed that some cavities are so big that they contain smaller nanoparticles inside *(Figure 9, left)*. Indeed, nanoparticles of 1.62 microns diameters have been measured *(Figure 9, centre).* The presence of spherical nanoparticles was confirmed by TEM after staining them with uranyl acetate *(Figure 9, right).*

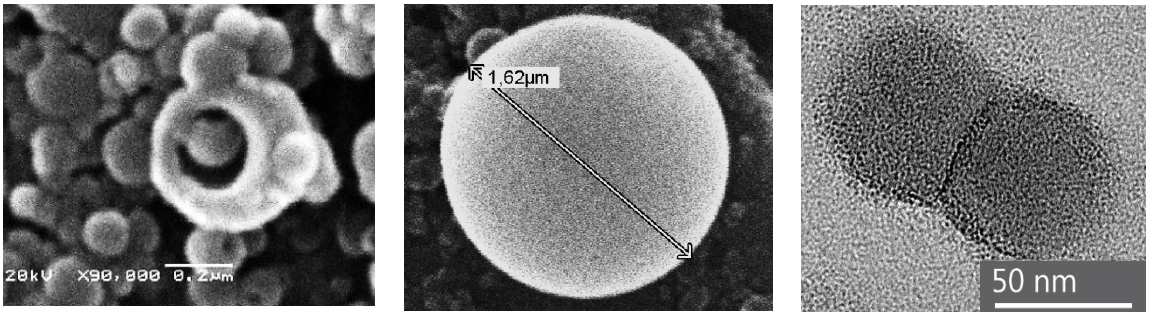

Figure 9. *SEM images of CH08 nanostructures in THF-H_2O at 80 % water ratio.*

[48] A. Saini, K. R. J. Thomas, *RSC Adv*. **2016**, *6,* 71638−71651.

The structures with a central cavity are very abundant in CH08 mixtures, and this morphology is the predominant one. Then CH09 was also imaged. It forms bigger aggregates than those of CH08. These super-aggregates have been shown to reach a height of 300 nm at 70% w.r. *(Figure 10, left).* Besides that, CH09 forms stunning chains of nanovesicles. *(Figure 10, centre and right).*

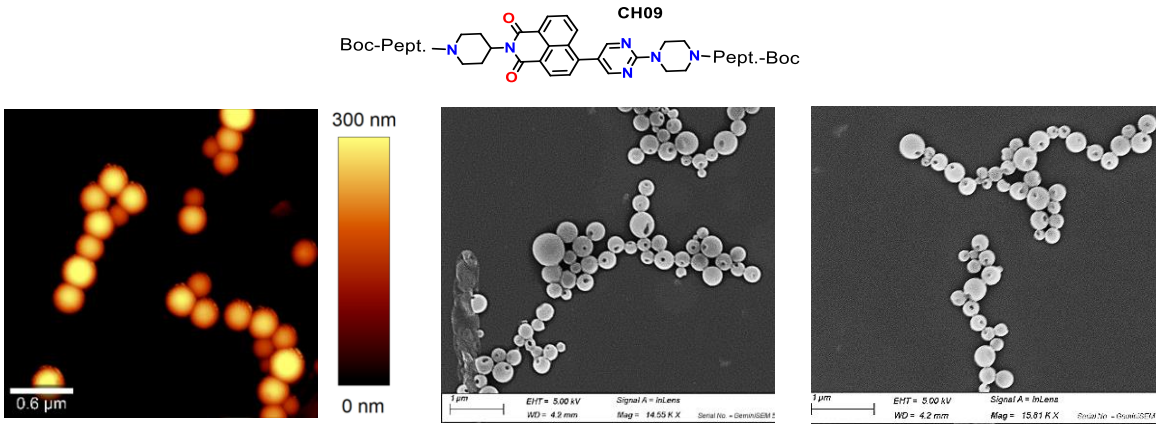

Figure 10. *Images of CH09 in THF-H_2O at 70% w.r.: (left) By AFM. (Centre and right) By FESEM*

In contrast, CH10 forms smaller and isolated nanospheres and vesicles; only small aggregates have been found *(Figure 11).*

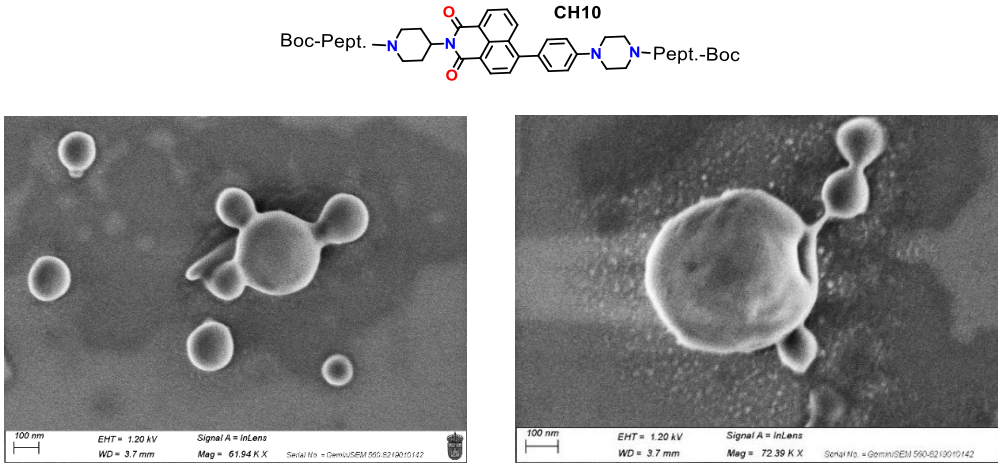

Figure 11. *FESEM images of CH10 in THF-H_2O: (left) 70% w.r. (right) 80% w.r.*

6.2. MONOFUNCTIONALIZED NMIS IMAGES

CH11 has been also measured at low and high-water percentages to determine the change on the nanoparticles sizes as the water ratio increases. Concretely, an increase of 124 nm is produced from 40% to 70% water ratio *(Figure 12, left and centre).*

As it was expected, when the AIE phenomenon takes place, this species forms hollow nanovesicles *(Figure 12, right).*

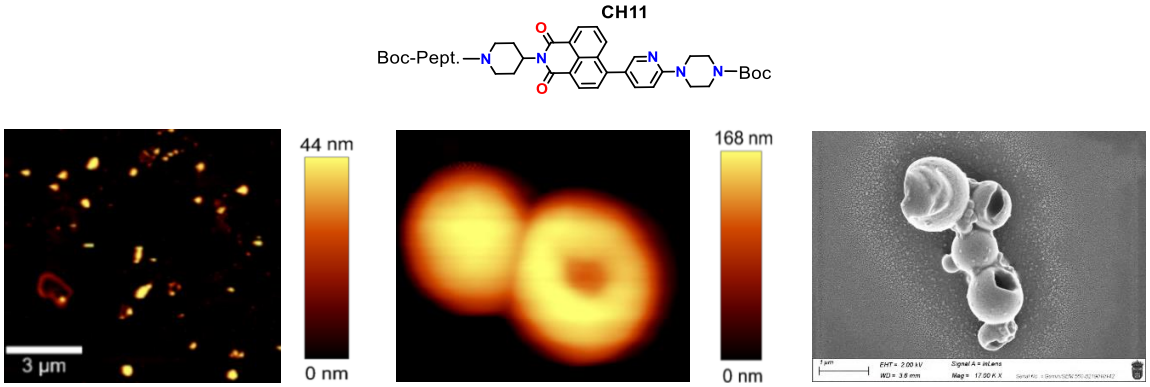

Figure 12. *AFM images of CH11 in THF-H_2O: (left) 40% w.r. (centre) 70% w.r.(right) FESEM image at 70% w.r.*

In contrast, the prevalent structure found in CH12 samples are large aggregates of several nanospheres *(Figure 13).*

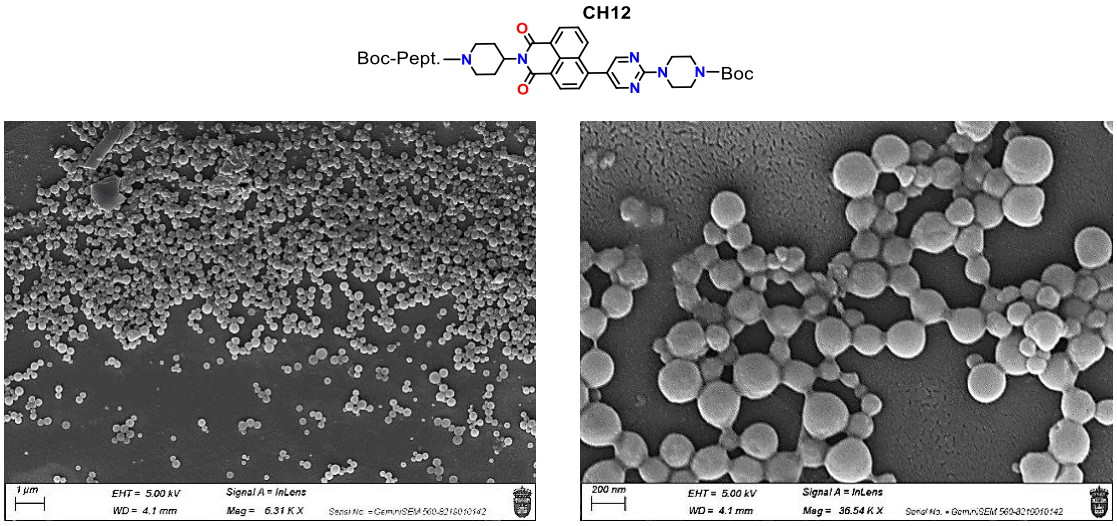

Figure 13. *FESEM images of CH12 in THF-H_2O at 80% w.r.*

Finally, CH16 was seen to form vesicles and fibers *(Figure 14).*

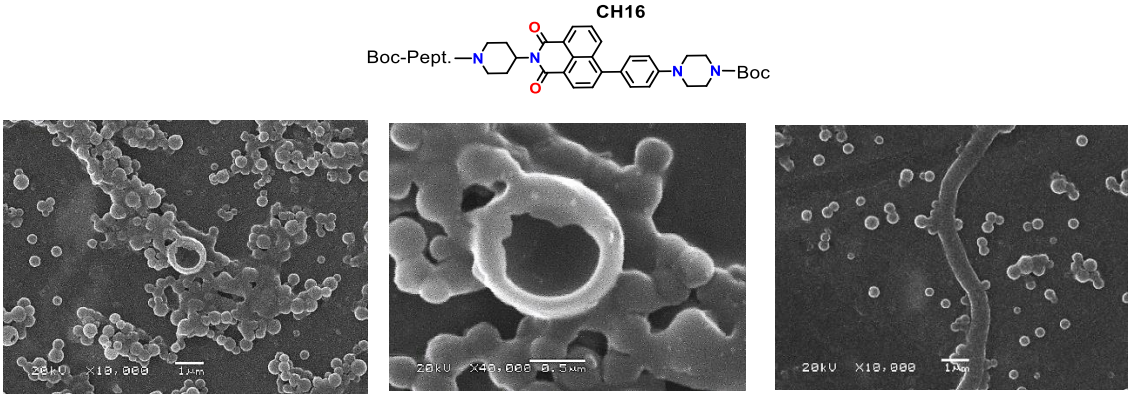

Figure 14. *SEM images of CH16 in THF-H_2O at 80% w.r.*

6.3. SOFTNESS AND ENHANCED FLOURESCENCE OF AGGREGATES

As mentioned in the objectives of the chapter, these compounds are expected to be used in biological environments, so it is desirable the nanostructures be soft and flexible due to the possibility of colliding with organelles inside cells or other particles and being broken. Fortunately, these NMIs' nanoparticles are very soft, and it is known due to the measurements made with the atomic force microscope, whose cantilever's tip does not resist heights of more than 250 nm unless the sample is highly soft and deformable. CH09 aggregates reach heights of 300 nm, and they could be measured without damaging the AFM tip, so they are attractive as soft nanocarriers.

The softness of the nanoparticles' surface was also demonstrated by changing typing mode in AFM. In this case, a stronger tip let us drill holes on the nanoparticles of CH08. So, it was possible to perforate solid nanoparticles, observing how their surface was completely smooth and deformable. In *Figure 15* it is possible to see the punctured vesicles *(right)* obtained from the intact ones *(left).*

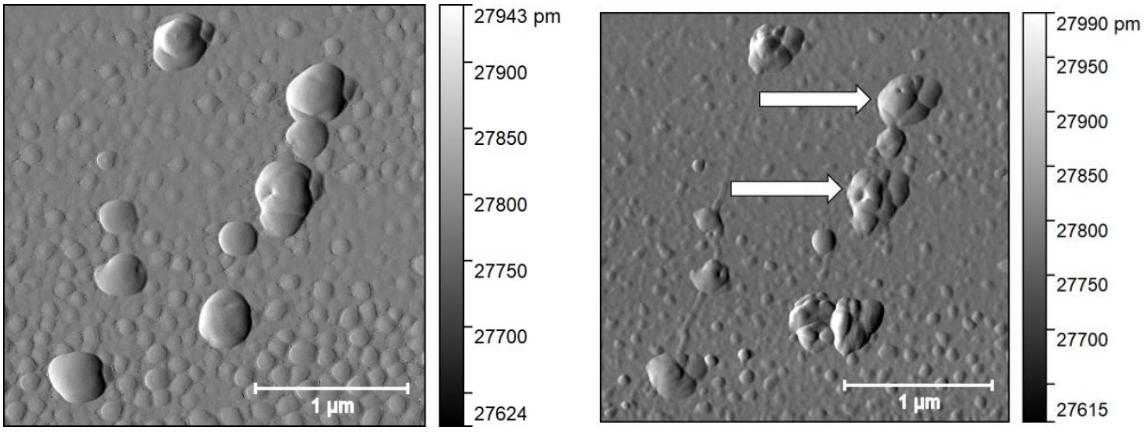

***Figure 15**. "Drilling a hole" by AFM typing on the surface of CH08.*

On the other hand, in previous sections we have observed that the aggregated induced emission effect takes place upon the formation of nanovesicles in mixtures with high water ratios. However, we wanted to verify whether the aggregates also exhibit strong fluorescence outside of solution. This was confirmed, using an AFM instrument coupled to a fluorescence microscope (placed in the instrumental techniques laboratory of the UVa). It was observed that the nanoparticles deposited on the silicon plate displayed intense fluorescence, confirming that the fluorescence is an intrinsic property of the aggregates and not solely dependent on the solvated environment *(Figure 16)*.

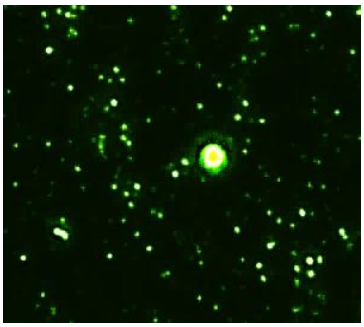

***Figure 16**. Fluorescence of CH12 nanoparticles formed in an 80% w.r. mixture (THF-H_2O).*

6.4. NANOPARTICLES' SIZES

Once the nanoparticles have been imaged, it is possible to determine which is the average size of them by making dynamic light scattering (DLS) measures of the most representative samples. It has been shown that the smallest nanoparticles are formed by CH08 at 80% w.r. (THF-H_2O) with an average diameter of 129.8 nm, whereas CH11 at 80% w.r. forms the greatest nanoparticles with an average diameter of 338.9 nm *(Table 12)*. Herein is only represented a small part of the results obtained by DLS, but all the information is completely detailed in the Supporting Information of this chapter.

Table 12. *DLS results of (a) CH08 and (b) CH11. The average sizes of aggregates are shown below*

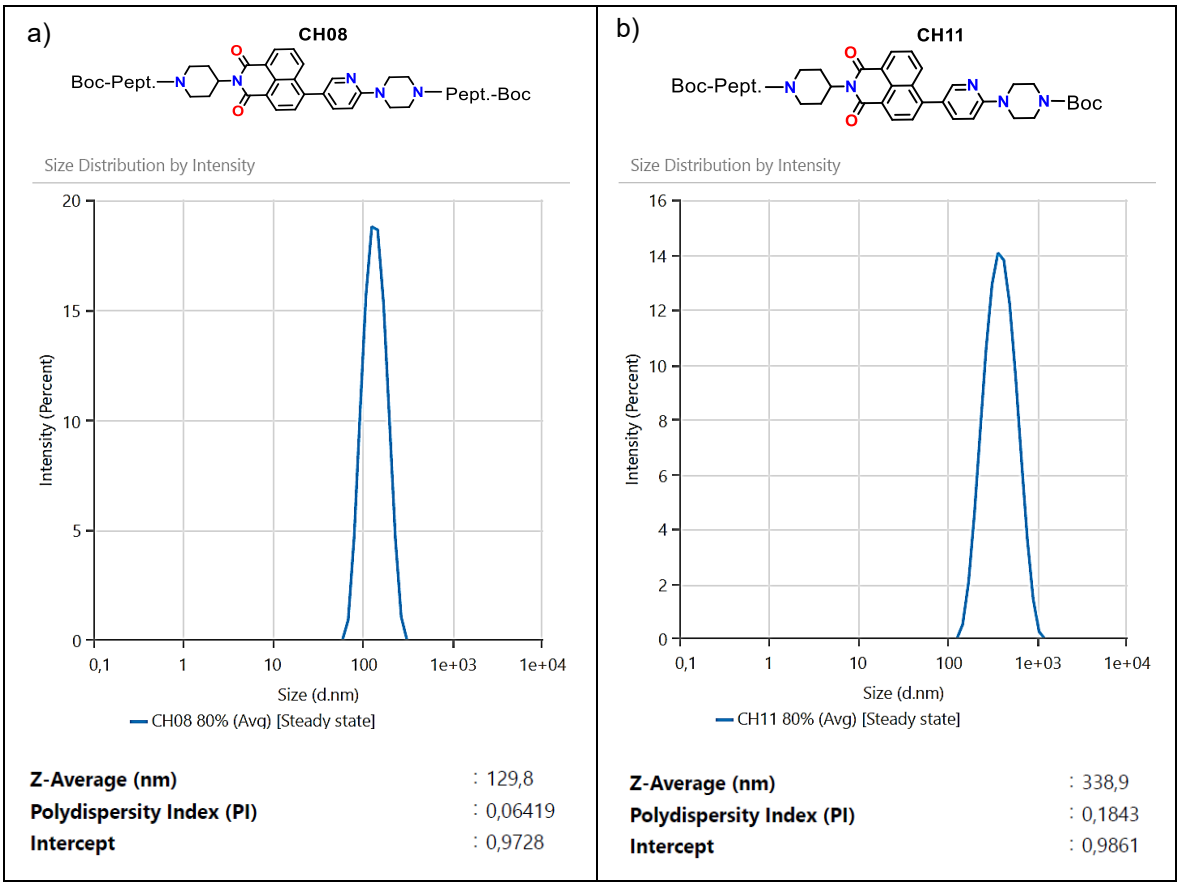

These results are only an average. This means that most of the particles in the sample are close to the average size. However, this doesn't mean that there aren't some larger particles, since vesicles of even one micron were seen in the sample of CH08 (it was shown in the images of the previous section). But DLS allows us to get an idea of the predominant particles' size.

7. MOLECULAR DYNAMICS SIMULATION

Once we had discovered that these compounds form nanovesicles, we wanted to verify if these structures could be predicted by computational calculations. It was hypothesized that the aromatic moieties of distinct CH08 molecules would perform stacking interactions with each other. Thus, to achieve atomic-level insights into the structure of nanovesicles, we collaborated with a specialized group to build a model by using molecular dynamics (MD) simulations lasting 400 nanoseconds. This technique, which explores the dynamic behaviour of molecular systems, provides crucial information about the structural characteristics and self-assembly of supramolecular systems.[49]

Notably, the MD simulations indicate that the aromatic naphthalimide core forms stable π-π stacking interactions and adopts a distinct curvature towards a vesicular structure *(Figure 17b)*. On average, the bending angle is approximately 147°, and it suggests that the simulated model accurately represents the curvature of the nanovesicle wall.

This becomes particularly evident when we expand the model to replicate the stacking interactions of the aromatic core *(Figure 17c)*. Based on our calculations, the estimated thickness of the CH08-associated assembly is around 5 nm. Meanwhile, analysing the microscopy images, the thickness of the nanovesicle wall is approximately 20 nm. This suggests that the nanovesicle wall is composed of an average of four stacked and curved molecular entities, as further modelized in *Figure 17c* and expanded in *Figures 17e* and *17f.*

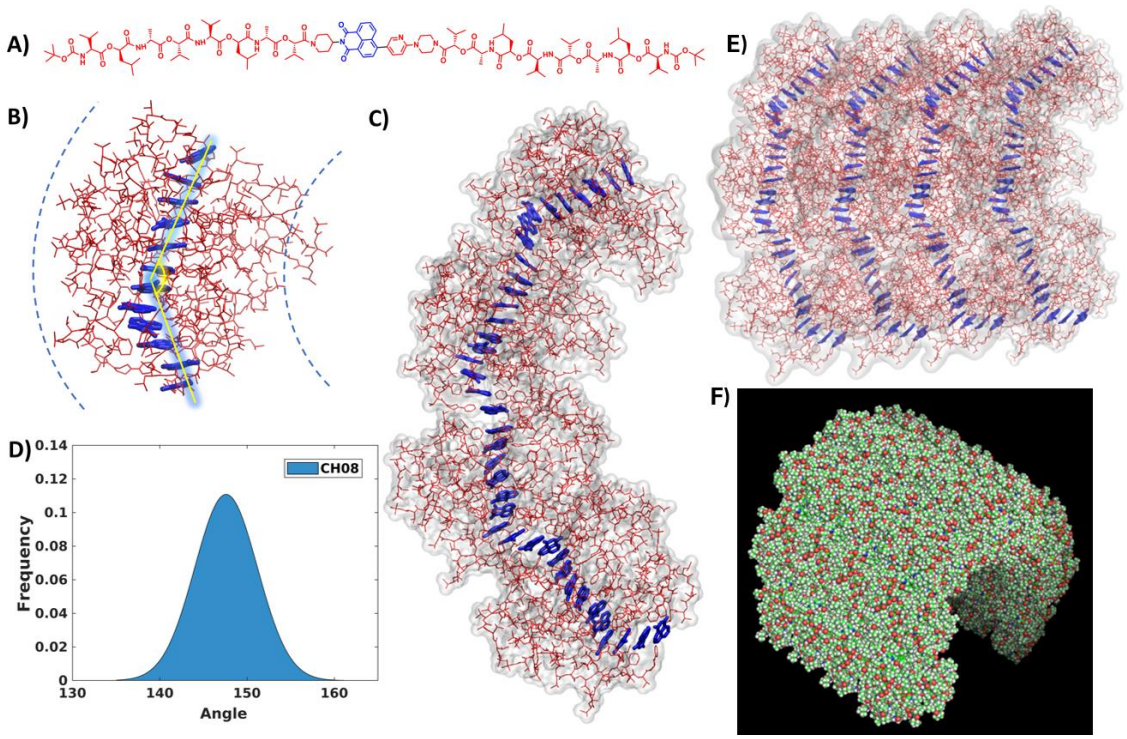

Figure 18. *A) Structure of CH08. The aromatic NMI core is shown in blue, while the depsipeptide chains are shown in red. B) Representative structure as extracted from a molecular dynamics trajectory of 12 stacked CH08 monomers showing the tilt angle measured between the central monomer and the top and bottom monomers. C) An extended model generated by replicating the already simulated structures. D) Tilt angle distribution observed during the MD simulation. E) A structural model showing the interaction of four stacked CH08 sets of molecules. F) The CPK model of the curvature of the four stacked CH08 molecular assemblies from E).*

[49] P. W. J. M. Frederix, I. Patmanidis, S. J. Marrink, *Chem. Soc. Rev.* **2018**, *47,* 3470−3489

8. CHIRAL ENTITIES: CPL AND CIRCULAR DICHROISM

Another key aspect in the formation process of these nanostructures is the influence of rigidity on the overall assembly. The stacking of basic chiral groups of the depsipeptide chain bonded to the core dye, results in chiral nanoentities that exhibit macroscopic effects, such as circularly polarized luminescence (CPL) and circular dichroism (CD) signals. It has been shown that these signals become detectable only upon the full development of the nanostructure. The latter affirmation was discovered because when measurements were taken with freshly prepared samples, no signals of CPL or CD were detected. However, if the measurements were carried out after the samples had rested for 24 hours, a response was detected. That it is because the nanoparticles need time to be formed, so the CPL and DC responses depend on the aggregated nanostructure of the compounds in the studied THF-H_2O mixtures. Here below the CPL and DC signals of CH09 (70% w.r.) and CH11 (80% w.r.) are shown as representative examples of all synthesized compounds *(Table 13).*

Table 13. *(a) CD spectra of CH09 and (c) the one of CH11. CPL spectra of (b) CH09 and (d) CH11 (10 averaged spectra, λ_{exc}= 390 nm and t(acq.) = 1 ms/nm)*

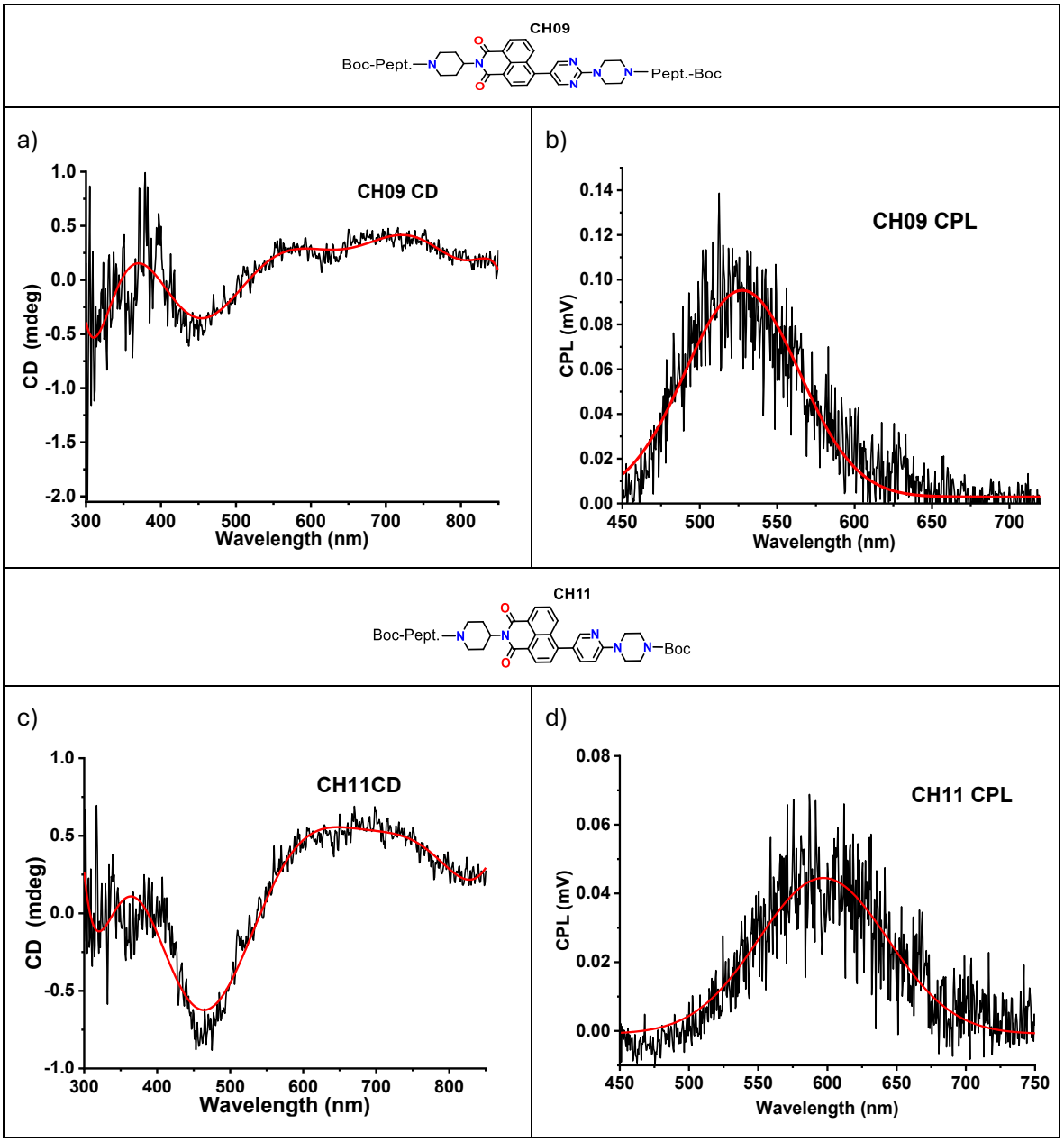

Notice that both CPL and DC are positive. When DC is positive means that the samples absorb right-circularly polarized light preferentially; and the CPL signal is the intensity difference between the left- and right-circularly polarized light emitted by the chiral molecule when it is excited by unpolarized light. In this case, the intensity of the emitted left-circularly polarized light is greater, so the signal is positive. The theoretical bases of CPL technique will be deeply described in Chapter 4.

9. DEPROTECTED AIE-GENS-DEPSIPEPTIDE HYBRIDS

We have seen that these AIEgens form nanovesicles, and this morphology could be useful for biological applications and use them for cell transport.[50] As an ideal objective, the nanoparticles might be attached to specific antibodies, nucleotide or protein sequences enabling them to recognize target cells and to deliver selectively their content.[51]

We decided to study these compounds inside cells, determine their biocompatibility and observe how the synthetized molecules interact with the different cellular organelles. Thanks to the AIE effect, if a homogeneous fluorescence is observed throughout the whole cellular surface, it means that the molecule doesn't have a specific destination in the cell.[52] Otherwise, if the most intense light comes from a reduced area, it is because the molecules are forming nanoaggregates there, in a particular compartment of the cell. So, it is possible to discover the target organelle. However, to do these studies it is necessary to slightly modify the hybrids' structure. The terminal amines are protected with a tert-butoxycarbonyl group, and this ester group has been shown to impede the entrance into cells.

9.1. DEPROTECTION REACTION.

The terminal protecting groups must be removed from the studied compounds *(Figure 18).* To get it, in a 50 ml flask, provided with a magnetic stirrer, the protected NMI is dissolved in 25 ml of $CHCl_3$. Next, 2 ml of trifluoroacetic acid is added to the mixture and the reaction is stirred for 3 hours at room temperature. Once the reaction has finalized, the solvents are removed under reduced pressure. Then, the products are obtained, with yields above 95%.

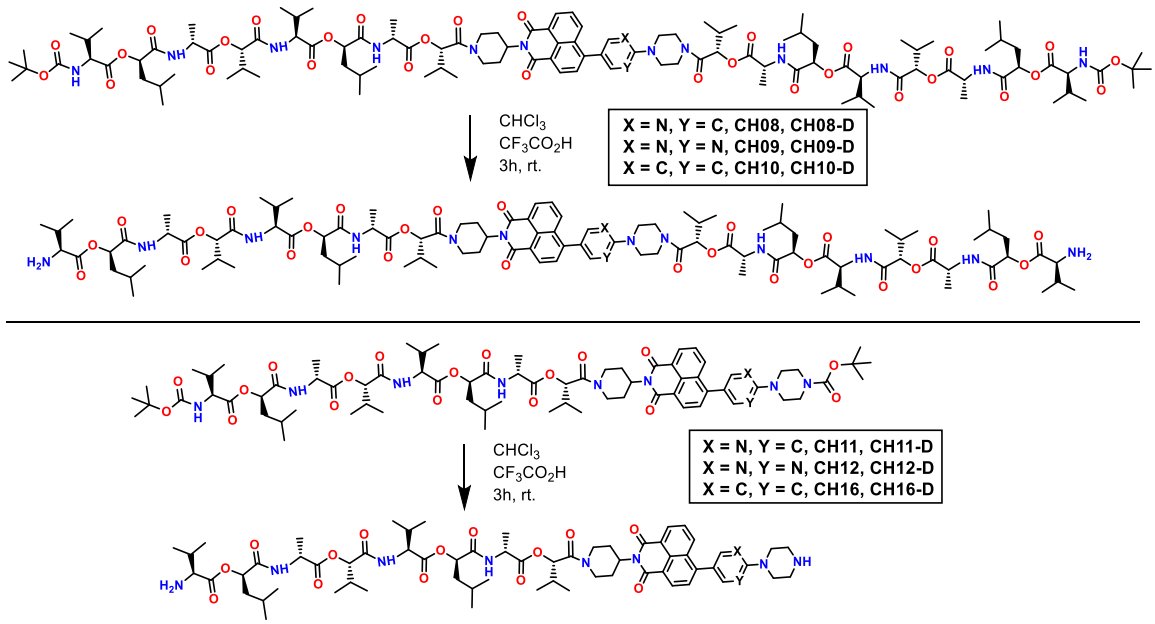

Figure 18. *Scheme reaction for the deprotection of terminal amines.*

[50] P. Choudhury, K. Das, P. K. Das, *Langmuir* **2017,** *33(18),* 4500−4510.
[51] S. Mitragotri, P. Stayton, *MRS Bull.* **2014,** *39*(*3*), 219−223.
[52] W. Qin, D. Ding, J. Liu, W. Z. Yuan, Y. Hu, B. Liu, B. Z. Tang, *Adv. Funct. Mater.* **2012,** *22*, 771−779.

The deprotected compounds are wanted to be studied inside cells, however, it is necessary to know if they still form nanovesicles after deprotection.

9.2. MORPHOLOGY AND SIZE OF DEPROTECTED COMPOUNDS

As it was done with the protected compounds, these ones were imaged using microscopy techniques. In this case, FESEM images were taken. Nanovesicles were observed, so the nanostructure is kept despite the presence of free terminal amines in the chemical structure. These amines could interact with the water of the mixtures and affect the formation of aggregates; however, it has been demonstrated that the aggregates are preserved after deprotection. Herein the most representative examples of each group of compounds are shown.

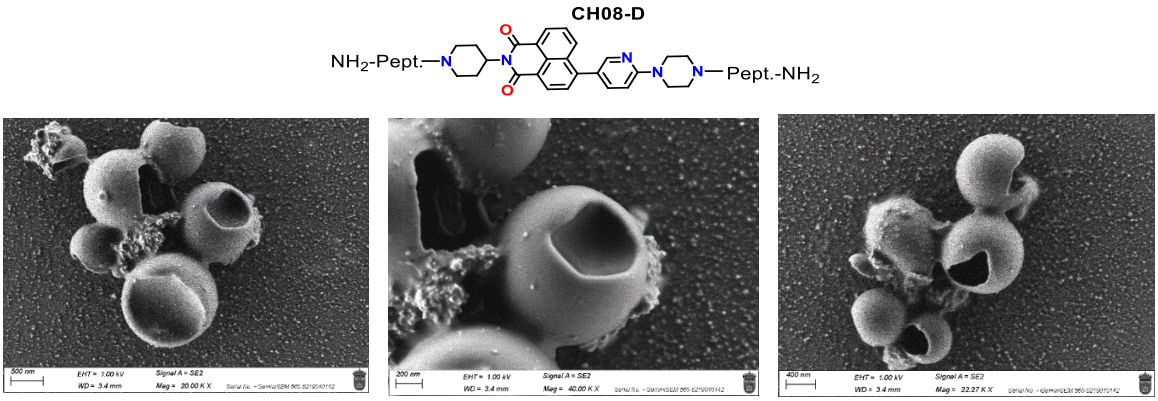

Figure 19. *FESEM images of CH08-D in THF-H_2O at 80% w.r.*

The wall of the nanovesicles formed by CH08-D were easily measured. It has been seen that they measure 20 nm approximately as their precursor did.

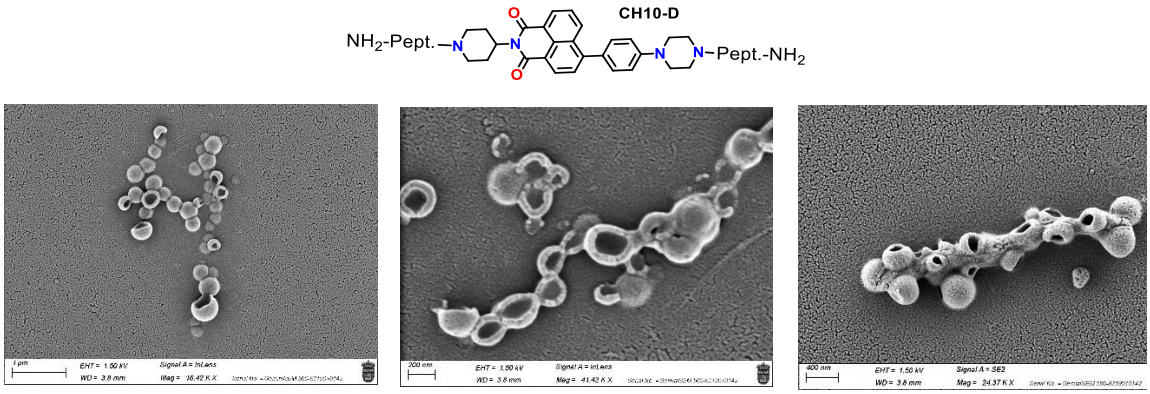

Figure 20. *FESEM images of CH10-D in THF-H_2O at 80% w.r.*

As seen in the image on the right above, some nanovesicles formed by CH10-D are aggregated in the form of a fiber a few microns long.

9.2.1. Nanoparticles' size of deprotected compounds: bigger aggregates

The nanovesicles observed in *Figure 19* seem to be much bigger than the ones observed in the images of the protected compounds. That observation is confirmed with DLS measurements. To maintain the reference examples that were shown with the precursors, the average sizes of CH08-D and CH11-D in THF-H_2O mixtures are shown in *Table 14.* Notice that the nanoparticles grow from 338.9 nm (protected structure) to 713.1 nm in the case of CH11-D at 90% w.r., and from 129.8 nm to 800.9 nm in the case of CH08-D at 80% w.r. This increase in size occurs with all deprotected compounds, but the most remarkable growth is observed for the examples below.

Table 14. *DLS results of (a) CH08-D and (b) CH11-D. The average sizes of aggregates are shown below*

a)

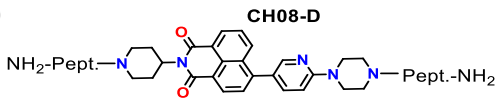

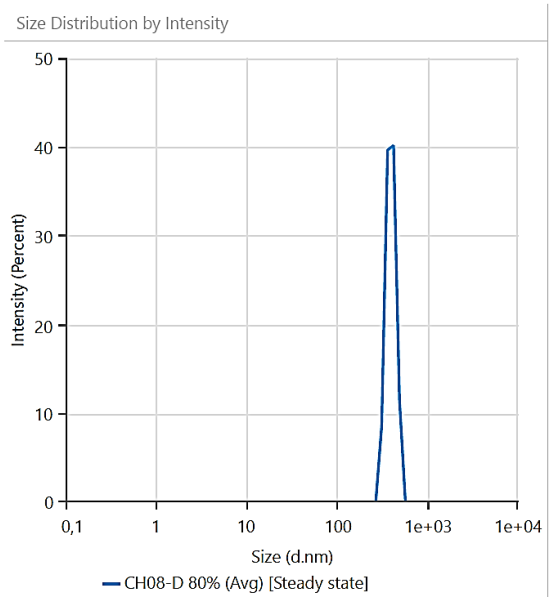

Z-Average (nm)	: 800,9
Polydispersity Index (PI)	: 0,6802
Intercept	: 0,8991

b)

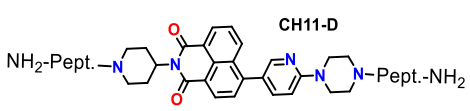

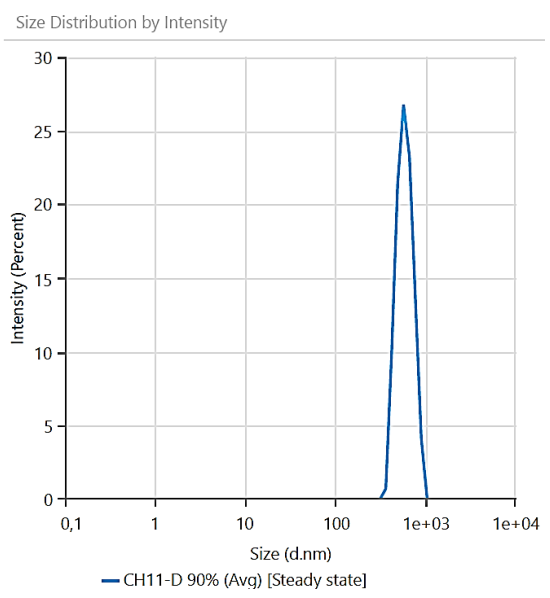

Z-Average (nm)	: 713,1
Polydispersity Index (PI)	: 0,3284
Intercept	: 0,9065

9.3. STUDY OF DEPROTECTED SPECIES INSIDE CELLS

Since deprotected compounds are able to cross the cellular membrane, it is possible to determinate their target organelle. Some published research has proved that cells keep their stability in water with low concentrations of a biocompatible solvent as DMSO or EtOH.[53] In this case, it is preferable to dissolve the compounds in DMSO. But first we checked the integrity of AIEgen characteristics in DMSO/water by AFM (study detailed in Supporting Information, p. S87). Spherical nanoparticles of CH11 were still detected in this mixture of solvents. *(Figure 21).*

[53] H. Gao, X. Zhang, C. Chen, K. Li, D. Ding, *Adv. Biosys.* **2018**, *2 (9),* 1800074.

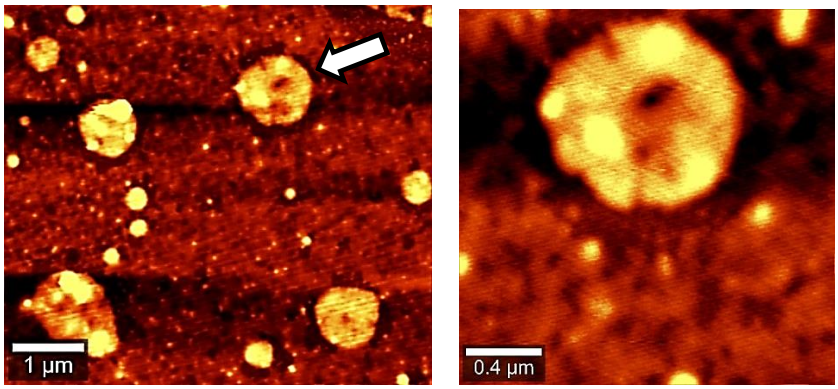

Figure 21. *Nanovesicles of CH11 in a mixture of DMSO and water (90%).*

To determine the destination of the compounds inside the cells we studied colocalization in lung tumor cells (A549). Using confocal laser scanning microscopy (CLSM) we saw that the nanovesicles showed positive colocalization with endoplasmic reticulum (ER) *(Figure 22)* stained with ER Tracer Blue (AAT Bioquest). The study by stimulated emission depletion (STED) super-resolution microscopy, revealed that the nanovesicles' size was consistent with measurements obtained from AFM and FESEM, confirming the integration of the vesicles into living cells *(Figure 22).*

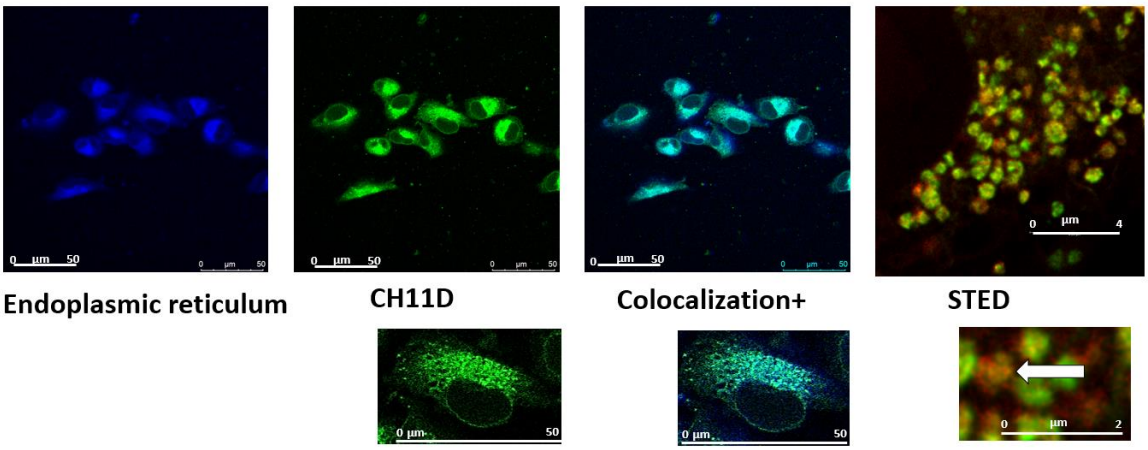

Figure 22. *Confocal laser scanning microscopy (CLSM) and STED super-resolution microscopy of CH11-D.*

To achieve these results, the cells were previously cultured in DMEM (Dulbecco's Modified Eagle Medium) with 10% of fetal bovine serum (FBS) and antibiotics (1% penicillin-streptomycin-amphothericin B) at 37°C with 5% CO_2. For imaging experiments, cells were seeded in glass-bottom dishes and grown for 24 hours before being treated with 1 µM of test compounds for 1 hour. The ER was stained with ER-Tracker™ Blue dye (500 nM) for 30 minutes, followed by washing with phosphate-buffered saline to remove the dye excess and finally fresh medium was added. Cells were then fixed with 4% paraformaldehyde, permeabilized with 0.1% Triton X-100, and blocked with 1% bovine serum albumin (BSA) for 1 hour at room temperature. Imaging was performed using a Leica TCS SP8 STED 3X microscope. For CLSM, λ_{exc} = 470 nm and λ_{em} = 670 nm were employed to visualize the compounds.

The analysis of confocal microscopy photographs involves the use of different metrics to evaluate the colocalization of fluorescent signals in the obtained images. In this context, the Pearson's coefficient and the Manders' coefficients are two of the most commonly used metrics to quantify the relationship between two sets of image data.

The Pearson's correlation coefficient (PCC) measures the linear correlation between the pixel intensities of two images. Its value ranges from -1 to 1, where 1 indicates a perfect correlation, 0 indicates no correlation, and -1 indicates a perfect inverse correlation. This coefficient is particularly useful for determining whether the intensities of the two fluorescence channels move together, suggesting that the labelled molecules in both images are colocalized. On the other hand, the Manders' coefficient (M1 and M2) represents a more specific measurement of colocalization. M1 represents the fraction of the signal from one channel that overlaps with the other channel, while M2 represents the fraction of the signal from the second channel that overlaps with the first. A value of M1 or M2 close to 1 indicates a high overlap between the signals of the two channels, suggesting effective colocalization.

Thus, colocalization coefficients were calculated with ImageJ software. For CH11-D, Pearson's correlation coefficient (Rr, no threshold) was 0.81, meaning a strong positive correlation between the intensity distributions of CH11-D and the ER probe; Manders' coefficients: M1 (CH11-D overlapping ER probe) was 0.890 whereas M2 (ER probe overlapping CH11-D) was 0.616; these values indicated that 89.0% of CH11-D signal overlaps with the ER probe, and 61.6% of the ER probe signal overlaps with CH11-D throughout the entire field of view.

9.3.1. Biocompatible vs antiproliferative species

Once the target organelle of the deprotected compounds was known, a biocompatibility study in three different carcinoma cell lines was carried out. For this purpose, MTT tests were performed. The MTT assay is a typical cell survival assay to evaluate cell viability in response to synthesized compounds. This is a colorimetric assay that measures the reduction of the yellow-coloured 3-(4,5-dimetylthiazol-2-yl)-2,5-diphenyl tetrazolium bromide (MTT) by the mitochondrial enzyme succinate dehydrogenase into a dark purple insoluble salt, formazan, which is exocytosed and precipitated *(Figure 23).* Since the reduction of MTT (which enters cells by endocytosis), can only occur in metabolically active cells, the intensity of the resulting purple colour correlates with cell viability.[54]

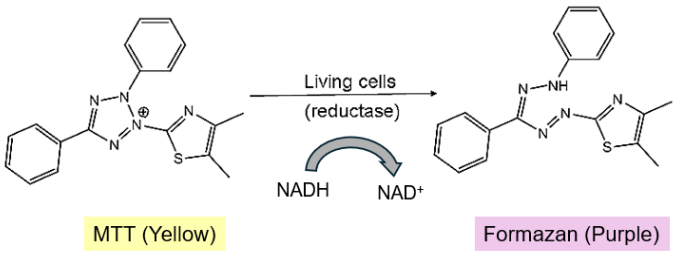

***Figure 23**. Mechanism of MTT reduction in Formazan salt.*

A549 (human lung adenocarcinoma) cells were cultured in Dulbecco's Modified Eagle Medium (DMEM) whereas A2780 (Human ovarian carcinoma) and A2780cis (Cis-platin resistant human ovarian carcinoma) cells were cultured in RPMI 1640. Culture media were supplemented with 1% Glutamine, 10% FBS and 1% Penicillin, Streptomycin and amphotericin B.

On the one hand, compounds with two depsipeptide chains were found to be biocompatible in all mentioned cell lines. Studies at 72 hours in A549 confirmed that biocompatibility is stable over time. The results of CH08-D, CH09-D and CH10-D are very similar between them. Here below the assays of CH08-D are shown as a representative example of the

[54] J. van Meerloo, G. J. L. Kaspers, J. Cloos, *Cell Sensitivity Assays: The MTT Assay.* In I. Cree, *Cancer Cell Culture. Methods in Molecular Biology,* Humana Press. Vol 731, Portsmouth, **2011**, pp. 237−245.

mentioned biocompatibility *(Figure 24).* Notice how the cell survival is maintained after 72 hours of incubation.

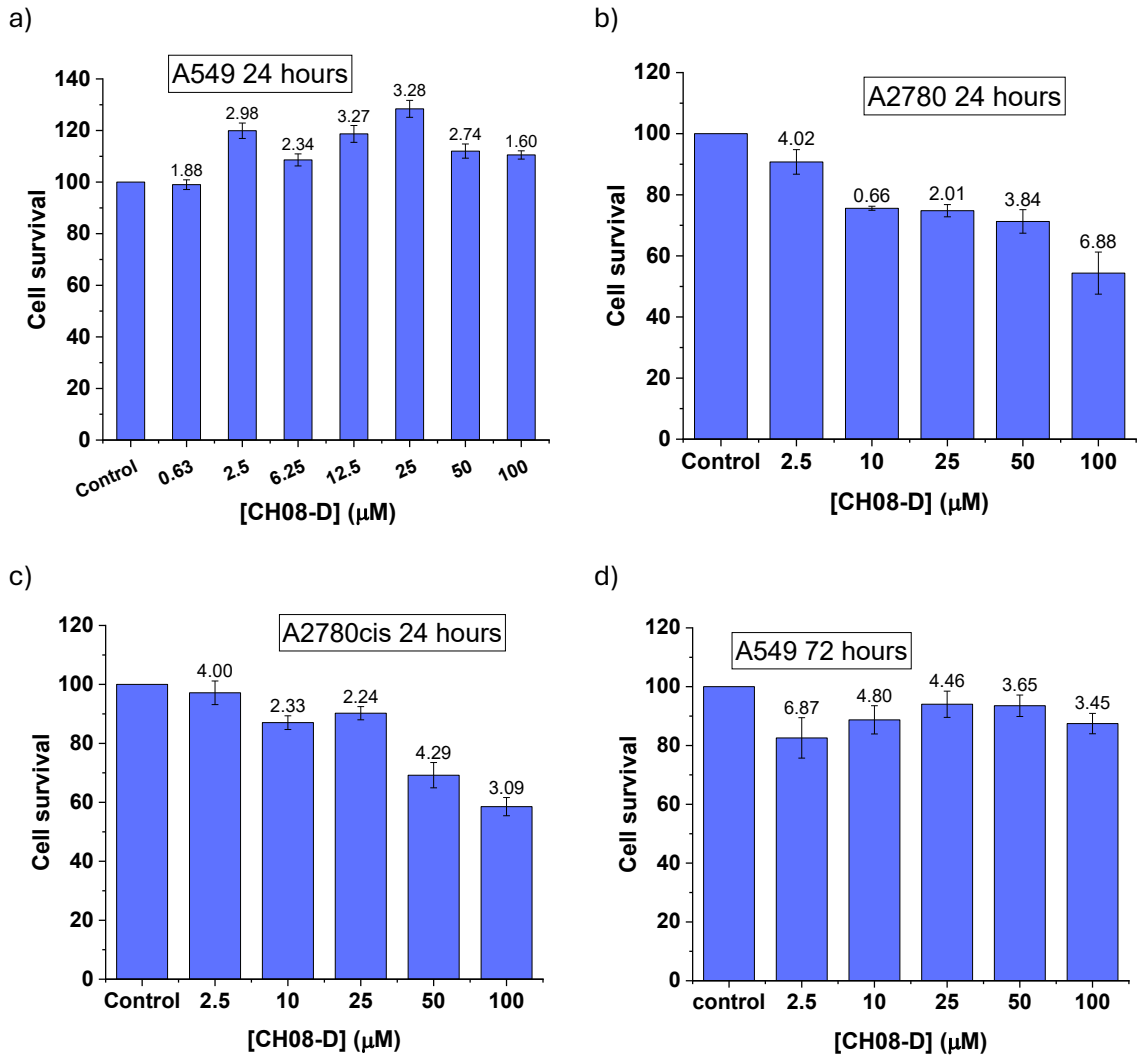

Figure 24. *Biocompatibility plots of CH08-D in (a) A549 for 24 h, (b) A2780 for 24 h, (c) A2780cis for 24 h (d) A549 for 72 h. Standard deviations (SD) are shown as percentages obtained from 3 independent experiments.*

On the other hand, compounds with a single depsipeptide sequence were found to be cytotoxic after 24 hours of incubation. It is believed that cytotoxicity is associated with the presence of the free terminal amino group of piperazine. This amine group can interact with some acidic groups of certain proteins inside the cells, thus resulting in an interference with some cellular process that ends with their apoptosis. It must be added that the cytotoxicity of the starting naphthaleneimides without any depsipeptide chain could not be performed because of their low solubility in the cell media, that leaded to their precipitation and atmospheric oxidation. Here the assays of CH12-D are shown as a representative example of the mentioned antiproliferative activity *(Figure 25).* Notice how the cytotoxicity increases after 72 hours.

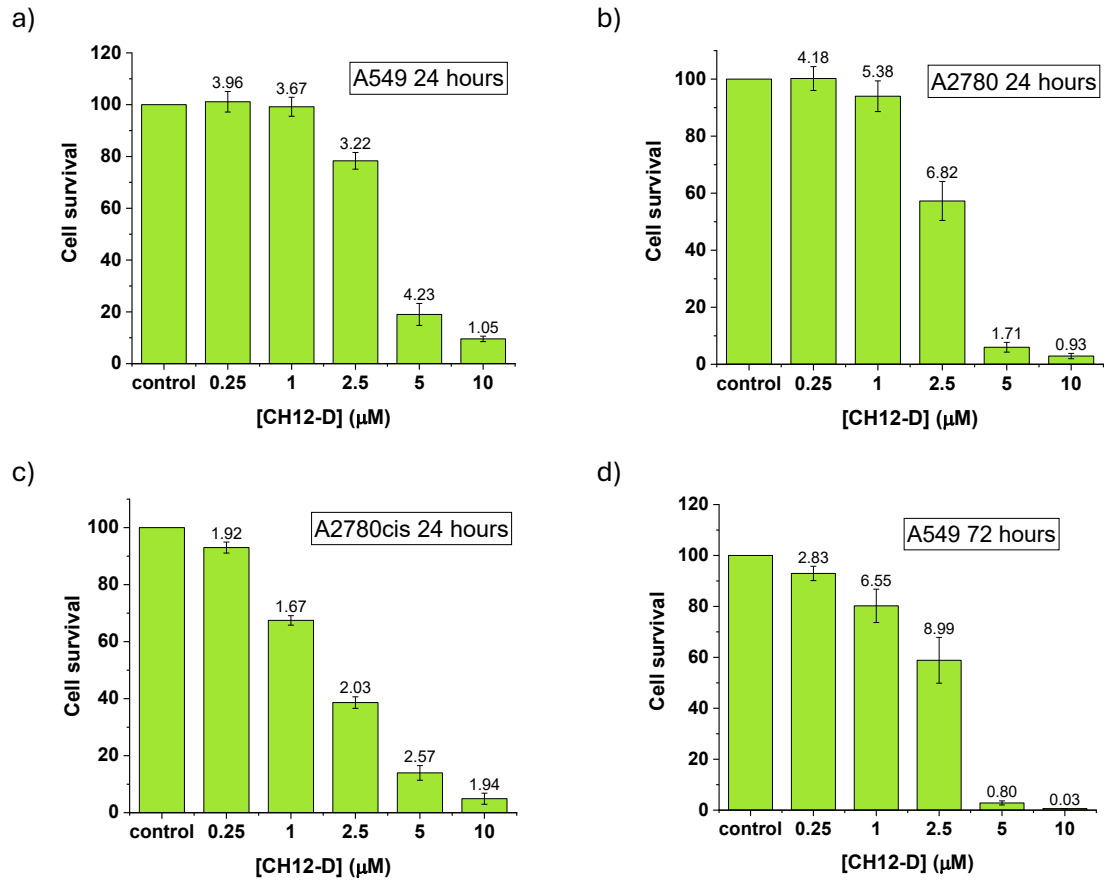

Figure 25. *Cytotoxicity plots of CH12-D in (a) A549 for 24 h, (b) A2780 for 24 h, (c) A2780cis for 24 h (d) A549 for 72 h. SD are shown as percentages obtained from 3 independent experiments.*

The half-maximal inhibitory concentration (IC_{50}) was calculated for all semifunctionalized compounds. It's a measure of the quantity of a drug is needed to reduce the cell survival by half. Thus, the IC_{50} in the three different carcinoma cell lines are shown in *Table 15.* Cis-diamminedichloroplatinum (II), (CDDP) is included as positive control.

Table 15*. The IC_{50} (μM) of deprotected compounds. Standard errors (SE) obtained from 3 independent experiments*

	A549 24 h	**A549 72 h**	**A2780 24 h**	**A2780cis 24 h**
CH11-D	6.1 ± 0.5	3.6 ± 0.7	4.4 ± 0.4	4.0 ± 0.3
CH12-D	3.8 ± 0.5	2.6 ± 0.1	2.4 ± 0.1	1.6 ± 0.1
CH16-D	12.3 ± 0.8	6.05 ± 0.2	4.6 ± 0.6	4.1 ± 0.3
CDDP	46.3 ± 3.9	4.6 ± 0.3	8.0 ± 0.9	29.8 ± 2.7

Notice that the most pronounced cytotoxicity is that of CH12-D, with a pyrimidine unit in its structure (2 nitrogen atoms), followed by CH11-D with a pyridine unit (1 nitrogen atom), and finally CH16-D, with a phenyl unit (no nitrogen atoms). It must be added that the IC_{50} decreases after 72 hours, confirming their dose- and time- dependent activity. It is also possible to compare the results with those of cisplatin (positive control), which is known to be a potential antitumoral drug. The results show that the studied compounds are even more cytotoxic than cis-platin, especially in ovarian carcinoma cells. So, these compounds (especially CH12-D) represent a competitive alternative to this popular drug. According to

the results, it is possible to modulate the NMIs' cytotoxicity depending on the number of depsipeptide chains bonded to the aromatic core. The presence of the second depsipeptide branch makes the compounds change from being highly cytotoxic to biocompatible.

10. SUPRAMOLECULAR STRUCTURES INCLUDING PREIMPLANTATION FACTOR

Once the compounds have been deprotected, it is possible to functionalise them by bonding a natural peptide, the preimplantation factor (PIF). The idea is to construct supramolecular species suitable to transport PIF into the cells. To achieve this, the bond between the studied compounds and PIF must be labile in the intracellular space, allowing its release in the target organelle of the cell. Hence, a structural modification of deprotected compounds was done, so they were bonded to a bicycloderivative with a highly reactive triple bond *(Figure 26, Structure A).* The preimplantation factor was also modified, and a terminal lysine of the PIF sequence bonded to an azide group was added *(Figure 26, Structure B).* Thus, a typical reaction in bioconjugation was performed. The supramolecular products *(Figure 26, Structure C)* are the result of an ordinary click reaction between the terminal azide group of the PIF-Lys-N_3 and the tensioned triple bond of the terminal bicycloderivative. It must be added that we made another supramolecular compound with a scrambled PIF *(Figure 26, Structure D,)*, in order to determinate if this modification on the PIF's natural structure has relevance in its activity inside the cells.

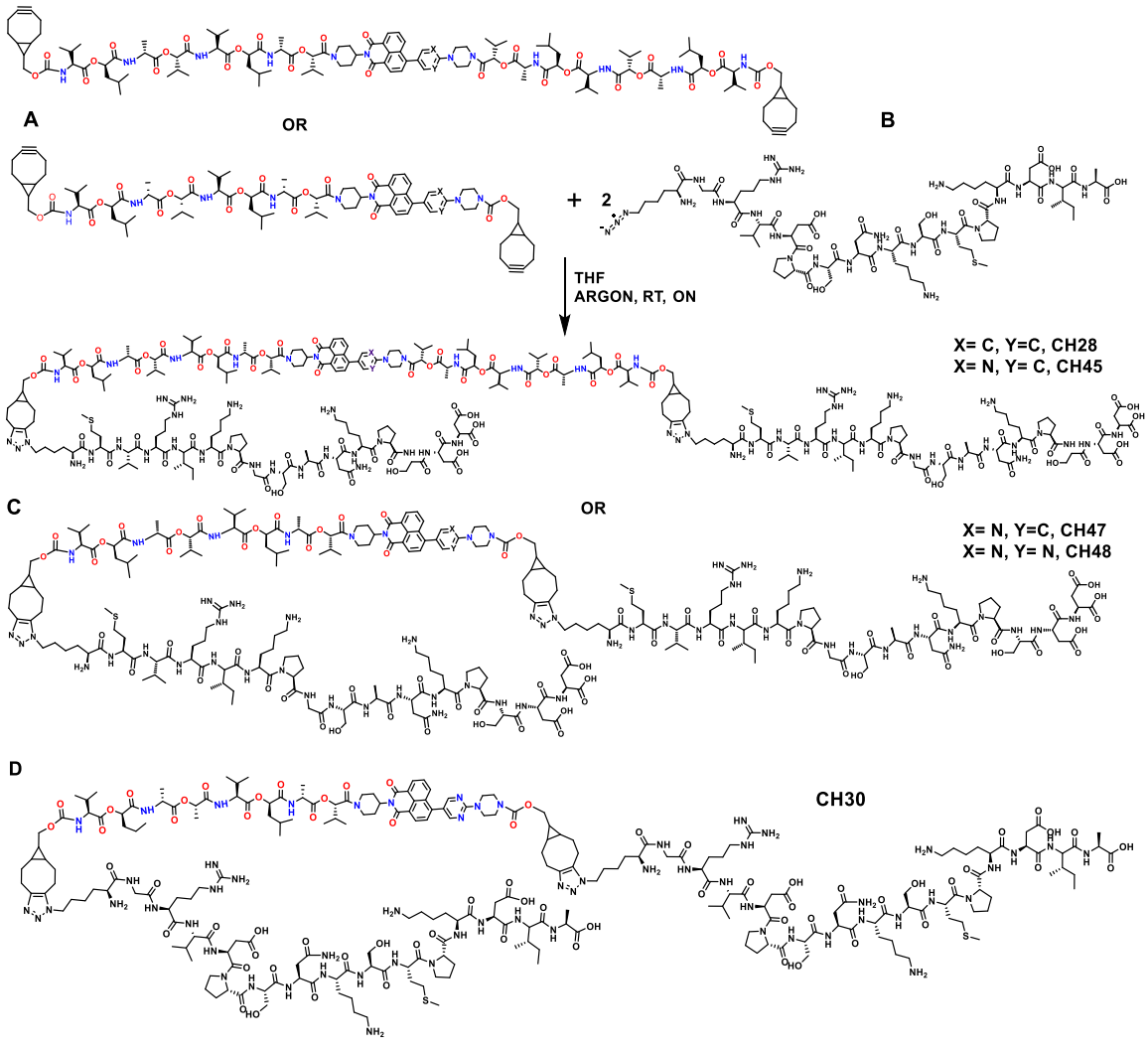

***Figure 26**. Click reaction scheme to obtain supramolecular structures of AIEgens and PIF.*

In *Figure 26*, it is observed that both type of compounds with two depsipeptide branches and those with a single branch have been bonded to PIF. The next step is to study whether it changes the biocompatibility of these new supramolecular species and their target organelle. First, we studied the fluorescence properties of these compounds and the formation of nanoparticles in mixtures of THF and high-water percentages. As a representative example, in *Figure 27* some nanovesicles formed by CH45 are shown.

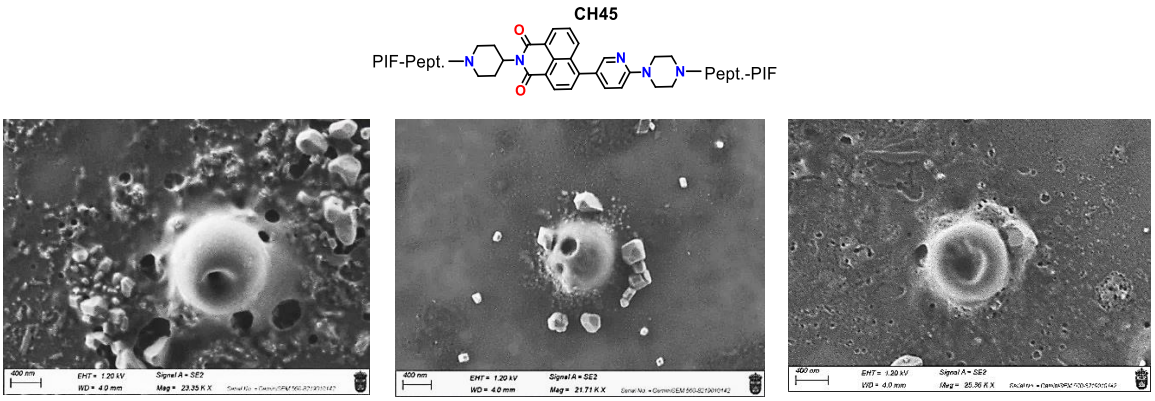

Figure 27. *FESEM images of CH45 in THF-H_2O at 80% w.r.*

10.1. STUDY OF PIF-BONDED SUPRAMOLECULAR SPECIES INSIDE CELLS

The methodology for determining the compounds' destination within the cells is the same as that followed in the previous section. The ER was stained with its specific dye (ER Tracer Blue) and confocal laser scanning microscopy was used, revealing that these supramolecular compounds, like deprotected species did, go to the endoplasmic reticulum. Stimulated emission depletion (STED) super-resolution microscopy showed that the size of the nanoparticles inside the cells matched that found by imaging microscopy, so they were integrated into living cells. In *Figure 28* the results for CH28 (two depsipeptide chains) and CH48 (one depsipeptide chain) are shown. The studied cell line is A549 too.

a)

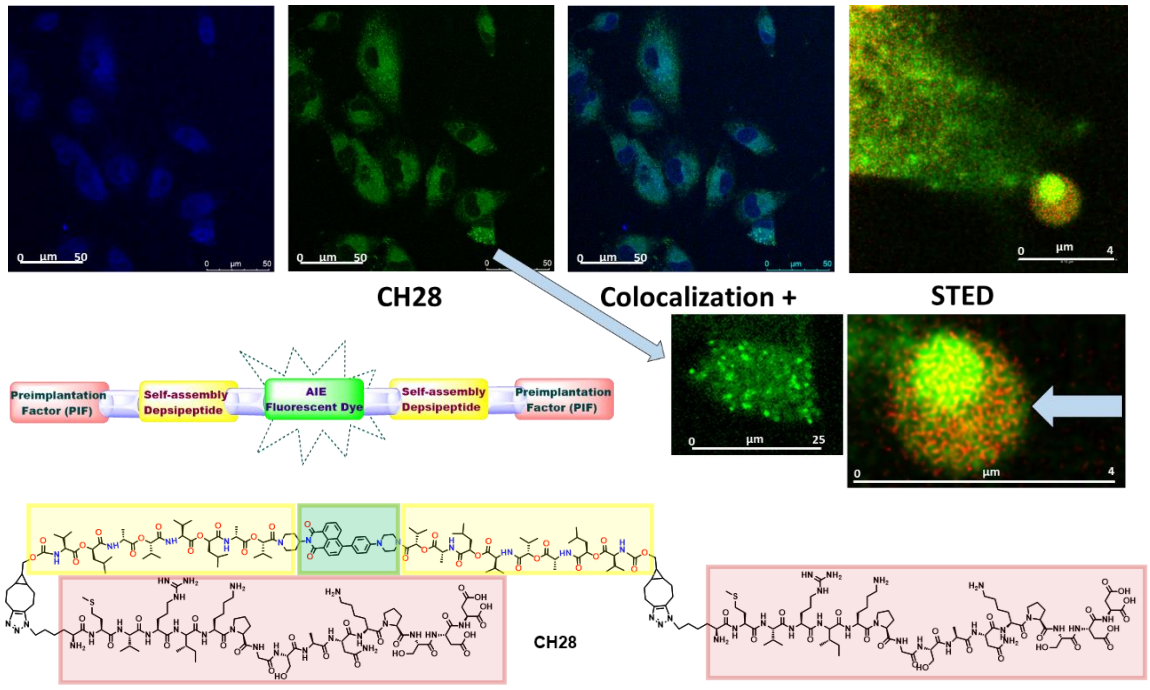

b)

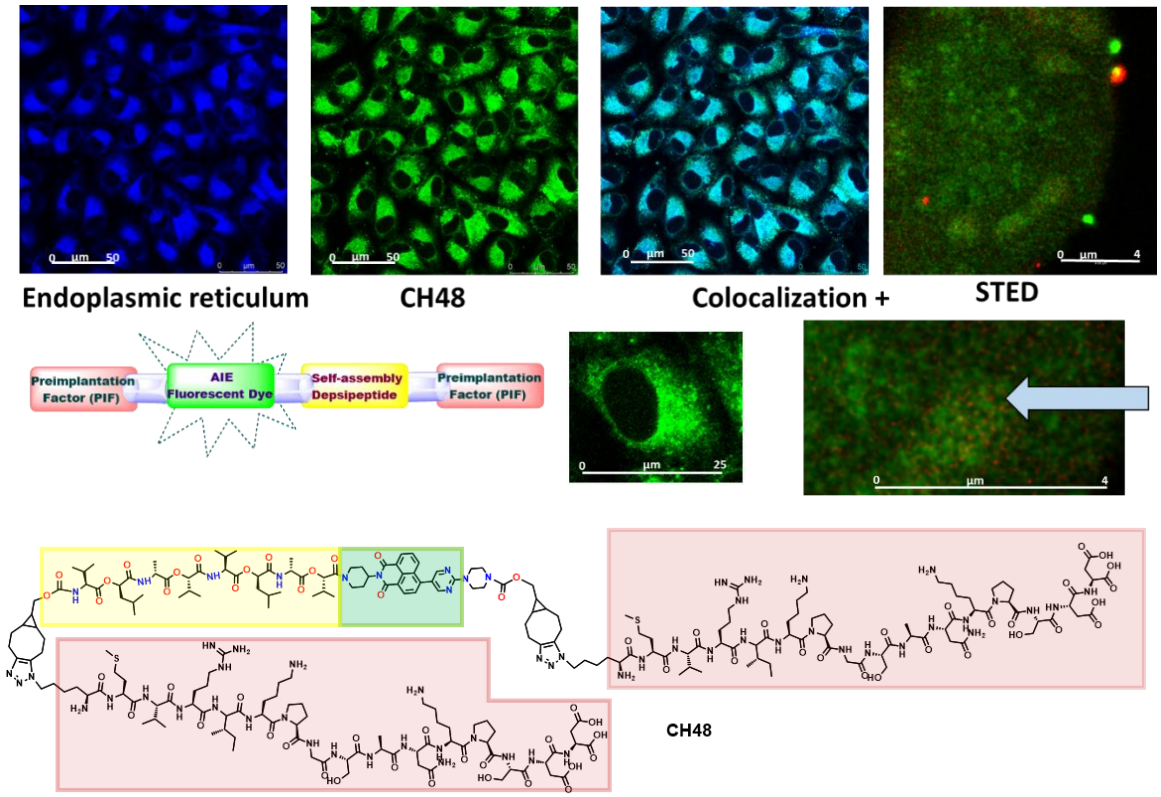

Figure 28. *Confocal laser scanning microscopy (CLSM), STED super-resolution microscopy and structures of (a) CH28 and (b) CH48.*

The concentration of compounds for CLSM was 1μM and λ_{exc} = 470 nm and λ_{em} = 670 nm. To evaluate the spatial overlap between the two signals, colocalization coefficients were calculated with ImageJ. For CH28, the analysis yielded the next results: Pearson's correlation coefficient (Rr, no threshold) was 0.63, suggesting a moderate positive correlation between the intensity distributions of CH28 and the ER probe. Manders' coefficients were also calculated: M1 (CH28 overlapping the ER probe) was 0.692, and M2 (ER probe overlapping CH28) was 0.642. These values indicate that 69.2% of the CH28 signal coincides with the ER probe, while 64.2% of the ER probe signal overlaps with CH28.

For CH48, the analysis yielded similar findings: Pearson's correlation coefficient (Rr, no threshold) was 0.68, also reflecting a moderate positive correlation with the ER probe. The Manders' coefficients were M1 (CH48 overlapping the ER probe), 0.667 and M2 (ER probe overlapping CH48), 0.586, meaning that 66.7% of the CH48 signal was located in areas containing the ER-specific probe, while 58.6% of the ER probe signal coincided with CH48.

10.1.1. Biocompatible vs antiproliferative species

To determine the biocompatibility of the compounds, MTT assays were performed, as it was done previously with deprotected species. Cell cultures of lung tumor cells A549, human ovarian carcinoma cell line A2780 (cisplatin-sensitive) and A2780cis (cisplatin-resistant) were carried out following the same protocol described in the previous section, with the same growth media and antibiotics.

The study revealed that compounds with two depsipeptides and two PIF units were biocompatible after 24 and 72 hours. This was expected since PIF is a natural peptide, and the two-branch precursors were also noncytotoxic. The labile bond with the PIF breaks as time goes by, hence, once it is released inside the cell, the remainder structure is a biocompatible AIEgen. In *Figure 29* the assays of CH28 are shown as a representative example of the mentioned biocompatibility. Notice how the cell survival is maintained after 72 hours of incubation in A549.

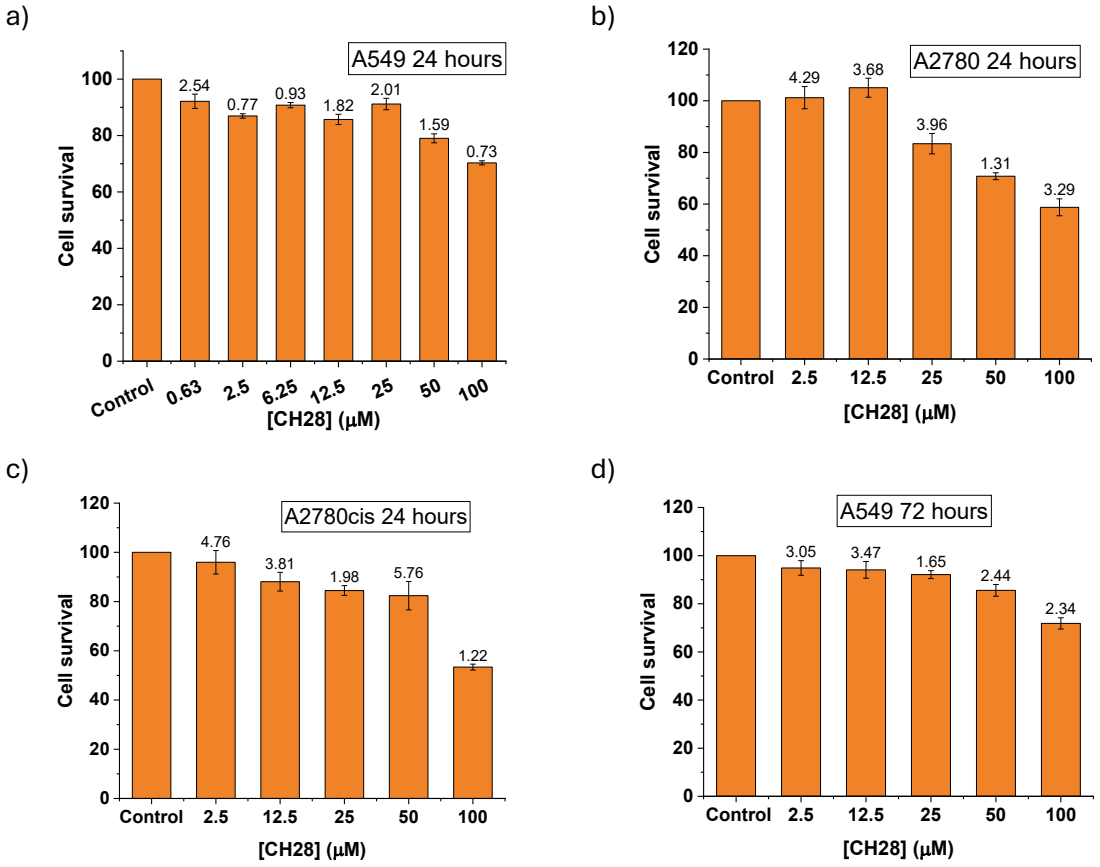

Figure 29. *Biocompatibility plots of CH28 in (a) A549 for 24 h, ((b) A2780 for 24 h, c) A2780cis for 24 h d) A549 for 72 h. Standard deviations (SD) are shown as percentages obtained from 3 independent experiments.*

In contrast, PIF derivatives with a single depsipeptide branch were slightly cytotoxic after 24 hours of incubation (IC_{50} 55−85 μM) in A549 cells, while after 72 hours there was a noticeable increase in cytotoxicity (IC_{50} 23−49 μM). The cytotoxicity of these compounds was also significantly higher (IC_{50} 13−46 μM) in the ovarian cancer series (A2780/A2780cis). These results were also expected since the starting AIEgens were cytotoxic, so it is probable that PIF units act as a protective envelope, and as time goes by, the labile bond with this active peptide breaks, and the cytotoxic AIEgen is released inside the cell. This is why these compounds exhibit time-related cytotoxicity. Here the assays of CH48 are shown as a representative example of the mentioned time-dependent cytotoxicity *(Figure 30)*. Notice how the cytotoxicity increases after 72 hours.

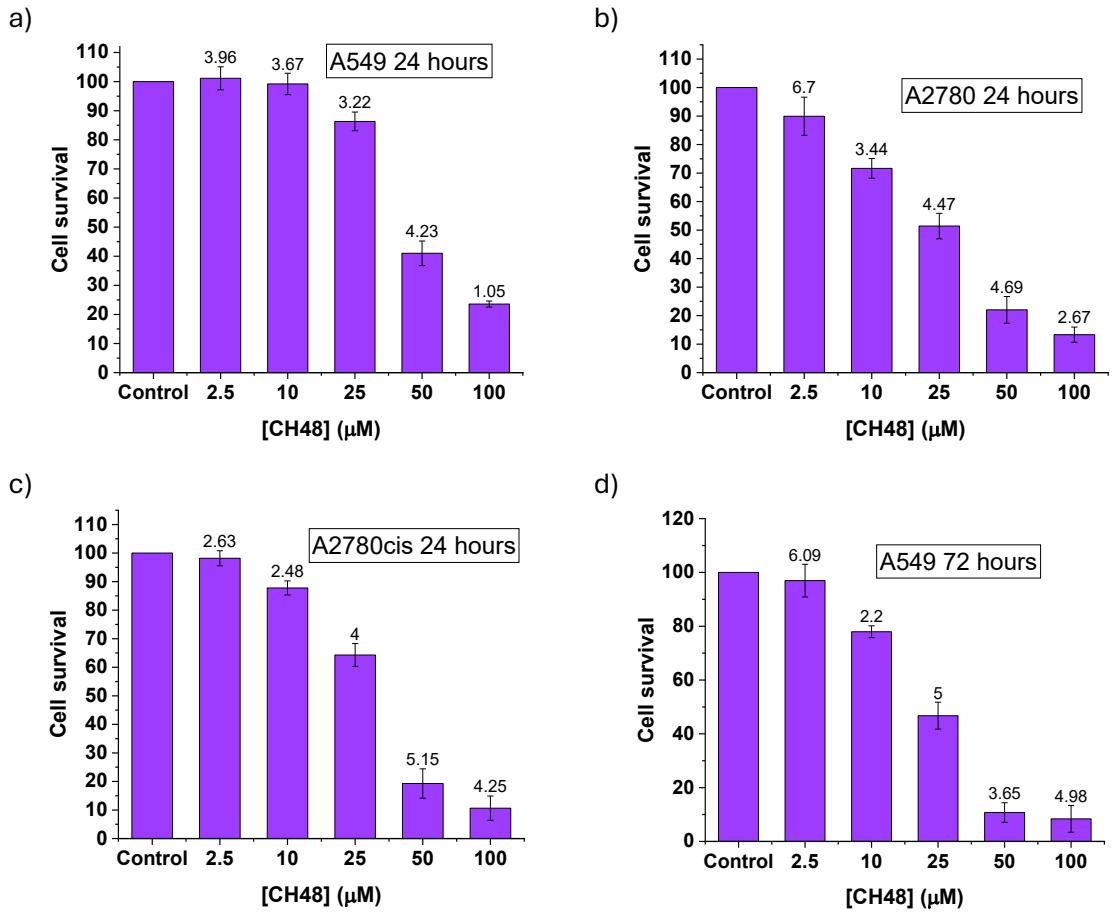

Figure 30. *Cytotoxicity plots of CH48 in (a) A549 for 24 h, (b) A2780 for 24 h, (c) A2780cis for 24 h (d) A549 for 72 h. Standard deviations (SD) are shown as percentages obtained from 3 independent experiments.*

The IC_{50} of the different PIF derivatives are shown in *Table 16*. Cis-diamminedichloroplatinum (II), (CDDP) is included as positive control.

Table 16*. IC_{50} (μM) of PIF derivatives. SE obtained from 3 independent experiments*

	A549 24 h	**A549 72 h**	**A2780 24 h**	**A2780cis 24 h**
CH28	>100	>100	>100	>100
CH45	>100	>100	>100	>100
CH47	84.5 ± 9.1	48.5 ± 2.1	13.1 ± 0.6	45.5 ± 3.4
CH48	54.8 ± 2.9	22.7 ± 2.6	20.9 ± 1.2	29.5 ± 0.8
CH30	>100	43.6 ± 2.3	>100	>100
CDDP	46.3 ± 3.9	4.6 ± 0.3	8.0 ± 0.9	29.8 ± 2.7

Considering all the IC_{50} values shown in the table above, we can state that is possible to use those biocompatible species (CH28, CH45) to transport sensitive drugs such as PIF which easily degraded in biological environments. Once the PIF is delivered, the remainder structure is noncytotoxic and would be phagocyted or eliminated as waste material by the cells.

On the other hand, some AIEgens, (CH47, CH48) act as Trojan horses. The cytotoxic species have a physiologically innocent outer coating that allows them to remain in cells for a while without killing them. However, over time, this envelope (PIF) is released, delivering the cytotoxic cargo that promotes cell apoptosis. In other words, it acts like a Trojan horse that initially appears innocent but later causes cell death.

Last, but not least, as reported at the beginning of this section, it was also synthesized a compound (CH30) that combines an AIEgen with a single depsipeptide branch (CH12-D) with a biologically inactive PIF unit, the PIF scramble. It was surprising to see that this compound does not exhibit the same antitumoral activity as its analogues with active PIF (CH47, CH48). CH30 is biocompatible after 24 hours and shows mild cytotoxicity after 72 hours. It is likely that, since PIF scramble has no biological activity, it does not interact within cells and is not released in the same way nor at the same rate as natural PIF does, thus proving that the physiological action of the natural PIF is necessary to exert activity in cells.

11. CHANGE ON THE GEOMTERY OF THE DYE'S CORE

From the findings obtained from these studies, we have gained a comprehensive understanding of how to precisely control the environmental and chemical conditions necessary for the successful formation of nanovesicles. Additionally, we have developed the ability to regulate how substances can pass through cell membranes and remain inside them and to manage the potential toxic effects these materials have on living cells.

The development of a reliable proof of concept has allowed us to predict the type of nanostructures formed. As a practical application of this, we have modified the molecular structure of the naphthalimide's core, altering its geometry and then incorporating depsipeptide chains. These changes have led to the successful formation of nanovesicles that closely resemble those produced in previous trials.

11.1. SYNTHESIS OF META-SUBSTITUTED AIE-GENS

In the previous studies, the central dye was substituted at the 4-position of the naphthalene ring, forming para-substituted dyes. However, the functionalization of the naphthalenemonoimide at the 3-position was then performed, leading to meta-substituted dyes. Thus, a meta-substituted NMI carrying a pyridine unit in its structure and with deprotected piperazine and piperidine groups *(Figure 31, Structure A)* was linked to two depsipeptide chains, giving rise to a new hybrid AIEgen *(Figure 31, Structure C)*. The synthesis' conditions and steps followed are the same to those described in the section 4 to obtain para-substituted hybrids.

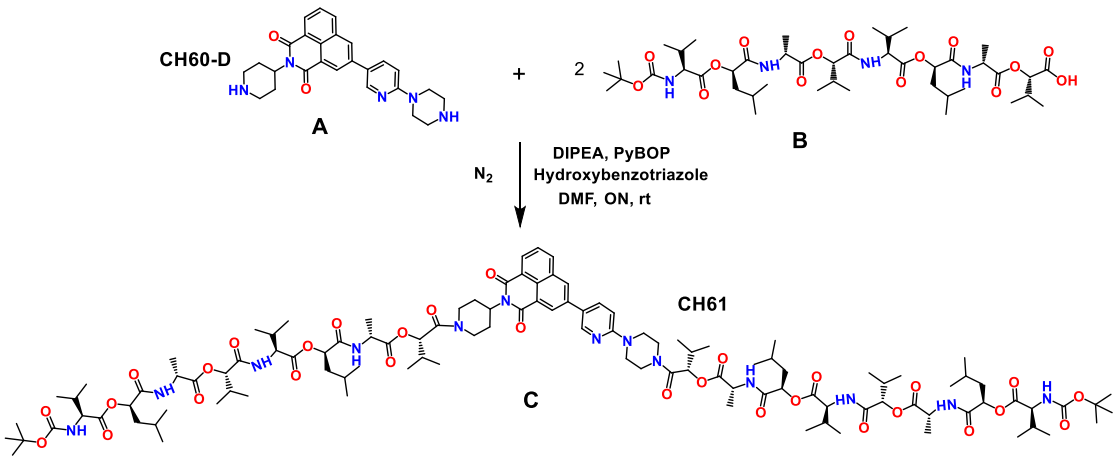

Figure 31. *Scheme reaction to obtain a meta-substituted AIEgen hybrid with two depsipeptide chains (CH61).*

11.2. FLUORESCENCE PROPERTIES OF THE META-SUBSTITUTED AIEGEN

11.2.1. Solvatochromism assays

Solvatochromism studies were performed under the same conditions as those of para-substituted compounds *(Figure 32)*. As expected, the results were very similar to those obtained for its analogue, CH08. Maximum emission was observed in low-polarity solvents such as toluene and diethyl ether, due to the interactions of the aliphatic regions of the molecule with the solvent, which prevents aggregation and favours fluorescence in solution. It is worth mentioning that this compound is partially soluble in water, and it is certainly emissive there. Finally, a bathochromic shift occurs when the solvent polarity increases as with its para-substituted analogues. The same explanations as those given in section 5 for two-branch depsipeptide compounds applies to this compound.

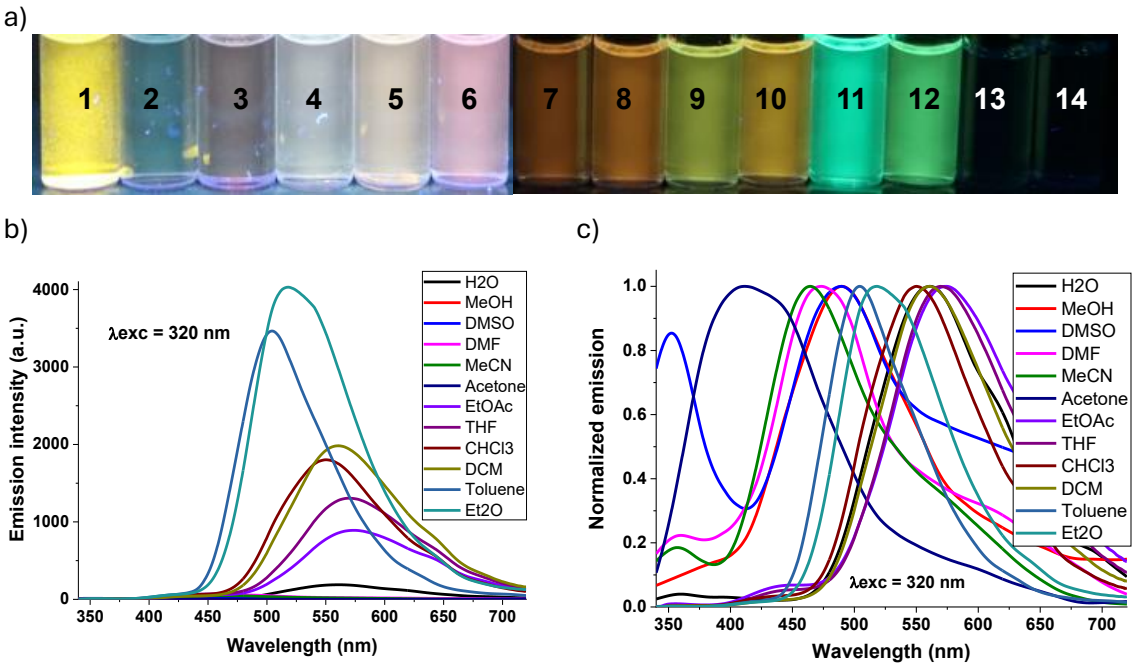

Figure 32. *(a) Solvatochromism assays of CH61 under UV light (366 nm). (b,c) Emission spectra (λ_{exc} = 320 nm, C = 10^{-5} M).*

11.2.2. Water-organic solvent ratio assays

As it was done with the para-substituted compounds, we studied the fluorescence of CH61 in mixtures of THF and water and how it changes as the polarity of the mixture increases *(Figure 33)*.

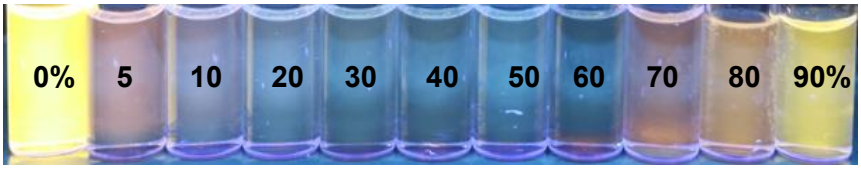

Figure 33. *THF-Water ratio assays of CH61 (C=10^{-5} M) using UV light (366 nm).*

It is observed that above 70% w.r. the colour of the emitted light changes from blue to orange. This fact agrees with the formation of aggregates at high water percentages and the subsequent energy stabilization. AIE effect takes place above 70% w.r., however, it is not very noticeable; thus, the assay was repeated in a mixture of MEOH and water *(Figure 34)*.

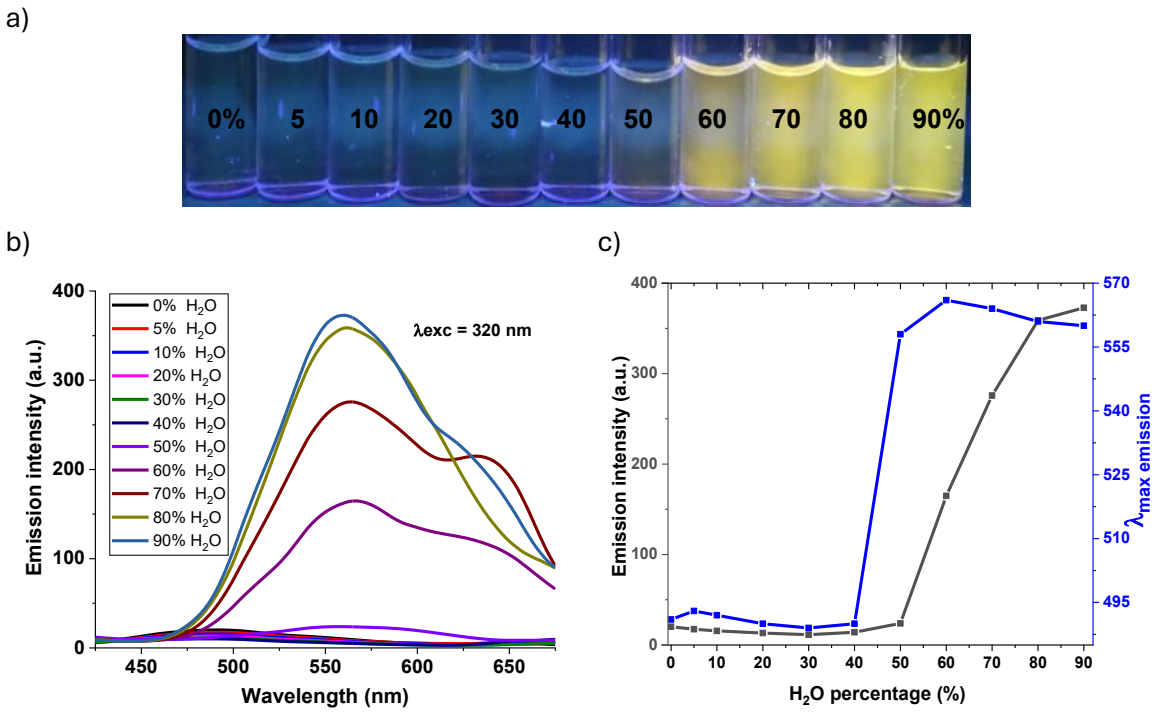

Figure 34. (a) *MeOH-Water ratio assays of CH61(C=10^{-5} M) using UV light (366 nm). (b) Emission intensity of CH61 at different w.r. λ_{exc} = 320 nm. (d) Emission intensity (grey) and λ_{max} emission (blue) at same conditions.*

With this new solvent, the formation of aggregates takes place at lower water ratios. The change in the colour of the emitted light (from blue to yellow) is observed above 60 % w.r. The AIE effect is corroborated in *Figure 34b,* where it is observed that the highest emission intensity takes place at 90%w.r. In *Figure 34c* we can see how the grey curve (emission intensity) suddenly increases above 60% w.r. due to the formation of aggregates.

11.3. NANOVESICLES FORMATION

Once we saw the conditions where the AIE effect occurred, it was verified by field emission scanning electron microscopy that this meta-substituted compound, like its para-substituted analogue (CH08), forms nanovesicles in mixtures of THF and high-water ratios *(Figure 35)*.

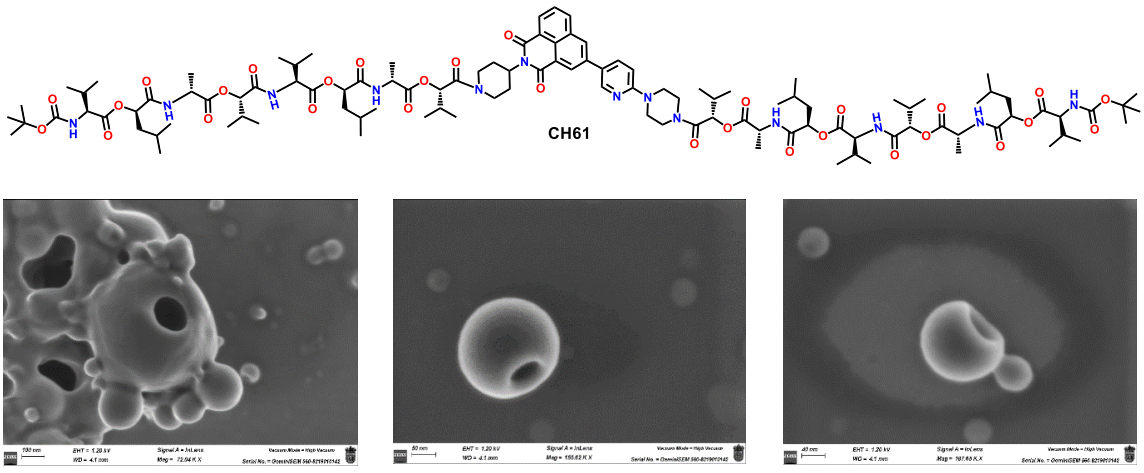

Figure 35. *FESEM images of CH61 in THF-H_2O: (left) 80% w.r. (centre and right) 90% w.r.*

Since the AIE effect also appears in mixtures of MeOH and water, they were also imaged by FESEM, finding nanovesicles as well, but in this case, at lower water percentages *(Figure 36)*.

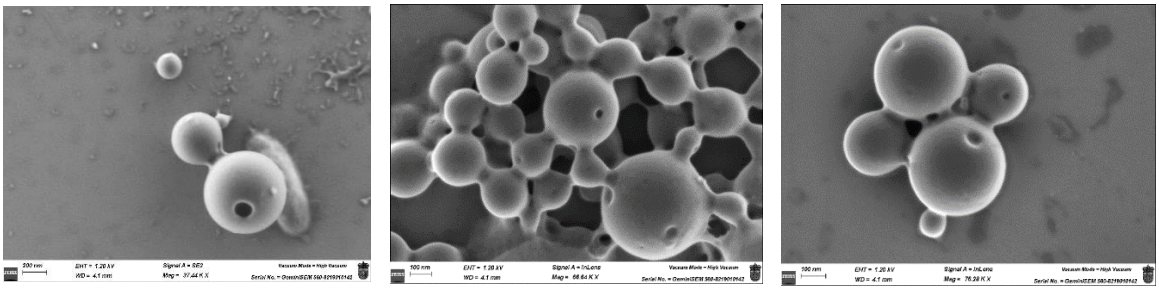

Figure 36. *FESEM images of CH61 in MeOH-H_2O: (left) 50% w.r. (centre and right) 60% w.r.*

11.4. META-SUBSTITUTED DEPROTECTED SPECIES

As done with the para-substituted compounds, the tert-butoxycarbonyl groups of the depsipeptide chain were removed, thus obtaining CH61-D *(Figure 37)*. The same synthesis procedure described in section 9.1 was followed, using trifluoroacetic acid in chloroform.

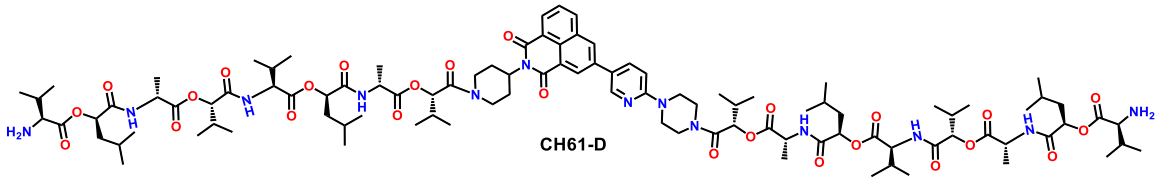

Figure 37. *Structure of the deprotected species CH61-D.*

This resulting species, with two free terminal amines, also forms nanovesicles in mixtures of THF and high-water content *(Figure 38)*.

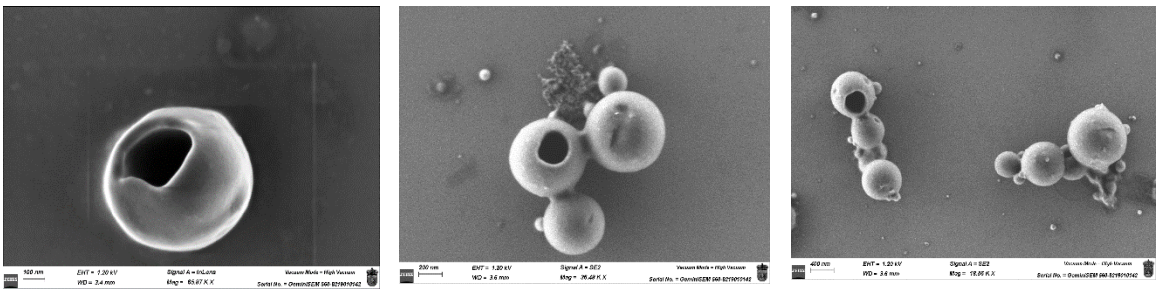

Figure 38. *FESEM images of CH61-D in THF-H_2O: (left) 80% w.r. (centre and right) 90% w.r.*

This meta-substituted species has been shown to exhibit the same behaviour as its para-substituted analogue. This deprotected species will probably be biocompatible due to the presence of two depsipeptide chains, as its analogue CH08 was. Thus, compounds with this geometry can be likely used for the same applications as the para-substituted species.

This shows that nanovesicles formation depends both on the specific aggregation of the NMI, giving rise to the aggregation-induced emission phenomenon, and on its attachment to a depsipeptide chain, which favours non-linear stacking, as shown by molecular dynamics simulation calculations. The presence of both factors leads to nanovesicle formation, and the two aspects are shared by para- and meta-substituted NMIs.

12. CONCLUSIONS

In this chapter, a novel strategy has been successfully validated for the formation of hollow organic nanovesicles through a bottom-up approach, based on the self-assembly of hybrid systems composed of depsipeptide chains and aggregation-induced emission luminogens. These AIEgens serve a dual function in this system: first, they act as essential building blocks that contribute to the formation of the vesicle structure, and second, they work as fluorescent indicators, providing visual evidence of the nanovesicle's formation and structural characteristics.

Initially, solvatochromism studies and Lippert-Mataga analysis were performed to evaluate the sensitivity of the synthesized compounds to solvent polarity. These studies revealed that pyridine-substituted derivatives exhibited the highest sensitivity to changes in polarity, while phenyl derivatives showed the least. Furthermore, the aggregation-induced emission effect (responsible for vesicle formation) was observed in mixtures of THF and water with water contents above 70%.

Once this AIE behavior was identified, imaging techniques such as atomic force microscopy, field emission scanning electron microscopy, and transmission electron microscopy confirmed the formation of spherical, hollow nanovesicles. These observations were further supported by molecular dynamics simulations, which showed that the NMI cores tend to stack with a slight curvature, favoring vesicle formation. The flexibility provided by the depsipeptide chains plays a key role in this process, facilitating the angular stacking of the NMI chromophores and stabilizing the supramolecular architecture. It must be mentioned that dynamic light scattering analyses showed that the vesicles' diameter increases significantly upon removal of the tert-butoxycarbonyl protecting group from the compounds.

Complementary studies revealed that the assembled nanostructures display optical activity. Circular dichroism measurements exhibited positive signals, indicating preferential absorption of right-handed circularly polarized light. Meanwhile, CPL experiments revealed left-handed polarized emission when the compounds were excited with unpolarized light, further confirming the chiral nature of the compounds.

On the other hand, biological studies showed that these nanovesicles are internalized by human cancer cells and localize predominantly in the endoplasmic reticulum. Interestingly, their biological activity is strongly dependent on their molecular design. When the fluorescent dye is bonded to two depsipeptide chains, the nanovesicles display excellent biocompatibility, showing no harmful effects to the cells. Hence, they have been shown to effective nanocarriers of the preimplantation factor. In contrast, the compounds composed of only one depsipeptide chain exhibit high cytotoxicity. Actually, the effectiveness in the promotion of apoptosis equalled or even surpassed that of cisplatin, a widely used chemotherapeutic agent, across various tested cancer cell lines. Notably, this cytotoxic effect can be modulated by incorporating physiological envelopes such as PIF, opening the door to use these supramolecular species as Trojan horses for cancer cell treatment research.

This ability to modulate biological activity and therapeutic impact through minor adjustments in chemical composition or cargo loading represents a significant advancement in biomedicine. It opens up a wide array of potential applications, particularly in the fields of targeted drug delivery, cancer therapy, and intracellular diagnostics. The ideal next step would be bonding the depsipeptide-AIEgen hybrids to specific antibodies, nucleotide or protein sequences enabling them to recognize target cells and to deliver selectively their content.[55]

Finally, a structural modification of the AIE dye component was explored by shifting the substitution pattern of the NMI unit from para- to meta-position. Despite this change in

[55] S. Mitragotri, P. Stayton, *MRS Bull.* **2014,** *39* (*3),* 219−223.

geometry, the new hybrid compounds were still able to self-assemble into stable nanovesicles in water-rich THF mixtures, indicating that they may also serve as effective and robust nanocarriers [56]

[56] C. Hernando-Muñoz, A. Revilla-Cuesta, I. Abajo-Cuadrado, C. Andreini, T. Torroba, N. Busto, D. Fernández, G. Perdomo, G. Acosta, M. Royo, J. Gutierrez Reguera, A. Spinello, G. Barone, D. Black, R. Pal, *ACS Appl. Mater. Interfaces* **2025**, *17 (6)*, 10097−10107.

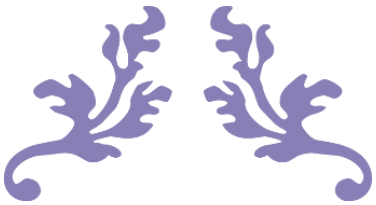

CHAPTER 2A

Short amino acid sequences on Aggregation-Induced Emission Luminogens

ABSTRACT

This chapter explores the design, synthesis, and self-assembly behaviour of a series of aggregation-induced emission luminogens functionalized with short amino acid chains. Concretely, NMI cores were conjugated to different sequences, composed of valine, alanine and certain synthetic amino acids in varying combinations and lengths. Thus, it was studied how the number and identity of amino acids influence the formation of nanostructures in aqueous mixtures. The results revealed that there is a critical transition in self-assembly behaviour depending on the size of the peptide bonded to the dye core; the larger and the more complex amino acids are, the sharper nanovesicles observed. This chapter confirms that the peptide's size has a noticeable effect on π-π interactions, playing this a key role in driving vesicle formation. The findings provide new insights into the relationship between molecular design and supramolecular organization, useful in the development of new nanomaterials for bioimaging and drug delivery. The Supporting Information of this chapter includes the structural characterization of all intermediates and final compounds, as well as a great variety of fluorescence characterization and microscopy images.

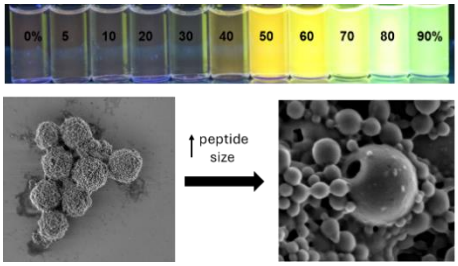

Figure 1. *Structural transition as the peptide size increases. From ordinary aggregates to beautiful nanovesicles.*

1. INTRODUCTION

It is known that aggregation-induced emission is associated with the formation of nanoaggregates, and some studies confirm that amino acids attached to dyes also favour this phenomenon and the consequent formation of nanostructures. Amino acids serve as versatile building blocks in the design of self-assembling systems due to their biocompatibility, chirality, and capacity for hydrogen bonding. Their side chains impart tuneable hydrophobicity/hydrophilicity and steric properties to molecular constructs, influencing the morphology and stability of aggregates.[1] For instance, l-phenylalanine-appended naphthalimide derivatives have been shown to self-assemble into spherical nanoparticles exhibiting green fluorescence due to AIE.[2] Furthermore, the conjugation of cyclic dipeptides to naphthalimide derivatives has been reported to induce AIE, facilitating the detection of phenolic drugs. This highlights the role of peptide structures in modulating the photophysical properties of dye conjugates.[3] Recent studies have also explored the controlled self-assembly of tyrosine derivatives doped with various amino acids, leading to the formation of full-colour fluorescent nanomaterials. The inclusion of different amino acids enabled precise modulation of the chemical structure and optical properties of the resulting chromophores, resulting in broad-spectrum fluorescence emissions through AIE.[4]

It must be added that hydrophobic residues (i.e. valine, alanine) enhance the tendency of molecules to associate through the hydrophobic effect, while polar or charged residues (e.g., glutamic acid, lysine) influence solubility and electrostatic interactions.[5] Some studies of supramolecular peptide assemblies (only amino acids are combined here) revealed that the size and identity of the peptide sequence determine their supramolecular architecture.[6] Thus, depending on the nature of the residues, a type of interaction will be favoured (hydrogen bonding, electrostatic or hydrophobic), giving rise to a wide variety of

[1] S. Zhang, *Nat. Biotechnol.* **2003,** *21* (10), 1171−1178.
[2] P. Choudhury, K. Das K, P. K. Das, *Langmuir* **2017,** *33* (18), 4500−4510.
[3] C. Balachandra, T. Govindaraju, *J.Org. Chem.* **2020,** *85* (3), 1525−1536.
[4] Y. Shen, Y. Sun, Y. Liang, X. Xu, R. Su, Y. Wang, W. Qi, *Nanoscale Horiz.* **2025,** *10,* 158−164.
[5] R.Qing, S. Hao, E. Smorodina, D. Jin, A. Zalevsky, S. Zhang, *Chem Rev.* **2022,** 122 (18), 14085−14179.
[6] X.Yan, P. Zhu, J. Li, *Chem. Soc. Rev.* **2010,** *39* (6), 1877–1890.

nanostructures ranging from nanotubes, beta sheets or spheres.[7] It can therefore be stated that short-chain peptides have a natural tendency to form nanostructures by themselves. Therefore, their binding to NMIs have a structural effect on these dyes.

In the previous chapter, molecular dynamics simulation studies revealed that the π-π stackings between the aromatic rings of naphtalenemonoimides attached to a depsipeptide chain are not entirely linear but rather exhibit certain curvature. This curvature favours the growth of aggregates in the form of spherical nanoparticles. Furthermore, the presence of the depsipeptide chain not only supports self-assembly but also provides flexibility to the structure, allowing the spheres to be hollow rather than solid. Hence, from these findings, we sought to evaluate how the presence of specific amino acid sequences shorter than the depsipeptide, affected the stacking of the dye rings. That is, we wanted to discover at what peptide's size the system is sufficiently flexible to turn from amorphous aggregates to well-defined vesicular nanostructures.

The depsipeptide of the previous chapter was made from amino and hydroxy acids with hydrophobic side chains: valine, alanine and leucine. So, in aqueous media, these side chains tend to assembly between them by hydrophobic interactions. Hence, it is suggested that the bonding of amino acids with hydrophobic moieties will favour the nanovesicles formation. In this chapter we will use alanine, valine and other non-natural amino acids with aliphatic regions and double or triple bonds, which are highly hydrophobic, with alternating chirality between adjoining aminoacids to maintain the intermolecular interactions that are characteristic of natural depsipeptides and facilitated the formation of hollow nanovesicles described in the last chapter.

This chapter will contribute to the broader understanding of how amino acid conjugation affects the self-assembly and photophysical properties of aromatic dyes, paving the way for the design of advanced functional nanomaterials.

2. OBJECTIVES

The primary objective of this chapter is to investigate how the molecular design of amino acid-conjugated dyes influences their self-assembly behaviour and the formation of nanostructures in aqueous environments. To achieve this, the study focuses on the following specific goals:

- To design and synthesize a series of AIEgens based on naphthalenemonoimide (NMI) cores functionalized with short peptide sequences composed of both natural (e.g., valine, alanine) and synthetic unsaturated amino acids of alternated chirality.
- To explore the role of amino acid identity and sequence length in modulating the supramolecular self-assembly of the NMI-peptide conjugates.
- To characterize the morphology and structural features of the self-assembled aggregates formed in aqueous mixtures, with particular emphasis on nanovesicle formation.
- To elucidate the influence of peptide chain complexity on π-π stacking interactions and stablish the critical peptide size threshold at which the system transitions from disordered, amorphous aggregates to ordered, vesicle-like nanostructures. Also considering the role of hydrophobic side chains in the vesicle formation.
- To establish structure-function relationships between peptide design and nanomaterial architecture, aiming to provide insight into rational design principles for future applications in bioimaging and drug delivery systems.

[7] L. A. Abramovich, E. Gazit, *Chem. Soc. Rev.* **2014,** *43*, 6881−6893.

3. SMALL NMI DERIVATIVES: D-ALANINE OR L-VALINE UNITS

First, NMI derivatives linked to isolated units of S-valine or R-alanine were synthesized. The resulting structures, whether mono- or bifunctionalized ones, will be intermediates for the obtention of bigger amino acid-bonded structures.

This synthesis starts from an NMI, either completely deprotected or semi-protected with a Boc protecting group. So, the mechanism consists in the nucleophilic attack of the free terminal amino groups of the NMI, to the carboxylic acid group of alanine or valine *(Figure 2).* For the reaction to work, a hindered amine, such as diisopropylethylamine (DIPEA), is added to the mixture to promote deprotonation of the carboxylic acid and activate it. To favour the reaction, the electropositivity of the carbonyl group is also increased by the addition of activating groups such as PyBOP and hydroxybenzotriazole (exact quantities of reagents are described in the Supporting Information of chapter 2A.)

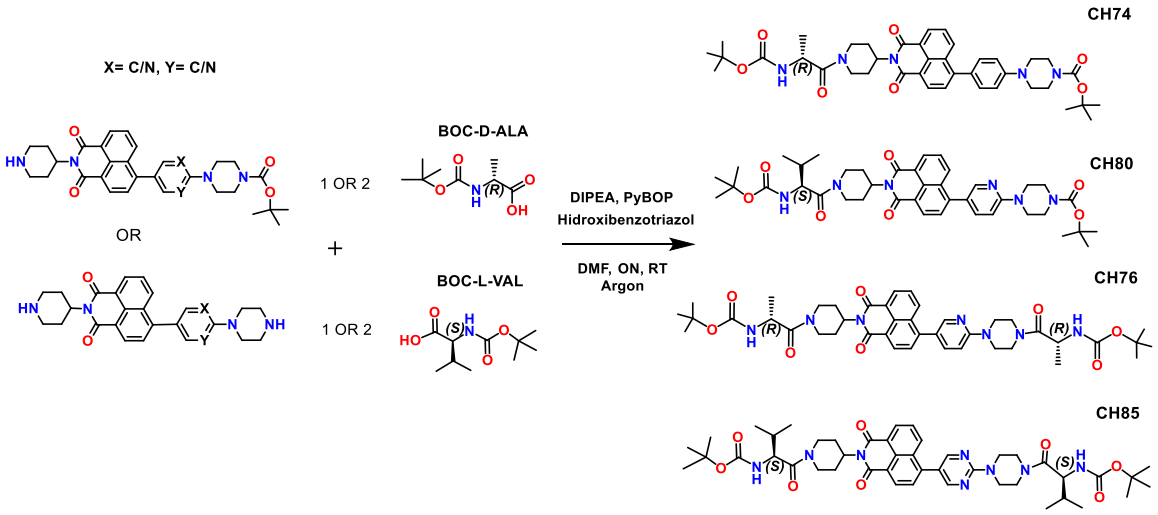

***Figure 2**. Scheme reaction for the synthesis of NMIs mono- and bi-functionalized with alanine or valine.*

3.1. AGGREGATION-INDUCED EMISSION OF SMALL NMI DERIVATIVES

The complete spectroscopic study of these species is described in the Supporting Information. However, among their fluorescence properties, the most interesting aspect is determining whether these species give rise to the aggregation-induced emission phenomenon. In this case, mixtures of THF with increasing amounts of water were studied. In *Table 1,* the photographs under UV light of CH74 and CH76 (10^{-5} M) are shown as representative examples of mono- and bi-functionalized species respectively.

***Table 1**. Water-solvent ratio assays of small NMI derivatives using UV light (366 nm)*

Structure	THF-H_2O mixtures
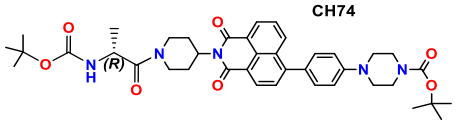	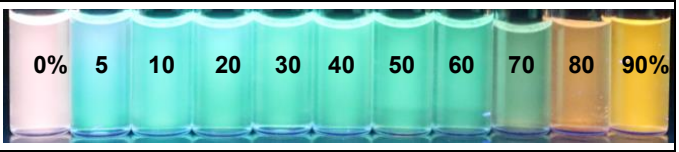
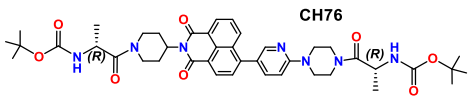	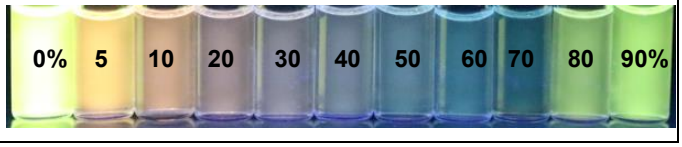

A small increase in fluorescence intensity is observed above 80% water, so there is a small AIE effect. But what is more noticeable is the change in colour of the emitted light at high water percentages, which turns from blue to orange or green. A red shift in the emission wavelength occurs. It is likely that, as aggregates form, the molecules experience an energy stabilization that results in emission at lower energy or longer wavelengths.

3.2. MORPHOLOGY OF THE AGGREGATES

Since we know that aggregates must be formed at high water percentages, their morphology was studied by scanning electron microscopy (FESEM), which revealed that solid nanoparticles with irregular surfaces were formed *(Figures 3* and *4)*.

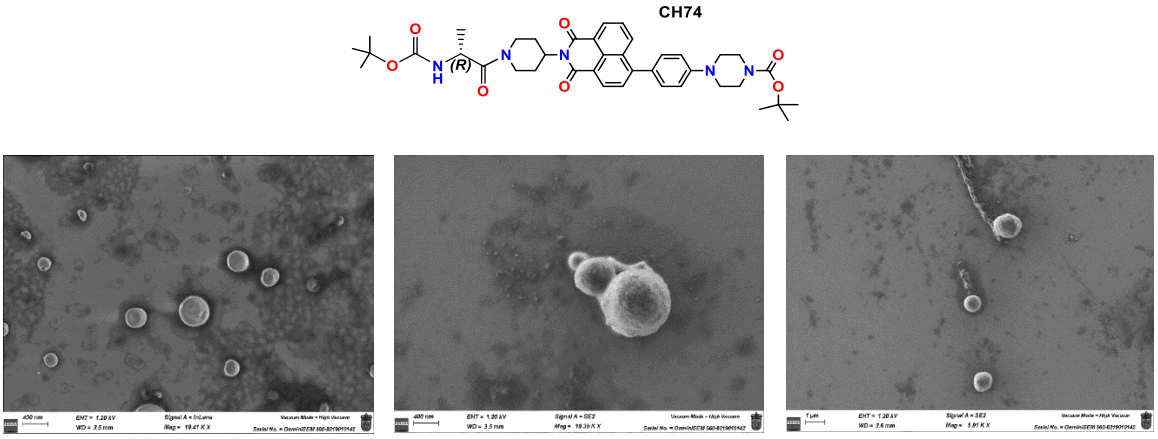

Figure 3. *FESEM images of CH74 in THF-H_2O: (left) 80% w.r. (centre and right) 90% w.r.*

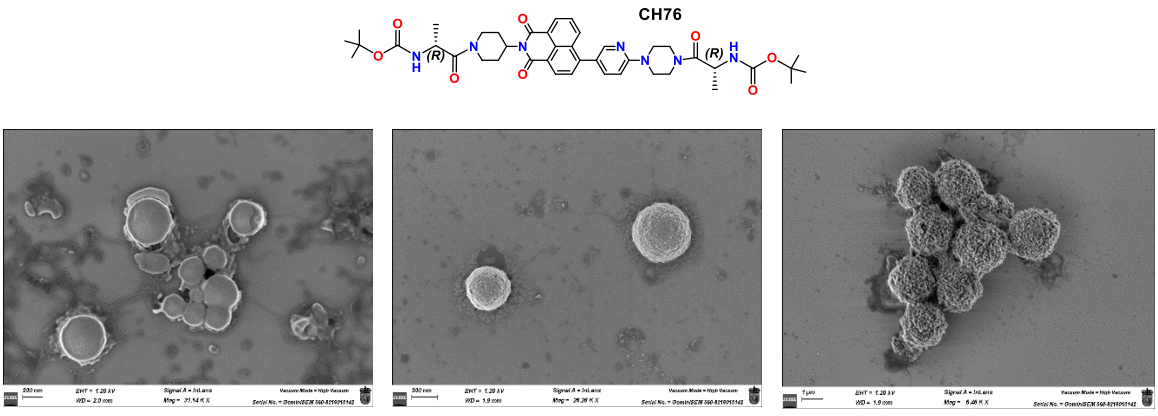

Figure 4. *FESEM images of CH76 in: (left and centre) THF-H_2O at 80% w.r. (right) MeOH-H_2O at 90% w.r.*

These images show that a single amino acid unit is not enough for vesicles formation. A longer chain is required to give flexibility to the system. The aggregation between only the aromatic rings of the NMI, without the presence of long amino acid chains, favours the formation of solid and bulky, but not hollow, spherical nanoparticles. So, in order to give more flexibility to the species, more units of D-alanine and L-valine were added to these structures.

4. EXPANDING THE AMINO ACID SEQUENCES

In order to join new amino acids to the previous species, it is necessary to carry out a deprotection reaction with trifluoroacetic acid *(Figure 5),* so that the terminal amines get free to react with a new acid group.

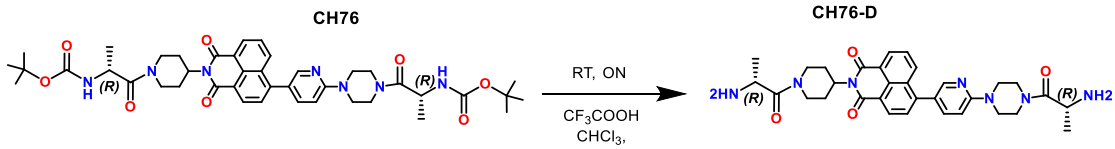

***Figure 5**. Deprotection reaction of CH76 as an example.*

Once the compounds from the previous section were deprotected, the amino acid chain was extended. Thus, CH78 and CH82 were synthesized in a single step following the reaction of *Figures 6a* and *6b.* Whereas CH79 was obtained in several steps *(Figure 6c)*, requiring the synthesis of an intermediate, CH75.

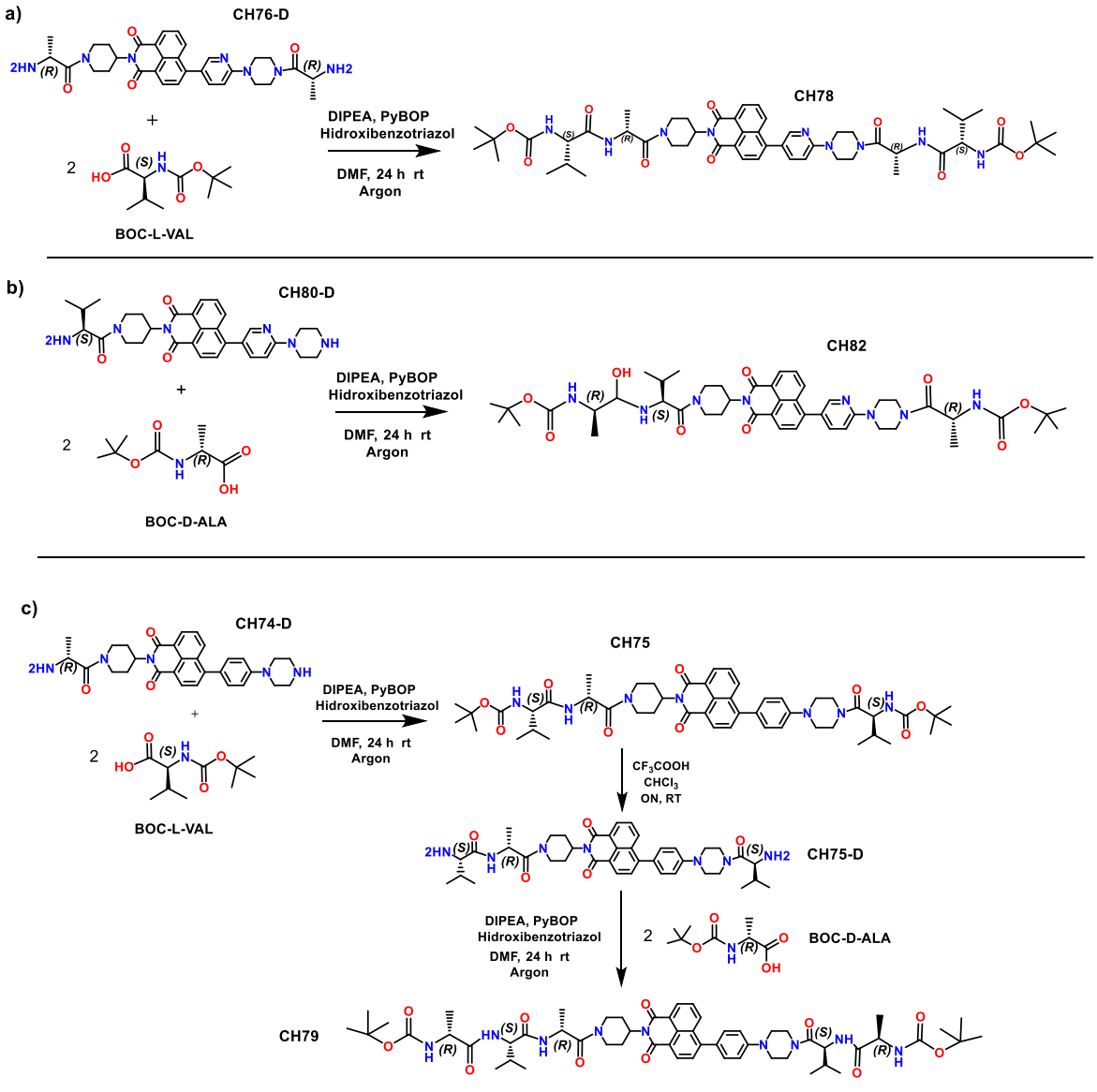

***Figure 6.** Steps followed to obtain CH78, CH82 and CH79.*

4.1. WATER RATIO ASSAYS OF LONGER AMINO ACID CHAIN DERIVATIVES

Fluorescent emission of the NMIs in mixtures of THF with increasing amounts of water was studied *(Table 2).* In this case, only CH78 and CH79 were evaluated, since CH82 was used as an intermediate to synthesize another compound from it, which will be discussed later in this chapter. The work concentration is 10^{-5} M.

***Table 2**. Water-solvent ratio assays of longer amino acid chain NMI derivatives using UV light (366 nm)*

Structure	THF-H_2O mixtures
Boc-L-Val-D-Ala— **CH78** —D-Ala-L-Val-Boc	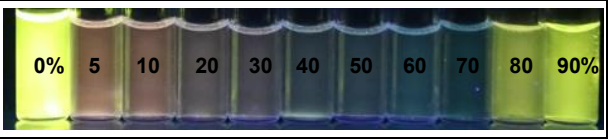
Boc-D-Ala-L-Val-D-Ala— **CH79** —L-Val-D-Ala-Boc	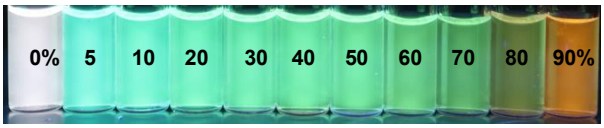

The photographs above show a moderate increase in fluorescence above 80% water. What is more noticeable is the change in the colour of the emitted light from bluish to yellow or orange. As the species studied in the previous section, light emission in shifted toward longer wavelengths, probably due to the energy stabilization that occurs when aggregates are formed in highly polar media. This qualitative analysis is quantified in *Figure 7*, where the grey curve increases slightly from 80% water (small AIE effect), while the blue curve increases sharply (red shift).

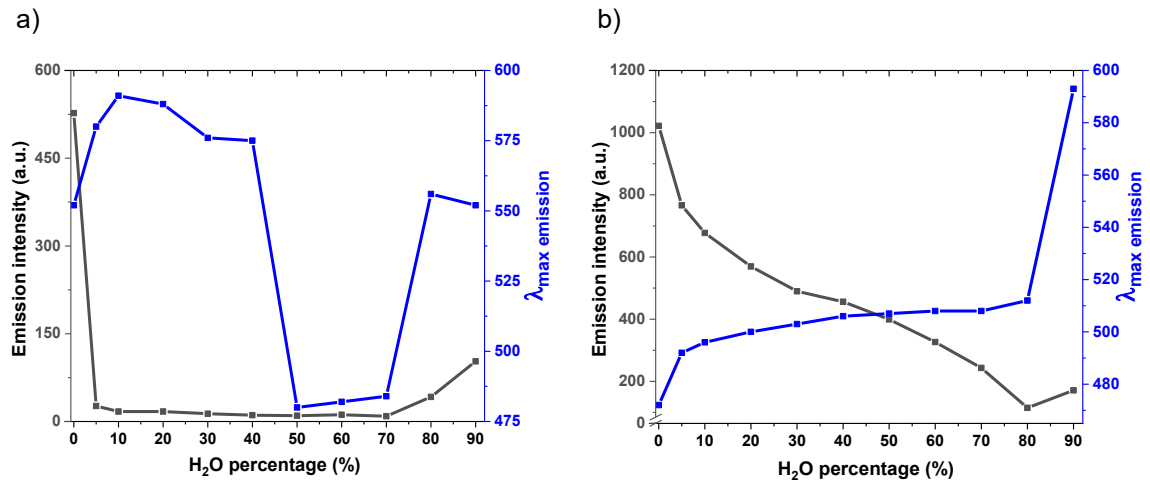

***Figure 7.** Emission intensity (grey) and λ_{max} emission (blue) of (a) CH78 and (b) CH79 at different w.r. λ_{exc} = 375/370 nm (THF-Water).*

It has been observed that these compounds have a less pronounced AIE effect than the compounds that were linked to a longer depsipeptide chains (studied in Chapter 1). It must be mentioned that the AIE effect of CH78 (pyridine) is higher than the one of CH79 (phenyl). In Chapter 1, studies of Lippert and Mataga revealed that compounds of pyridine were the most sensitive to the environment polarity, and the phenyl ones were the least sensitive. Also, the AIE effect of pyridine derivatives was the highest one, and this tendency is conserved with the compounds studied in this chapter. The ACQ effect, typically observed at medium water percentages, is not observed with phenyl derivatives, as it was not observed in Chapter 1 with CH16, it is not observed with CH79.

4.2. MORPHOLOGY OF THE AGGREGATES

As the amino acid chain has become longer, the morphology of the aggregates is expected to be different from the solid, irregular surface nanoparticles of the previous section. So, FESEM was employed to obtain images of CH78 and CH79 in mixtures of high-water percentage *(Figures 8* and *9).*

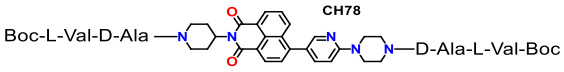

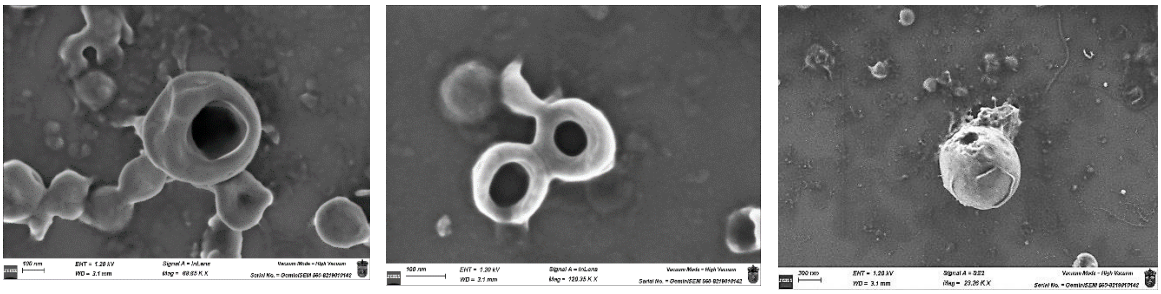

Figure 8. *FESEM images of CH78 in THF-H_2O: (left and centre) 70% w.r. (right) 90% w.r.*

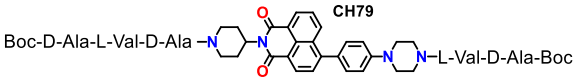

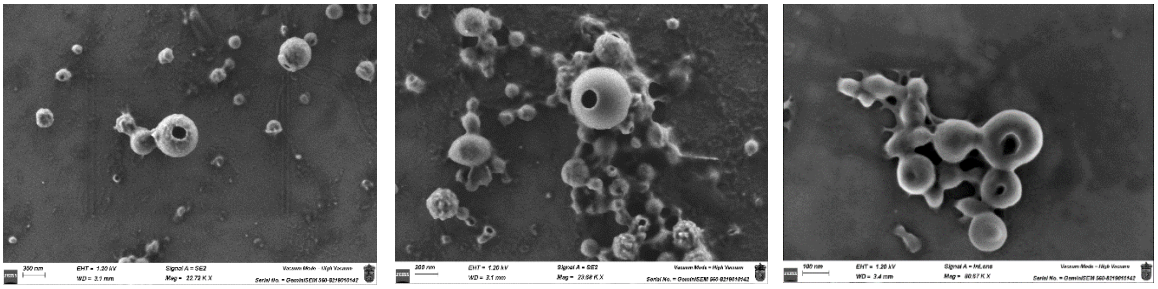

Figure 9. *FESEM images of CH79 in: (left and centre) THF-H_2O at 90% w.r. (right) MeOH-H_2O at 90% w.r.*

Nanovesicles have been observed. So, it can be said that when a dipeptide is joined to the dye, nanovesicles can be formed, however, most of them were mixed with amorphous aggregates. Moreover, these nanovesicles are not as abundant as those found when the dye is bonded to a longer depsipeptide. Thus, the longer the amino acid chain, the more beautiful and abundant vesicles are. It must be also mentioned that CH79 only forms nanovesicles at 90% of water, and that is the polarity at which a small increase in fluorescence and red shift was observed. At lower water percentages, virtually no nanoparticles are observed.

5. UNSATURATED AMINO ACIDS LINKED TO NMIS

It has been shown that a single dipeptide is sufficient for vesicle formation. Furthermore, it is known that the hydrophobic side chains of amino acids provide flexibility to the alternated peptide, potentially promoting vesicle formation. Hence, we made a series of derivatives that, in addition to alanine or valine, contain an amino acid which have an aliphatic chain with a terminal triple bond *(Figure 10b, 10c)*, thus promoting hydrophobic interactions between the peptides bonded to the NMIs cores. Alongside, an amino acid with a terminal double bond was linked to a starting semi-protected dye, then, through a metathesis reaction using the Hoveyda-Grubbs catalyst, a compound with two NMIs linked through a dipeptide with a central double bond was obtained *(Figure 10c)*. The products studied in this section (CH83, CH84, CH86-BIS) are the result of several synthetic steps described in the following scheme. The quantities of reagents and the specific procedure are described in detail in the Supporting Information of this chapter.

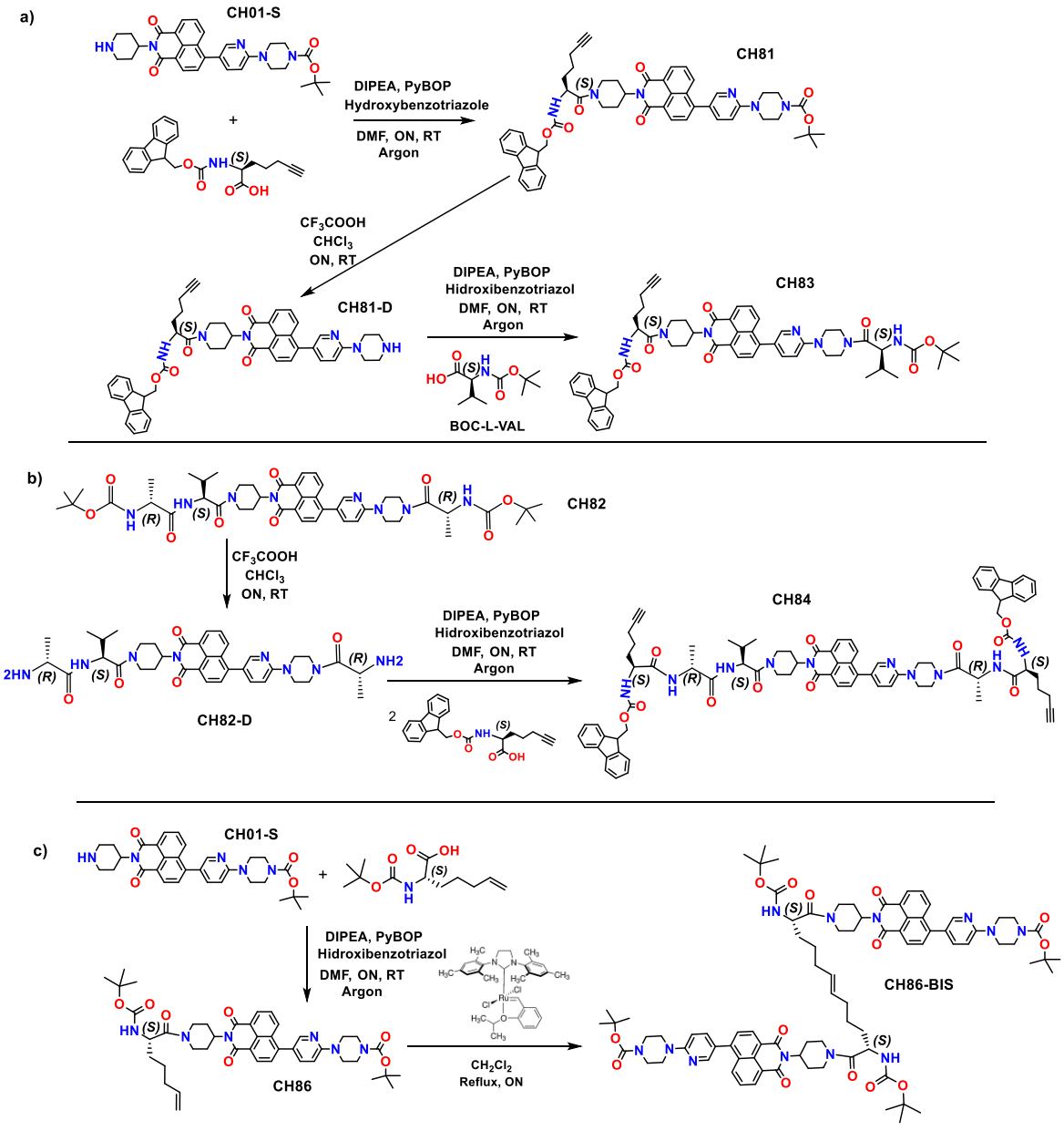

Figure 10. *Reactions followed to obtain synthetic amino acid NMI derivatives: CH83, CH84 and CH86-BIS.*

5.1. WATER RATIO ASSAYS OF SYNTHETIC AMINO ACID NMI DERIVATIVES

As was done in previous sections, the emission intensity of CH83, CH84 and CH86-BIS (10^{-5} M) in mixtures of THF with increasing amounts of water is studied *(Table 3)*.

***Table 3**. Water-solvent ratio assays of synthetic amino acid NMI derivatives using UV light (366 nm).*

Structure	THF-H_2O mixtures
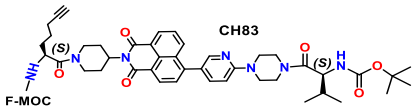	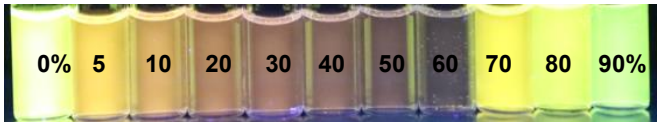
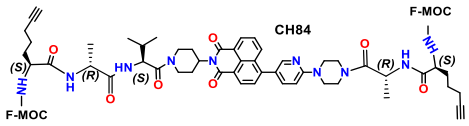	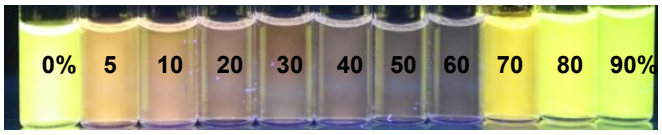
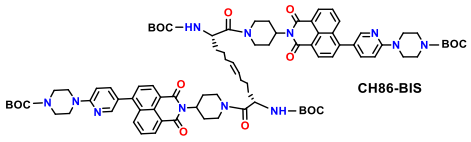	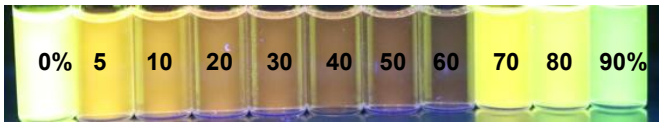

A change of the emission intensity and colour is observed when the water ratio is modified. In mixtures with intermediate water percentages (20-60%) the fluorescence emission is weaker due to the aggregation-caused quenching effect. However, at higher water ratio (above 70 %), the species experience an enhancement of fluorescence emission due to the higher agglomeration and the bigger nanoparticles formation. In addition, it is observed an important change in the colour of the emitted light. It changes from orange-brown to yellow (above 70% w.r.). In contrast to previously observed with other compounds, the aggregates likely experience energy destabilization to higher energy levels, resulting in an emission at higher energies or shorter wavelengths. All the compounds have a pyridine unit in their structure, so they have similar fluorescence behaviour. Taking CH84 and CH86-BIS as representative examples, this qualitative study was quantified with the emission spectra of the different mixtures. In *Figure 11* it is observed that the highest emission intensity takes place at 0% w.r. (the fluorophores are in solution, and no aggregate is formed), but the grey curve (emission intensity) suddenly decreases at intermediate water percentages (5-60%), and above 70% it increases again. That is because the AIE effect takes place. It is also observed that the blue curve (λ_{max} emission) declines sharply from 70% w.r.

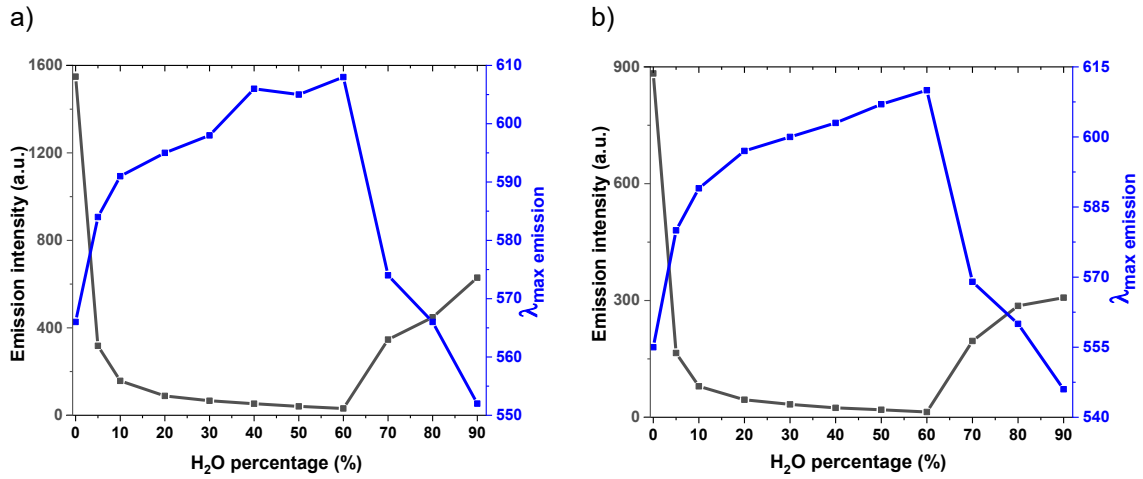

***Figure 11.** Emission intensity (grey) and λ_{max} emission (blue) of (a) CH84 and (b) CH86-BIS at different w.r. λ_{exc} = 375/390 nm. (THF-Water).*

5.2. MORPHOLOGY OF THE AGGREGATES

The AIE effect is much more noticeable with this group of unsaturated amino acids than NMIs with only valine and alanine. Therefore, the nanostructures formed are also expected to be better defined. FESEM was employed to obtain images of the three compounds in mixtures of high-water percentage *(Figures 12, 13* and *14).*

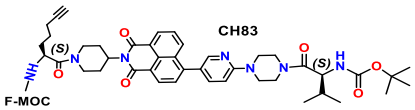

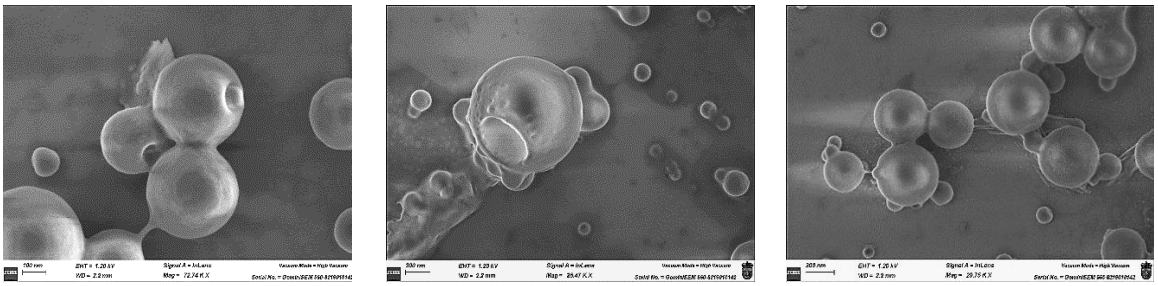

Figure 12. *FESEM images of CH83 in THF-H_2O: (left) 70% w.r. (centre and right) 80% w.r.*

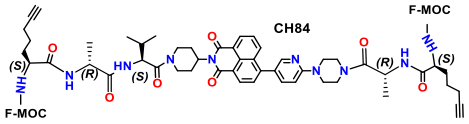

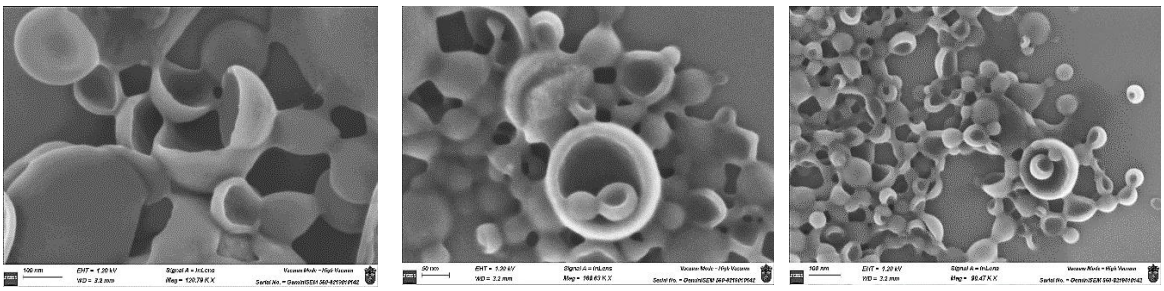

Figure 13. *FESEM images of CH84 in THF-H_2O: (left) 80% w.r. (centre and right) 90% w.r.*

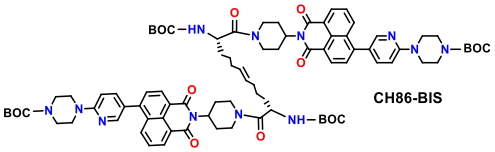

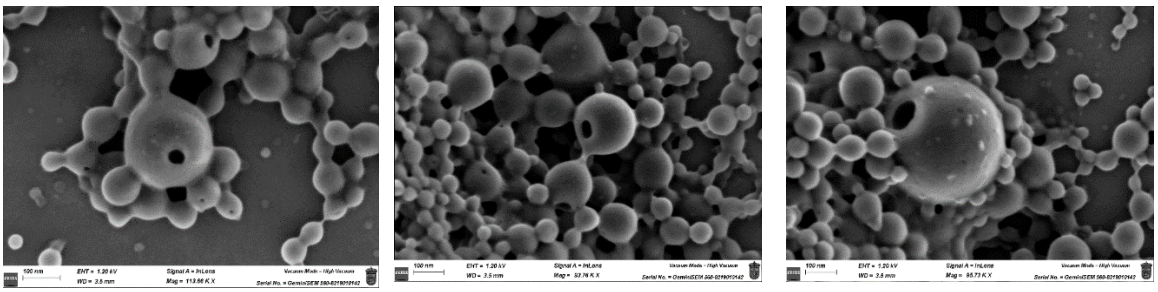

Figure 14. *FESEM images of CH86-BIS at 90% w.r. in: (left) THF-H_2O, (centre and right) MeOH-H_2O w.r.*

The nanovesicles formed were observed to be more abundant and defined than in the previous cases of this chapter. Something eye-catching of these compounds is that at 90% water, the number of aggregated nanoparticles increases, but their size is smaller. They form aggregates of hundreds of small vesicles, especially CH86-BIS, and among those small aggregated nanoparticles, certain bigger nanovesicles are found.

It can be stated that the presence of unsaturation moieties in the amino acids linked to the NMI favour the formation of vesicles; this corroborates that hydrophobic interactions between amino acids give flexibility to the system that allows the nanospheres (formed by π-π interactions between the NMI cores) to be not compact but hollow.

6. A NEW UNSATURATED HYBRID: TESTOSTERONE DERIVATIVE

The previous chapter discussed the importance of vesicles in biomedical applications. Cellular assays were also performed, but without any specific cell recognition markers. Thus, in the Chapter 3, a modified testosterone will be used as a cell-type selective marker, and detailed studies will be conducted on its activity when bound to naphthalenimides. However, this modified testosterone was also bonded to one of the compounds described in this chapter, CH83, and its structural effect on nanovesicle formation is herein evaluated.

To synthesize this derivative, it was first necessary to remove the F-Moc protecting group from CH83, thus leaving a free terminal amine *(Figure 15).* The deprotection reaction was carried out in THF with 25% piperidine under nitrogen atmosphere. Once the reaction had finalized the solvent and the excess of THF and piperidine were evaporated under reduced pressure. The excess of fulvene was removed with hexane (the deprotected product is not soluble there) obtaining CH83-F-D.

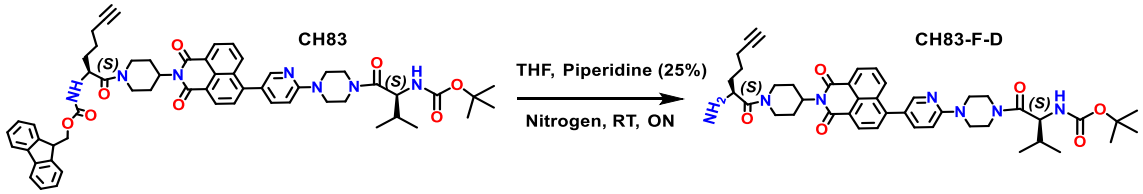

Figure 15. *Scheme reaction of basic deprotection of fluorenylmethoxycarbonyl protecting group (Fmoc).*

Then, to obtain the final product (CH88), the just deprotected amine reacts by nucleophilic attack of the acid group present in the modified testosterone[8] *(Figure 16).* The reagents amounts and conditions are fully described in the Supporting Information of this chapter.

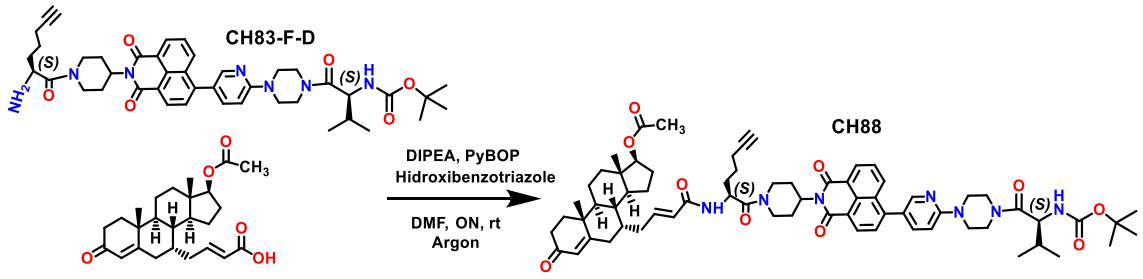

Figure 16. *Reaction scheme to obtain CH88.*

Then, this compound was analysed as it was done with the rest of compounds.

[8] A.-R. Vesper, J. Lacroix, R. C.-Gaudreault, H.-A. Tajmir-Rihai, G. Bérubé, *Steroids* **2016**, *115*, 98–104.

6.1. WATER RATIO ASSAYS AND MORPHOLOGY OF THE AGGREGATES

The THF-water mixtures photographed under UV light are shown in *Figure 17*. Also, the emission plot of CH88 in that mixture of solvents is collected below.

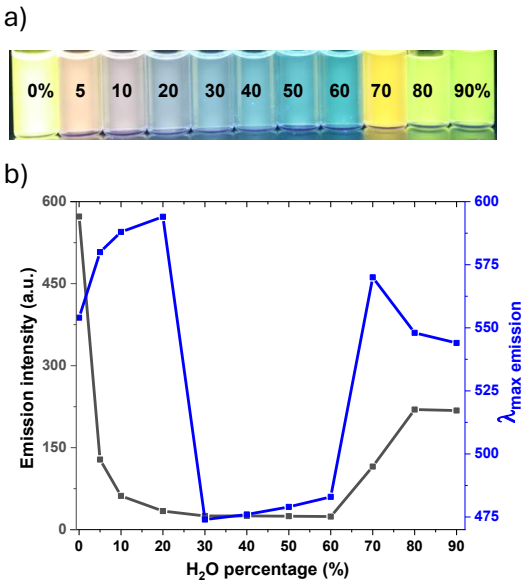

Figure 17. *(a) THF-H_2O ratio assays of CH88 ($C=10^{-5}$ M) using UV light (366 nm). (b) Emission intensity (grey) and λ_{max} emission (blue) of CH88 at different w.r. λ_{exc} = 390 nm.*

A change of the emission intensity and colour is observed when the water ratio is modified. In mixtures with intermediate water percentages (10-60%) the fluorescence emission is weaker due to the aggregation-caused quenching (ACQ) effect. However, at higher water ratio (above 70 %), the species experiences an enhancement of fluorescence emission. This qualitative analysis is quantified with the emission spectra of the mixtures. In *Figure 17b* it is observed that the highest emission intensity takes place at 0% w.r. (the fluorophore is in solution and no aggregate is formed), but the next is 80% w.r. In *Figure 17b* it can be noticed how the emission intensity (grey curve) suddenly decreases at intermediate water percentages (5-60%), and at 70% and above it increases again. That is because the AIE effect takes place. In addition, it is observed an important change in the colour of the emitted light. It changes from blue to yellow at 70% w.r. and green above that value. Unlike compounds that did not contain testosterone, CH88 experiences a red shift when aggregates are formed *(Figure 17c, blue curve).* In this case, energetic stabilization occurs, resulting in an emission at lower energies or longer wavelengths.

Once AIE effect has been observed, FESEM images of high-water ratio mixtures were obtained *(Figure 18)*. These revealed that the presence of the hormone also favours the formation of nanovesicles and allows the system to have sufficient flexibility to form them.

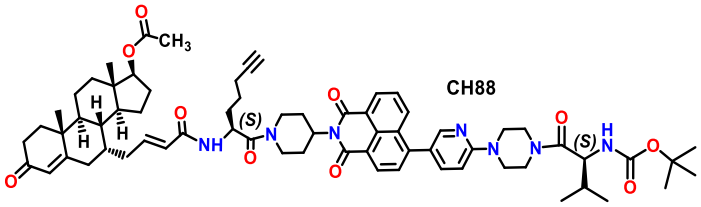

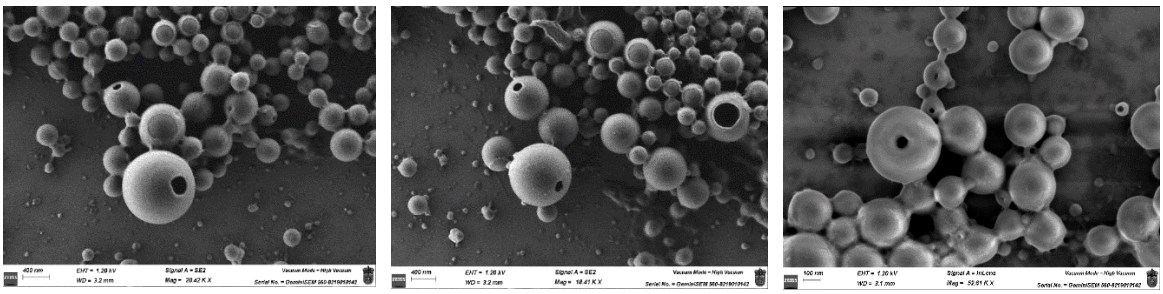

Figure 29. *FESEM images of CH88 in THF-H_2O: (left and centre) 80% w.r. (right) 90% w.r.*

7. CONCLUSIONS

This chapter has demonstrated that the self-assembly behaviour of aggregation-induced emission luminogens based on naphthalimide cores is strongly governed by the molecular design of the peptide sequences conjugated to them. By systematically varying the identity, length, and complexity of amino acid chains (comprising both natural and synthetic residues) with alternate chirality, the study revealed a clear structure-function relationship that dictates the morphology and organization of the resulting nanostructures.

A key finding is the existence of a critical peptide size threshold, a dipeptide, beyond which the system transitions from compact aggregates to well-defined nanovesicular architectures. This transition correlates with enhanced π-π stacking interactions, modulated by both the unsaturations and hydrophobicity of the alternated amino acid residues. Larger and more complex sequences, particularly those with hydrophobic side chains, promote more organized and uniform vesicle formation, highlighting the role of molecular crowding and non-covalent interactions in directing supramolecular assembly.

Additionally, it was observed that compounds incorporating pyridine units instead of phenyl rings in their structure formed more defined and uniform vesicles. These pyridine-containing conjugates also exhibited a more pronounced aggregation-induced emission (AIE) effect, suggesting that the electronic and polar nature of the pyridine ring may enhance self-assembly tendency of the NMI cores. This tendency was also observed in chapter one, where it was seen that the best nanovesicles belonged to pyridine derivatives.

Through comprehensive structural and fluorescence characterization, the work provides fundamental insights into the principles underlying nanomaterial formation from peptide-dye conjugates: it is not necessary to create a long labor-intensive depsipeptide, instead, with a correct design of the linked short peptide, vesicles can also be obtained. These insights lay the groundwork for the rational design of peptide-based AIEgens with tailored self-assembly properties, holding promising potential for applications in targeted bioimaging and drug delivery schemes.

CHAPTER 2B

Amino acid-based AIEgens as reducing agents for metal nanoparticles formation

ABSTRACT

This chapter explores the role of amino acid-bearing AIEgens as multifunctional agents in the green synthesis of metallic nanoparticles. These compounds permit the reduction of metal ions under mild conditions, facilitating the bottom-up formation of gold and silver nanostructures with controlled morphology. The ability of amino acids to both reduce metal ions and stabilize the resulting particles, along with structure-directing capability of AIEgens when aggregate, offers a flexible and surfactant-free method to produce branched gold nanostructures and silver coatings on vesicles. This work highlights the strategy employed to develop simplified, eco-friendly routes to complex metal nanomaterials, expanding the tools for advanced and functional nanostructure fabrication. Additionally, it has been found that the branched gold nanostructures exhibit catalytic activity in carbon-carbon cross-coupling reactions, specifically demonstrating efficiency in Suzuki-type coupling reactions, thereby opening new avenues for their application in sustainable green catalysis. The morphology of the resulting nanostructures was characterized by using Scanning Electron Microscopy and Transmission Electron Microscopy. In addition, Energy-dispersive X-ray spectroscopy was used to verify their elemental composition. The full characterization of the metallic nanostructures is included in the Supporting Information of chapter 2B.

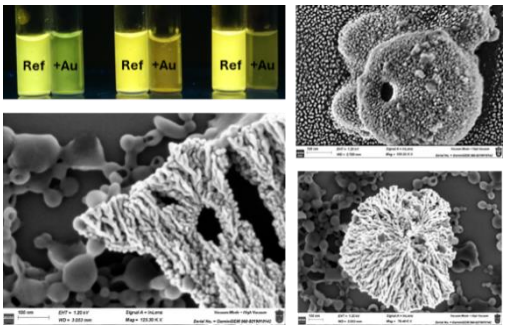

***Figure 1**. AIEgens promoting the formation of gold and silver nanoparticles.*

1. INTRODUCTION

Recent advances have expanded the utility of AIEgens beyond their luminescent properties, revealing their potential as active chemical agents in redox processes. In addition, some amino acids have demonstrated the ability to reduce metal ions under mild conditions.[1] This redox capability opens new avenues for the bottom-up synthesis of metallic nanostructures, which are of significant interest due to their high surface area, plasmonic properties, and catalytic activity.

Several studies have demonstrated AIE-activity in noble metal nanoparticles such as gold and silver. In a pioneering report, aggregation-induced emission was observed in gold nanoclusters whose surface motifs influenced both optical and structural properties, indicating a strong interplay between molecular aggregation and metallic core formation.[2] Similarly, Ag–Au bimetallic nanoclusters have been synthesized using AIE-active ligands, highlighting how these molecules can stabilize and modulate the growth of complex metal nanostructures.[3,4]

Naturally occurring biomolecules such as amino acids, have shown intrinsic redox capabilities that enable the reduction of metal ions, including Au(III), to their elemental metallic states. Further studies have demonstrated the efficacy of specific amino acids in reducing Au(III) ions. For example, tryptophan has been shown to spontaneously reduce aqueous chloroaurate ions, with the indole group playing a crucial role in the reduction

[1] A. M. Figat, B. Bartosewicz, M. Liszewska, B. Budner, M. Norek, B. J. Jankiewicz, *Langmuir* **2023,** *39* (25), 8646−8657.
[2] D. Bain, S. Maity, A. Patra, *Chem. Commun.* **2020,** *56,* 9292−9295.
[3] T. Chen, S. Yang, J. Chai, Y. Song, J. Fan, B. Rao, H. Sheng, H. Yu, M. Zhu, *Sci. Adv*. **2017,** *3* (8). e1700956.
[4] S. Jin, W. Liu, D. Hu, X. Zou, X. Kang, W. Du, S. Chen, S. Wei, S. Wang, M. Zhu, *Chem. Eur. J.* **2018,** *24* (15), 3712−3715.

process.[5] Similarly, aspartic acid, arginine, threonine, glycine and valine have exhibited significant reducing activity towards Au(III) species, leading to the formation of gold nanoparticles under various conditions *(Figure 2)*.[6]

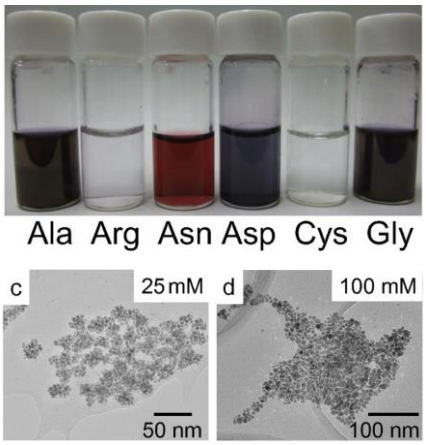

Figure 2. *Up: gold colloidal solutions using different aminoacids. Down: TEM images of gold nanoparticles.*

These findings emphasise the potential of amino acids as environmentally benign and biocompatible agents for the green synthesis of metal nanoparticles. The amides can coordinate with metal ions and facilitate electron transfer through the formation of transient metal-ligand complexes. These amino acids serve as a dual function as both reducing and stabilizing agents.[7] The aggregation of the AIEgens is also important to get the final gold and silver nanostructures, since they act as structure-directing elements. Their environmentally benign nature makes them especially attractive for green synthesis approaches, where the elimination of harsh reductants and surfactants is desirable.

The utilization of AIEgens in the synthesis of metal nanostructures is very attractive. Their intrinsic fluorescence enables in situ monitoring of nanostructure formation, since the resulting metal-AIE hybrid systems change the initial chromophore's fluorescence. Besides that, their ability to induce reduction under mild conditions offers an eco-friendly alternative to traditional synthetic routes.

On the other hand, the formation of carbon-carbon bonds is a fundamental transformation in organic synthesis, with cross-coupling reactions playing a central role in the development of pharmaceuticals, agrochemicals, and functional materials.[8] Among these, the Suzuki–Miyaura coupling has emerged as one of the most widely used methods due to its broad substrate scope, mild conditions, and tolerance of functional groups. Traditionally, such reactions have relied heavily on homogeneous palladium-based catalysts, which, although highly effective, present limitations in terms of cost, recovery, and metal contamination of products.

In recent years, heterogeneous catalysis using gold nanoparticles (AuNPs) under environmentally benign conditions has attracted considerable attention as a promising alternative to palladium. For instance, ultrasmall Au nanoclusters (<2 nm) have enabled Suzuki–Miyaura cross-couplings in mixtures of ethanol and water with high selectivity and recyclability when clusters are capped with thin ligand layers.[9] In other cases, to improve its efficiency, gold is combined with supports and stabilizers, as is the case of certain Au catalysts supported on CuO-ZnO, which effectively catalyse Suzuki reactions in water.[10] Moreover, some authors demonstrate that metallic gold nanoparticles, when properly stabilized on active carbon, can catalyse cross-couplings in aqueous media under air, illustrating both the sustainability and efficiency of Au-based catalytic systems. In addition they performed hot filtrations test, confirming the predominance of heterogeneous catalysis.[11] Other authors reported AuNPs supported on graphene as active catalyst for the Suzuki reaction of aryl halides with arylboronic acids in water under aerobic conditions.[12] It must be added that some researchers have provided mechanistic insights into C-C bond-

[5] P. Selvakannan, S. Mandal, S. Phadtare, A. Gole, R. Pasricha, S. D. Adyanthaya, M. Sastry, *J. Colloid. Interface Sci.* **2004,** *269* (1), 97-102.
[6] T. Maruyama, Y. Fujimoto, T. Maekawa. *J. Colloid Interface Sci.* **2015,** *447,* 254-257.
[7] D. Nemkova, S. Saikova, A. Krolikov, *Crystals.* **2025**, *15*, 72.
[8] C. S. Horbaczewskyj, I. J. S. Fairlamb, *Org. Process Res. Dev.* **2022**, *26* (8), 2240-2269.
[9] Q. Shi, Z. Qin, H. Xu, G. Li, *Nanomat.* **2019,** *9*, 838.
[10] J. Albadi, A. Momeni, A. Mansournezhad, *Jordan J. Chem.* **2017,** *12* (4), 237-244.
[11] J. Han, Y. Liu, R. Guo, *J. Am. Chem. Soc.* **2009**, *131* (6), 2060-2061.
[12] Y. Li, X. Fan, J. Qi, J. Ji, S. Wang, G. Zhang, F. Zhang, *Mater. Res. Bull.* **2010,** *45,* 1413-1418.

forming reactions catalysed by gold nanoparticles. Their study highlights that AuNPs, particularly those below 5 nm, can promote Suzuki-type couplings through a catalytic cycle involving oxidative addition, transmetalation, and reductive elimination. The authors emphasized the influence of nanoparticle size, support, and reaction conditions on catalytic performance. Importantly, they discussed evidence for a dual catalytic behaviour, where heterogeneous surface activity may coexist with leached Au(I)/Au(III) species, suggesting a quasi-homogeneous pathway in some systems. These findings underscore the mechanistic complexity and versatility of gold-based catalysts in cross-coupling chemistry.[13] Moreover, recent advances have demonstrated that gold nanoparticles, supported on polymeric resins via sorption-reduction (without additional ligands) exhibit catalytic activity due to their high surface-to-volume ratio and the presence of undercoordinated atoms at the metal-support interface. Unlike bulk gold, which is catalytically inert, AuNPs enable the Suzuki-Miyaura coupling in water-containing mixtures. This activity is attributed to electronic effects at the nanoscale, such as quantum confinement and d-band modulation, which enhance adsorbate interactions and facilitate key steps like oxidative addition. In addition, in that work they performed a filtration of the resin-supported catalyst showing a minimal leaching or deactivation over multiple runs.[14] These examples illustrate that well-engineered gold nanostructures, especially those stabilized in green media, can act as effective, sustainable C-C coupling catalysts.

Hence, in the present work, branched gold nanostructures, synthesized from amino acid-based AIEgens in a THF-water solution, provide an excellent platform for efficient Suzuki-type couplings. These nanodendrites significantly advance the field by combining abundant active sites with mild, green reaction conditions. So, this work opens new avenues for multifunctional nanomaterials that combine catalytic functionality with optical properties.

Altogether, this chapter explores the novel application of alternated peptide-bearing AIEgens as active chemical agents in the formation of gold nanodendrites as well as silver covers on the surface of the nanovesicles. The findings presented herein contribute to a broader understanding of how molecular structure and photophysical properties can be leveraged for nanomaterial synthesis, leading to simplified, surfactant-free, and tuneable pathways toward complex metal nanostructures. Finally, this work also contributes to the understanding of gold-catalysed C-C bond formation and to promote the development of recyclable, sustainable catalytic systems for use in green chemistry.

2. OBJECTIVES

In this chapter it is desired to explore the multifunctional role of AIEgens bonded to alternated amino acids in the eco-friendly generation of metallic nanostructures. The work focuses on their utility as both reducing and stabilizing agents, their influence on nanostructure morphology, and their potential catalytic performance. To get it, the next specific objectives must be achieved:

- To select those amino acid-bearing AIEgens from the previous chapter which form nanovesicles at high water percentages.
- To use the selected compounds as reducing and stabilizing agents for the synthesis of gold and silver nanostructures under mild, environmentally friendly conditions. Concretely, in a short generation time, at room temperature in water-containing mixtures and avoiding the use of surfactants or hazardous reagents.
- To evaluate the effect of metallic nanoparticle formation on the optical properties of the compounds, specifically their visible absorption, colour of emitted light, and aggregation-induced emission, in high-water-content solutions. This will be quantified by

[13] G. Li, R. Jin, *Nanotechnol. Rev.* **2013,** *2* (5), 529−545.

[14] D. Shah, H. Kaur, *J. Mol. Catal. A: Chem.* **2014**, *381*, 70–76.

comparative analysis of their absorption and emission spectra against established references.

- To perform a rigorous characterization of the synthesized gold nanodendrites and silver nanoparticles using Scanning Electron Microscopy and Energy-Dispersive X-ray Spectroscopy (EDX) in order to evaluate their morphology and confirm their elemental composition.
- To employ Transmission Electron Microscopy (TEM) to analyse the growth mechanism of gold nanodendrites relative to the nanovesicles, determining their nucleation site. High-resolution TEM will also reveal atomic-scale details, including the gold atom arrangement and crystallographic planes.
- To employ dynamic light scattering (DLS) to determine the average size of the gold nanodendrites.
- To investigate the catalytic activity of the synthesized branched gold nanostructures in carbon-carbon cross-coupling reactions, specifically evaluating their efficiency in Suzuki-type coupling as a model of sustainable catalytic application.

3. COMPOUNDS WHICH PROMOTE METALLIC NANOPARTICLES FORMATION

From the compounds synthesized in the preceding chapter, those exhibiting the most intense aggregation-induced emission in high-water content mixtures, and forming nanovesicles under these conditions, were selected. It was found that these conditions were met by compounds with the longest amino acid chains, which consequently resulted in a greater number of amide bonds. These amide bonds will facilitate the reduction of gold and silver cations to their elemental forms. Furthermore, compounds featuring aliphatic chains containing double or triple bonds were also observed to form nanovesicles. Given their electron-rich nature, these species are also likely candidates for the reduction of gold and silver cations. The formation of nanovesicles by these compounds is crucial, as the nanovesicles themselves act as stabilizers for the resulting metal nanoparticles, preventing their collapse and maintaining long-term stability. Compounds are shown in *Figure 3*.

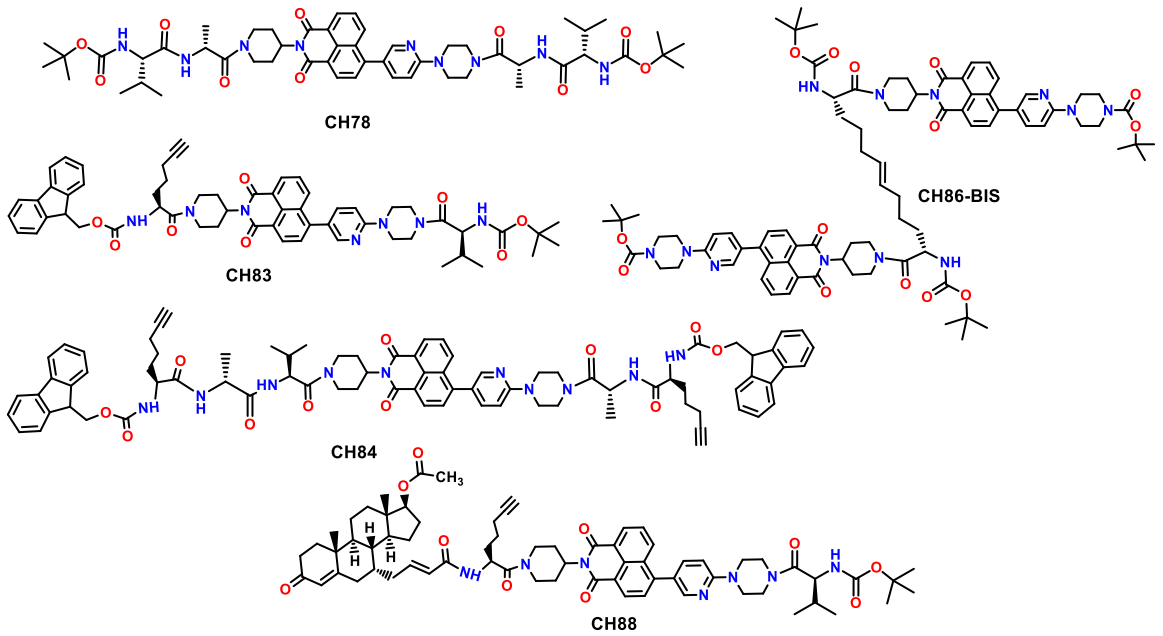

Figure 3. *Compounds selected as precursors for metallic nanoparticles formation.*

4. STUDY OF THE OPTICAL CHANGES OF MIXTURES WITH GOLD

The methodology followed to prepare all organic compound-gold solution mixtures was the similar in all cases. First, the water percentage where the best nanovesicles are formed is selected. It was 90% w.r. for all compounds except for CH78, which was mixed with gold(III) at 80% of water. Then, each compound dissolved in THF, was combined with an excess of gold salt (8 equivalents of $HAuCl_4 \cdot 3\ H_2O$) dissolved in water. The amounts used of each solution were those necessary to get a final concentration of the organic species of 10^{-5} M in a mixture of 90% or 80% w.r.

First, freshly prepared samples were imaged under white and UV light of 366 nm *(Table 1, left column).* And after 24 hours the mixtures were imaged again *(Table 1*, *right column)* in order to find any change in the colour of the samples and in their emission intensity. The presence of optical changes is an indicator of the interaction between the gold and the organic compound.

Table 1. *Optical changes of the samples. (left: under white light, right: under UV light, 366 nm)*

Compound	Freshly prepared samples	After 24 hours
CH78	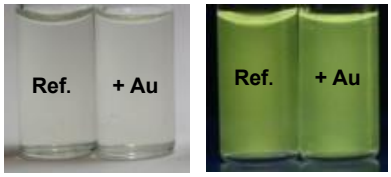	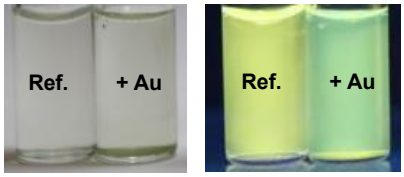
CH83	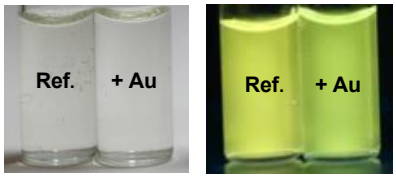	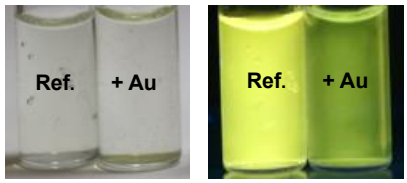
CH84	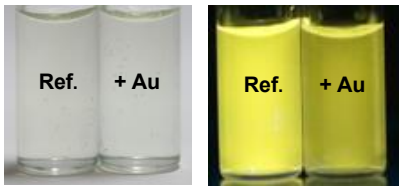	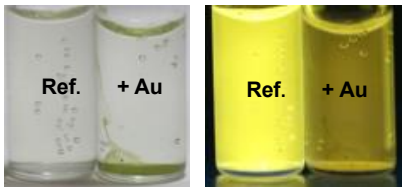
CH86-BIS	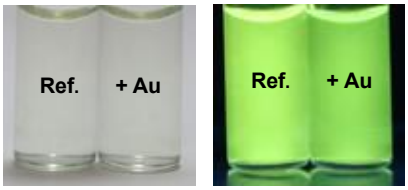	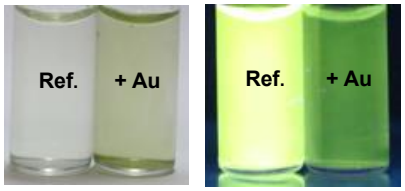
CH88	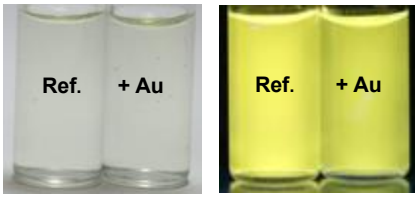	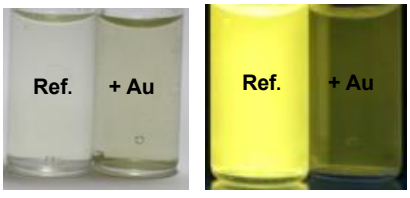

In all cases, a clear decrease in emission intensity is observed after 24 hours of evolution. In addition, in some mixtures, a colour change of the vial is noticeable (under visible light), going from colourless to yellow. However, these changes are very slight, and for better analysis, normalized absorption and emission spectra were acquired.

The spectra of CH86-BIS are shown in the next figure as a representative example, but the spectra of all mixtures are collected in the Supporting Information of this chapter.

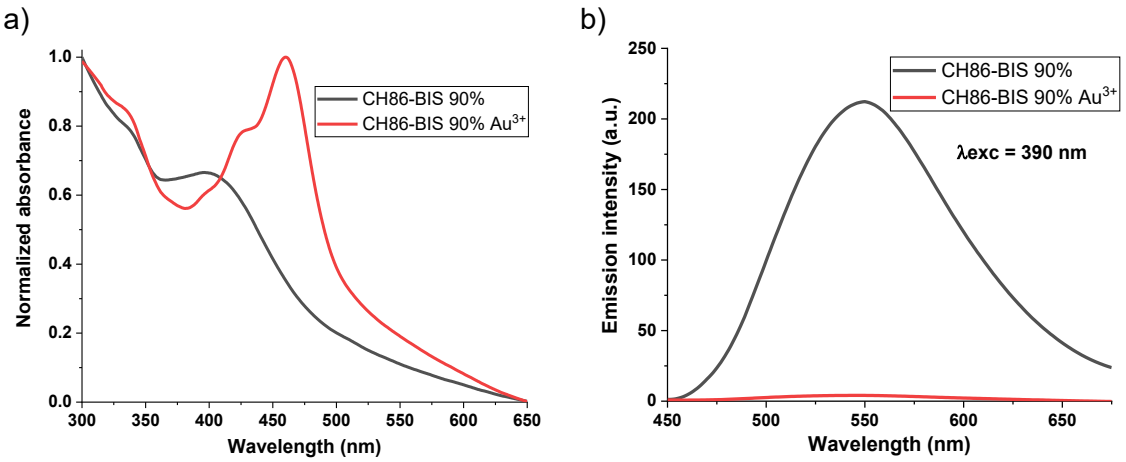

***Figure 4**. CH86-BIS at 90% w.r. in THF with gold(III), (a) Normalized absorption spectra of reference (black) and mixture (red) (b) Emission spectra of reference (black) and mixture (red).*

In the absorption spectra it is observed that there is a shift towards longer wavelengths when gold is present in the sample (red curve). It explains the yellow colour of the mixture under white light. On the other hand, the emission spectrum demonstrates a marked decrease in fluorescence intensity approaching the baseline. This indicates that interaction with gold(III) effectively quenches the fluorescence emission. It must be mentioned that the mixtures do not exhibit the characteristic bright colours, such as red or blue, typically associated with the formation of gold nanoparticles. Some reports confirmed that gold nanodendrites typically exhibit colours in the red region of the spectrum. This optical behaviour can be attributed to their complex morphology, which supports multiple plasmonic resonances and generates intense localized electromagnetic fields.[15] In this case, the surface plasmon resonance of the gold appears to be suppressed, likely due to interactions with the organic matter present in the solution, which may inhibit the gold optical properties.

5. ELECTRON MICROSCOPY OF THE MIXTURES

Before studying the mixtures of organic compounds and gold(III), a blank test was performed, by preparing a gold(III) solution ($HAuCl_4 \cdot 3\ H_2O$) $8 \cdot 10^{-5}$ M in a THF-H_2O mixture at 90% w.r. By this way we checked that no representative gold nanostructures were formed. Then, the images of each studied compound are presented in the next different subsections. It must be mentioned that a great quantity of additional images is collected in the Supporting Information.

5.1. GOLD NANOSTRUCTURES FROM CH78

Scanning electron microscopy.

After 24 hours of stillness, the sample of CH78 (10^{-5} M) at 80% w.r. in THF/H_2O mixed with gold(III) [($HAuCl_4 \cdot 3\ H_2O$) $8 \cdot 10^{-5}$ M] (8 equivalents) was imaged. Stunning big dendrites of gold (in white at the images) were found (*Figure 5*).

[15] S. Eustis, M. A.-Sayed, *Chem. Soc. Rev.* **2006**, *35* (3), 209–217.

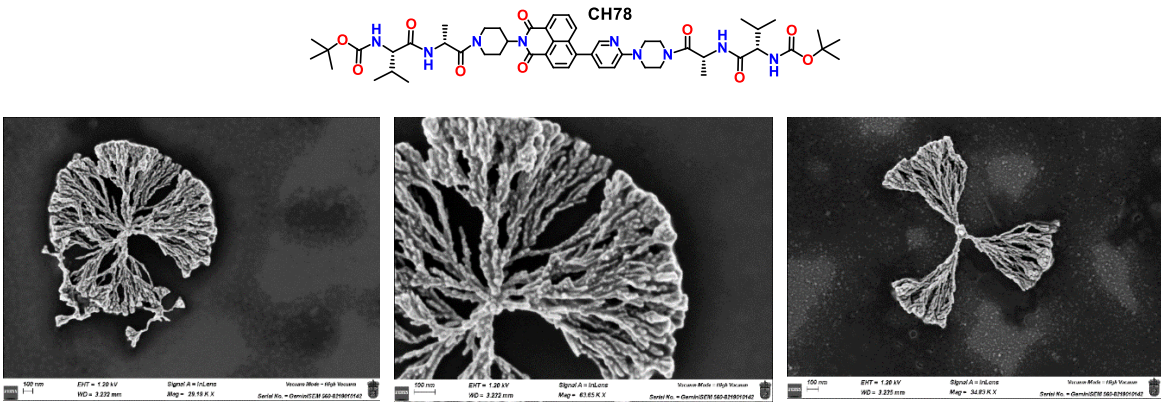

Figure 5. *FESEM images of gold nanodendrites formed in the studied mixture (CH78 80% w.r.)*

Transmission electron microscopy

The obtained nanodendrites were also imaged by TEM. In the right corner of *Figure 6* it can be observed how the nanodendrite is actually surrounded by organic matter (pale grey around the black gold).

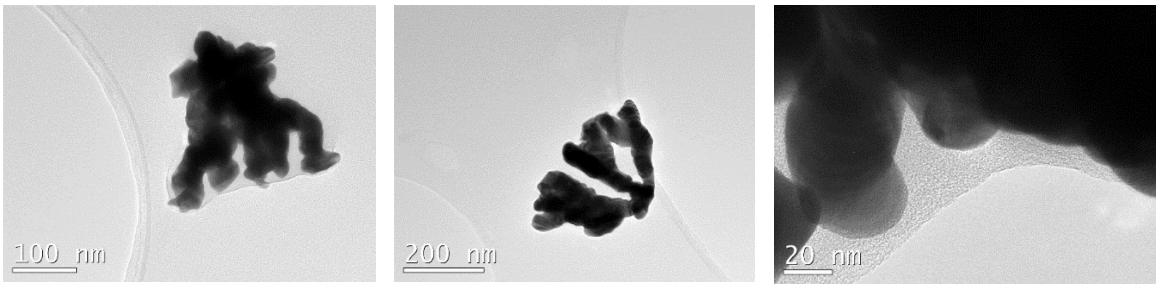

Figure 6. *TEM images of gold nanodendrites formed in the studied mixture (CH78 80% w.r.)*

The covering of the dendrite by the organic compound was not appreciated in FESEM images but it is confirmed by this technique. It could explain the inhibition of the optical properties of the gold plasmon and explain why the solutions do not become red or blue as typically occurs with gold nanoparticles colloids.

5.2. GOLD NANOSTRUCTURES FROM CH83

Scanning electron microscopy

After 24 hours of stillness, the sample of CH83 (10^{-5} M) at 90% w.r. in THF mixed with gold(III) was imaged. Big dendrites of gold (in white) are combined with nanovesicles of CH83 (in grey). In *Figure 7* it can be seen how the dendrites are outside the vesicles, but gold and organic matter are interacting, so the gold plasmon is also inhibited.

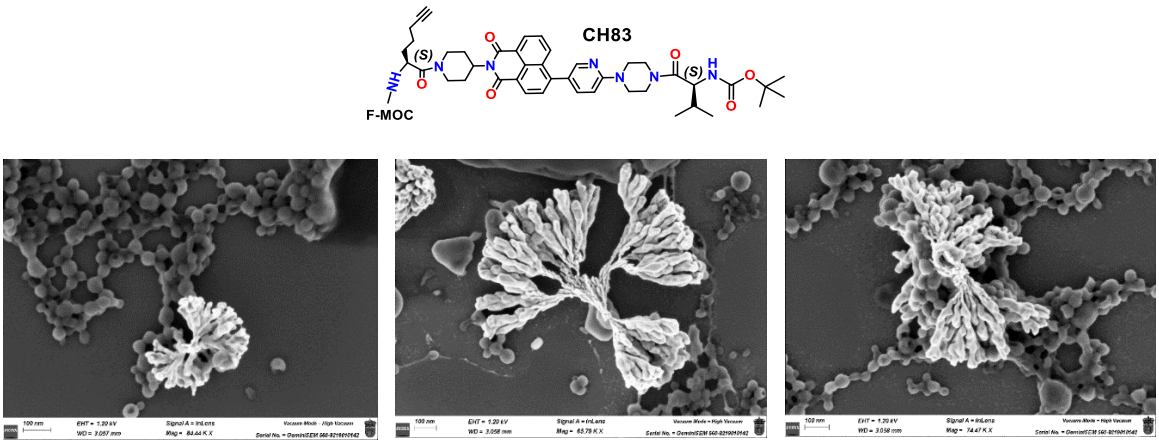

Figure 7. *FESEM images of gold nanodendrites formed in the studied mixture (CH83 90% w.r.)*

Energy-Dispersive X-ray Spectroscopy

Then, an elemental analysis was performed by Energy-Dispersive X-ray Spectroscopy (EDX) to verify the composition of each observed structure. First a localized analysis was made *(Figure 8).* The results confirmed that dendrites are made of gold, the vesicles of carbon/nitrogen/oxygen and the plate of silicon.

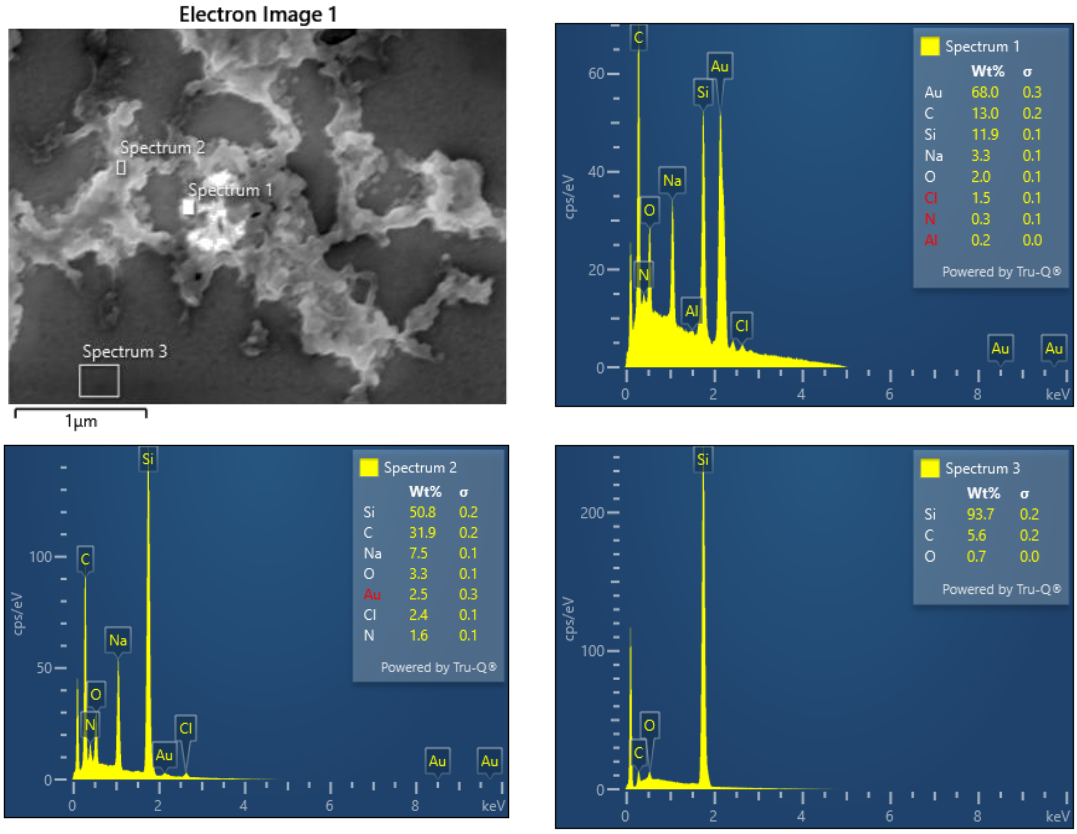

Figure 8. *Punctual EDX spectra of CH83 (90% w.r.): gold nanodendrites and carbon vesicles.*

It should be noted that silicon is detected in all spectra: since the electron beam has a high penetrating power, once it passes through the gold or carbon and collides with the silicon plate, it also detects this element even if it is below the sample. The analysis of spectrum 1 reveals that gold is found as pure element with a mass percentage of 68% *(Figures 9* and *10),* thus confirming that the reduced gold has been formed by the compound.

Spectrum 1							
Element	Line Type	Apparent Concentration	k Ratio	Wt%	Wt% Sigma	Standard Label	Factory Standard
C	K series	19.24	0.19238	12.96	0.16	Pure Element	Yes
N	K series	0.66	0.00457	0.31	0.06	BN	Yes
O	K series	4.07	0.03568	2.01	0.05	SiO2	Yes
Na	K series	8.90	0.07627	3.27	0.06	Albite	Yes
Al	K series	0.47	0.00425	0.16	0.05	Al2O3	Yes
Si	K series	36.84	0.33782	11.88	0.13	SiO2	Yes
Cl	K series	3.81	0.03635	1.45	0.15	NaCl	Yes
Au	M series	112.22	1.12222	67.96	0.28	Pure Element	Yes
Total:				100.00			

Figure 9. *Compositional analysis of spectrum 1. Reduced gold is found.*

Then an EDX mapping was performed:

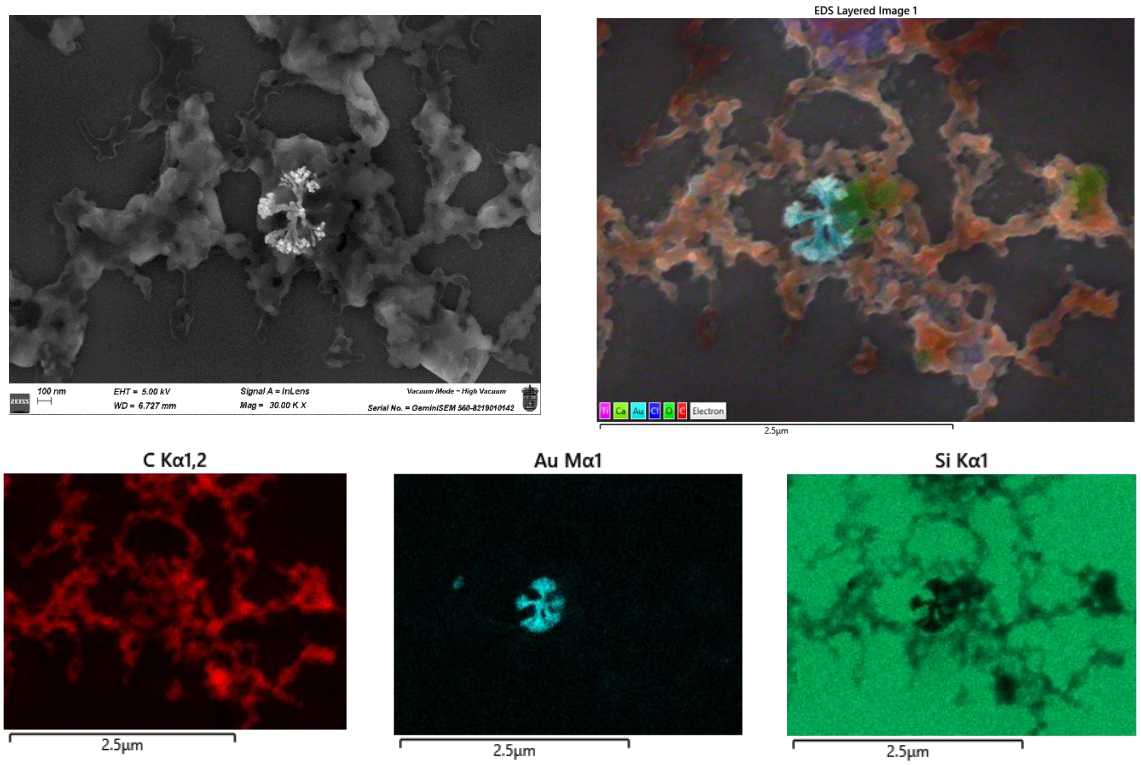

Figure 10. *EDX mapping spectra: gold nanodendrites (blue) and carbon vesicles of CH83 (red).*

High resolution transmission electron microscopy

HR-TEM was employed to characterize the gold nanodendrites at the atomic scale. The high resolution of this equipment enables direct visualization of the crystallographic arrangement and atomic lattice structure of the gold atoms within the dendrite. Initially, low-magnification images were acquired to observe the overall morphology of the dendrites *(Figure 11).*

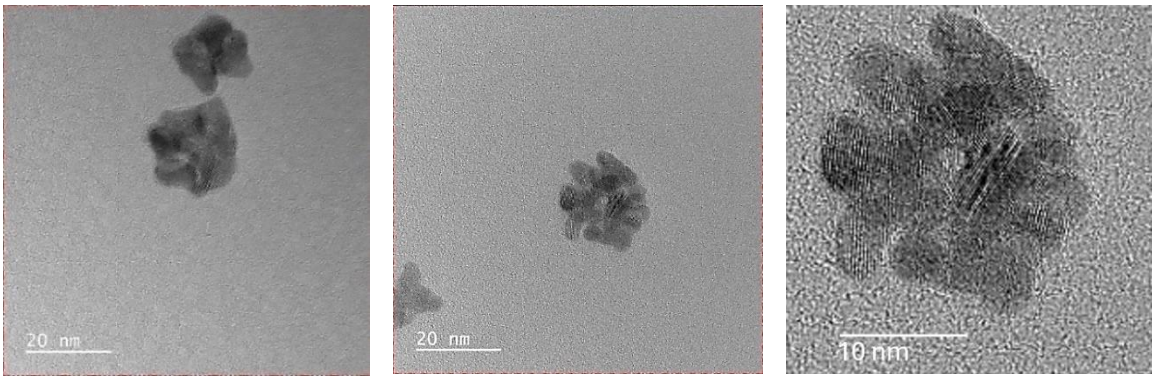

Figure 11. *HR-TEM images of gold nanodendrites formed in studied mixtures (CH83 90% w.r.)*

Then, specific regions of interest were digitally magnified to resolve atomic-scale structural details *(Figure 12, right).*

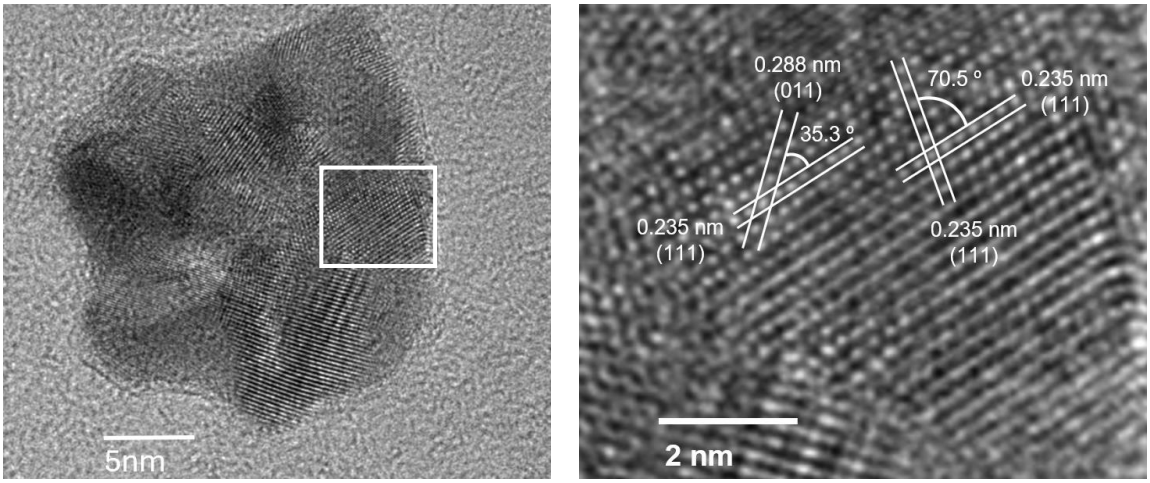

Figure 12*. HR-TEM images of different crystallographic planes. Viewed along [110] zone axis.*

To understand the atomic-scale analysis made in the right panel of *Figure 13*, it is necessary to give a brief theoretical background. In this section it is essential to consider that gold crystallizes in a face-centred cubic (FCC) structure with a lattice parameter of a = 4.078 Å.[16] The spatial arrangement of atoms can be described by crystallographic planes denoted by Miller indices (hkl). These indices are integral values that represent the orientation of a given plane within the unit cell and are directly related to the interplanar spacing through the following equation:[17]

$$d_{hkl} = \frac{a}{\sqrt{h^2 + k^2 + l^2}} \quad \text{Eq. 1}$$

Where d_{hkl} is the interplanar spacing, ***a*** is the lattice parameter of gold (4.078 Å), and *h,k,l* are the Miller indices of the plane. Using this relationship, it is possible to calculate the expected distances between atomic planes and compare them with the measured spacings observed in HR-TEM images. These comparisons enable the identification of specific crystallographic planes and zone axes in the imaged nanostructures. Based on this, if we see the right image of *Figure 13,* the measured interplanar spacing of approximately 2.35 Å

[16] F. J. Osonga, V. M. Kariuki, V. M. Wambua, S. Kalra, B. Nweke, R. M. Miller, M. Çeşme, O. A. Sadik, *ACS Omega* **2019,** *4* (4), 6511-6520.
[17] W. D. Callister, D. G. Rethwisch, *Materials Science and Engineering: An Introduction*. John Wiley & Sons, Hoboken, tenth edition, **2018,** chapter 3.

corresponds to the (111) crystallographic planes and interplanar distances of 2.88 Å correspond to planes (011).

On the other hand, the angles between crystallographic planes can also be used to confirm their identity. Theoretical angles between planes in a crystal lattice can be calculated based on the Miller indices of the corresponding planes. For a cubic system such as face-centred cubic, the angle (θ) between two planes ($h_1k_1l_1$) and ($h_2k_2l_2$) is given by the following expression:[18]

$$cos\theta = \frac{h_1h_2 + k_1k_2 + l_1l_2}{\sqrt{h_1^2 + k_1^2 + l_1^2}\sqrt{h_2^2 + k_2^2 + l_2^2}} \quad \text{Eq. 2}$$

This equation allows for theoretical prediction of the angles between any two crystallographic planes. By comparing the measured angles obtained from the HR-TEM images with the calculated values, one can verify the identity of the observed planes and determine the zone axis along which the crystal is being viewed. Taking this into account, the angles between the identified planes in *Figure 12* were measured, obtaining that between two planes (111) there is an angle of 70.5 degrees, and between the planes (111) and (011) there is an angle of 35.3º. These experimental results are consistent with the predictions made by the previous equation (Eq. 2). The angles obtained also verify that the family of planes is imaged along the [110] zone axis. So, this mathematic study provides an additional confirmation of the structural analysis. It must be added that in the low magnification images of the dendrites *(Figure 12, left)*, it is possible to observe the (111) planes in multiple orientations within the same particle, indicating a polycrystalline nature.[19]

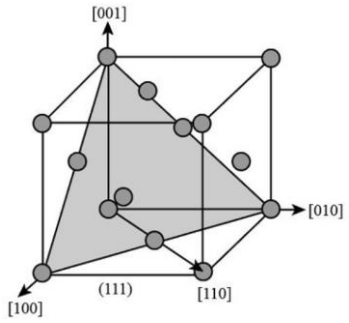

Figure 13. *FCC unit cell with one (111) plane shaded in grey.*

To better understand the experimental observations *Figure 13*[20] shows a face-centred cubic unit cell, where one of the (111) planes is highlighted in grey. In the experimental analysis made before, the planes were viewed along the [110] crystallographic direction, which is also drawn in *Figure 14.* It must be added that in the right panel of *Figure 13*, planes (111) are better distinguishable than any other plane of the lattice; that is because in FCC crystals, the (111) planes are the closest-packed atomic planes, meaning that atoms are disposed with the highest possible packing density. This dense atomic arrangement and regular spacing make (111) planes to produce strong and well-defined contrast in HR-TEM images.[21]

[18] C. Kittel, *Introduction to Solid State Physics*. John Wiley & Sons, Hoboken, eighth edition, **2018,** chapter 2.

[19] Y. Q. Wang, W. S. Liang, C. Y. Geng, *Nanoscale Res. Lett*. **2009,** *4* (7), 684−688.

[20] Adapted from: Ø. Storesund Hetland, *Atomistic Implications of Stacking Fault Energy on Dislocation - Void Interactions.* Master thesis. Norwegian University of Science and technology. **2012.**

[21] A. M. Khan, A. A. Al-Ghamdi, M. I. Khan, K. Ahmad, V. Kumar, S. M. Al-Hartomi, *Mater. Sci. Eng. B* **2017,** *220*, 26–32.

5.3. GOLD NANOSTRUCTURES WITH CH84

Scanning electron microscopy

As was done with the previous compounds, after 24 hours of stillness, the mixture of hydrated auric chloride and CH84 (10^{-5} M) at 90% w.r. in THF, was imaged. In this case, the largest dendrites of all this work have been imaged, and it is probably because CH84 contains two terminal triple bonds and five amide groups, which make it an effective reducing agent for gold. Some of the dendrites measure several microns, and they are combined with small nanovesicles of CH84 (grey in *Figure 14*). As occurred with CH83, the gold nanostructures are so big that they are on the outside of the vesicles.

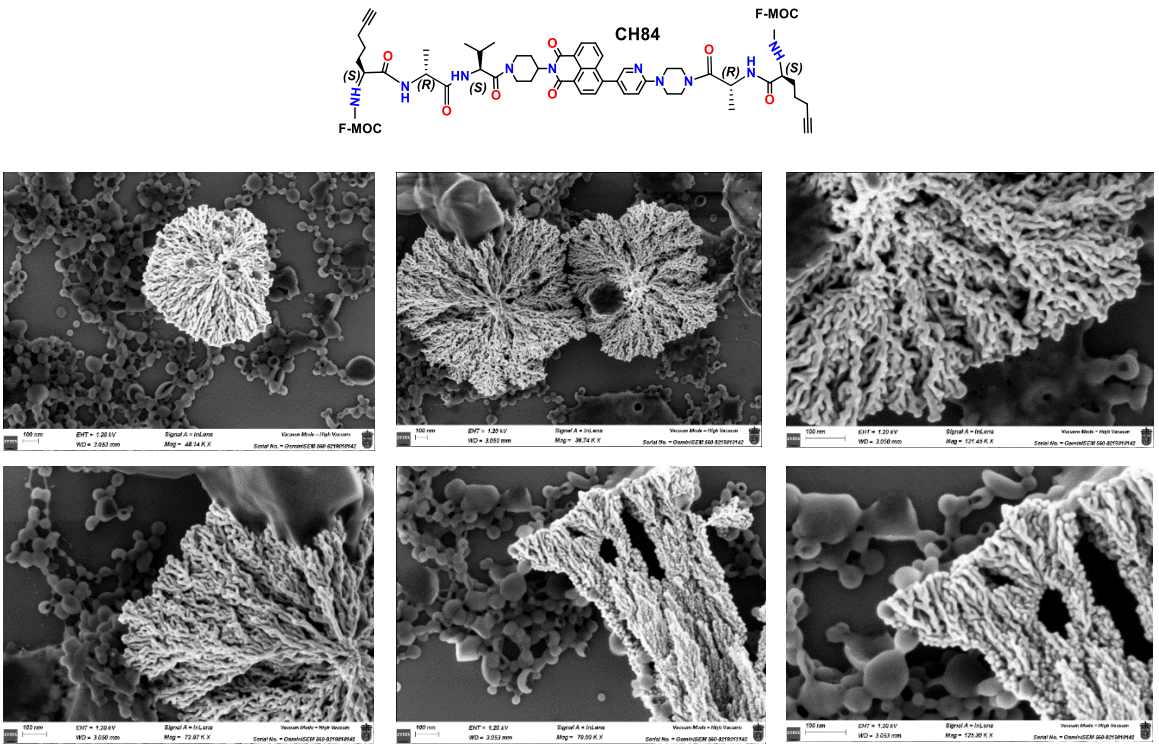

Figure 14. *FESEM images of gold nanodendrites formed in the studied mixture (CH84 90% w.r.)*

Energy-Dispersive X-ray Spectroscopy

A punctual elemental analysis was performed to corroborate the elemental composition of the structures seen in the FESEM images (*Figure 15*).

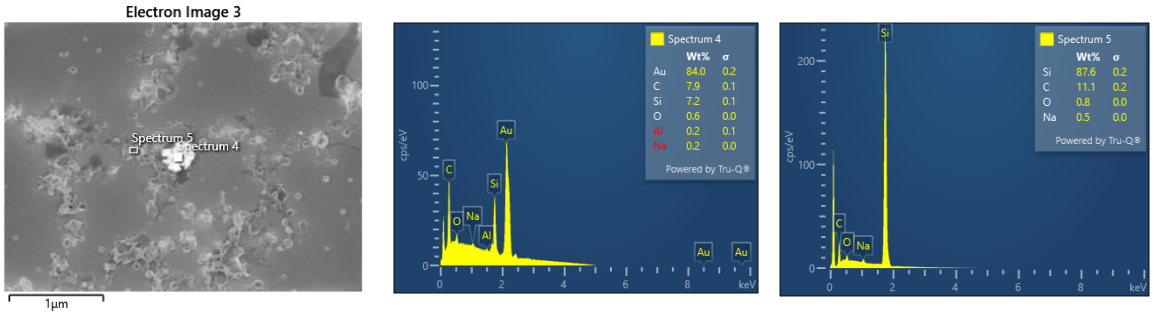

Figure 15. *Punctual EDX spectra of CH84 (90% w.r.): gold nanodendrites and carbon vesicles.*

As happened with the previous compound, the analysis of spectrum 4 reveals that the nanodendrites are made of elemental gold with a mass percentage of 84% *(Figure 16)*, thus confirming that auric chloride has been reduced to gold by CH84.

Spectrum 4							
Element	Line Type	Apparent Concentration	k Ratio	Wt%	Wt% Sigma	Standard Label	Factory Standard
C	K series	12.17	0.12166	7.86	0.12	Pure Element	Yes
O	K series	1.15	0.01008	0.57	0.05	SiO2	Yes
Na	K series	0.50	0.00427	0.18	0.04	Albite	Yes
Al	K series	0.68	0.00616	0.22	0.05	Al2O3	Yes
Si	K series	23.86	0.21876	7.21	0.10	SiO2	Yes
Au	M series	148.46	1.48461	83.97	0.19	Pure Element	Yes
Total:				100.00			

Figure 16. *Compositional analysis of spectrum 4. Pure gold is found.*

High resolution transmission electron microscopy

As was done with the previous compound, the dendrites were characterized at the atomic scale using HR-TEM. Images were first taken at low magnification *(Figure 17) and* then enlarged to analyse the crystallographic planes visible in a portion of the dendrite.

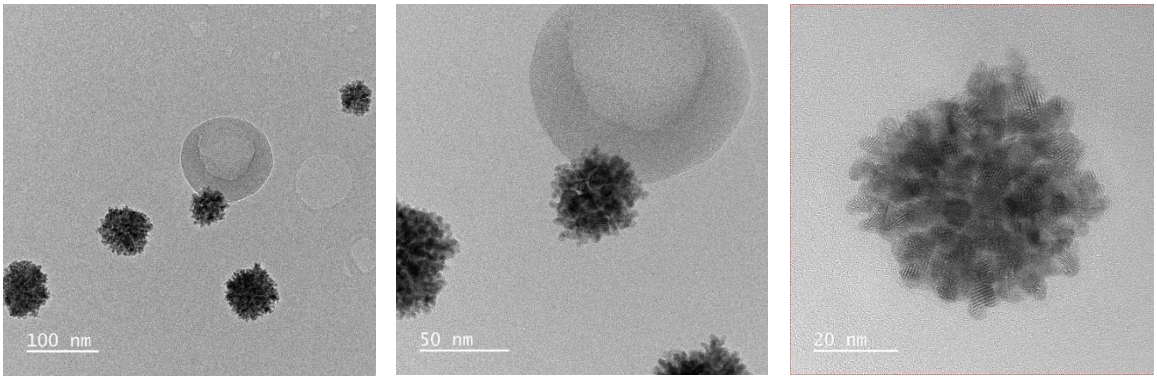

Figure 17. *HR-TEM images of gold nanodendrites formed in studied mixtures (CH84 90% w.r.)*

The nanodendrite observed on the far-right side of *Figure 17,* was digitally magnified (*Figure18*):

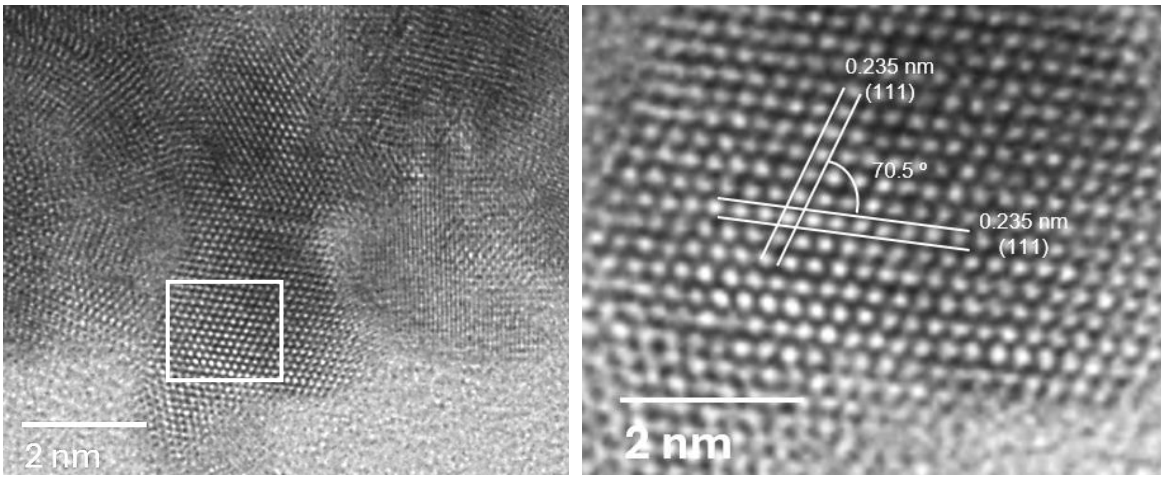

Figure 18*. Enlarged HR-TEM images of (111) crystallographic planes. Viewed along [110] zone axis.*

In the left panel of *Figure 18*, (111) planes appear in different orientations across different regions of the nanodendrite, confirming its polycrystalline nature. Unlike the previous compound, where multiple families of crystallographic planes were visible, in this case only the {111} facet can be distinguished. The right image of *Figure 18* reveals a lattice arrangement composed of equilateral triangles or regular hexagons. This geometry, resulting from the intrinsic cubic symmetry of the FCC structure, typically appears under imaging conditions where only the most densely packed planes are visible.[22] The appearance of these equilateral triangles in the right side of *Figure 18* is consistent with gold nanocrystals oriented along the [110] zone axis. In this projection, inclined {111} planes intersect at angles of 70.5°, generating the characteristic triangular lattice.

5.4. GOLD NANOSTRUCTURES WITH CH86-BIS

Scanning electron microscopy

After 24 hours of stillness, the sample of CH86-BIS (10^{-5} M) at 90% w.r. in THF mixed with gold(III) was imaged. In this case, the gold dendrites are smaller than those imaged in the previous sections; these new dendrites are of a similar size to the nanovesicles. They are intermingled among the nanovesicles, resembling nanofingers protruding from within them (*Figure 19*).

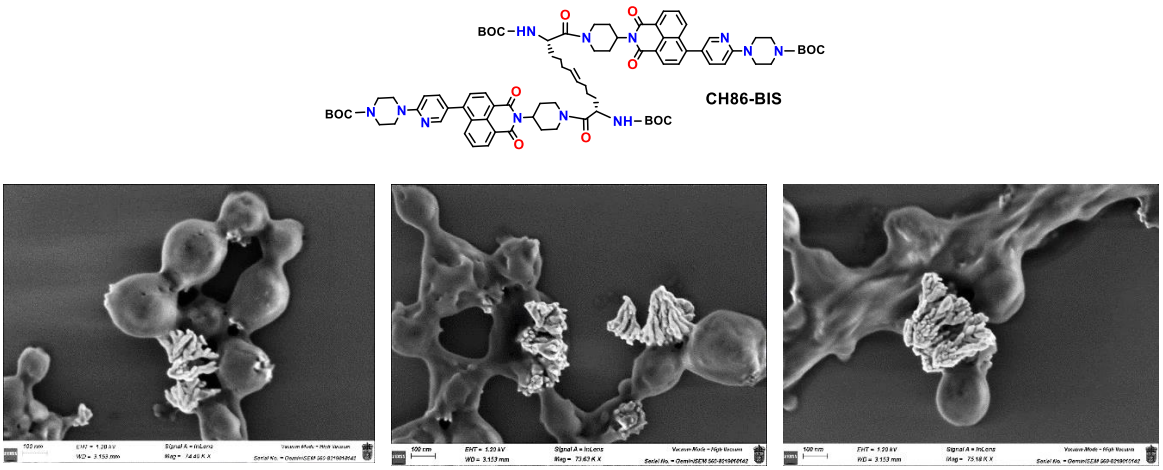

Figure 19. *FESEM images of gold nanodendrites protruding from the vesicles (CH86-BIS 90% w.r.)*

Transmission electron microscopy

This technique allows us to corroborate the earlier hypothesis that the dendrites originate from within the vesicles. In this case, the reduction of gold(III) occurs inside them. While FESEM imaging revealed only the portions of the dendrites protruding from the vesicle interiors, or those dendrites which had completely emerged, TEM imaging clearly demonstrates that the nanodendrites originate and grow inside the vesicles. The organic matter appears in grey, surrounding the gold structures, which are observed in black *(Figure 20)*.

[22] N. Bhattarai, S. Khanal, P. R. Pudasaini, S. Pahl, D. R. Urbina. *Int. J. Nanotechnol. Mol. Comput.* **2011**, *3* (3), 15–28.

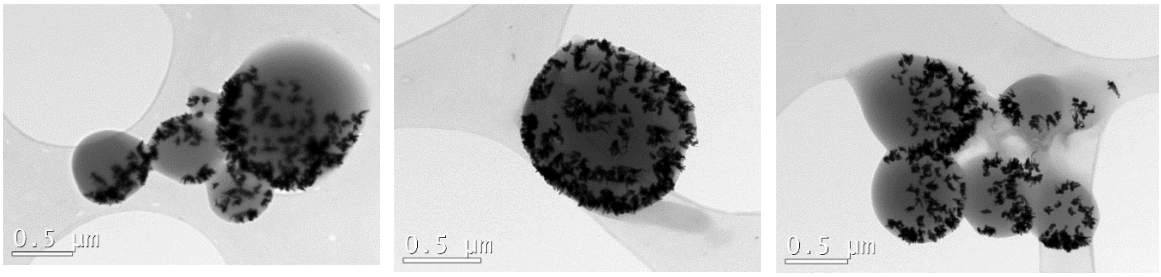

Figure 20. *TEM images of gold nanodendrites within the organic vesicles (CH86-BIS 90% w.r.)*

5.5. GOLD NANOSTRUCTURES WITH CH88

Scanning electron microscopy

Finally, after 24 hours of stillness, the mixture of hydrated auric chloride and CH88 (10^{-5} M) at 90% w.r. in THF, was imaged. Like the previous compound, the small-sized dendrites seem to emerge from the interior of the vesicles (*Figure 21*).

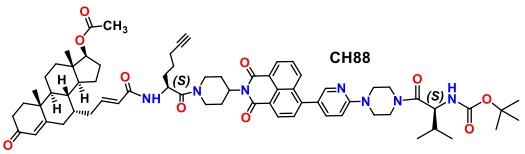

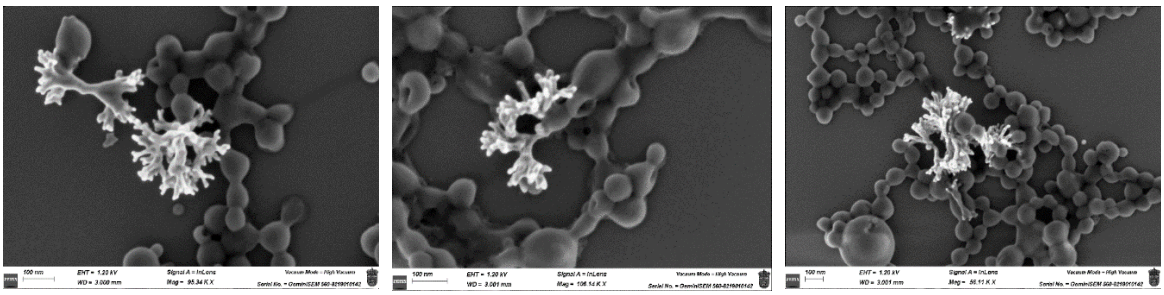

Figure 21. *FESEM images of gold nanodendrites protruding from the vesicles (CH88 90% w.r.)*

Transmission electron microscopy

From to the TEM images, we can confirm our hypothesis. The gold(III) is reduced inside the vesicles, which are formed before. Then, the nanodendrites grow within their cavities (*Figure 22*).

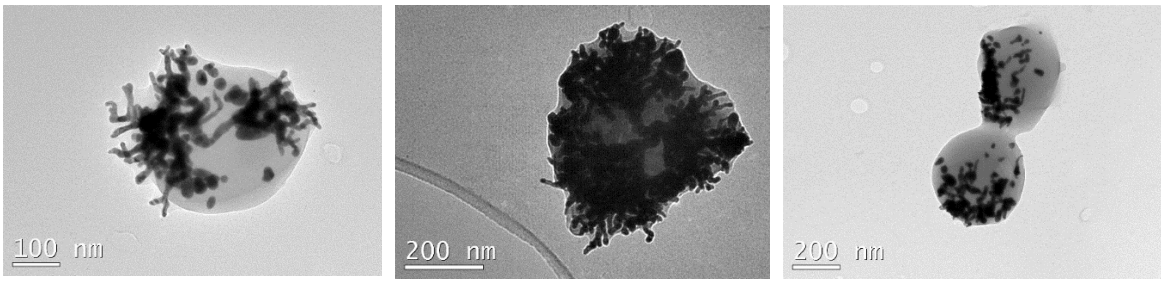

Figure 22. *TEM images of gold nanodendrites within the organic vesicles (CH88 90% w.r.)*

5.6. SUMMARY: INFLUENCE OF STRUCTURE ON NANODENDRITE GROWTH

From the results obtained, it can be concluded that distinct behaviours are observed in the formation of gold nanodendrites, depending on the specific compound involved.

On the one hand, compounds CH83 and CH84 exhibit a strong reducing capacity due to the presence of multiple amide bonds and triple bonds. This high reducing power causes the rapid formation of gold nanodendrites, which occurs before the vesicle formation. As a result, dendrites are observed on the surface of the vesicles rather than being integrated within them. Moreover, since they grow externally, these dendrites can reach very large sizes, this being consistent with reports of unconfined dendritic growth in reducing environments.[23]

In contrast, CH78 is also a compound with a high reducing capability, attributed to the presence of four amide bonds. In this case, dendrites are found embedded within the organic matrix. It is likely that vesicle formation and gold reduction occur simultaneously, which is reflected in TEM images showing dendrites enveloped by an amorphous organic shell. This suggests that the concurrent gold reduction process may interfere with the complete development of well-defined vesicular structures. And it is consistent with the large size of the imaged nanodendrites.

Finally, compounds CH86-BIS and CH88 exhibit a special behaviour: vesicle formation occurs first, followed by the reduction of gold inside them. This implies a slower reduction rate, allowing gold dendrites to be formed and grow inside the nanovesicles. FESEM and TEM images confirm this fact, as the dendritic structures appear to emerge from the interior of the vesicles. For CH86-BIS, this behaviour is consistent with its lower reducing potential, as it lacks triple bonds and contains only two amide groups. In the case of CH88, although it contains a triple bond (suggesting a potentially higher reducing power), it is hypothesised that the presence of a testosterone moiety in its structure promotes faster vesicle formation. Thus, the delayed formation of nanodendrites inside the vesicles is not necessarily due to a lower intrinsic reducing ability, but rather due to the accelerated self-assembly process. Some bibliography support that when dendrites grow within vesicles, their size is physically constrained by the internal cavity,[24] thus explaining the observation of smaller dendritic structures compared to those formed externally.

6. EFFECT OF SEQUENTIAL ADDITION OF REAGENTS ON GOLD NANODENDRITE FORMATION

The previous theory was established based on experiments in which the hydrated auric chloride and the organic compound were added simultaneously to the solution and left to evolve for 24 hours. However, we aimed to investigate how the gold nanodendrites would form when the auric chloride and the organic compound were added to the solution at different times.

So, another experiment was carried out, first the organic compound solution was prepared and then aged for 24 hours to give time for vesicles to form. After this time, 8 equivalents of the hydrated auric chloride solution were added, and the system was left to evolve for other 24 hours. The results are shown in the next section, and they seem to confirm the proposed theory. When the nanovesicles formation is forced to occur first, gold always grows within these structures. Consequently, in all cases, the resulting nanodendrites are confined by the vesicles. Under these new conditions, even compounds containing triple bonds produce small nanodendrites that appear to emerge from within the vesicles, as vesicle formation has been directed to precede the gold(III) reduction.

[23] X. Cao, S. Chen, W. Li, J. Li, L. Bi, H. Shi, *AIP Adv.* **2018**, *8* (10), 105133.
[24] J-D. Jang, H. Seo, Y.J. Yoon, S.H. Choi, Y.S. Han, T.H. Kim, *Sci. Rep.* **2022,** *12* (1), 4548.

Yet the optical results measured 24 hours after gold addition were comparable to those observed when gold(III) and compounds were simultaneously added. As in the previous case, the presence of organic material surrounding the vesicles inhibits the emission of the gold plasmon resonance, so the solutions are colourless or pale yellow. In addition, the AIE effect of the mixture sharply decreases when gold(III) is added, as occurred before.

6.1. STUDY OF CH78 WHEN GOLD(III) ADDITION IS DONE 24 HOURS APART

In *Figures 23a* and *23b,* it can be observed that the mixture of CH78 with gold(III) experiences a red shift of the absorption band respect to the reference, which is manifested as a yellow colour of the vial under visible light; however, the typical red hues associated with gold dendrite formation are not observed. Additionally, a decrease in the fluorescence emission intensity of the fluorophore is evident in *Figure 23c*. In the lower row, the nanodendrites appear significantly smaller compared to those formed when gold reduction occurred simultaneously with the self-assembly of the organic compound.

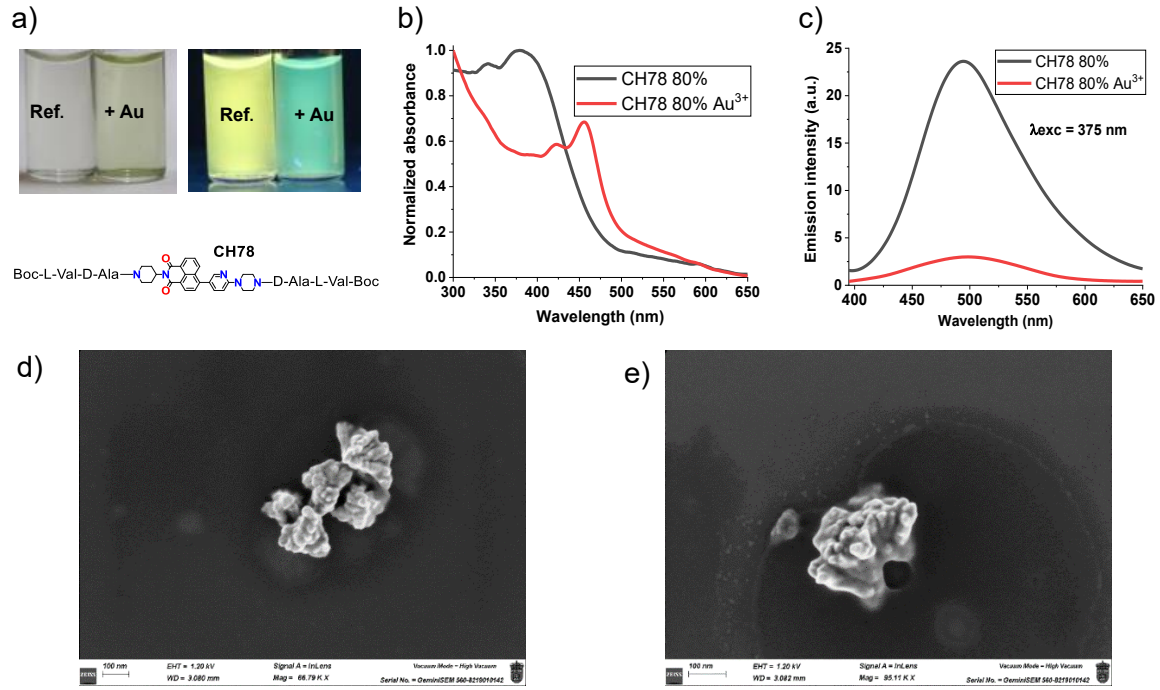

Figure 23. *(a) Photographs taken 24 h after gold addition. (b) Normalized absorption spectra of reference (black) and mixture (red). (c) Emission spectra of reference (black) and mixture (red). (d, e) FESEM images of nanodendrites with CH78 at 80%.*

6.2. STUDY OF CH83 WHEN GOLD(III) ADDITION IS DONE 24 HOURS APART

As occurred with the previous compound, the mixture gradually turns yellow over time *(Figure 24a);* however, the gold plasmon resonance remains inhibited, and no red coloration is detected. Notably, in this case, gold dendrites now emerge from within the vesicles, as the system has been directed to promote this behaviour. It must be reminded that this compound had high reducing power so, when gold((III) and the compound were added simultaneously, large dendrites were observed, since they were probably formed faster than the vesicles; however, under these new conditions, dendrite formation occurs after formation of the vesicles and gold dendrites are confined by the vesicle size.

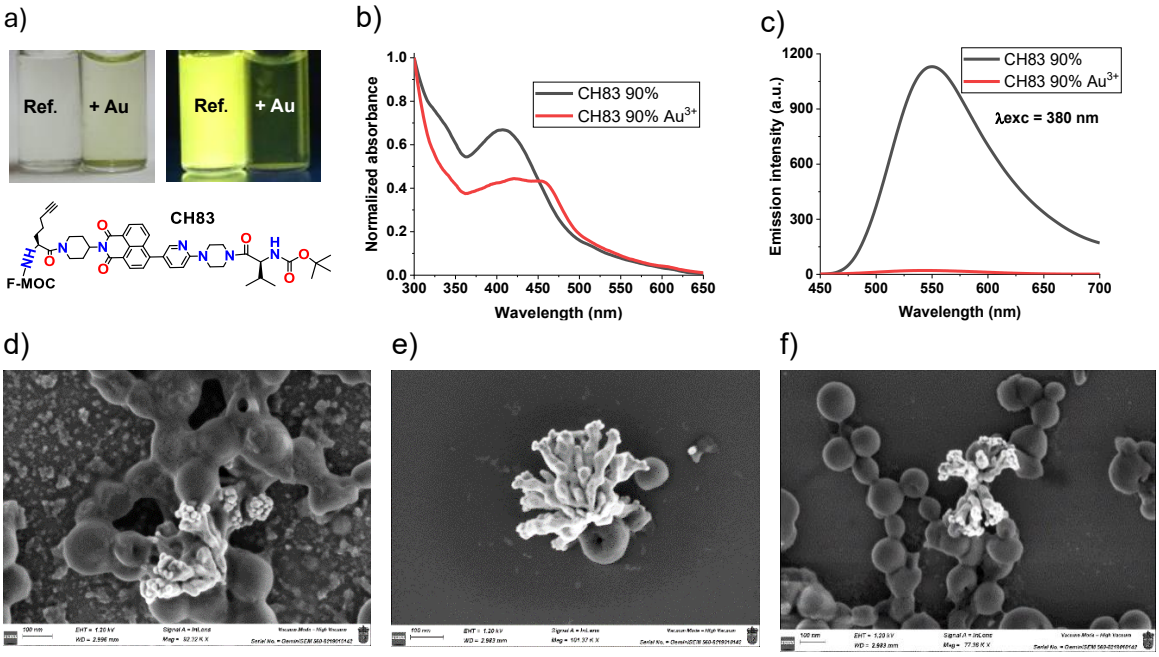

Figure 24. *(a) Photographs taken 24 h after gold addition. (b) Normalized absorption spectra of reference (black) and mixture (orange). (c) Emission spectra of reference (black) and mixture (red). (d, e, f) FESEM images of nanodendrites with CH83 at 90%.*

6.3. STUDY OF CH84 WHEN GOLD(III) ADDITION IS DONE 24 HOURS APART

The optical changes are similar to those observed before *(Figure 25, top row).* In this case, the mixture under visible light does not turn as yellow as with the previous compound, but a clear quenching of the AIE effect is observed in the emission spectrum *(Figure 25c).* The FESEM images show how the gold nanodendrites are very small and are embedded between the vesicles of CH84. In contrast to the structures observed with simultaneous addition, large nanodendrites are no longer present.

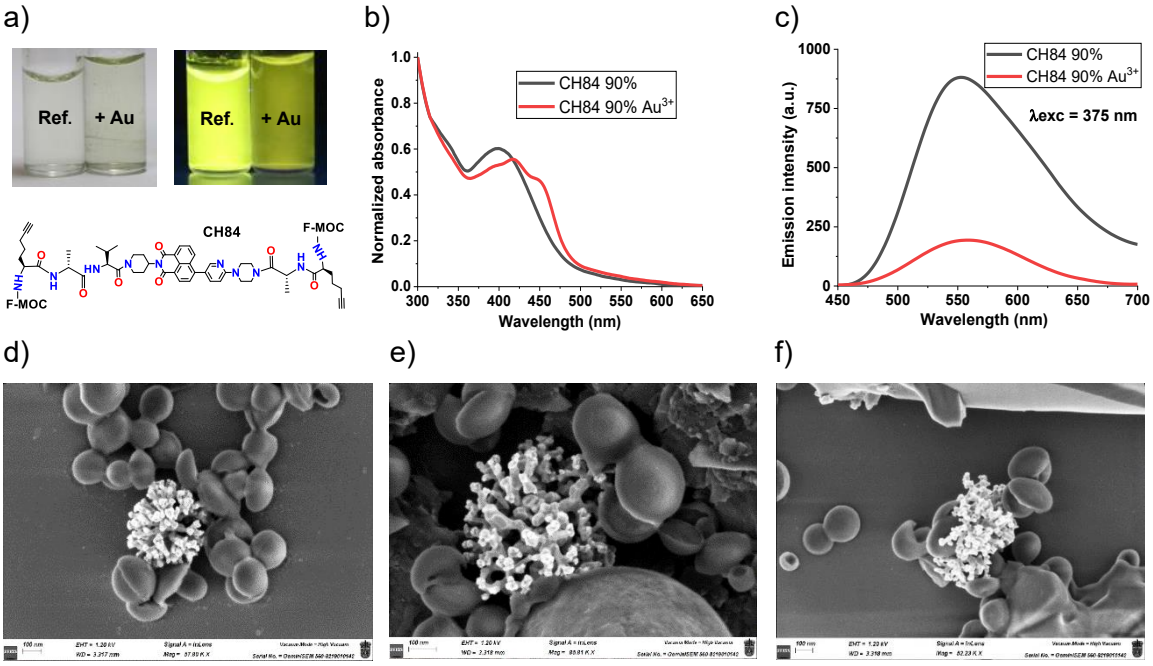

Figure 25. *(a) Photographs taken 24 h after gold addition. (b) Normalized absorption spectra of reference (black) and mixture (orange). (c) Emission spectra of reference (black) and mixture (red). (d, e, f) FESEM images of nanodendrites with CH84 at 90%.*

6.4. STUDY OF CH86-BIS WHEN GOLD(III) ADDITION IS DONE 24 HOURS APART

This compound exhibits one of the lowest reducing power, and consequently, in the simultaneous addition experiments, it was already observed that gold dendrites are formed inside vesicles. This theory is supported by the new experiment, which clearly shows that vesicles formation takes place before gold nucleation. Like in the previous case, nanodendrites are now observed to emerge from within the vesicles. Regarding the optical changes, they are very similar to those reported in the previous cases, including those observed under simultaneous addition conditions. A red shift of the absorption band occurs, manifested as a yellow coloration of the mixture under visible light *(Figure 26a)*. In this case, the emission spectrum shows a marked quenching of fluorescence upon gold addition *(Figure 26c)*.

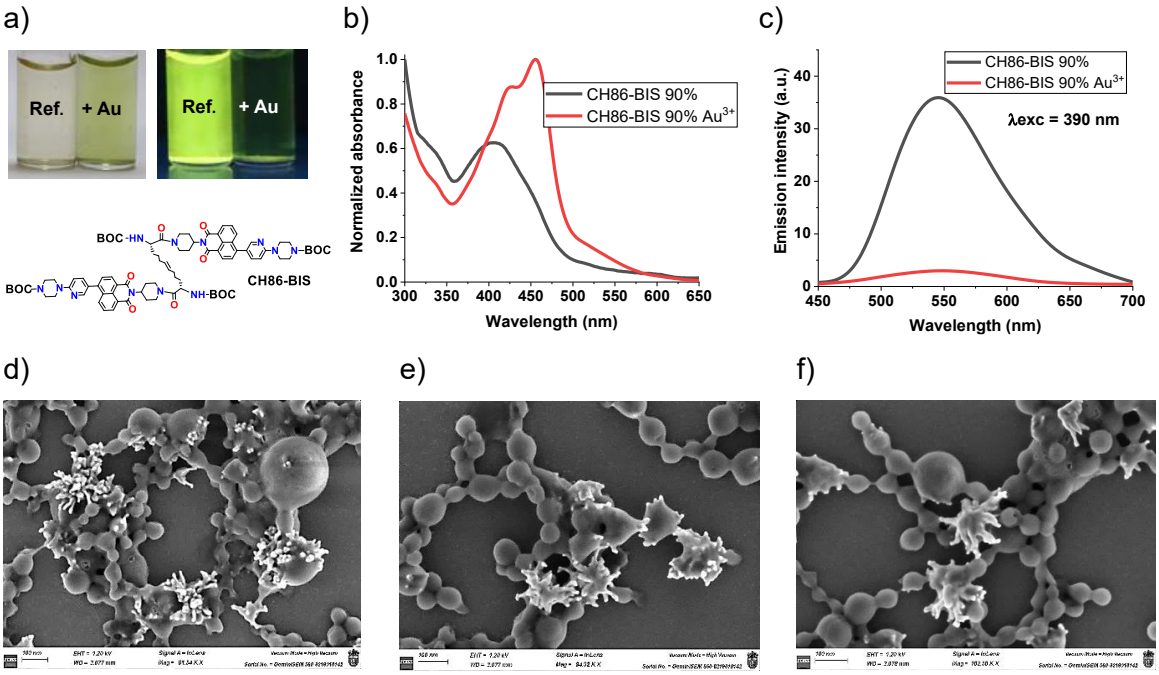

Figure 26. *(a) Photographs taken 24 h after gold addition. (b) Normalized absorption spectra of reference (black) and mixture (orange). (c) Emission spectra of reference (black) and mixture (red). (d, e, f) FESEM images of nanodendrites with CH86-BIS at 90%.*

6.5. STUDY OF CH88 WHEN GOLD(III) ADDITION IS DONE 24 HOURS APART

Finally, the results for CH88 are presented. Since this compound contains a triple bond, we could expect a similar behaviour to the other compounds with triple bonds. However, as explained before, the presence of the testosterone moiety in the structure promotes very fast vesicle formation. Consequently, in simultaneous addition experiments, the nanodendrites were embedded within the vesicles because gold reduction occurred after self-assembly of the vesicles. This is further confirmed by the current experiment, where it is assured that vesicles are formed first in the absence of gold, and the auric chloride was added 24 hours later, resulting in nucleation within the vesicles. FESEM images of *Figure 27* clearly show the nanodendrites protruding from the vesicles as occurred before. Regarding the optical changes, in this case, the red shift of the absorption band and the resulting yellow coloration of the solution are more pronounced than in the previous cases, as is the quenching of the AIE effect *(Figure 27, top row)*.

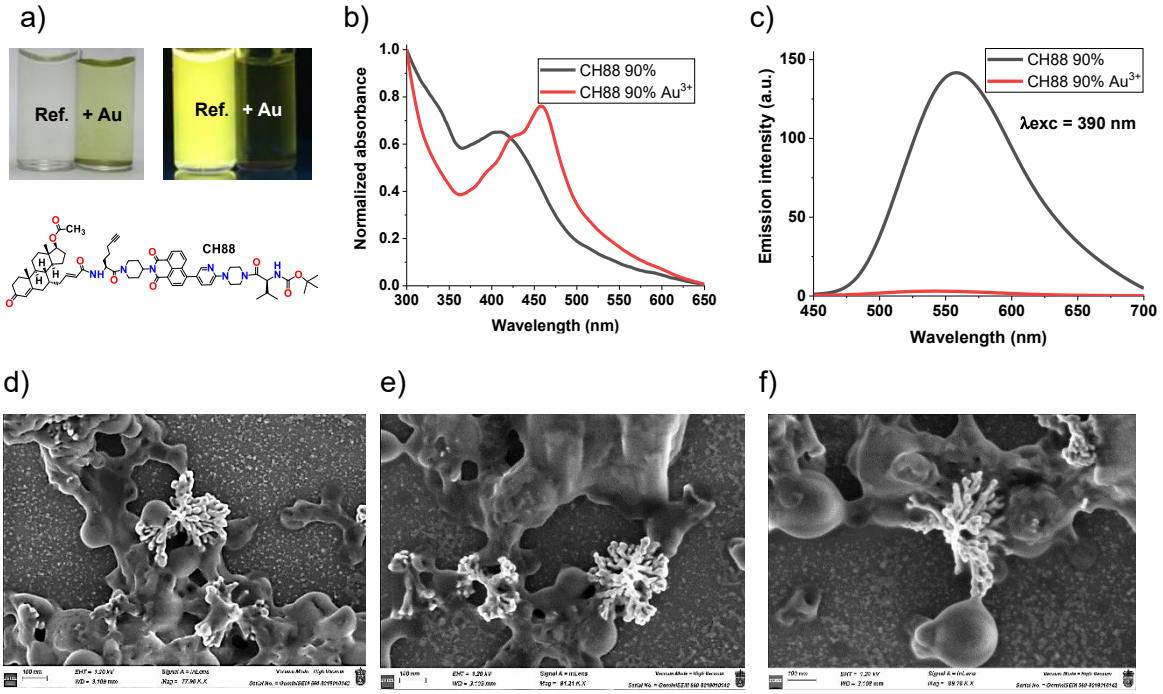

Figure 27. *(a) Photographs taken 24 h after gold addition. (b) Normalized absorption spectra of reference (black) and mixture (orange). (c) Emission spectra of reference (black) and mixture (red). (d, e, f) FESEM images of nanodendrites with CH88 at 90%.*

7. SIZE OF NANODENDRITES: A COMPARATIVE STUDY BY DLS

Summary: In this section, the size of the nanostructures formed by each compound combined with gold(III) is studied using DLS. In this study we compare the size of nanostructures formed by each individual compound in THF-water mixtures with the size of the nanostructures from the same compounds combined with gold(III). Two different conditions were tested: simultaneous addition of gold(III), and its addition 24 hours later. The results show a clear trend: after addition of gold(III), the size of aggregates measured by DLS increases significantly. This is due to a strong interaction between the gold(0) and the organic structures, leading DLS to detect superaggregates that incorporate both the gold nanodendrites and the organic vesicles. This size increase has one explanation for compounds CH83 and CH84, which possess high reducing power, whereas the size increase when gold(III) is added has a different explanation for CH86-BIS and CH88, which seem to self-assemble prior to gold(0) nucleation. On the other hand, mixtures of gold(III) with CH78 also exhibit an increase in size of nanostructures; however, the evolution pattern observed is distinct from that of the other compounds.

In the next table the DLS results of CH83 and CH84 are collected. As can be seen in *Table 2*a, isolated CH83 forms nanovesicles with an average size of approximately 172 nm (blue curve). When gold(III) is added simultaneously to the organic compound, the average size increases significantly to 449.7 nm (orange curve). In this case, the dendrites are formed outside the vesicles and can reach larger sizes. In contrast, when gold(III) is added 24 hours apart, an intermediate size of 284 nm is observed (green curve). This is because the gold dendrites now grow inside the vesicle, leading to the formation of superaggregates that combine both structures. As a result, DLS detects a signal larger than the one corresponding to nanovesicles from the isolated compound. A similar behaviour is observed for CH84, the other compound with a high reducing power. However, in this second case, the increase is less notorious *(Table 2b).*

***Table 2**. DLS results of CH83 and CH84 at 90% w.r. Samples of single compounds and gold-mixtures*

a)

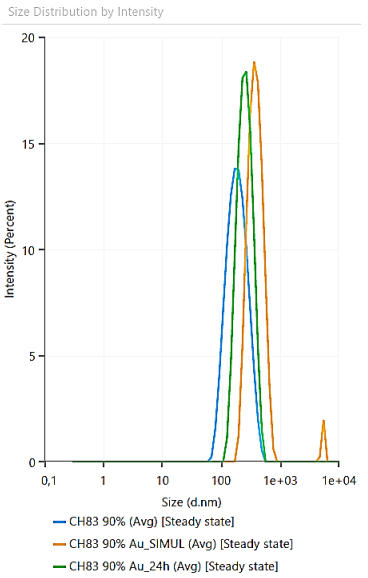

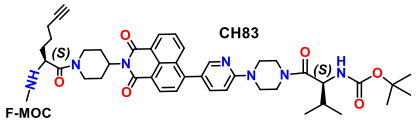

Isolated CH83.

Z-Average (nm)	: 172
Polydispersity Index (PI)	: 0,1274
Intercept	: 0,9786

Simultaneous addition of gold(III).

Z-Average (nm)	: 449,7
Polydispersity Index (PI)	: 0,3565
Intercept	: 0,8439

Gold(III) addition 24 hours apart.

Z-Average (nm)	: 284
Polydispersity Index (PI)	: 0,3646
Intercept	: 0,8945

b)

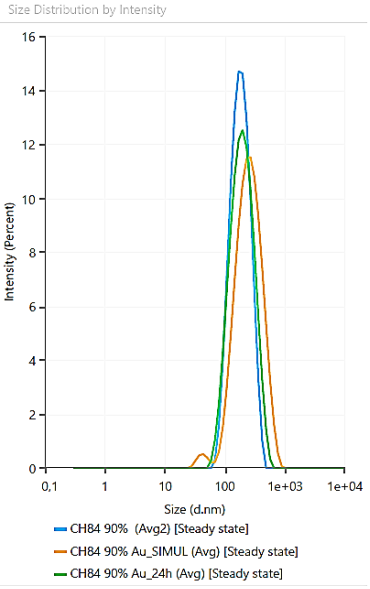

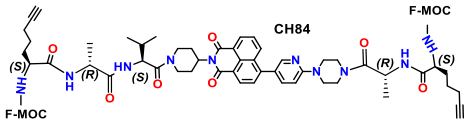

Single CH84.

Z-Average (nm)	: 162,9
Polydispersity Index (PI)	: 0,1514
Intercept	: 0,9696

Simultaneous addition of gold(III).

Z-Average (nm)	: 221
Polydispersity Index (PI)	: 0,2355
Intercept	: 0,8875

Gold(III) addition 24 hours apart.

Z-Average (nm)	: 174,3
Polydispersity Index (PI)	: 0,2202
Intercept	: 0,9448

On the other hand, the analysis of CH86-BIS *(Table 3a)* shows that when the single compound is dissolved in THF-water, the vesicles have an average size of 109.1 nm (blue curve). Upon addition of gold(III), either simultaneously or after a 24-hour delay, the aggregate size measured by DLS increases significantly to 561 and 405.1 nm (orange and green curves respectively). While both conditions lead to size growth due to the formation of dendrites inside the vesicles, the degree of this increase differs. In the case of simultaneous addition, the organic material and gold precursors co-assemble and grow together from the beginning, forming large hybrid aggregates that integrate organic vesicles and gold dendrites inside them. In contrast, when gold is added after a 24-hour delay, the vesicular aggregates have already formed and stabilized at a smaller size, close to that of the organic compound alone. Upon addition of gold(III), nucleation and growth occur mainly inside and between these pre-existing vesicles, leading to the formation of superaggregates that increase the average size, but not as dramatically as in the case of simultaneous

growth. This tendency is also observed for CH88, since with this compound the gold nanodendrites always grow inside the vesicles.

***Table 3**. DLS results of CH86-BIS and CH88 at 90% w.r. Samples of single compounds and gold-mixtures*

a)

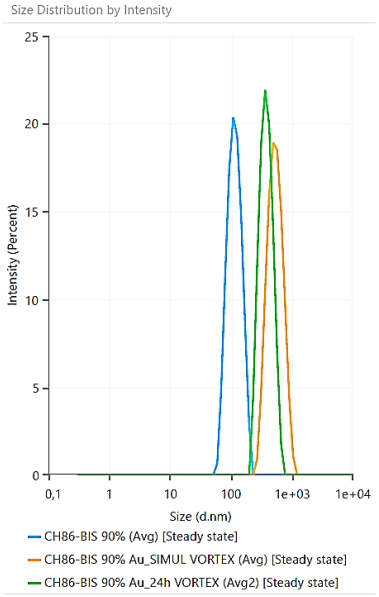

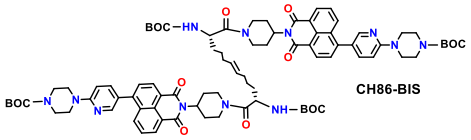

Single CH86-BIS.

Z-Average (nm)	: 109,1
Polydispersity Index (PI)	: 0,05288
Intercept	: 0,9835

Simultaneous addition of gold(III).

Z-Average (nm)	: 561
Polydispersity Index (PI)	: 0,2579
Intercept	: 0,8481

Gold(III) addition 24 hours apart.

Z-Average (nm)	: 409,3
Polydispersity Index (PI)	: 0,2212
Intercept	: 0,8415

b)

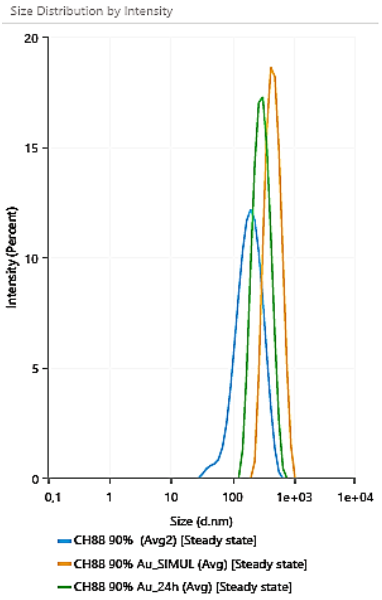

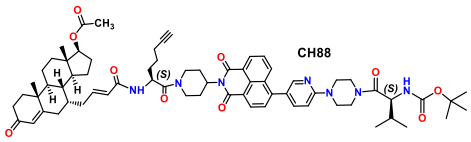

Single CH88.

Z-Average (nm)	: 164,1
Polydispersity Index (PI)	: 0,1878
Intercept	: 0,9797

Simultaneous addition of gold(III).

Z-Average (nm)	: 462,3
Polydispersity Index (PI)	: 0,194
Intercept	: 0,811

Gold(III) addition 24 hours apart.

Z-Average (nm)	: 299,8
Polydispersity Index (PI)	: 0,1924
Intercept	: 0,828

CH78 exhibits an opposite growth trend compared to the rest of compounds. Previous observations showed that the nanodendrites formed in this system tend to become embedded within the organic matrix, likely due to nucleation occurring at a rate similar to that of the self-assembly process. Isolated CH78 displays an average size of 152 nm. When gold(III) is added simultaneously, DLS detects an average aggregate size of approximately 346.7 nm. However, when gold is added 24 hours after the organic aggregation, the measured size increases, reaching around 405 nm. This suggests that the delayed addition of gold(III) leads to the collapse and clustering of the already-formed organic aggregates, resulting in the formation of larger superaggregates in which the gold nanodendrites become embedded, thereby yielding even larger hybrid structures *(Table 4)*.

***Table 4**. DLS results of CH78 at 80% w.r. Samples of single compound and gold-mixtures*

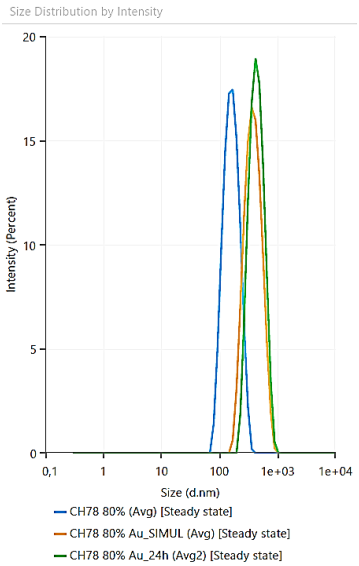

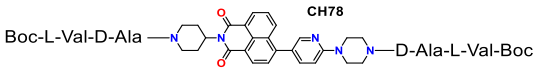

Isolated CH78.

Z-Average (nm)	: 152
Polydispersity Index (PI)	: 0,09046
Intercept	: 0,9767

Simultaneously addition of gold.

Z-Average (nm)	: 346,7
Polydispersity Index (PI)	: 0,1358
Intercept	: 0,8641

Gold addition 24 hours apart.

Z-Average (nm)	: 405,1
Polydispersity Index (PI)	: 0,1476
Intercept	: 0,8753

8. GOLD NANOPARTICLES AS SUZUKI-MIYAURA CATALYSTS

The Suzuki-Miyaura cross-coupling reaction, widely utilized in the formation of biaryl and sp^2-sp^2 carbon-carbon bonds, has traditionally been catalysed by homogeneous palladium complexes. However, as seen in the introduction, recent advances have demonstrated that metallic gold (Au^0) nanoparticles can act as efficient heterogeneous catalysts for this transformation, expanding the scope of transition-metal catalysis in cross-coupling chemistry. In addition, gold nanoparticles have gained significant attention due to its high catalytic efficiency, chemical inertness, and recyclability.[13]

The mechanism of the gold-catalysed Suzuki reaction in a heterogeneous context is hypothesized to occur at the surface of gold nanoparticles, which offer high surface-to-volume ratios and unique electronic properties. The catalytic cycle involves three mechanistic steps analogous to traditional palladium catalysis: oxidative addition, transmetalation, and reductive elimination *(Figure 28).*

Oxidative addition: The process begins with adsorption of the aryl halide (Ar-X) onto coordinatively unsaturated surface atoms (edges or corners) of the Au^0 nanoparticles, thereby activating the C-X bond through surface-mediated interactions. This adsorption can induce local oxidation of gold atoms to Au(I) or Au(III), enabling oxidative addition-like reactivity, even though gold, in its bulk metallic form, is typically considered catalytically inert. [25]

Transmetalation: Subsequently, the arylboronic acid or ester ($Ar'–B(OH)_2$ / $Ar'–B(OR)_2$), activated in the presence of a base, undergoes transmetalation, transferring the aryl moiety to the surface-bound Au-Ar intermediate. This step results in the formation of a bis-aryl species at the metal interface, yielding a surface complex of the type Au(Ar)(Ar′).[26]

Reductive elimination: the resulting Au(Ar)(Ar′) species undergoes reductive elimination, producing the desired biaryl compound (Ar-Ar′) and regenerating the catalytically active Au^0 surface. The ease of reductive elimination is significantly influenced by the geometric

[25] A. S. K. Hashmi, *Chem. Rev*. **2007,** *107* (7), 3180–3211.
[26] H. Tsunoyama, H. Sakurai, N. Ichikuni, Y. Negishi, T. Tsukuda, *Langmuir* **2004**, *20*, 11293–11296.

constraints and electronic properties of the gold nanoparticle surface. This step closes the catalytic cycle and maintains turnover.[6]

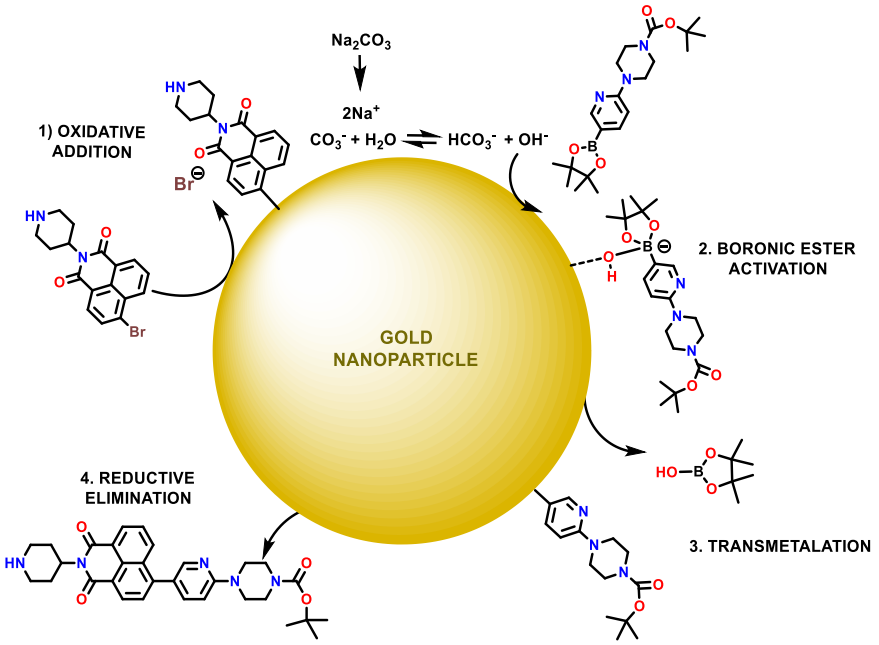

Figure 28. *Catalytic process of Suzuki-Miyaura reaction on a gold nanoparticle surface.*

Although some controversy remains over whether the catalysis is purely heterogeneous or involves leaching of Au(I) species into solution (i.e., a quasi-homogeneous cycle),[27] several studies suggest that the solid gold surface plays a dominant role, especially when leaching is minimal or reversible.[28] So, it can be stated that heterogeneous gold catalysis represents a sustainable and efficient platform for Suzuki couplings but, the success of this system depends critically on nanoparticle size, surface morphology, and metal-support interactions.

8.1. USE OF GOLD NANODENDRITES AS CATALYSTS

Based on the previous background, we wanted to evaluate if the gold nanodendrites were able to catalyse the Suzuki reaction. This reaction has been extensively studied by our research group, since the starting naphthalimides (described in the introduction of Chapter 1) are synthesized via this route. We typically used tetrakis(triphenylphosphine)palladium(0) as catalyst and a solvent mixture of toluene, butanol, and water. However, this method is not considered environmentally friendly. Therefore, we explored an alternative approach, performing the reaction in a 90:10 mixture of H_2O:THF, and employing the CH84-derived gold nanodendrites as the catalyst.

We selected CH84 since with this compound, the nanodendrites are formed on the exterior of the nanovesicles, providing a larger active gold surface for catalysis. Moreover, these dendritic structures display a high degree of folding (surface defects), numerous nanofingers, and are more abundant than those formed by any other compound tested. Concretely, the catalyst was formed by 1.09 mg of auric chloride and 0.48 mg of CH84 in 5 ml of a THF-H_2O (90% w.r.) mixture. The following section describes the synthetic process

[27] F. Mohammadparast, A. P. Dadgar, R. T. A. Tirumala, S. Mohammad, C. O. Topal, A. K. Kalkan, M Andiappan, *J. Phys. Chem. C* **2019**, *123* (18), 11539−11545.

[28] M. Sankar, Q. He, R. V. Engel, M. A. Sainna, A. J. Logsdail, A. Roldan, D. J. Willock, N. Agarwal, C. J. Kiely, G. J. Hutchings, *Chem. Rev.* **2020,** *120* (8), 3890−3938.

of a naphthalimide via this gold-catalysed Suzuki-Miyaura reaction (the product that is going to be synthesized is the one represented in the previous diagram of *Figure 28*).

8.1.1. Synthesis of *N*-(piperidin-4-yl)-4-[2-((4-*N*'-Boc)piperazin-1-yl)pyridin-5-yl]naphthalen-1,8-dicarboxylmonoimide (CH01-S)

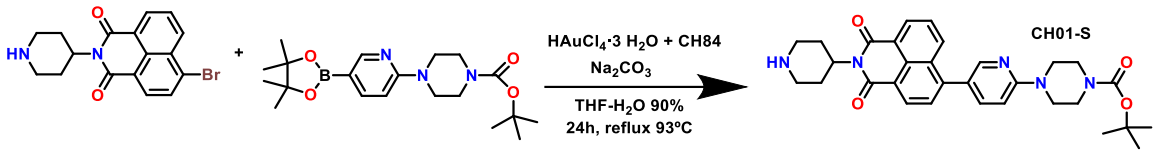

Figure 29. *Synthetic scheme to obtain CH01-S.*

In a 50 ml flask, provided with a magnetic stirrer, 10 mg of *N*-piperidine-4-bromonaphtalene-1,8-dicarboxylmonoimide (1 eq. 27.8 µmol), 11.4 mg of 2-(4-Boc-piperazine)pyridine-5-boronic acid pinacol ester (1.05 eq., 29.2 µmol) and 29.5 mg of sodium carbonate (10 eq. 0.3 mmol) were dissolved under argon atmosphere in 1 ml of THF to ensure the complete dissolution of the organic reagents. Then, 9 ml of distilled water were added. Finally, 5 ml of the catalyst (from 0.1 eq. of $HAuCl_4 \cdot 3H_2O$ mixed with 0.0125 eq. of CH84 in THF-H_2O (1:9)) were added preserving the inert atmosphere. The mixture was stirred overnight at reflux of 93ºC. Once the reaction had finalized, the solvent was evaporated under reduced pressure and the solid dissolved in DCM. Then, in a separatory funnel the product was washed with water (3x20ml). The organic extracts were combined, dried over anhydrous Na_2SO_4 and the solvent was evaporated under reduce pressure. Finally, the product was purified by column chromatography (SiO_2) employing a DCM-MeOH mixture, gradually increasing the MeOH content from 0 % to 7%. Finally, 8.5 mg of CH01-S were obtained.

Discussion of results

8.5 mg of product were obtained, meaning a 56% yield. Although this yield is lower than what is typically achieved with classical palladium-based catalysts, it is still a satisfactory result considering that the reaction was carried out under eco-friendly conditions. This experiment also demonstrates that the gold nanodendrites, once formed, are stable in THF-water mixtures even under reflux conditions. Moreover, it must be mentioned that due to column chromatography, the final product could be efficiently separated, as it exhibits a considerable different elution rate compared to both the gold catalyst and CH84.

Then, it was hypothesized that the reaction yield could be improved by employing classical solvents. Therefore, the reaction was repeated using the same amounts of reagents but dissolved in a mixture of toluene:butanol:THF/water in a 4:1:2 ratio. The gold nanodendrites were prepared as before in a 5 ml THF-water (1:9) mixture; then, 10 ml of toluene and 2.5 ml of butanol were added. The reaction was carried out under an argon atmosphere and refluxed overnight at 105 °C. Nevertheless, the result was unsatisfactory. TLC analysis of the crude mixture revealed a very faint spot corresponding to the final product, indicating a low reaction yield. Furthermore, the ^{1}HNMR spectrum of the crude mixture showed that a significant amount of unreacted starting materials remained there. Given the very low amount of final product, column purification was not carried out, since the yield was estimated to be less than 10%.

This experiment highlights that gold nanodendrites are not active in this classical solvent system; they likely redissolve or disaggregate under these conditions, making them catalytically inactive. Thus, the most effective conditions for this reaction with gold nanodendrites are those employing THF-water, being them more eco-friendly than other methods typically used.

9. SILVER NANOPARTICLES FORMATION

Once it was known that these compounds are able to reduce gold, the same study was conducted with silver. In this case, a silver perchlorate solution ($AgClO_4 \cdot 2\ H_2O$) $8 \cdot 10^{-5}$ M, was first analysed in a THF-water mixture containing 90% water, to determine the type of structures formed by silver(I) in the absence of organic compounds. Subsequently, all compounds selected in this chapter were studied in the presence of silver(I), but only CH83 and CH88 yielded favourable results. It was surprising to find that silver forms tiny and spherical nanoparticles that coat the surface of the nanovesicles. It must be mentioned that this type of particles had not been observed in the blank sample, when only silver was studied. The formation of a metallic layer was similar for both compounds independently to their reduction power: it is estimated that vesicle formation occurs first, followed by their coating with reduced silver. It must be mentioned that, in this case, optical changes were studied only qualitatively.

9.1. SILVER NANOPARTICLES ON CH83

CH83 (10^{-5} M in THF) was combined with an excess of silver (8 equivalents of $AgClO_4 \cdot 2\ H_2O$ dissolved in water), then additional water was added to reach a solvent mixture of 90% H_2O and 10% THF. The first objective was to see if there are changes in the NMI's emission and, therefore, interaction with the metal. *Figure 30* shows that no visible colour changes occur in the mixture. However, under UV light, a slight increase in the AIE effect is observed compared to the silver-free reference, thus indicating a possible interaction with the metal. After conducting the optical analysis, FESEM images were acquired, revealing a film of silver nanoparticles coating the gold vesicles (*Figure 31*).

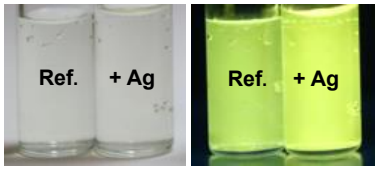

Figure 30. *Optical changes after 24 h of evolution (CH83 at 90% w.r. mixed with silver).*

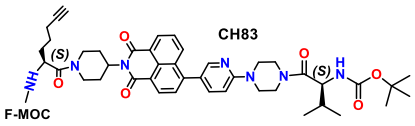

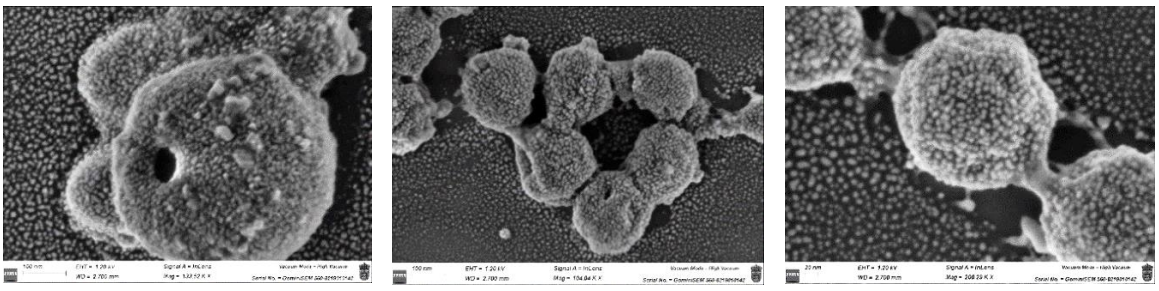

Figure 31. *Silver nanoparticles covering the nanovesicles' surface (CH83 90% w.r.)*

Then, the silver nanoparticles were reimaged using Backscattered electrons (BSEs). These are high-energy electrons that are reflected or scattered back from a sample by atomic nuclei. These BSEs, unlike secondary electrons, originate from deeper within the sample and are used to image the sample's elemental composition and topography. White particles are made of silver and grey surface is carbon *(Figure 32).*

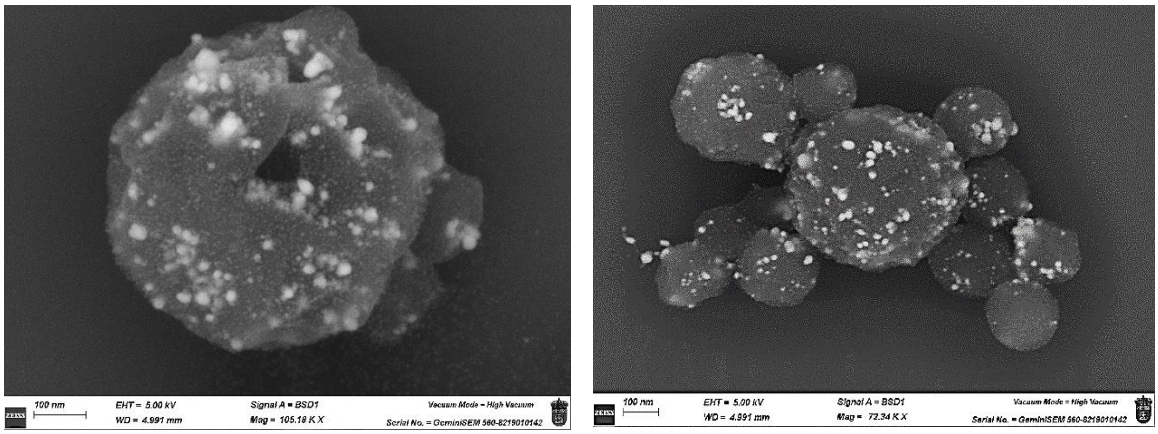

Figure 32. *BSEs image: silver nanoparticles covering the nanovesicle's surface of CH83 at 90% w.r.*

Then, the elemental analysis using Energy Dispersive X-ray Spectroscopy mapping confirmed that there is a silver coat (blue) on the carbon surface of the vesicles (red).

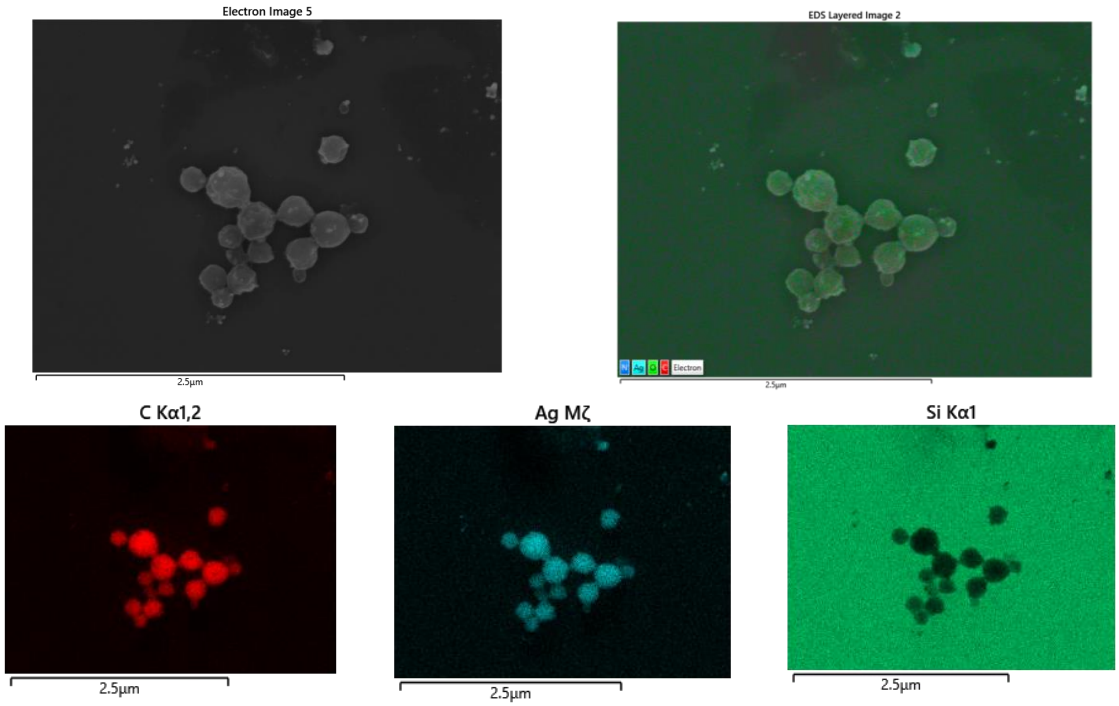

Figure 33. *EDX mapping spectra: silver nanoparticles (blue) covering the CH83 nanovesicles surface (red).*

9.2. SILVER NANOPARTICLES ON CH88

Subsequently, CH88 was also mixed with 8 equivalents of $AgClO_4 \cdot 2\ H_2O$, and the resulting mixture (THF-Water 90%) was left to evolve for 24 hours. After this period, photographs were taken, revealing that under 366 nm UV light, the colour of the emitted light changes from green (reference) to yellow (silver-containing mixture), indicating a possible interaction with silver(I). However, under visible light there is no change in the colour of the vial.

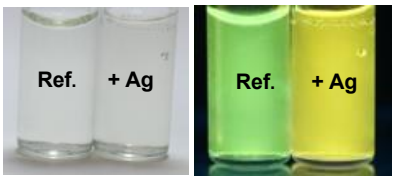

Figure 34. *Optical changes after 24 h of evolution (CH88 at 90% w.r. mixed with silver(I)).*

After conducting the optical analysis, FESEM images were acquired, revealing silver coating on the nanovesicles' surface.

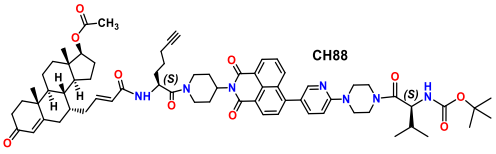

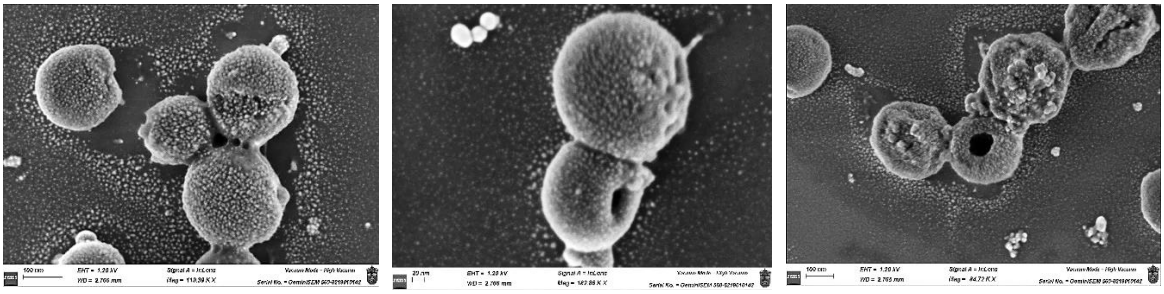

Figure 35. *Silver nanoparticles covering the nanovesicles' surface (CH88 90% w.r.)*

These two compounds have been identified as capable of promoting the reduction of silver(I), resulting in the formation of a film on the vesicle's surface. However, this deposition is not completely selective. Around the vesicles, on the silicon plate, some silver nanoparticles are also deposited. It is worth mentioning that during FESEM imaging, as the sample was scanned, elemental silver appeared to be concentrated exclusively in areas where nanovesicles were present, whereas no deposition was observed in regions with no organic material. Nonetheless, once silver(I) is reduced on the nanovesicle surface, a portion of it tends to deposit around the vesicles, directly on the near silicon substrate.

In the elemental mapping analysis of CH83, it was clearly observed that the highest concentration of silver (blue spheres) is located on the surface of the vesicles. This suggests that silver(I) reduction occurs after the self-assembly of naphthalimides and the subsequent vesicles formation.

10. CONCLUSIONS

In this chapter it has been shown how the studied amino acid-bearing AIEgens can act as reducing, stabilizing, and structure-directing agents for the green synthesis of metal nanostructures. Particularly, gold nanodendrites and silver films on nanovesicles have been created. From the experiments conducted, it was established that the presence of amide bonds and aliphatic unsaturations influence the reduction capacity of the compounds and their nanostructure.

As a preliminary step in the investigation of the interactions between gold and the various compounds, the optical properties of the resulting mixtures were analysed. Those measurements revealed that all gold-containing mixtures exhibit a clear quenching of fluorescence and a bathochromic shift in the absorption spectrum, indicating interactions between the metal and the organic compound. However, characteristic plasmonic features of gold nanoparticles were suppressed due to the close association with organic matter.

Then, electron microscopy confirmed the successful formation of gold nanodendrites. It was discovered that the morphology of these nanostructures is highly dependent on the compound structure. Concretely when auric chloride is added to the mixture at the same time as the organic compounds, the following results were obtained:

- CH83 and CH84, with strong reducing capabilities, promote the formation of large, external dendrites due to rapid gold nucleation occurring before vesicle assembly.
- CH78 displays intermediate behaviour, with gold nanodendrites and organic vesicles forming at the same time, leading to partially embedded dendrites.
- CH86-BIS and CH88 allow the formation of small dendrites inside the vesicles, due to a slower reduction rate or accelerated vesicle self-assembly, respectively.

Then, new experiments were performed, adding gold(III) to the mixture with a 24-hour delay. These experiments confirmed that pre-formation of vesicles leads to internal gold nucleation regardless of the reducing power of the compound, offering an attractive strategy for controlling size and localization of the dendrites formed by CH83 and CH84. These observations were further supported by DLS analysis, which showed an increase of the measured sizes upon gold addition, corresponding to the formation of superaggregates comprising both organic and inorganic components.

Catalytic tests demonstrated that CH84-derived gold nanodendrites are able to catalyse the Suzuki-Miyaura cross-coupling reaction in THF-water mixtures, yielding the desired biaryl compound under mild and eco-friendly conditions. Although the catalytic yield (56%) was moderate compared to conventional palladium catalysts, it underscores the potential of these nanostructures in green catalysis. Their catalytic activity is likely related to the high density of surface defects present along the dendritic branches, where each small protrusion can behave as an individual nanoparticle and act as an active site for catalysis. It must be mentioned that the dendritic gold structures lost catalytic activity in classical organic solvents, highlighting the importance of solvent compatibility for gold nanodendrites stability and performance.

Finally, silver nanoparticle formation was successfully induced by CH83 and CH88, resulting in a uniform coating of the nanovesicle surface. EDX and BSE imaging confirmed the deposition of silver on organic structures, indicating that vesicle assembly precedes silver reduction.

Overall, this study highlights the versatility of AIE-active amino acid derivatives as sustainable, multifunctional species for the synthesis of attractive metallic nanostructures. These findings open new avenues in the development of environmentally friendly methods for the fabrication of optically and catalytically functional nanomaterials.

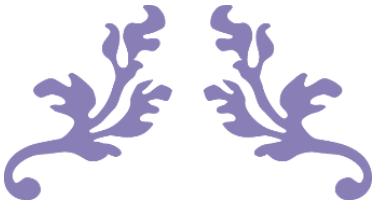

CHAPTER 3

Modified testosterone on Aggregation-Induced Emission Luminogens

ABSTRACT

Prostate cancer is a major medical concern today, with the androgen receptor (AR) playing a central role in disease development and progression. This chapter explores the design and application of fluorescent antitumoral agents based on organic dyes conjugated to testosterone for selective imaging and potential therapy of prostate cancer. Studies were conducted using both AR-positive (LNCaP) and AR-negative (PC-3) cell lines, which serve as complementary models to assess compound behaviour in androgen-sensitive and androgen-insensitive prostate cancer contexts. This study introduces novel probes that combine chemically modified testosterone with naphthalimide-based aggregation-induced emission fluorophores. These conjugates demonstrate promising targeting properties, efficient cellular uptake, and self-assembly into nanovesicles in aqueous environments, offering the possibility of use these vesicles as antitumoral agents while monitored by fluorescence techniques. The integration of hormone specificity with advanced photophysical and structural properties represents a powerful strategy in the development of targeted diagnostic and therapeutic tools for prostate cancer.

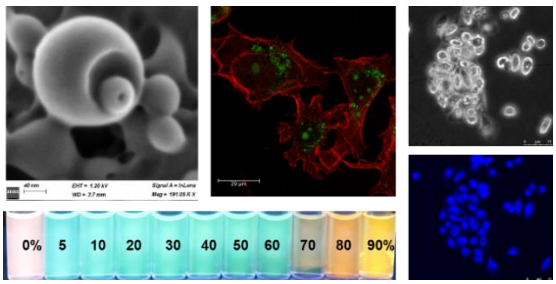

Figure 1. *Nanovesicle of new NMI-testosterone AIEgens and images inside prostate cancer cells.*

1. INTRODUCTION

Prostate cancer remains a leading cause of cancer-related morbidity and mortality among men worldwide. Central to its pathogenesis is the androgen receptor, a nuclear transcription factor activated by androgens such as testosterone and dihydrotestosterone (DHT). Upon activation, AR translocates to the nucleus, regulating the expression of genes critical for prostate cell proliferation and survival.[1] In prostate cancer, AR signalling continues to play a pivotal role, even in advanced stages of the disease. This receptor is overexpressed in prostate cancer cells, making it a strategic target for selective drug delivery and imaging.

The AR comprises several functional domains: the N-terminal domain, DNA-binding domain, hinge region, and ligand-binding domain. Alterations in AR, including point mutations, overexpression, and the emergence of constitutively active splice variants, have been implicated in the development of castration-resistant prostate cancer (CRPC), a stage where the disease progresses despite androgen deprivation therapy.[2]

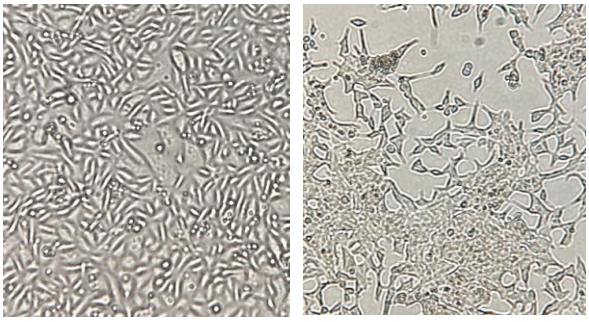

Figure 2. *Cell cultures of PC-3 (left) and LNCaP (right).*

In vitro studies of prostate cancer often utilize established cell lines to elucidate the molecular mechanisms underpinning disease progression and therapeutic resistance. The LNCaP and PC-3 cell lines are extensively utilized models in prostate cancer research.[3] LNCaP cells express functional AR and are androgen-sensitive, making them suitable for studying androgen-dependent mechanisms. Conversely, PC-3 cells

[1] E. P. Gelmann , *J. Clin. Oncol*. **2002**, *20,* 3001−3015.
[2] K. Fujita, N. Nonomura, *World J. Mens Health* **2019,** *37* (3), 288−295.
[3]A. Chlenski, K. Nakashiro, K.V. Ketels, G. I. Korovaitseva, R. Oyasu, *Prostate* **2001,** *47 (*1), 66−75.

lack functional AR and are androgen-insensitive.[4]

Based on the well-established premise that prostate cancer cells exhibit an increased affinity for androgens, numerous studies have explored the conjugation of hormones with antitumoral agents as a strategy to enhance cellular selectivity. Moreover, it is of particular interest when antitumor agents possess intrinsic fluorescence, as this feature enables the monitoring of their cellular destination through fluorescence-based imaging techniques.

In the 80's century, it was explored the development of several testosterone-fluorescein conjugates. Some species retained immunoreactivity with anti-testosterone antibodies, indicating their potential utility in immunofluorescence applications.[5] However, not all androgen-fluorophore conjugates have proven effective. For instance, fluorescein-labelled dihydrotestosterone derivatives exhibited variable fluorescence in prostate tissues, with significant non-specific binding and autofluorescence observed. These limitations underscore the importance of careful design and validation of such probes for specific applications.[6] Nonetheless, these studies laid the groundwork for the development of more advanced fluorescent probes specifically designed to target prostate cancer cells.

Thus, following this research line, a promising study recently emerged, and it serves as a precedent for this chapter. This approach involved the synthesis of testosterone derivatives linked to BODIPY fluorophores. These steroid-BODIPY conjugates have demonstrated efficient cellular uptake in LNCaP, and exhibit selectivity as compared to normal cells, so they have been studied as promising imaging and anticancer agents.[7]

In parallel, some bioimaging studies of prostate cancer cells have been done with infrared dyes. Researchers synthesized a compound named Abi-780 by conjugating the near-infrared fluorescent dye IR-780 with abiraterone, an androgen biosynthesis inhibitor. This conjugate retained the imaging capabilities of IR-780 and demonstrated selective accumulation in prostate cancer cells over normal prostate epithelial cells. In vitro studies showed that Abi-780 inhibited prostate cancer cell proliferation.[8] In addition, other study investigated the use of heptamethine carbocyanine dyes, for near-infrared fluorescence imaging of prostate cancer. These dyes exhibited selective uptake in prostate cancer cells (PC-3, DU-145, and LNCaP) over normal prostate epithelial cells suggesting their potential for non-invasive prostate cancer imaging.[9] These studies highlight the potential of combining fluorescent dyes with androgen-related compounds to improve prostate cancer imaging and therapy.

So, in this work testosterone was selected as a targeting ligand due to the well-documented androgen dependence of prostate cancer cells, which exhibit a high affinity for this steroid hormone. Its conjugation to the probes confers cellular selectivity, enabling preferential accumulation in prostate-derived cancer cells over non-prostate or non-tumoral cell types. Moreover, given the frequent overexpression of the androgen receptor in prostate cancer tissues, these compounds likely demonstrate enhanced binding and uptake in cancerous cells relative to normal prostate epithelial cells, thus supporting their potential as selective biomarkers or antitumoral agents within this cellular context.

[4] H. J. Kim, Y. I. Park, M. S. Dong, *Toxicol. In Vitro* **2006,** *20* (7), 1159−1167.

[5] C. Evrain, K. M. Rajkowski, N. Cittanova, M. F. Jayle, *Steroids* **1980,** *35* (6), 611−619.

[6] A. Lämmel, M. Krieg, G. Klötzl, Prostate. **1983,** *4* (3), 271−282.

[7] A. F. Amendoeira, A. Luz, R. Valente, C. Roma-Rodrigues, H. Ali, J. E. van Lier, F. Marques, P. V. Baptista, A. R. Fernandes, *Int. J. Mol. Sci.* **2023**, *24*, 3600.

[8] X. Yi, J. Zhang, F. Yan, Z. Lu, J. Huang, C. Pan, J. Yuan, W. Zheng, K. Zhang, D. Wei, W. He, J. Yuan, *Int. J. Oncol*. **2016,** *49* (5), 1911−1920.

[9] J. Yuan, X. Yi, F. Yan, F. Wang, W. Qin, G. Wu, X. Yang, C. Shao, L. W. Chung, *Mol. Med. Rep.* **2015,** *11* (2), 821−828.

So, taking into account that naphthalimide derivatives have been demonstrated to be promising AIE-active compounds due to their favourable photophysical properties and ease of functionalization, we have conjugated chemically modified testosterone to naphthalimide-based AIE luminogens. This has made possible to create fluorescent probes that leverage the specificity of testosterone, thus facilitating selective targeting of prostate cancer cells *(Figure 3).* Throughout this chapter we will see how these conjugates cross the cellular membranes and localize in different parts of the cell depending on the number of testosterone units bonded to the naphthalimide core.

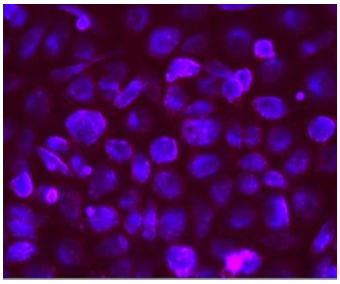

Figure 3. *NMI-testosterone hybrid inside PC-3 cell line.*

Furthermore, we know that naphthalimide aromatic rings stack through π-π interactions, giving rise to the aggregation-induced emission phenomenon useful in the design of fluorescent probes. Additionally, in the previous chapter we demonstrated how hydrophobic moieties bound to the NMI cores provide flexibility to the system, favouring the formation of nanovesicles. In this case, testosterone linked to the aromatic rings of NMI are ideal candidates for the formation of AIEgens that self-assemble into vesicles in high-water environments such as the intracellular medium.

In summary, the integration of testosterone's targeting capability with the advantageous photophysical properties of AIE-active naphthalimide derivatives presents a compelling strategy for the development of selective fluorescent probes and specific antitumoral agents.

2. OBJECTIVES

The main objective of this work is to develop and evaluate novel fluorescent probes based on testosterone-conjugated naphthalimide derivatives for specific antitumor activity in prostate cancer cells, with the possibility of monitoring it by fluorescence techniques. To get this, some specific objectives must be achieved:

- To design and synthesize new testosterone-naphthalimide conjugates and verify their aggregation-induced emission, leveraging the π–π stacking interactions of the aromatic NMI cores.
- To characterize the photophysical properties of the compounds, confirming their fluorescence behaviour and stability under biologically relevant conditions.
- To use scanning electron microscopy to study the self-assembly of the conjugates into nanovesicles in organic solvent-water mixtures and determine the role of testosterone in their formation.
- To evaluate the selective cellular uptake of the conjugates in AR-negative (PC-3) and AR-positive (LNCaP) prostate cancer cell lines and explore the potential of these species as antitumoral agents, testing their cytotoxicity against both cancer cell lines.
- To determine their target organelle, using endoplasmic reticulum, mitochondria and lysosome specific dyes. Confocal microscopy and colocalization test will be used to achieve this objective. The software ImageJ will be employed to determine the colocalization correlation coefficients.

3. SYNTHESIS OF AIE-GEN-TESTOSTERONE HYBRIDS

In this chapter, two groups of compounds are designed. On the one hand, deprotected compounds of the Chapter 1, with only one depsipeptide chain, were linked to two modified testosterone units *(Figure 4a)*. On the other hand, the initial unfunctionalized dyes were directly linked to one or two testosterone units *(Figure 4b, c)*.

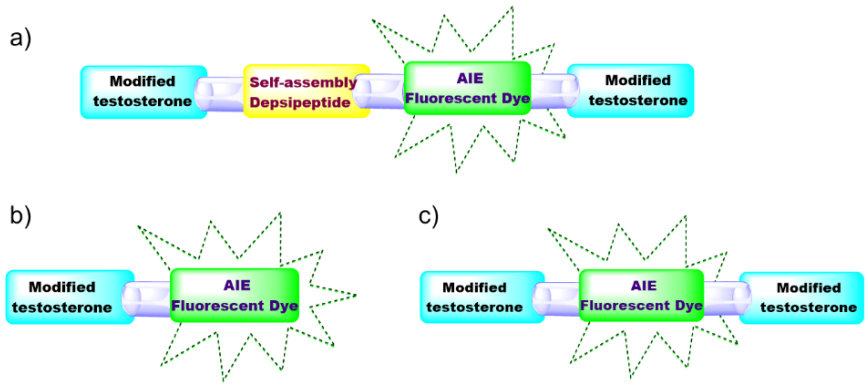

Figure 4 *Schematic structure of new AIEgen-testosterone hybrids.*

All compounds described in this section have similar synthetic reaction mechanisms which consist in the nucleophilic attack of free amine groups to the carboxylic acid group of the modified testosterone's chain. Hence, amide bonds are formed. Due to the similarity between the synthetic reactions herein studied, their experimental conditions and steps to be followed are similar. Only the nature of starting NMIs and the amount of the other reagents change, and they are deeply described in the Supporting Information section, as well as their full characterization. The common methodology is shown in *Figure 5.*

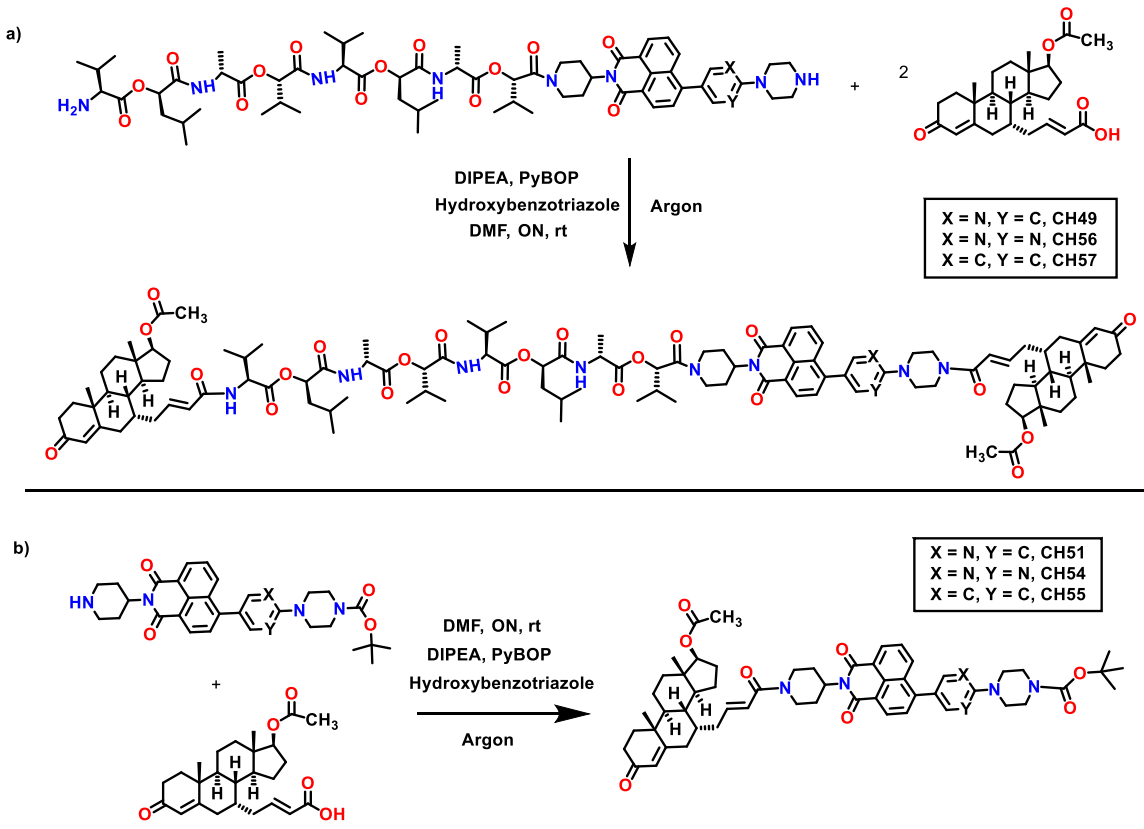

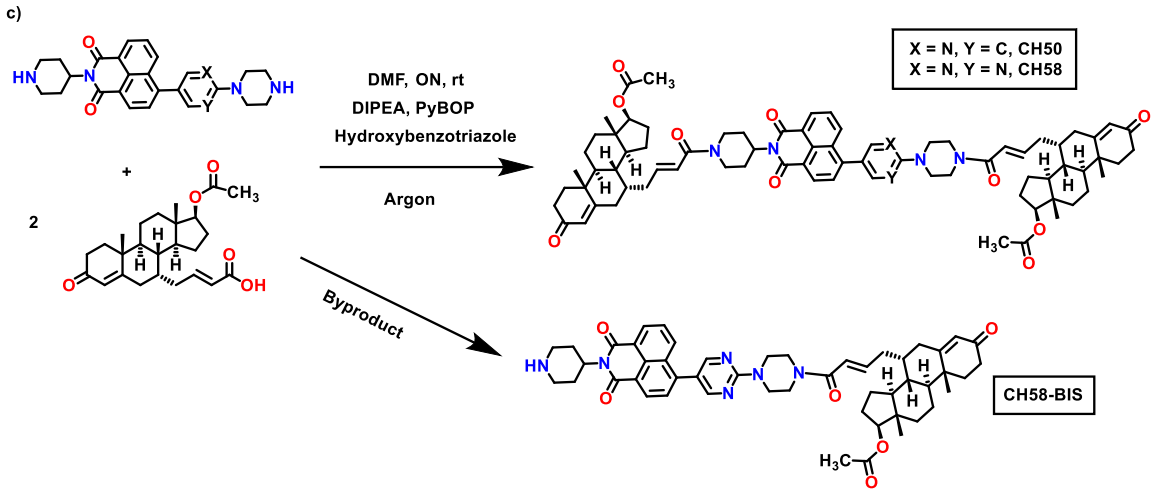

Figure 5. *Synthesis of the three different models of AIEgen-testosterone hybrids.*

It is worth mentioning that the product CH58-BIS was obtained as a reaction byproduct and will be one of the most attractive compounds in this chapter due to the presence of the free piperidine amine, which appears to have significant cytotoxic activity, as will be seen later.

4. FLUORESCENCE PROPERTIES OF SYNTHESIZED HYBRIDS

4.1. SOLVATOCHROMISM ASSAYS

Herein, the solvent polarity effect on the position and intensity of the absorption and emission bands is studied. In *Table 1*, the employed solvents are ordered from highest to lowest polarity, according to the Snyder polarity index.

Table 1. *Employed solvents in solvatochromism assays.*

1. H_2O	4. DMF	7. EtOAc	10. THF	13. Hexane
2. MeOH	5. MeCN	8. THF	11. Toluene	14. MCH
3. DMSO	6. Acetone	9. $CHCl_3$	12. EtO_2	

Then, the 14 different solutions (10^{-5} M) of each compound were photographed under UV light of 366 nm *(Tables 2,3)*.

Table 2*. Solvatochromism assays of depsipeptide-AIEgen-testosterone hybrids under UV light (366 nm)*

Structure	Solvents (1-14)
CH49 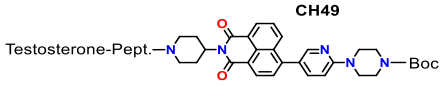	
CH56 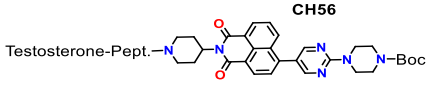	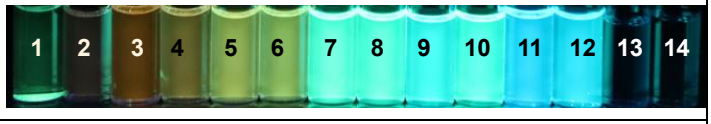
CH57 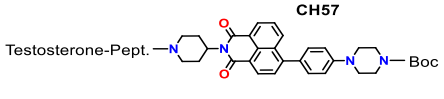	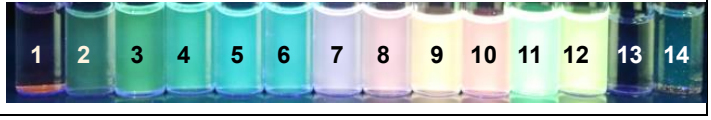

***Table 3**. Solvatochromism assays of AIEgen-testosterone hybrids under UV light (366 nm)*

Structure	Solvents (1-14)
CH51 Testosterone—N—Boc	
CH54 Testosterone—N—Boc	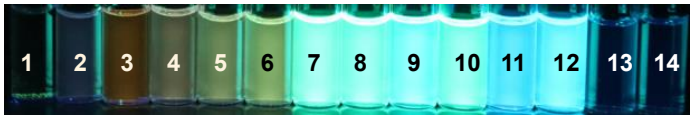
CH55 Testosterone—N—Boc	
CH50 Testosterone—N—Testosterone	
CH58 Testosterone—N—Testosterone	
CH58-BIS HN—Testosterone	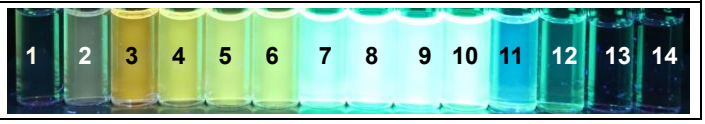

As happened with compounds of Chapter 1, it is observed that the fluorescence intensity of all NMIs increases as the solvent polarity decreases. In high polarity solvents, the species establish interactions between their aromatic cores and aggregate, so a little ACQ effect is observed. However, at moderate polarities, the aliphatic regions (including testosterone units) interact with the solvent, and no aggregate is formed, showing therefore a bright fluorescence. Finally, most of the compounds are not fluorescent in the least polar solvents as hexane and methylcyclohexane and that's because they are less soluble in these media. In the case of CH49, CH56 and CH57 it is explained because the depsipeptide chain with amide polar groups hinder the interactions between the aliphatic regions of the structure and the solvent when the environment polarity is too low. These statements are supported by their normalized absorption spectra, where neither hexane nor cyclohexane curves appear *(Table 4, Fig.a)*. It should be noted that CH56 is moderately soluble in water due to its increased polarity arising from the presence of a pyrimidine unit in its structure. Consequently, the absorption spectrum also shows the signal in water *(Table 4, Fig.a)*. Regarding monofunctionalized species, CH51 and CH55 are fluorescent both in hexane and MCH, and that is probably because of the presence of a tert-butoxycarbonyl group which can better interact with nonpolar solvents, making these compounds quite soluble; so, in their normalized absorption spectra MCH and hexane appear (see Supporting Information). However, CH54 contains a pyrimidine unit in its structure, which renders it slightly more polar. As a result, despite the presence of a Boc protecting group, it is insoluble in both hexane and MCH *(Table 4, Fig.b)*. To illustrate the points just discussed, the following table presents the normalized absorption spectra of CH56 and CH54.

***Table 4**. Normalized absorption spectra of (a) CH49 and (b) CH51*

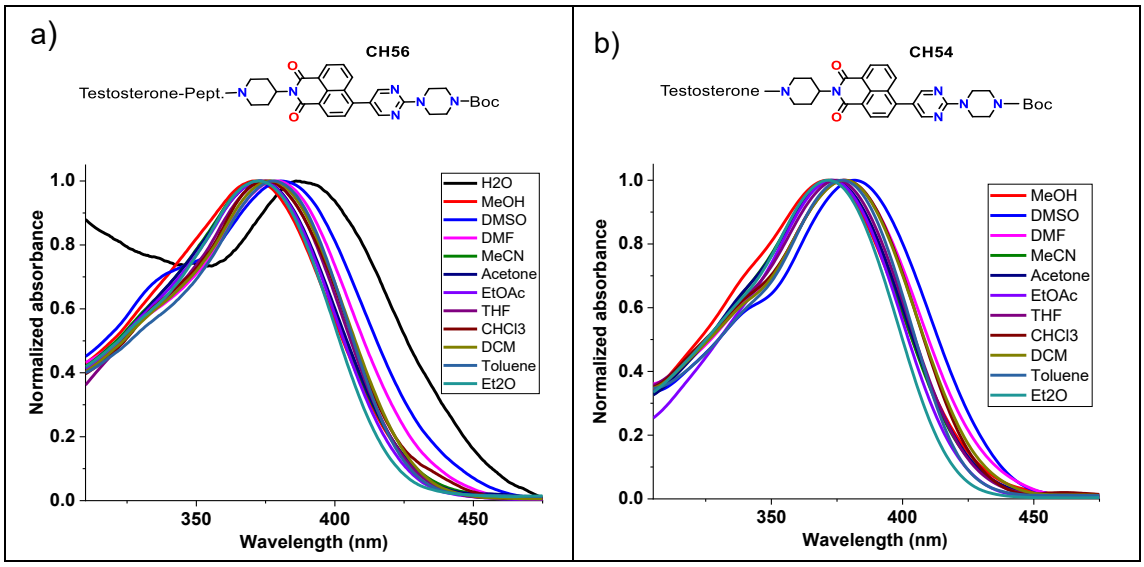

The differences between the emission intensities of the compounds in the different solvents can be clearly seen in the emission spectra of the compounds. in *Table 5.*, the spectra of CH56 and CH54 are shown as representative examples of the general behaviour.

***Table 5**. Emission spectra of (a) CH56 and (b) CH54. λ_{exc} = 375 nm*

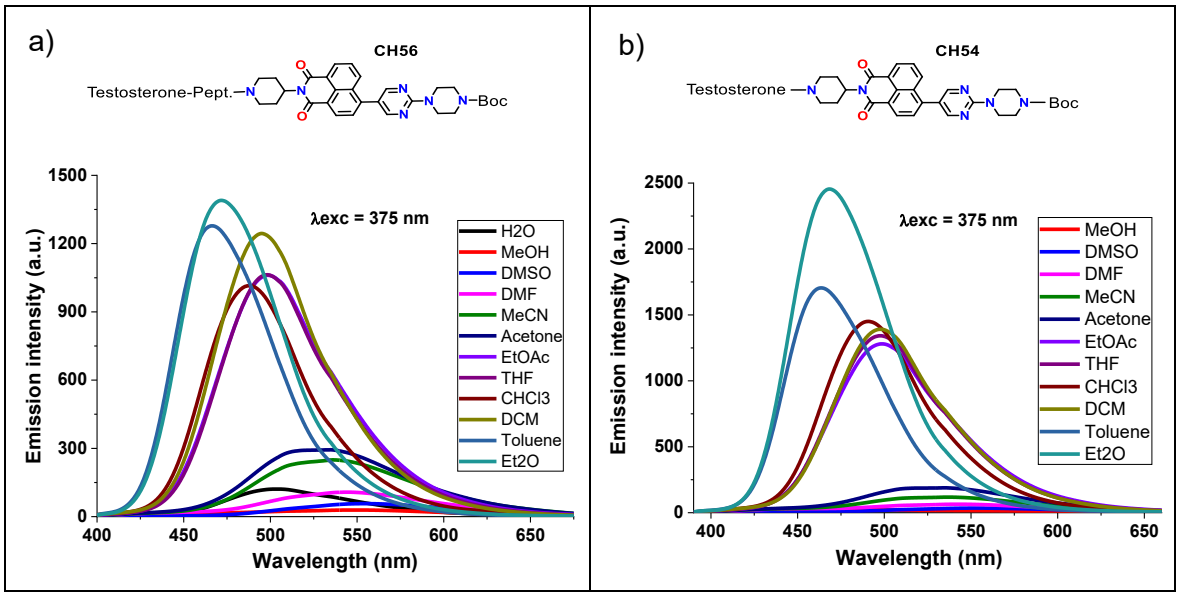

In both spectra, the curves representing the most polar solvents, such as MeOH, DMSO, and DMF, are indistinguishable as they lie along the baseline (mentioned ACQ effect). This supports the earlier qualitative observation that low fluorescence is present. The spectra further confirm that emission intensity increases as solvent polarity decreases. CH56 and CH54 exhibit their strongest fluorescence in diethyl ether and toluene, the least polar solvents where they also show good solubility.

Additionally, the absorption and emission spectra help identify the most suitable solvent for next studies. Absorption spectra indicate which solvents are most effective for the compounds' analysis. From these, the ideal solvent must be miscible with water and not to produce excessively strong fluorescence from the NMIs. Tetrahydrofuran is selected as it meets all these criteria.

Returning to the photographs in *Tables 2* and *3*, in general, it can be observed that a red shift occurs as the polarity of the solvent increases. This occurs for species containing pyridine and pyrimidine in their structure. On the other hand, CH55 and CH57 (with a phenyl group) break with this phenomenon, as was the case with the phenyl compounds in Chapter 1, where it was seen that the presence of nitrogen atoms was essential for the energy stabilization of the aggregates formed in high polar solvents, and therefore for the detection of the mentioned red shift. Considering pyridine and pyrimidine compounds, this fluorescence behaviour and the effect of the solvent polarity on the position of the bands, can be studied in more detail by the interpretation of their normalized emission spectra. CH56 (with depsipeptide), CH54 (one testosterone and Boc) and CH58 (two testosterone units) are selected as representative examples *(Table 6)*.

***Table 6**. Normalized emission spectra of (a) CH56, (b) CH54 and (c) CH58. λ_{exc} = 375 nm*

a)

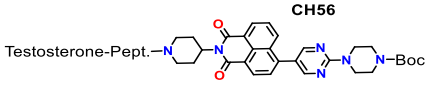

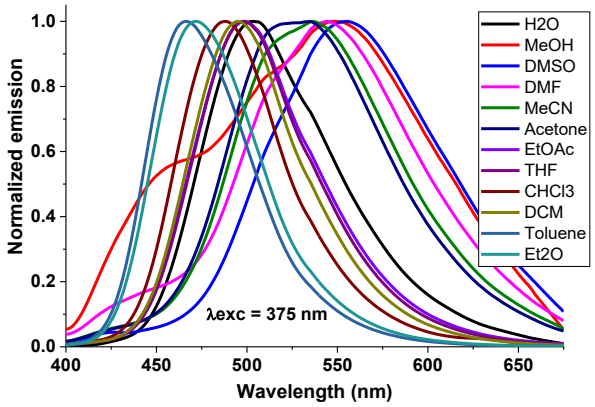

b)

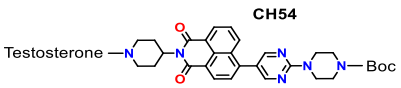

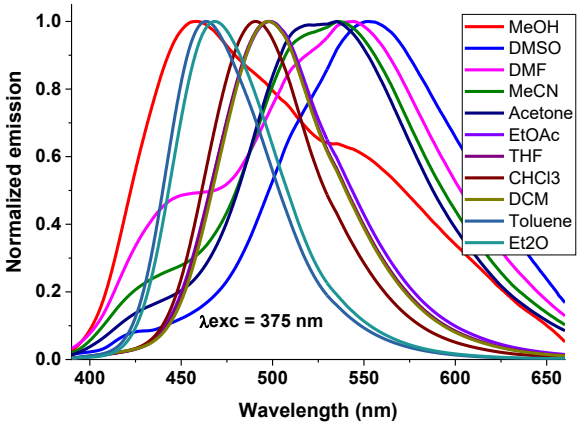

c)

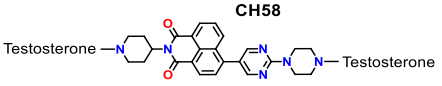

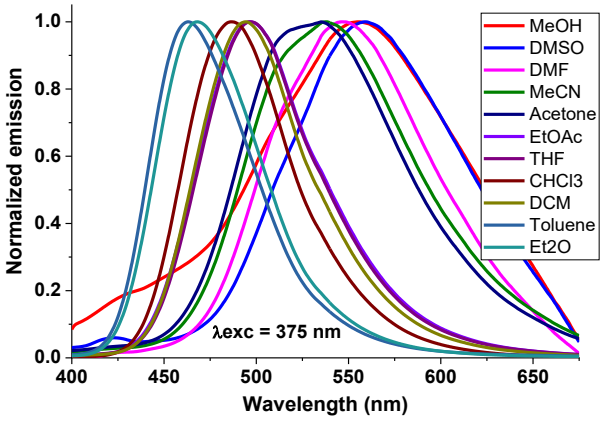

First, it must be said that methanol is not considered in this study because it can interact by hydrogen bonds and breaks with general theory. Observe that all three spectra demonstrate a shift of the maximum emission peaks toward longer wavelengths as the polarity of the solvent increases. This bathochromic shift can be quantified by calculating the difference in peak wavelengths between the most and least polar solvents. For example, in the CH56 spectrum, the emission maximum shifts by 83 nm (from 472 nm in Et_2O to 555 nm in DMSO). Similarly, CH54 exhibits a bathochromic shift of 84 nm, as its emission peak moves from 468 nm in diethyl ether to 552 nm in DMSO. Finally, CH58 has a bathochromic shift of 91 nm, corresponding to the difference between Et_2O (469 nm) and DMSO (560 nm). These findings are consistent with literature, which shows that when the electron-accepting core of NMIs is modified with donor groups like amines or hydroxyls, the emission spectrum displays a red-shifted intramolecular charge transfer band accompanied by a pronounced solvatochromic effect.[10]

As was done in chapter one, the observed bathochromic shifts can also be explained in terms of molecular energy levels. Upon excitation to the first singlet state, a molecule possesses excess vibrational energy, which is quickly dissipated to the surrounding environment. In addition, the dipole moment of a fluorophore typically increases in the excited state compared to the ground state. As a result, the excited fluorophore interacts more strongly with the solvent, leading to greater stabilization and a lowering of its energy levels. This stabilization effect becomes more pronounced with increasing solvent polarity, causing the emission to occur at lower energies, or longer wavelengths.[11]

4.2. WATER-ORGANIC SOLVENT RATIO ASSAYS

It has been shown that these NMIs tend to aggregate in polar solvents. As seen in previous chapters, mixtures of THF with increasing amounts of water are an ideal medium for the detection of the aggregation-induced emission phenomenon. Therefore, these tests were carried out with the testosterone derivatives herein studied. The prepared mixtures (methodology described in the Supporting Information) have been photographed under UV light of 366 nm to determine if these NMIs exhibit the already mentioned AIE phenomenon *(Table 7)*. The solutions' concentration is 10^{-5} M.

***Table 7**. Water-solvent ratio assays of different testosterone-NMI hybrids, using UV light (366 nm)*

Structure	THF-H_2O mixtures
CH49 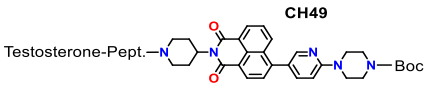	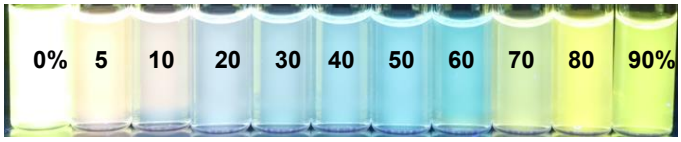
CH56 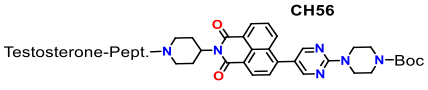	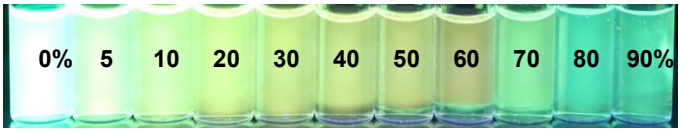
CH57 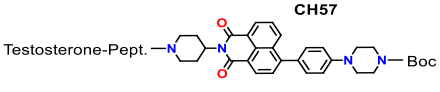	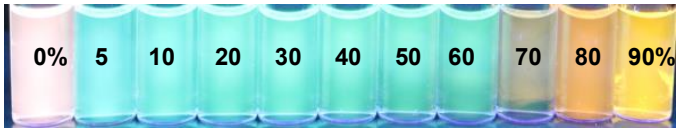

[10] S. Dhar, S. S. Roy, D. K. Rana, S. Bhattacharya, S. Bhattacharya, S. C. Bhattacharya, *J. Phys. Chem. A.* **2011,** *115* (11), 2216−2224.
[11] C. Le Droumaguet, A. Sourdon, E. Genin, O. Mongin, M. Blanchard-Desce, *Chem. Asian J.* **2013**, *8*, 2984-3001.

CH51 Testosterone — Boc	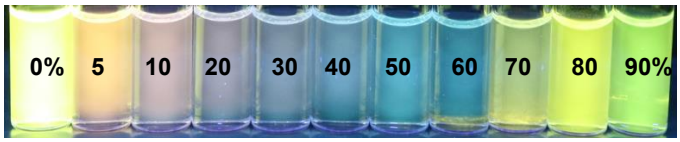
CH54 Testosterone — Boc	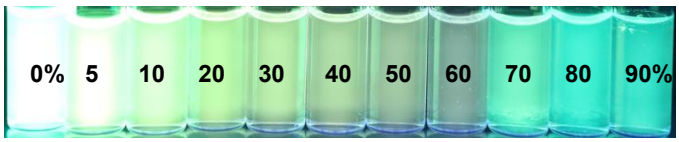
CH55 Testosterone — Boc	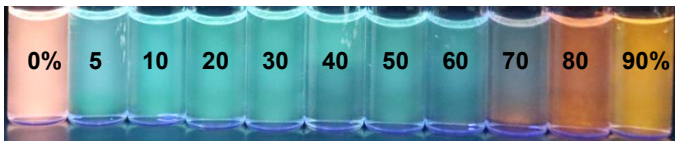
CH50 Testosterone — Testosterone	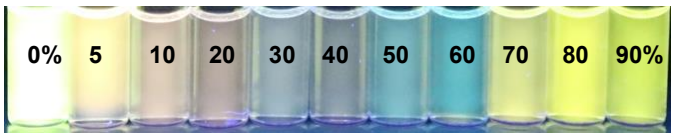
CH58 Testosterone — Testosterone	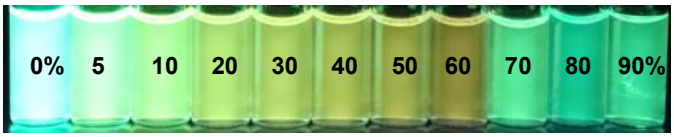
CH58-BIS Testosterone	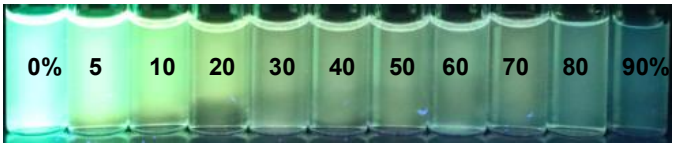

In the photographs, it can be observed that the phenyl and pyridine compounds exhibit a colour shift toward longer wavelengths starting at 70% of water. This is consistent with the aggregate formation and energy stabilization mentioned above. Furthermore, in the same compounds, it is observed a change of the emission intensity as the water ratio is modified. In pure THF (0% w.r.) the fluorescence emission is very high because the species are in solution, and no aggregate is formed. In mixtures with a low water content (10-60%), fluorescence emission goes weaker due to the aggregation-caused quenching effect. However, when the water content exceeds 70%, there is a marked increase in fluorescence emission, attributed to greater molecular aggregation and the formation of larger nanoparticles. This observation confirms that at higher water ratios, the fluorophores form nanoaggregates big enough to exhibit the AIE effect. In this state, non-radiative decay processes are suppressed because of the increased structural rigidity of the nanoaggregates. However, it must be mentioned that CH58-BIS do not show the AIE effect. Its fluorescence decreases as the water ratio increases, and it is probably because of the presence of a free amine group which easily interacts with the polar medium.

Moreover, it must be pointed that CH56 and CH54 (pyrimidine derivatives) do not fit with the statements above, since ACQ is not observed at low water percentages, and there is not an increase of fluorescence intensity at high water ratios. Thus, the assays were repeated in mixtures of methanol and water, and an intense AIE effect was observed above 50% w.r. Also, a displacement to longer wavelengths at high water percentages was noticed *(Table 8)*.

***Table 8**. Water-MeOH ratio assays of CH56 and CH54, using UV light (366 nm)*

Structure	MeOH-H_2O mixtures
CH56 Testosterone-Pept.–N–Boc	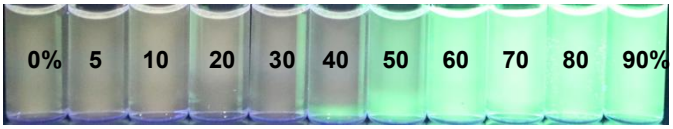
CH54 Testosterone–N–Boc	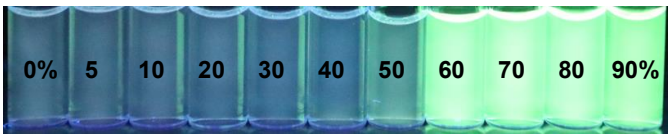

This qualitative analysis can be quantified with the emission spectra of the different mixtures. CH51 (pyridine, in THF) and CH54 (pyrimidine, in methanol) have been selected as representative examples of each group of behaviours. In *Table 9, Fig.a* it is observed how the emission intensity (grey curve) of CH51 suddenly decreases at intermediate water percentages, and above 60% w.r. it increases again. The shift of the emitted light to longer wavelengths, when the aggregates are formed, is also verified. The blue curve suddenly increases above 60% w.r. In the case of CH54, in methanol, the changes in the emission intensity and colour appear at lower w.r. In *Table 9, Fig.b*, it can be noticed how the emission intensity (grey curve) suddenly increases above 50% w.r. The shift of the emitted light to longer wavelengths when the aggregates are formed is also observed, since the blue curve suddenly increases above 50% w.r. too.

***Table 9.** Emission intensity (grey) and λ_{max} emission (blue) of (a) CH51 in THF at different w.r. (b) CH54 in MeOH at different w.r. λ_{exc} = 375 nm*

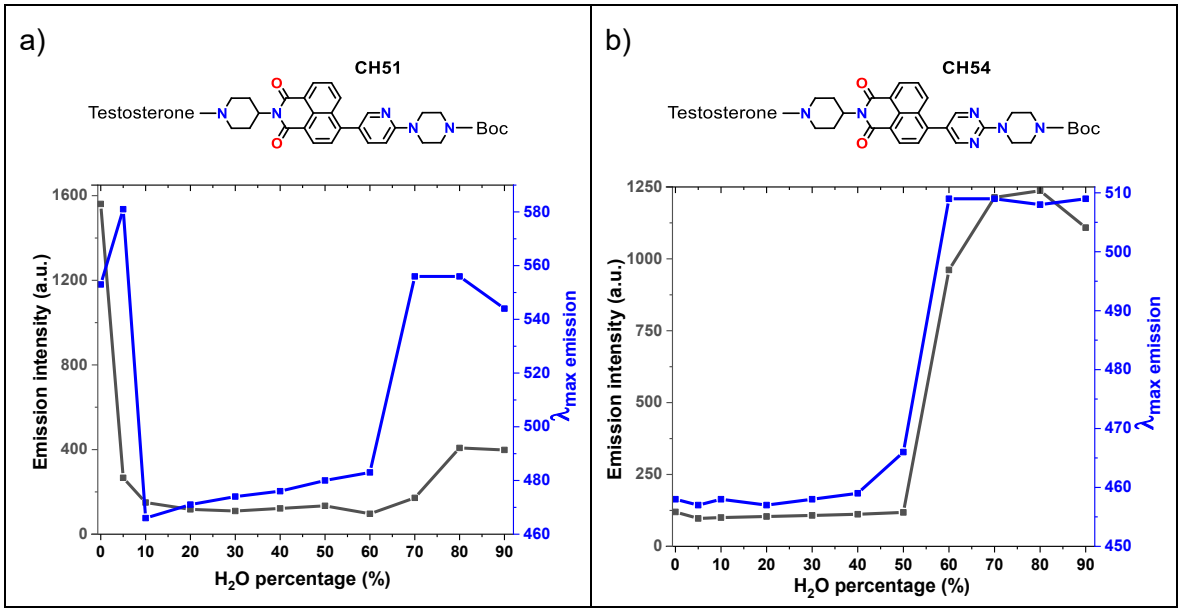

5. NANOPARTICLES MORPHOLOGY AND SIZE

This section includes several pictures obtained by field emission scanning electron microscopy (FESEM) located in the technologic scientific park of the University of Burgos. In this section, the mixtures where the AIE effect is observed are studied. Here below are first collected the nanoparticles observed for species bonded to both testosterone and a depsipeptide chain, and then the species with only testosterone moieties.

5.1. TESTOSTERONE-AIEGEN-DEPSIPETIDE HYBRIDS: IMAGES

A great deal of nanovesicles have been observed for the three derivatives. First, CH49 was imaged in mixtures of THF and water of high-water content.

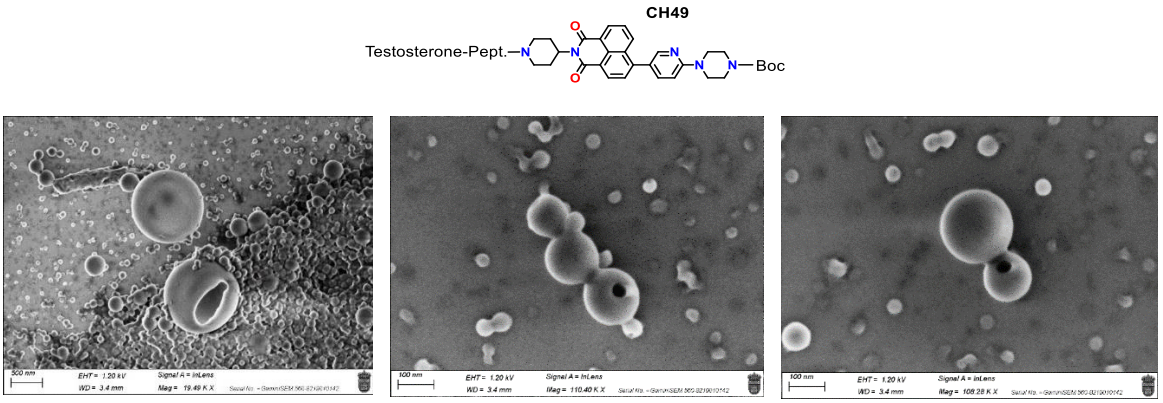

Figure 6. *FESEM images of CH49 in THF-H_2O: (left) 80% w.r. (centre and right) 90% w.r.*

On the other hand, CH56 was seen to show noticeable AIE effect in MeOH-H_2O mixtures; so, it was also imaged in this mixture of solvents. It was seen that the spherical nanoparticles formed in methanol are smaller than those formed in THF. Additionally, in MeOH mixtures, the nanoparticles' size decreases as the water ratio increases but the number of aggregated particles increases *(Figure 7).*

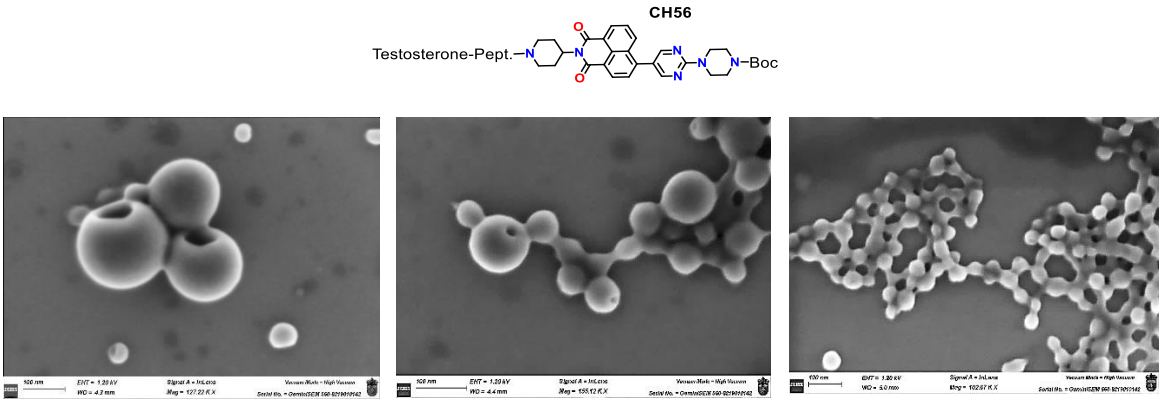

Figure 7. *FESEM images of CH56 in: (left) THF-H_2O at 90% w.r. (centre) MeOH-H_2O at 60% w.r (right) MeOH-H_2O at 70% w.r.*

CH57 was also imaged in both methanol and THF mixtures. Since the AIE effect appears in MeOH at lower water percentages than in THF, so does the appearance of nanoparticles. It must be remarked that nanovesicles capable to host smaller ones inside them were observed at 90% w.r. in THF *(Figure 8, centre).*

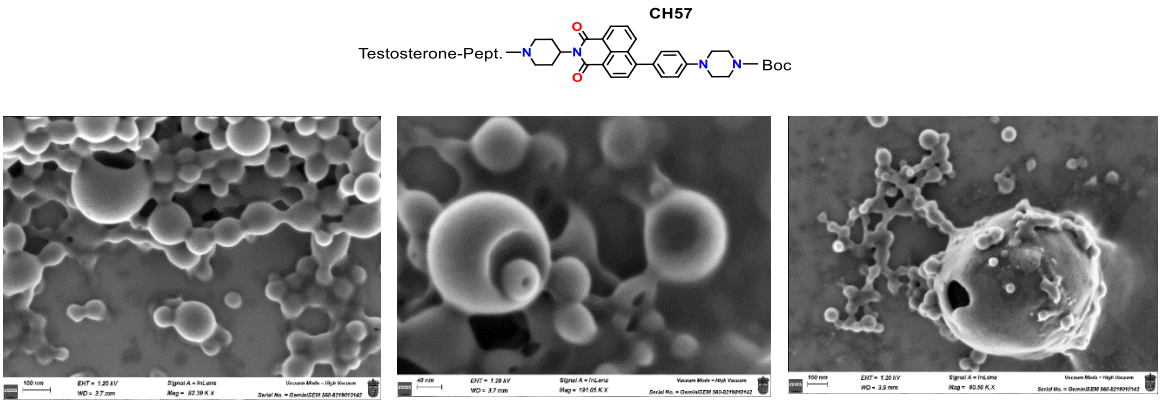

Figure 8. *FESEM images of CH57 in: (left) THF-H_2O at 80% w.r. (centre) THF-H_2O at 90% w.r. (right) MeOH-H_2O at 60% w.r.*

5.2. TESTOSTERONE-AIEGEN-BOC HYBRIDS: IMAGES

CH51 forms nanovesicles above 70% w.r.; however, the most stunning ones were imaged at 90% w.r. in THF-H_2O mixtures *(Figure 9).*

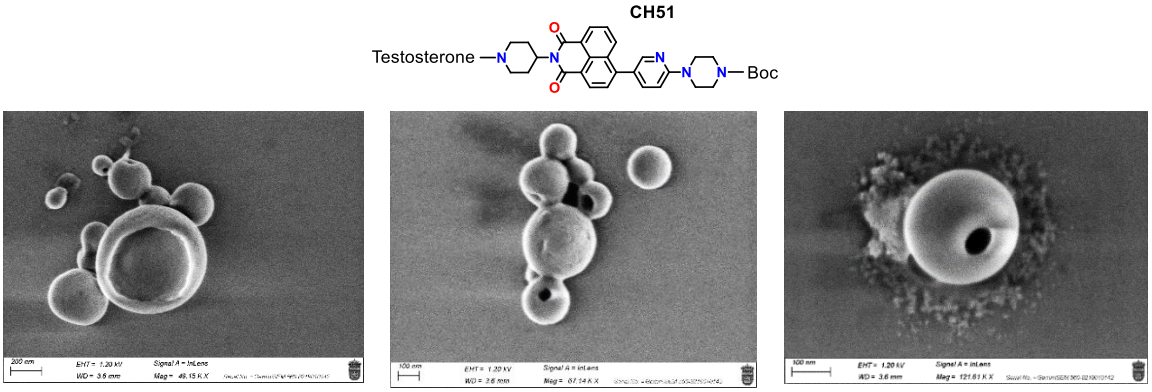

Figure 9. *FESEM images of CH51 in THF-H_2O at 90% w.r.*

CH54 is a pyrimidine derivative and the AIE effect was only noticeable in MeOH-H_2O mixtures. So, nanovesicles have been there observed.

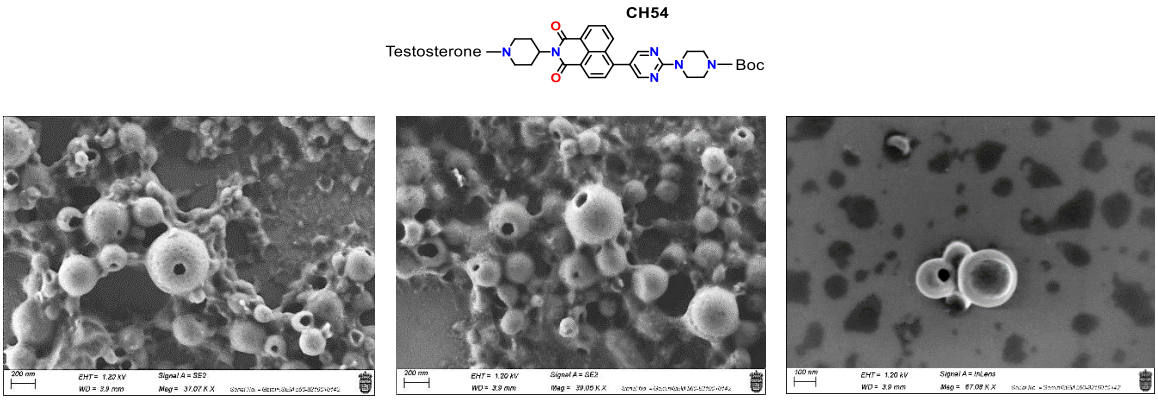

Figure 10. *FESEM images of CH54 in MeOH-H_2O at 80% w.r.*

CH55 also forms nanovesicles *(Figure 11)*, however they are very small and difficult to focus with microscope, so the images' sharpness is not as good as those images of its analogues.

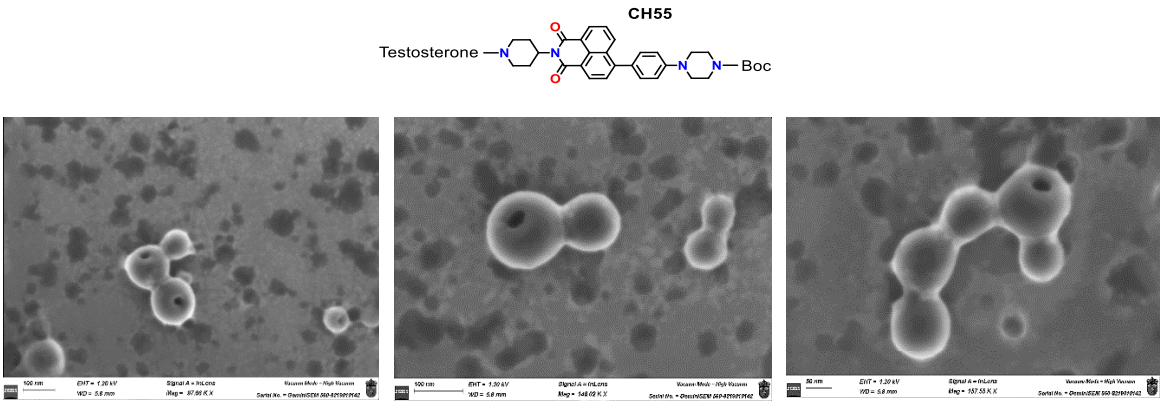

Figure 11. *FESEM images of CH54 in THF-H_2O at 90% w.r.*

As it was seen in previous chapters, the semi-functionalized species, containing a pyridine unit, form better nanovesicles than those of pyrimidine or phenyl moieties.

5.3. TESTOSTERONE-AIEGEN HYBRIDS: IMAGES

In this section CH58 and CH58-BIS are studied. Both are pyrimidine containing NMIs. In CH58, the presence of two testosterone units (hydrophobic units bonded to the naphthalene core) favours the nanovesicles formation *(Figure 12).*

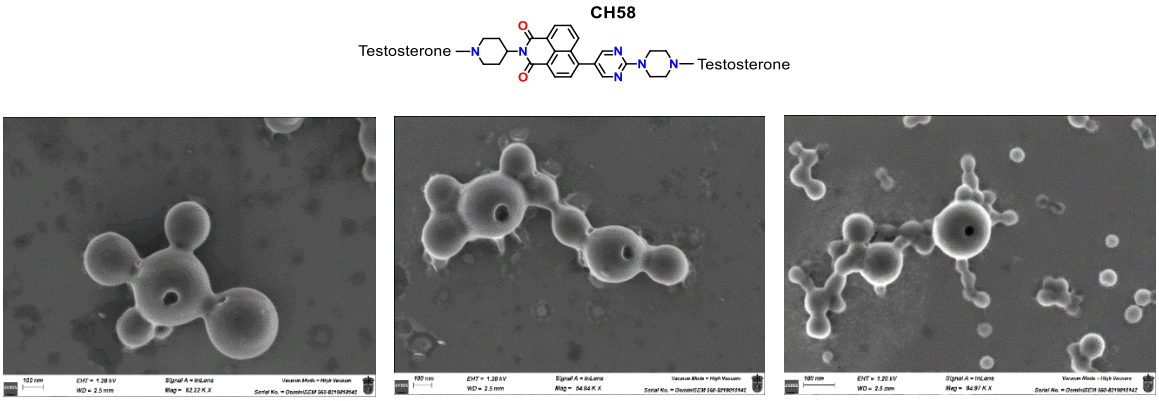

Figure 12. *FESEM images of CH58 in THF-H_2O: (left and centre) at 80% w.r. (right) at 90% w.r.*

Then, CH58-BIS was studied. Although it has a free terminal amine group, it forms stunning nanovesicles *(Figure 13).*

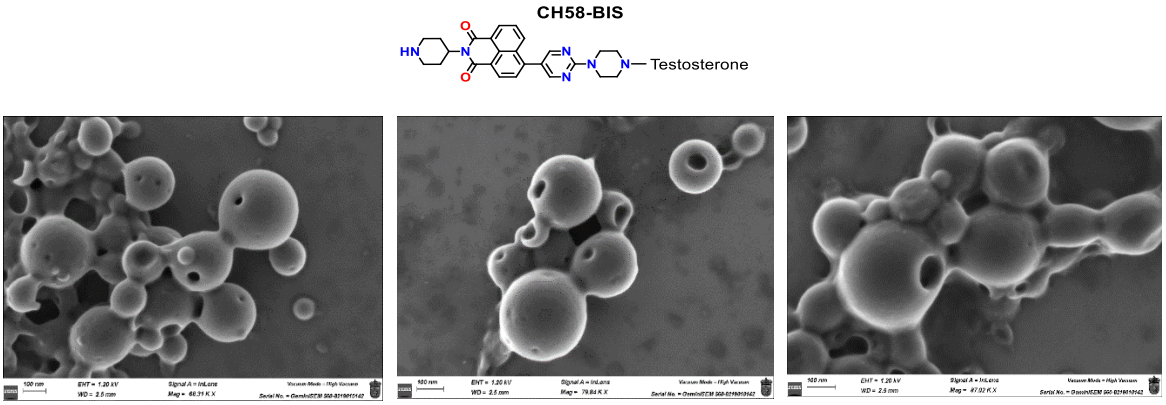

Figure 13. *FESEM images of CH58-BIS in THF-H_2O: (left and centre) at 70% w.r. (right) at 80% w.r.*

5.4. NANOPARTICLES' SIZES: DLS MEASURES

Once the nanoparticles have been imaged, the average size of them is determined by dynamic light scattering (DLS) in mixtures of THF and water with high-water content. The measurements of all compounds are collected in the Supporting Information of this chapter, however, here below are shown some representative examples. It has been seen that pyrimidine derivatives are the largest ones, while phenyl derivatives are the smallest. It has also been observed that the presence of an unprotected amine causes the size to increase considerably, as occurs with CH58-BIS. This growth phenomenon associated with deprotection was also noticed in Chapter 1 of this thesis. Thus, the smallest species is CH55 at 90% water, with an average diameter of 143.1 nm. The rest of the pyridine and pyrimidine species measure around 200-280 nm; for example, CH56 at 90% w.r. has an average diameter of 224.5 nm. Finally, it was found that CH58-BIS at 80% reaches a size of 1611 nm *(Table 10)*.

Table 10. *DLS of (a) CH55 (b) CH56 (c) CH58-BIS. The average sizes of aggregates are shown below*

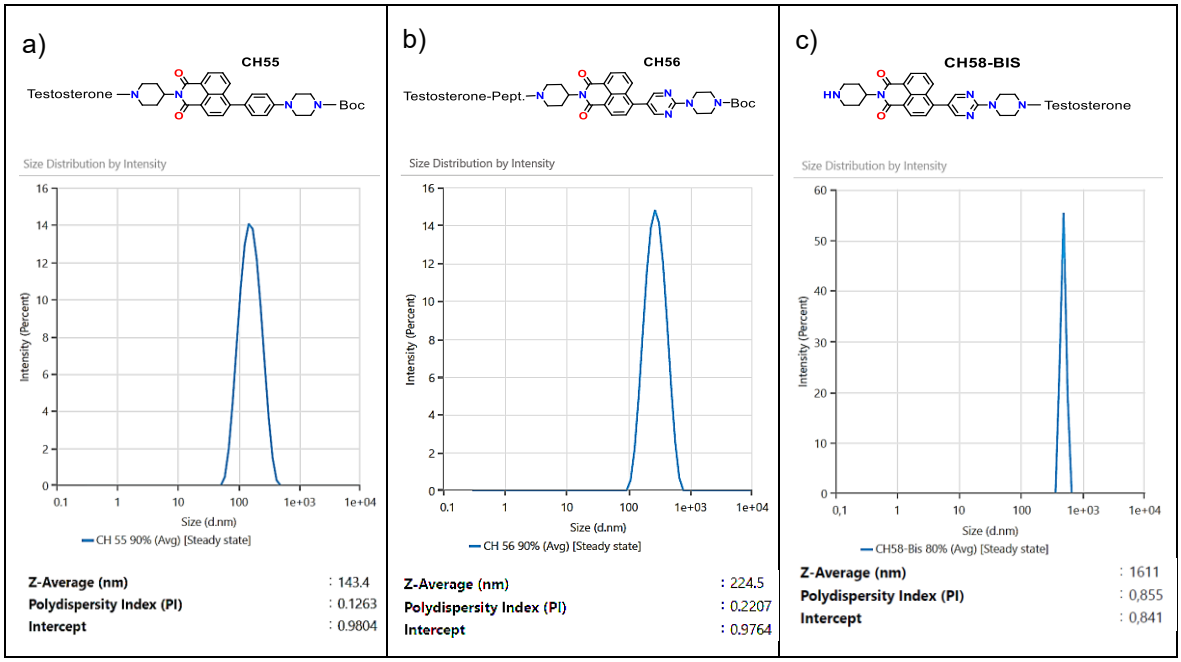

6. DEPROTECTED AIE-GEN-TESTOSTERONE HYBRIDS

As described in the introduction, these AIEgens contain testosterone, a molecule that should be recognized by prostate cancer cells. Thus, the next step is to test them and determine whether these species are suitable for use as antitumor agents for prostate cancer therapy.

However, to perform these analyses, the structure of the hybrids must be slightly modified. It is necessary to remove the tert-butoxycarbonyl group, thus allowing the compounds pass through the cell membrane. We also tried deprotecting the acetate group in the hormone and leaving it in the alcohol form to see if the ester's presence affects cytotoxicity or may avoid cell entry.

6.1. DEPROTECTION REACTION

To deprotect both the Boc group and the acetate, a mixture of HCl and methanol is required *(Figure 14).* Thus, the products are dissolved in MeOH and then, a mixture of HCl in methanol (3M) is added until the final HCl concentration is 5N (relative to the concentration of AIEgen). The mixture is stirred overnight at 40 ºC. Once the reaction has finalized, the solvents are removed under reduced pressure. Then, the products are obtained as hydrochlorides, with yields above 95%.

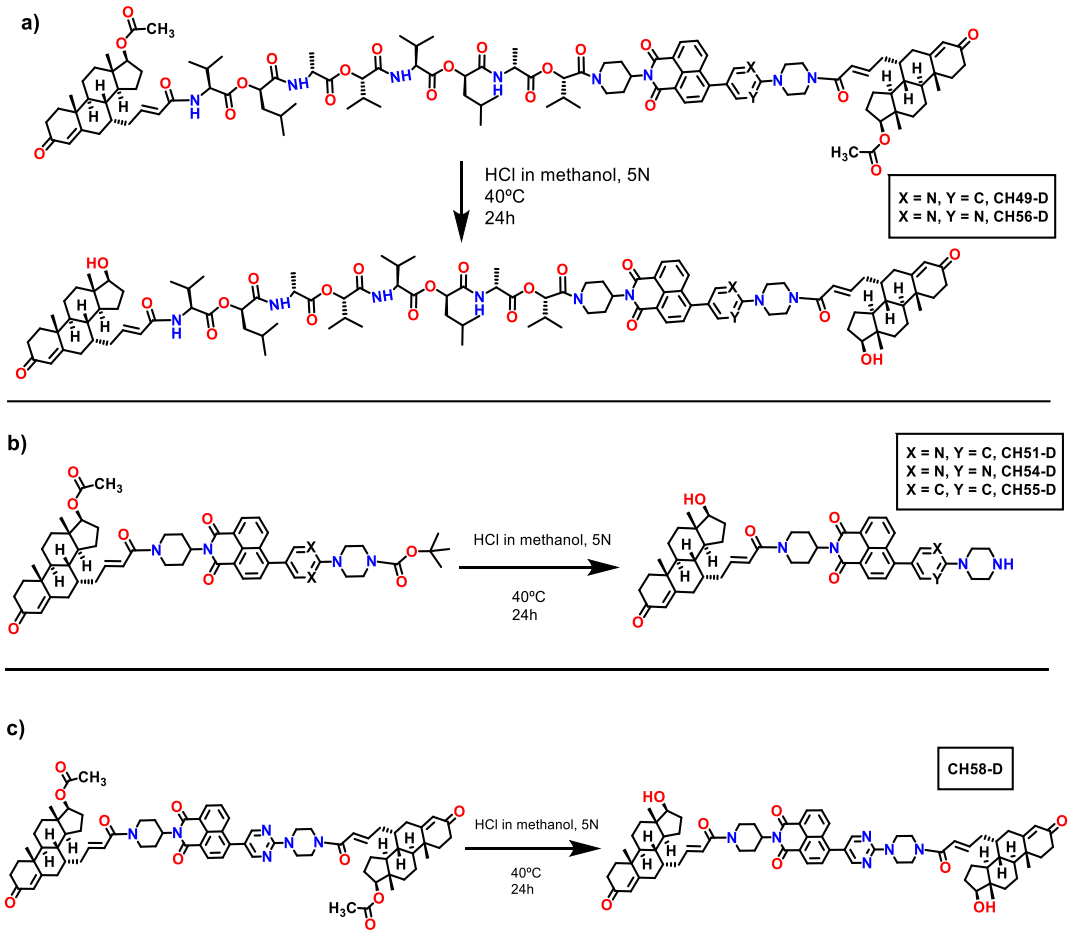

Figure 14. *Deprotection of terminal amines and acetate group in the different types of hybrids.*

7. CYTOTOXIC ACTIVITY AND INTRACELLULAR LOCALIZATION STUDIES

All deprotected compounds are able to be tested inside cells. In addition, those compounds with the depsipeptide chain and still bearing the acetyl group on the testosterone moiety will also be evaluated. Two prostate cancer cell lines have been selected: PC-3 (no androgen sensitive) and LNCaP (androgen sensitive). In this section, we examine the biocompatibility of the compounds and analyse how the synthesized molecules interact with various cellular organelles. As instance, due to the AIE effect, a uniform fluorescence distributed across the entire cell surface should indicate that the molecule does not have a specific intracellular destination.[12] In contrast, if the fluorescence is concentrated in a limited area, it would suggest that the molecules could be forming nanoaggregates within a specific cellular

[12] W. Qin, D. Ding, J. Liu, W. Z. Yuan, Y. Hu, B. Liu, B. Z. Tang, *Adv. Funct. Mater.* **2012,** *22*, 771−779.

compartment. The specific organelle, in which the compounds will accumulate, will be identified through confocal microscopy.

7.1. ACTIVITY AND TARGET ORGANELLE INSIDE PC-3 CELL LINE

In this section, the cytotoxic or biocompatible activity of the compounds will be analysed, and secondly, their target organelles will be determined.

7.1.1. Biocompatible vs antiproliferative species in PC-3 cell line

To determine the cytotoxicity of the compounds, MTT assays were performed by biologists following the next protocol: PC-3 cells were cultured in F12K medium which contains L-glutamine and sodium bicarbonate. They were mixed with 10% of fetal bovine serum (FBS) and antibiotics (1% penicillin-streptomycin-amphothericin B) at 37°C with 5% CO_2. Initially, approximately 30000 cells were seeded per well in a 96-well plate. After incubation, the medium was replaced with fresh medium containing increasing concentrations of test compounds (from 10 mM DMSO stock solutions, to a final concentration of DMSO <0.5%). After 24, 48 and 72 hours, the medium was removed, and 100 µl/well of MTT solution (5 mg/ml) was added, reaching a final concentration of 0.5 mg/ml. Plates were incubated for 4 hours, followed by the addition of 100 µl/well of pure DMSO. The plates were incubated for 15 minutes to allow complete solubilization of the formazan crystals. Absorbance at 595 nm, (proportional to the number of viable cells), was measured using a BioTek Cytation 5 multiwell plate reader.

In the case of species with a depsipeptide chain, both compounds with protected and unprotected ester were studied. The results revealed that the presence of acetate or alcohol does not alter the species' ability to cross the cell membrane; however, the presence of the alcohol group produces a slight increase in the toxicity of the compounds. On the other hand, a significant difference in cytotoxicity was observed between species with a depsipeptide chain, those with only one testosterone and one free amine, and those with two testosterone units. The cytotoxicity studies of all compounds are deeply described in the Supporting Information of this chapter.

Depsipeptide-containing hybrids.

Depsipeptide-containing species exhibit moderate toxicity which increases as time goes by. The number of survivor cells is represented versus increasing probe's concentration. The graphs for CH56 are shown as representative examples of this group of compounds *(Figure 17).*

a) b)

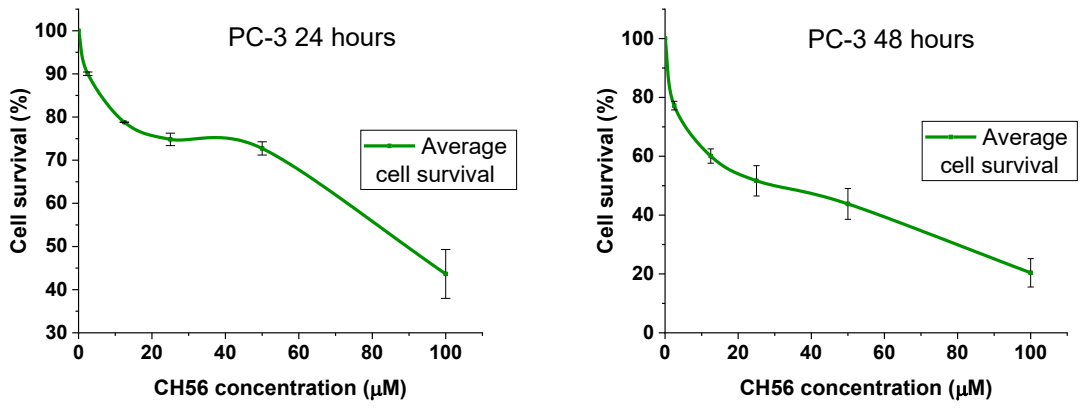

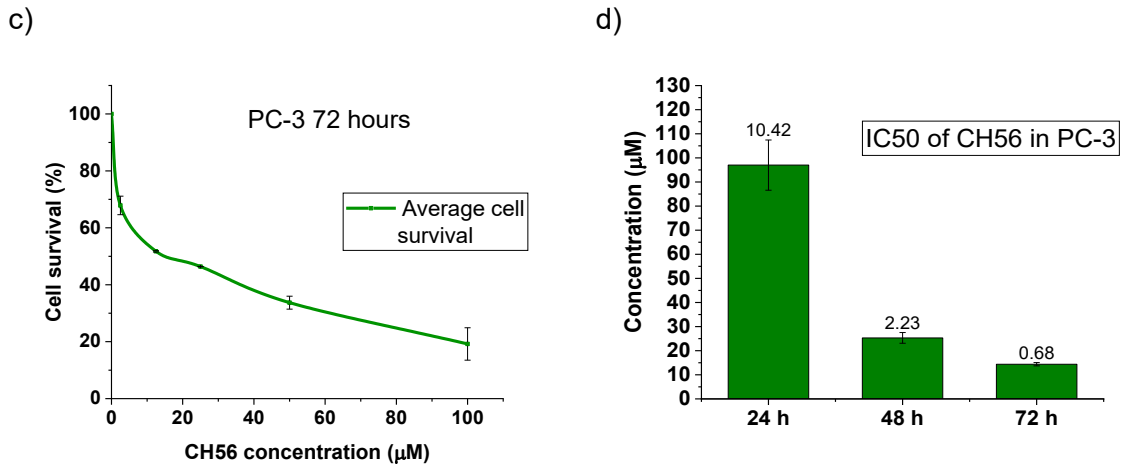

***Figure 17**. PC-3 cell line survival after (a) 24 h, (b) 48 h and (c) 72 hours in the presence of increasing concentrations of CH56. (d) IC_{50} at different times labelled with standard errors (SE).*

The half-maximal inhibitory concentration (IC_{50}) in PC-3 cells was calculated for all both protected and deprotected compounds *(Table 11).*

***Table 11**. IC_{50} (μM) of depsipeptide-containing hybrids. SE obtained from 4 independent experiments.*

	PC-3 24 h	**PC-3 48 h**	**PC-3 72 h**
CH49	320.1 ± 5.4	325.5 ± 47.8	67.5 ± 6.8
CH49-D	39.1 ± 3.4	15.6 ± 2.3	11.1 ± 1.8
CH56	97.0 ± 10.4	25.3 ± 2.2	14.4 ± 0.7
CH56-D	50.7 ± 5.1	17.5 ± 2.3	10.4 ± 1.5
CH57	101.9 ± 11.2	79.2 ± 9.9	51.9 ± 5.6

Notice that the most pronounced cytotoxicity after 72 hours is that of CH56-D, with a pyrimidine unit in its structure (2 nitrogen atoms), followed by CH49-D with a pyridine unit (1 nitrogen atom). It must be added that the IC_{50} notably decreases after 72 hours in both protected and deprotected species, confirming their dose- and time- dependent activity. In addition, the acetylated species are biocompatible after 24 hours (IC_{50} ≥100 μM), however, as time goes by, they become slightly cytotoxic. It is assumed that depsipeptide chain is degraded by the action of proteases inside the cells, so the species becomes cytotoxic as the depsipeptide chain is degraded.

Hybrids with a free amine group.

Species with an unprotected NH group have been shown to be much more cytotoxic compared to the previous compounds. This subsection includes species with the unprotected NH of piperazine (CH51-D, CH54-D, CH55-D) and a species with the unprotected NH of piperidine (CH58-BIS). The graphs of survival cells and IC_{50} plots of CH54-D are shown as representative examples of this group of compounds *(Figure 18).*

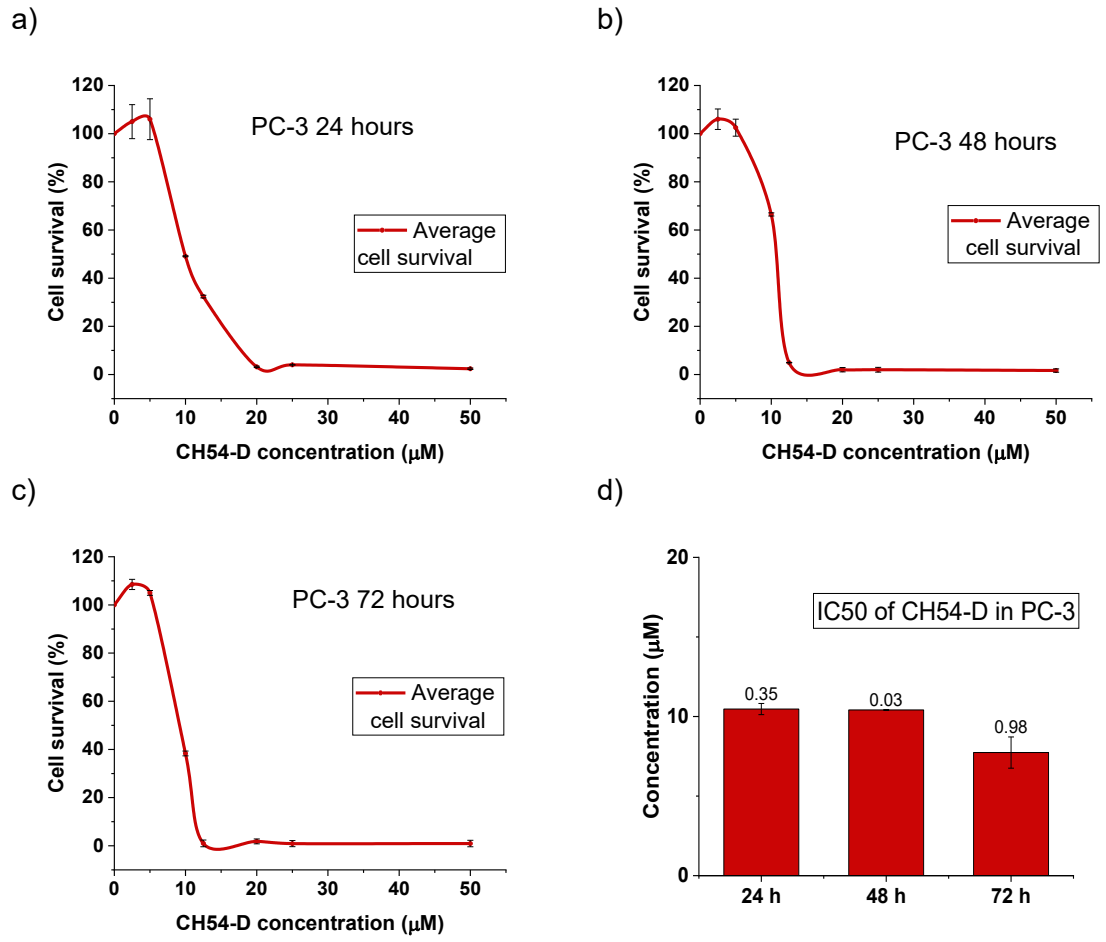

***Figure 18**. PC-3 cell line survival after (a) 24 h, (b) 48 h and (c) 72 hours in the presence of increasing concentrations of CH54-D. (d) IC_{50} at different times labelled with standard errors (SE).*

The half-maximal inhibitory concentration in PC-3 cells was calculated for all deprotected species *(Table 12)*.

***Table 12**. IC_{50} (μM) of free amine-containing hybrids. SE obtained from 4 independent experiments*

	PC-3 24 h	**PC-3 48 h**	**PC-3 72 h**
CH51-D	19.4 ± 0.2	15.7 ± 0.9	14.8 ± 1.2
CH54-D	10.5 ± 0.4	10.4 ± 0.0	7.7 ± 1.0
CH55-D	16.6 ± 1.5	13.3 ± 0.6	12.8 ± 0.5
CH58-BIS	7.1 ± 0.1	6.7 ± 0.1	6.6 ± 0.7

It can be observed that cytotoxicity has been shown to be higher when the piperidine group is unprotected (CH58-BIS) compared to those with the unprotected piperazine (CH51-D, CH54-D, CH55-D). It is supposed that the NH groups should interact with acid groups of some protein or enzyme inside the cell, inhibiting or altering biological processes essential for its survival. Furthermore, if the species with unprotected piperazine are compared between them, it is observed that once again the most cytotoxic compound is the one that contains a pyrimidine group in its structure, CH54-D. The more cytotoxicity of pyrimidine derivatives could be likely explained because that this type of structure with two nitrogen atoms interacts more selectively with some enzymatic receptor, altering the correct functioning of the cell; but this is only a probable theory. The specific cytotoxic mechanism

of the species is not yet discovered. Finally, it is also observed that the IC_{50} barely changes over time. For example, the cytotoxicity of CH58-BIS is high after 24 hours (7.1 μM), with hardly any changes over time (6.6 μM after 72 hours). The small differences observed can even be attributed to the standard deviation of the measurements. So, these compounds have a high cytotoxic efficiency from early stages inside the cells.

Two testosterone-containing hybrids.

In this case, a pyrimidine compound with two testosterone groups was evaluated. It was tested in its acetyl derivative (CH58) and in its deprotected alcoholic form (CH58-D), and in both cases it was shown to be completely biocompatible over time. The cell survival graphs for CH58 are represented in *Figure 19.*

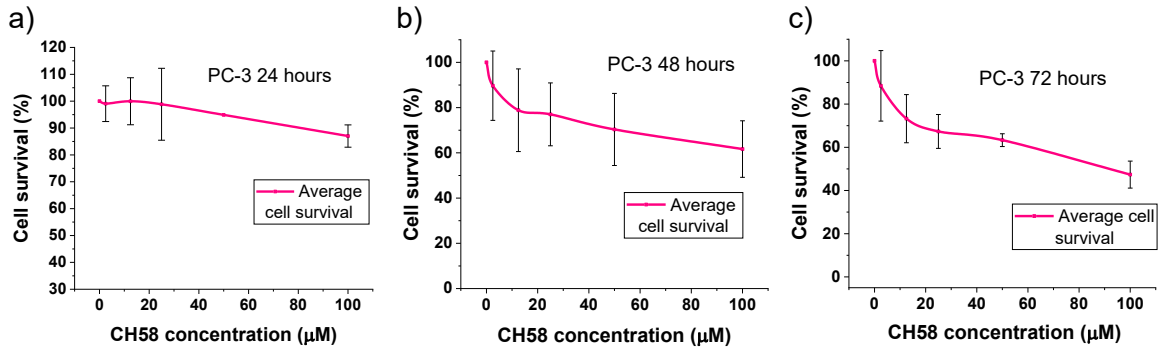

***Figure 19**. PC-3 cell line survival after (a) 24 h, (b) 48 h and (c) 72 hours in the presence of increasing concentrations of CH58.*

The IC_{50} was in both cases above 100 μM. It can be stated that the presence of two testosterone units makes the compounds biocompatible in PC-3 cells, even if they contain a pyrimidine unit in its structure. These compounds lack unprotected amine groups, and thus they probably do not disrupt any essential biological processes.

7.1.2. Target organelle of compounds in PC-3 cell line

To determine the intracellular destination of the compounds, we used confocal laser scanning microscopy (CLSM). First, the cells were stained with phalloidin, a probe that selectively binds to filamentous actin, thereby outlining the cytoskeleton. This allowed us to assess the spatial distribution of the compounds within the cells and revealed that they did not accumulate in the nucleus but rather in the cytoplasmic region. Based on this preliminary localization pattern, we selected specific organelle dyes for the lysosomes, mitochondria, and endoplasmic reticulum, as these organelles were considered the most likely targets for the compounds. To carry out image acquisition, prior preparation of the cells was necessary (made by biologists). First, cells were seeded in 12 mm sterile coverslips in cell culture plates of 24 well at a density of 5 x 10^4 cells per well and allowed to grow for 24 hours. Then, cells were incubated with 15 μM of the compounds under study for 12h. Then, the medium was removed, and the organelles were stained using different dyes. Mitochondrial staining was carried out using Mitochondrial Staining Kit - Red Fluorescence - Cytopainter (ab112145). Lysosomes were stained with Lysosomal Staining Reagent - Deep Red-Cytopainter (ab176829). And for ER, the ER Staining Kit - Red Fluorescence - Cytopainter (ab139482) was employed. Briefly, a 1 mM stock solution was diluted in serum-free growth medium to a final concentration of 500 nM. Both cell lines were incubated with the staining solution for 30 minutes at 37°C with 5% CO_2. After incubation, the cells were washed three times with phosphate-buffered saline (PBS) to remove excess dye. Cells were fixed with 4% paraformaldehyde in PBS for 15 minutes at room temperature, followed by three washes with PBS. Then, we visualized the cells in a Leica TCS SP8 lightning apparatus.

The excitation and emission wavelengths employed for each dye are collected in the next table.

***Table 13**. Excitation and emission wavelengths employed for each dye*

	λ excitation (nm)	**λ emission (nm)**
Testosterone-NMI hybrid	360	500
Endoplasmic reticulum dye	580	677
Mitochondria dye	580	600
Lysosomes dye	596	619

Destination of cytotoxic species

First, phalloidin-stained cells were imaged. In *Figure 20* we can see that CH51-D (green) is located in areas proximal to the nucleus. Given that the endoplasmic reticulum is characteristically concentrated in this perinuclear region, these preliminary results provide an early indication of its potential accumulation site, guiding the subsequent organelle-specific staining experiments.

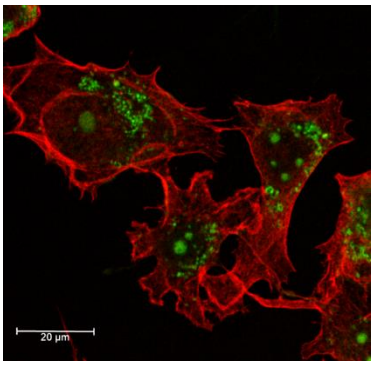

***Figure 20.** Confocal microscopy image of CH51-D (green) inside PC-3 cells stained with phalloidin.*

Then, CLSM results confirmed that cytotoxic species (CH51-D and CH54-D) colocalize with endoplasmic reticulum. In *Table 14,* the intracellular localization of compound CH51-D along with stained mitochondria, lysosomes, and endoplasmic reticulum are shown. While CH51-D displays regions of apparent overlap with both mitochondria and lysosomes, this is likely due to the fact that these organelles are widely distributed throughout the cytoplasm in a three-dimensional arrangement. As a result, some degree of spatial overlap is inevitable, including within areas where the endoplasmic reticulum is present. However, quantitative colocalization analysis performed with ImageJ software, confirmed that the highest degree of colocalization occurs with the endoplasmic reticulum, supporting it as the primary target organelle of CH51-D.

***Table 14**. Confocal microscopy images of stained mitochondria, lysosomes, endoplasmic reticulum and the localization of CH51-D inside the PC-3 cells. Overlapped channels are shown in the right column*

	Stained organelle	CH51-D	Overlapped channels
Mitochondria	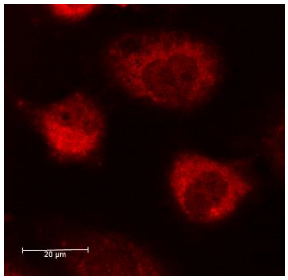	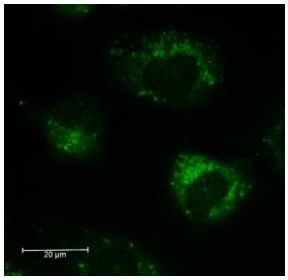	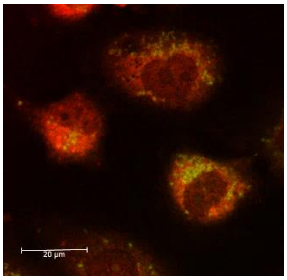

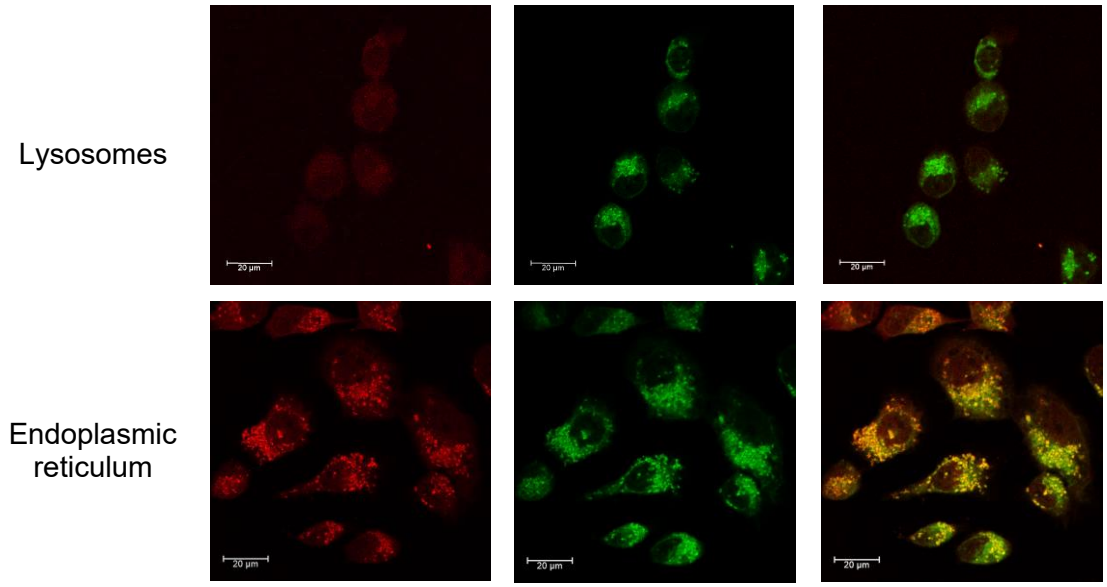

The Pearson's correlation coefficient measures the degree of linear correlation between the intensity values of two fluorescent signals, indicating how similarly they vary across the image. In our analysis, the intensity profiles of CH51-D and the endoplasmic reticulum signal varied in a highly similar manner within the cell, yielding a high Pearson's correlation coefficient of 0.86 (calculated using ImageJ without applying thresholding). In contrast, for lysosomal and mitochondrial markers, regions of maximum fluorescence intensity did not completely coincide with those of CH51-D, resulting in markedly lower Pearson's coefficients, both below 0.5, thus indicating low correlation.[13] Then, to evaluate the spatial overlap between the signals of ER and CH51-D, we also calculated Manders' coefficients. M1 (CH51-D overlapping the ER probe) was 0.635, and M2 (ER probe overlapping CH51-D) was 0.485. These values indicate that 63.5% of the CH51-D signal coincides with the ER probe, while 48.5% of the ER probe signal overlaps with CH51-D. M2 has a lower value, likely because the stained endoplasmic reticulum occupies a larger volume within the cell than the compound, so not all ER regions contain CH51-D. In practical terms, Manders' coefficients above 0.5 generally indicate a moderate to strong degree of colocalization in cell imaging studies.[14] Therefore, the present results suggest a substantial association of CH51-D with the endoplasmic reticulum, consistent with the Pearson's correlation findings.

Then, CH54-D was also studied by confocal microscopy, and it shows the same behaviour as CH51-D. It colocalizes with endoplasmic reticulum too, as observed in the next figure.

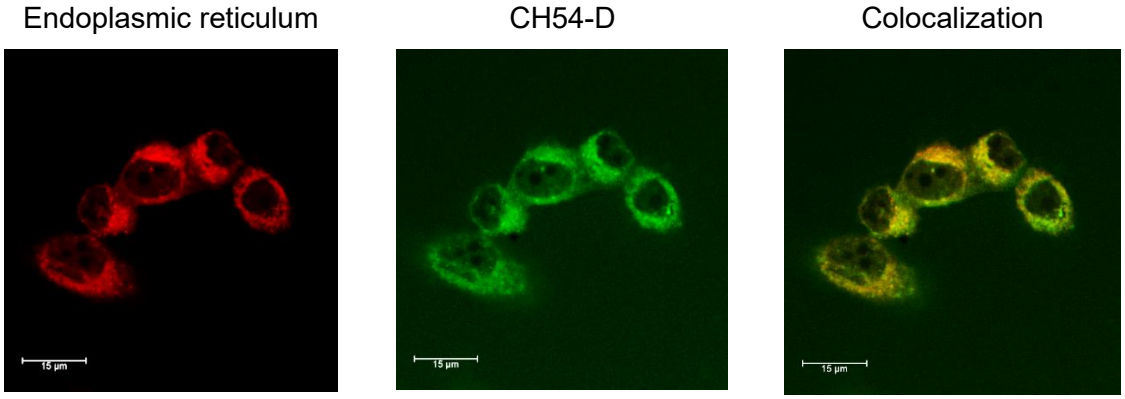

Figure 21. *Colocalization of CH54-D with endoplasmic reticulum in PC-3-cells.*

[13] S. Botle, F. P. Cordelières, *J. Microsc.* **2006,** *224,* 213−232.
[14] K. W. Dunn, M. M. Kamocka, J.H. McDonald, *Am. J. Physiol. Cell. Physiol.* **2011,** *300* (4), 723−742.

In this case, colocalization coefficients were also determined with ImageJ software. Pearson's correlation coefficient (Rr, no threshold) was 0.93, suggesting a very high positive correlation between the intensity distributions of CH54-D and the ER probe. Manders' coefficients were also calculated: M1 (CH54-D overlapping the ER probe) was 0.188, and M2 (ER probe overlapping CH54) was 0.707. These values indicate that 18.8 % of the CH54-D signal coincides with the ER probe, while 70.7 % of the ER probe signal overlaps with CH54-D. The observed discrepancy between Mander's coefficients can be attributed to the presence of extracellular CH54-D, as indicated by the slightly green background in the central image. Consequently, a fraction of the fluorescence signal lies outside the cellular boundaries, leading to a marked decrease in the M1 coefficient. It is well established that Manders' coefficients are very sensitive to background noise and signals outside the region of interest, such as extracellular fluorescence.[12, 15] So, in this case, the extracellular noise is artificially reducing M1 value. This conclusion is further supported by the high Pearson's coefficient, which had already indicated a very high degree of colocalization.

Destination of biocompatible species

On the other hand, the study by confocal microscopy of CH58 (a biocompatible compound bearing two testosterone units) revealed that it does not colocalize with any cytoplasmatic organelle. First, PC-3 cells were stained with phalloidin, which facilitated the preliminary assessment of the compound's localization within the cell. As seen in *Figure 22* the compound appears to be aggregated in the periphery of the cell, near the plasma membrane. Then, mitochondria, lysosomes and endoplasmic reticulum were also stained. In the next table we can see that there is not overlap with any of them.

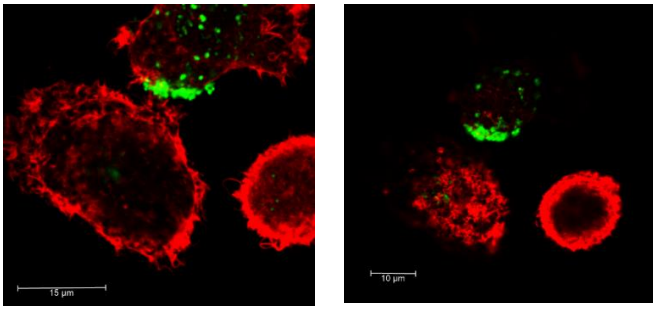

Figure 22. *Confocal microscopy images of CH58 inside PC-3 cells stained with phalloidin.*

Table 15*. Confocal microscopy images of stained mitochondria, lysosomes, endoplasmic reticulum and the localization of CH58 inside the PC-3 cells. Overlapped channels are shown in the right column*

	Stained organelle	CH58	Overlapped channels
Mitochondria	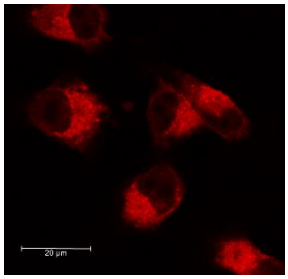	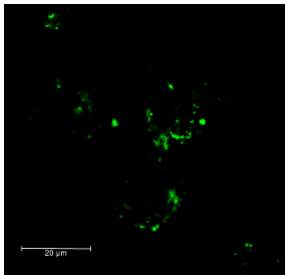	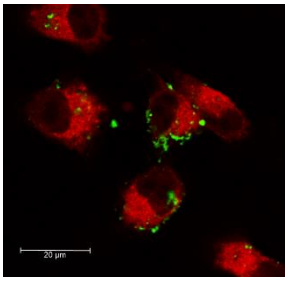

[15] Y. Wu, V. Zinchuk, O. Grossenbacher-Zinchuk, E. Stefani*, Interdiscip. Sci. Comput. Life. Sci*. **2012,** *4,* 27–37.

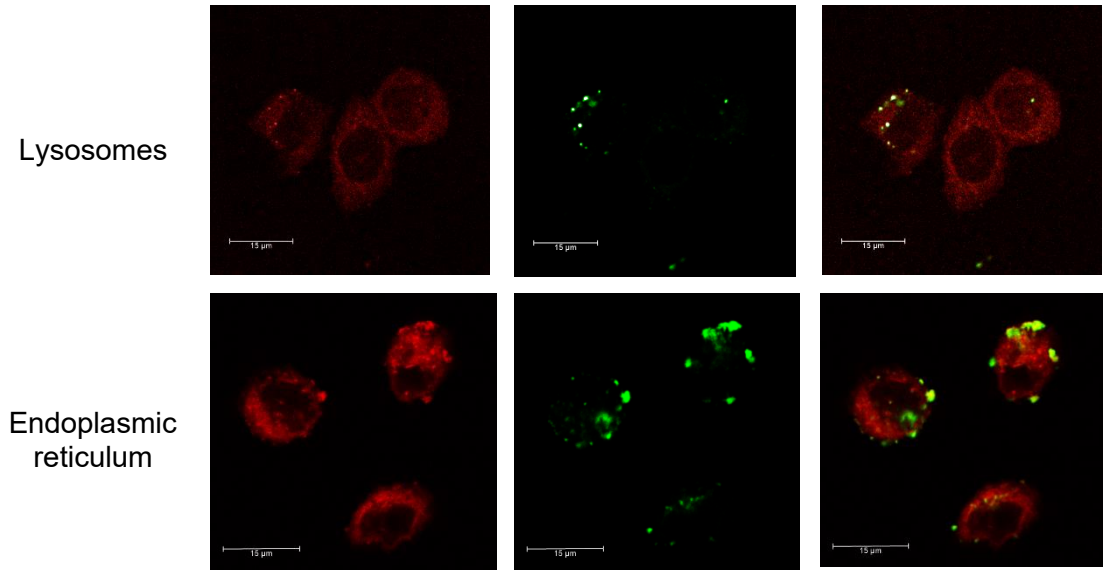

As observed, this biocompatible compound containing two hydrophobic testosterone units does not colocalize with any of the studied organelles; instead, it forms aggregates near the plasma membrane. This behaviour is likely due to the hydrophobic nature of testosterone, which confers on the molecule greater affinity for the lipid-rich plasma membrane than for the endoplasmic reticulum, where the cytotoxic compounds tend to localize. It is probable that the interaction with the endoplasmic reticulum of the cytotoxic compounds is driven by the presence of the naphthalimide core or the free terminal amine groups, which may interact with essential intracellular proteins or enzymes, thereby promoting cell death. In contrast, the presence of the two testosterone units increases the molecule's affinity for the plasma membrane, making the cellular destination primarily dictated by the hydrophobicity of testosterone rather than by the naphthalimide core. In addition, it is probable that this different location is directly related to its lack of toxicity.

7.2. ACTIVITY AND TARGET ORGANELLE INSIDE LNCaP CELL LINE

As was done in the previous section, the antitumor activity of the compounds will be evaluated in this new cell line, and the target organelle will be also identified.

7.2.1. Biocompatible vs antiproliferative species in LNCaP cell line

To determine the cytotoxicity of the compounds, MTT assays were performed following a similar protocol to the followed with PC-3 cells. The only difference is that in this case, the culture medium is RPMI-1640, since LNCaP cell line exhibits more delicate growth requirements than PC-3, and the enriched nutrient composition of this new medium is better suited to meet its specific metabolic demands.

The results presented in this section follow the same behaviour pattern as that observed in the PC-3 cell line. Compounds containing a depsipeptide chain exhibit low cytotoxicity, which increases slightly as time goes by. However, species with an unprotected terminal amino group are markedly more cytotoxic and the values are stable over time. Finally, compounds bearing two testosterone moieties prove to be biocompatible. From a general perspective, the overall cytotoxicity of the compounds is slightly lower in this cell line compared to PC-3. A detailed analysis of each compound group is presented below.

Depsipeptide-containing hybrids

In this cell line, compounds containing a depsipeptide (both acetylated and alcoholic forms) exhibit low initial cytotoxicity, which increases to moderate levels after 72 hours of

incubation. To maintain consistency with the previous cell line, the cytotoxicity graphs of CH56 are shown in *Figure 23.*

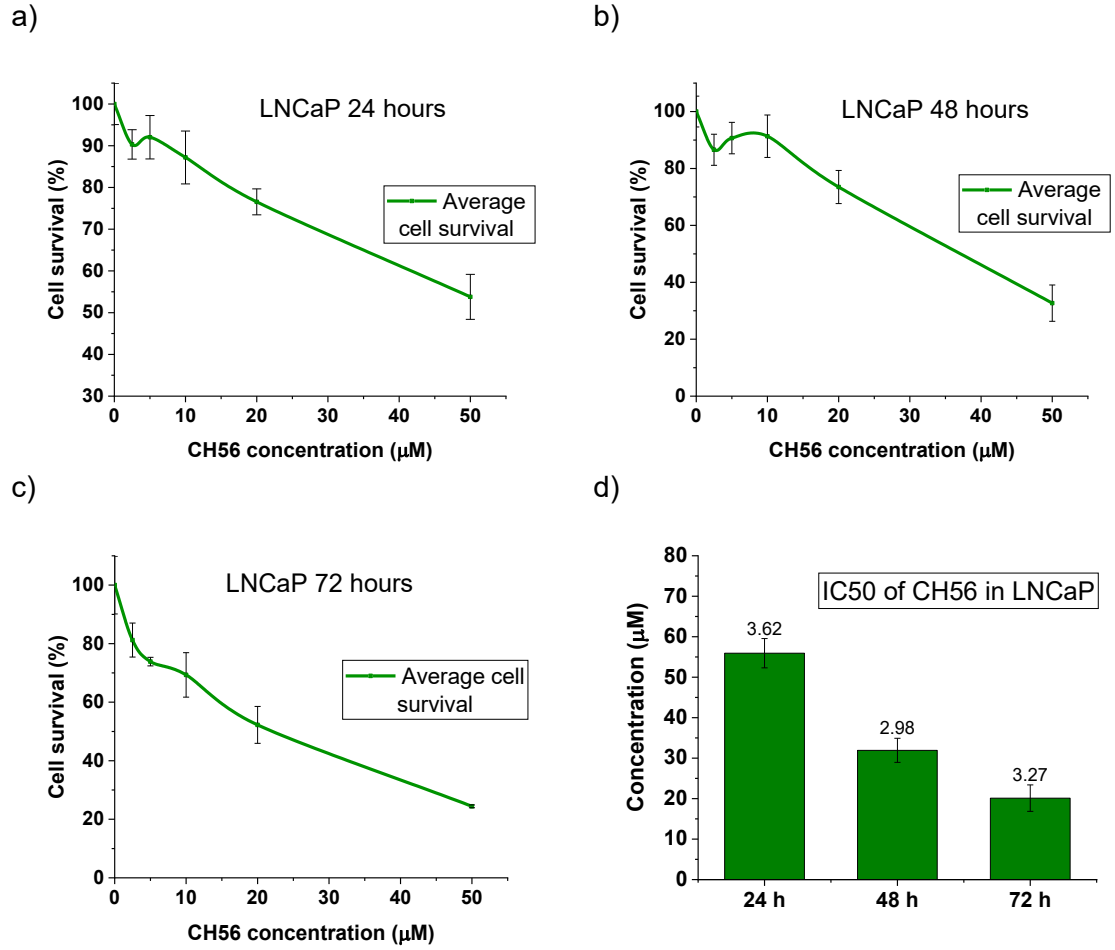

***Figure 23**. LNCaP cell line survival after (a) 24 h, (b) 48 h and (c) 72 hours in the presence of increasing concentrations of CH56. (d) IC_{50} at different times labelled with standard errors (SE).*

The half-maximal inhibitory concentration (IC_{50}) in LNCaP cells was calculated for all both protected and deprotected compounds *(Table 14)*. However, it is worth mentioning that CH49, (containing the acetyl group), resulted to be unstable and could not be studied.

***Table 16.** IC_{50} (μM) of depsipeptide-containing hybrids. SE obtained from 4 independent experiments*

	LNCaP 24 h	**LNCaP 48 h**	**LNCaP 72 h**
CH49-D	116.3 ± 8.1	61.0 ± 3.7	35.5 ± 2.3
CH56	55.9 ± 3.6	31.9 ± 3.0	20.1 ± 3.3
CH56-D	144.7 ± 2.8	46.1 ± 4.3	29.5 ± 2.3
CH57	>1000	>1000	52.9 ± 4.2

As observed with PC-3 cells, the most cytotoxic compounds are those containing a pyrimidine moiety in their structure. A time-dependent increase in toxicity was also detected, which may be attributed to the degradation of the depsipeptide chain within the intracellular environment as time goes by. After 72 hours, cytotoxicity values fall within the 20-50 μM range, whereas in PC-3 cells, values decreased to as low as 10 μM at the same time point. This difference may be explained by the slower metabolism of this particular cell line.

Hybrids with a free amine group

As was done with the PC-3 cells, this section includes the compounds with a terminal unprotected amine group. So, here are collected the compounds from which the Boc group has been removed from the piperazine ring (CH51-D, CH54-D, and CH55-D) as well as the one with a free piperidine (CH58-BIS). These compounds exhibit moderate-high cytotoxicity, and to maintain consistency with the previous cell line series, the results for CH54-D are presented as a representative example *(Figure 24).*

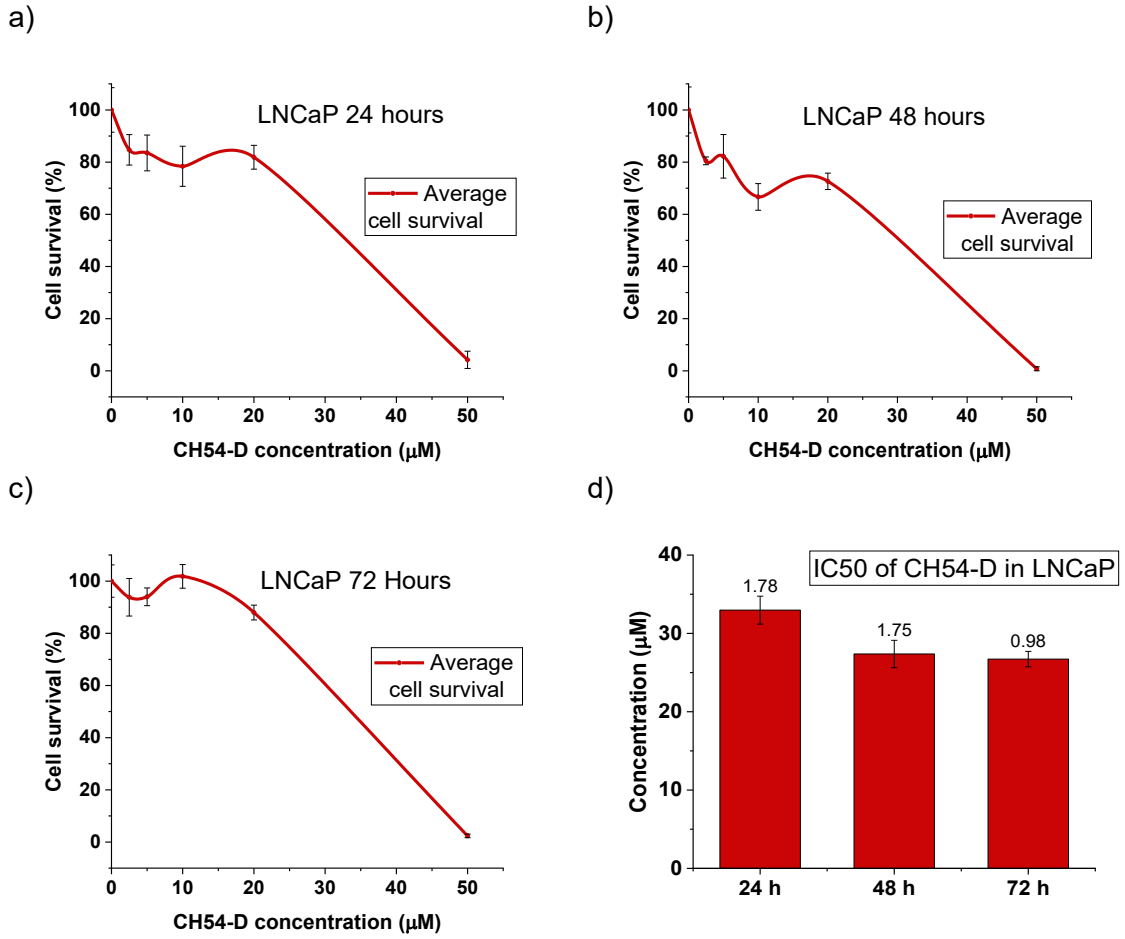

***Figure 24**. LNCaP cell line survival after (a) 24 h, (b) 48 h and (c) 72 hours in the presence of increasing concentrations of CH54-D. (d) IC_{50} at different times labelled with standard errors (SE).*

The half-maximal inhibitory concentration in LNCaP cells was calculated for all deprotected species *(Table 15).*

***Table 17**. IC_{50} (μM) of free amine-containing hybrids. SE obtained from 4 independent experiments*

	LNCaP 24 h	LNCaP 48 h	LNCaP 72 h
CH51-D	26.1 ± 2.2	18.3 ± 0.2	14.3 ± 0.6
CH54-D	33.0 ± 1.8	27.4 ± 1.8	26.7 ± 1.0
CH55-D	28.8 ± 2.2	27.6 ± 1.3	28.5 ± 1.0
CH58-BIS	12.2 ± 0.2	12.0 ± 0.4	10.9 ± 0.1

The table shows that cytotoxicity remains stable over time. In contrast to the depsipeptide-containing compounds, which require a latency period for the release of the depsipeptide chain, and subsequent induction of cell death, the compounds in this series possess an NH group from the beginning. This functional group is likely responsible for the immediate cytotoxic response, as it can directly interact with intracellular targets (such as proteins). The absence of a protective group enables the amine to interact with biologically relevant components as soon as the compound enters the cell, leading to early cytotoxicity.

The antitumoral activity is similar for all compounds bearing an unsubstituted piperazine, with IC_{50} values around 20-30 micromolar. Notably, CH58-BIS displays a markedly lower IC_{50}, (10 μM) suggesting that having an unsubstituted piperidine is more effective in the search for antitumor agents.

As with the depsipeptide-hybrids, these compounds are less cytotoxic to LNCaP cells than to the PC-3 line. Nonetheless, their consistent activity still positions them as promising antitumor candidates for this cell line.

Two testosterone-containing hybrids

Finally, the compound bearing two testosterone units was evaluated in both its acetylated-protected form (CH58) and its deprotected, alcoholic form (CH58-D). As observed in the PC-3 cells, in the LNCaP cell line both compounds exhibit good biocompatibility, with IC_{50} values exceeding 1000 μM at 24 and 48 hours and approaching 100 μM after 72 hours of incubation. The biocompatibility plots of CH58 are shown in *Figure 25.*

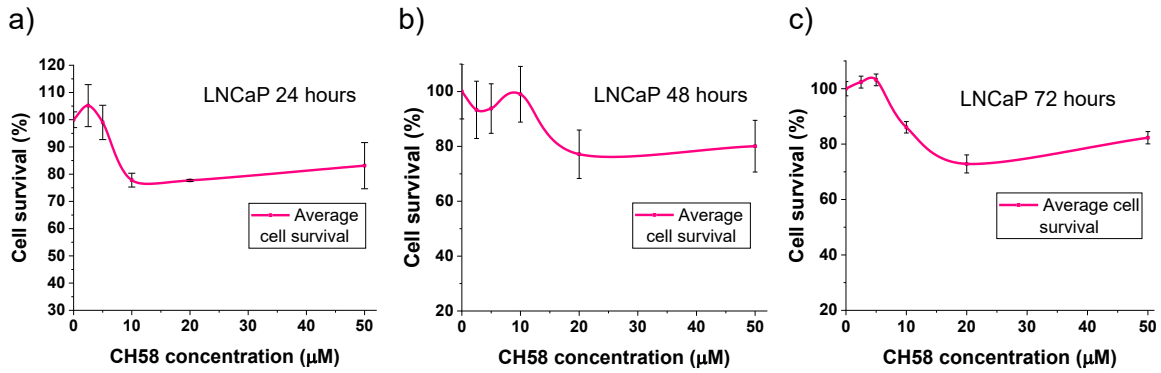

***Figure 25**. LNCaP cell line survival after (a) 24 h, (b) 48 h and (c) 72 hours in the presence of increasing concentrations of CH58.*

The compounds bearing two testosterone units were found to be biocompatible. This is a particularly interesting result, as it highlights the possibility of modulating the cytotoxicity of the molecules according to the number of testosterone moieties conjugated to the fluorophore. Based on the results obtained throughout the different sections, it becomes evident that a tuneable cytotoxic profile can be achieved depending on the desired therapeutic goal.

Highly cytotoxic agents can be obtained through the presence of a free NH group; alternatively, compounds incorporating a biocompatible depsipeptide exhibit delayed cytotoxicity, acting as "Trojan horses" (similar to those described in Chapter 1) as the cytotoxic fragment (NH group) is released over time.

Finally, compounds bearing two testosterone units demonstrate to be non-cytotoxic and are suitable for use as cellular biomarkers in prostate cancer cell lines. The amine-testosterone linkage is stable under intracellular conditions and resists enzymatic degradation, preventing the release of free NH groups and, consequently, avoiding cytotoxic effects.

7.2.2. Target organelle of compounds in LNCaP cell line

Visualization of the compounds within LNCaP cells was carried out following the same protocol used for PC-3 cells, however, in this case the compounds concentration inside the cells were 10 μM. The same organelle fluorescent dyes, excitation and emission wavelengths and confocal microscopy apparatus were employed.

The results in LNCaP cells are similar to those obtained for PC-3. Whereas cytotoxic species such as CH51-D localize to the endoplasmic reticulum, compounds bearing two testosterone units remain close to the plasma membrane.

Destination of cytotoxic species.

First are collected the results for CH51-D, a pyridine derivative with one testosterone unit and one free amine group. LNCaP cells were also stained with phalloidin (red), so, we can see how the compound (green) is located around the nucleus *(Figure 26)*. It shows the same location pattern as observed in PC-3 cells.

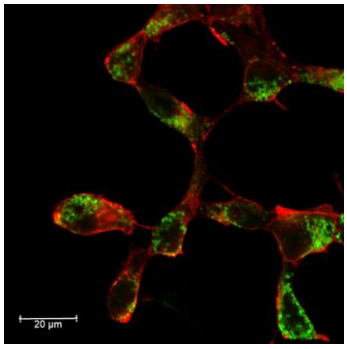

Figure 26. *Confocal microscopy image of CH51-D (green) inside LNCaP cells stained with phalloidin (red).*

To ensure that the subcellular localization of the compound was consistent in both LNCaP and PC-3 cells, additional colocalization studies were performed using mitochondrial, lysosomal, and endoplasmic reticulum markers. The results revealed a high degree of colocalization with the endoplasmic reticulum, whereas the correlation coefficients obtained with ImageJ for lysosomes and mitochondria indicated that these were not the primary target organelles. The partial spatial overlap observed with these latter organelles can be explained by their uniform distribution throughout the cytoplasm, which, as previously discussed, makes a certain degree of coincidence unavoidable. In the next table the CLSM images are collected.

Table 18*. Confocal microscopy images of stained mitochondria, lysosomes, endoplasmic reticulum and the localization of CH51-D inside the LNCaP cells. Overlapped channels are shown in the right column*

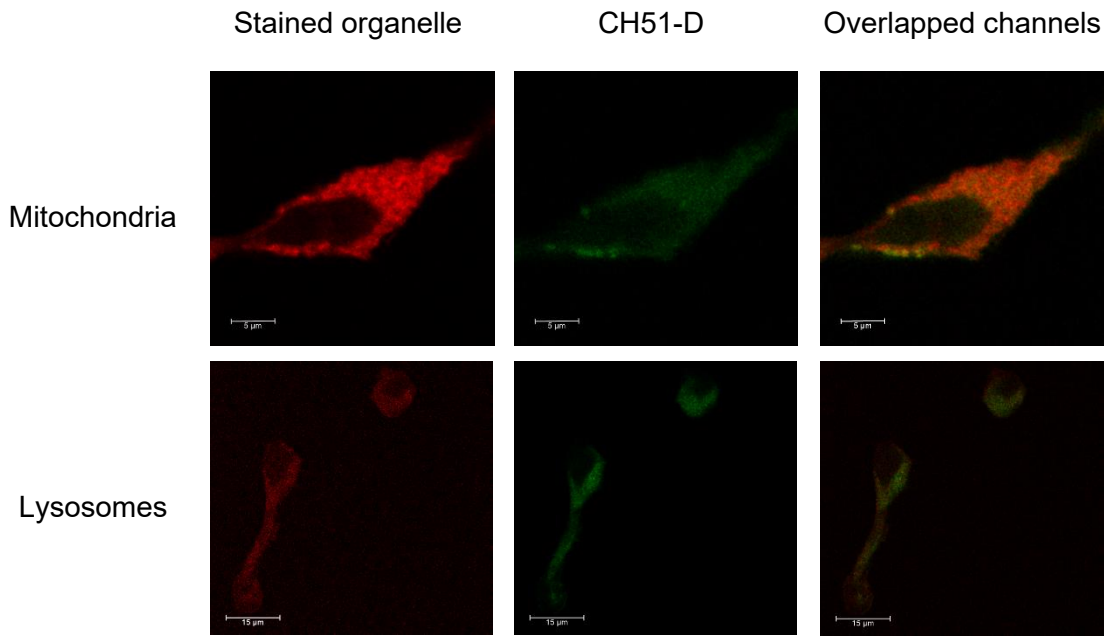

Endoplasmic reticulum	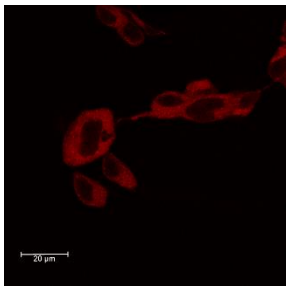	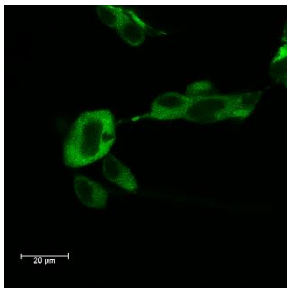	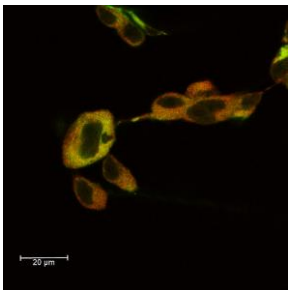

As shown in the channel overlay images (right column of the table above), colocalization with mitochondria is characterized by a predominantly red signal, whereas lysosomal colocalization is marked by a predominance of green fluorescence. This observation indicates that the regions of highest intensity for the two fluorophores analysed in each image are not fully coincident. In contrast, when examining the endoplasmic reticulum, the overlay produces a uniform yellow signal, arising from the complete overlap between the red channel (endoplasmic reticulum) and the green channel (CH51-D). This complete signal merging suggests that this organelle is the primary intracellular destination of the compound. Following this qualitative assessment, colocalization coefficients were quantified using the ImageJ software. The values for colocalization with mitochondria and lysosomes were close to, but did not exceed, 0.5. However, for endoplasmic reticulum, Pearson's correlation coefficient (Rr, no threshold) was 0.91, suggesting a very high positive correlation between the intensity distributions of CH51-D and the ER probe. Manders' coefficients were also calculated: M1 (CH51-D overlapping the ER probe) was 0.612, and M2 (ER probe overlapping CH51-D) was 0.472. These values indicate that 61.2 % of the CH51-D signal coincides with the ER probe, while 47.2 % of the ER probe signal overlaps with CH51-D.

Destination of biocompatible species

This section examines the intracellular localization of CH58 in LNCaP cells, the same biocompatible compound with two testosterone moieties previously characterized in PC-3 cells. The new cells were first stained with phalloidin, and confocal images revealed that the product is located at the cell periphery as occurred with PC-3 cell line *(Figure 27).*

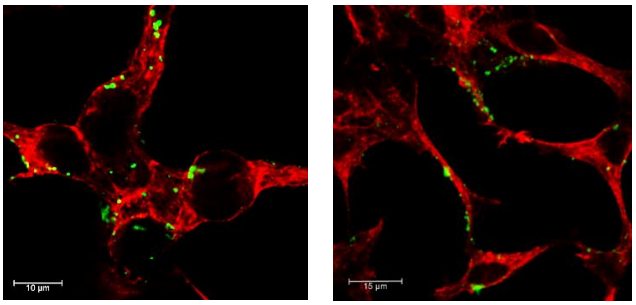

Figure 27. *CLSM images of CH58 inside LNCaP cells stained with phalloidin (red).*

As done in the previous analysis, the distribution of lysosomes, mitochondria and endoplasmic reticulum was compared with that of CH58, revealing no correspondence with any of them. The compound forms aggregates near the plasma membrane *(Table 19).*

***Table 19**. Confocal microscopy images of stained mitochondria, lysosomes, endoplasmic reticulum and the localization of CH58 inside the LNCaP cells. Overlapped channels are shown in the right column*

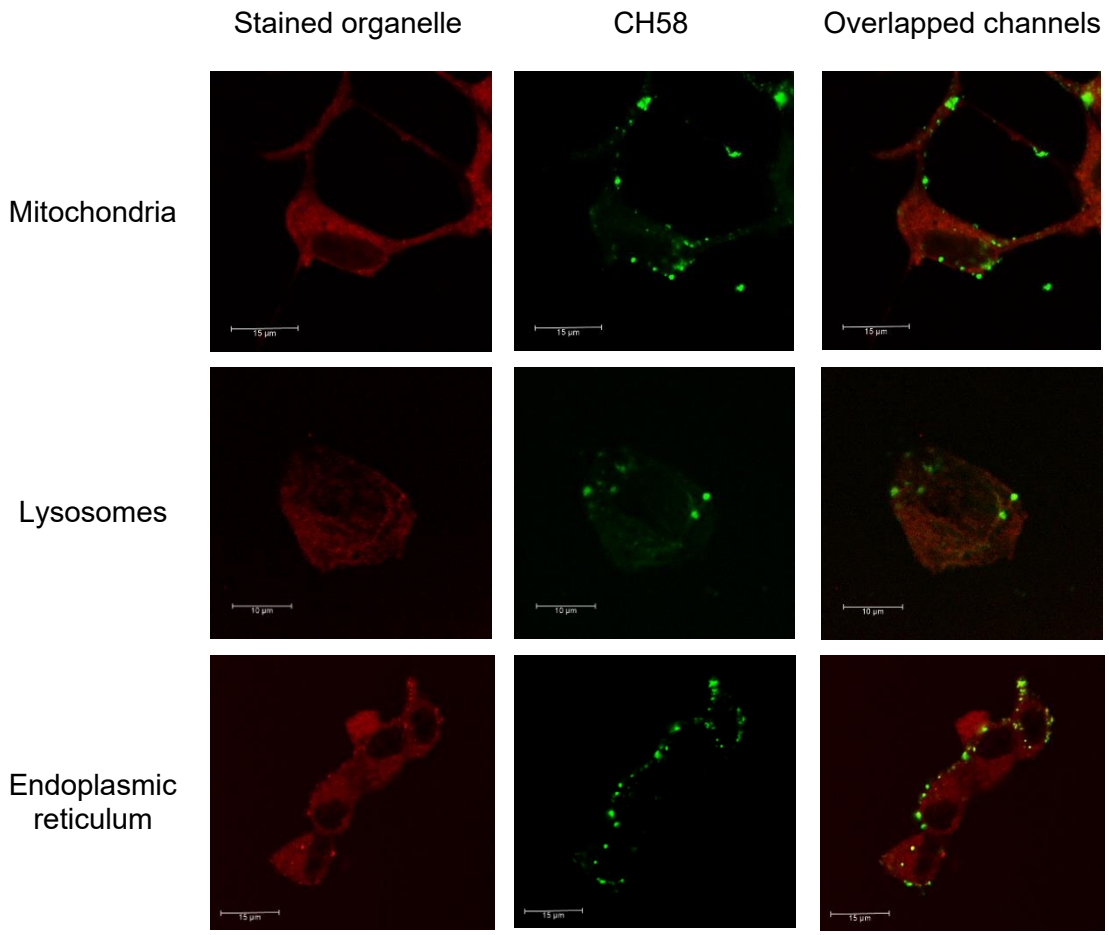

7.2.3. Conclusions from confocal microscopy results

From the microscopy images presented in the section above, it is possible to extract some conclusions. The cytotoxic compounds predominantly target the endoplasmic reticulum. It is known that LNCaP cells, being androgen-sensitive, express functional androgen receptors, which under normal conditions would be expected to interact with steroidal structures such as the testosterone moiety present in the designed compounds. It was therefore initially hypothesized that the testosterone-functionalized molecules might bind to the AR and follow a cytoplasmic or nuclear distribution pattern, as previously described for endogenous and synthetic androgens. However, confocal microscopy studies revealed a strong and preferential accumulation of the cytotoxic compounds in the endoplasmic reticulum, suggesting that their intracellular trafficking is driven more by physicochemical properties or NMI-based targeting motifs than by steroid-receptor interactions.

This observation is particularly promising, as it indicates that the presence of the testosterone unit does not lead to sequestration by the androgen receptor nor alters the compounds' intracellular destination. As a result, the cytotoxic potential of the molecules is preserved, regardless of AR-mediated pathways. This behaviour not only reinforces their mechanistic stability across androgen-responsive environments but also positions these compounds as attractive candidates for therapeutic applications, especially in hormone-

sensitive prostate cancer models where AR signalling and activation by androgens often complicates treatment efficacy.[16]

8. CONCLUSIONS

In this chapter, a new series of fluorescent testosterone-naphthalimide hybrids has been successfully developed. These compounds were designed to target prostate cancer cells and act as antitumoral agents. In addition to their therapeutic potential, they offer the advantage that the cellular uptake can be monitored through fluorescence-based imaging techniques.

Firstly, a range of testosterone-naphthalimide conjugates was synthesized, including derivatives functionalized with one or two testosterone units and others containing depsipeptide chains. Solvatochromic studies revealed a bathochromic shift of emission maxima as the solvent polarity increases, while water/organic solvent ratio experiments. demonstrated a pronounced AIE effect in mixtures with high water ratio.

Scanning Electron Microscopy confirmed that these compounds self-assemble into nanovesicles in the mixtures where the AIE phenomenon takes place, with morphology and size influenced by the structure of the NMI core. In addition, dynamic light scattering analyses revealed that pyrimidine-containing derivatives produced the largest aggregates, while phenyl-based compounds formed smaller vesicles.

Regarding biological evaluation, the synthesized hybrids exhibit tunable cytotoxicity against prostate cancer cell lines, depending on their structural features. The presence of a free amine group led to immediate and potent cytotoxic effects, particularly in CH58-BIS (unprotected piperidine), with IC_{50} values below 10 μM in both PC-3 and LNCaP cells. In contrast, compounds with a depsipeptide chain showed moderate, time-dependent cytotoxicity, suggesting intracellular degradation of the peptide moiety as time goes by. This process would release the active naphthalimide, allowing it to act freely within the cell. Compounds bearing two testosterone moieties, such as CH58 and CH58-D, showed high biocompatibility, indicating their suitability as selective fluorescent probes or biomarkers for prostate cancer cells. This ability to modulate cytotoxicity through structural modifications (particularly the number of testosterone units) opens the possibility to tailor the hybrids for either diagnostic or therapeutic purposes.

Cellular uptake assays using both AR-positive (LNCaP) and AR-negative (PC-3) prostate cancer cell lines confirmed efficient internalization of the conjugates. Despite initial expectations, the intracellular localization was not primarily governed by androgen receptor interactions. Confocal microscopy and colocalization studies revealed preferential accumulation of the cytotoxic compounds in the endoplasmic reticulum, regardless of androgen receptor presence, suggesting that intracellular trafficking is more influenced by the physicochemical nature of the fluorophores (NMI core) than by steroid-receptor binding. Interestingly, biocompatible conjugates exhibited greater accumulation near the plasma membrane, which is likely due to the presence of two testosterone units. These hydrophobic moieties may enhance the affinity of the conjugates for membrane regions, thereby reducing the influence of the naphthalimide core on subcellular localization.

In summary, the conjugation of testosterone to AIE-active naphthalimide dyes results in versatile molecules that exhibit desirable fluorescence properties, selective cellular uptake, controlled cytotoxicity, and clear subcellular localization. These findings support the potential of this class of compounds as attractive agents for treatment of prostate cancer, with the possibility of modulating the cytotoxicity depending on the intended applications.

[16] a) M. Ehsani, F. O. David, A. Baniahmad, *Cancers* **2021,** *13* (7), 1534. b) I. Coutinho, T. K. Day, W. D. Tilley, L. A. Selth, *Endocr. Relat. Cancer.* **2016,** *23* (12), 179−197.

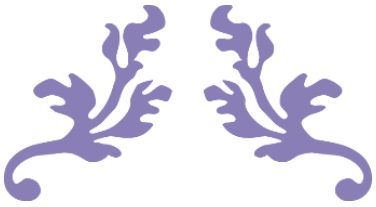

CHAPTER 4

Chiral urea moieties on Aggregation-Induced Emission Luminogens

ABSTRACT

In this chapter, we report the design and synthesis of chiral naphthalimide derivatives bearing chiral urea moieties, which exhibit aggregation-induced emission in mixtures with high water content. When the AIE is observed, these chiral NMI compounds self-assemble into helical fibers, driven by specific molecular interactions, the particular geometry of the core dye and the inherent chirality of the substituents. Due to the structural design, we successfully directed the formation of left-handed fibers imaged by scanning electron microscopy. Notably, enantiomeric pairs (R and S) of the NMI derivatives displayed mirror-image circular dichroism (CD) signals but unexpectedly emitted circularly polarized luminescence (CPL) of the same handedness, attributed to the supramolecular interactions at the aggregated state. Furthermore, these organic left-handed fibers served as chiral templates for the growth of silver nanoparticles. The metallization process was confirmed by elemental analysis using energy-dispersive X-ray spectroscopy (SEM-EDX). This work highlights a strategy for the rational design of chiral aggregation-induced emission luminogens and their use as scaffolds for the synthesis of metal coverings.

The Supporting Information of this chapter includes the synthetic routes, structural and fluorescence characterization tests as well as microscopy images of the nanostructures.

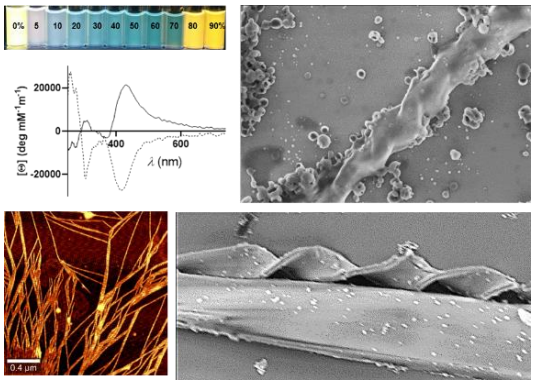

Figure 1. *Chiral NMIs derivatives: helical nanofibers, AIE and CD in aqueous mixtures.*

1. INTRODUCTION

The rational design of chiral organic molecules capable of self-assembling into well-defined supramolecular structures has become a central topic in supramolecular chemistry and materials science.[1] When building blocks possess chiral centres, supramolecular chirality is frequently generated during the assembly process, enabling the transfer of chirality from the molecular to the supramolecular level. Thereby, supramolecular chirality arises from the asymmetric spatial organization of the building blocks during self-assembly or co-assembly.[2] Among the various classes of functional molecular architectures, helical supramolecular structures derived from small chiral organic building blocks stand out due to their potential in optoelectronics, chiral recognition, enantioselective catalysis, the generation of circularly polarized luminescence as well as their emerging applications in biomaterials and biotechnology, and in the development of stimuli-responsive systems for sensing, molecular switching, and information storage.[3] These helices often result from non-covalent interactions such as hydrogen bonding, π-π stacking, and solvation effects, which collectively enable precise control over their handedness and morphology.[4]

Some studies reveal that incorporating a chiral unit into AIEgens structures can improve their circularly polarized luminescence performance in the solid state, as well as increase the dissymmetry factors of their self-assembled helical structures.[5] For example, it has been shown that the bonding of L-leucine to the tetraphenylethylene structure, makes this AIEgen show chiroptical activity. Although the core of the AIEgen structure has not inherent chirality, introducing leucine as a chiral side group allows the molecule to transfer molecular chirality

[1] W. Gong, W. Wang, J. Dong, X. Pan, Y. Liu, H-B. Yang, X. Y. Cui, *CCS Chem.* **2023,** *5*, 2736–2759.
[2] B. Liu, K. Guo, N. Wang, A. Hao, P. Xing, *J. Phys. Chem. C* **2022,** *126* (30), 12643−12650.
[3] E. Yashima, N. Ousaka, D. Taura, K. Shimomura, T. Ikai, K. Maeda, *Chem. Rev.* **2016,** *116* (22), 13752−13990.
[4] M. Kataria, S. Seki, *Chem. Eur. J.* **2025,** *31*, e202403460.
[5] C. Liu, J. C. Yang, J. W. Y. Lam, H. T.Feng, B. Z. Tang, *Chem. Sci.* **2022,** *13,* 611−632.

to the supramolecular level during the aggregation process. This chiral induction leads to the formation of helical nanostructures that are active in circular dichroism and show circularly polarized luminescence. Thus, leucine acts as a stereochemical driver, enabling the material to become optically active upon aggregation, highlighting the importance of chiral moieties bonding in the design of responsive chiroptical materials.[6] With the same purpose, some researchers combined chiral amines with pentaphenylpyrrole (PPP) derivatives achieving this way optical activity in their aggregated state. While the PPP serves as an AIE-active core, it is the presence of chiral side chains, that enables the transfer of chirality to the supramolecular assemblies. Upon aggregation, these chiral molecules self-assemble into helical nanofibers, displaying aggregation-induced circular dichroism and CPL signals.[7]

These examples show how the integration of aggregation-induced emission with supramolecular chirality is an attractive field in chemistry research. Recent studies have revealed that π-conjugated chromophores, such as naphthalenediimides and naphthalenemonoimides are also ideal platforms for constructing such systems. These chromophores can be engineered to promote directional self-assembly and often exhibit strong electronic interactions that are essential for CPL behaviour. Moreover, functionalization with chiral units provides a methodology to guide the appearance of helicity in the aggregated state.[8] It has been shown that the self-assembly of certain NDI-based macrocycles can lead to supramolecular helices with CPL signals that are inverted relative to those of the monomers, indicating that formation of aggregates may change the expected handedness of the CPL signals. That work offers a fascinating insight into how supramolecular interactions can dominate over the intrinsic chirality of the monomer. In this case R-enantiomers conducted to right-handed helices and S-enantiomers to left-handed ones *(Figure 2)*, while the CPL signals exhibited the opposite handedness relative to the helical sense.[9]

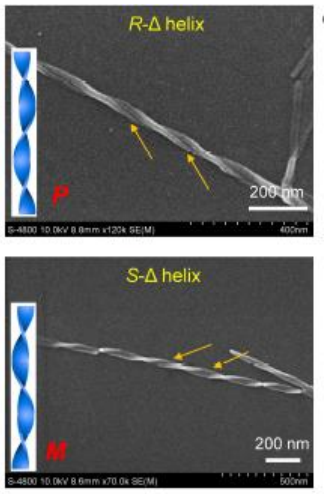

Figure 2. *SEM images of NDIs assembled in R and S helices.*[9]

In addition, some researchers explored the development of supramolecular polymers that exhibit both aggregation-induced emission and circularly polarized luminescence. They discovered that while isolated AIEgens and chiral units did not display significant chiroptical activity on their own, their combination through supramolecular assembly leads to notable chiral optical properties. Specifically, the achiral AIEgens, when incorporated into a chiral matrix, exhibited induced circular dichroism signals upon aggregation. This phenomenon is attributed to the efficient transfer and amplification of chirality from the chiral host to the achiral AIEgens during the self-assembly process. The resulting supramolecular gels demonstrated enhanced fluorescence and chiral properties, culminating in pronounced CPL signals. This study underscores the potential of combining AIE and supramolecular chemistry to design advanced chiroptical materials.[10]

These bibliographical findings highlight the importance of tailoring the chemical structure by the modification of the molecular core and its substituents. In this chapter, we extend this approach to NMI cores bearing both R and S enantiomers of (naphthyl)ethylcarboxamides. These molecules are designed to undergo AIE and to self-assemble into helices in aqueous-

[6] H. Li, J. Cheng, H. Deng, E. Zhao, B. Shen, J. W. Y. Lam, K. S. Wong, H. Wu, B. S. Li B. Z. Tang, *J. Mater. Chem. C.* **2015,** *3,* 2399−2404.
[7] L. Zhang, K. Liang, L. Dong, P. Yang, Y. Li, X. Feng, J. Zhi, J. Shi, B. Tong, Y. Dong, *New J. Chem.* **2017,** *41,* 8877−8884.
[8] S. Liu, F. Li, Y. Wang, X. Li, C. Zhu, Y. Cheng, *J. Mater. Chem. C.* **2017,** *5,* 6030−6036.
[9] S. Wu, X. Song, J. Lu, W. Hao, M. Liu, *Angew. Chem. Int. Ed.* **2025,** *64,* e202421108.
[10] H. Yan, Y. He, D. Wang, T. Han, B. Z. Tang, *Aggregate* **2023,** *4,* e331.

organic solvent mixtures. These helices always exhibit left-handedness, regardless of the R/S configuration of the enantiomers. In addition, while the CD signals of enantiomers are mirror images, the CPL signals show the same handedness, indicating that they are generated by supramolecular mechanisms that will be deeply explained in this chapter.

Furthermore, these chiral organic helices serve as templates for the growth of silver nanoparticles, indicating that is possible to transfer chirality from the organic matrix to metallic nanostructures. This approach opens promising applications in chiral plasmonics, asymmetric catalysis, and nanoscale photonics. The ability to transfer chiral arrangement to silver nanoparticles has been studied primarily in polymers. For example, some researchers have synthesized chiral poly(phenylacetylene) polymers that naturally adopt a helical conformation due to the presence of chiral side chains. These helical polymers act as templates for the controlled alignment of silver nanoparticles along their backbone. By introducing Ag^+ ions, which are subsequently reduced to form metallic silver nanoparticles, the researchers achieve a selective decoration of the helical polymer chains. The resulting nanocomposite features AgNPs arranged in a helical pattern, following the geometry of the polymer.[11]

In summary, this work contributes to the expanding field of chiral functional materials by illustrating how molecular chirality, supramolecular organization, and photophysical behaviour can be previously designed. By manipulating the molecular structure at the atomic level, we achieve control over macroscopic properties such as helicity and CPL, offering promising new directions for the design of chiral nanoscale materials.

2. OBJECTIVES

This chapter is focused on the design of chiral MNIs with aggregation-induced emission and self-assembling into helical fibers. It will be explored how molecular design can be employed to control supramolecular chirality and photophysical properties at the nanoscale. To get it, specific objectives must be achieved:

- To design and synthesize chiral naphthalenemonoimide derivatives functionalized with chiral urea moieties capable of exhibiting aggregation-induced emission in aqueous mixtures.
- To investigate the self-assembly behaviour of the synthesized NMI derivatives and characterize the formation of left-handed helical fibers using Scanning Electron Microscopy (SEM) and Transmission Electron Microscopy (TEM).
- To support the formation of helices with molecular dynamic simulation calculations, which also predict the self-assembly in this form of nanostructures.
- To analyse the chiroptical properties of the NMI enantiomers, including fluorescence anisotropy, circular dichroism, and circularly polarized luminescence, and to clarify how supramolecular interactions influence the generation of CPL signals.
- To use organic helical fibers as chiral templates for the growth of silver nanohelices and to confirm their composition using Scanning Electron Microscopy combined with Energy Dispersive X-ray spectroscopy.
- To change the geometry of the NMIs, functionalizing them in the meta position. It was discovered that in this case, helical fibers are not formed. This highlights the importance of specific geometry.

[11] M. Núñez-Martínez, S. Arias, E. Quiñoá, R. Riguera, F. Freire, *Chem. Mat.* **2021,** *33* (12), 4805−4812.

3. SYNTHESIS OF AIEGEN-CHIRAL UREA HYBRIDS

The chiral NMIs herein studied are divided in two families: (a) products containing two chiral urea moieties and (b) products with only one chiral urea moiety *(Figures 3a, 3b)*.

***Figure 3**. Schematic structure of new hybrid of AIEgens and chiral urea moieties.*

All compounds described in this section have the same synthetic reaction mechanism which consists in the nucleophilic attack of the free amine group present in the piperazine and/or piperidine of the NMI to the isocyanate group of the chiral moiety. Hence, two urea bonds are formed when a completely deprotected NMI is functionalized *(Figure 4a)*, but only one urea bond is created when the isocyanate is joined to a semi-protected structure *(Figure 4b)*.

Due to the similarity between the six synthetic reactions of this report, their experimental conditions and steps to be followed are the same. Only the nature of starting NMIs and the amount of all reagents change, and they are deeply described in the Supporting Information section, as well as their structural characterization. The common methodology is summarised herein after and shown in *Figure 4*.

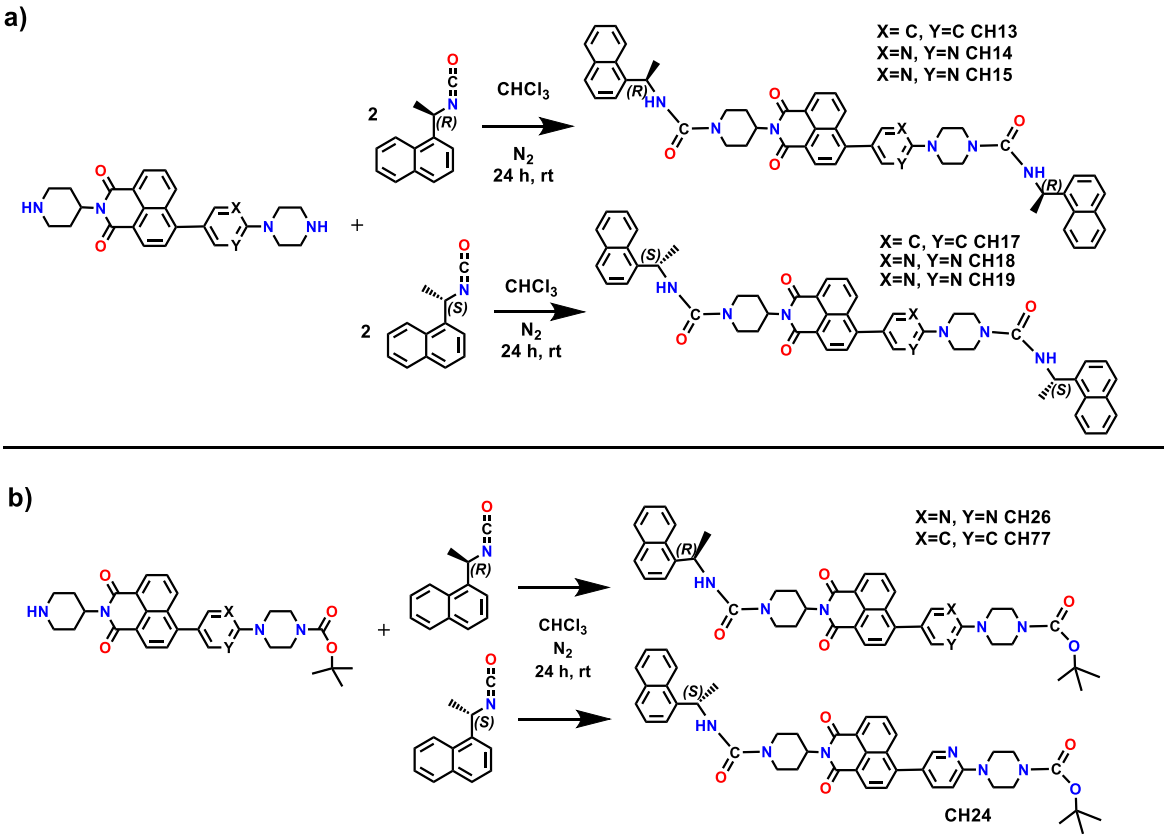

***Figure 4.** Synthetic route to obtain (a) Two chiral urea-AIEgen hybrids (b) One chiral urea-AIEgen hybrids.*

Experimental procedure: in a 50 ml flask, provided with a magnetic stirrer, the unfunctionalized NMI (1 eq.) is dissolved in 20 ml of chloroform. Then, inside of a nitrogen atmosphere glovebox, 1 or 2 equivalents (depending on the starting NMI) of (R/S)-(-/+)-1-(1-naphthyl)ethyl-isocyanate are added using a Hamilton microsyringe. Keeping the dry and inert atmosphere, the reaction mixture is stirred overnight at room temperature.

Once the reaction has finalized, the corresponding product is purified by column chromatography (SiO_2) employing a DCM-MeOH mixture, gradually increasing the MeOH content from 0 % to 2-3%. Finally, the products are obtained with yields ranging from 50 to 90%, depending on the nature of the starting NMIs.

4. FLUORESCENCE PROPERTIES OF SYNTHETISEZ HYBRIDS

4.1. SOLVATOCHROMISM ASSAYS

Here, the solvent polarity effect on the position and intensity of the absorption and emission bands is studied. In *Table 1*, the employed solvents are ordered from highest to lowest polarity, according to the Snyder polarity index.

Table 1. *Employed solvents in solvatochromism assays*

1. H_2O	4. DMF	7. EtOAc	10. THF	13. Hexane
2. MeOH	5. MeCN	8. THF	11. Toluene	14. MCH
3. DMSO	6. Acetone	9. $CHCl_3$	12. EtO_2	

Then, the 14 different solutions (10^{-5} M) of each compound were photographed under UV light of 366 nm. Bi- and monofunctionalized compounds are separately collected *(Tables 2, 3)*.

Table 2*. Solvatochromism assays of two chiral urea-AIEgen hybrids under UV light (366 nm)*

Structure	Solvents (1-14)
CH13: PHENYL NMI + 2 UREA (R)	
CH17: PHENYL NMI + 2 UREA (S)	
CH14: PYRIMIDINE NMI + 2 UREA (R)	
CH18: PYRIMIDINE NMI + 2 UREA (S)	
CH15: PYRIDINE NMI + 2 UREA (R)	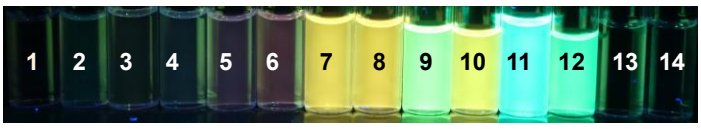
CH19: PYRIDINE NMI + 2 UREA (S)	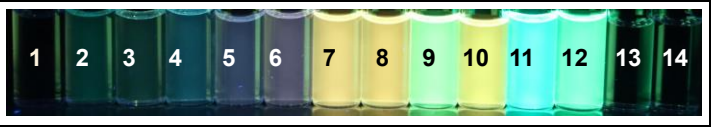

***Table 3**. Solvatochromism assays of one chiral urea-AIEgen hybrids under UV light (366 nm)*

Structure	Solvents (1-14)
CH24: PYRIDINE NMI + 1 UREA (S)	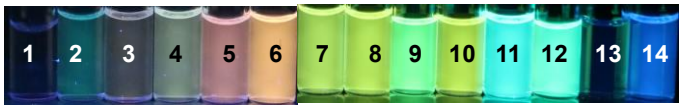
CH26: PYRIMIDINE NMI + 1 UREA (R)	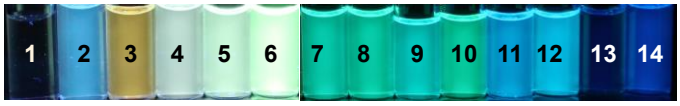
CH77: PHENYL NMI + 1 UREA (R)	

As happened with compounds of Chapter 1, it is observed that the fluorescence intensity of all NMIs increases as the solvent polarity decreases. In high polarity solvents, the species establish interactions between their aromatic cores and aggregate, so a little ACQ effect is observed. However, at intermediate polarities, the aliphatic regions (including chiral moieties) interact with the solvent and no aggregate is formed, showing therefore a bright fluorescence. Finally, compounds with two urea groups are not fluorescent in the least polar solvents as hexane and methylcyclohexane. They are less soluble in these media because the polar urea bonds hind the interactions between the aliphatic regions of the structure and the solvent when the environment polarity is too low. These statements are supported by their normalized absorption spectra, where neither hexane nor cyclohexane curves appear *(Table 4, Fig.a)*. On the other hand, species with only one urea moiety, are fluorescent in MCH, and that is probably because of the presence of a tert-butoxycarbonyl group which can better interact with nonpolar solvents, making these compounds quite soluble; hence, MCH appears in their normalized absorption spectra *(Table 4, Fig.b)*. As CH14 and CH26 are representative examples of both types of behaviours, their spectra are collected below.

***Table 4**. Normalized absorption spectra of (a) CH14 and (b) CH26*

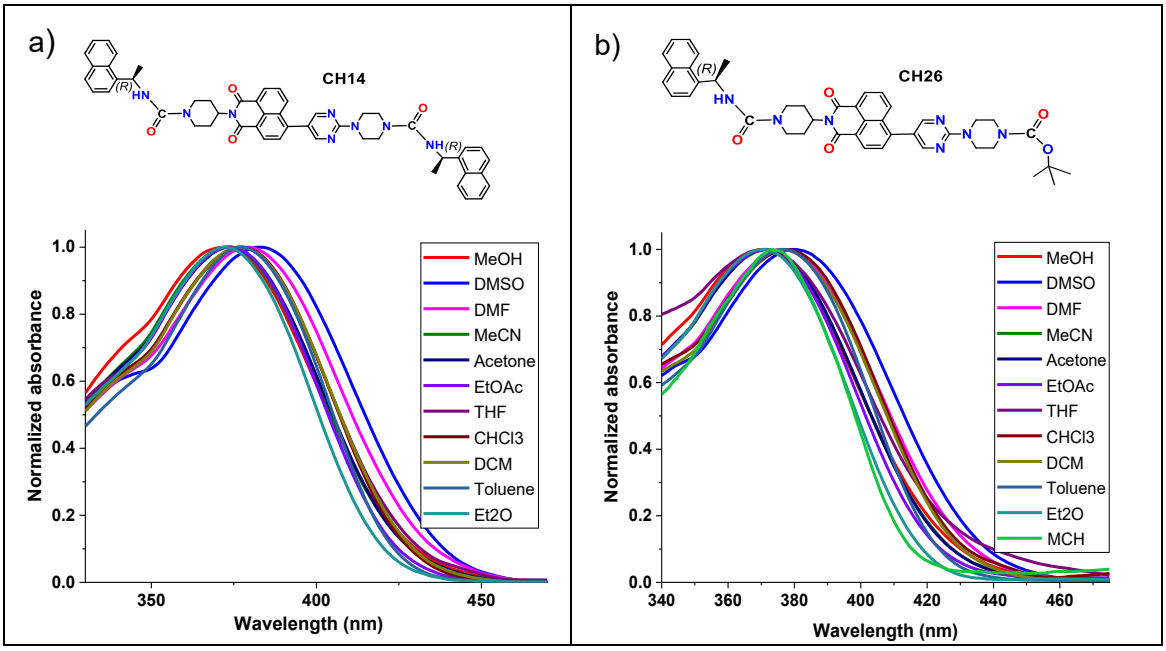

The differences between the emission intensities of the compounds in the different solvents can be corroborated with the emission spectra of the compounds. In *Table 5* the spectra of CH14 and CH26 are shown as representative examples of the general behaviour. As seen in the photographs, the most intense signals are those of the least polar solvents where the compounds are soluble, as diethyl ether or toluene, whereas the signals of MeOH, DMSO or DMF are near the baseline due to the ACQ effect that appears in those polar solvents. It must be mentioned that the signal in water does not appear because no compound is soluble there (it was already observed in the photographs).

***Table 5**. Emission spectra of (a) CH14 and (b) CH26. λ_{exc} = 375/370 nm*

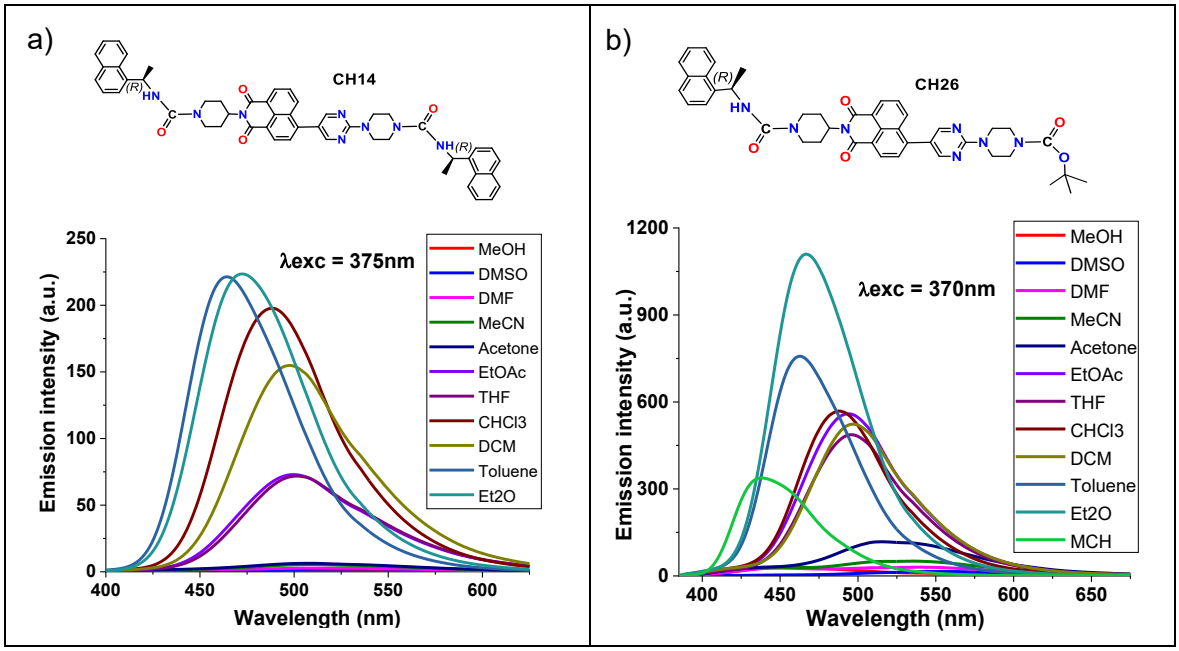

Additionally, from the absorption and emission spectra it can be identified the most suitable solvent for next studies. The ideal solvent must be miscible with water and the NMIs should show moderate fluorescence there. Tetrahydrofuran is selected as the best solvent.

Alternatively, normalized emission spectra can be studied to detect shifts in the position of the emission bands as changing solvent polarity. In the case of phenyl compounds, no clear pattern is observed. However, as in the previous chapter, the derivatives containing pyridine and pyrimidine show a bathochromic shift as solvent polarity increases. This shift is clearly seen in the CH15 and CH19 photographs in *Table 2*, where the vials changed from blue in diethyl ether (nonpolar) to yellow in ethyl acetate (polar). This bathochromic shift occurs because the aggregates formed in high polarity solvents lead to energy stabilization, which results in an emission at lower energy or longer wavelengths. As seen in Chapter 1, this energy stabilization was less pronounced in phenyl compounds. The presence of nitrogen atoms in pyridine and pyrimidine derivatives appears to be essential for this stabilization to occur. This shift towards longer wavelengths is also clearly observed in the normalized absorption spectra of CH14 and CH26 *(Table 6).*

***Table 6**. Normalized emission spectra of (a) CH14, (b) CH26. λ_{exc} = 375/370 nm*

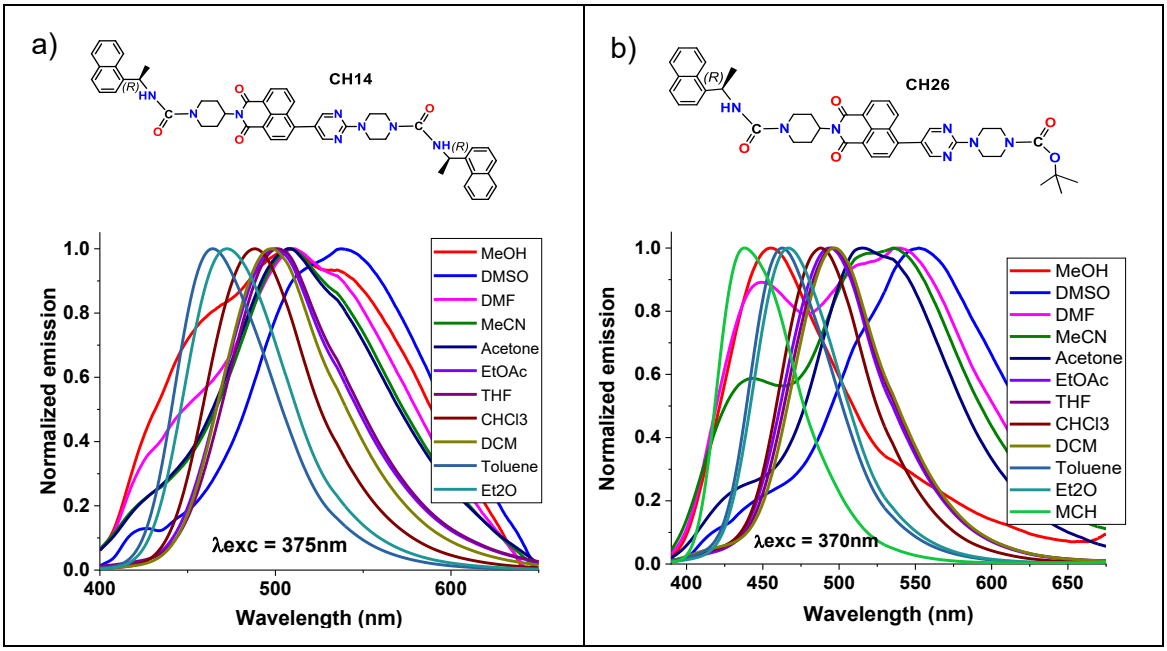

The bathochromic shift as solvent polarity increases can be obtained calculating the difference between the peak wavelengths of the most and the least polar solvents. It must be mentioned that methanol is not considered in this study because it can interact by hydrogen bonds and breaks with general theory. Thus, in the CH14 spectrum, the emission maximum is shifted 74 nm (from 464 nm in toluene to 538 nm in DMSO). Likewise, CH26 exhibits a bathochromic shift of 74 nm, since its emission peak moves from 447 nm in MCH to 521 nm in DMSO. This phenomenon can be explained with the same theory of aggregation and the relaxation of excited states in polar solvents as reported in the solvatochromism section of chapters 1 and 3.

4.2. FLUORESCENCE ANISOTROPY

Fluorescence anisotropy (r) is a measurement of how a molecule changes its orientation in space, with respect to the time between absorption and emission events. There are some fluorophores that once they have been excited with polarized light, its emission is also polarized. The degree of polarization of the emitted light is described in terms of anisotropy.

The origin of anisotropy is the presence of transition moments for absorption and emission in specific directions within the fluorophore structure. In homogeneous solutions the ground-state fluorophores are randomly oriented. If the sample is excited with polarized light, some of the excited molecules will have their transition moments oriented along the electric vector of the exciting light, consequently, a part of the emitted light will retain that polarization based on how fast the molecules are rotating in solution. The faster change of orientation, the more depolarized the emitted light is. The slower the motion, the more retention of polarization.[12]

The emission can become depolarized by different processes, and it depends upon the fluorophore under investigation. The fluorescence anisotropy also depends on the fluorescence lifetime of the molecule. If the fluorescence lifetime is longer than the rotational correlation time of the molecule, the fluorophore can reorient significantly during the excited state, causing the emitted light to be depolarized; but if the lifetime is shorter, the emission

[12] J. R. Lakowicz, *Principles of Fluorescence Spectroscopy*, Springer Science + Business Media, Singapore, third edition, **2006,** chapter 10, pp. 353-360.

will retain the polarization of the excitation light.[13] In this section, the fluorescence anisotropy of compounds with two chiral urea units is studied.

Experimental procedure

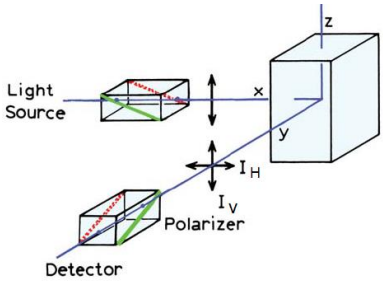

Figure 5. *Diagram of a fluorescence anisotropy experiment.*

As is shown in *Figure 5*,[10] two polarizers are used. One of them is placed in the excitation light path and the other in the emission light path of a fluorometer.

Four arrangements are possible. First, fluorescence is measured with both polarizers set at vertical orientation. Then, the excitation one rotates 90 degrees, and the emission polarizer keeps vertical. In the third experiment, both polarizers are horizontal, and in the last assay the excitation polarizer is horizontal while the emission one is vertical.

Experimental results

The experimental results for all compounds containing two chiral urea moieties are very similar. Therefore, the following table presents the graphs for one representative pair of enantiomers: CH14 (R, R) and CH18 (S, S) (pyrimidine derivatives).

Table 7*. Fluorescence anisotropy plots of (a) CH14 and (b) CH18 (b). (λ_{exc} = 375 nm, C=10^{-5} M). Solvent: toluene*

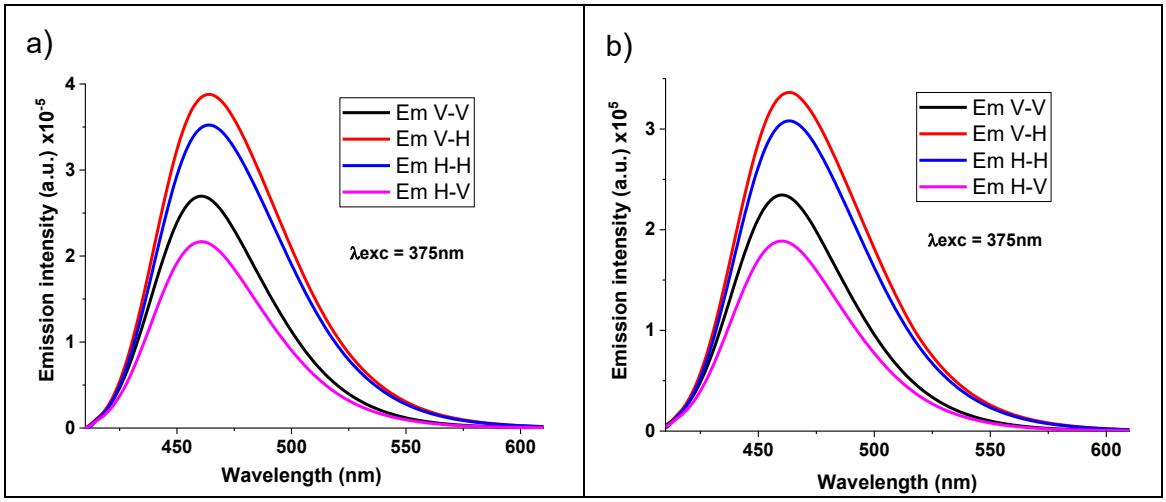

In both graphs it is observed that the highest emission intensity (red) takes place when compounds are excited with vertically polarized light, and the second polarizer is horizontally orientated. Under these conditions, there is a depolarization of the incident light (low anisotropy). In this case, a greater number of molecules are excited when the incident light is vertically polarized (most of them have this particular axis of orientation). However, a depolarization of light takes place, since the maximum emission is detected when the second polarizer is horizontally oriented. That is explained because the fluorescent lifetime is longer than the time it takes for the molecule to change its orientation. This results in an emission of light at different angle than the incident light. However, the next highest emission (blue) occurs when both polarizers are horizontally oriented. In this case, the system is able to maintain the polarization of the light. Molecules with horizontally oriented

[13] I. E. Steinmark, P. H. Chung, R. M. Ziolek, B. Cornell, P. Smith, J. A. Levitt, C. Tregidgo, C. Molteni, G. Yahioglu, C. D. Lorenz, K. Suhling, *Small.* **2020**; *16,* 1907139.

transition moments retain this orientation, resulting in high anisotropy along the horizontal axis. Consequently, it can be stated that these compounds show fluorescence anisotropy on the horizontal axis, and it is independent of the chirality of the molecules.

4.3. WATER-ORGANIC SOLVENT RATIO ASSAYS

Throughout this thesis it has been shown that mixtures of THF with increasing amounts of water are an ideal medium for the detection of the aggregation-induced emission phenomenon. Therefore, the THF-water tests were carried out with the chiral urea derivatives herein studied. The mixtures were prepared using the same methodology as followed in previous chapters, with a final concentration of 10^{-5} M and then photographed under UV light of 366 nm *(Table 8)*.

***Table 8**. Water-solvent ratio assays of different chiral urea-NMI hybrids, using UV light (366 nm)*

Structure	THF-H_2O mixtures
CH13: PHENYL NMI + 2 UREA (R)	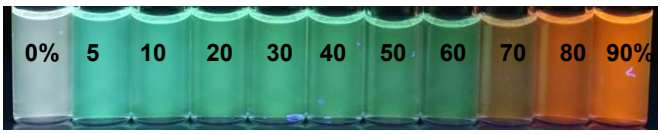
CH17: PHENYL NMI + 2 UREA (S)	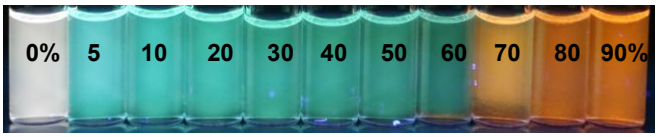
CH14: PYRIMIDINE NMI + 2 UREA (R)	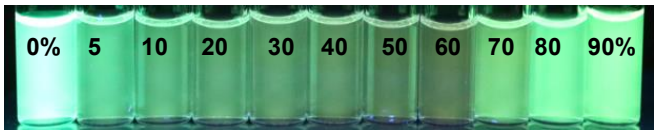
CH18: PYRIMIDINE NMI + 2 UREA (S)	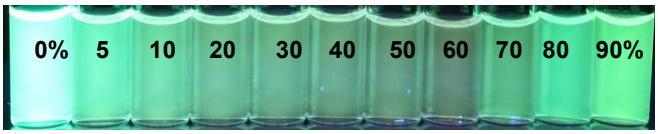
CH15: PYRIDINE NMI + 2 UREA (R)	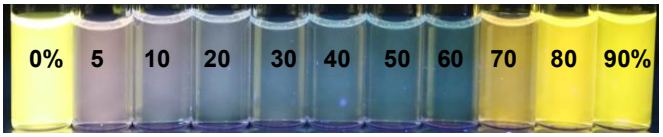
CH19: PYRIDINE NMI + 2 UREA (S)	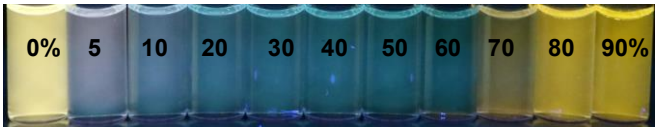
CH24: PYRIDINE NMI + 1 UREA (S)	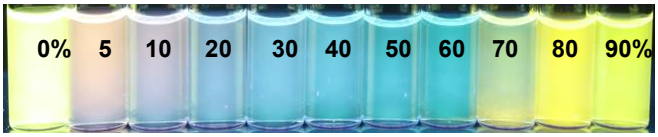
CH26: PYRIMIDINE NMI + 1 UREA (R)	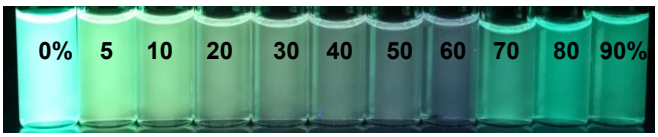
CH77: PHENYL NMI + 1 UREA (R)	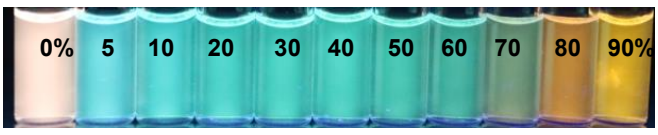

In the photographs, it can be observed that most of compounds exhibit a colour shift toward longer wavelengths starting at 70% water. This is consistent with the aggregate formation and energy stabilization explained in previous chapters. It is also observed how the emission intensity varies as the water content changes. In pure THF, the emission intensity is very high since the species are in solution and no aggregate is formed; however, when small amounts of water are added (between 5 and 60% water) fluorescence emission is very weak due to the aggregation quenching effect. However, at higher water content (above 70%), the species experience a sudden increase in fluorescence emission due to increased agglomeration and the formation of nanostructures. This experiment therefore confirms that, at high water content, these fluorophores form nanoaggregates large enough to exhibit the AIE effect, whereby non-radiative relaxation processes are restricted due to the structural rigidity of the aggregates, as explained in previous chapters.

These changes can be better observed in the emission spectra of the different mixtures. CH15 and CH24 are representative examples of each group of compounds. In *Table 9* it is observed how the emission intensity (grey curve) of both compounds suddenly decreases at intermediate water percentages, and above 60% w.r. it increases again. The shift of the emitted light to longer wavelengths when the aggregates are formed is also verified. The blue curve suddenly increases above 60% w.r.

Table 9. *Emission intensity (grey) and λ_{max} emission (blue) of (a) CH15 (b) CH24 in THF at different w.r.*
λ_{exc} = 380 nm

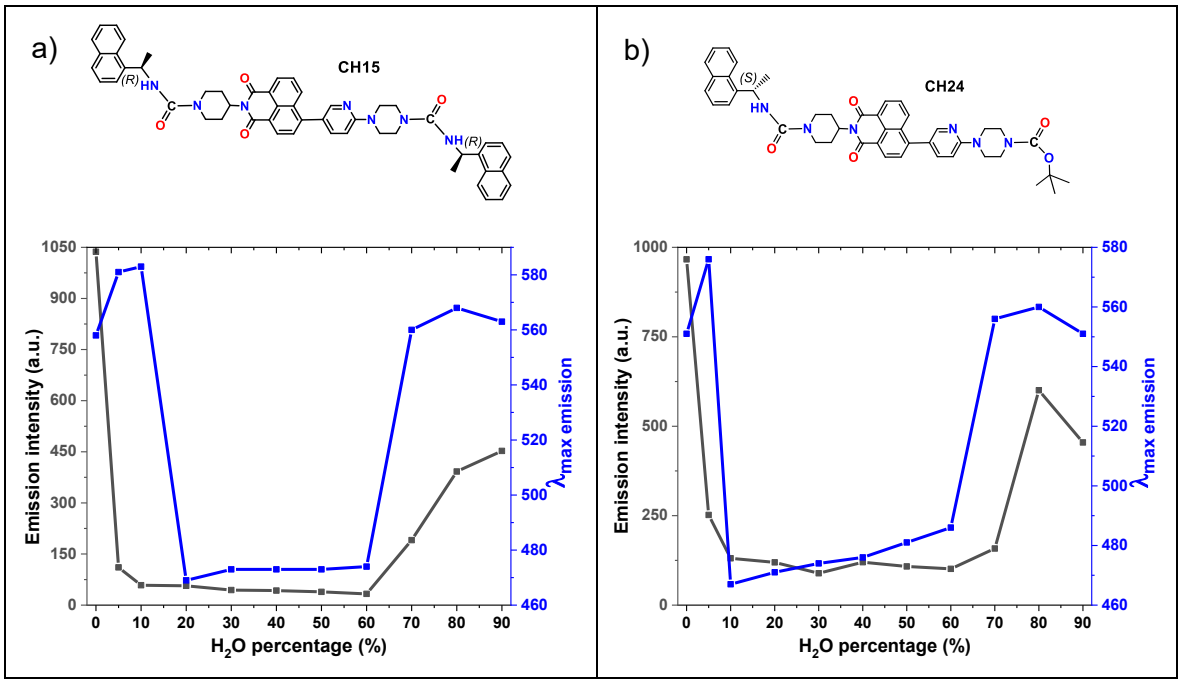

5. NANOSTRUCTURES MORPHOLOGY

Since the aggregation-induced emission effect occurs in mixtures above 70% water ratio, these mixtures have been examined by microscopy techniques to determine the structures responsible of the AIE effect. Hence, this section includes several pictures obtained by atomic force microscopy (AFM), field emission scanning electron microscopy (FESEM) and transmission electron microscopy (TEM).

5.1. IMAGES OF SPECIES WITH TWO CHIRAL UREA MOIETIES

First, AFM images were obtained, revealing the formation of fibers that only measure 3-7 nm high. *Figure 6* shows some of the most representative images of the compounds with two chiral urea units.

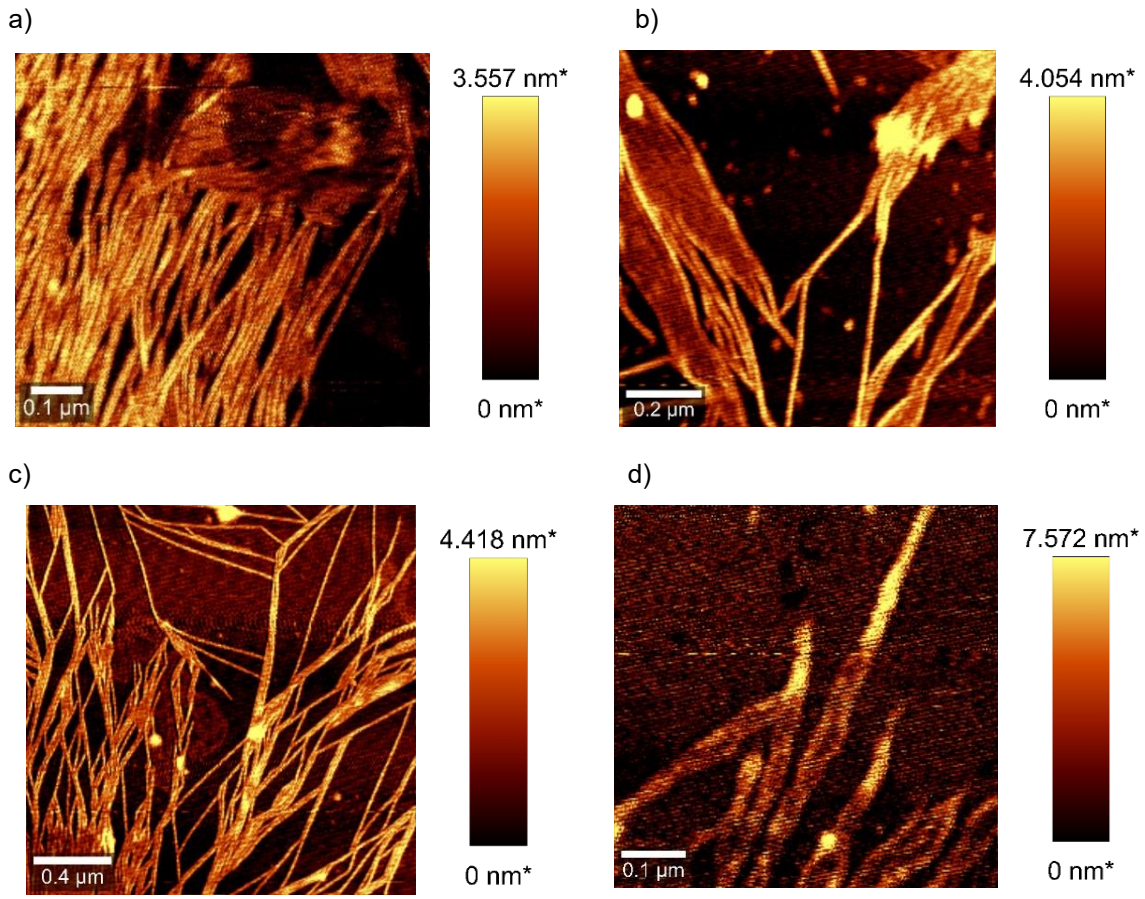

Figure 6. *AFM images of (a) CH13 at 90% w.r. (b) CH15 (at 80% w.r. (c) CH17 at 70% w.r. (d) CH18 at 70% w.r.*

Once nanofibers were observed, FESEM was employed to determine their surface's morphology. The images showed that most of those fibers were chiral and measured several microns long (see the length in *Figure 7b*). The formation of helical nanofibers at high water ratios is common to all compounds and a great deal of images of them are collected in the Supporting Information of this chapter. In *Figure 7,* some representative examples are shown.

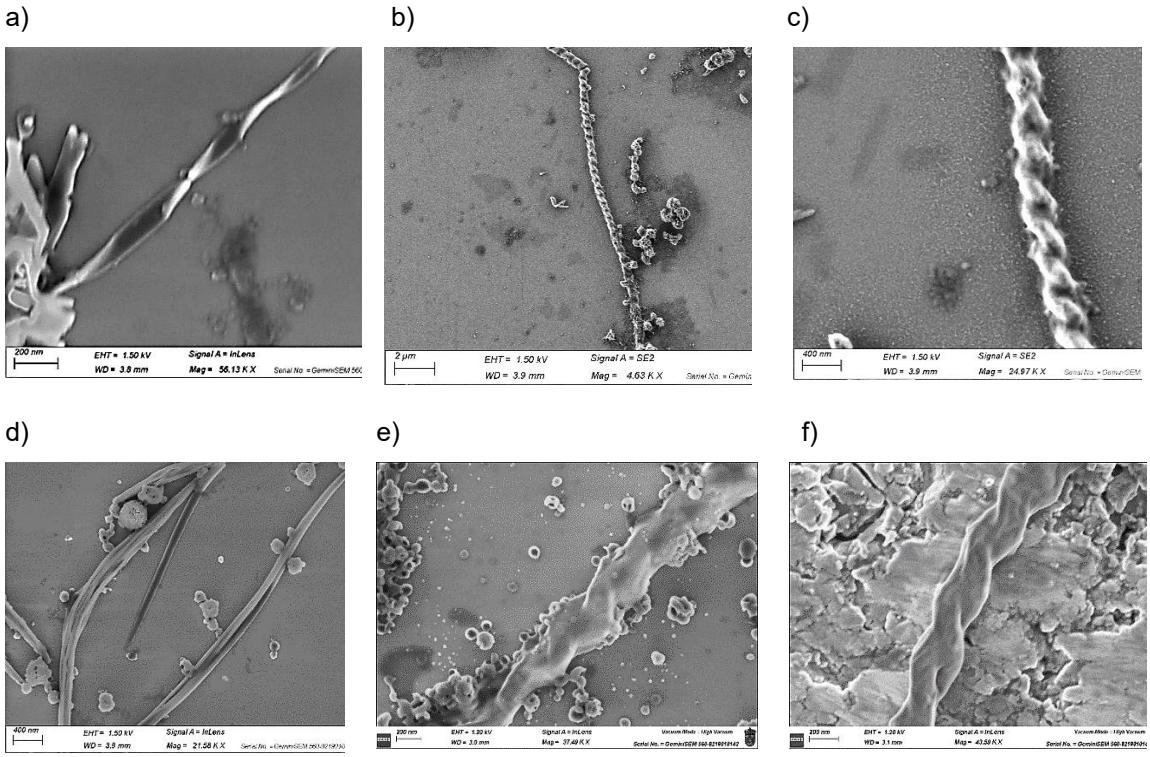

Figure 7. *FESEM images of (a) CH15 at 80% w.r. (b, c) CH17 at 70% w.r. (d) CH17 at 80% w.r. (e, f) CH19 at 90% w.r.*

Notice that there are two types of fibers: thicker ones with a clear helicity, and thinner ones. The latter tend to form helices, but their helical shape is not observed in all images. It was surprising to discover that all helices have the same handedness: both R and S compounds form left-handed fibers. To corroborate the formation of these fibers, they were examined under a transmission electron microscope, which required prior staining with a 2.5% wt. uranyl acetate solution. In *Figure 8* are collected some representative examples.

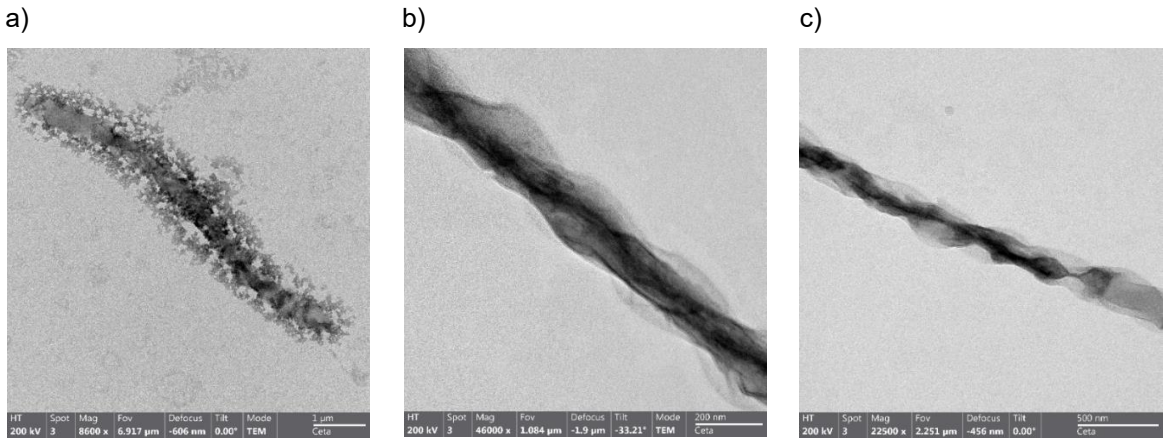

Figure 8. *TEM images of (a) CH15 at 80% w.r. (b, c) CH17 at 90% w.r.*

These results let us state that the AIE effect is associated with the formation of chiral nanofibers in mixtures with high-water content.

5.2. IMAGES OF SPECIES WITH ONE CHIRAL UREA MOIETY

Species with only one chiral urea moiety were visualized by FESEM. The number of chiral nanofibers is lower than in the case of compounds with two urea groups, but left-handed fibers are also formed. In *Figure 9*, the most beautiful and well-formed helices are shown; it must be mentioned that lot of images in mixtures with different water percentages are collected in the Supporting Information of this chapter.

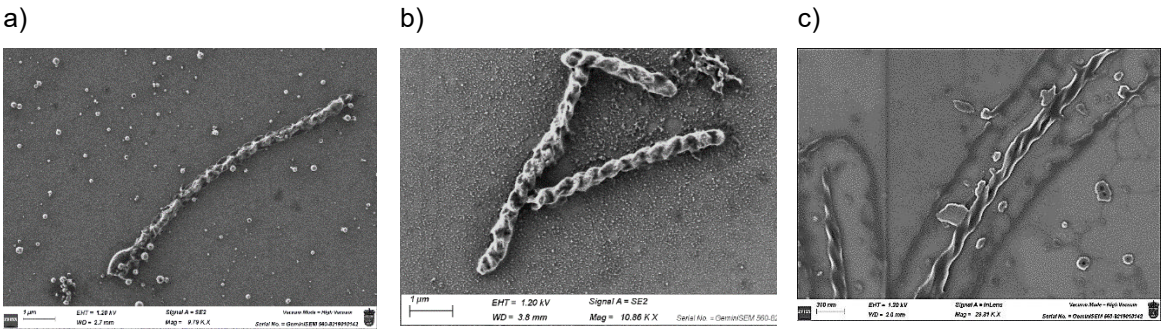

Figure 9. *FESEM images of (a) CH24 (pyridine, S) at 90% w.r. (b) CH26 (pyrimidine, R) at 70% w.r. (c) CH77 (phenyl, R) at 80% w.r.*

It is worth noting that some semi-functionalized species were deprotected. The tert-butoxycarbonyl group was removed from CH24 and CH26 resulting in CH24-D and CH26-D. It was necessary to use hydrochloric acid dissolved in methanol, since this method prevents from breaking the urea bond and only attacks the Boc-protecting group of piperazine. Trifluoroacetic acid could not be used, as it breaks the urea bond. The deprotection reactions are shown in *Figure 10.*

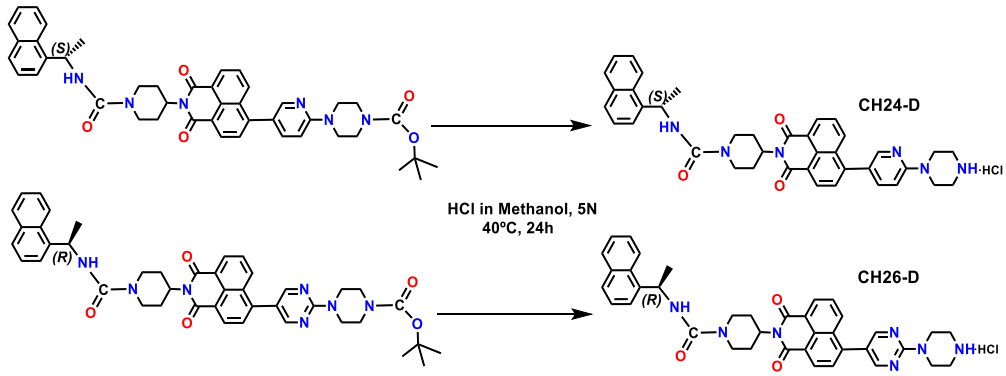

Figure 10. *Deprotection scheme for the synthesis of CH24-D and CH26-D.*

These species, as its precursors, were completely characterized, and their spectroscopic analysis is fully described in the Supporting Information of this chapter. It must be added that once the species were deprotected, the AIE effect at high water ratios disappeared. In this case, the interactions between the free amine of the piperazine and water are dominant. Then, these species were visualized by scanning electron microscopy, and the images revealed that if the Boc group is removed, the helices are no longer formed. These observations reveal that both piperazine and piperidine must be functionalized for supramolecular arrangement and self-assembly into chiral fibers to occur. In mixtures with high-water percentage, the free amino group likely interacts strongly with the environment, preventing association into fibers. Instead of helical fibers, in the case of CH24-D, nanotubes are formed above 80% w.r. *(Figure 11)*. Interestingly, during the imaging process, an unexpected phenomenon was observed: as the electron beam interacted with the sample, the elongated structures began to break apart and develop holes. This damage

surprisingly revealed that the structures were not solid as initially assumed, but rather hollow on the inside, confirming that they were, in fact, nanotubes.

a) b) c)

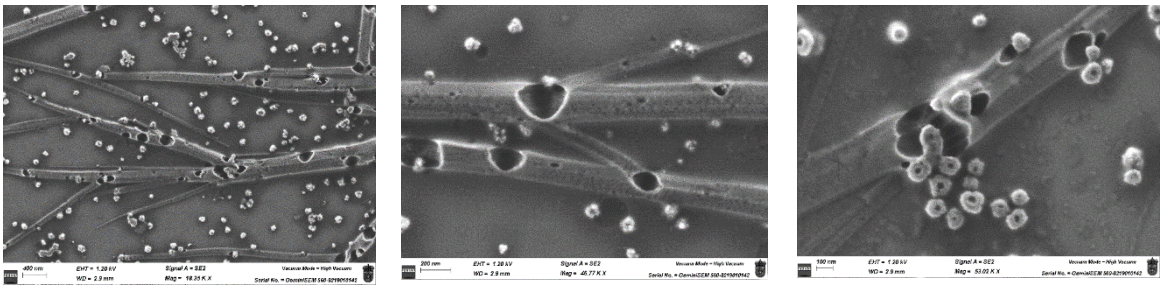

***Figure 11**. FESEM images of CH24-D at (a, b) 80% w.r. (c) at 90% w.r.*

On the other hand, unlike the previous one, CH26-D forms irregular structures with a cottony texture *(Figure 12)*. In both cases, the helicity exhibited by the protected species has been lost.

a) b) c)

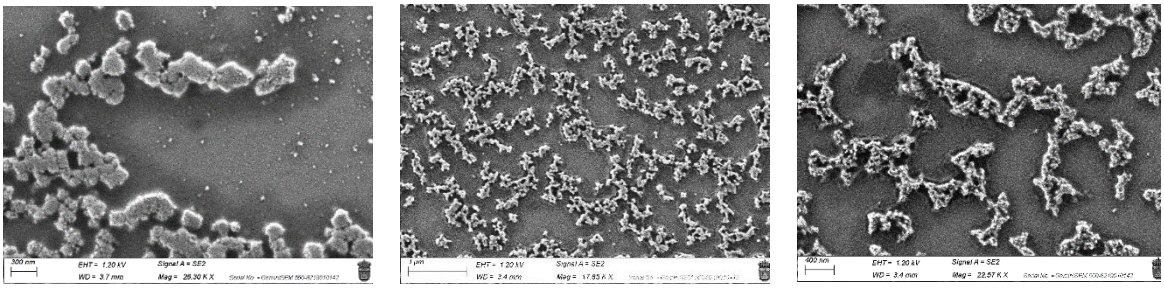

***Figure 12**. FESEM images of CH26-D at (a) 50% w.r. (b, c) at 70% w.r.*

6. MOLECULAR DYNAMICS SIMULATION

Once we had discovered these compounds form helical fibers, we wanted to verify if these structures could be predicted by computational calculations using MacroModel tool. It was hypothesized that the aromatic moieties of distinct CH19 molecules would perform stacking interactions with each other. Thus, to achieve atomic-level insights into the structure of fibers, the computational chemists developed a model using molecular dynamics simulations lasting 500 nanoseconds. This technique enables the prediction of how organic building blocks will self-assemble into specific supramolecular nanostructures.[14]

If we go back to Chapter 1 of this thesis, molecular dynamics simulation studies were also conducted with depsipeptide naphthalimide derivatives, and it was seen how the NMIs stacked head-to-tail, and due to the depsipeptide chains that offered flexibility to the system, they curved into a vesicle shape. However, in this case, the assembly does not occur in this way. Chiral urea moieties are formed by a bulky naphthalene group that prevents the aromatic nucleus of the NMIs from stacking head-to-tail. This steric hindrance causes each NMI to be displaced by a certain angle with respect to the previous one, and this small rotation repeated over thousands of molecules gives rise to the formation of a helix. Regardless of whether the attached chiral group is R or S, the rotation of one NMI with respect to the other always results in the formation of a left-handed helix.

[14] K. E. Jelfs, *Ann. N. Y. Acad. Sci.* ***2022,*** *1518* (1), 106–119.

We considered the possibility of exploring what would happen if CH19 were able to form right-handed helices. To investigate this, molecular dynamics simulations were performed. Initial energy-minimized structures (without time evolution) indicated that the formation of such helices was, in principle, possible *(Figure 13a).* However, when the system was allowed to evolve over 500 nanoseconds, the intermolecular order rapidly deteriorated, the stacking distances were disrupted and the system collapsed *(Figure 13b).* This confirms that right-handed helices are not stable over time.

a) b)

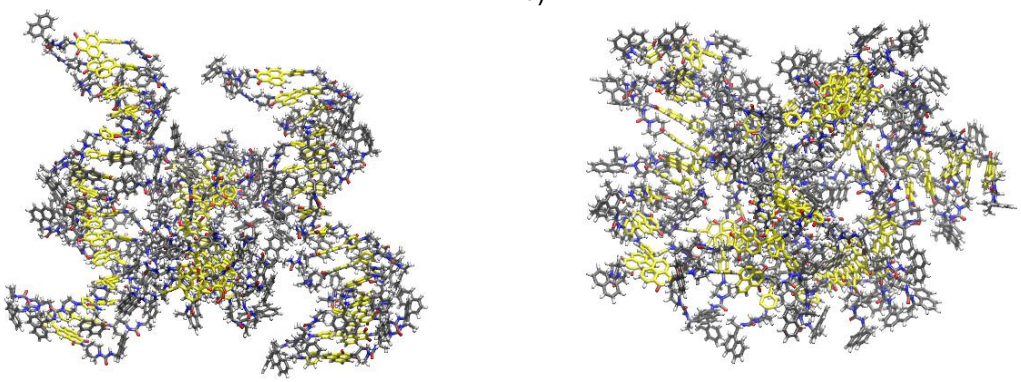

Figure 13*. (a) First frame of theoretical right-handed helices for CH19. (b) Last frame: at 500 ns of evolution: the system collapses and the helices disappear.*

In contrast, simulations performed for left-handed helices demonstrated temporal stability under the same conditions. This explains why only left-handed helices are observed in electron microscopy images. The next figure illustrates this simulation for CH19 molecules. In *Figure 14a* two helices composed of 16 interacting molecules (core distances of 4.15 Å) are shown, exhibiting the slight rotational offset mentioned previously. The aromatic cores are represented in yellow and the chiral urea moieties are drawn in grey. In *Figure 14b* it is shown how after 500 ns of molecular dynamics simulation, the internal organization of the system remains intact. It is observed how the rotational alignment between aromatic cores is preserved throughout the evolution.

a) b)

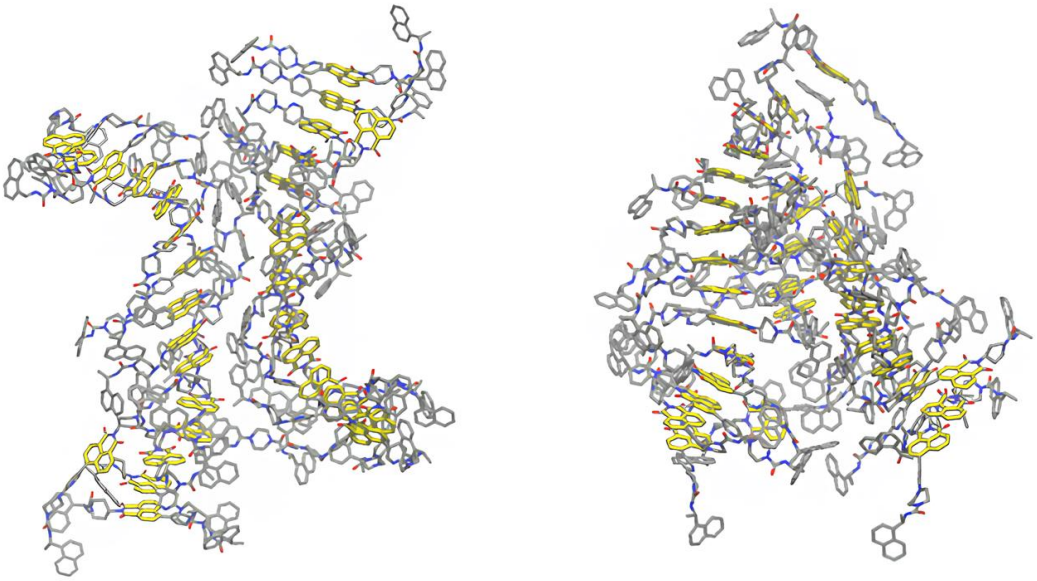

Figure 14. *(a) First frame of left-handed helices of CH19. (b) Last frame: preserved left-handed helices after 500 ns of evolution.*

7. SPECTROSCOPY OF CHIRAL UREA DERIVATIVES

7.1. CIRCULAR DICHROISM

Dichroism is a characteristic property of certain anisotropic materials that absorb light differently depending on the polarization or direction of the incident beam. In the specific case of circular dichroism (CD), this differential absorption occurs between right- and left-circularly polarized light, providing crucial structural information about chiral molecules.

Linearly polarized light can be mathematically decomposed into two circularly polarized components which rotate in opposite directions. When such light passes through an optically active medium, each circular component may interact differently with the chiral centres of the molecules within the medium. If these components are absorbed to different extents, the transmitted light becomes elliptically polarized. This phenomenon is known as circular dichroism, and its magnitude is typically expressed in terms of molar ellipticity (θ).[15]

Derivatives with two chiral urea moieties

In the present work, the urea derivatives under study were analysed by pairs of enantiomers in mixtures of high-water content where chiral fibers were imaged. It was observed that the R enantiomers exhibit circular dichroism signals in one direction, whereas their S counterparts display CD signals in the opposite direction, so there is a mirror-image inversion of the CD response. In *Table 10,* the CD results of the enantiomers with two chiral urea units are collected. Notice that CH13, CH14 and CH15 (R) show positive signals, whereas their S enantiomers CH17, CH18 and CH19 show negative CD.

Table 10. *Molar ellipticity vs wavelength of compounds in different THF-water mixtures (80% w.r., red; 90% w.r., black). (a) CH13 (plain) and CH17 (dotted) (b) CH14 (plain) and CH18 (dotted). (c) CH15 (plain) and CH19 (dotted).*

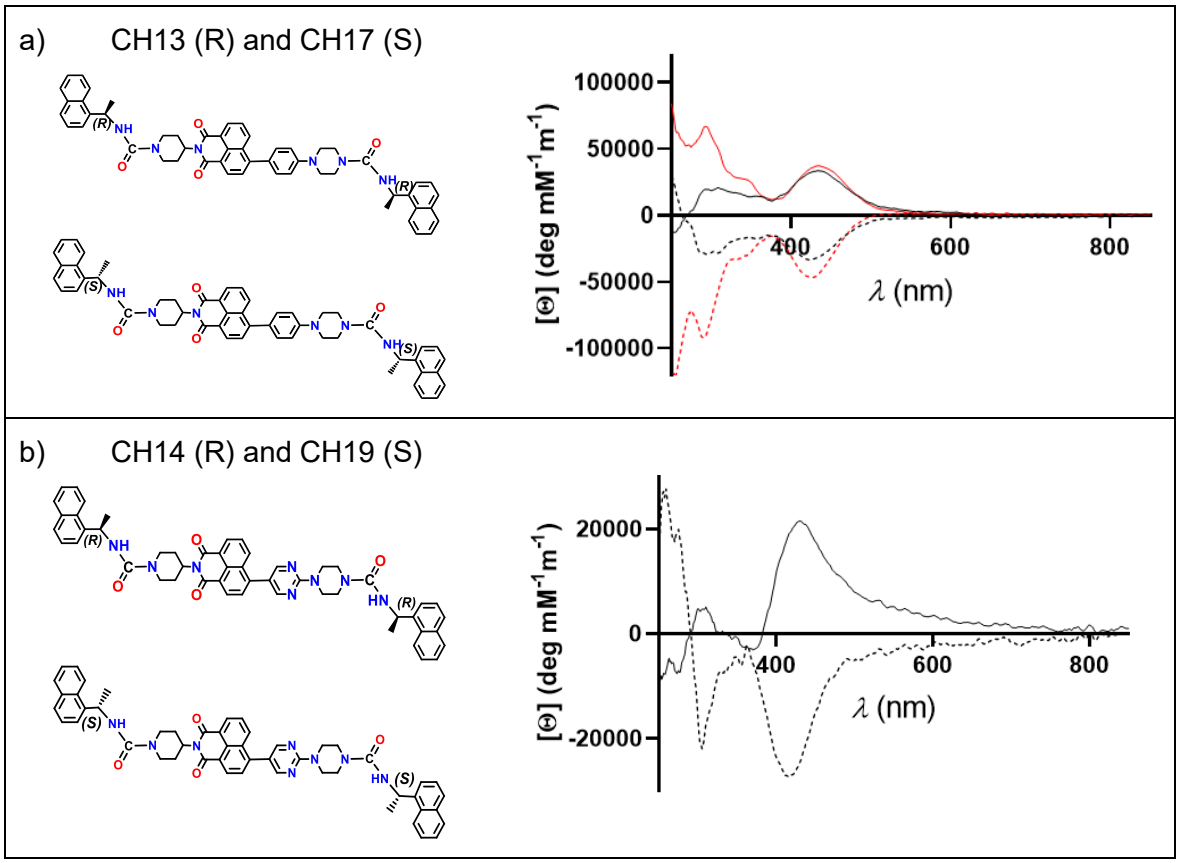

[15] A. J. Miles, R. W. Janes, B. A. Wallace, *Chem. Soc. Rev.* **2021,** *50*, 8400−8413.

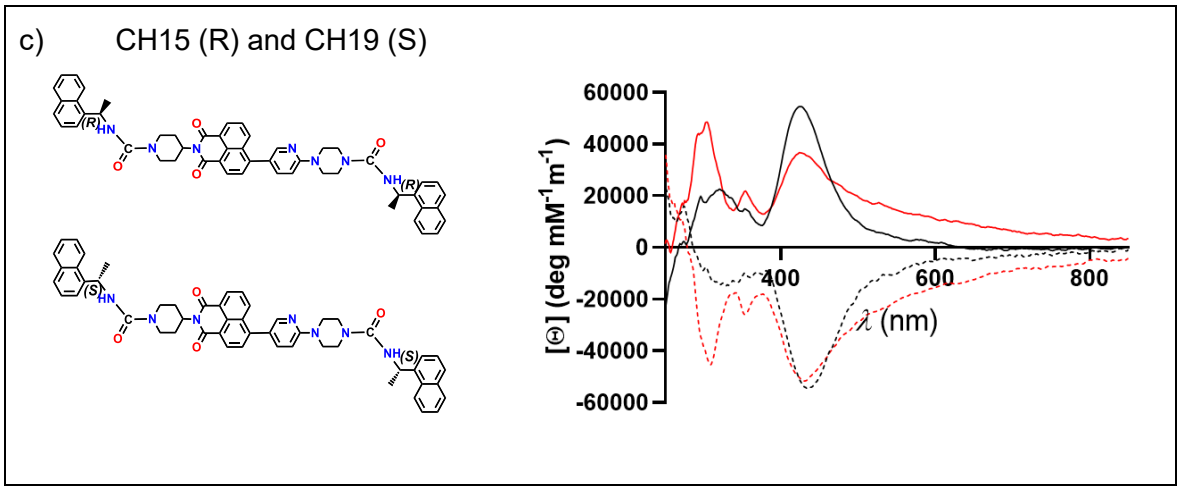

This study demonstrates that molecules are able to deflect polarized light in the opposite direction, depending on the stereochemistry of the chiral centres. CD spectra, like molecules, are non-superimposable mirror images. It must be mentioned that the molar ellipticity signals reach their maximum values for the phenyl and pyridine derivatives *(Table 10 a, c)* reaching 6000 deg mM^{-1} m^{-1}, while the pyrimidine derivatives *(Table 10 b)* reach values of 2000 deg mM^{-1} m^{-1}. In both cases, these are intense CD signals.

Derivatives with one chiral urea moiety

Compounds CH24 and CH26 with a single chiral urea moiety were also analysed by circular dichroism *(Table 11)*. The signals obtained turned out to be much less intense than those of compounds with two urea groups (10-100 times less intense). This makes sense, since there are fewer active optical centres in each molecule, resulting in less activity in circular dichroism. It is worth comparing both species; CH26 (R) shows positive cotton effect or positive dichroism. At 90% w.r. it is positive from 250 to 400 nm, and at 80% w.r. from 375 to 420 nm approximately. The signals are 10 times more intense than those of CH24, reaching values of 600 deg mM^{-1} m^{-1}. On the other hand, CH24 (S) shows negative cotton effect or negative dichroism. It is more notorious at 80% water ratio, but only reaches -20 deg mM^{-1} m^{-1}.

Table 11. *Molar ellipticity vs wavelength of compounds in different THF-water mixtures (70% w.r., black; 80% w.r., red and 90% w.r., blue). (a) CH24 (b) CH26*

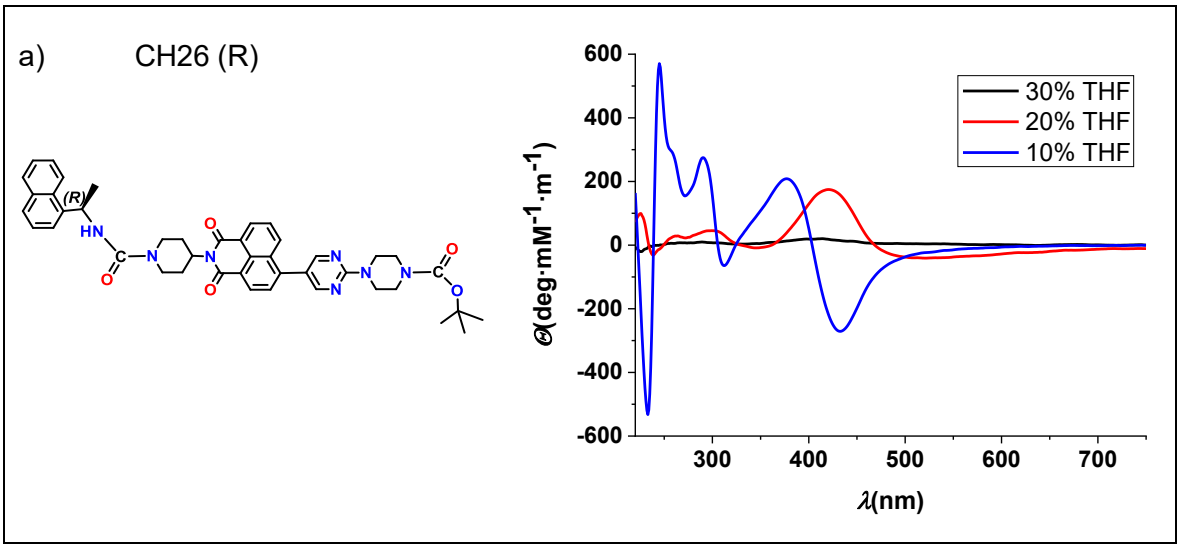

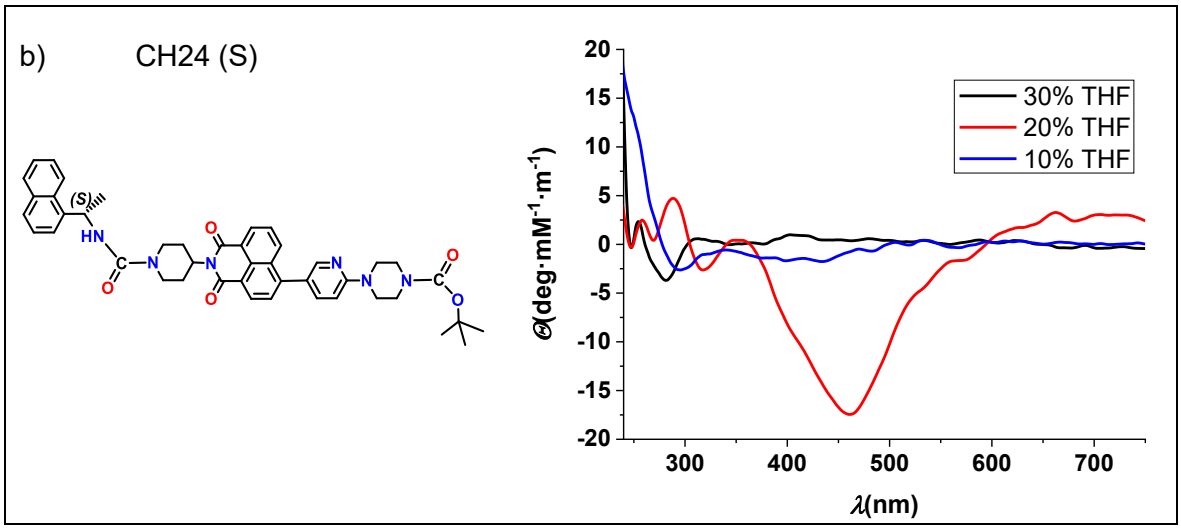

7.2. CIRCULARLY POLARIZED LUMINISCENCE (CPL)

Circularly Polarized Luminescence (CPL) is a powerful chiroptical spectroscopic technique that measures the differential emission of left- and right-circularly polarized light from chiral luminescent species. While circular dichroism measures the differential absorption of circularly polarized light, CPL provides complementary information by examining the chirality of the emitted light in the excited state.

This technique is particularly valuable for understanding the excited-state properties and supramolecular assemblies.

The degree of polarization is quantified by the luminescence dissymmetry factor ($g_{luminiscence}$). It is a value that indicates the difference in intensity between the left- and right-circularly polarized light emitted by a chiral molecule when excited by unpolarized light. It is defined as: [16]

$$g_{lum} = \frac{2(I_L - I_R)}{I_L + I_R} \quad \text{Eq. 1}$$

where I_L and I_R are the intensities of left- and right-circularly polarized emitted light, respectively.

It is known that CPL is sensitive to electronic transitions of chiral chromophores, and the signals depend on the spatial arrangement of molecules.[17] As occurred in Chapter 1, the CPL signals are only detected when the nanostructures are formed, since if measurements are taken with freshly prepared samples, no signal of CPL is detected. It is known that the samples need to rest for 24 hours to enable the formation of chiral nanofibers. So, CPL measurements of the enantiomer pairs with two chiral urea moieties were made in mixtures of THF and 90% water ratio. The results corresponding to the pair CH15 (R) and CH19 (S) are collected in *Figure 15.* Firstly, the sum of the intensity of circularly polarized light towards the right and towards the left (L+R) is represented, and secondly the difference between them, which is what would be the CPL signal. It was observed that this difference is always negative, for both R and S compounds. It means that all species emit mostly to the right, and that may seem to be contradictory to the common left-handed helicity of the fibers. However, it has an explanation that will be discussed later in this section.

[16] J. P. Riehl, F. S. Richardson, *Chem. Rev.* **1986,** *86* (1), 1−16.
[17] T. Zhao T, J. Han, P. Duan, M. Liu M. *Acc. Chem. Res.* **2020,** *53* (7), 1279−1292.

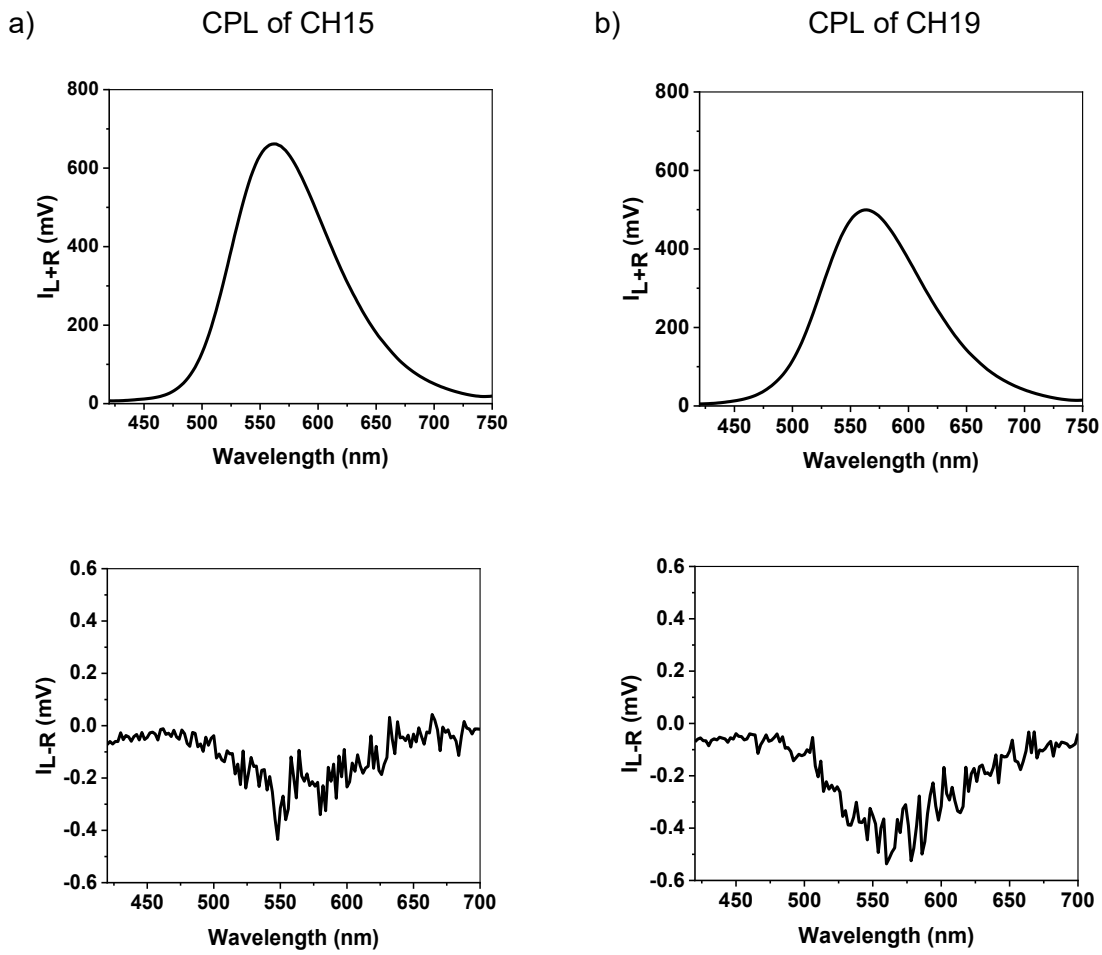

Figure 15. *(a) CH15 and (b) CH19 CPL signals. Up: (I_{L+R}), down: (I_{L-R})*

The g_{lum} index is also represented in *Figure 16.* It is negative and higher for CH19 (S).

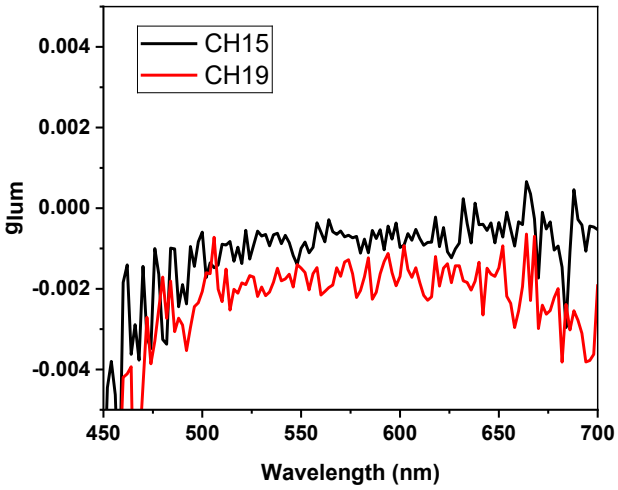

Figure 16. *g_{lum} of CH15 (black) and CH19 (red).*

Although the individual chiral units in the studied system adopt left-handed helical conformations, CPL measurements reveal a negative dissymmetry factor (g_{lum}), corresponding to emission of right-handed circularly polarized light. At first glance, this might appear contradictory, as one might expect the handedness of the CPL signal to reflect the intrinsic molecular helicity. However, this apparent discrepancy can be rationalized in the

context of exciton coupling and supramolecular organization.[18] In chiral systems where chromophores are closely packed in supramolecular aggregates, such as helices, fibers, or stacked assemblies, the interaction between transition dipole moments of neighbouring chromophores leads to exciton coupling.[19] In other words, their excited states can couple, leading to the formation of delocalized excitonic states, in which the excitation is not confined to a single molecule but is instead distributed over several interacting chromophores. This coupling can profoundly affect the chiroptical properties, including CPL.[20,] That is because the dissymmetry factor can also be expressed in terms of magnetic and electric dipole moments:[21]

$$g_{lum} = 4\cos\theta \frac{|m|\,|\mu|}{|m^2|\,|\mu^2|} \quad \text{Eq. 2}$$

Where m and μ are the magnetic and electric transition dipole moments respectively and θ is the angle between them. In our case, the CPL signal is governed not by the helicity of the individual helices, but by the nature of the excitonic states that arise from molecular association. It must be added that in these situations, the sign of the CPL signal does not depend on whether the monomer units are R or S, but rather on how the transition dipoles are arranged and interact within the aggregate.[22]

The collective excited-state properties of the supramolecular assembly can give rise to chiral exciton states that possess different rotational strengths and electric transition dipole/magnetic dipole interactions than the individual molecules.[23] In the case here studied, it has been observed that positive g_{lum} does not reflect the left-handedness of the supramolecular helices. It actually results from the formation of new excitonically coupled states that emerge upon aggregation. It is worth to remind that we found that CPL signals were only detectable after 24 h, corresponding to the time required for the formation of the aggregates (helices). This delay confirms that the CPL-active species are not present in the monomeric state, and supports the conclusion that exciton coupling within the aggregated state is essential for CPL generation. Notably, the formation of left-handed fibers alone is not sufficient to define the CPL sign: it is the supramolecular excitonic interactions (not supramolecular chirality itself) that determine the handedness and intensity of the emitted CPL. All these statements support the observation of a negative g_{lum} value, despite the presence of left-handed helices in the system.

[18] S. Ma, B. Zhao, J. Deng, *ACS Cent. Sci.* **2023,** *9* (7), 1409−1418.
[19] S. Ghorai, S. Show, A. Das, *Angew. Chem. Int. Ed.* **2025,** 64, e202500879.
[20] S. Yang, S. ZZhang,F. Hu, J. Han, *Coord. Chem. Rev.* **2023**, *485*, 215116.
[21] T. He, W. Zhao, M. Lin, B. Sun, Y. Chen, H. L. Zhang, G. Long, *J. Phys. Chem. Lett.* **2024**, *15* (39), 9844−9851.
[22] R. Tempelaar, A. Stradomska, J. Knoester, F. C. Spano*, J. Phys. Chem. B* **2011,** *115* (36), 10592−10603.
[23] J. Kumar, T. Nakashima, T. Kawai, *J. Phys. Chem. Lett*. **2015,** *6* (17), 3445−3452.

8. NANOHELIX AS TEMPLATES FOR SILVER NANOPARTICLES

The ability to control the spatial arrangement of nanoparticles on supramolecular templates opens exciting possibilities in the development of chiral nanomaterials with tailored optical, or catalytic properties. In this context, helical fibers represent an ideal scaffold for directing the organization of inorganic nanoparticles in a chiral manner.

In this part of the work, we describe a novel approach to functional nanostructure fabrication through the selective deposition of silver nanoparticles onto pre-formed helical fibers derived from chiral building blocks. To get it, the chiral compounds (10^{-5} M) were combined with 8 equivalents of $AgClO_4 \cdot 2\ H_2O$ in mixtures of THF and high-water percentage. The mixtures were then left to stand for 24 hours (the time required to form the fibers). After that time, the structures formed were imaged with FESEM. We observed that silver nanoparticles spontaneously nucleated and assembled specifically along the surface of the chiral helices. We also confirmed that the silver was deposited selectively by performing elemental analysis with Energy-Dispersive X-ray Spectroscopy coupled to the microscope. CH14 at 70% w.r., CH15 at 70% w.r. and CH19 at 90% w.r. were seen to form stunning fibers, so they were used as representative examples for this study.

8.1. DEPOSITION OF SILVER ON CH14 FIBERS AT 70% W.R.

Fluorescence changes

The mixture was prepared to see if there are changes in the NMI's emission and, therefore, interaction with the metal. First, freshly prepared compound mixed with silver(I) in THF was imaged under white and UV light of 366 nm. And after 24 hours the mixtures were imaged again.

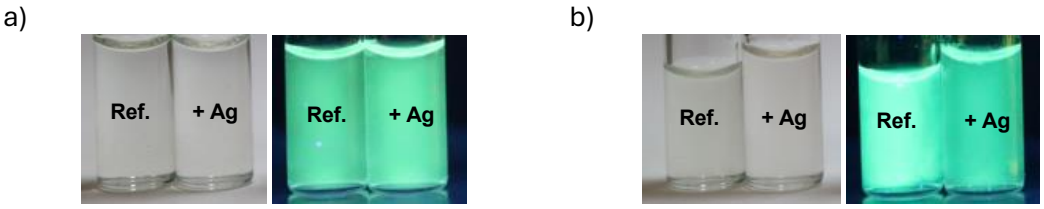

***Figure 17**. CH14 at 70% w.r. in THF with silver(I), (a) Freshly prepared mixtures (b) After 24 hours of preparation.*

After 24 hours a slight change is observed in the AIE effect of the mixture, indicating a probable interaction with silver.

Study of nanostructures

Then, after being left to stand for 24 hours, the sample of CH14 (10^{-5} M) at 70% w.r. in THF mixed with silver(I) was imaged. Stunning nanoparticles of silver covered the surface of the nanohelices *(Figure 18)*.

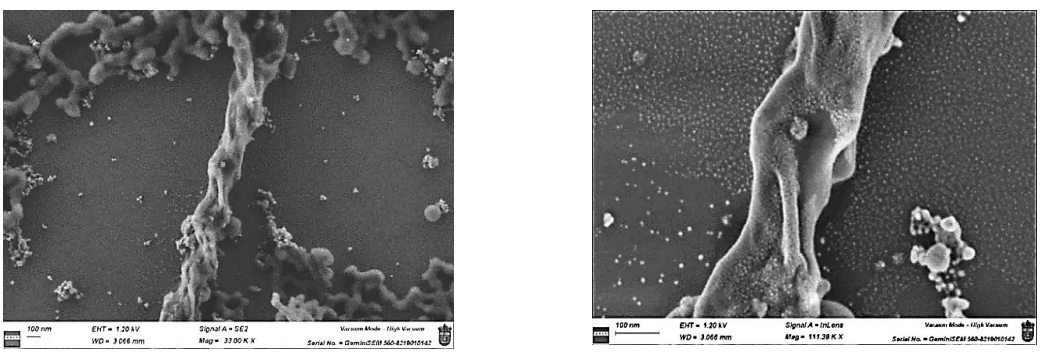

***Figure 18.** Silver nanoparticles covering the fibers' surface (CH14 70% w.r.)*

Then, the elemental analysis using Energy Dispersive X-ray Spectroscopy (EDX) mapping confirmed that there is a silver coat on the carbon surface of the fibers *(Figure 19).*

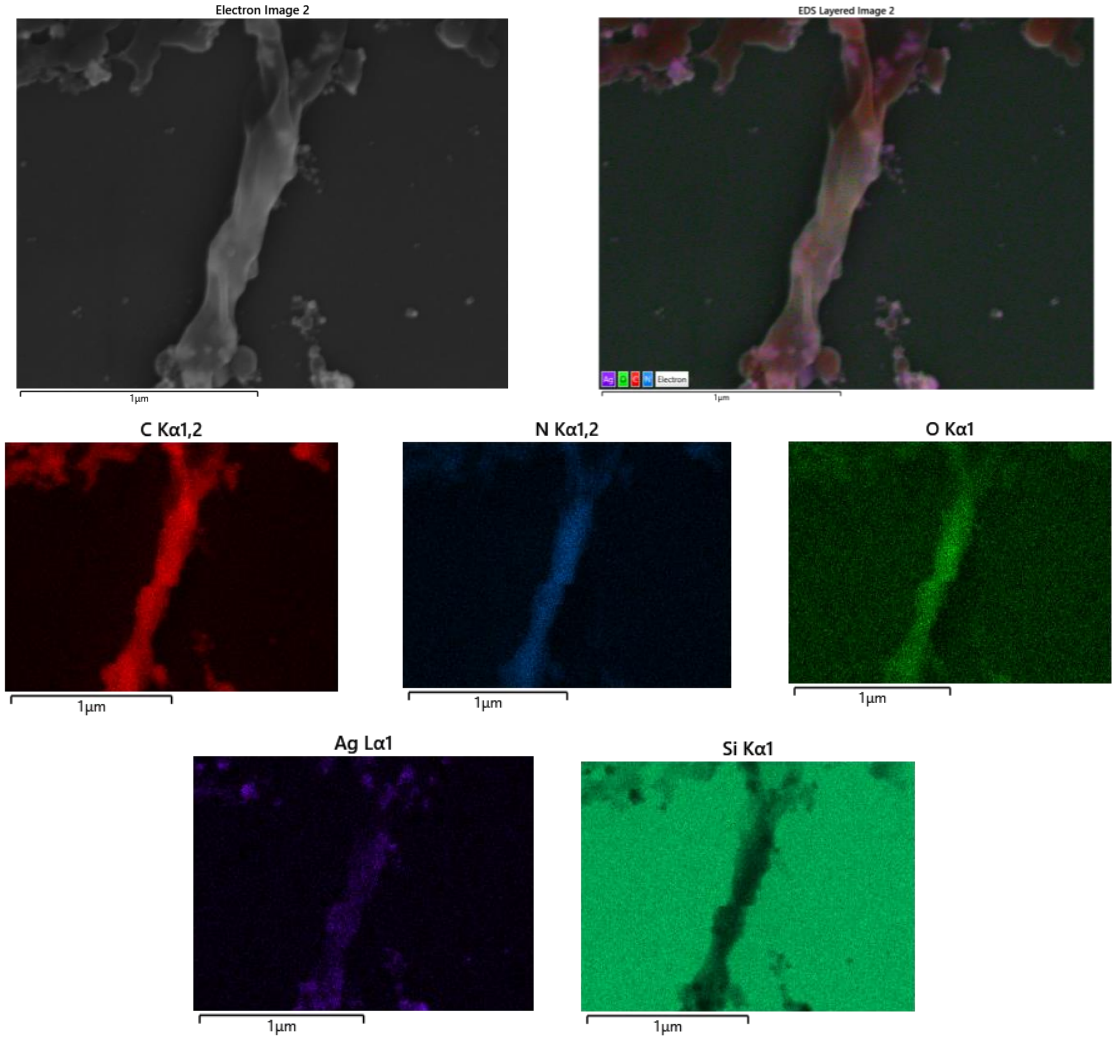

Figure 19. *EDX mapping spectra: silver nanoparticles (purple) covering the nanofibers' surface (red).*

The X-ray beam causes silver to oxidize easily, explaining why a high oxygen content (green) appears in the elemental analysis.

8.2. DEPOSITION OF SILVER ON CH15 FIBERS AT 70% W.R.

Fluorescence changes

As it was done with the previous compound, freshly prepared compound mixed with silver(I) in THF was imaged under white and UV light of 366 nm. And after 24 hours the mixtures were imaged again.

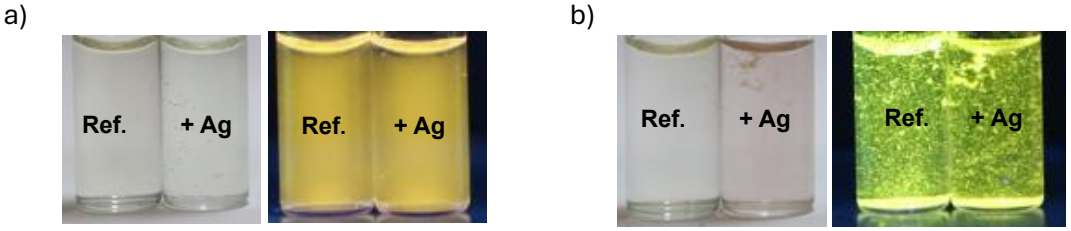

Figure 20*. CH15 at 70% w.r. in THF with silver, (a) Freshly prepared mixtures (b) After 24 hours of preparation.*

After 24 hours a slight change on the solution colour is observed; it evolves from colourless to pale pink under white light. This change suggests interaction between the silver and the organic compound.

Study of nanostructures

After being left to stand for 24 hours, the sample of CH15 (10^{-5} M) at 70% w.r. in THF mixed with silver(I) was imaged. Striking nanoparticles of silver cover the surface of the organic matter *(Figure 21).*

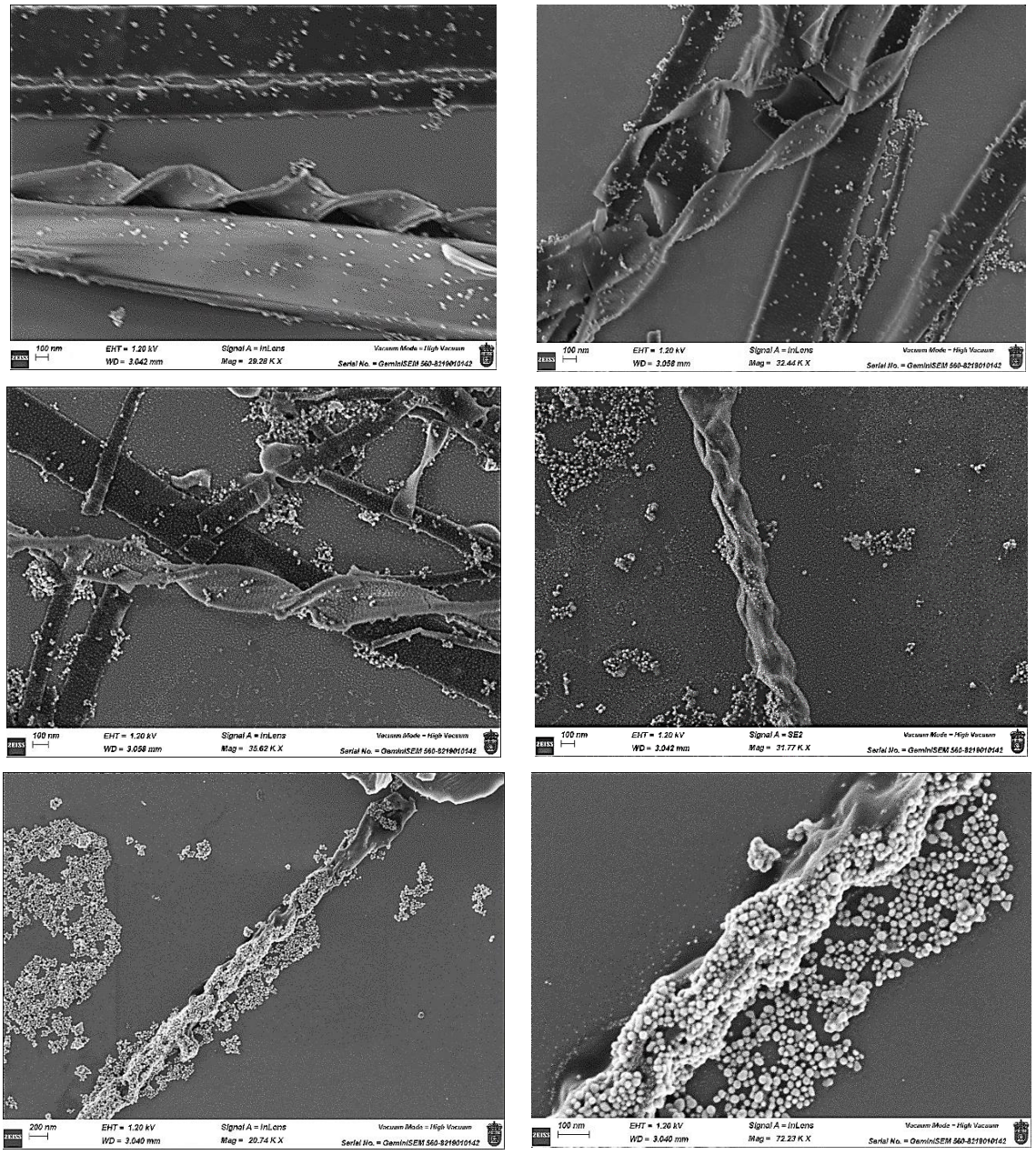

Figure 21. *Silver nanoparticles covering the fibers' surface (CH15 70% w.r.)*

Then, the elemental analysis was performed by EDX to verify the composition. First a localized analysis was made *(Figure 22).* The results confirmed that the surface of the fiber is covered by silver.

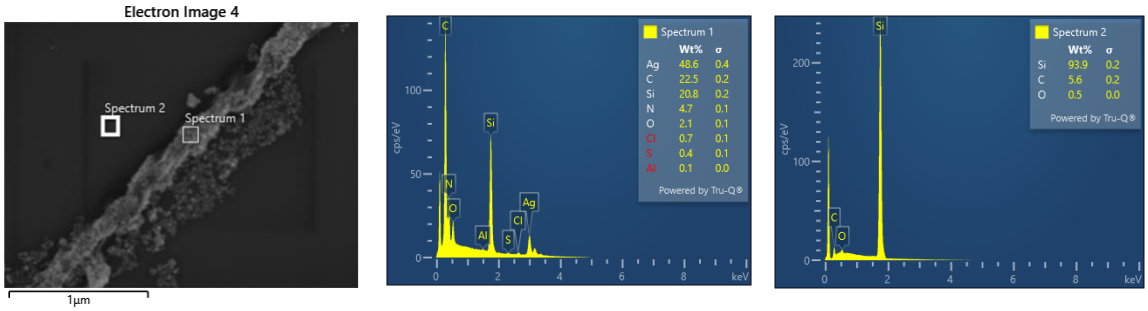

Figure 22. *Punctual EDX spectra of CH15 (70% w.r.): silver on nanohelix.*

The analysis of spectrum 1 reveals that silver is found as pure element with a mass percentage of 48.6 % *(Figure 23),* thus confirming that silver has been reduced without the presence of surfactants or specific reducing agents.

Spectrum 1							
Element	Line Type	Apparent Concentration	k Ratio	Wt%	Wt% Sigma	Standard Label	Factory Standard
C	K series	45.93	0.45931	22.49	0.21	Pure Element	Yes
N	K series	9.50	0.06564	4.74	0.10	BN	Yes
O	K series	3.76	0.03295	2.08	0.06	SiO2	Yes
Al	K series	0.39	0.00352	0.13	0.04	Al2O3	Yes
Si	K series	63.13	0.57888	20.81	0.19	SiO2	Yes
S	K series	1.04	0.01100	0.40	0.08	FeS2	Yes
Cl	K series	2.02	0.01927	0.72	0.11	NaCl	Yes
Ag	L series	93.75	0.93755	48.63	0.40	Pure Element	Yes
Total:				100.00			

Figure 23. *Compositional analysis of spectrum 1. Elemental silver is found.*

Then, the elemental analysis (EDX mapping) confirmed that there is a silver coat on the carbon surface of the fibers *(Figure 24).* It must be mentioned that oxygen was also found due to the easy oxidation of silver, however it has been omitted in the figure.

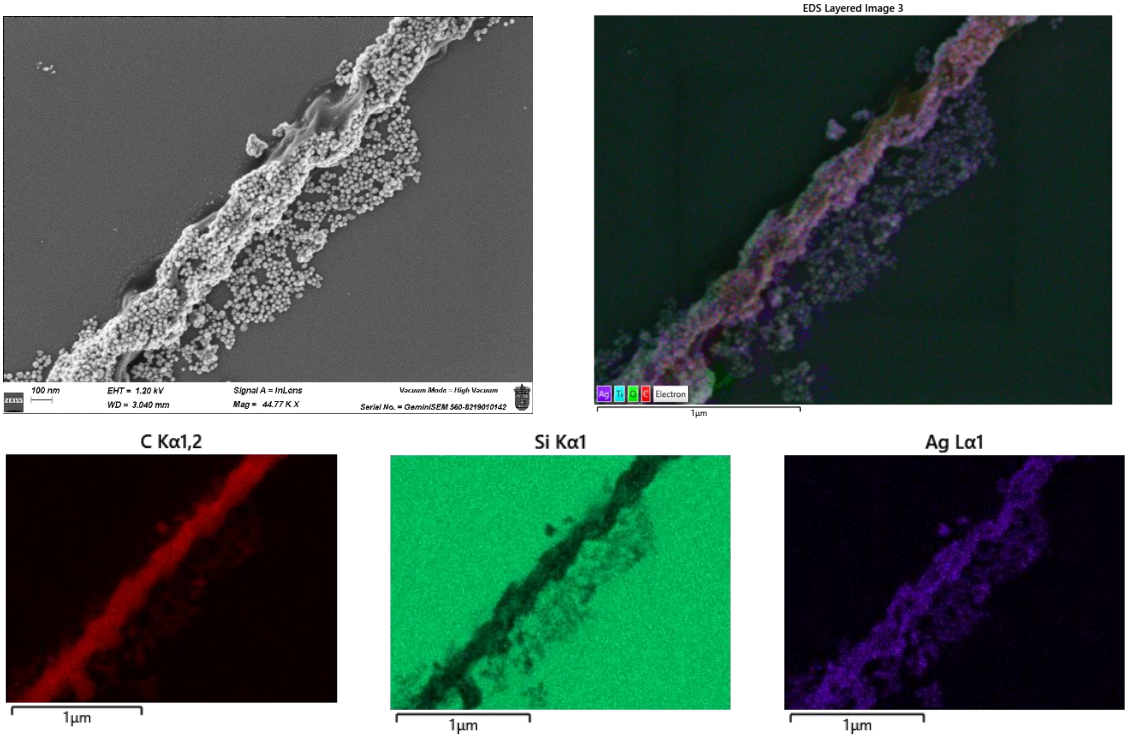

Figure 24. *EDX mapping spectra: silver nanoparticles (purple) covering the nanofibers' surface (red).*

8.3. DEPOSITION OF SILVER ON CH19 FIBERS AT 90% W.R.

Fluorescence changes

As in previous cases, it is wanted to see if there are changes in the NMI's emission when it is mixed with silver(I), thus suggesting interaction with the metal. First, freshly prepared compound mixed with silver(I) in THF was imaged under white and UV light of 366 nm. And after 24 hours the mixtures were imaged again.

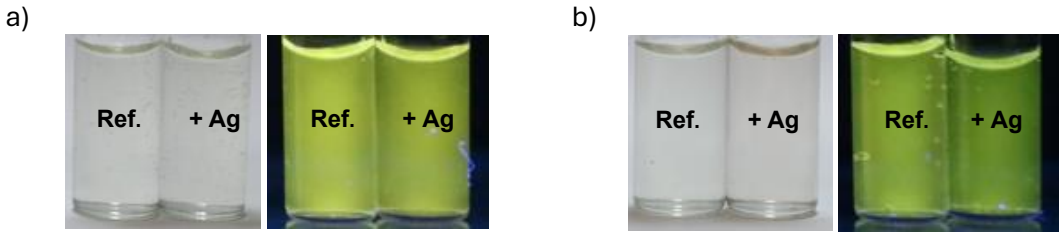

***Figure 25**. CH19 at 90% w.r. in THF with silver, (a) Freshly prepared mixtures (b) After 24 hours of preparation.*

After 24 hours a slight change on the solution colour is observed; it evolves from colourless to pale pink.

Study of nanostructures

Then, after being left to stand for 24 hours, the sample of CH19 (10^{-5} M) at 90% w.r. in THF mixed with silver(I) was imaged. Small nanoparticles of silver cover the surface of the nanohelices *(Figure 26)*.

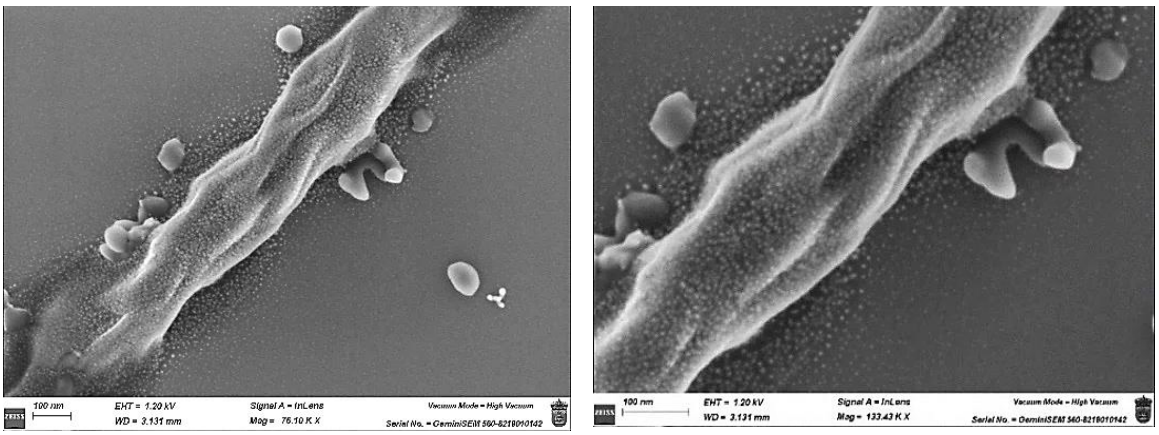

***Figure 26.** Silver nanoparticles covering the fibers' surface (CH19 90% w.r.)*

Then, the elemental analysis (EDX mapping) confirmed the silver coat on the carbon surface of the fibers *(Figure 27)*.

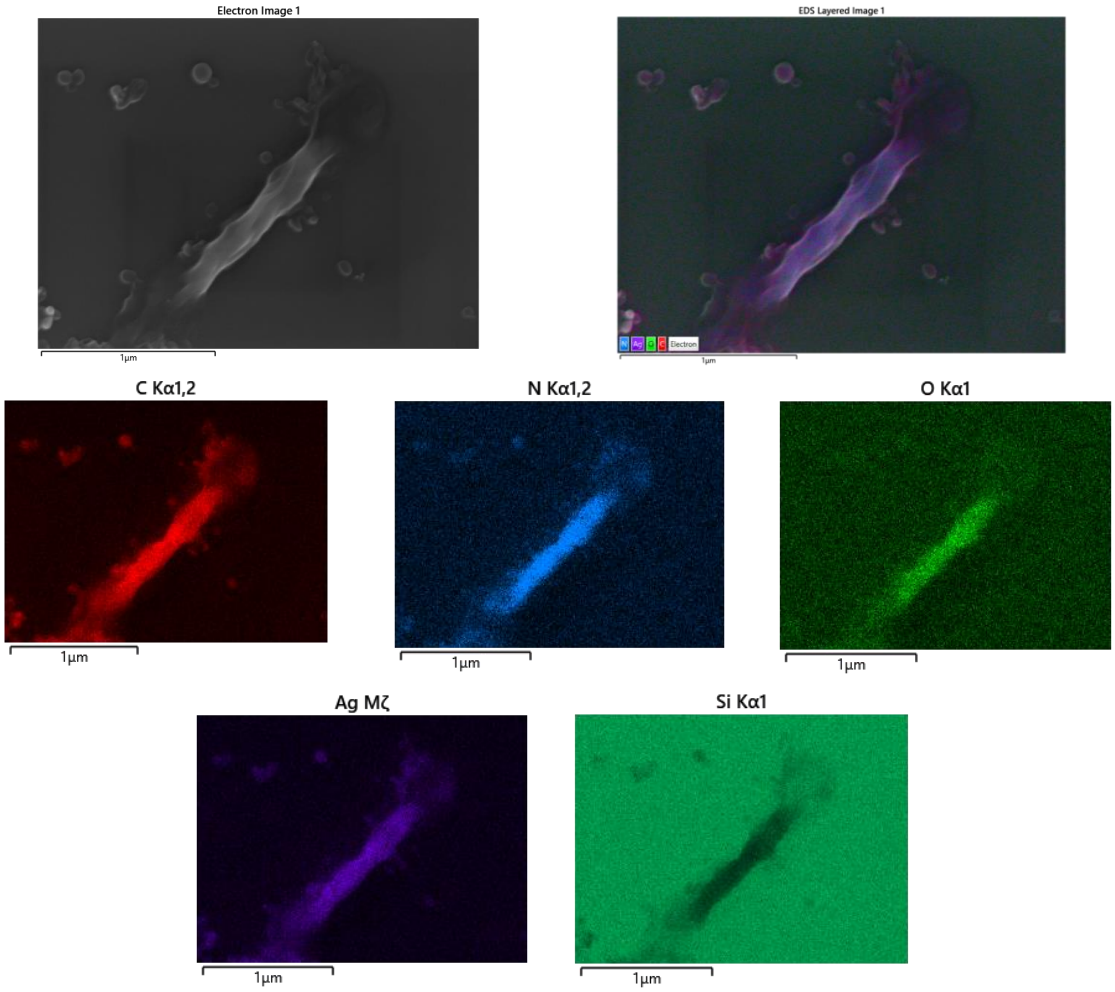

Figure 27. *EDX mapping spectra: silver nanoparticles (purple) covering the nanofibers' surface (red).*

This strategy highlights a simple and effective method for generating metallic coverings on helical nanostructures. The ideal objective for these silver nanoparticles would be to form chiral helices and to fully preserve the helicity of the templates. Thus far, we have only achieved selective coating on the organic material. Although a few nanoparticles have been observed deposited around some of the helices (images of CH15), scanning across the sample during FESEM imaging revealed that silver deposition occurred exclusively in regions where helices were present, rather than randomly across the silicon substrate. So, it can be stated that we have achieved a selective deposition of silver nanoparticles on chiral organic helices. Nevertheless, further efforts are required to obtain a more homogeneous deposition of nanoparticles that fully preserves the helicity of the chiral templates. However, the observation of selective deposition on the helices represents an important first step in this research, as it has been accomplished.

9. CHANGE ON THE GEOMETRY OF THE DYE'S CORE

As it was done in Chapter 1, a new series of compounds was designed by modifying the geometry of the naphthalimide core through meta-substitution. In this case, only semi-functionalized species were synthesized, incorporating a single chiral urea moiety and a tert-butoxycarbonyl substituent. The objective is to investigate whether altering the geometry of the dye affects the π-π stacking interactions between the aromatic cores and to determine if the system is still capable of self-assembling into chiral helices. The results revealed that, upon modifying the core geometry, the steric hindrance caused by the bulky urea units (previously preventing head-to-tail stacking between naphthalimide moieties) disappeared. This change facilitated the formation of nanovesicles (similar to those observed in previous chapters) in which the NMIs are stacked, and the side chains promote the formation of hollow spherical aggregates. These findings underscore the important role of the aromatic core geometry in directing the self-assembly behaviour and suggest that precise structural design is essential for promoting the formation of helical nanofibers.

9.1. SYNTHESIS OF META-SUBSTITUTED CHIRAL AIE-GENS

The experimental steps and regents necessary to synthetize these compounds are similar to the ones used for the synthesis of para-substituted derivatives. The specific reagents amounts, yields and structural characterization of the compounds are described in full in the Supporting Information of this chapter. The reaction scheme with the new structures is shown in *Figure 28.*

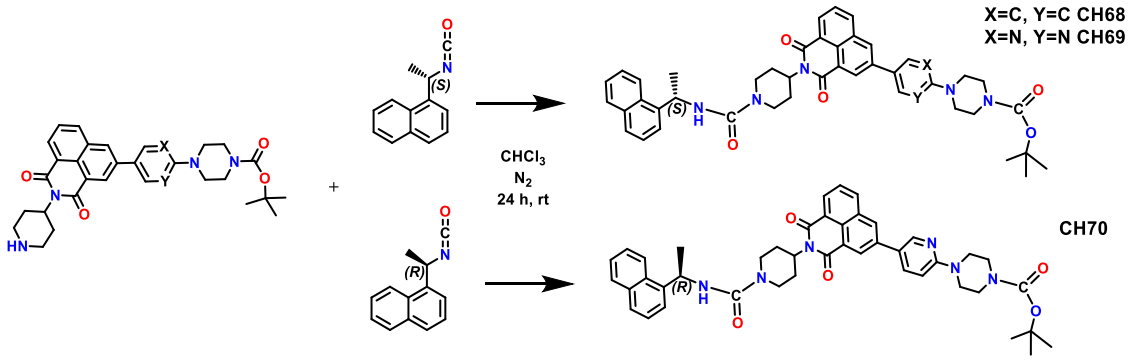

Figure 28. *Synthesis scheme of meta-substituted chiral AIEgens.*

9.2. FLUORESCENCE PROPERTIES

Regarding the fluorescence lifetimes, the meta-substituted compounds show noticeably longer lifetimes, in the range of 12 to 15 nanoseconds, compared to the para-substituted analogues, which exhibit shorter lifetimes between 3 and 5 nanoseconds. This difference is likely related to variations in the electronic distribution and molecular conformation induced by the substitution pattern.[24]

9.2.1. Solvatochromism assays

Solvatochromism studies were performed under similar conditions as those of para-substituted compounds. As expected, the results were very similar to those obtained for its analogues. The highest emission intensities were observed in low-polarity solvents such as toluene and diethyl ether, which is attributed to favourable interactions between the solvent and the molecule's aliphatic regions. These interactions inhibit aggregation in solution, thereby enhancing fluorescence. As their para-substituted analogues, these compounds

[24] J. Dai, X. Zhang, *Chem. Biomed. Imaging* **2023,** *1* (9), 796−816.

are scarcely soluble in hexane and methylcyclohexane, due to the presence of the Boc group. As the polarity of the solvent increases, a bathochromic shift in the emission spectrum is observed, consistent with the behaviour of the para-substituted analogues. However, in this case, this shift is only observed from MCH to ethyl acetate, since the highest polar solvents break with this tendency. The underlying photophysical behaviour can be explained using the same arguments previously discussed in Section 4 for the semifunctionalized species. In *Figure 29* are collected the solvatochromism assays of CH70 (pyridine, R) and its emission spectra as representative example. The solvents employed are numbered following the Snyder polarity index collected in *Table 1* of this chapter.

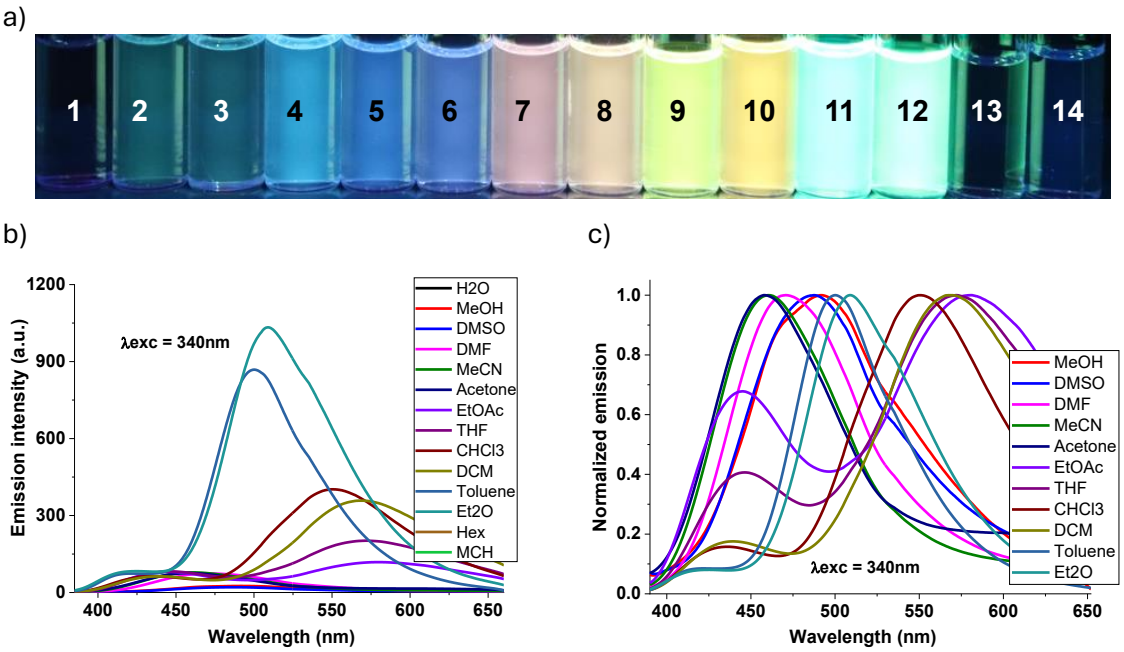

Figure 29. *(a) Solvatochromism assays of CH70 under UV light (366 nm). (b,c) Emission spectra (λ_{exc} = 340 nm, C = 10^{-5} M).*

9.2.2. Water-organic solvent ratio assays

As it was done with the para-substituted compounds, these compounds (10^{-5} M) were studied in mixtures of THF and water to determine how the fluorescence changes as the polarity of the mixture increases *(Table 12).*

Table 12*. Water-solvent ratio assays of meta-substituted hybrids, using UV light (366 nm)*

Structure	THF-H_2O mixtures
CH68: PHENYL NMI + 1 UREA (META) (S)	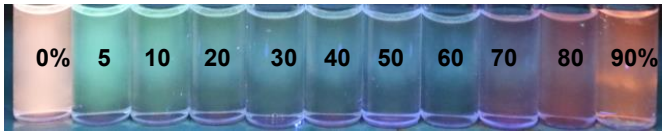
CH69: PYRIMIDINE NMI + 1 UREA (META) (S)	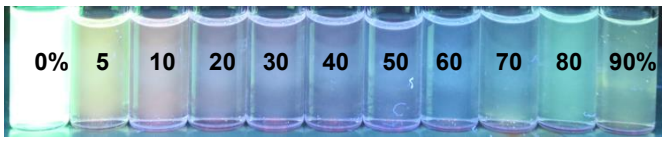
CH70: PYRIDINE NMI + 1 UREA (META) (R)	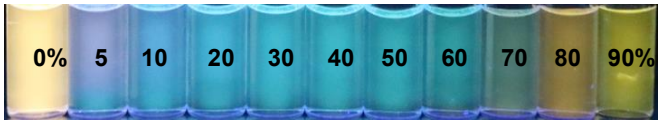

In the case of compounds CH68 and CH70, the AIE phenomenon is observed above 70% of water. However, this increase in fluorescence emission is not observed in the pyrimidine derivative, CH69. Nevertheless, in all three cases, a shift toward longer wavelengths takes place at high-water percentages. This is consistent with the formation of aggregates in these mixtures. The intensities and wavelengths of the emitted light were measured to corroborate the previous qualitative analysis. In *Table 13*, the spectra of CH68 and CH70 are collected. Notice how the blue (wavelength) and grey (intensity) curves rise above 70% w.r.

Table 13. *Emission intensity (grey) and λ_{max} emission (blue) of (a) CH68 (b) CH70 in THF at different w.r.*
λ_{exc} = 320/ 340 nm

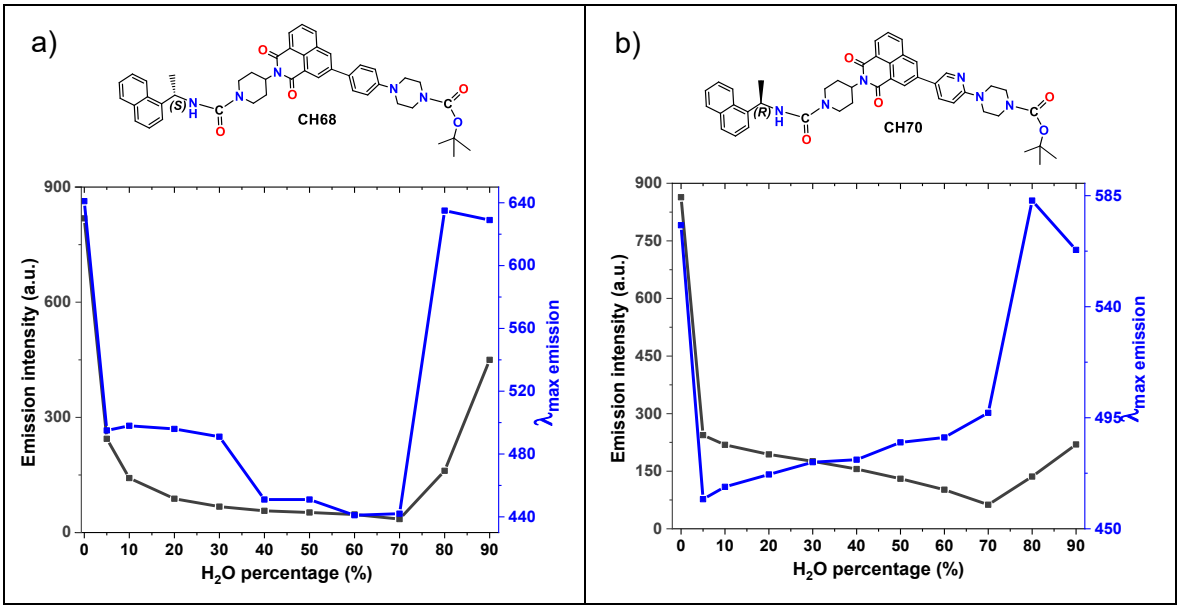

9.3. NANOPARTICLES FORMATION

Once it has been seen the meta-substituted species also form aggregates in mixtures of THF and high-water ratio, their morphology was studied by FESEM. It was observed that the three studied compounds form the same type of nanostructure regardless of whether the urea's stereochemistry is R or S. In this case, the meta-geometry prevents the bulky urea groups from hindering the head-to-tail stacking of the NMIs, allowing them to aggregate into nanovesicles. In the next figures some images of the different compounds are collected.

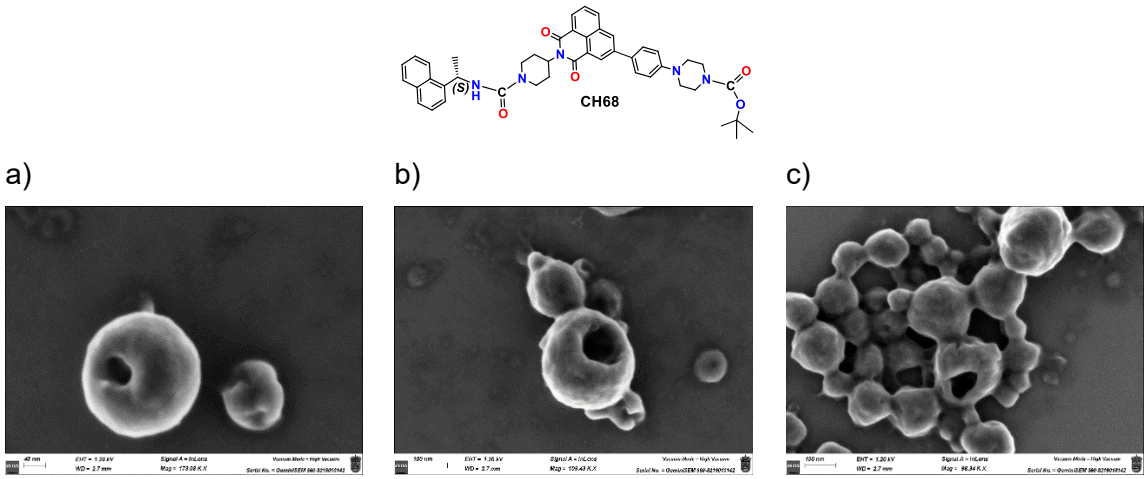

Figure 30. *FESEM images of CH68 in THF-H_2O: (a, b) at 80% w.r. (c) at 90% w.r.*

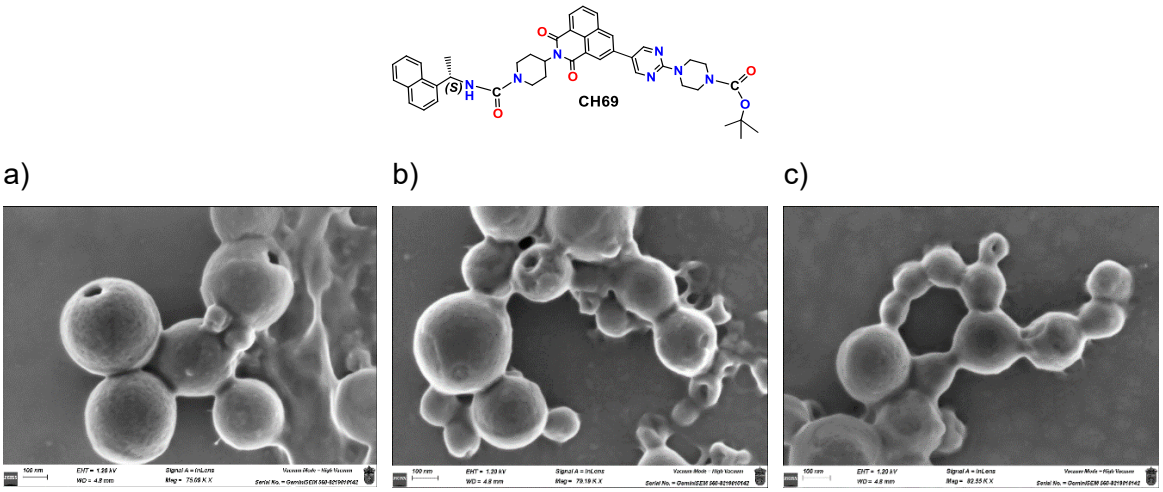

Figure 31. *(a, b, c) FESEM images of CH69 in THF-H_2O at 80% w.r.*

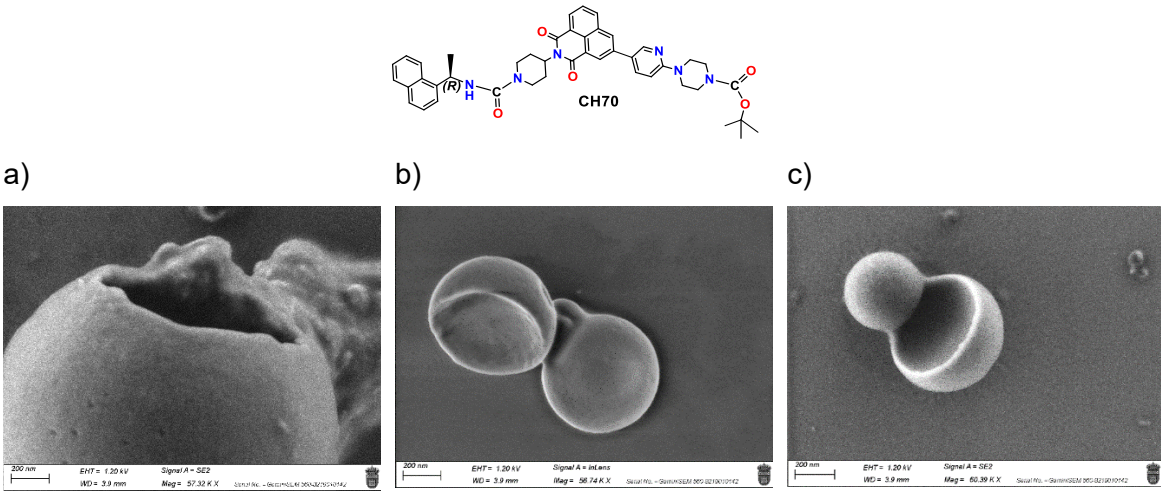

Figure 32. *FESEM images of CH70 in THF-H_2O: (a) at 80% w.r. (b, c) at 90% w.r.*

As occurred in other chapters where compounds assembled into hollow spheres, the most well-defined nanovesicles are those formed by pyridine derivatives. Particularly, CH70 was found to generate vesicles that are more abundant, uniform, and structurally well-formed.

10. CONCLUSIONS

In this chapter, we have demonstrated the successful design and synthesis of naphthalimide derivatives functionalized with chiral urea moieties, which exhibit aggregation-induced emission in aqueous media. The carefully tuned molecular structure enabled the controlled self-assembly of these compounds into left-handed helical fibres, driven by specific non-covalent interactions, the specific geometry of the dye and the inherent chirality and bulky size of the substituents.

Microscopy techniques (FESEM and TEM) confirmed the formation of the chiral fibers, while the self-assembly mechanism was clarified through molecular dynamics simulations. These simulations revealed that the bulky urea units hinder efficient head-to-tail π-π stacking of the NMI aromatic cores. Consequently, the chromophores adopt a displaced arrangement relative to one another, which results in a helical supramolecular architecture.

On the other hand, chiroptical characterisation of the enantiomeric compounds revealed mirror-image circular dichroism spectra. Concretely, the R enantiomers exhibited positive Cotton effects, while the S enantiomers showed negative ones, consistent with their mirror-image chirality. Furthermore, compounds bearing two chiral urea units displayed significantly stronger CD signals compared to those containing only a single optically active urea moiety. In contrast, the circularly polarised luminescence signals were consistently right-handed, regardless of the absolute configuration of the chiral centres and the formation of left-handed fibers. That is because in this case, the CPL signals are not directly determined by the supramolecular chirality of the system, but rather by excitonic interactions arising upon molecular aggregation.

Then, as application for these organic helical fibers, we demonstrated that they could serve as chiral templates for the growth of silver nanoparticles. The metallisation was confirmed by energy-dispersive X-ray spectroscopy (FESEM-EDX). The selective growth of silver on the fibers suggests specific interactions between the chiral surface and the silver species during nucleation and growth. These findings contribute to a deeper understanding of how supramolecular chirality can influence the spatial organization of nanoparticles and may pave the way for the development of new functional materials with chiroptical or electronic applications.

Finally, we also investigated the influence of the dye geometry on self-assembly. When the substitution pattern on the NMI core was altered from para to meta positions, an important change in the resulting nanostructures was observed. In this new geometry, the steric hindrance posed by the urea groups does not prevent effective head-to-tail stacking. Consequently, the system no longer forms helices but instead self-assemble into nanovesicles, similar to those observed in previous chapters. These results highlight the pivotal role of chromophore geometry in the helices formation.

Altogether, this chapter offers a comprehensive strategy for the rational design of chiral AIE luminogens, revealing how subtle changes in molecular design can direct supramolecular chirality, optical activity, and nanostructure formation.

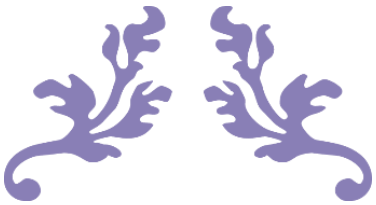

CHAPTER 5

Ruthenium and iridium complexes on 1,8-naphthalimides: Photophysics, nanostructure and applications

ABSTRACT

In this chapter, a new series of hybrid compounds based on naphthalimide fluorophores covalently linked to ruthenium(II) and iridium(III) complexes is described. These systems exhibit aggregation-caused quenching in THF-water mixtures with high water content, indicating intermolecular interactions in the aggregated state. Transient absorption spectroscopy reveals a multistep excited-state evolution in these compounds, beginning with ultrafast charge transfer processes between the organic chromophore and the metal centre, followed by the formation of long-lived metal-centred triplet states. These triplet states are capable of sensitizing molecular oxygen to its reactive singlet state ($^1\Delta_g$ O_2). Hence, the compounds were evaluated in human embryonic kidney cells (HEK-293) and showed promising light-induced toxicity, likely due to the effective production of singlet oxygen and other reactive oxygen species. So, they are attractive agents for photodynamic therapy. On the other hand, these compounds are able to promote the reduction of gold(III) ions in THF-water mixtures, yielding elemental gold nanoparticles. Interestingly, the resulting gold nanostructures lack the characteristic surface plasmon resonance (SPR) band typically observed in colloidal gold, indicating that the organic shell formed by the naphthalimide-metal complexes effectively suppresses the SPR response. This combined behaviour makes them relevant for further exploration in therapeutic and nanomaterial applications.

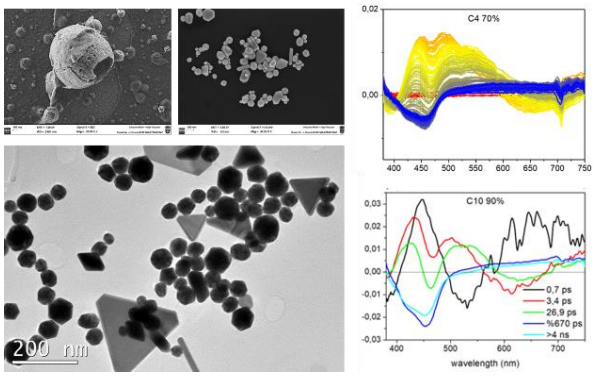

Figure 1. *Nanostructure, gold nanoparticles and transient absorption spectra of NMI-metal hybrids.*

The morphology of both organic and metallic nanostructures was characterized using Scanning Electron Microscopy and Transmission Electron Microscopy. In addition, Energy-Dispersive X-ray Spectroscopy was used to verify their elemental composition. The full analysis of both organic and metallic nanostructures is included in the Supporting Information of Chapter 5, along with the structural characterization and the fluorescence assays of the chemical compounds described in this chapter.

1. INTRODUCTION

Organometallic complexes of ruthenium and iridium have emerged as attractive systems in photophysical and photochemical research due to their distinctive electronic configurations, which facilitate diverse excited-state processes. Their ability to undergo efficient metal-to-ligand charge transfer (MLCT) transitions, coupled with their adjustable photophysical properties, renders them suitable for applications in photodynamic therapy, solar energy conversion and molecular electronics.[1]

In aqueous environments, the behaviour of these complexes is significantly influenced by their tendency to aggregate. High water content often induces aggregation, leading to phenomena such as aggregation-induced emission or aggregation-caused quenching, depending on the specific molecular architecture and interactions. For example, in donor-π-acceptor systems, aggregation can modulate intramolecular charge transfer, altering the lifetimes and energies of excited states.[2] In addition it has been shown that certain iridium(III) complexes have been designed to exhibit AIE characteristics, maintaining or

[1] R. Kuhrt, P. Y. Hob, M. Hantuscha, F. Lisselb, O. Blacque, M. Knupfera, B. Büchner, *RSC Adv.* **2020,** 10, 43242-43247.
[2] R. Chen, Q. Zhang, L. Zhang, C. Liu, *Chemosensors.* **2025**, *13*, 14.

even enhancing their luminescence upon aggregation, which is advantageous for biological applications where aqueous solubility is essential.[3]

Transient absorption spectroscopy (TAS) operates as a crucial technique to unravel the excited-state dynamics of these complexes. Through TAS, it is possible to monitor the formation and decay of excited states, providing insights into processes like charge transfer, intersystem crossing (ISC), and triplet state formation. Studies have demonstrated that the aggregation state significantly affects these dynamics. For example, in ruthenium polypyridyl complexes, ultrafast transient absorption measurements have revealed that the MLCT excited states can decay via multiple pathways, including internal conversion and ISC, with the rates influenced by the ligand environment and solvent interactions.[4]

The generation of singlet oxygen ($^1\Delta_g O_2$) is a critical aspect of photochemical applications, including photodynamic therapy and environmental remediation. Organometallic complexes can sensitize $^3O_2$ to $^1O_2$ via energy transfer from their triplet excited states. The efficiency of this process is dependent on factors like triplet state energy, lifetime, and the presence of aggregation.[5] Notably, certain metal-organic frameworks (MOFs) have been engineered to optimize triplet exciton formation. Additionally, the already mentioned iridium complexes with AIE properties have demonstrated robust capabilities in generating singlet oxygen upon aggregation, highlighting their potential in therapeutic applications. The resulting singlet oxygen is a highly reactive species capable of inducing oxidative damage to cellular components such as lipids, proteins, and nucleic acids, ultimately leading to cell death.[3]

On the other hand, recent studies have explored the incorporation of perylenediimide (PDI) ligands into ruthenium and iridium complexes, aiming to enhance their photophysical properties and their use in photodynamic therapy. These PDI-based complexes exhibit strong absorption in the visible region and efficient intersystem crossing, leading to high singlet oxygen generation upon light irradiation.[6]

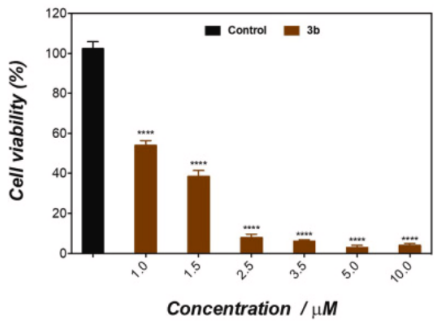

Figure 2. *Photocytotoxicity of porphyrin-iridium complex in melanoma cells.*

Furthermore, the development of ruthenium and iridium complexes bearing porphyrin moieties has shown promising results in photodynamic therapy applications. These complexes combine the favourable photophysical properties of the metal centres with the strong light-harvesting abilities of porphyrins, resulting in effective photosensitizers capable of inducing significant cytotoxic effects upon light activation *(Figure 2)*.[7]

Understanding the interplay between aggregation, excited-state dynamics, and $^1O_2$ generation is essential for the rational design of organometallic complexes with tailored photophysical properties. This chapter explores these aspects, providing a comprehensive analysis of the transient absorption behaviour and singlet oxygen sensitization of selected organometallic compounds in varying aqueous environments, with a focus on their potential applications in photodynamic therapy.

On the other hand, the synthesized naphthalimide derivatives, covalently linked to ruthenium(II) and iridium(III) complexes via amide bonds, exhibit aggregation in THF-water mixtures with high water content. This aggregation leads to a pronounced fluorescence quenching, indicative of aggregation-induced quenching behaviour. Remarkably, under

[3] W. Zhu, S. Liu, Z. Wang, C. Shi, Q. Zhang, Z. Wu, G. Li, D. Zhu, *Molecules* **2023,** *28* (23), 7914.
[4] J. F. Endicott, M. D. J. Uddin, H. B. Schlegel, *Res. Chem. Intermediat.* **2002,** *28*, 761–777.
[5] K. Wang, C. T. Li, G. L. Zhang, *Natl. Sci. Rev.* **2025***, 12* (4), nwaf024.
[6] L. Mauri, A. Colombo, C. Dragonetti, F. Fagnani, D. Roberto, *Molecules* **2022**, *27*, 7928.
[7] M. M. N. Moura A. D. F. Kelly, J. C. Biazzotto, J. A. Prandini, C. Lodeiro, M. A. F. Faustino, M. M. Q. Simoes, R. S. da Silva, M. G. P. M. S. Neves, *Dyes Pigm.* **2022,** *205,* 110501.

these same aqueous conditions, the addition of auric chloride results in the formation of elemental gold nanoparticles with spherical and polygonal shapes, suggesting that the metal-organic complexes can promote gold(I) ion reduction. This behaviour may be attributed to the redox-active nature of the Ru(II) and Ir(III) centres. Interactions between ruthenium and gold have been reported in the literature, where ruthenium complexes act as stabilizing agents of gold nanoparticles.[8]

However, ruthenium and iridium complexes are frequently combined with gold nanoparticles to exploit synergistic optical properties. In such systems, the phosphorescence of the metal complex couples with the localized surface plasmon resonance (LSPR) of gold, resulting in enhanced emission intensity, altered excited-state lifetimes, and improved photophysical performance for applications such as biosensing, imaging, and photocatalysis.[9] For instance, cyclometalated Ir(III) complexes embedded on silica-coated gold cores demonstrate dual photodynamic and photothermal therapeutic action while retaining strong luminescence, thanks to plasmon-enhanced energy transfer processes.[10] Similarly, $[Ru(bpy)_3]^{2+}$ adsorbed onto gold nanospheres demonstrated adjustable optical absorption spectra and enhanced stability, facilitating plasmon-enhanced spectroscopy.[11]

In contrast, in the present study, the hybrid naphthalimide-Ru/Ir complexes form an organic cover on the gold nanoparticles' surface that inhibits the gold plasmon resonance, thus suppressing the plasmon-enhanced emission and damping off the LSPR band.[12] This phenomenon is consistent with reports showing that dense organic or ligand shells around gold nanoparticles can significantly red-shift or quench the LSPR peak due to changes in the local dielectric environment and refractive index of the shell.[13] This behaviour emphasizes the critical influence of surface coverage on plasmonic modulation, offering valuable insights into the design of multifunctional nanomaterials where emission, redox activity, and plasmon response must be carefully balanced for specific applications.

2. OBJECTIVES

In this chapter, the photophysical behaviour, aggregation properties, and biological activity of newly synthesized hybrid naphthalimide–ruthenium(II)/iridium(III) complexes are investigated. Particular attention is also given to their ability to generate gold nanoparticles. To address these aspects, the following specific objectives are proposed.

- To characterize the aggregation behaviour of the compounds in THF-water mixtures with high water content.
- To determine the nature of the nanostructures formed upon aggregation, with particular emphasis on identifying the possible formation of nanovesicles. To get it, Scanning Electron Microscopy will be employed.
- To elucidate the excited-state dynamics of these compounds via Transient Absorption Spectroscopy, detailing the charge transfer processes and the formation of long-lived metal-centred triplet states capable of sensitizing singlet oxygen.
- To evaluate the photodynamic activity of the compounds. This will be done through cytotoxicity studies in HEK-293 cells under both dark and light conditions, determining this way the increase in toxicity upon light exposure.

[8] S. A. M. Osborne, Z. Pikramenou, *Faraday Discuss.* **2015,** *185,* 219−231

[9] X. H. N. Xu, S. Huang, W. Brownlow, K. Salaita, R. B. Jeffers, *J. Phys. Chem. B* **2004,** *108* (40), 15543−15551.

[10] A. Candreva, L. Ricciardi, E. I. Szerb, M. A. La Deda, *Nanomat.* **2024,** *14 (19)*, 1543.

[11] U. Yunusa, N. Warren, D. Schauer, P. Srivastava, E. Sprague-Klein, *Nanoscale* **2024,** *16,* 5601−5612.

[12] J. Zhou, B. Tang, *In Situ Localized Surface Plasmon Resonance Spectroscopy for Gold and Silver Nanoparticles*, In: Challa S.S.R. Kumar Editor, *In-situ Characterization Techniques for Nanomaterials,* Springer-Verlag, **2018,** chapter 4, pp. 107−157.

[13] M.P. Mcoyi, K.T. Mpofu, M. Sekhwama, P. Mthunzi-Kufa, *Plasmonics.* **2025**, *20*, 5481−5520.

- To investigate the ability of these complexes to reduce gold(III) ions to elemental gold nanoparticles in THF-water mixtures, and to characterize the morphology and elemental composition of the resulting nanostructures using Scanning Electron Microscopy, Transmission Electron Microscopy, and Energy-Dispersive X-ray Spectroscopy.
- To evaluate the effect of light exposure during the formation of gold nanoparticles on their size, shape, and plasmonic properties, comparing samples synthesized under white light illumination and in the dark.
- To analyse the impact of gold nanoparticle formation on the absorption and emission spectra of the hybrid complexes to understand the interaction between the organic matter and the plasmon resonance of gold nanoparticles.

3. SYNTHESIS OF NMI-METAL COMPLEXES HYBRIDS

The organometallic compounds herein studied are divided in two families: (a) one product containing two equal metal centres (b) products containing one metal complex *(Figures 3a, 3b)*.

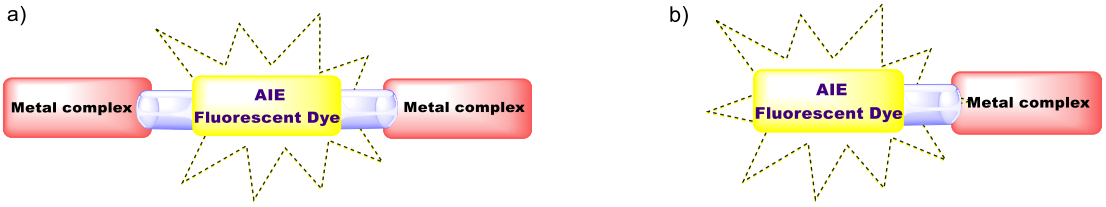

***Figure 3**. Schematic structure of new hybrid of NMIs and metal complexes.*

All compounds described in this section have similar synthetic reaction mechanisms which consist in the nucleophilic attack of the free amine group present in the piperazine and/or piperidine of the NMI to the carboxylic acid group of an amino acid that carries one of the ligands of the metal complex (either ruthenium or iridium). In this way, two amide bonds are formed when fully deprotected naphthalimide is functionalized. In this case, only one hybrid with two metal centres has been synthesized, and both of them were iridium complexes *(Figure 4a)*. Whereas only one amide bond is formed when the metal centre is bonded to a semi-protected NMI *(Figure 4b)*.

Due to the resemblance between the four synthetic reactions herein studied, their experimental conditions and steps to be followed are similar. Only the nature of starting NMIs and the amount of the other reagents change, and they are deeply described in the Supporting Information section, as well as their characterization. The common methodology is as follows:

In a 25 ml flask, provided with a magnetic stirrer, the unfunctionalized NMI (1 eq.) is mixed with 1 or 2 equivalents (depending on the starting NMI) of the metal complex. There are two possible metallic moieties: Ir(ppy)2(4-([2,2'-bipyridin]-4-yl)butanoic acid)][PF_6] or [Ru(bpy)$_2$(4-methyl-4'-carboxypropyl-2,2'-bipyridine)][PF_6]$_2$, both commercial compounds. Subsequently, 2 equivalents of hydroxybenzotriazole monohydrate, 2 equivalents of PyBOP and 4 equivalents of DIPEA (*N*,*N*-diisopropylethylamine) are added to the flask. Then, under argon atmosphere the mixture of solids is dissolved in 3 ml of anhydrous DMF. Keeping the inert atmosphere, the reaction mixture is stirred overnight at room temperature.

Once the reaction has finalized, 15 ml of ethyl acetate are added to the crude reaction mixture and then poured in a separatory funnel. Next, small amounts of water (5x10 ml) are added to drag out the DMF. After that, the ethyl acetate is removed under reduced pressure. The product is purified by column chromatography (SiO_2) employing a DCM-MeOH mixture, gradually increasing the MeOH content from 0% to 3-5%. Finally, the products are obtained with yields ranging from 70 to 84% depending on the starting NMI.

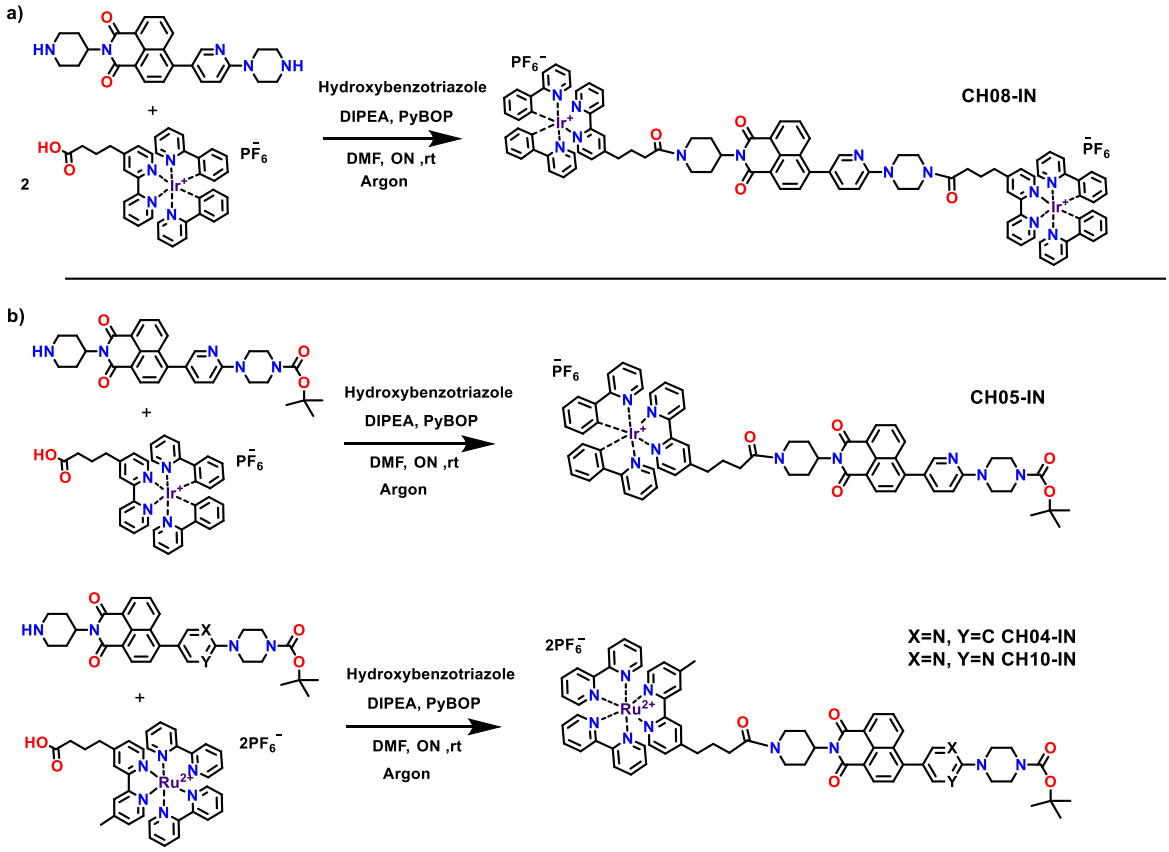

Figure 4. *Synthetic route to obtain (a) Two metal complexes-NMI hybrid (b) One metal complex-NMI hybrids.*

4. FLUORESCENCE PROPERTIES OF METAL COMPLEX-NMI HYBRIDS

4.1. SOLVATOCHROMISM ASSAYS

In this section, the solvent polarity effect on the position and intensity of the absorption and emission bands is studied. In *Table 1*, the employed solvents are ordered from highest to lowest polarity, according to the Snyder polarity index.

Table 1. *Employed solvents in solvatochromism assays*

1. H_2O	4. DMF	7. EtOAc	10. THF	13. Hexane
2. MeOH	5. MeCN	8. THF	11. Toluene	14. MCH
3. DMSO	6. Acetone	9. $CHCl_3$	12. EtO_2	

Then, the 14 different solutions (10^{-5} M) of each compound were photographed under UV light of 366 nm *(Table 2).* As it will be observed, in this case, the behaviour is not exactly the same as in the previous chapters, since here there are metal centres that interact with highly polar solvents, while the central naphthalimide dye interacts more favourably with low-polarity solvents. In the case of CH08-IN, the presence of two metal units predominantly governs the solvatochromic response of the molecule, especially with respect to the colour of the emitted light.

***Table 2**. Solvatochromism assays of metal complex-NMI hybrids under UV light (366 nm)*

Structure	Solvents (1-14)
CH04-IN 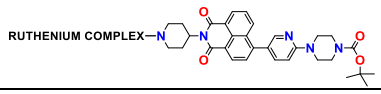	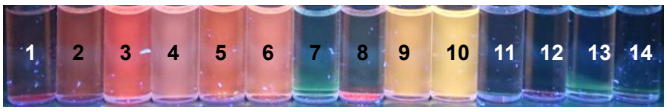
CH10-IN 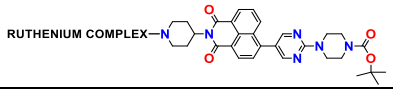	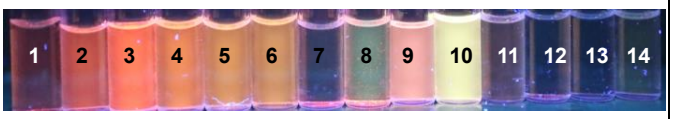
CH05-IN 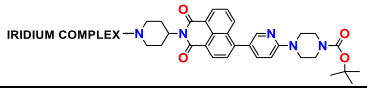	
CH08-IN 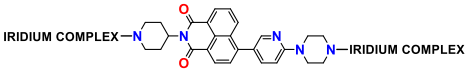	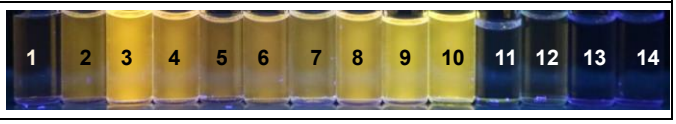

In this case, there is no clear pattern of increasing or decreasing fluorescence as the polarity of the solvent changes. In three compounds, strong fluorescence is observed in DMSO, and that is because the metal centre is interacting with this solvent. At moderately high polarities, the fluorescence decreases (from acetonitrile to ethyl acetate), followed by a pronounced increase in lower-polarity solvents, such as chloroform and dichloromethane. In this range, the solvatochromic response is governed by the naphthalimide core. Moreover, it is observed that at very low polarities the compounds no longer emit, with the vials appearing colourless. This effect is especially evident in the case of CH08-IN, which, due to the presence of two metal centres, shows no emission in toluene, likely due to its low solubility in this solvent. Another remarkable observation is the slight emission of vial number one, corresponding to water, where the compounds exhibit certain solubility. This can be attributed to the fact that the isolated metal complexes were soluble in water, and thus, when bonded to the naphthalimide core, they impart a certain degree of solubility to the final hybrid molecule.

This qualitative analysis can be supported by the normalized absorption spectra of the compounds, which provide valuable information regarding their solubility in different solvents. In *Table 3,* the spectra of CH10-IN (one ruthenium complex) and CH08-IN (two iridium complexes) are collected as representative examples.

***Table 3**. Normalized absorption spectra of (a) CH10-IN and (b) CH08-IN*

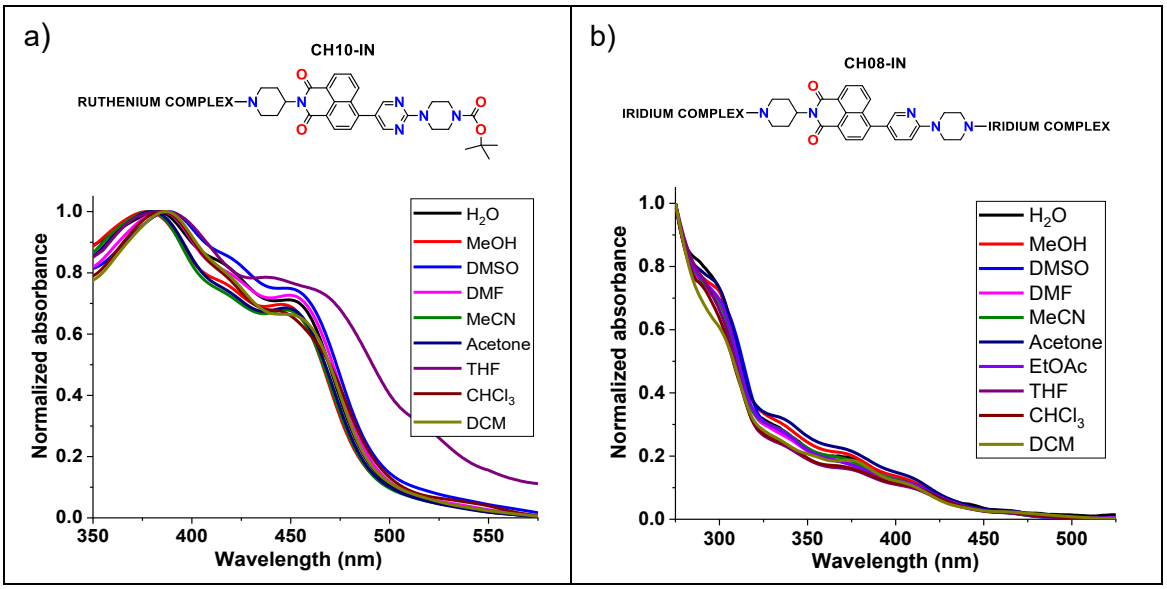

On the other hand, the differences between the emission intensities of the compounds in the different solvents can be corroborated with their emission spectra. In *Table 4* the spectra of CH10-IN and CH08-IN are collected. As seen in the photographs, the most intense signals are those of solutions in the least polar solvents where the compounds are soluble, such as DCM or $CHCl_3$ (although as described before, it is also intense in DMSO), whereas the signal in water is near the baseline.

***Table 4**. Emission spectra of (a) CH10-IN and (b) CH08-IN. λ_{exc} = 380/300 nm*

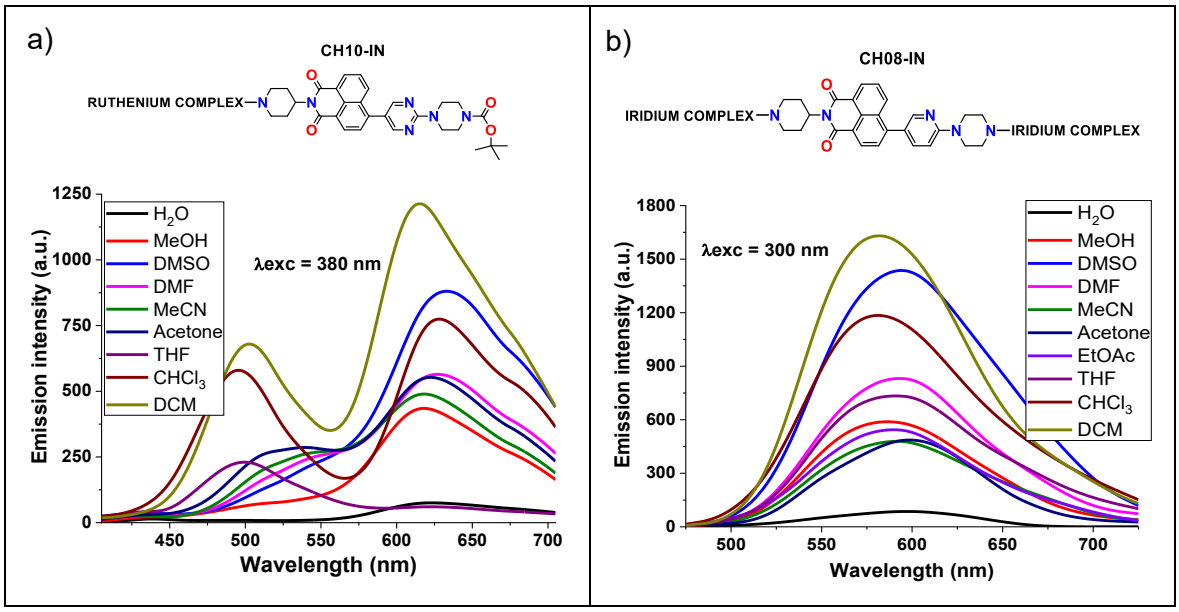

Additionally, from the absorption and emission spectra it can be identified the most suitable solvent for the next studies. The ideal solvent must be miscible with water and the NMIs should show moderate fluorescence there. Tetrahydrofuran is selected as the best solvent.

Alternatively, due to the normalized emission spectra *(Table 5),* it is possible to determine the shift in the position of the emission bands as the solvent polarity changes. Two distinct behaviours are observed: in one hand, the compounds containing a single metal complex exhibit a red shift in their emission bands as the polarity of the solvent increases; that is, they show a bathochromic shift. It is probably because in the most polar solvents, the naphthalimide cores undergo π-π stacking, leading to aggregate formation. These aggregates stabilize the system's energy, thus resulting in emission at longer wavelengths. But it must be mentioned that the shifts are not very pronounced, as the emitted light ranges between yellow and orange hues, reflecting the influence of the iridium or ruthenium centres. In contrast, in the case of CH08-IN, the emission is governed by the two iridium complexes. As a result, the emission occurs at virtually the same wavelength across all solvents (there is no appreciable shift), which explains why the vials appear yellow in all the photographs.

All these observations can be better appreciated in the next table, which shows the normalized emission spectra of CH10-IN and CH08-IN. From the spectrum of CH10-IN, the exact bathochromic shift can be determined calculating the difference between the peak wavelengths of the most and the least polar solvents. It must be mentioned that methanol is not considered in this study because it can interact by hydrogen bonds and breaks with general theory. Thus, in the CH10-IN spectrum, the emission maximum is shifted 18 nm since its emission peak moves from 615 nm in DCM to 633 nm in DMSO. It is worth noting that, although the DCM signal in compound CH10-IN displays two bands, only the most intense one (at longer wavelengths) has been considered. On the other hand, the analysis of the normalized emission spectrum reveals that the THF band is significantly shifted toward shorter wavelengths compared to the other solvents, even though THF is not the

least polar solvent in which the compound is soluble. In this case, the emission maximum appears at 500 nm. Therefore, considering the difference between the emission maximum in DMSO (633 nm) and that in THF, the bathochromic shift would be 133 nm. In contrast, the absence of a bathochromic shift in compound CH08-IN is supported by *Table 5, Fig. b*, where it is observed that all the emission bands appear at practically the same wavelength.

***Table 5**. Normalized emission spectra of (a) CH10-IN, (b) CH08-IN. λ_{exc} = 380/300 nm*

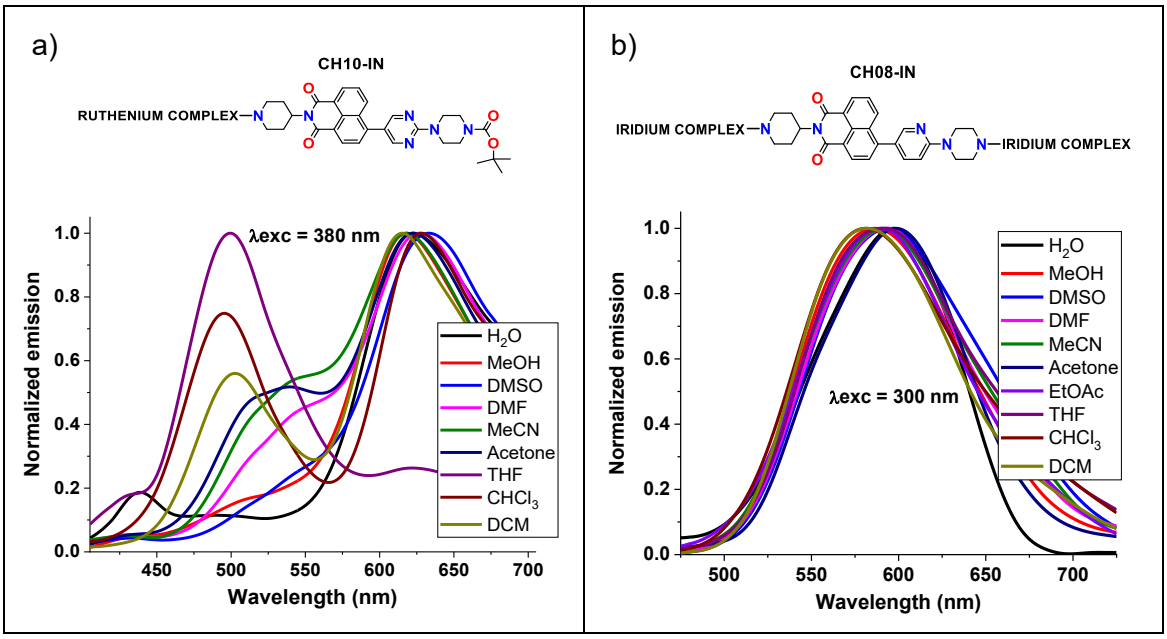

4.2. WATER-ORGANIC SOLVENT RATIO ASSAYS

As in previous chapters of this thesis, this section examines the behaviour of the organometallic compounds in THF-water mixtures, in order to determine whether aggregates are formed as the water content increases. The mixtures were prepared according to the methodology described in previous chapters, with a final concentration of 10^{-5} M. Then, they were photographed under UV light at 366 nm *(Table 6)*.

***Table 6**. Water-solvent ratio assays of different metal complex-NMI hybrids, using UV light (366 nm)*

Structure	THF-H_2O mixtures
CH04-IN 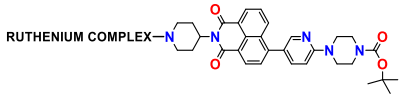	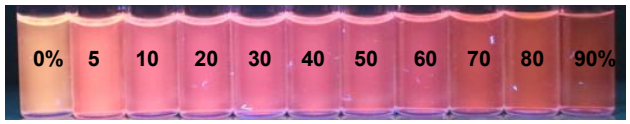
CH10-IN 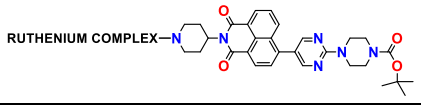	
CH05-IN 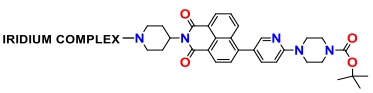	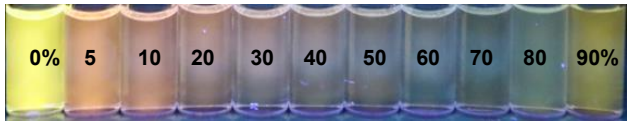
CH08-IN 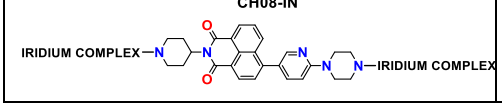	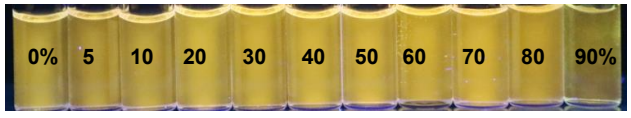

In the photographs, it can be observed that monofunctionalized compounds exhibit a colour shift toward longer wavelengths at 90% water. This is consistent with the aggregate formation and energy stabilization mentioned above. It is also observed for these compounds how the emission intensity varies as the water content changes. In pure THF, the emission intensity is very high since the species are in solution and no aggregate is formed; however, when water is added, fluorescence emission becomes weaker due to the ACQ effect.

Furthermore, in the case of ruthenium derivatives (CH04-IN and CH10-IN), fluorescence quenching is particularly pronounced at high water content. Whereas for CH05-IN (one iridium centre), quenching occurs from as low as 5% water. In contrast, CH08-IN, which contains two metal complexes, does not exhibit significant changes in fluorescence intensity upon water addition. This is because the emission is governed by the iridium complexes rather than by NMI stacking, and therefore the ACQ effect is not prominent. However, at 90% water, a slight decrease in emission intensity can be observed, which may be attributed to the appearance of some π-π stacking interactions between the NMIs. It is likely that at this high-water content, these interactions become strong enough to influence the emission.

Paying attention to monofunctionalized complexes, a subtle difference in behaviour between ruthenium and iridium complexes can be observed. *Table 7* shows the emission spectra (intensity and wavelength vs water percentage) of the compounds CH04-IN and CH05-IN. It can be seen that in the case of CH04-IN, quenching becomes more pronounced with increasing water content, whereas in the case of the iridium complex, the ACQ effect remains constant across all mixtures (grey curve). A common feature, however, is a red shift in the emission wavelength (blue curve sharply rises) at 90% water, which is consistent with aggregate formation and system stabilization. It must be also mentioned that the emission wavelengths differ slightly; while the ruthenium complex emits in the orange region, the iridium complex emits from blue to yellow depending on the water content of the mixture.

Table 7. *Emission intensity (grey) and λ_{max} emission (blue) of (a) CH04-IN (b) CH05-IN in THF at different w.r. λ_{exc} = 380 nm*

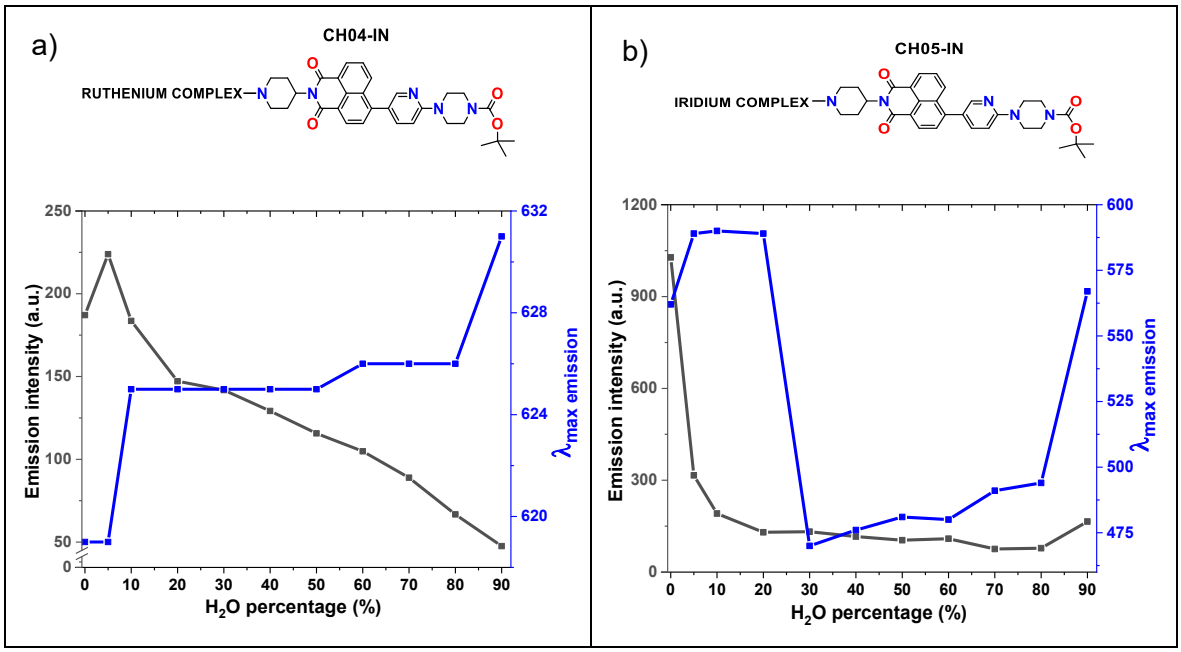

5. NANOPARTICLES MORPHOLOGY

First, it should be noted that in the previous section, the emission tests in THF-water mixtures were conducted at a concentration of 10^{-5} M; hence, the nanostructures formed by these compounds at that concentration are available in the Supporting Information of this chapter. However, future studies within this chapter had to be performed at a tenfold higher concentration of 10^{-4} M. For a comprehensive analysis of these studies, it is necessary first to determine the nanostructures formed by the compounds at this increased concentration. So, this section includes several pictures obtained by field emission scanning electron microscopy (FESEM) of the mixtures (10^{-4} M) with a high-water content.

5.1. NANOSTRUCTURES OF CH04-IN

First, CH04-IN was imaged. Very big nanovesicles have been observed and their walls seem to be formed by several layers *(Figure 5).*

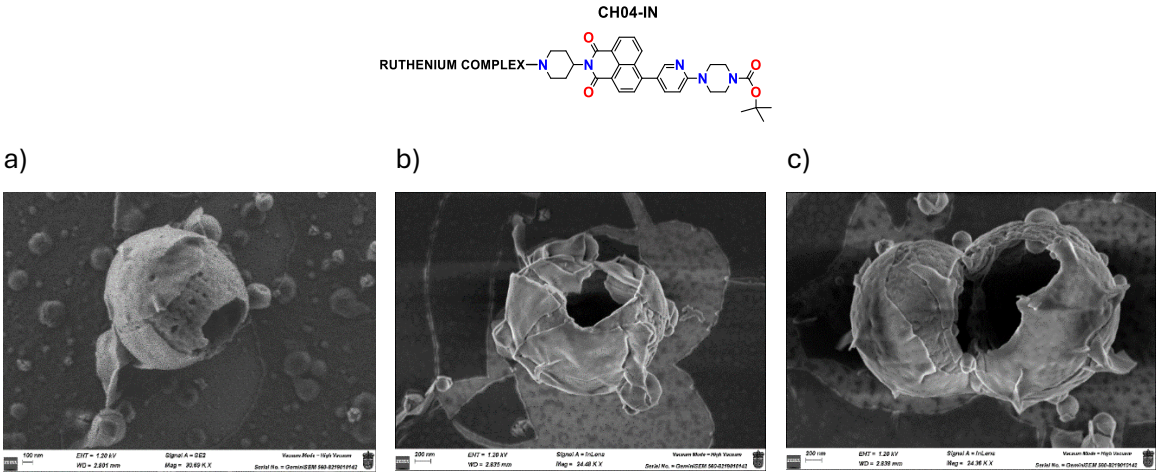

Figure 5. *FESEM images of CH04-IN in THF-H_2O. (a) 70% w.r. (b, c) 80% w.r. (10^{-4} M)*

Then, an EDX analysis was conducted to determine whether the ruthenium and carbon content was homogeneous inside and outside the vesicles. So, an elemental analysis of the vesicle cavity and wall was performed, in order to clarify if the NMIs could be arranged in such a way that the ruthenium complex is preferentially positioned in a specific region of the vesicle. However, the results showed the elemental distribution was homogeneous throughout all the vesicles *(Figure 6).*

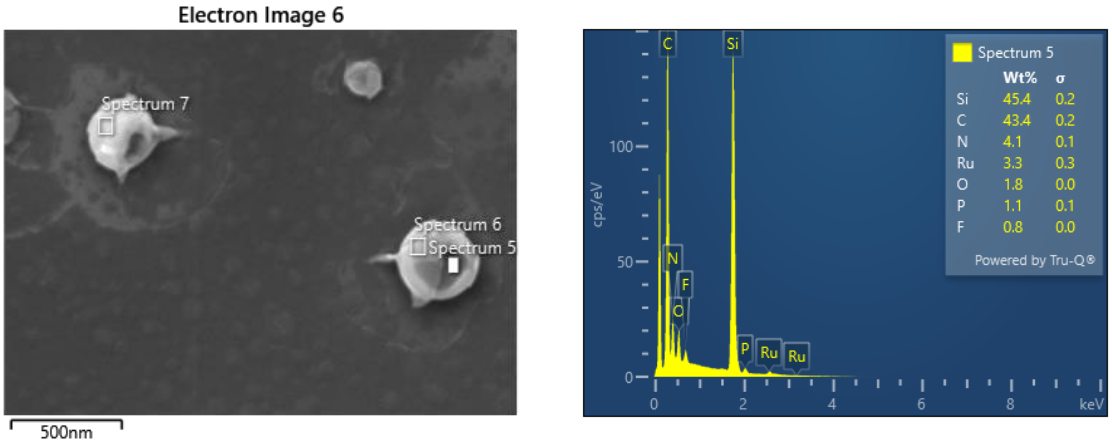

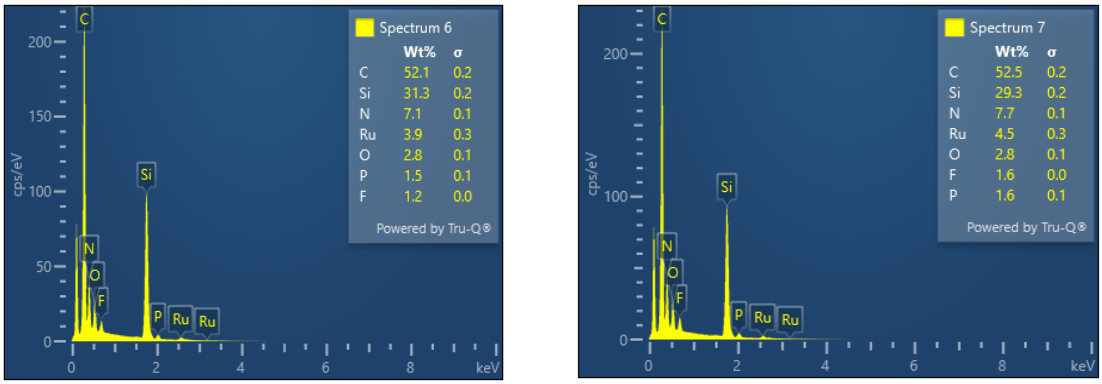

Figure 6. *Punctual EDX spectra of CH04-IN (70% w.r.)*

As observed, ruthenium accounts for approximately 3-4% of the total elemental composition, with very similar values across all regions of the vesicle.

5.2. NANOSTRUCTURES OF CH10-IN

Similar to the previous semi-functionalized ruthenium compound, CH10-IN forms large nanovesicles with an irregular surface.

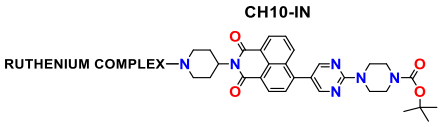

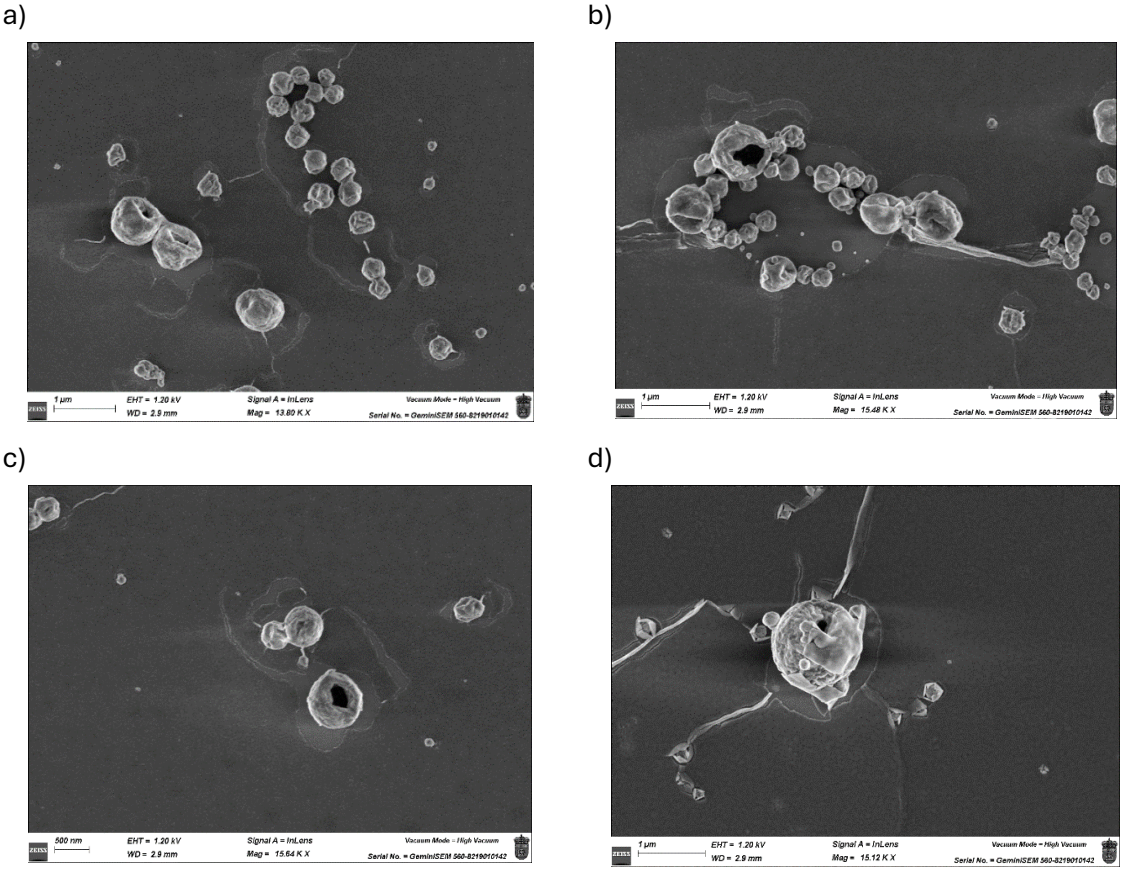

Figure 7. *FESEM images of CH10-IN in THF-H_2O: (a, b, c) 70% w.r. (d) 80% w.r. (10^{-4} M)*

5.3. NANOSTRUCTURES OF CH05-IN

CH05-IN (iridium) exhibits a somewhat different behaviour compared to the other compounds. It forms well-defined and homogeneous nanovesicles, which tend to aggregate in a similar way to that observed in the previous chapters (NMI units bonded to amino acids). In this case, aggregates of homogeneous vesicles are formed, and they can be observed at both 10^{-5} M and 10^{-4} M concentrations. For this reason, microscopy images at 10^{-5} M are also included for comparison *(Figure 8)*. Although aggregation is evident at both concentrations, the number of vesicles is significantly higher in the more concentrated solutions *(Figure 9)*.

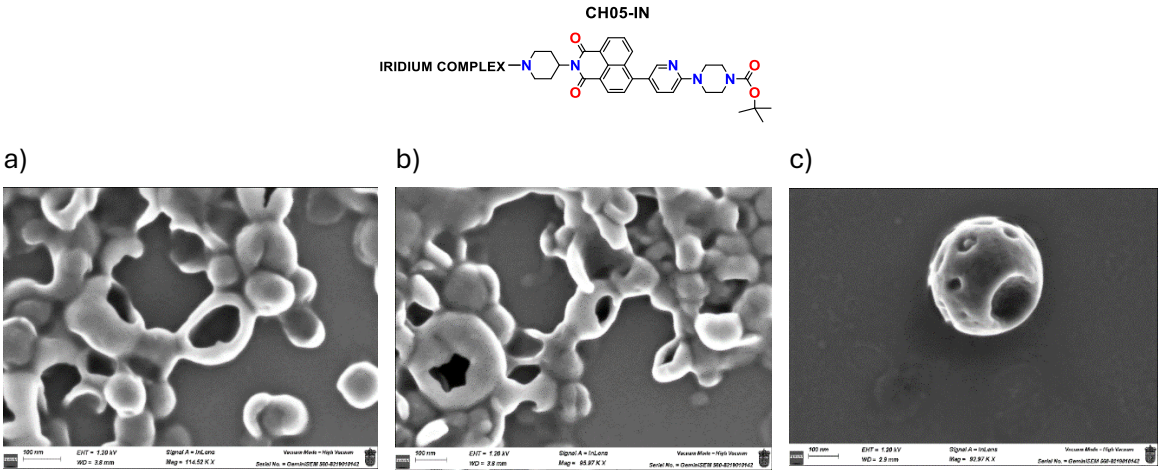

Figure 8. *FESEM images of CH05-IN in THF-H_2O: (a, b) 70% w.r. (c) 80% w.r. (10^{-5} M)*

In the previous figure, it can be observed that the vesicles do not have a double-layered wall, nor are they as large as those observed for the two previously described compounds. In this case, the vesicles are much smaller and appear as aggregated structures, what is further supported by the following images recorded at 10^{-4} M.

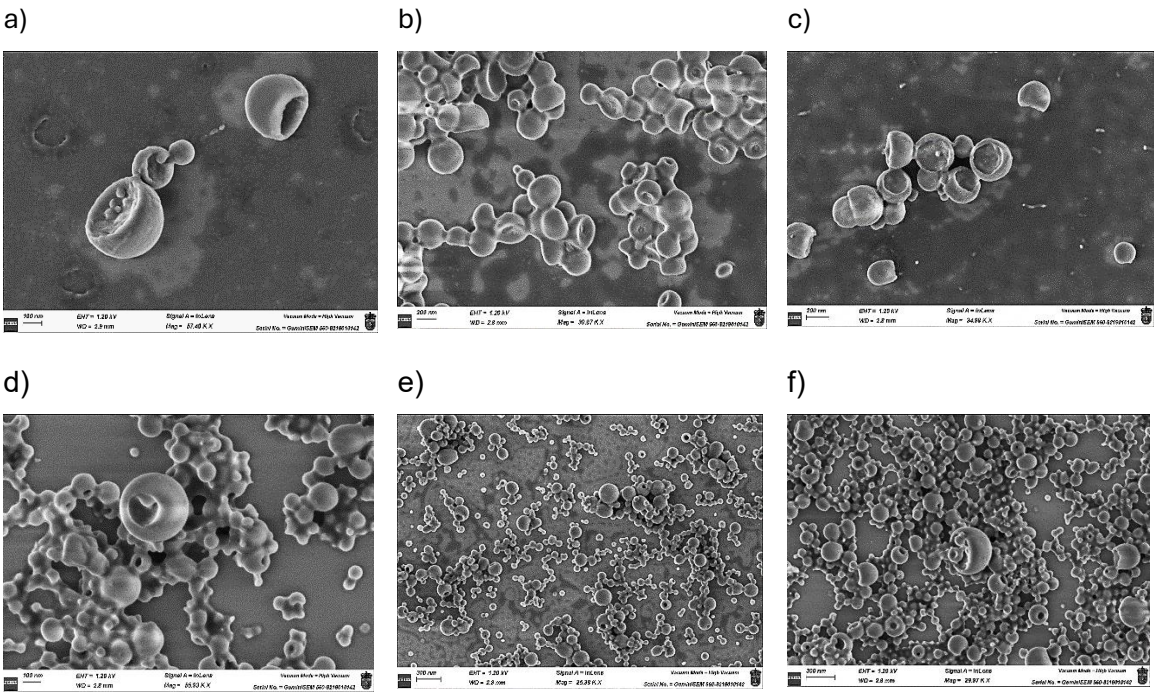

Figure 9. *FESEM images of CH05-IN in THF-H_2O: (a, b, c) 70% w.r. (d, e, f) 80% w.r. (10^{-4} M)*

5.4. NANOSTRUCTURES OF CH08-IN

In this last case, the compound contains two iridium centres and, similarly to the ruthenium-based compounds, forms large vesicles with irregular walls. These structures were only found at high concentrations (10^{-4} M).

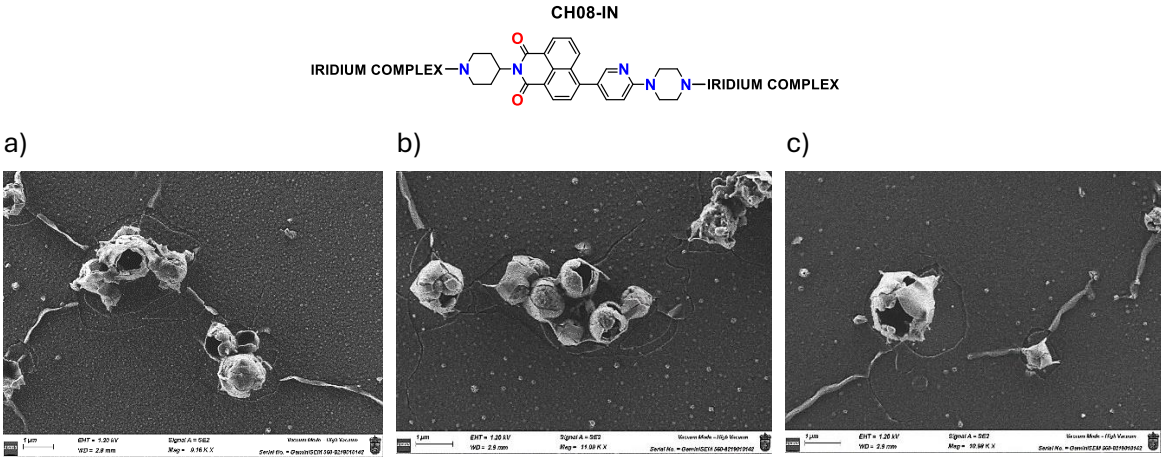

Figure 10. *FESEM images of CH08-IN in THF-H_2O: (a) 70% w.r. (b, c) 80% w.r. (10^{-4} M)*

6. THEORETICAL BACKGROUND OF EXCITED-STATE DYNAMICS

In the next section, the ultrafast excited-state behaviour of the organometallic compounds is studied. To get it, transient absorption spectroscopy (TAS) has been performed by chemical-physics experts. Our focus includes the formation of intermediate excited states, stimulated emission, and the formation of long-lived triplet states. Here below is a brief theoretical introduction about this technique and its fundamentals.

6.1. PRINCIPLES OF TRANSIENT ABSORPTION SPECTROSCOPY

Transient absorption spectroscopy, also known as pump-probe spectroscopy, is a nonlinear optical technique used to monitor ultrafast changes in a sample's absorbance following photoexcitation. The experiment involves two laser pulses:[14]

- *Pump pulse:* A strong, ultrashort laser pulse excites the sample to an electronic excited state, creating a non-equilibrium population and depleting the ground state.
- *Probe pulse:* A weaker, broadband pulse, delayed in time, measures how the sample's absorbance evolves after excitation.

By recording the change in optical density (ΔA(λ, t)) at various time delays, TAS reveals the dynamics of excited-state processes with femtosecond resolution. The optical density is defined as:[15]

$$\Delta A\,(\lambda, t) = -log_{10}\frac{I_{probe,\ pump-on\,(\lambda,t)}}{I_{probe,\ pump-off\,(\lambda,t)}} \qquad \text{Eq. 1}$$

Where $I_{probe,\ pump\text{-}on}$ is the intensity of the probe pulse transmitted through the sample after excitation by the pump pulse, measured at wavelength λ and delay time t. It represents the "excited" state of the system. Whereas $I_{probe,\ pump\text{-}off}$ is the intensity of the probe pulse

[14] J. A. Cina, *Getting Started on Time-Resolved Molecular Spectroscopy*. Oxford University Press. **2022,** chapter 3. pp 47−76.
[15] N. Li, Y. Ma, W. Sun, *Molecules* **2024**, *29*, 3995.

transmitted through the sample without any prior excitation (i.e., with the pump pulse turned off). This serves as the baseline or reference transmission.

The logarithmic ratio quantifies the relative change in transmission due to photoexcitation. A positive ΔA indicates increased absorption (e.g., due to excited-state absorption), while a negative ΔA implies reduced absorption or increased transmission, often due to ground-state bleaching (GSB) or stimulated emission (SE). All these new spectral concepts are explained below. For better understanding it can be expressed in terms of absorbance:

$$\Delta A\ (\lambda, t) = A_{probe,\ pump-on} - \ A_{probe,\ pump-off} \qquad \text{Eq. 2}$$

Spectral features in Transient Absorption Spectra

Transient absorption spectra show important signals that help identify what happens to molecules after they are excited. The three main types of spectral features are:[16]

- *Ground State Bleach (GSB):* a negative ΔA signal arising from depletion of ground-state population after excitation. It appears at wavelengths where the ground state originally absorbed. If the ground state is depleted, the transmission is higher, which results in a quotient of the logarithm greater than one, and therefore in a negative optical density.
- *Excited State Absorption (ESA):* a positive ΔA signal due to further absorption by excited species (e.g., $S_1 \rightarrow S_n$ or $T_1 \rightarrow T_n$ transitions). ESA bands provide evidence of intermediate states and their dynamics.
- *Stimulated Emission (SE):* it occurs when an excited molecule returns to a lower energy state (typically the ground state) by emitting a photon that is coherent with an incident probe photon. If the probe pulse interacts with an excited population (e.g., in S1) at a wavelength corresponding to the excited-state emission band, the emitted photons will add to the transmitted probe signal. This leads to an apparent increase in transmission, which manifests as a negative ΔA signal, similar in sign to GSB but distinct in origin and spectral position. SE typically appears at longer wavelengths (red-shifted) compared to excitement.

In addition to these primary spectral features, transient absorption spectroscopy is particularly powerful for determining the formation and decay of long-lived excited states, especially triplet states. In the case of organometallic complexes, photoexcitation often leads spin-orbit coupling, which facilitates intersystem crossing from initially formed singlet excited states (S_n) to long-lived triplet excited states (T_n). It is typical to observe metal-to-ligand charge transfer (^{3}MLCT) states.[17] Triplet states are characterized by two unpaired electrons with parallel spins. Due to their longer lifetimes (ranging from nanoseconds to microseconds, or even longer) compared to singlet excited states (typically picoseconds or less), triplet states are often the key intermediates responsible for photochemical reactions, energy transfer, or photocatalytic activity. Their long lifetime allows them more time to interact with other molecules or undergo chemical transformations.[18]

[16] R. Berera, R. van Grondelle, J. T. M. Kennis, *Photosynth. Res.* **2009,** *101,* 105–118.

[17] A. Stamoulis, M. Mato, P. C. Bruzzese, M. Leutzsch, A. Cadranel, M. Gil-Sepulcre, F. Neese, J. Cornella, *J. Am. Chem. Soc.* **2025,** *147* (7), 6037−6048.

[18] C. Daniel, *Absorption Spectroscopy, Emissive Properties, and Ultrafast Intersystem Crossing Processes in Transition Metal Complexes: TD-DFT and Spin-Orbit Coupling.* In: N. Ferré, M. Filatov, M. H. Rotllant, *Density-Functional Methods for Excited States, Topics in Current Chemistry*, Springer Internat., **2016,** Vol 368. pp. 377−414.

6.2. ASSOCIATED DIFFERENCE SPECTRA AND KINETIC ANALYSIS

Transient absorption signals are inherently multidimensional, encompassing spectral (wavelength) and temporal (delay time) information. These signals often include overlapping features from different excited-state processes, such as ground-state bleaching, stimulated emission, and excited-state absorption. This overlap makes it difficult to interpret the data directly, especially when several species or states are involved.[19] This highlights the need to separate these contributions for clearer analysis. So, to get it, a powerful analytical tool is employed:

Evolution-Associated Difference Spectra (EADS), sometimes called species-associated or decay-associated spectra, are used to better understand the complex signals measured in transient absorption experiments. To separate the overlapping signals, a mathematical analysis called global fitting is applied. Through this method, the time-resolved absorption changes are modelled as a sum of exponential decays, where each decay component corresponds to a particular species or process.[20] So, each component is represented in one ADS, highlighting its individual contribution to the overall time-resolved response. In other words, ADS help identify which part of the spectrum comes from which step in the process, and how fast that step happens. This makes it much easier to understand the full sequence of changes that the molecule undergoes after being excited by light.

7. TIME-RESOLVED SPECTROSCOPIC ANALYSIS

Once the theoretical bases of excited-states spectroscopy have been established, it is possible to analyse the organometallic compounds described in this chapter. Nevertheless, before proceeding with it, it is important to note that previous analyses were done. First, the two employed metal complexes were independently studied by ultrafast transient absorption spectroscopy. In both cases, the spectral features and excited-state dynamics observed were found to be consistent with those reported in the literature for related Ru(II) and Ir(III) complexes bearing bipyridine and phenylpyridine ligands.[21,22] This includes the characteristic formation of long-lived ^{3}MLCT states and typical ground-state bleach. In most documented cases, no triplet d-d excited state (^{3}dd) is detected, confirming that ^{3}MLCT is the dominant and long-lived excited state governing the observed dynamics.[23] On the other hand, transient absorption of the isolated naphthalimide core (without functionalization) was also studied. The results showed no intermediate excited states or any significant transient signals. Only upon coordination to the metal centre it is possible to observe charge transfer processes and notable transient absorption activity, which is described in the following sections.

7.1. EXCITED-STATES: ANALYSIS OF CH04-IN

Transient absorption analysis

In previous studies it has been shown that CH04-IN experiences an emission quenching in mixtures with high water percentage (above 70% w.r.) due to aggregation processes. It was also seen that CH04-IN forms irregular nanovesicles in those mixtures at 10^{-4} M. In *Figure 11* transient absorption spectra are reported, recorded at 10^{-4} M in two pure solvents (methanol and tetrahydrofuran) and in three different THF-water mixtures: 70%, 80%, and 90% w.r., exciting at 350 nm.

[19] I. H. M. van Stokkum, D. S. Larsen, R. van Grondelle, *Biochim. Biophys. Acta, Bioenerg*. **2004,** *1657* (2–3), 82–104.
[20] J. E. Loefroth, *J. Phys. Chem.* **1986,** *90* (6), 1160−1168.
[21] P. Müller, P, K. Brettel, *Photochem. Photobiol. Sci.*, **2012,** *11,* 632–636.
[22] G. J. Hedley, A. Ruseckas, I. D. W. Samuel, *Chem. Phys. Lett.* **2008,** *450* (4-6), 292−296.
[23] N. H Damrauer, G. Cerullo, A. Yeh, T. R. Boussie, C. V. Shank, J. K. McCusker, *Science* **1997,** *275,* 54−57.

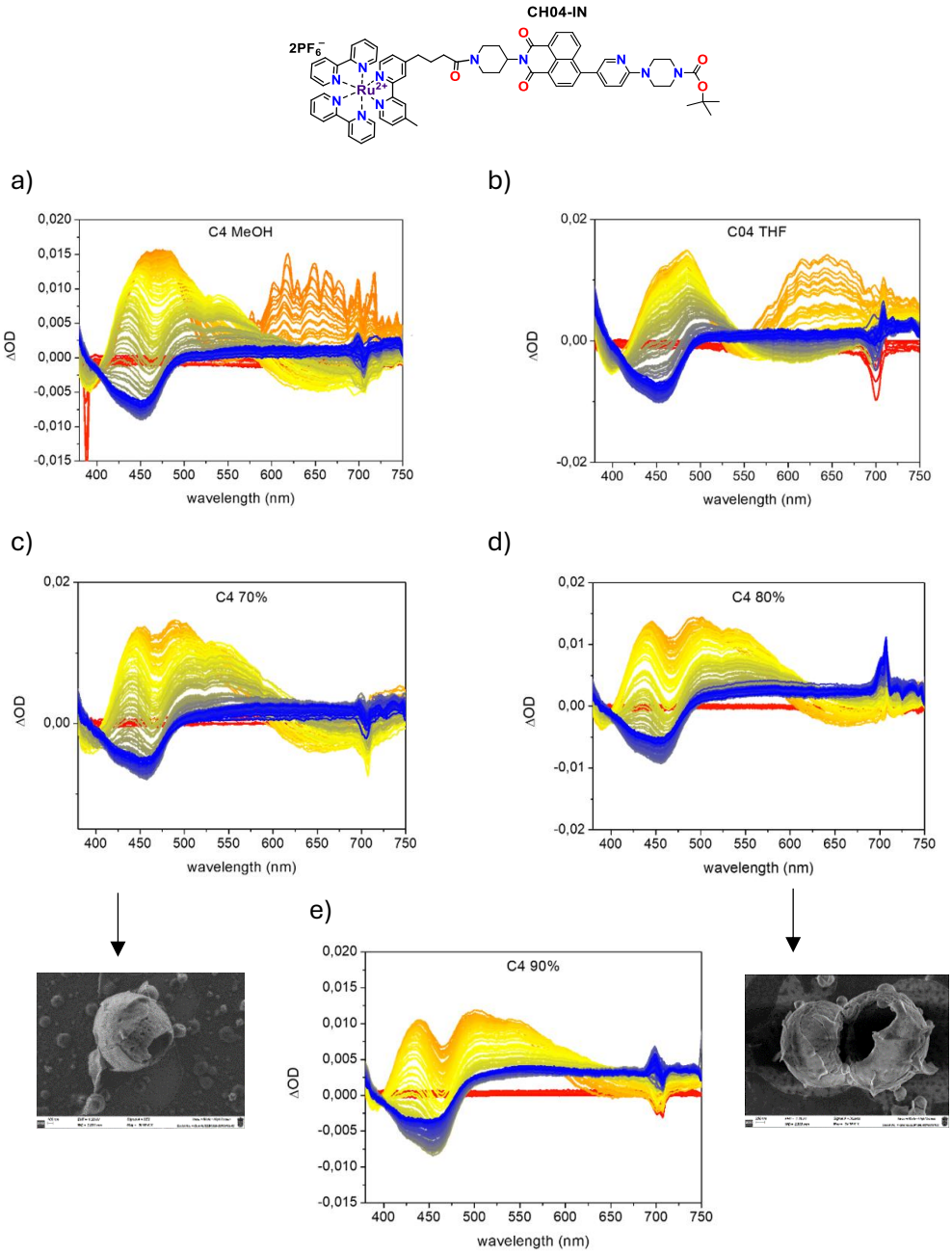

Figure 11. *Transient Absorption Spectra of CH04-IN in (a) methanol, (b) THF, (c) THF:H_2O 70% H_2O, (d) THF:H_2O 80% H_2O, (e) THF:H_2O 90% H_2O. The respective FESEM images of the vesicles are shown.*

The spectra are colour-coded according to delay time, ranging from red (near time zero) to blue (end of the delay scan at 3.5 ns). Orange corresponds to the first few picoseconds after excitation, with the evolution of the spectral features progressing from yellow to blue as time increases.

It is observed that the spectral features of the aggregates in the THF-water mixtures resemble those of the compound in pure methanol more than in pure THF. This behaviour can be attributed to the higher polarity of the THF-water mixtures (water ε = 78.5), which is more comparable to methanol (ε = 32.6) than to THF (ε = 7.4).

The long living state (blue) appears largely unaffected by the solvent environment and is likely ascribed to the triplet state of the ruthenium complex, consistent with previous studies.

Evolution-Associated Spectra and Kinetic Analysis

As described in the theoretical section, it is possible to decompose these spectra in different components and determine their associated lifetimes. For this purpose, the evolution-associated difference spectra are obtained and reported in *Figure 12*.

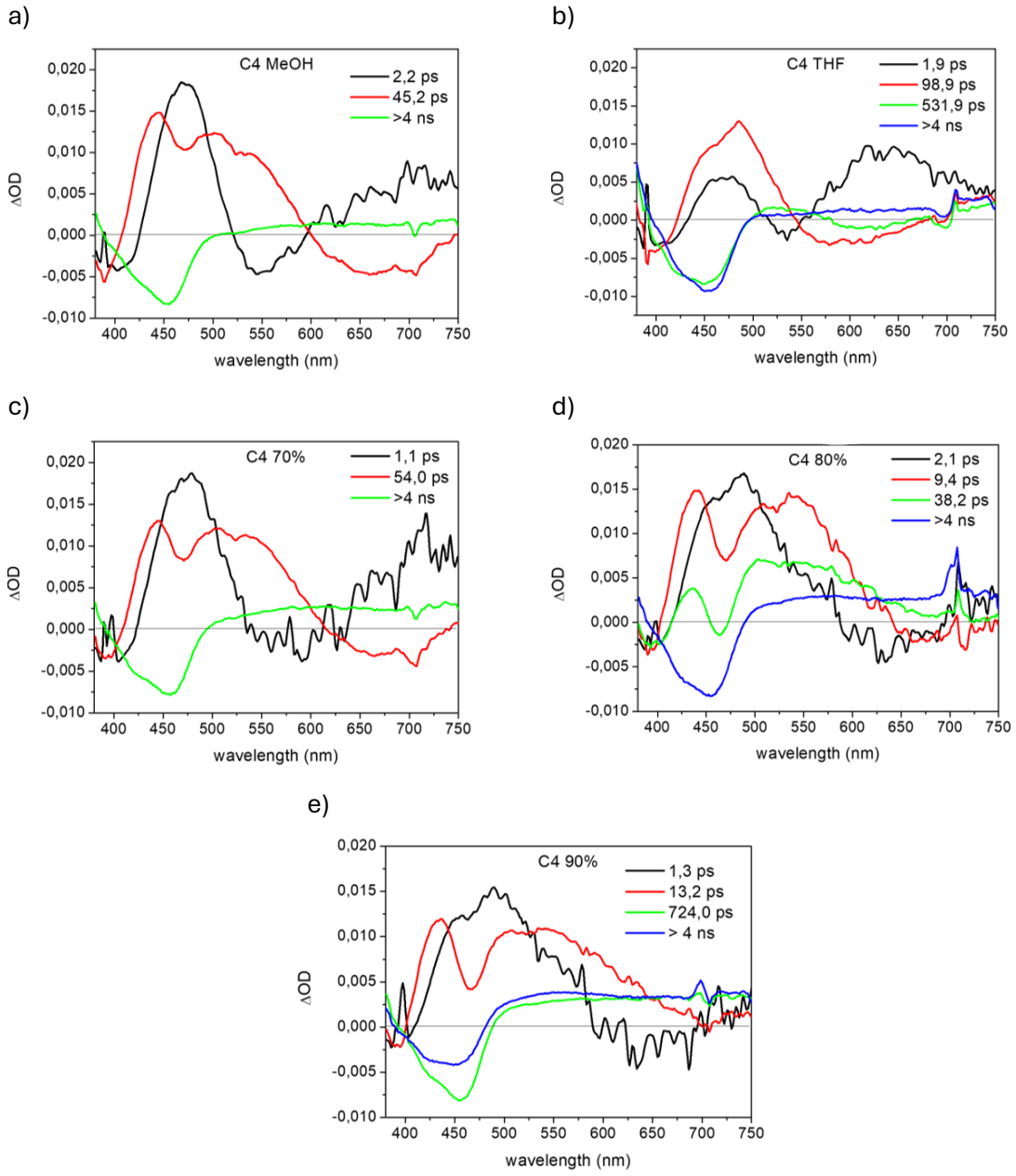

Figure 12. *Evolution Associated difference Spectra of CH04-IN in (a) methanol, (b) THF, (c) THF:H_2O 70% H_2O, (d) THF:H_2O 80% H_2O, (e) THF:H_2O 90% H_2O.*

As observed, these graphs reveal the evolution of excited states and the dynamics of energy transfer within the molecule at different times.

The excitation wavelength was 350 nm, at which both the Ru complex and the organic ligand can be excited. At the short timescale the transient spectra are dominated by positive bands, attributed to excited state absorption signals (ESA), which evolve on a fast timescale of a few picoseconds (evolution from black to red lines). Successively the spectral shape evolves, indicating the relaxation towards a different state, which could involve an energy

or charge transfer process (red lines). We observe a variation in the shape of the positive band, and the formation of a negative signal in the 600-750 nm region, that can be assigned to a stimulated emission (as previously mentioned, it appears shifted toward longer wavelengths). In the 80% and 90% water-containing samples, the stimulated emission band is observed on a shorter timescale, suggesting a different excited-state relaxation pathway in excess water conditions.

The final state (blue line) corresponds to the formation of a metal centred triplet state (it is a negative signal because there is a ground-state bleaching, since the population has been previously promoted to excited states). The timescale of the relaxation towards this triplet state appears to be dependent on the environment and its polarity. Comparing methanol and THF, triplet formation occurs within 45 ps in methanol, and >200 ps in THF. In THF-water mixtures, the relaxation towards the triplet state becomes faster by increasing the water percentage (54 ps in 70% H_2O/THF; 38 ps in 80% H_2O/THF and 13 ps in 90% H_2O/THF). The lifetime of the final state exceeds the temporal resolution of the measurements.

The fact that the excited triplet state appears faster as the water content increases is noteworthy. This behaviour is likely related to the aggregation of the naphthalimide units, which tend to stack in aqueous-rich environments. Such aggregation facilitates intermolecular interactions. These close contacts between chromophores in the aggregated state may promote energy transfer between different molecules, thereby enabling more efficient population of the triplet state through intermolecular pathways, rather than through purely intramolecular processes. This effect becomes more pronounced as the water content increases, since aggregation is enhanced and, consequently, the efficiency of intermolecular energy transfer increases. The temporal difference in the formation of the triplet state can be further determined through a kinetic analysis.

Kinetic traces of the triplet state

The kinetic traces at the maximum of the negative band, indicative of triplet formation, are normalized and superimposed, highlighting that the relaxation towards the triplet state becomes faster by increasing the water content.

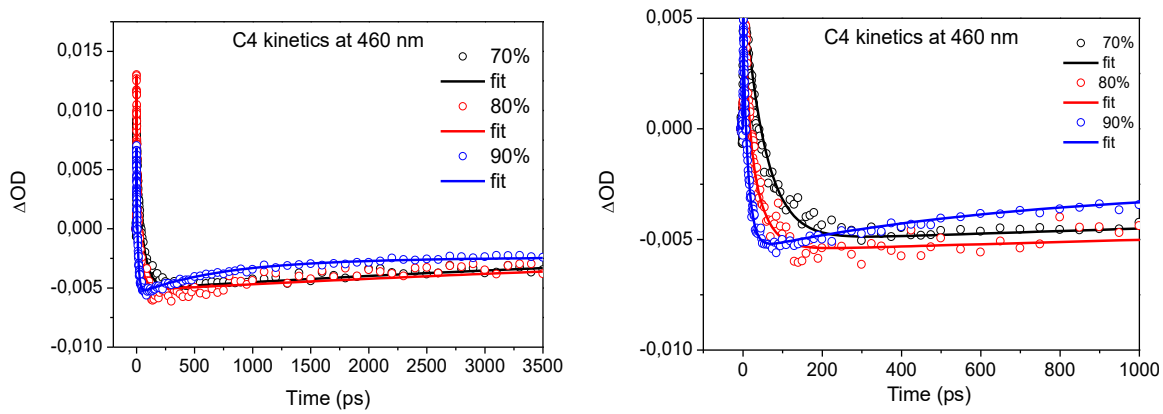

Figure 13. *Kinetic traces at 460 nm of CH04-IN in THF:H_2O 70% (black), THF: H_2O 80% (red), THF:H_2O 90% (blue).*

7.2. EXCITED-STATES: ANALYSIS OF CH10-IN

Before starting with the transient absorption measurements, it is necessary to examine the steady-state emission spectra of the compound in THF-water mixtures with increasing water content *(Figure 14),* as this compound exhibits a particular behaviour under these conditions.

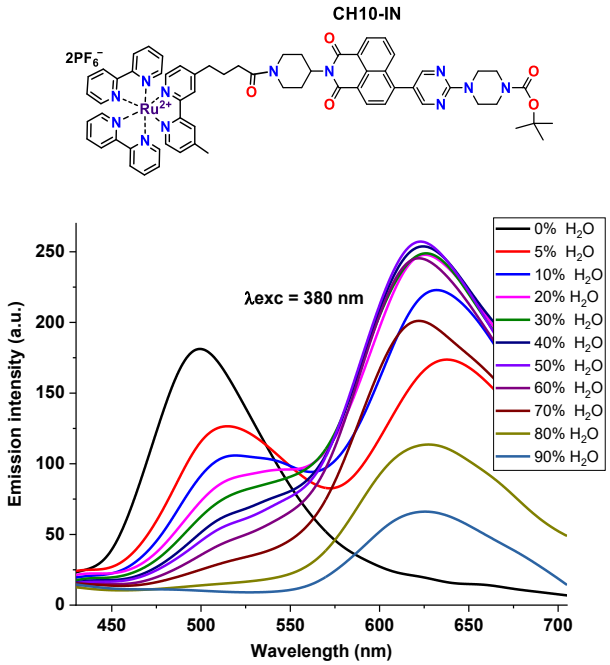

Figure 14. *Emission intensity of CH10-IN at different w.r. λ_{exc} = 380 nm.*

As observed, in mixtures with low water percentage, there are two emission bands (red line 5% w.r.) and, as the water ratio increases, one of the bands disappears. CH10-IN exhibits a different behaviour compared to the previously studied ruthenium compound CH04-IN. Although CH10-IN contains only one additional nitrogen atom, the gradual addition of water does not lead to a simple aggregation caused quenching effect. Instead, it is observed an evolution in the emission profile: the initial single-band emission characteristic of the monomer (black, pure THF) evolves into a dual-band structure upon increasing water content (5-60% w.r.). At higher water concentrations (>70%), the monomer-associated band is nearly absent, while the new emission band associated to a dimeric form in the aggregates becomes dominant. Hence, the charge transfer processes that will be observed in the next section are likely attributed to intermolecular exchange between the two moieties comprising the dimer.

Transient absorption analysis

The following section analyses the transient absorption spectra of a compound similar to the previous one (featuring a ruthenium complex), but in this case instead of a pyridine unit CH10-IN has a pyrimidine moiety. FESEM images revealed that at high water percentages this compound also forms big vesicles, due to aggregation processes.

In *Figure 15* transient absorption spectra are reported, recorded at 10^{-4} M in pure tetrahydrofuran and in three different THF-water mixtures: 70%, 80%, and 90% water by volume, exciting at 350 nm. In the same way as the previous compound, the spectra are colour-coded according to delay time, ranging from red (near time zero) to blue (end of the delay scan at 3.5 ns). Orange corresponds to the first few picoseconds after excitation, with the evolution of the spectral features progressing from yellow to blue as time increases.

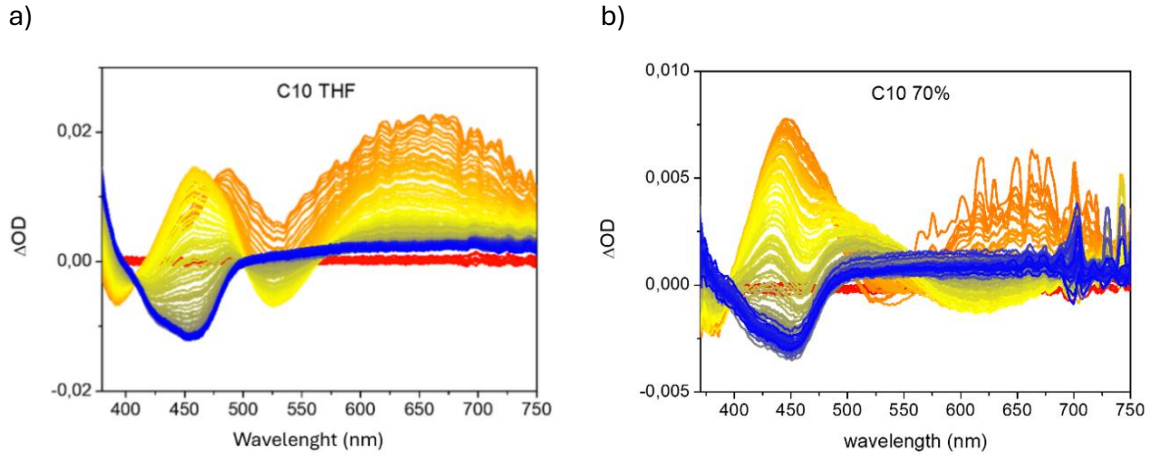

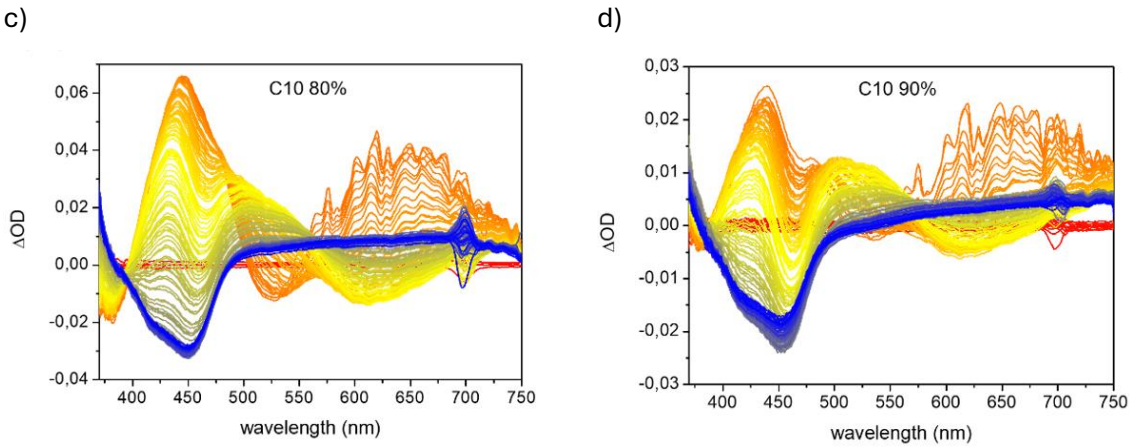

Figure 15. *Transient Absorption Spectra of CH10-IN (a) THF, (b)THF:H_2O 70% H_2O, (c)THF:H_2O 80% H_2O, (d) THF:H_2O 90% H_2O.*

The spectral features are similar to those observed for compound CH04-IN, with two notable differences: in pure THF, the stimulated emission band around 620-630 nm is absent, and a distinct signal appears at 520 nm. This signal only appears in pure THF, just like the monomer emission band observed in the steady-state emission spectrum, which appeared at the same wavelength as this distinct signal in transient absorption. In contrast, the stimulated emission at 620-630 nm is clearly observed in the water-containing samples, which is consistent with the dimer formation previously identified in the steady-state emission spectra. Interestingly, this stimulated emission occurs at the same wavelength as the dimer emission band in the steady-state spectra, further supporting the assignment of this feature to the aggregated species. As in the case of compound CH04-IN, the final state (blue) is attributed to the metal centred triplet state.

Evolution-Associated Spectral and Kinetic Analysis

To better understand the previously discussed spectra, they were deconvoluted into Evolution-Associated Difference spectra, allowing us to analyse the spectral features associated with each kinetic component over time.

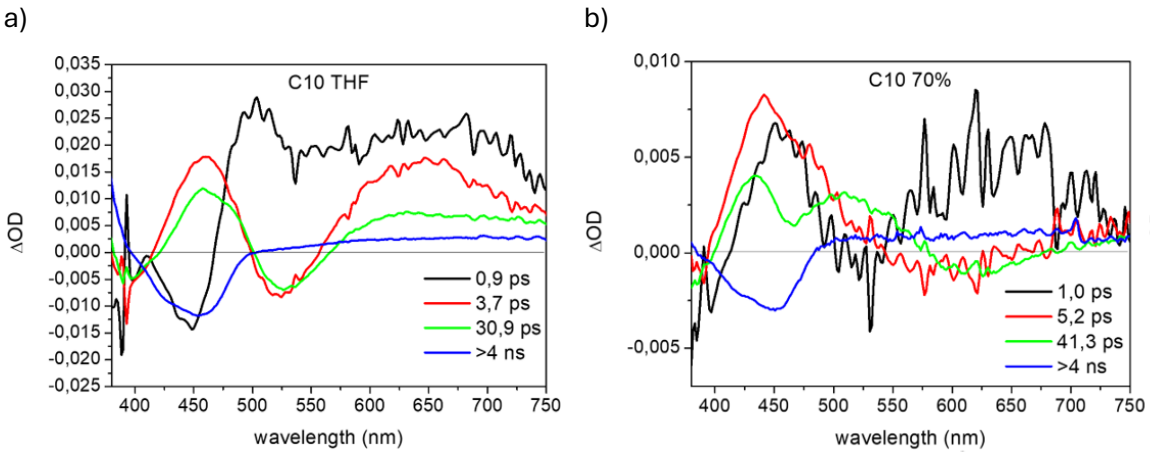

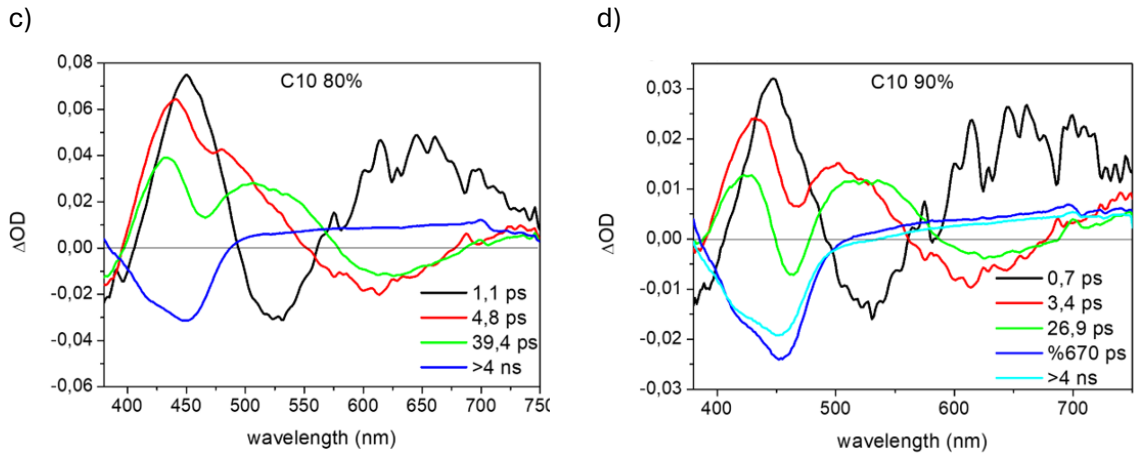

Figure 16. *Evolution Associated difference Spectra of CH10-IN in (a)THF, (b) THF:H_2O 70%, (c) THF:H_2O 80%, (d) THF:H_2O 90%*

The behaviour of the CH10-IN samples is qualitatively similar to that of CH04-IN. In this case, the photodynamics appears to be less sensitive to the polarity of the environment. As observed previously, at high water content, a stimulated emission signal appears (seen as red and green negative curves at longer wavelengths). Notably, the formation of the triplet state occurs on a comparable timescale in both pure THF and THF-water mixtures (approximately 30-40 ps) with only a slight acceleration observed as the water content increases. However, at 90% water, a modest but clear enhancement in the rate of triplet-state formation is detected, indicating that even in this less polarity-sensitive system, aggregation or dimer formation still subtly influence the excited-state relaxation dynamics. It is worth noting that the red curves, as observed in the spectra of CH04-IN, can be associated with energy transfer processes. These processes may occur between two different NMI units, as well as between the naphthalimide core and the metal centre within the same molecule.

Kinetic traces of the triplet state

The kinetic traces at the maximum of the negative band (460 nm) indicating triplet formation are normalized and superimposed, highlighting that the relaxation towards the triplet state appears at similar time at 70 and 80% w.r. It is a little faster at 90% w.r.

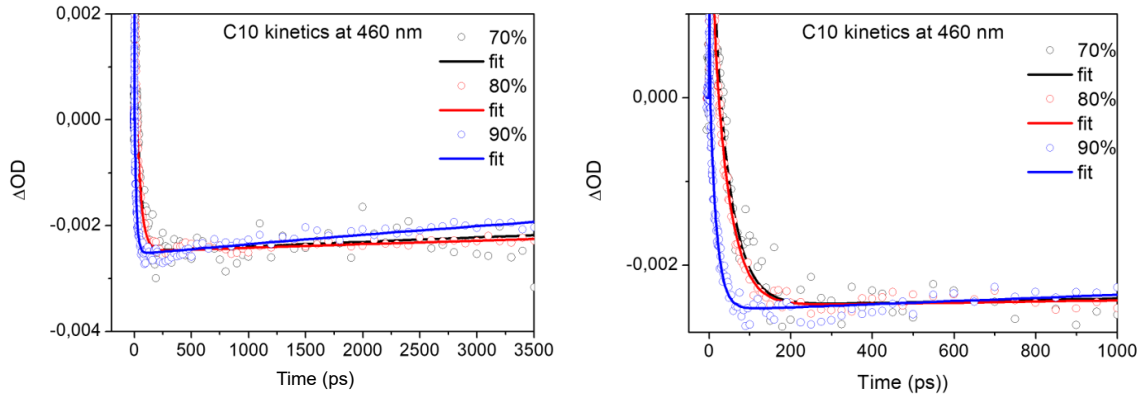

Figure 17. *Kinetic traces at 460 nm of CH10-IN in 70% H_2O/THF (black), 80% H_2O/THF (red), 90% H_2O/THF (blue).*

7.3. EXCITED-STATES: ANALYSIS OF CH05-IN

Transient absorption analysis

In this case, the compound contains an iridium complex instead of ruthenium, and it has been observed that in water-rich mixtures it forms well-defined aggregates composed of a large number of uniform vesicles. In *Figure 18* transient absorption spectra are collected, recorded at 10^{-4} M in two pure solvents (methanol and tetrahydrofuran) and in mixtures of THF and water (above 70% w.r.). The samples were excited at 350 nm. The spectra follow the same colour code as used for the previous compounds. In this case, the absence of a negative band at longer wavelengths suggests that stimulated emission does not occur.

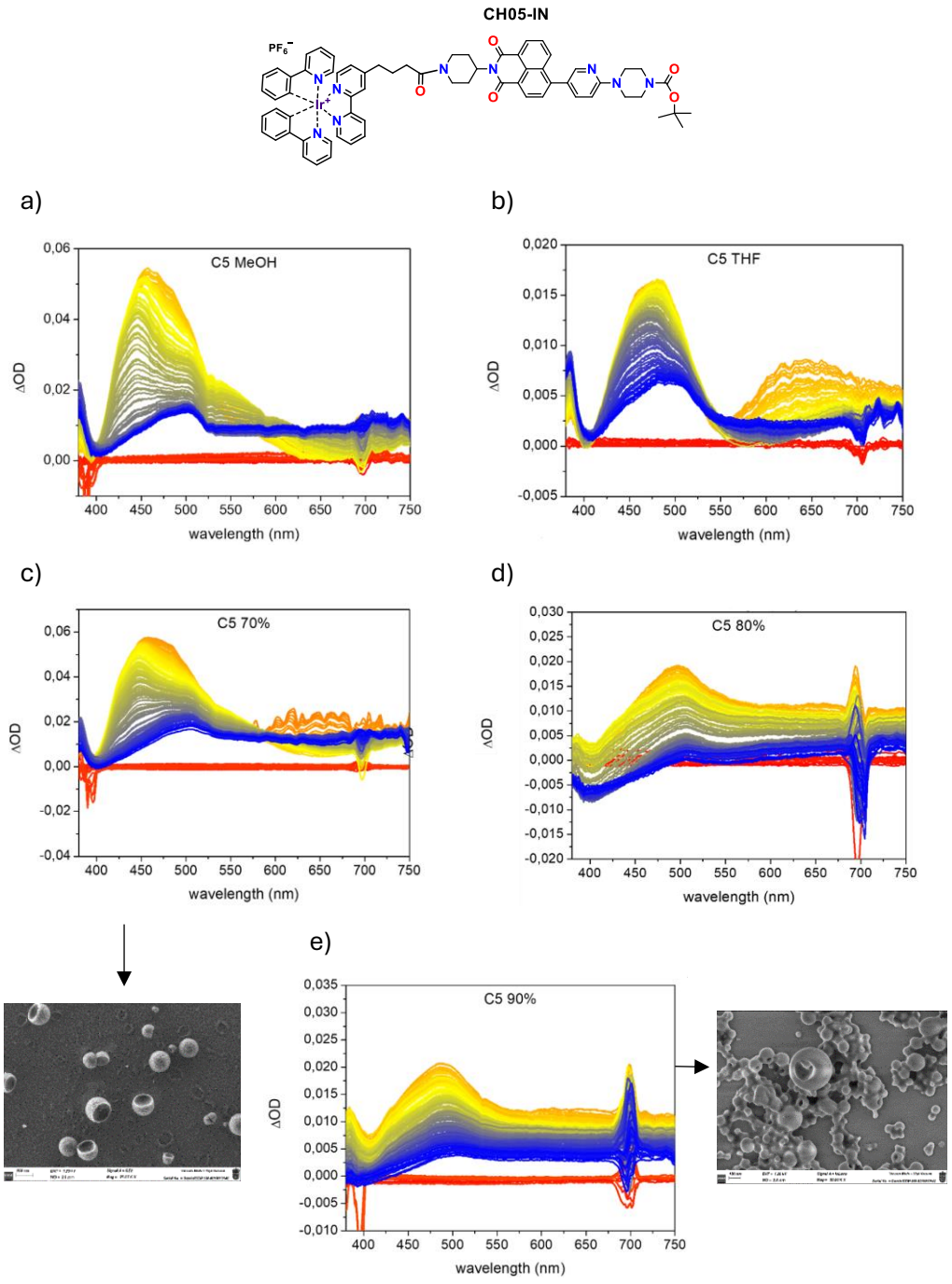

Figure 18. *Transient Absorption Spectra of CH05-IN in (a) methanol, (b) THF, (c) THF:H_2O 70% H_2O, (d) THF:H_2O 80% H_2O, (e) THF:H_2O 90% H_2O. The respective FESEM images of the aggregates are also shown.*

Evolution-Associated Spectral and Kinetic Analysis

To better understand the transient absorption graphs, evolution associated difference spectra have been obtained *(Figure 19).*

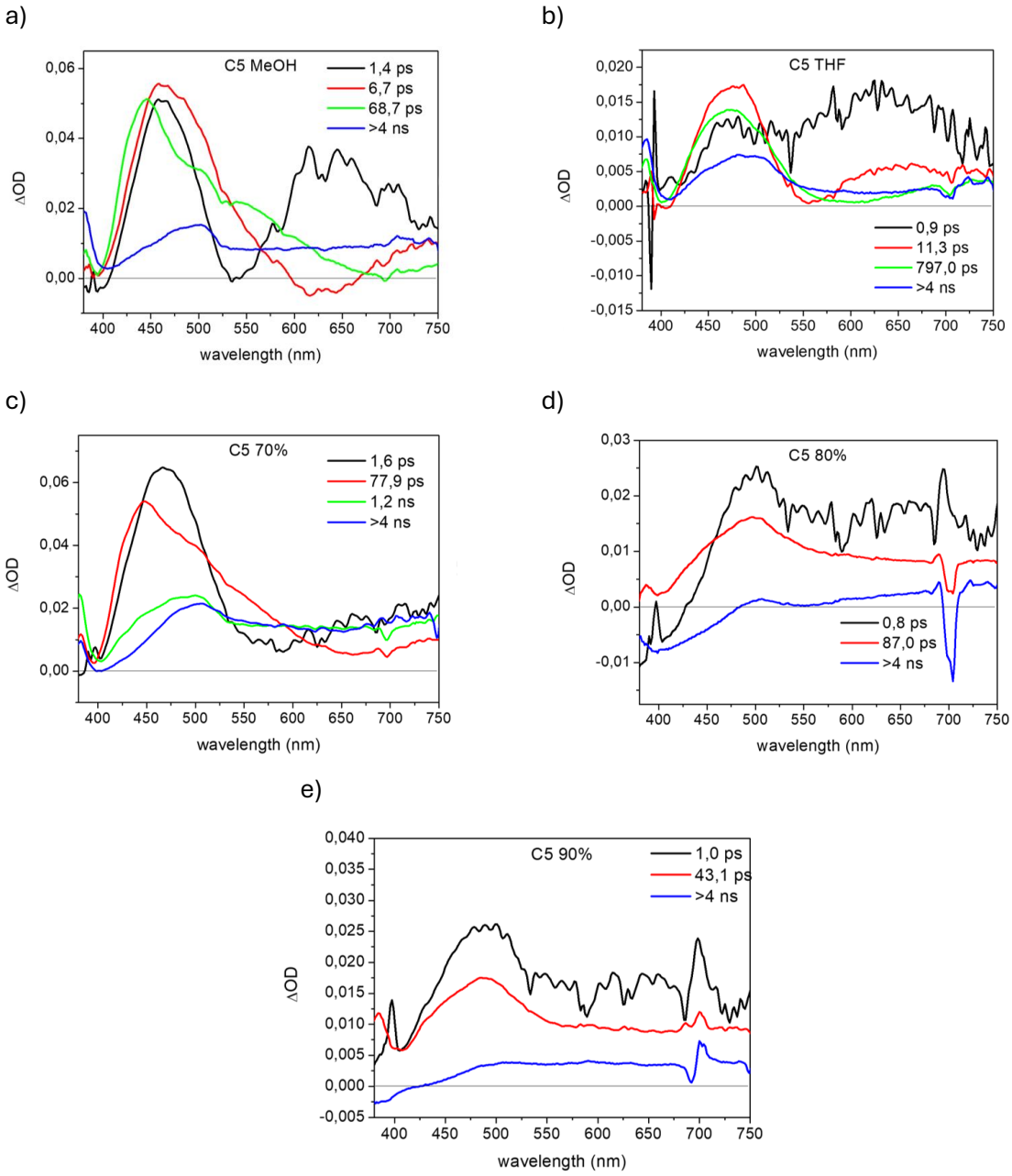

Figure 19. *Evolution Associated difference Spectra of CH05-IN in (a) methanol, (b) THF, (c) THF:H_2O 70% H_2O, (d) THF:H_2O 80% H_2O, (e) THF:H_2O 90% H_2O.*

For compound CH05-IN, the excited-state dynamic varies with the environment. Triplet formation is observed in both methanol and THF, and it occurs much faster in the polar solvent (about 70 ps in methanol and about 800 ps in THF, corresponding with the evolution from green to blue component). Upon water addition, the triplet state is still clearly observed only in the THF:H_2O 70% H_2O mixture, where it is formed in about 1.2 ns. By increasing the water content, the spectral shape of the long living component changes and slightly deviates from what observed in pure solvents, reflecting both a lower degree of triplet state formation

and its appearance at longer timescales. In this case, aggregation has the opposite effect compared to the previous compounds, delaying the formation of the triplet state.

Kinetic traces of the triplet state

For CH05-IN, the kinetic traces at the maximum of the long-lived state (500 nm) and in the red region (660 nm) are superimposed between the three different water ratios, revealing a similar behaviour for the 80% H_2O and 90% H_2O samples, while the 70% H_2O sample follows a distinct kinetic pathway.

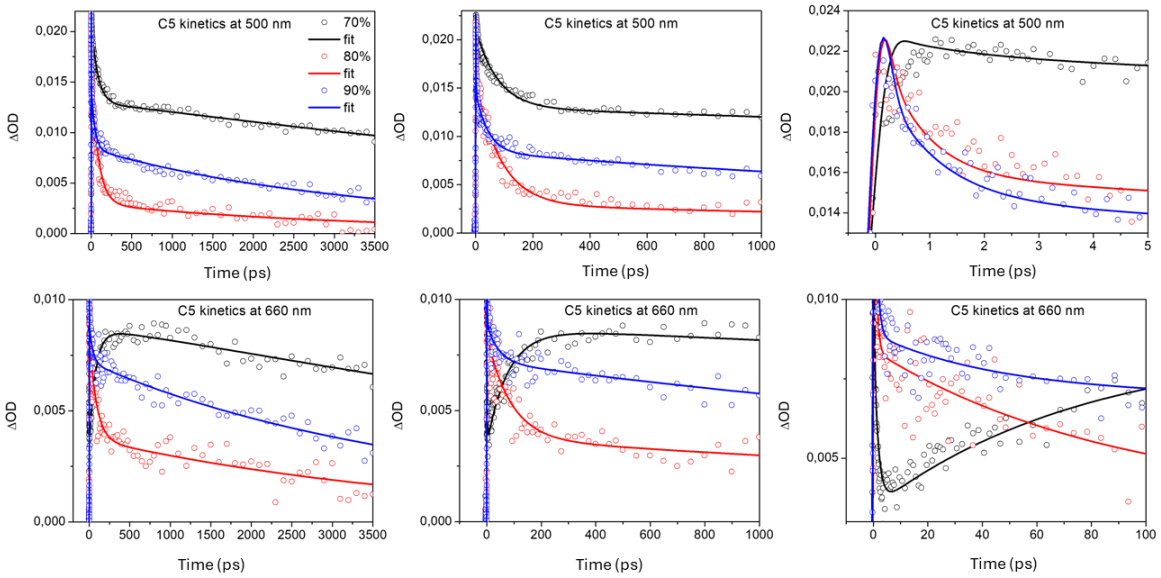

Figure 19. *Top line: kinetic traces at 500 nm of CH05-IN in THF:H_2O 70% H_2O (black), THF:H_2O 80% H_2O (red), THF:H_2O 90% H_2O (blue). Bottom line: kinetic traces of CH05-IN at 660 nm in the same mixtures.*

7.4. EXCITED-STATES: ANALYSIS OF CH08-IN

Transient absorption analysis

This compound differs from the previous ones in that it contains two iridium metal centres instead of just one. In THF-water mixtures with high water content, it forms large and irregular nanovesicles. *Figure 20* shows the transient absorption spectra recorded at a concentration of 10^{-4} M in pure THF and in THF-water mixtures containing 70%, 80%, and 90% water. As in previous cases, the excitation wavelength was 350 nm. The spectra are colour-coded according to the temporal evolution, with red representing time near to zero, followed by orange (first picoseconds after excitation) then, as time increases the spectral features progress from yellow to blue (end of the delay scan at 3.5 ns).

Here, the predominance of the blue colour suggests a more significant role of the iridium complexes in the excited-state dynamics, which aligns with the fact that this molecule contains two metal centres.

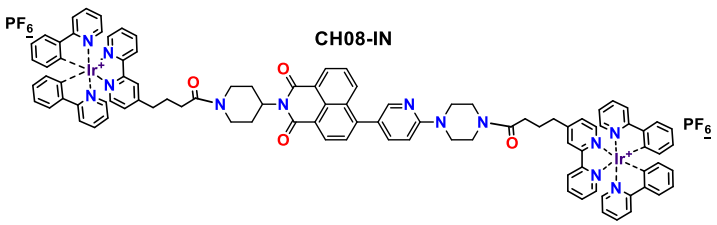

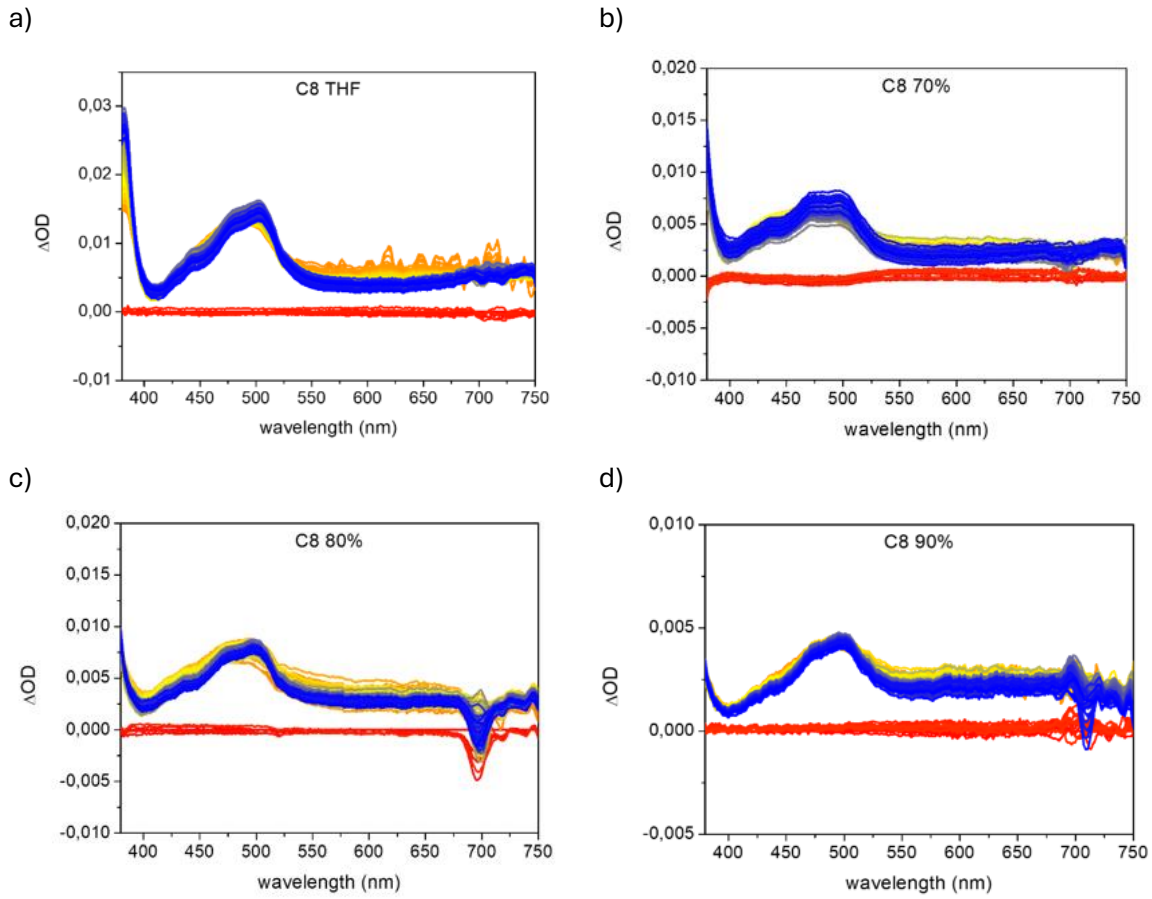

Figure 20. *Transient Absorption Spectra of CH08-IN (a) THF, (b) THF:H_2O 70% H_2O, (c)THF:H_2O 80% H_2O, (d) THF:H_2O 90% H_2O.*

Evolution-Associated Spectral and Kinetic Analysis

To better understand the previously discussed spectra, they were deconvoluted into Evolution-Associated Difference spectra, allowing us to analyse the spectral features associated with each kinetic component over time. The spectra recorded in pure THF and in mixtures of THF-H_2O are collected in the next figure.

So, in *Figure 21* it can be observed that the excited state dynamics of CH08-IN is minimally influenced by the solvent. The results indicate that the samples behave very similarly both in pure THF and in THF-water mixtures. In the figures, it can be observed all samples undergo triplet formation on a very fast timescale (<1ps) and no significant spectral evolution is observed over the investigated temporal window. This behaviour can be correlated with the structural characteristics of the molecule: the presence of two iridium centres imposes rigidity and limits conformational flexibility, possibly decreasing the influence of the organic moiety. In contrast, the other compounds, which feature only a single ring, exhibit greater structural freedom. Specifically, in those more flexible systems, π-π interactions between the metal-containing ring and the NMI moiety are possible, enabled by the possibility of bringing the two fragments into proximity through rotation around the single-bond linker, determining a more complex excited-state behaviour and a marked solvent dependence. In conclusion, although this compound has been shown to undergo aggregation at high water content, the presence of two metal centres appears to dominate the photophysical behaviour of the system. As a result, neither aggregation-induced effects nor intra- or intermolecular energy transfer processes are observed under the studied conditions.

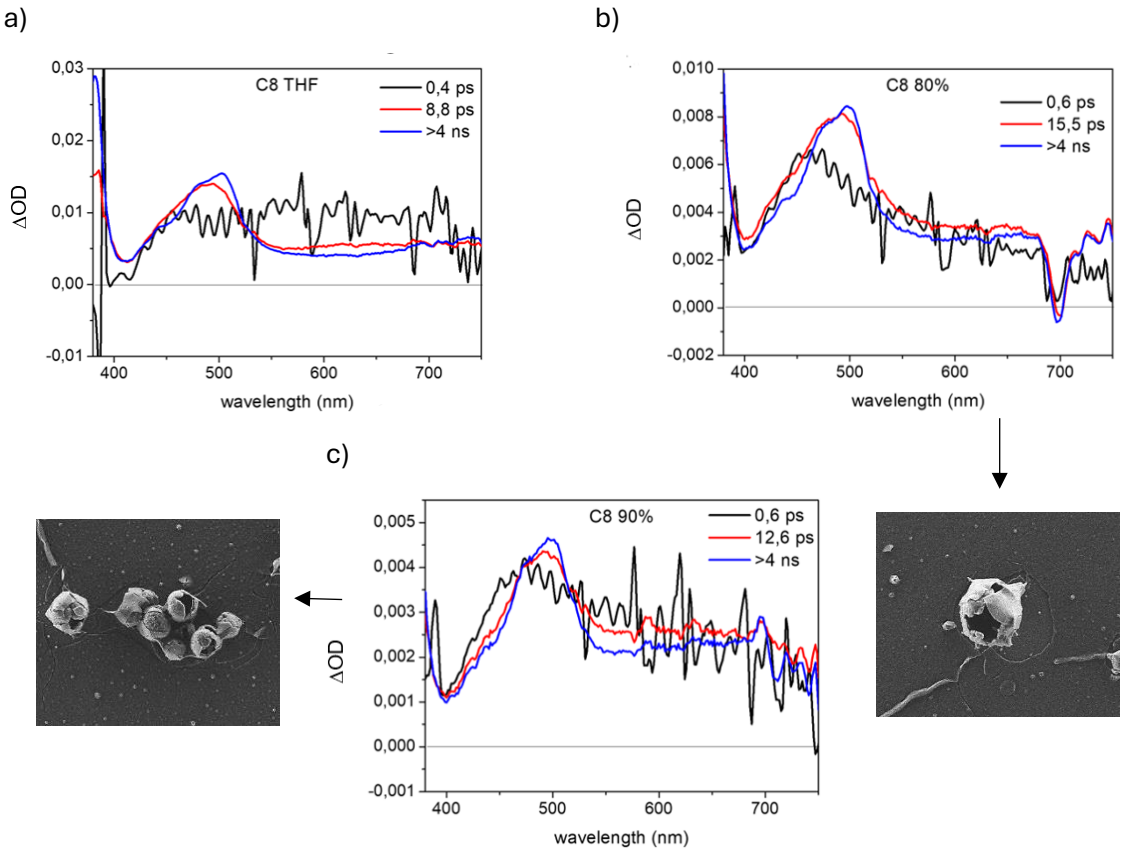

Figure 21. *Evolution Associated difference Spectra of CH08-IN in (a)THF, (b) THF:H_2O 80% H_2O, (c) THF:H_2O 90% H_2O. FESEM images of some vesicles are also shown.*

Kinetic traces of the triplet state

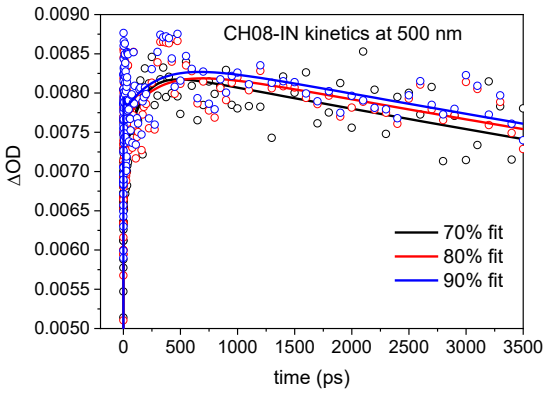

Figure 22*. Kinetic traces at 500 nm of CH08-IN in THF:H_2O 70% H_2O (black), THF:H_2O 80% H_2O (red), THF:H_2O 90% H_2O (blue).*

To confirm that CH08-IN exhibits similar behaviour and occurs on the same timescale across the three solvent mixtures, the kinetic traces at the maximum of the long-lived state (500 nm) were superimposed. The resulting overlap reveals a comparable response for the three samples *(Figure 22)*.

8. DETERMINATON OF SINGLET OXYGEN QUANTUM YIELD

After confirming that these compounds exhibit a long-lived triplet excited state, their ability to generate singlet oxygen was evaluated. Singlet oxygen is a reactive oxygen species of considerable importance in photochemical processes as photodynamic therapy which has an important role in this chapter. The detection of $^1O_2$ was performed using phosphorescence spectroscopy, by monitoring its characteristic emission at 1270 nm, corresponding to the $^1\Delta_g \rightarrow {}^3\Sigma_g^-$ transition.

The determination involves a relative approach, comparing the emission intensity of singlet oxygen at 1270 nm generated by the molecule under study to that produced by a reference compound with a known quantum yield under identical experimental conditions.

The quantum yield of the sample and reference are related by following equation:[24]

$$\Phi_{\Delta}^{PS} = \Phi_{\Delta}^{REF} \cdot \frac{I_{PS}}{I_{REF}} \cdot \frac{A_{REF}}{A_{PS}} \cdot \left(\frac{n_{PS}}{n_{REF}}\right)^2 \qquad \text{Eq. 3}$$

Where:

- Φ_{Δ}^{PS} is the singlet oxygen quantum yield of the photosensitizer under study.
- Φ_{Δ}^{REF} is the known singlet oxygen quantum yield of the reference compound.
- I_{PS}, I_{REF} are the integrated singlet oxygen emission intensities (at 1270 nm) for the photosensitizer and the reference, respectively.
- A_{PS}, A_{REF} are the absorbance values of the photosensitizer and the reference at the excitation wavelength.
- n_{PS}, n_{REF} are the refractive indices of the solvent used for the photosensitizer and the reference.

However, this formula is only used when a single measurement per sample is made, and the individual intensities are compared with the corrected absorbances.[25]

In the present case, measurements were carried out in air-saturated acetonitrile solutions at room temperature. A continuous monochromatic excitation source (400 nm for iridium complexes and 440 nm for ruthenium compounds) was employed. Then, the singlet oxygen quantum yield of the photosensitizers under study (PS) was determined by measuring fluorescence spectra for a series of acetonitrile solutions at different concentrations with the ^{1}MLCT absorbance values within the range of 0.04 to 0.25 in a 1 cm optical path length quartz cuvette. The absorbance range was chosen to ensure that the system remained in the linear regime of the Lambert-Beer law and to minimize reabsorption or inner filter effects, which could otherwise distort the emission intensity.[24] For each solution, the integrated intensities of emission were plotted as a function of the solution absorption ($1\text{-}10^{-Abs}$) at the excitation wavelength. The slope of the linear regression was proportional to the singlet oxygen quantum yield of the sample (Φ_{Δ}^{PS}). This relation can be deduced from the previous formula.[26]

In the Equation 3, when the solvent used for the test sample and the reference is the same, the refractive index factor can be omitted since the quotient is equal to 1, thus obtaining:

[24] J. R. Lakowicz, *Principles of Fluorescence Spectroscopy,* Springer Science + Business Media, Singapore, third edition, **2006,** chapter 2, pp. 55−56.
[25] P. De Bonfils, C. S. Altamirano, X. Moreau, P. Nun, A. D. Laurent, G. Gunther, V. Coeffard, *Photochem. Photobiol*. **2023,** *99 (2),* 642−651.
[26] R. Bresolí-Obach, J. Torra, R. P. Zanocco, A. L. Zanocco, S. Nonell, *Singlet Oxygen Quantum Yield Determination Using Chemical Acceptors.* In J. Espada (eds) *Reactive Oxygen Species. Methods in Molecular Biology*. Vol 2202. Humana, New York, **2021,** chapter 14, pp. 165−188.

$$\Phi_{\Delta}^{PS} = \Phi_{\Delta}^{REF} \cdot \frac{I_{PS}}{I_{REF}} \cdot \frac{A_{REF}}{A_{PS}} \qquad \text{Eq. 4}$$

Then, we want to represent integrated emission intensity at 1270 nm (I) vs. ($1-10^{-A}$).

First, we can consider that $slope = \frac{I}{1-10^{-A}} \propto \frac{I}{A}$ (only when A is small).

If all data points lie on a straight line, we can consider:

$$slope_{PS} \propto \frac{I_{PS}}{A_{PS}}; \qquad slope_{REF} \propto \frac{I_{REF}}{A_{REF}};$$

And, substituting into the original formula, we obtain:

$$\Phi_{\Delta}^{PS} = \Phi_{\Delta}^{REF} \cdot \frac{I_{PS}}{I_{REF}} \cdot \frac{A_{REF}}{A_{PS}} \approx \Phi_{\Delta}^{REF} \cdot \frac{slope_{PS}}{slope_{REF}} \qquad \text{Eq. 5}$$

And Eq. 5 is the formula we used to obtain the desired quantum yields. In our case, $[Ru(phen)_3]Cl_2$ was used as a standard reference with a known oxygen quantum yield of 0.38 ± 0.06 in acetonitrile.[27] Since the measurements for the samples and for the standard reference were carried out in acetonitrile, the value of the ratio between the diffraction indices (η) is equal to 1. From these measurements, the obtained singlet oxygen quantum yields of the investigated photosensitizers are collected in *Table 8.*

Table 8. *Singlet oxygen quantum yields of the studied photosensitizers. Using $[Ru(phen)_3]Cl_2$ as reference in acetonitrile. Highlighted in orange the ruthenium compounds and in blue the iridium ones*

	CH04-IN	CH10-IN	CH05-IN	CH08-IN
Oxygen quantum yield (Φ_{Δ})	0.46 ± 0.06	0.46 ± 0.06	0.20 ± 0.06	0.43 ± 0.06

Singlet oxygen quantum yield (Φ_{Δ}) is a critical parameter in assessing the potential of metal-based complexes for photodynamic therapy (PDT), as the efficacy of this treatment relies on the generation of reactive oxygen species upon light activation. The ruthenium complexes CH04-IN and CH10-IN exhibit high singlet oxygen quantum yields of 0.46, indicating strong photosensitizing ability and efficient generation of singlet oxygen under the experimental conditions. These values are close to the upper range typically considered favourable for PDT applications, supporting their potential use in therapeutic contexts.[28] The iridium complexes CH05-IN and CH08-IN exhibited singlet oxygen quantum yields (Φ_{Δ}) of 0.20 and 0.43, respectively. While CH05-IN displays moderate photogeneration efficiency, CH08-IN performs comparably to the ruthenium-based compounds, underscoring its potential as a photosensitizer. Notably, despite its lower Φ_{Δ}, CH05-IN can still exert significant intracellular photodynamic effects, as reported for similar Ir(III) complexes in the literature.[29] In addition, the overall efficacy is influenced not only by singlet oxygen production but also by factors such as cellular uptake and subcellular distribution.[30] Overall, these results indicate that both ruthenium and iridium complexes in this study are capable

[27] L. Casula, G. E. Giacomazzo, L. Conti, M. Fornasier, B. Manca, M. Schlich, C. Sinico, T. Rheinberger F. R. Wurm, C. Giorgi, S. Murgia, *J. Colloid Interface Sci*. **2024,** *670,* 234−245.

[28] M.A. Unegowda, A. Manalac, M. Weersink, H.D. Cole, S. A. McFarland, L. Lilge, *Coord. Chem. Rev*. **2022**, *470,* 214712.

[29] Y. Xu, X. Wang, K. Song, J. Du, J. Liu, Y. Miao, Y. Li, *RSC Adv.* **2021,** *11* (25), 15323−15331.

[30] A. Rovira, E. Ortega-Forte, C. Hally, M. Jordà-Redondo, D. Abad-Montero, G. Vigueras, J. I. Martínez, M. Bosch, S. Nonell, J. Ruiz, V. Marchán *J. Med. Chem.* **2023,** *66* (12), 7849−7867.

of generating singlet oxygen with high efficiency, making them promising candidates for further development as PDT photosensitizers.

9. BIOLOGICAL EVALUATION: STUDY IN HECK-293 CELL LINE

In addition to their photophysical characterization, the biological behaviour of the synthesized compounds was evaluated in human embryonic kidney cells (HECK-293), in order to assess their potential application in photodynamic therapy. This section includes cellular uptake studies using fluorescence microscopy to visualize and confirm internalization, followed by cytotoxicity assays performed under both dark and irradiated conditions. These experiments provide insight into the compounds' cellular interaction and phototherapeutic efficacy, contributing to a comprehensive understanding of their suitability as photosensitizers in PDT.

9.1. CELLULAR UPTAKE

The ability of the compounds to cross the cell membrane was evaluated by cellular uptake studies. Widefield fluorescence microscopy revealed that all of them are efficiently internalized by the cells. Remarkably, cellular entry was observed even for those compounds bearing a tert-butoxycarbonyl protecting group, despite the findings in other chapters indicating that this group typically hinders membrane permeability. This highlights the high affinity and strong capacity of these organometallic compounds to be taken up by cells. This capacity is likely attributable to the presence of the metal centre, which distinguishes these new compounds from those discussed in previous chapters. The fluorescence signal was clearly detected within the cytoplasm, indicating successful membrane permeation *(Figure 23)*. However, no accumulation in the nucleus was observed, suggesting that nuclear uptake does not occur under the tested conditions. Although the compounds localize in the cytoplasmic space, the specific target organelle could not be identified with the current experimental setup. Images were acquired using λ_{exc} = 405 nm, and emission filtered at 515, 588, and 700 nm using a multi-band filter system.

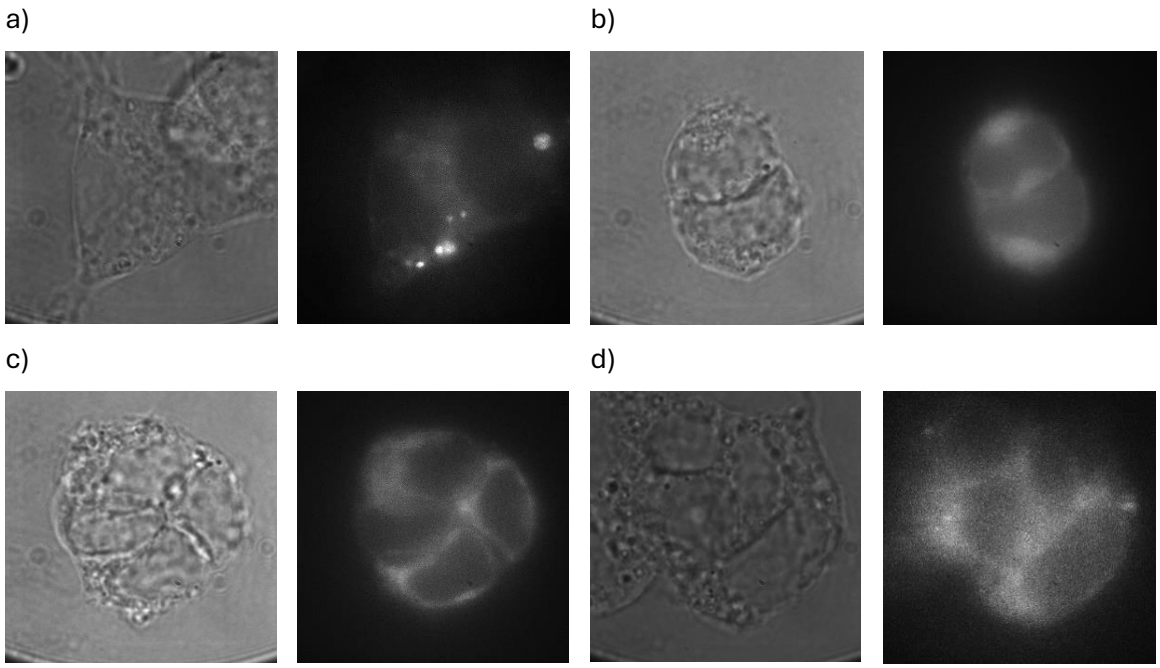

Figure 23. *Cellular uptake in HECK-293 cells. (a) CH04-IN 750 nM, 1h. (b) CH10-IN 1 µM, 1 h. (c) CH05-IN 250 nM, 1 h. (d) CH08-IN 100 nM, 1 h. For each compound, left: phase contrast microscopy, right: fluorescence microscopy.*

9.2. CYTOTOXICITY ASSAYS FOR PHOTODYNAMIC THERAPY

Cell viability assays were also performed using HEK-293 cancer cells. Initially, cytotoxicity was assessed after 72 hours of incubation with the compounds without prior light irradiation. These experiments provided the intrinsic cytotoxic profile of the products in the absence of photoactivation. Subsequently, the experiments were repeated under irradiation conditions: cells with each organometallic compound were exposed to 415 nm light for 30 minutes, followed by the same 72-hour incubation period. Cell viability was then re-evaluated. Under these conditions, a notable decrease in cell viability was observed.

In *Figure 24,* the survival cells are represented versus concentration of each compound, both under dark conditions (black) and under light irradiation (red).

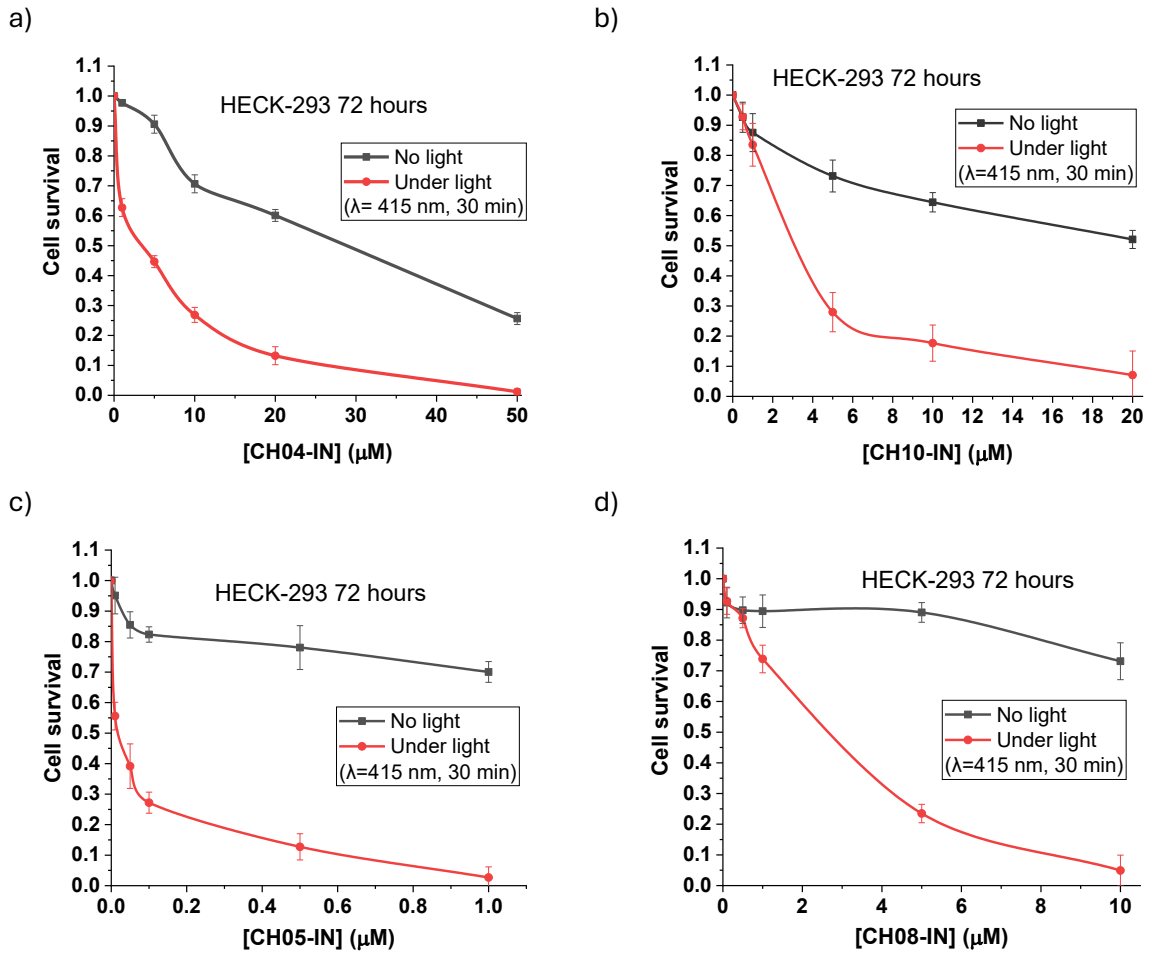

Figure 24. *Cell survival after 72 h in the presence of increasing concentrations of (a) CH04-IN, (b) CH10-IN, (c) CH05-IN, (d) CH08-IN. Without light exposure (black) and after light activation (red).*

Then, the IC_{50} values of each compound were calculated for both conditions and are collected in the next table.

Table 9. *IC_{50} values (μM) after 72 hours of incubation in HECK-293 cells. Standard errors obtained from 3 independent experiments. Ruthenium compounds are highlighted in orange, and iridium ones in blue*

	CH04-IN	CH10-IN	CH05-IN	CH08-IN
No light	28.6 ± 0.7	21.2 ± 0.8	2.5 ± 0.5	23.4 ± 0.8
Light exposure	3.5 ± 0.3	3.4 ± 0.5	0.03 ± 0.00	3.0 ± 0.2

First, it is worth highlighting that all the studied organometallic compounds exhibit intrinsically cytotoxicity, as evidenced by their IC_{50} values under dark conditions. These values are competitive within the landscape of anticancer agents,[31] even in the absence of photoactivation.[32]

Upon light exposure, a notable decrease in IC_{50} values was observed for all compounds, indicating a significant phototherapeutic enhancement. In particular, compounds CH04-IN, CH10-IN, and CH08-IN demonstrated a one-order-of-magnitude reduction in IC_{50} following irradiation, dropping from approximately 20.30 μM in the dark to 3-4 μM post-activation. It must be reminded that these same compounds formed large and irregular isolated vesicles in aqueous mixtures. Moreover, these three products showed high singlet oxygen quantum yields ($\Phi_\Delta \approx 0.45$), confirming their excellent potential as photosensitizers for photodynamic therapy.[33]

In contrast, compound CH05-IN exhibit a particularly high intrinsic cytotoxicity, with a IC_{50} value as low as 2.5 μM under dark conditions; that value makes it the most potent among all compounds analysed in this thesis. Upon irradiation, its IC_{50} decreased further, reaching values in the nanomolar range (30 nM), which is surprising, since this behaviour is not correlated with singlet oxygen generation. CH05-IN displayed a relatively low singlet oxygen quantum yield ($\Phi_\Delta = 0.20$), suggesting that alternative mechanisms may be contributing to its cytotoxic action.

Structurally, CH05-IN was observed to form numerous uniform vesicular aggregates in aqueous environments (a clear contrast to the irregular and widely spaced structures formed by the other compounds). This distinct aggregation profile may influence its cellular uptake or intracellular localization, thereby enhancing its ability to induce cell damage upon photoactivation. It is plausible that this compound exhibits more efficient aggregation at the cellular target site, increasing its phototoxic impact. In summary, the distinct aggregation behaviours and photophysical properties observed suggest that molecular self-assembly and structural organization may play a critical role in modulating biological activity. Hence, further investigation of compounds structurally analogous to CH05-IN (especially those capable of forming similarly ordered vesicular aggregates) could be key to understanding whether this unique aggregation mode consistently correlates with enhanced cytotoxicity. Such studies may provide deeper insight into the relationship between supramolecular organization and therapeutic efficacy, guiding the rational design of more potent photoactivatable anticancer agents.

Overall, the organometallic species developed in this study represent highly promising candidates for cancer treatment via photodynamic therapy.[34] Since the IC_{50} values obtained after light activation fall within the low micromolar and nanomolar range, these compounds are exceptionally attractive within the context of biomedical research.[35,36] These results emphasize the therapeutic relevance of the compounds and underscore the need for continued investigation as phototoxic species. In fact, the species bearing a tert-butoxycarbonyl group have been deprotected, yielding piperazine derivatives with a free terminal amine. This decision was based on findings from previous chapters, where Boc removal was associated with increased cytotoxicity. However, cellular studies with these particular compounds have not yet been conducted and are part of future research that will complement the findings presented in this chapter.

[31] J. Ismail, W. Shebaby, S. A. Atallah, R. I. Taleb, S. Kawrani, W. Faour, M. Mroueh, *Biomed.* **2025**, 13, 520.
[32] B. S. McGhie, J. R. Aldrich-Wright, *Biomed.* **2022**, *10*, 578.
[33] S. Mathai, T. A. Smith, K. P. Ghiggino, *Photochem. Photobiol. Sci.* **2007,** *6,* 995–1002.
[34] R. J. Mitchell, D. Havrylyuk, A. C. Hachey, D. K. Heidary, E. C. Glazer, *Chem. Sci.* **2025**, *16*, 721–734.
[35] J. Han, K. Li, M. Yang, J. Fan, X. Peng, *Chem. Sci.* **2025**, *16*, 12397–12407.
[36] Y. Wu, S. Li, Y. Chen, W. He, Z. Guo, *Chem. Sci.* **2022**, *13*, 5085–5106.

10. RUTHENIUM AND IRIDIUM COMPOUNDS AS MEDIATORS IN METAL NANOPARTICLES' FORMATION

Beyond their role as photosensitizers and cytotoxic agents in photodynamic therapy, the organometallic ruthenium and iridium complexes have been found to exhibit an unexpected behaviour when mixed with gold(III) and silver(I) salts. It must be reminded that these compounds in mixtures of THF and water with high water content, self-assemble into aggregates and display aggregation-caused quenching effect.

Taking into account this aggregation propensity, we explored the ability of these complexes to act as reducing or templating agents in the formation of noble metal nanoparticles. Remarkably, when they are mixed with auric or silver salts and left evolve for 24 hours, the resulting mixtures yield well-defined metallic nanoparticles, indicating that these organometallic species can mediate the nucleation and growth of metal nanostructures under mild conditions. This novel function represents an important advance in the versatility of these compounds, expanding their potential far beyond biomedical applications and into the field of nanomaterials synthesis, where controlled nanoparticle formation remains a central challenge. Moreover, this approach does not require the use of surfactants or additional stabilizing agents, offering a significantly cleaner and more straightforward route to metal nanoparticle generation. The methodology and the results are described in the next subsections. It must be mentioned that CH08-IN is not included in this study since it is not effective in the generation of noble metal nanoparticles.

10.1. SPECTROSCOPIC CHANGES UPON GOLD ADDITION

The methodology followed to prepare all organic compound-gold(III) solution mixtures was similar across all experiments. First, the optimal water content for nanovesicle formation was determined (70% w.r. for CH04-IN and CH05-IN, and 80% for CH10-IN). Each compound, previously dissolved in THF, was then combined with an aqueous solution of $HAuCl_3 \cdot 3H_2O$ (8 equivalents). The solutions were mixed to achieve a final organic compound concentration of 10^{-5} M in THF-water mixtures of 70 or 80% w.r. Although at this concentration, no vesicle formation was observed for the ruthenium complexes, control experiments carried out at higher concentrations demonstrated that these compounds are not effective in promoting the formation of gold nanoparticles.

The experiments were first performed allowing the samples to evolve under dark conditions. Then, since it is known these compounds interact with light and are photosensitive, the experiments were repeated allowing the samples to evolve for 24 hours under white light. First, photographs of the mixtures were taken under visible and ultraviolet light, both before and after 24 hours of the addition of the gold salt. However, no significant changes in the colour of the solutions were observed (neither under dark conditions nor with light irradiation). As an example, the mixtures containing CH04-IN are shown in *Figure 25.*

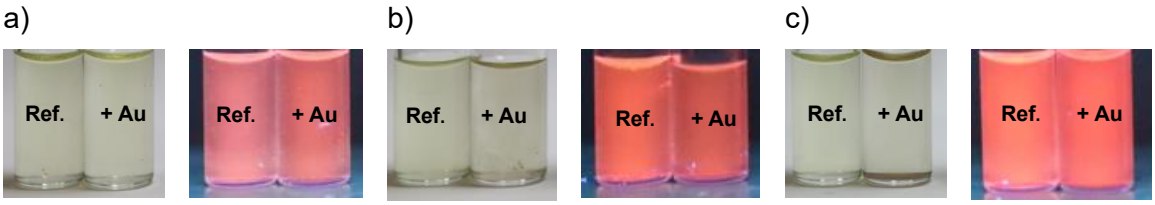

Figure 25. *CH04-IN at 70% w.r. in THF with gold(I), (a) Freshly prepared mixtures (b) After 24 hours of evolution in darkness (c) After 24 hours under white light.*

It can be seen that the typical red or blue coloration associated with the formation of colloidal gold nanoparticles is absent. A similar behaviour was previously observed in Chapter 2B of this thesis. This lack of colour change can be attributed to the presence of organic matter in the medium, which inhibit the surface plasmon resonance of the gold nanoparticles.

Since the qualitative changes are very slight, and for better analysis, absorption and emission spectra were acquired both under dark conditions and under light. The spectra of CH04-IN are shown in *Figure 26* as a representative example, but the ones of all mixtures are collected in the Supporting Information of this chapter.

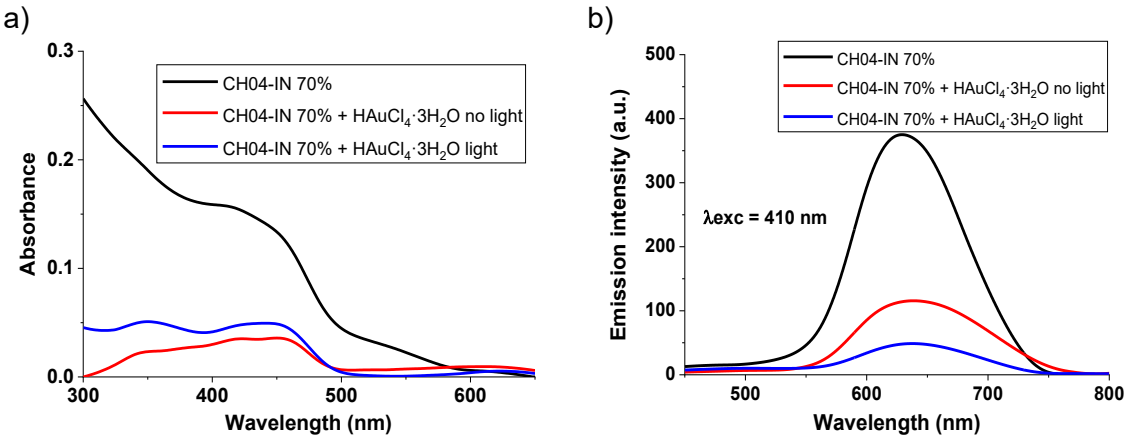

***Figure 26**. CH04-IN at 70% w.r. in THF with $HAuCl_4 \cdot 3\ H_2O$, (a) Absorption spectra of reference (black) and mixtures (blue: under light, red: darkness) (b) Emission spectra of reference (black) and mixtures (blue: under light, red: darkness).*

A marked decrease in both absorption and emission intensity is observed after the formation of gold nanoparticles. This reduction in optical intensity suggests that the gold interact with the NMIS' cores, leading to the quenching of their photophysical properties.

Once the optical changes in the mixtures have been characterized, the presence of gold nanoparticles is further confirmed through microscopy techniques. The corresponding images and elemental analysis are presented in the following sections, organized according to the different organic precursor used.

10.2. GOLD NANOPARTICLES USING CH04-IN

Scanning electron microscopy.

After 24 hours of stillness under dark and light conditions, CH04-IN (10^{-5} M) at 70% w.r. in THF mixed with $HAuCl_4 \cdot 3\ H_2O$ was imaged.

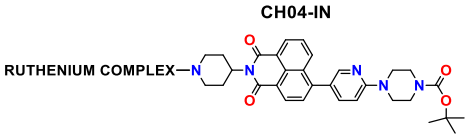

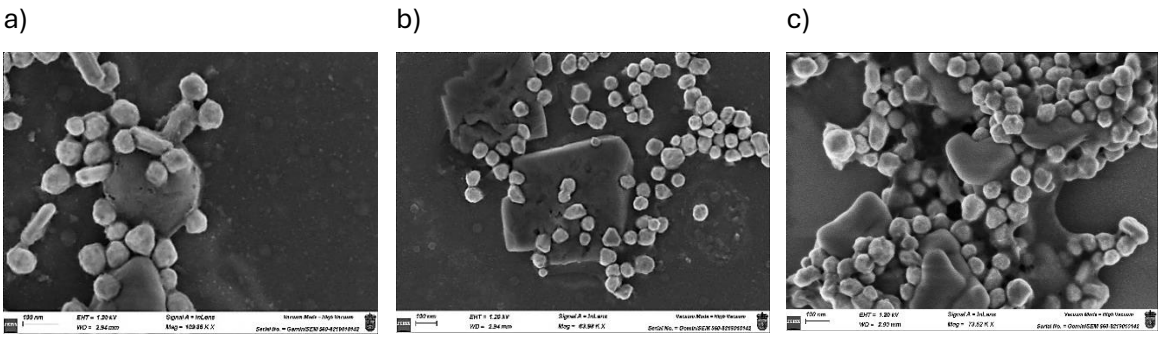

Figure 27. *FESEM images of gold nanoparticles formed when CH04-IN at 70% w.r. is mixed with $HAuCl_4 \cdot 3\ H_2O$. (a, b) under dark conditions (c) under light exposure.*

Notice that the formation of well-defined pseudospherical and/or polygonal gold nanoparticles occurs under both dark and light-irradiated conditions, indicating that the nanoparticle generation process is independent of the lighting method. In both cases, the nanoparticles are mixed with organic structures.

The experiment was repeated using anhydrous auric chloride ($AuCl_3$), under darkness and under white light, but the results were similar to those obtained before. In the next figure some gold nanoparticles obtained with anhydrous auric chloride are shown.

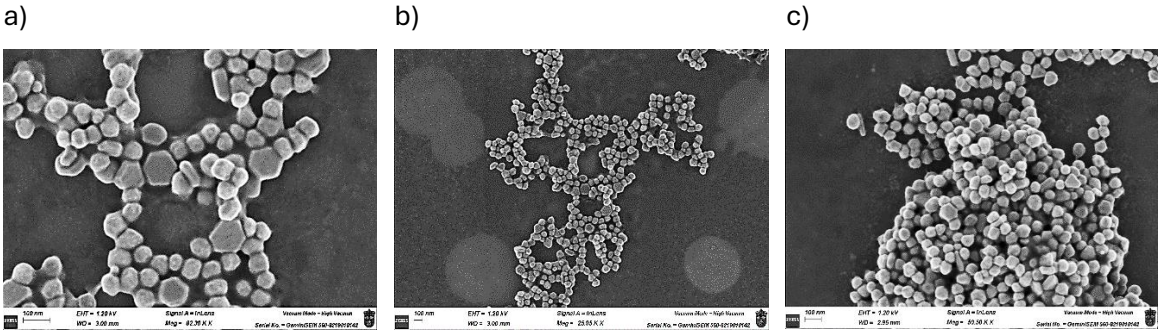

Figure 29. *FESEM images of gold nanoparticles formed when CH04-IN at 70% w.r. is mixed with $AuCl_3$ (a, b) under dark conditions (c) under light exposure.*

Transmission electron microscopy

The CH04-IN mixture was left to evolve under dark conditions and then characterized by TEM. Medium-resolution TEM images were obtained for samples prepared with both hydrated and anhydrous gold (III) chloride. In both cases, comparable results were obtained *(Figure 30),* revealing morphologies consistent with those previously observed by FESEM.

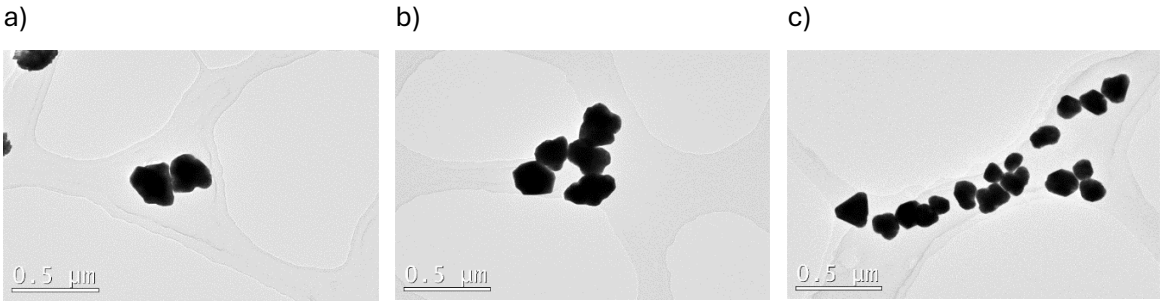

Figure 30. *TEM images of gold nanoparticles formed when CH04-IN at 70% w.r. is mixed with (a, b) $HAuCl_4 \cdot 3\ H_2O$ and (c) $AuCl_3$.*

10.3. GOLD NANOPARTICLES USING CH10-IN

As light irradiation was shown not to affect the type of gold nanoparticles formed, this section includes only the results obtained from the evolution of the sample kept in the dark.

Scanning electron microscopy

CH10-IN (10^{-5} M) at 80% w.r. in THF mixed with $HAuCl_4 \cdot 3\ H_2O$ or with $AuCl_3$ was left to evolve for 24 hours and then was imaged. The results were similar with both precursors.

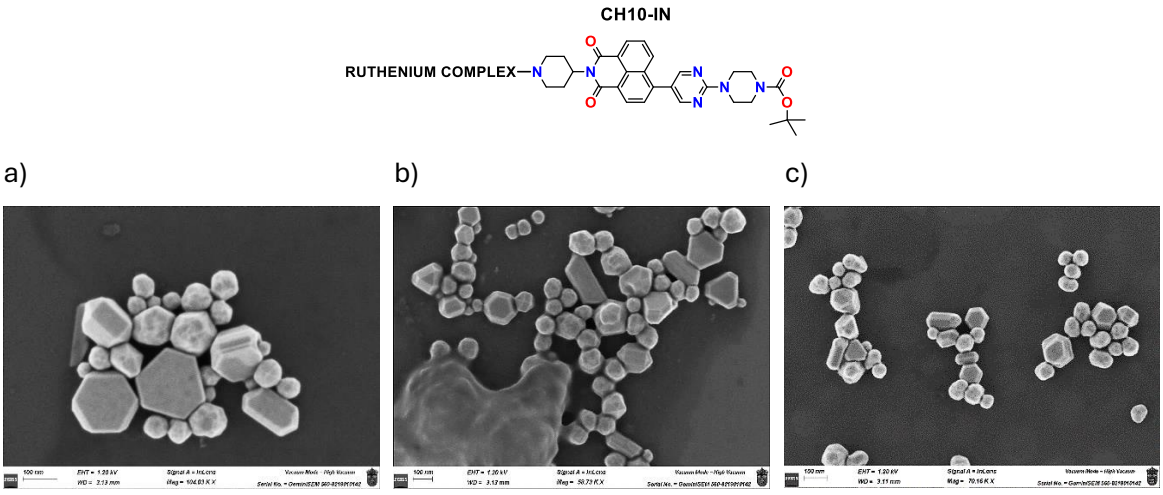

Figure 31. *FESEM images of gold nanoparticles formed when CH10-IN at 80% w.r. is mixed with (a, b) $HAuCl_4 \cdot 3\ H_2O$, (c) $AuCl_3$.*

Unlike the previous case, the gold nanoparticles (appearing as brighter regions in the images) are not pseudospherical but exhibit polygonal shapes. As observed before, they appear associated with organic material *(Figure 31b).* It must be mentioned that more images of these experiments, using both auric chloride salts as precursors, are collected in the Supporting Information of this chapter.

To verify the composition of the nanoparticles, elemental mapping analysis was performed using Energy-Dispersive X-ray Spectroscopy *(Figure 32).* The results revealed the presence of an organic layer on the surface of the gold nanoparticles, corresponding to the CH10-IN compound. This was confirmed by the presence of a carbon (red) signal on the surface of the gold nanoparticles (purple).

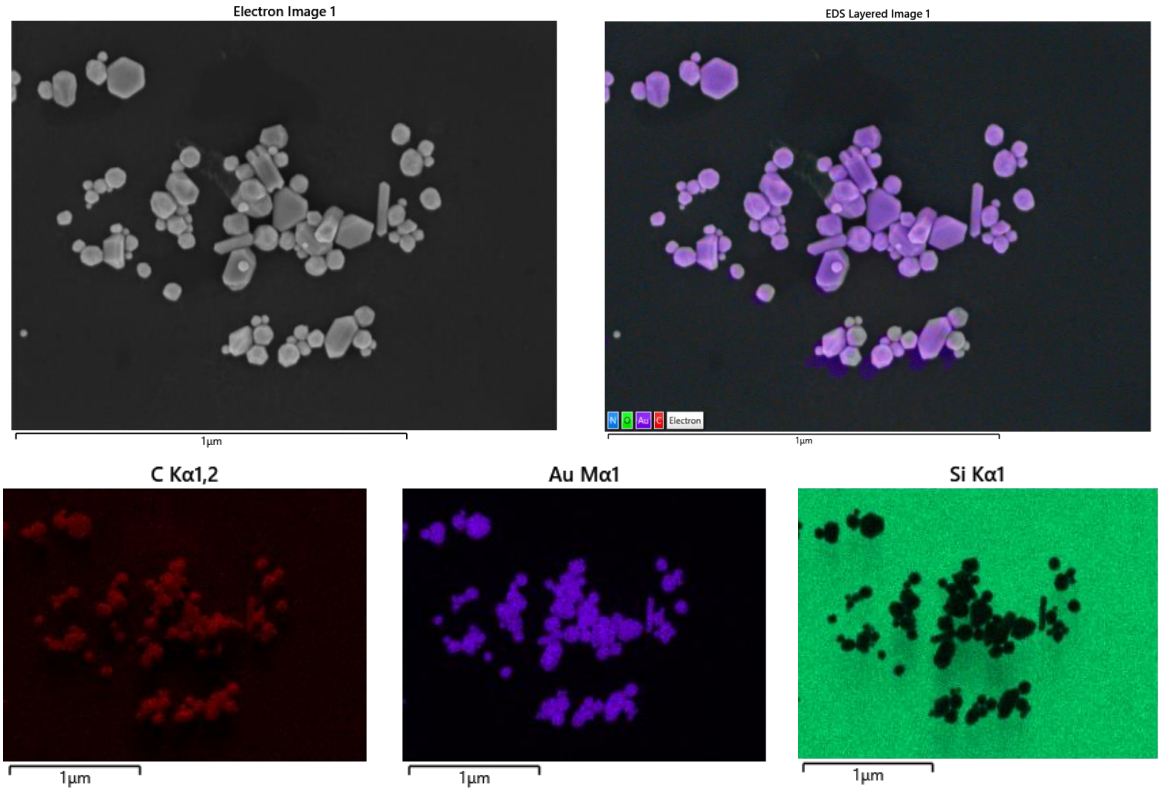

Figure 32. *EDX mapping spectra: gold nanoparticles (purple) and carbon cover of CH10-IN (red).*

Then, to determine the proportion of gold and carbon, punctual EDX analyses were performed. Initially, the sample was analysed using a voltage of 5 kV, which provides lower electron penetration depth. Under these conditions, the surface carbon was detected. *(Figure 33).*

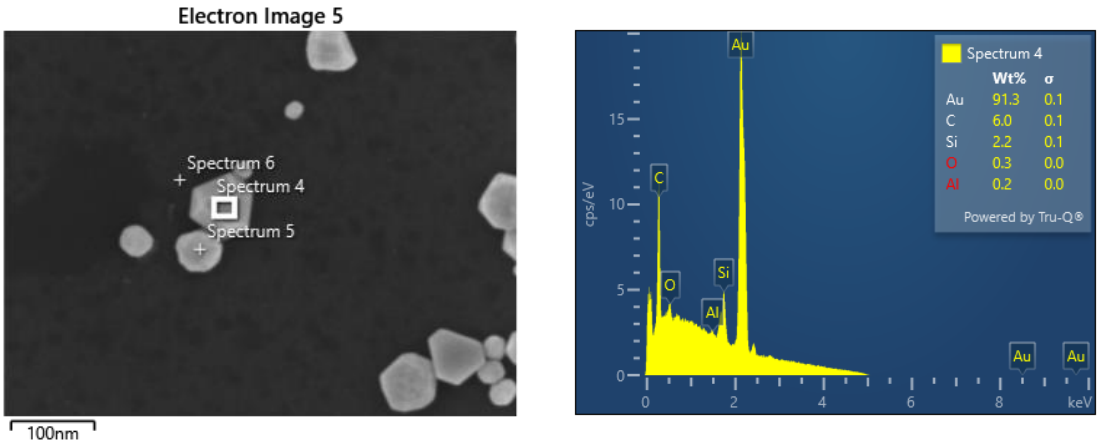

Figure 33. *Punctual EDX spectra of CH10-IN (80% w.r.) mixed with gold (5 kV).*

The analysis of spectrum 4 reveals that gold is found as pure element with a mass percentage of 91.3 % *(Figure 34),* and carbon covers the nanoparticle with a mass percentage of 6%.

Spectrum 4

Element	Line Type	Apparent Concentration	k Ratio	Wt%	Wt% Sigma	Standard Label	Factory Standard
C	K series	11.49	0.11490	6.02	0.11	C Vit	Yes
O	K series	2.04	0.00686	0.32	0.04	SiO2	Yes
Al	K series	0.92	0.00661	0.20	0.05	Al2O3	Yes
Si	K series	10.13	0.08023	2.16	0.07	SiO2	Yes
Au	M series	198.40	1.98405	91.30	0.15	Au	Yes
Total:				100.00			

Figure 34. *Compositional analysis of spectrum 4. Gold and carbon are found.*

Subsequently, a punctual EDX analysis was performed at an accelerating voltage of 10 kV, which allows for greater electron penetration. In this case, the carbon percentage increased, indicating the presence of carbon at the base of the nanoparticle as well. This suggests that the gold nanoparticles are embedded within a thin carbon film that fully envelops them, both at the base and on the exposed surface. This confirms that CH10-IN, which is present around the particles, mediates the gold reduction.

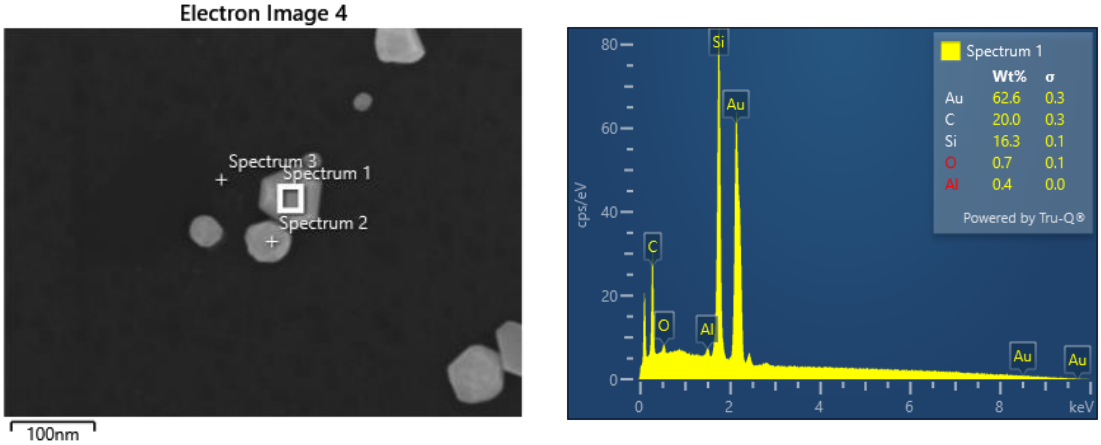

Figure 35. *Punctual EDX spectra of CH10-IN (80% w.r.) mixed with gold (10 kV).*

As observed, the carbon content increases to approximately 20% *(Spectrum 1, Figure 36).* However, due to the higher electron penetration at 10 kV, the silicon signal (corresponding to the plate) also increases.

Spectrum 1							
Element	Line Type	Apparent Concentration	k Ratio	Wt%	Wt% Sigma	Standard Label	Factory Standard
C	K series	8.90	0.08899	19.98	0.32	C Vit	Yes
O	K series	1.08	0.00363	0.68	0.09	SiO2	Yes
Al	K series	0.77	0.00552	0.41	0.05	Al2O3	Yes
Si	K series	31.47	0.24933	16.28	0.15	SiO2	Yes
Au	M series	67.80	0.67802	62.65	0.33	Au	Yes
Total:				100.00			

Figure 36. *Compositional analysis of spectrum 1. Carbon and silicon content increase.*

Transmission electron microscopy

The mixtures were also examined by TEM, yielding similar results for the samples prepared with hydrated and anhydrous gold(III) chloride. In this section, a detailed analysis of the images obtained using $HAuCl_4 \cdot 3\ H_2O$ as the precursor is presented, whereas the TEM images of the nanoparticles synthesized from $AuCl_3$ are provided in the Supporting Information of this chapter. Preliminary medium-resolution TEM images revealed the formation of nanoparticles with diverse morphologies, including spheres, rods, and polygonal shapes *(Figure 37).*

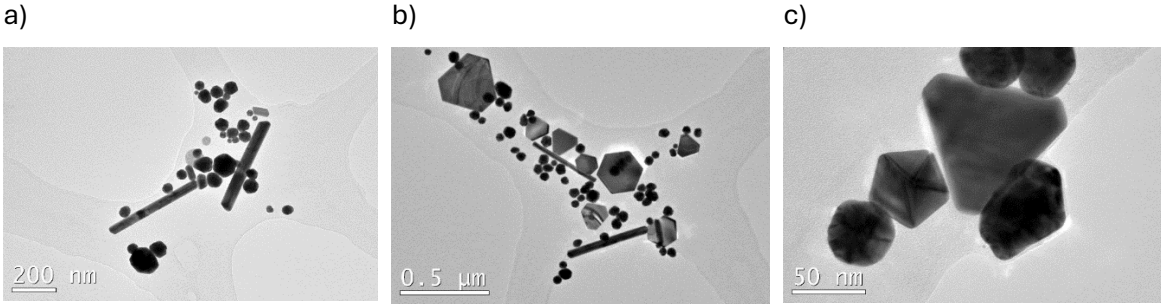

Figure 37. *Medium-resolution TEM images of gold nanoparticles formed when CH10-IN at 80% w.r. is mixed with $HAuCl_4 \cdot 3\ H_2O$.*

After obtaining a general overview of the formed nanostructures from medium-resolution TEM images, high-resolution TEM was employed, allowing us to visualize the spatial arrangement the atoms within the gold nanoparticles. Digital magnification of selected areas allows the visualization of distinct crystallographic planes. Given the face-centred cubic lattice of gold, with a lattice parameter of a = 4.078 Å, measurement of the interplanar spacings and angles between the observed planes enables their identification. To do that is necessary to use the formulas based on Miller indices and the theoretical crystallographic framework deeply described in Chapter 2B. Taking this into account, we can state that the interplanar spacing of approximately 2.35 Å corresponds to the (111) crystallographic planes. Between them there is an angle of 70.5 degrees *(Figure 38b)*, which indicates that the family of planes is imaged along the [110] zone axis. In addition, in *Figure 38d* it is possible to see the (011) planes, with interplanar distances of 2.88 Å. The angle between the (111) and (011) planes is 35.3°, which is consistent with their geometry when viewed along the [110] zone axis.

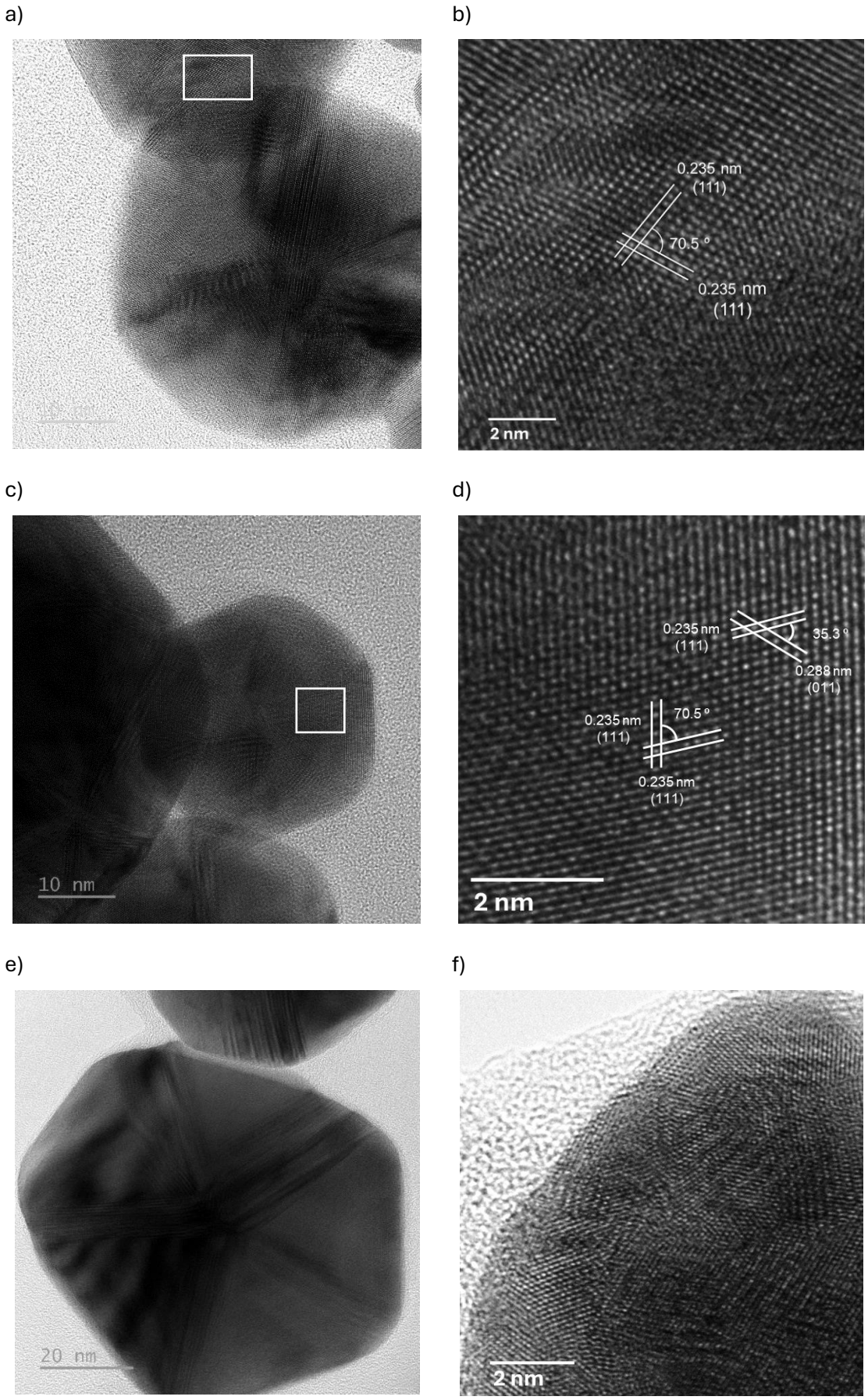

Figure 38. *HR-TEM images of CH10-IN at 80% w.r. when mixed with $HAuCl_4 \cdot 3\ H_2O$. Crystallographic planes seen along [110] axis.*

In *Figure 38f*, the (111) lattice planes can be observed in multiple orientations within the same particle. This indicates a polycrystalline structure, where the nanoparticle is composed of several crystalline domains (grains) separated by grain boundaries. In face-centred cubic metals such as gold, such multi-domain structures are often associated with growth via oriented attachment, in which smaller nanocrystals join together during growth while retaining different crystallographic orientations.[37] This mechanism can naturally lead to polygonal or faceted morphologies, as the merged grains define flat facets or edges. Indeed, coalescence accompanied by twinning or grain boundary formation has been directly observed in gold nanoparticles,[38] sometimes resulting in decahedral, or other polygonal shapes.[39] The polygonal particles observed here exhibit distinct lattice orientations depending on the region examined by high-resolution TEM, consistent with a polycrystalline and possibly twinned internal structure.

10.4. NOBLE METAL NANOPARTICLES USING CH05-IN

10.4.1. Formation of gold nanoparticles

Scanning electron microscopy

In first place, a solution of CH05-IN (10^{-5} M) at 70% w.r. in THF mixed with 8 equivalents of $HAuCl_4 \cdot 3\ H_2O$, remained under stillness for 24 hours under dark conditions and then it was imaged. It is important to note that, unlike the previous compounds, this iridium product formed nanovesicle aggregates at a concentration of 10^{-5} M. Hence, stunning spherical nanoparticles of gold (appearing bright and white coloured), combined with the nanovesicles formed by the organic compound (grey) are observed. In addition, gold not only forms spherical particles, but also polygonal structures were found *(Figure 39a-f)*.

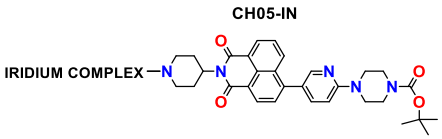

a) b) c)

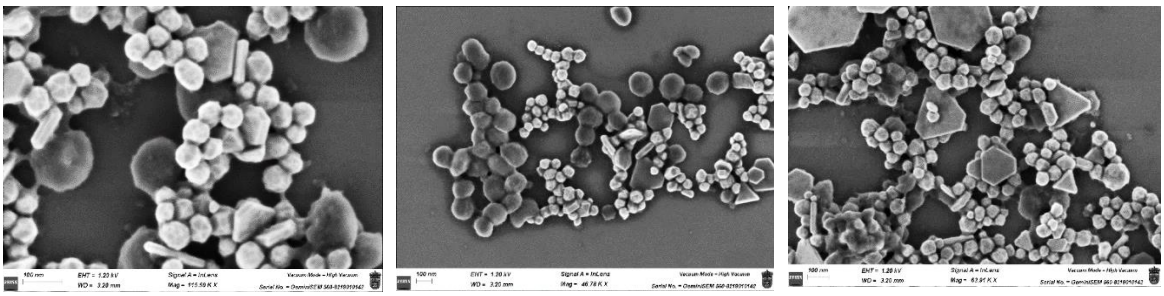

[37] B. Ingham, T. H. Lim, C. J. Dotzler, A. Henning, M. F. Toney, R. D. Tilley, *Chem. Mat.* **2011,** *23* (14), 3312−3317.
[38] C. Martín-Sánchez, A. Sánchez-Iglesias, J. A. Barreda-Argüeso, J. P. Itié, P. Chauvigne, L. M. Liz-Marzán, F. Rodríguez, *Nano Lett*. **2025**, *25* (9), 3588−3596.
[39] Y. Q. Wang, W. S. Liang, C. Y. Geng, *Nanoscale Res. Lett.* **2009;** *4*, 684.

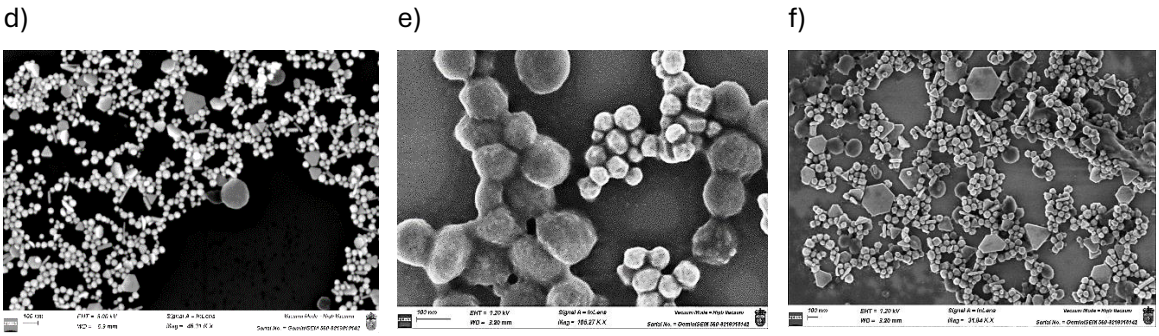

Figure 39. *(a-f) FESEM images of gold nanoparticles formed when CH05-IN at 70% w.r. is mixed with* $HAuCl_4 \cdot 3\ H_2O$ *(dark conditions).*

Then, the composition of the nanoparticles was verified by a punctual elemental analysis using EDX (Supporting Information). And then, an EDX mapping was also performed *(Figure 40).* As occurred with the previous compounds, an organic coating on the gold nanoparticles is observed. It can be confirmed by looking to the specific carbon distribution (image shown in red).

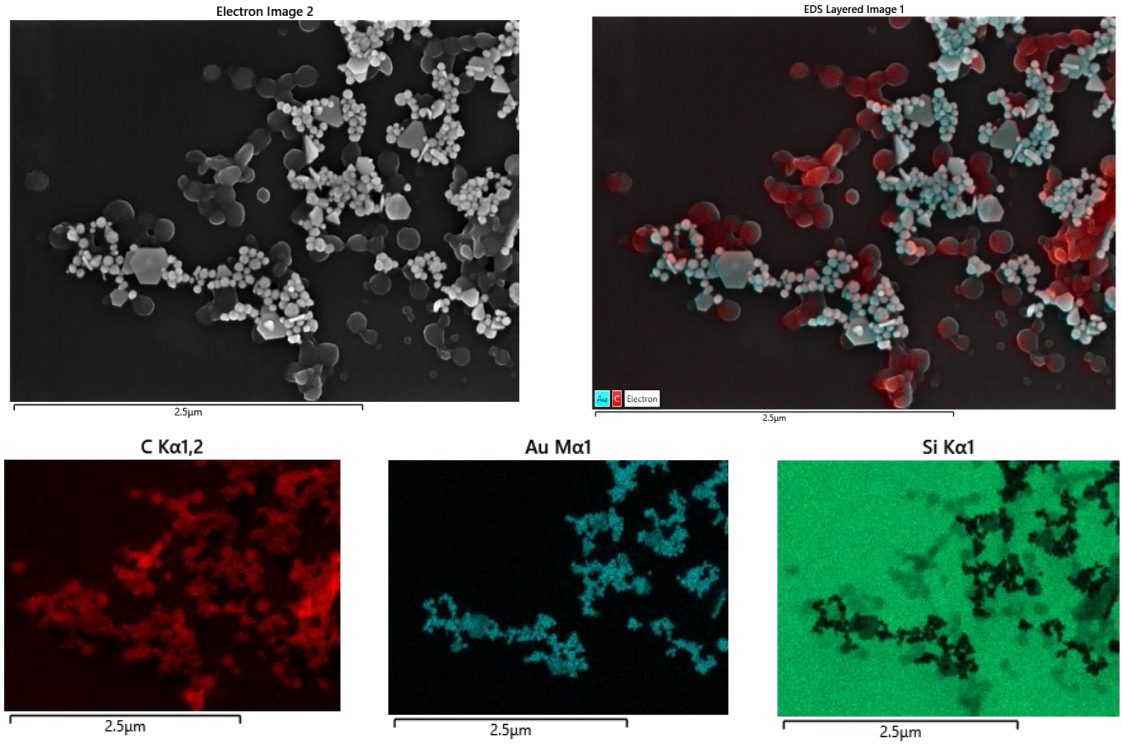

Figure 40. *EDX mapping spectra: gold nanoparticles (blue) and carbon vesicles of CH05-IN (red).*

Given that this compound features an iridium metal centre rather than ruthenium, the effect of light exposure was also investigated. We wanted to determine whether the metal substitution would lead to different gold nanoparticles after light irradiation. However, the results were very similar to those observed in the dark. To complete this study, the experiment was repeated using anhydrous auric chloride ($AuCl_3$) under both dark conditions and white light exposure. As expected, the results followed the same pattern as those obtained before. In the next figure some gold nanoparticles obtained with anhydrous auric chloride are shown.

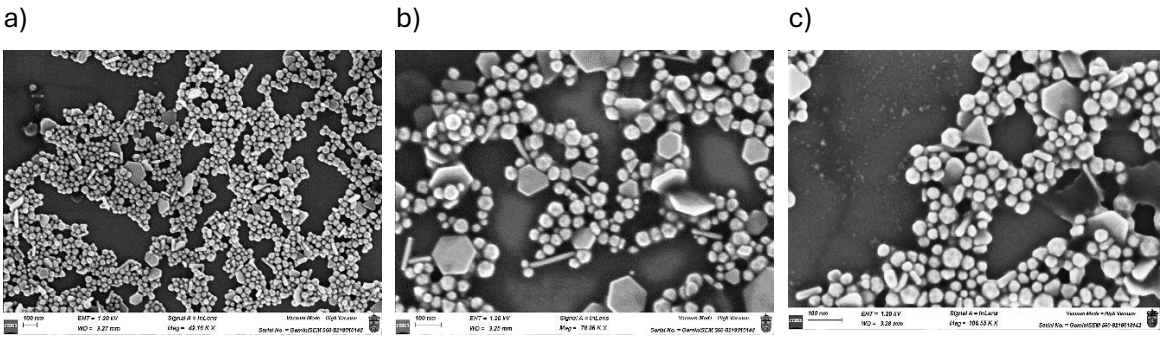

Figure 41. *FESEM images of gold nanoparticles formed when CH05-IN at 70% w.r. is mixed with $AuCl_3$. (a, b) under dark conditions (c) under light exposure.*

Transmission electron microscopy (TEM)

Finally, the samples prepared with $HAuCl_4 \cdot 3\ H_2O$ and evolved under dark conditions were analysed using TEM. The images confirmed the observations made with FESEM, revealing gold nanoparticles of various shapes, including spheres, rods and polygonal forms *(Figure 42)*.

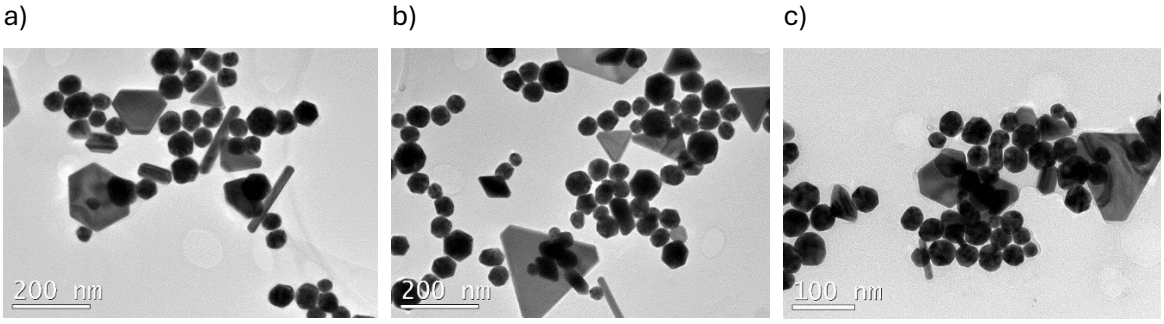

Figure 42. *(a, b, c) TEM images of gold nanoparticles formed when CH05-IN at 70% w.r. is mixed with $HAuCl_4 \cdot 3\ H_2O$.*

In some of the images, organic matter (pale grey) is combined with the gold nanoparticles *(Figure 43a*). Moreover, the nanovesicles formed by CH05-IN are clearly visible without the need for prior staining *(Figures 43b, 43c)*. This is attributed to the presence of iridium in the molecular structure of the compound, an element with a high atomic number, which enhances electron scattering and thereby increases contrast in transmission electron microscopy images.[40]

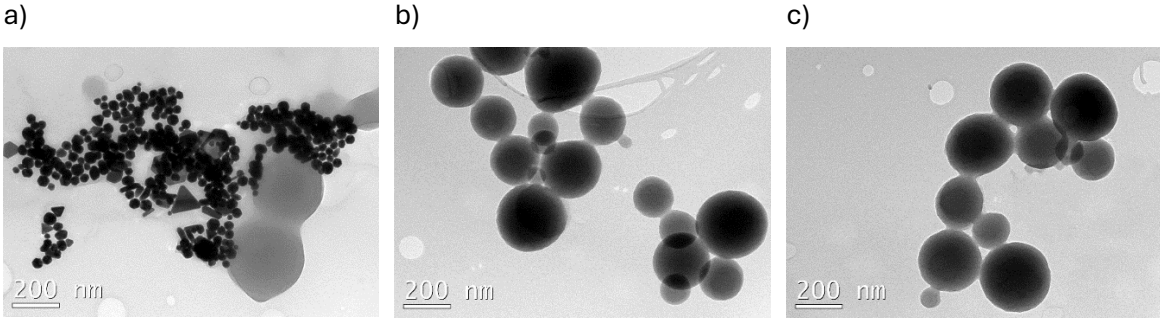

Figure 43. *TEM images of (a) gold nanoparticles mixed with vesicles of CH05-IN at 70% w.r. (b, c) nanovesicles formed by CH05-IN at 70% w.r.*

[40] R. F. Egerton, *Physical Principles of Electron Microscopy: An Introduction to TEM, SEM, and AEM*. Second edition, Springer: Cham, Switzerland, **2016,** chapter 4, pp 41–58.

10.4.2. Formation of silver nanoparticles

It was found that CH05-IN also promotes the formation of silver nanoparticles. For this purpose, the compound was mixed with 8 equivalents of $AgClO_4 \cdot 2\ H_2O$ in a solvent system composed of 70% water and 30% of THF, resulting in a final organic compound concentration of 10^{-5} M.

In this case, the spectroscopic analyses revealed that there are not significant changes in the emission spectra of the mixtures, although a decrease in absorbance was observed (see Supporting Information). Once again, the experiment was first performed leaving the samples to evolve under dark conditions and then, the experiments were repeated by leaving the samples to rest for 24 hours under white light. In this case, notable differences in the morphology and type of silver nanoparticles were observed between the two lighting conditions.

Study of silver nanoparticles when the sample evolves under dark conditions.

The mixture allowed to stand for 24 hours under dark conditions was imaged. The nanoparticles of silver (bright points) cover the surface of the organic aggregates *(Figure 44).*

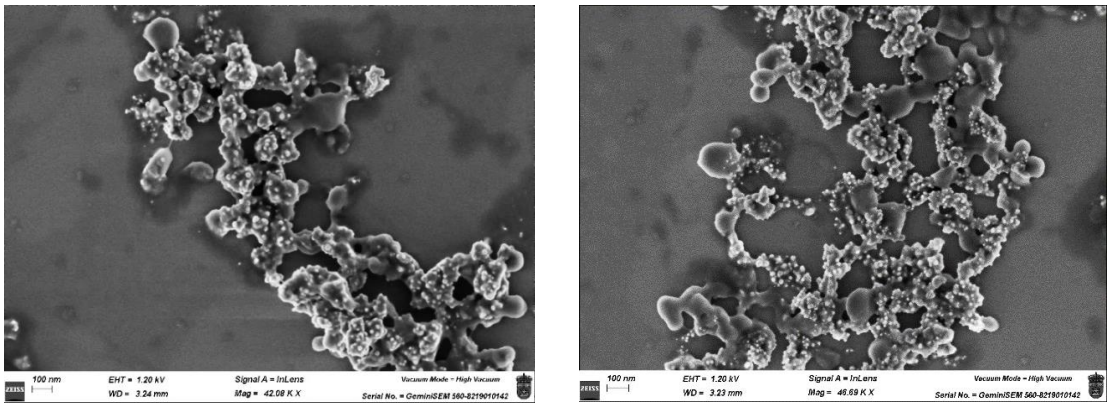

Figure 44. *Silver nanoparticles covering the organic particles' surface (CH05-IN 70% w.r., darkness).*

To verify the composition of the nanoparticles, an elemental mapping analysis was performed by EDX at 6 kV. It corroborated the silver particles cover the surface of the organic matter.

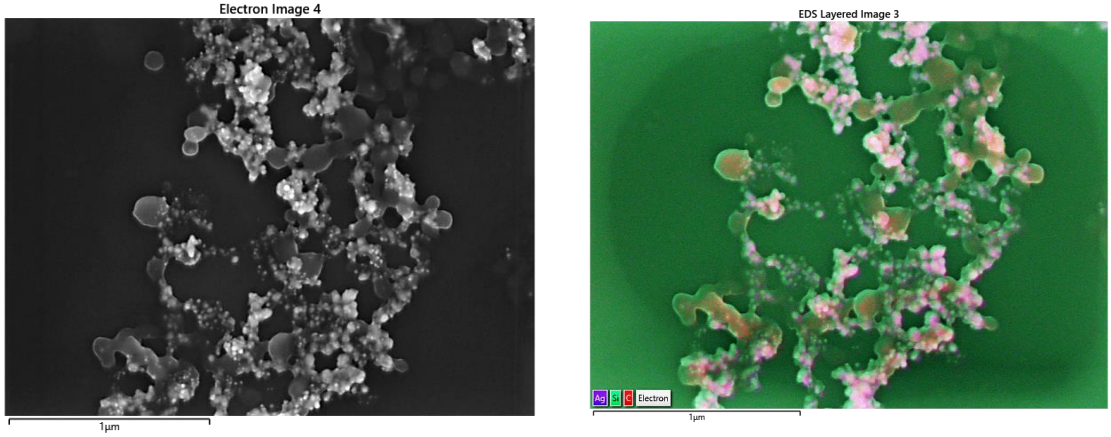

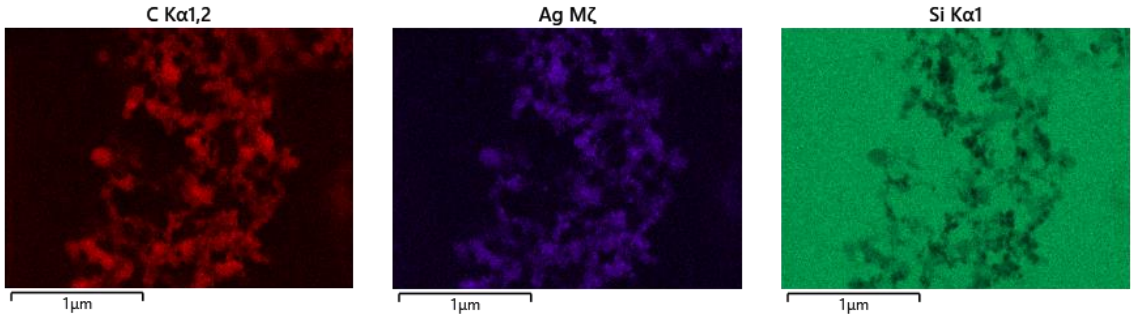

Figure 45. *EDX mapping spectra: silver nanoparticles (purple) covering the organic surface (red).*

Study of silver nanoparticles when the sample evolves under white light

Since silver(I) is known to be photosensitive,[41] before evaluating the behaviour of the organic compound in the presence of silver(I) under white light, we first verified whether a silver perchlorate solution ($8 \cdot 10^{-5}$ M in 70% water, 30% THF) would undergo spontaneous photoreduction. It was confirmed that, in the absence of the organic compound, no formation of elemental silver nanoparticles occurred upon light exposure. FESEM images revealed the presence of only unreacted flat silver(I) perchlorate crystals.

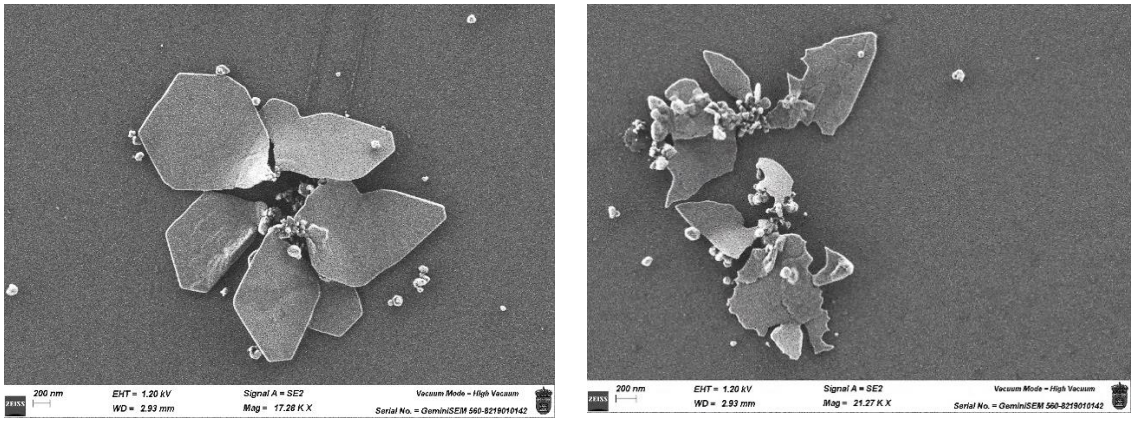

Figure 46*. Silver perchlorate plates formed in THF-H_2O at 70% w.r. (under light).*

Then CH05-IN (10^{-5} M) at 70% w.r. in THF mixed with silver(I) was allowed to stand for 24 hours under white light and then imaged. Stunning aggregates of silver nanoparticles were observed.

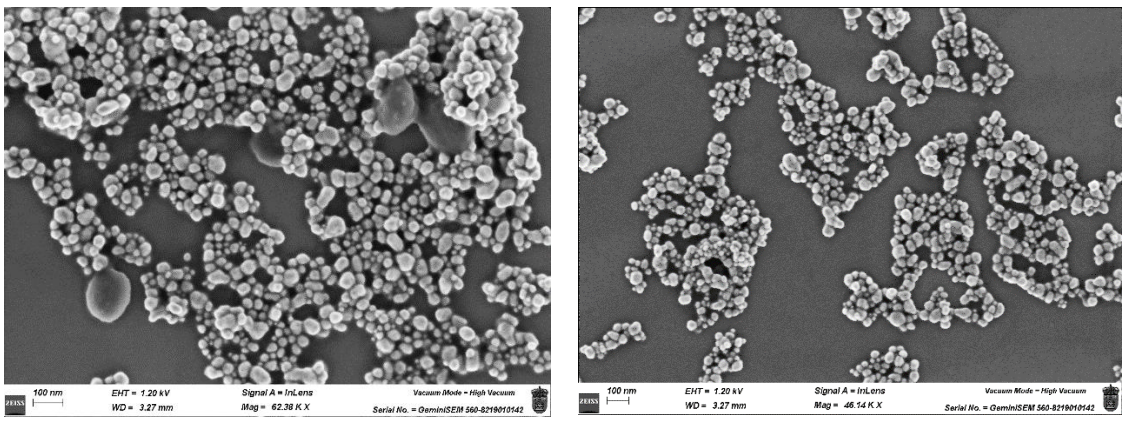

Figure 47. *Aggregates of silver nanoparticles formed with CH05-IN at 70% w.r.*

[41] H. M. Mahlamn, T. E. Willmarth, *Nature* **1964**, *202*, 590−591.

To verify the composition of the nanoparticles, a punctual elemental analysis was performed by Energy-Dispersive X-ray Spectroscopy at 6 kV. It corroborated the nature of the silver nanoparticles.

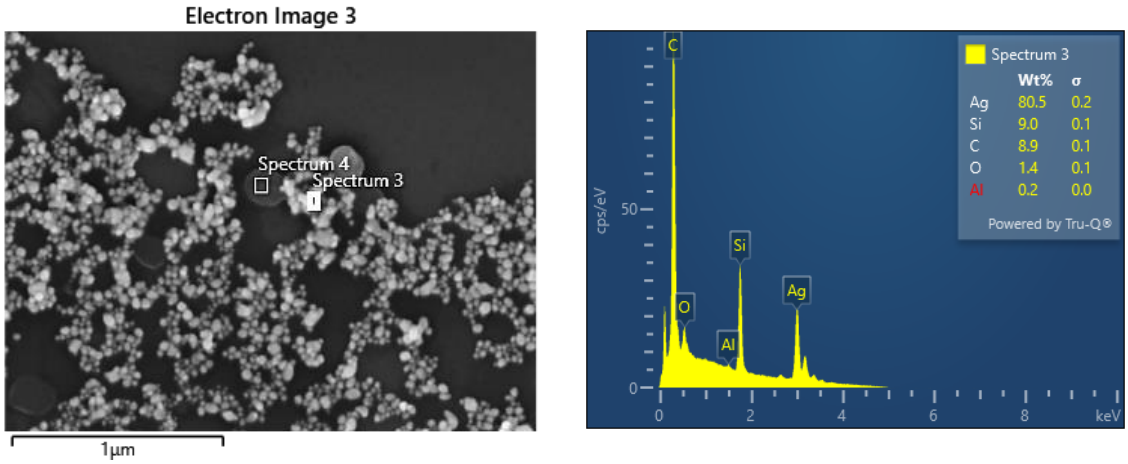

Figure 48. *Punctual EDX spectrum of silver NPs. formed with CH05-IN at 70% w.r. (under white light).*

The analysis of spectrum 3 reveals that silver is found as pure element with a mass percentage of 80.5 % *(Figure 49),* thus confirming that the silver has been successfully reduced.

Spectrum 3							
Element	Line Type	Apparent Concentration	k Ratio	Wt%	Wt% Sigma	Standard Label	Factory Standard
C	K series	23.51	0.23508	8.94	0.13	Pure Element	Yes
O	K series	2.38	0.02087	1.39	0.06	SiO2	Yes
Al	K series	0.59	0.00533	0.19	0.05	Al2O3	Yes
Si	K series	29.04	0.26630	8.97	0.12	SiO2	Yes
Ag	L series	174.54	1.74537	80.50	0.21	Pure Element	Yes
Total:				100.00			

Figure 49. *Compositional analysis of spectrum 3. Pure elemental silver is found.*

In this section it has been observed that upon mixing the silver precursor with the CH05-IN organic compound and exposing the system to white light, well-defined elemental silver nanoparticles are formed. This result is consistent with previous studies reporting light-induced reduction of silver ions in the presence of organic matter.[42] In those systems, organic compounds (especially those containing electron-donating groups) can mediate photochemical reduction processes, often through radical or electron transfer mechanisms.[43] Similarly, the molecular structure of CH05-IN, which incorporates π-conjugated systems and heavy iridium atoms, likely facilitates photoinduced electron transfer to Ag^+ ions, triggering their reduction to metallic silver under illumination. This coherence with the literature supports the idea that CH05-IN acts not only as a structural component but also as a photochemical reducing agent in the formation of silver nanoparticles.

[42] a) S. Xiong, X. Cao, H. Fang, H. Guo, B. Xing, *Sci. Total Environ*. **2021,** *775*, 145867. b) Y. Yin, M. Shen X. Zhou, S. Yu, J. Chao, J. Liu, G. *Environ. Sci. Technol.* **2014,** *48* (16), 9366−9373.
[43] a) W. C. Hou, B. Stuart, R. Howes, R. G. Zepp, *Environ. Sci. Technol*. **2013,** *47* (14), 7713-7721. b) H. Peng, H. Guo, P. Gao, Y. Zhou, B. Pan, B. Xing, *Sci. Total Environ.* **2021**, *779*, 146326.

11. CONCLUSIONS

In this chapter, new hybrid compounds based on naphthalimide fluorophores covalently linked to ruthenium(II) and iridium(III) complexes have been successfully synthesized and extensively characterized in terms of their photophysical properties, aggregation behaviour, photodynamic activity, and their ability to mediate noble metal nanoparticle formation.

First of all, it was seen that all synthesized compounds displayed aggregation-caused quenching in THF-water mixtures with high water content, indicating the formation of intermolecular interactions in aqueous-rich environments. The formation of nanovesicles was confirmed via FESEM imaging, revealing distinct morphologies depending on the metal centre and degree of functionalization. Ruthenium-based compounds formed large, irregular-surfaced vesicles that were widely spaced. A similar morphological pattern was observed for the CH08-IN compound, which contains two iridium centres. In contrast, the compound CH05-IN, which incorporates only one iridium centre, displayed a distinct behaviour: it forms small, well-defined vesicles with a high degree of aggregation.

Then, transient absorption spectroscopy revealed a multistep excited-state evolution in all compounds. Initial ultrafast energy transfer processes were detected, followed by the formation of long-lived metal-centred triplet states. The formation rate of these triplet states was found to be strongly dependent on solvent polarity and aggregation state. Ruthenium derivatives showed that the triplet state formation was faster as the water ratio increased, due to the enhanced intermolecular interactions. Evolution-associated difference spectra also verified the presence of stimulated emission in mixtures with high-water ratios, confirming that this phenomenon is also related to the formation of aggregates. However, the compound CH08-IN with two iridium centres, exhibited a distinct behaviour: its excited-state dynamics were dominated by the metal complexes, with ultrafast and direct formation of the triplet state, and without the detection of intermediate excited states. This confirms that its photophysical behaviour is conditioned by its rigid, metal-rich molecular architecture.

Given the efficient formation of long-lived triplet states in all compounds, their ability to generate singlet oxygen was subsequently evaluated. Ruthenium derivatives (CH04-IN and CH10-IN) exhibited average singlet oxygen quantum yields of approximately 0.46 ($\Phi_\Delta \approx 0.46$), while the iridium compounds showed variable values ($\Phi_\Delta = 0.20$ for CH05-IN and 0.43 for CH08-IN).

Once this ability to efficiently generate singlet oxygen was confirmed, the compounds were evaluated in biological systems. Fluorescence microscopy confirmed that all compounds were internalized efficiently into HEK-293 cells and localize in the cytoplasmic space (the specific organelle is not determined yet). Cytotoxicity assays under both dark and light conditions demonstrated significant cell death upon light activation, with IC_{50} values dropping to low micromolar or even nanomolar levels. Notably, CH05-IN exhibits exceptionally low IC_{50} values (0.03 μM under irradiation), despite its moderate singlet oxygen quantum yield, suggesting that alternative phototoxic mechanisms may be involved, probably related to its distinct self-assembly into highly ordered vesicles. These findings support the potential of these compounds as successful antitumoral agents in photodynamic therapy. In addition, they highlight the importance of continuing research in this direction, particularly toward the design of new compounds that not only exhibit high singlet oxygen generation efficiency but also replicate the aggregation-driven phototoxic mechanism observed in CH05-IN.

Finally, the monofunctionalized compounds were shown to mediate the reduction of gold(III) ions in THF-water mixtures, yielding well-defined metallic nanoparticles. The resulting gold nanoparticles lacked the typical surface plasmon resonance band, attributed to the strong interaction between the organic shell formed by the studied metallorganic compounds and the reduced gold. Moreover, CH05-IN also facilitated silver nanoparticle formation, with light exposure significantly influencing the morphology and distribution of the particles.

It can be concluded that the combined ability of these hybrid complexes to act as efficient photosensitizers in photodynamic therapy and as mediators for gold nanoparticle synthesis underlines their multifunctionality. These properties open promising research for dual biomedical and nanotechnological applications.

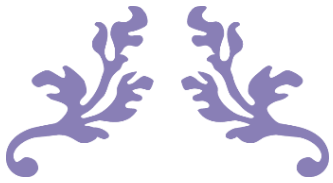

CONCLUSIONES FINALES

CONCLUSIONES FINALES

Esta tesis doctoral presenta un estudio integral sobre el diseño, síntesis y funcionalidad de agentes luminógenos derivados de naftalimida, con especial énfasis en sus propiedades de autoensamblaje, comportamiento fluorescente y aplicaciones en biomedicina y ciencia de nanomateriales.

Un aspecto clave en este trabajo es el desarrollo de sistemas agregados que se autoensamblan en forma de nanovesículas y fibras helicoidales. Estas estructuras supramoleculares se han logrado mediante un cuidadoso diseño molecular, uniendo a los núcleos de naftalimida distintas unidades, como péptidos, testosterona, ureas quirales o complejos metálicos. Es importante destacar que la formación de estas nanoestructuras ocurre en mezclas de disolvente orgánico con un alto contenido acuoso, lo que pone de manifiesto el importante papel del agua para que tenga lugar el autoensamblaje.

Los resultados demostraron que cambios sutiles en el diseño molecular (por ejemplo, la longitud peptídica, la naturaleza de las unidades aromáticas, la quiralidad de los sustituyentes o la identidad del centro metálico) tienen un impacto directo y predecible sobre la morfología, comportamiento fotofísico y función biológica de los agregados resultantes. Además, dependiendo de la naturaleza de los sustituyentes unidos al núcleo de naftalimida, los agregados pueden exhibir emisión inducida por agregación (el fenómeno predominante discutido en esta tesis) o apagamiento de la fluorescencia por agregación, (observado exclusivamente cuando se introducen complejos metálicos en el sistema).

En primer lugar, se demostró que los AIEgens unidos a depsipéptidos forman nanovesículas con actividad biológica modulable, dependiendo del número de cadenas depsipeptídicas unidas al núcleo de NMI. Cuando hay una única cadena depsipeptídica (dejando un grupo amina terminal libre), los compuestos presentan alta citotoxicidad. En contraste, la unión de dos cadenas depsipeptídicas conduce a sistemas biocompatibles capaces de transportar selectivamente cargas terapéuticas dentro de las células. Además, la conjugación de moléculas bioactivas, como el factor de preimplantación (PIF), da lugar a especies citotóxicas dependientes del tiempo, que actúan como caballos de Troya: inicialmente el sistema funciona como un portador biocompatible, y con el tiempo se vuelve citotóxico. Finalmente, cabe mencionar que todas las especies van al retículo endoplasmático.

Seguidamente se descubrió que no es necesario emplear cadenas largas de depsipéptidos (como en el primer capítulo) para lograr la formación de nanovesículas. Se comprobó que basta con alcanzar una longitud mínima del péptido D/L alternado, y que la presencia de cadenas alifáticas, insaturaciones y aminoácidos hidrofóbicos es esencial. Estos residuos proporcionan flexibilidad al sistema, permitiendo que los núcleos NMI se apilen con la curvatura suficiente para formar estructuras vesiculares. Una línea paralela de investigación reveló que estos AIEgens pueden actuar como agentes reductores y estabilizantes suaves en la síntesis de nanostructuras metálicas, incluyendo dendritas de oro y nanopartículas de plata. Además, las nanodendritas de oro demostraron actividad catalítica en acoplamientos Suzuki-Miyaura bajo condiciones respetuosas con el medio ambiente (mezclas acuosas), volviéndolas atractivas como catalizadores verdes.

Volviendo al contexto biomédico, también se desarrollaron híbridos de testosterona-naftalimida que actúan como agentes antitumorales fluorescentes con citotoxicidad modulable, útiles en el tratamiento del cáncer de próstata. Mediante la modificación del número y tipo de grupos funcionales (aminas libres, cadenas depsipeptídicas o unidades de testosterona), estos compuestos pueden comportarse como potentes agentes citotóxicos o sondas biocompatibles. La captación celular se estudió en células de cáncer de próstata AR-positivas (LNCaP) y AR-negativas (PC-3), y en ambos casos el orgánulo diana es el retículo endoplasmático para los compuestos citotóxicos (igual que en el capítulo uno), lo que sugiere que la localización celular de estos compuestos está dictada

principalmente por el núcleo de naftalimida, más que por interacciones con el receptor de andrógenos. En cambio, las especies biocompatibles se acumulan en las proximidades de la membrana, debido a la presencia de dos unidades de testosterona hidrofóbicas.

Apartándose del enfoque biomédico previamente descrito, este trabajo también explora el campo de los nanomateriales. Así, se sintetizaron híbridos quirales de NMI-urea que autoensamblan en fibras helicoidales levógiras, cuya formación está favorecida por efectos estéricos de los grupos voluminosos de urea. Los nuevos compuestos mostraron actividad óptica quiral clara, demostrada mediante dicroísmo circular y luminiscencia circularmente polarizada. Sorprendentemente, las señales de CPL tienen una componente mayoritaria hacia la derecha, siendo esto opuesto a la helicidad supramolecular levógira. Este comportamiento se atribuye a interacciones excitónicas en el estado agregado. Por otra parte, se vio que al modificar la geometría del núcleo de NMI se produce una transición de fibras helicoidales a nanovesículas, destacando el papel de la geometría del colorante en las interacciones π-π intermoleculares. Finalmente, se hicieron crecer nanopartículas de plata sobre la superficie de las hélices orgánicas, resaltando su potencial en el desarrollo de materiales nanostructurados quirales.

Finalmente, se sintetizaron nuevos derivados de NMI que incorporan complejos de iridio(III) o rutenio(II). A diferencia de los compuestos abordados en los apartados anteriores, estos híbridos muestran apagamiento por agregación en mezclas con alto contenido de agua. Se ha visto que actúan como fotosensibilizadores eficientes para terapia fotodinámica debido a su capacidad para generar oxígeno singlete. Destaca el compuesto CH05-IN, que mostró una fototoxicidad excepcional a concentraciones nanomolares, pero se cree que su citotoxicidad aumentada está impulsada por un mecanismo dependiente de la agregación más que por la generación de oxígeno singlete. Por otro lado, estos compuestos funcionan como mediadores en la formación de nanopartículas de oro y plata, lo que muestra su doble funcionalidad en aplicaciones fototerapéuticas y de nanomateriales.

Puede concluirse que estos resultados demuestran el gran poder del diseño molecular para controlar el autoensamblaje, las propiedades ópticas y la multifuncionalidad de los sistemas basados en naftalimida, dando lugar a posibles aplicaciones biomédicas y en el mundo de los nanomateriales.

FINAL CONCLUSIONS

FINAL CONCLUSIONS

This doctoral thesis presents a comprehensive study of the design, synthesis, and functionality of naphthalimide-based luminogens, with particular emphasis on their self-assembly properties, fluorescence behaviour, and applications in biomedicine or nanomaterials science.

A key point in this work is the development of versatile aggregated systems that self-assemble into well-defined nanostructures, including nanovesicles and helical fibers. These supramolecular architectures were achieved by careful molecular design, by modulating the peptide, steroidal, chiral urea, or metal-complex moieties attached to the NMI cores. Importantly, the formation of these nanostructures occurs in organic solvent-water mixtures with a high-water content, highlighting the role of aqueous environments in driving the self-assembly process. The findings consistently demonstrated that subtle changes in molecular design (e.g., peptide length, aromatic substituents, chirality, or metal center identity) have a direct and predictable impact on the morphology, photophysical behavior, and biological function of the resulting aggregates. Furthermore, depending on the nature of the substituents attached to the NMI core, the aggregates can exhibit either aggregation-induced emission (the predominant phenomenon discussed in this thesis) or aggregation-caused quenching, which is observed exclusively when metal complexes are introduced into the system.

In the first part of the thesis, depsipeptide-based AIE luminogens were shown to form nanovesicles with modifiable biological activity, depending on the number of the depsipeptide chains attached to the NMI core. When a single depsipeptide chain is present, (bearing an unprotected terminal amine group) the compounds exhibit high cytotoxicity. In contrast, the attachment of two depsipeptide chains leads to the formation of biocompatible systems capable of selectively delivering therapeutic cargos into the cells. Moreover, the conjugation of bioactive molecules, such as the preimplantation factor (PIF), results in the creation of time-dependent cytotoxic species, which act like Trojan horses: the system first behaves as a biocompatible carrier, and as time goes by, it becomes cytotoxic. Finally, it must be mentioned that all the studied species accumulate in the endoplasmic reticulum.

Subsequently, it was discovered that it is not necessary to use long depsipeptide chains (like that used in the first chapter) to achieve nanovesicle formation. Instead, a minimal length of D/L alternating peptide is required, where the presence of aliphatic chains, unsaturations and hydrophobic amino acids is essential. These residues provide flexibility to the system, allowing the NMI cores to stack with enough curvature to form vesicular structures. A parallel line of research revealed that these AIEgens can act as mild reducing and stabilizing agents in the synthesis of metal nanostructures, including gold dendrites and silver-coated vesicles. Moreover, the gold nanostructures showed catalytic activity in Suzuki-Miyaura couplings under eco-friendly conditions, making them attractive as green catalysts.

Returning to the biomedical context, this study next explored testosterone-naphthalimide hybrids as fluorescent antitumoral agents with modifiable cytotoxicity for prostate cancer treatment. By modifying the number and type of functional groups (e.g., free amines, depsipeptide chains, or testosterone units), these compounds could behave either as potent cytotoxic agents or biocompatible probes. Cellular uptake was studied in both AR-positive (LNCaP) and AR-negative (PC-3) prostate cancer cell lines. In both cases, the target organelle for the cytotoxic compounds was the endoplasmic reticulum, as also observed in chapter one. This suggests that the subcellular localization of these compounds is primarily dictated by the naphthalimide core rather than by interactions with the androgen receptor. In contrast, the biocompatible species accumulated near the plasma membrane, likely due to the presence of two hydrophobic testosterone units.

Breaking from the biomedical focus previously described, this work also explores the field of nanomaterials. Hence, we synthesized chiral NMI-urea hybrids that self-assemble into left-handed helical fibers, driven by the steric effects of the bulky urea groups. The new compounds showed clear chiroptical activity, as demonstrated by circular dichroism and circularly polarized luminescence. Unexpectedly, the CPL signals were always right-handed, opposite to the left-handed supramolecular helicity. This behaviour is attributed to excitonic interactions in the aggregated state. Additionally, modifying the substitution geometry of the NMI core led to a transition from helical fibers to nanovesicles, highlighting the role of dye geometry in the π-π stacking interactions. Finally, silver nanoparticles were successfully grown on the surface of the organic helices, highlighting their potential in the development of chiral nanostructured materials.

Finally, new hybrid luminogens incorporating iridium(III) and ruthenium(II) complexes were also synthesized. Unlike the compounds studied in earlier stages of this research, these hybrids exhibit aggregation-caused quenching in mixtures with high water content. They act as efficient photosensitizers for photodynamic therapy due to their capacity to generate singlet oxygen. Notably, CH05-IN showed exceptional phototoxicity at nanomolar concentrations, suggesting that its enhanced cytotoxicity is driven by an aggregation-dependent mechanism beyond classical singlet oxygen generation. On the other hand, these compounds serve as mild mediators for gold and silver nanoparticles formation, supporting their use in dual phototherapeutic and nanomaterials applications.

Altogether, these results demonstrate the power of molecular design in controlling the self-assembly, optical properties, and multifunctionality of naphthalimide-based systems across biomedical and nanomaterials applications.

FUTURAS LÍNEAS DE INVESTIGACIÓN

FUTURAS LÍNEAS DE INVESTIGACIÓN

A lo largo de la tesis se han tratado diversos aspectos y aplicaciones de los derivados fluorescentes de naftalimida, que van desde el autoensamblaje supramolecular y las propiedades quiral-ópticas hasta los usos biomédicos y nanotecnológicos. Sin embargo, algunos estudios permanecen abiertos para futuras investigaciones. Por ello, se proponen las siguientes líneas de trabajo que permitan continuar lo iniciado en la presente tesis:

- **Estudio del mecanismo de citotoxicidad:** tanto en el Capítulo 1 (AIEgens basados en depsipéptidos) como en el Capítulo 3 (conjugados testosterona-NMI), el mecanismo exacto responsable de los efectos citotóxicos de los compuestos aún no se ha determinado. Se ha observado que las moléculas que poseen un grupo amina libre presentan alta citotoxicidad y tienden a acumularse en el retículo endoplásmico. Esto resalta la necesidad de investigar más a fondo qué tipo de interacciones mantienen estos compuestos dentro de la célula, particularmente con enzimas o proteínas. Técnicas como la transcriptómica o la proteómica podrían ser de gran ayuda para identificar las biomoléculas afectadas. Una vez que se conozca el mecanismo citotóxico específico, será posible diseñar agentes terapéuticos más específicos y efectivos.
- **Aumentar el potencial catalítico de las nanodendritas de oro:** se ha visto que las nanodendritas de oro descritas en el Capítulo 2B son capaces de catalizar reacciones de acoplamiento Suzuki-Miyaura. Para continuar, se pretende optimizar su eficiencia catalítica en mezclas acuosas y evaluar su capacidad para catalizar otros tipos de reacciones de acoplamiento carbono-carbono.
- **Búsqueda de estructuras helicoidales más definidas**: se llevará a cabo la unión de moléculas quirales más grandes a los núcleos de NMI con el fin de controlar de manera más precisa el apilamiento entre las unidades de naftalimida. Los resultados actuales muestran que la sustitución con ureas voluminosas impide que las moléculas se dispongan en una configuración simple de cabeza con cola o perfectamente alineadas, introduciendo en su lugar un ligero giro entre NMI adyacentes. Esta distorsión es la que da lugar a la formación de nanohélices. A partir de estos hallazgos, se estudiará si sustituyentes quirales de mayor tamaño y diversidad pueden generar hélices más definidas, más abundantes y con una estructura más regular. Al mismo tiempo, estos experimentos permitirán determinar en qué medida los sustituyentes impiden el apilamiento típico de las NMI y dirigen al sistema hacia ensamblajes supramoleculares quirales que exhiben el efecto de emisión inducida por agregación.
- **Determinación del orgánulo diana de los compuestos organometálicos:** otro objetivo pendiente es determinar la localización celular específica de los compuestos organometálicos de rutenio e iridio y esclarecer si el destino celular está dirigido por la unidad de naftalimida, como se observó en compuestos previos, o si los complejos metálicos influyen en su dirección hacia un orgánulo concreto. En este contexto, es crucial examinar si el compuesto CH05-IN (que presenta un modo de agregación distinto y mayor citotoxicidad en comparación con sus análogos) posee un destino celular diferente a los demás. Una vez conocida la localización subcelular, los estudios deberán centrarse en determinar el mecanismo de acción asociado a estos compuestos, empleando técnicas como las ya mencionadas proteómica y transcriptómica y teniendo en cuenta que estos compuestos generan oxígeno singlete de forma efectiva.
- **Desarrollo de nuevos compuestos con citotoxicidad asociada al modo de agregación:** dado que CH05-IN ha mostrado una elevada fototoxicidad (probablemente relacionada con su capacidad de agregación en multitud de nanovesículas), resulta deseable diseñar y estudiar nuevos compuestos que sigan

su patrón estructural. Por ejemplo, sintetizar un análogo que contiene un anillo de pirimidina en lugar de piridina, coordinado a un complejo de iridio para evaluar si este nuevo compuesto presenta características similares de agregación, mantiene una baja generación de oxígeno singlete y conserva una fuerte eficacia en terapia fotodinámica. Estos estudios podrían ayudar a esclarecer el papel de la agregación en la potenciación de la citotoxicidad.

- **Evaluación de compuestos organometálicos con grupos Boc desprotegidos:** para dar continuidad a los estudios iniciados en el Capítulo 5, se han desprotegido los compuestos organometálicos que contienen grupos Boc, y estudios preliminares de microscopía de fluorescencia sugieren que estos nuevos productos se localizan en el núcleo de las células HECK-293. Es necesario realizar nuevos estudios para determinar su citotoxicidad, eficiencia en terapia fotodinámica y evaluar la colocalización mediante microscopía confocal para poder así caracterizar por completo esta nueva serie de compuestos.
- **Evaluación de la citotoxicidad de los compuestos en células no cancerosas:** es importante evaluar la citotoxicidad de los compuestos estudiados en los capítulos 1, 3 y 5 en líneas celulares no cancerosas, como los fibroblastos. Este paso es esencial para valorar la selectividad terapéutica de dichos compuestos. Para ello se ha de determinar si presentan un efecto citotóxico mayor en células cancerosas en comparación con células sanas. Esta evaluación resulta especialmente relevante en el caso de los compuestos que incorporan una unidad de testosterona. Se espera que éstas presenten una mayor afinidad por las células de cáncer de próstata debido a la sobreexpresión de receptores androgénicos en líneas celulares tumorales como LNCaP. No obstante, esta línea de investigación plantea un reto técnico importante: las células no cancerosas suelen presentar un crecimiento lento y ser difíciles de cultivar, lo que complica la realización de los ensayos de citotoxicidad. A pesar de estas dificultades, la confirmación de la selectividad de los compuestos hacia las células cancerosas frente a las células sanas constituye un objetivo clave dentro del desarrollo de agentes terapéuticos selectivos y eficaces.
- **Aplicaciones biológicas de las nanopartículas de plata:** las nanopartículas de plata generadas a partir de las fibras helicoidales (Capítulo 4), del complejo de iridio CH05-IN (Capítulo 5) y las obtenidas mediante los AIEgens funcionalizados con aminoácidos (CH83 y CH88 del Capítulo 2) resultan interesantes en aplicaciones biomédicas. La plata es bien conocida por sus potentes propiedades antimicrobianas,[1] ya que puede alterar las membranas bacterianas,[2] interferir en procesos metabólicos,[3] interrumpir la replicación del ADN y generar especies reactivas de oxígeno.[4] Por lo tanto, en futuras investigaciones se quiere explorar el potencial de estos sistemas recubiertos de plata en terapias antibacterianas o como agentes multifuncionales que combinen efectos antimicrobianos y fototóxicos (como en el caso de CH05-IN).

[1] A. S. Rodrigues, J. S. G. Batista, M. A. V. Rodrigues, V. C. Thipe, L. A. R. Minarini, P.S. Lopes, A. B. Lugão, *Front. Microbiol.* **2024,** *15*, 1440065.
[2] S. González-Fernández, N. Blanco-Agudín, D. Rodríguez, I. Fernández-Vega, J. Merayo-Lloves, L. M. Quirós, *Antibiotics* **2025**, *14*, 289.
[3] A. N. Kodintcev, *Chim. Tech. Acta.* **2022,** *9* (4), 20229402.
[4] I. X. Yin, J. Zhang, I. S. Zhao, M. L. Mei, Q. Li, C. H. Chu, *Int. J. Nanomedicine* **2020,** *15*, 2555−2562.

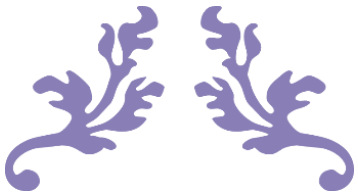

FUTURE RESEARCH LINES

FUTURE RESEARCH LINES

This thesis has explored diverse topics and applications, from supramolecular self-assembly and chiroptical properties to biomedical and nanotechnological uses of naphthalimide-based luminogens. However, some studies remain open for further investigation. Thus, the following research lines are proposed to continue the work herein started:

- **Mechanistic studies of cytotoxicity**: in both Chapter 1 (depsipeptide-based AIEgens) and Chapter 3 (testosterone-NMI conjugates), the exact mechanism behind the cytotoxic effects of the compounds is still unknown. It has been observed that molecules with an unsubstituted amine group are highly cytotoxic and tend to accumulate in the endoplasmic reticulum. This highlights the need for further studies to understand what types of interactions these compounds have inside the cell, particularly with enzymes or proteins. Techniques such as transcriptomics or proteomics could help identify the molecular targets affected. Once the specific cytotoxic mechanism is discovered, it would be possible to design more specific and effective therapeutic agents.
- **Improving the catalytic potential of gold dendrites**: the gold nanodendrites of Chapter 2B were shown to catalyse Suzuki-Miyaura coupling reactions. As a future research direction, it is desirable to improve their catalytic efficiency in aqueous mixtures and to test their ability to promote other types of carbon-carbon coupling reactions.
- **Towards more defined helical architectures:** we plan to test the attachment of larger chiral molecules to the NMI core in order to better control the way the units stack with each other. Our current results showed that these bulky urea substituents prevent the molecules from arranging in a simple head-to-tail or perfectly aligned manner, and instead introduce a small twist between adjacent NMIs. This distortion is what gives rise to the formation of nanoscale helices. Building on these findings, in future studies we will investigate whether larger and more diverse chiral substituents can produce helices that are more defined, more abundant, and more regular in structure. At the same time, these experiments will help determine to what extent the substituents consistently disrupt the typical NMI stacking and guide the system toward chiral supramolecular assemblies that display the aggregation-induced emission effect.
- **Determination of target organelle of organometallic compounds:** another important research direction involves determining the specific cellular localization of the organometallic compounds and discover whether it is directed by the naphthalimide core, as seen in previous compounds, or if the ruthenium and iridium metal complexes influence their target organelle. Within this line, it is also crucial to examine whether CH05-IN (which shows a different aggregation mode and higher cytotoxicity compared to analogues) has a distinct cellular destination. Once the cellular localization is established, further studies should focus on elucidating the mechanism of action associated with these compounds, using transcriptomics or proteomics as already mentioned in the first point and taking into account that these compounds effectively generate singlet oxygen.
- **Development of new aggregation-driven cytotoxic compounds**: Since CH05-IN has been shown to be high phototoxic (likely related to its ability to form aggregates composed of multiple nanovesicles) it is desirable to design and study new compounds following its structural pattern. For instance, an analogue bearing a pyrimidine ring instead of pyridine, coordinated to an iridium complex, should be synthesized to evaluate whether this new compound displays similar aggregation features, maintains low singlet oxygen generation, and still shows strong

photodynamic therapeutic efficacy. These studies could help to clarify the role of aggregation in enhancing cytotoxicity.

- **Evaluation of Boc-deprotected organometallic compounds**: to continue the studies started in Chapter 5, organometallic compounds bearing Boc-protected groups have been deprotected, and preliminary fluorescence microscopy studies suggest that these deprotected compounds tend to localize in the nucleus of HECK-293 cells. It is necessary to carry out comprehensive studies on their cytotoxicity, photodynamic therapy efficiency, and evaluate the colocalization using confocal microscopy to fully characterize this new series of compounds.
- **Evaluation of the cytotoxicity of the compounds in non-cancerous cells:** it is important to evaluate the cytotoxicity of the synthesized compounds from chapters 1, 3 and 5 in non-cancerous cell lines such as fibroblasts. This step is essential to assess the therapeutic selectivity of the products, by determining whether they exhibit greater cytotoxic effects on cancer cells compared to healthy ones. This is especially relevant for the compounds incorporating a testosterone moiety, which are expected to show increased affinity for prostate cancer cells due to the overexpression of androgen receptors in tumour cell lines (LNCaP). However, this line of research presents a notable technical challenge: non-cancerous cells, are typically slow-growing and difficult to cultivate, thus complicating the performance of cytotoxicity assays. Despite these difficulties, confirming the selectivity of the compounds toward cancer cells over healthy ones remains a key objective.

Biological applications of silver nanoparticles: silver nanoparticles generated from the helical fibers (Chapter 4), the CH05-IN complex (Chapter 5) and those synthesized using AIEgens with amino acids (CH83 and CH88 of Chapter 2) open interesting opportunities for biomedical applications. Silver is well known for its strong antimicrobial properties,[1] as it can disrupt bacterial cell membranes,[2] interfere with metabolic processes,[3] interrupt replication of DNA and generate reactive oxygen species.[4] Therefore, in future studies we want to explore the potential of these silver-coated systems in antibacterial therapies or as multifunctional agents combining antimicrobial and phototoxic effects (CH05-IN).

[1] A. S. Rodrigues, J. S. G. Batista, M. A. V. Rodrigues, V. C. Thipe, L. A. R. Minarini, P.S. Lopes, A. B. Lugão, *Front. Microbiol.* **2024,** *15*, 1440065.
[2] S. González-Fernández, N. Blanco-Agudín, D. Rodríguez, I. Fernández-Vega, J. Merayo-Lloves, L. M. Quirós, *Antibiotics* **2025**, *14*, 289.
[3] A. N. Kodintcev, *Chim. Tech. Acta.* **2022,** *9* (4), 20229402.
[4] I. X. Yin, J. Zhang, I. S. Zhao, M. L. Mei, Q. Li, C. H. Chu, *Int. J. Nanomedicine* **2020,** *15*, 2555−2562.

ANNEX

1. SCIENTIFIC CONTRIBUTIONS

1.1. PUBLICATIONS

Synthesis of Fluorogenic Arylureas and Amides and Their Interaction with Amines: A Competition between Turn-on Fluorescence and Organic Radicals on the Way to a Smart Label for Fish Freshness.

J. García-Tojal, J. V. Cuevas, M. J. Rojo, B. Díaz de Greñu, C. Hernando-Muñoz, J. García Calvo, M. M. Salgado, T. T. Torroba.

Molecules. **2021,** *26*, 1404.

DOI: https://doi.org/10.3390/molecules26051404

Journal classification: second quartile (Q2). Impact factor: 4.92.

New Fluorescent Reporters Capable of Ultrasensitively Detecting Trinitrotoluene on Surfaces: A Proof-of-Concept for Finding Hidden Nitroaromatics in the Workroom.

A. Revilla-Cuesta, I. Abajo-Cuadrado, M. Medrano, M. M. Salgado, G. Pecori, T. Rodríguez, C. Hernando-Muñoz, J. García-Calvo, J. Arcos, T. Torroba.

J. Photochem. Photobiol. A: Chem. **2023,** *444,* 114911.

DOI: https://doi.org/10.1016/j.jphotochem.2023.114911

Journal classification: first quartile (Q1). Impact factor: 5.141.

Pharmacological activation of insulin-degrading enzyme improves insulin secretion and glucose tolerance in diet-induced obese mice.

A. Sanz-González, I. Cozar-Castellano, C. Broca, J. Sabatier, G. A. Acosta, M. Royo, C. Hernando-Muñoz, T. Torroba, G. Perdomo, B. Merino.

Diabetes Obes. Metab. **2023,** *25,* 3268–3278.

DOI: https://doi.org/10.1111/dom.15225

Journal classification: first quartile (Q1). Impact factor: 5.8.

Chemical speciation of methylmercury and mercury(II) cations in fish by new fluorogenic naphthalimide alkynyl gold complexes: The ultimate test for detecting fish contamination.

A. Revilla-Cuesta, I. Abajo-Cuadrado, L. Quadrini, S. Failli, A. Rodriguez-Rubio, J. V. Cuevas, C. Hernando-Muñoz, J. García-Calvo, T. Torroba.

Sens. Actuators B : Chem. **2024,** *421,* 136492.

DOI: https://doi.org/10.1016/j.snb.2024.136492

Journal classification: first quartile (Q1). Impact factor: 8.0.

Self-assembling Depsipeptides on Aggregation-Induced Emission Luminogens: A New Way to Create Programmable Nanovesicles and Soft Nanocarriers.

C. Hernando-Muñoz, A. Revilla-Cuesta, I. Abajo-Cuadrado, C. Andreini, T. Torroba, N. Busto, D. Fernandez, G. Perdomo, G. Acosta, M. Royo, J. Gutierrez Reguera, A. Spinello, G. Barone, D. Black, Robert Pal.

ACS Appl. Mater. Interfaces. **2025,** *17* (6), 10097-10107.

DOI: https://doi.org/10.1021/acsami.4c19123

Journal classification: first quartile (Q1). Impact factor: 8.5.

1.2. ORAL COMMUNICATIONS AND POSTERS IN NATIONAL AND INTERNATIONAL CONGRESSES

Nuevos conjugados pseudopeptídicos fluorescentes con posibles aplicaciones biomédicas.

Carla Hernando Muñoz, Irene Abajo Cuadrado, Tomás Torroba Pérez.

VII Jornadas de doctorandos de la Universidad de Burgos.

ISBN 978-84-18465-23-9.

Burgos, Spain; 25/04/2022.

From fluorescent biomarkers to soft nanotransporters.

T. Torroba, C. Hernando, M. M. Salgado, A. Revilla, I. Abajo, N. Busto, J. Gutierrez, G. A. Acosta y M. Royo.

XXXVIII Reunión bienal de la RSEQ.

ISBN: 978-84-09-42159-6.

Granada, Spain; 27/06/2022 – 30/06/2022

Self-assembling depsipeptides on aggregation-induced emission luminogens as a new way to create programmable nanovesicles, soft nanocarriers and trojan horses of drug-peptide conjugates.

C. Hernando, M. M. Salgado, A. Revilla, I. Abajo, N. Busto, J. Gutierrez, G. Barone, A. Spinello and T. Torroba.

The International Symposium on Macrocyclic and Supramolecular Chemistry.

Reykjavik, Iceland; 25/06/ 2023 – 29/06/2023.

New fluorescent reporters capable of ultrasensitively detecting trinitrotoluene on surfaces: proof-of-concept detection of hidden nitroaromatics in the workroom.

I. Abajo, A. Revilla, M. Medrano, M. M. Salgado, G. Pecori, C. Hernando and T. Torroba.

XXXIX Reunión bienal de la RSEQ.

ISBN: 978-84-09-52207-1.

Zaragoza, Spain; 25/06/2023 – 29/06/2023.

Citotoxicidad modulable de conjugados depsipeptídicos fluorescentes y su utilidad como transportadores de macromoléculas con función farmacológica.

Carla Hernando Muñoz, Irene Abajo Cuadrado, Andrea Revilla Cuesta, Tomás Torroba Pérez.

IX Jornadas de Doctorandos de la Universidad de Burgos.

ISBN: 978-84-18465-83-3.

Burgos, Spain; 21/05/2024.

From hidden explosive sensors to environmental plastic degradation: opportunities of the locally directed supramolecular events on surfaces.

Andrea Revilla-Cuesta, Irene Abajo-Cuadrado, Carla Hernando-Muñoz, Cristian Almeida, Federica Bertocchini, Tomás Torroba.

Polymat Spotlight.

San Sebastián, Spain; 11/06/2024 – 14/06/2024

The Supramolecular Chemistry of a Cross Shaped Tetrameric Peryleneimide.

I. Abajo-Cuadrado, A. Revilla-Cuesta, M. M. Salgado, C. Hernando, M. Avella, T. Torroba.

XXIX RSEQ Biennial Meeting in Organic Chemistry.

Santa Cruz de Tenerife, Spain; 26/06/2024 – 28/06/2024.

Naphthalimide Derivatives: Structure-Dependent Control of AIE-gen Behavior.

A. Revilla-Cuesta, I. Abajo-Cuadrado, C. Hernando, T. Torroba.

XXIX RSEQ Biennial Meeting in Organic Chemistry.

Santa Cruz de Tenerife, Spain; 26/06/2024 – 28/06/2024.

Perylenediimide and indolo[3,2,1-jk]carbazole, a marriage of convenience with multiple advantages on the way to extended aromatic systems.

T. Torroba, C. Almeida, A. Revilla, I. Abajo, C. Hernando.

20th International Symposium on Novel Aromatic Compounds

Toronto, Canada; 11//08/2024 – 16/08/2024.

Desarrollo de nuevos AIEgens depsipeptídicos con aplicaciones biomédicas.

Carla Hernando Muñoz, Irene Abajo Cuadrado, Tomás Torroba Pérez.

XI Jornadas de investigadoras de Castilla y León. La aventura de la ciencia y la tecnología.

ISBN: 978-84-09-63913-7.

Burgos, Spain; 03/04/2025.

Development of new chiral AIEgen-carbamides with self-assembly into helicoidal fibers.

Carla Hernando Muñoz, Irene Abajo Cuadrado, Yeray Moreno Macías, Cristian Almeida Estévez, Tomás Torroba Pérez.

X Jornadas de Doctorandos de la Universidad de Burgos.

ISBN: 979-13-87585-13-6.

Burgos, España, 12/05/2025 – 13/05/2025.

Sustainable functional nanomaterials based on self aggregation: a new approach to active cell transport and nanoencapsulation.

T.Torroba, C.Hernando, I. Abajo, C. Almeida, Y. Moreno.

XL Reunión bienal de la RSEQ.

ISBN: 978-84-09-73753-6.

Bilbao, Spain; 30/06/2025 – 03/07/2025.

1.3. PROJECT DIRECTLY ASSOCIATED TO THE THESIS.

Project code: PID2022-142318NB-I00.

Title: Self-assembling depsipeptides on aggregation-induced emission luminogens as a new way to create programmable nanovesicles, soft nanocarriers and green functional nanomaterials (FLUONANOVESICLE).

Funding entity: Agencia Estatal de Investigación, Ministerio de Ciencia e Innovación.

Duration: 48 months. From 01/09/2023 to 31/08/2027.

Principal investigator: Tomás Torroba.

1.4. PhD THESIS FUNDING.

Reference: FPU 21/01473

Name: Convocatoria 2021 de las Ayudas para la Formación de Profesorado Universitario (FPU).

Funding entities: Ministerio de Ciencia, Innovación y Universidades.

Duration: from 19/12/2022 to 18/12/2026.

2. REAGENTS AND SOLVENTS

All reagents and solvents employed during the course of this Doctoral Thesis were obtained from a wide range of commercial suppliers, including but not limited to TCI, Sigma-Aldrich, Fluorochem, Activate Scientific, and BLD Pharmatech.

Thin-layer chromatography (TLC) was carried out on aluminum-backed plates coated with silica gel SiO_2 F-254 (Silicycle) and visualized under 366 nm UV light. Column chromatography was conducted using silica gel (particle size 40–63 μm) supplied by VWR BDH Chemicals.

3. APPARATUS

3.1. GENERAL TECHNIQUES

Absorption spectra: they were acquired with a Hitachi U-3900 spectrometer, in one-centimeter quartz cells at 25ºC.

Circular Dichroism (CD): the spectra were determined using a JASCO J-815 CD spectrometer and 1 mm path length quartz cells at room temperature. The scanning speed was adjusted to 200 nm/min, and three accumulations were acquired.

Dynamic light scattering (DLS): these measurements were taken with a Zetasizer Advance Pro Red Label apparatus.

Emission spectra: were recorded with a Hitachi F-7000 FL or a modular Edinburgh Instruments FLS980 spectrofluorometers, in one-centimeter quartz cells at 25ºC.

Fluorescence Lifetime Decays (τ): Chromophore solutions were freshly prepared in a concentration of 1-10 μM in the corresponding solvent. The decay was fitted (black) with a sum of two exponentials by convolution with the instrumental response function (red). The quality of the fit was judged by $\chi 2$ values and the plot of the weighted residues. Measurements were made with a modular spectrometer Edinburgh Instruments FLS980, with a source excitation pulsed laser of 366 – 380 nm picosecond diode. One-centimeter quartz cells, at 25ºC, were employed.

Fluorescence Quantum Yields (ØF): Fresh solutions made from high-purity dyes (or mixtures of dye with an additive) and solvent were used. Integrating sphere was used as the method and three measurements were performed for each sample in order to calculate the average. Solutions were prepared in a concentration of 1-10 μM in the corresponding solvent. The excitation wavelength is indicated in each case. Measurements were made with a modular spectrometer Edinburgh Instruments FLS980. One-centimeter quartz cells, at 25ºC, were employed.

High resolution mass spectra (HRMS): MALDI-TOF mass spectra were measured with a MALDI-TOF Bruker Autoflex Mass Spectrometry instrument, using DCTB (*trans*-2-[3-(4-tert-butylphenyl)-2-methyl-2-propenylidene] malononitrile) or DIT (dithranol) as matrixes, in modes positive or negative. The atomic mass of the molecular ion (and/or fragments) per elementary charge were reported in dimensionless quantities. Whereas ESI-TOF mass spectra were measured with a 1260 Infinity liquid chromatograph (Agilent) coupled to a 6460 Triple Quad mass spectrometer (Agilent) with a triple quadrupole (QQQ) analyzer using ESI as the ionization source.

Infrared Spectra (IR): they were recorded with a JASCO FT/IR-4200 spectrometer equipped with an ATR accessory model JASCO ATR PRO ONE.

Melting points (m.p.): they were determined on an electrothermal melting point Gallenkamp apparatus.

Nuclear magnetic resonance (NMR): the spectra were recorded with Varian Mercury-300 and Bruker Advance NEO 4500 500 MHz, spectrometers at room temperature (25ºC), with $CDCl_3$ or CD_3OD as solvents. Chemical shifts (δ) were reported in parts per million (*ppm*) relative to the residual solvent peaks, rounded to the nearest 0.01 for ^{1}H-NMR and 0.1 for ^{13}C-NMR. Spin-spin coupling constants (*J*) in ^{1}H-NMR were given in Hz, rounded to the nearest 0.1 Hz. Peak multiplicity was indicated as follows: *s* (singlet), *d* (doublet), *t* (triplet), *q* (quartet), *m* (multiplet) and *br* (broad). Relative integrals were given in ^{1}H-NMR too. All ^{13}C NMR were recordered with complete proton decoupling. Carbon types, structure assignments and attribution of peaks were determined from ^{13}C-DEPT-NMR. NMR spectra were analyzed using MestReNova NMR data processing software.

PEM-CPL spectrometer: CPL measurements were performed using a custom-built modular spectrometer. The setup included a broadband laser-driven light source (EQ 99, Elliot Scientific) coupled to a monochromator (Acton SP-2155) to select the excitation wavelength. Emission was collected at 90° relative to the excitation beam and passed through a photoelastic modulator (PEM), a linear polariser, and a second monochromator before detection by a photomultiplier tube (PMT). Signal acquisition employed lock-in amplification, enabling detection of the CPL signal as the ratio 2·AC/DC. Calibration was done using Hg-Ar and calibrated lamps (Ocean Optics), and system validation was carried out with LEDs and a λ/4 plate to produce circularly polarised light. Emission spectra were collected with 0.5 nm step size and 5 nm spectral resolution. Data were averaged over multiple scans and smoothed using a Savitzky–Golay algorithm; final dissymmetry factors were calculated from raw data with an estimated uncertainty of ±10%.

Singlet oxygen quantum yield (Φ_Δ): phosphorescence signals were collected by using a N_2 cooled InGaAs photodiode, on a spectrophotofluorometer Horiba FluoroMax, 1 cm optical path length cuvettes were used.

Solvatochromism Tests: All samples were freshly prepared in each different solvent. Photos were taken with a Canon (EOS M3) camera with a 22 mm lens. The solvents were, if it is not said otherwise: 1: H_2O, 2: MeOH (methanol), 3: DMSO (dimethylsulfoxide), 4: DMF (*N*,*N'*-dimethylformamide), 5: MeCN (acetonitrile), 6: Acetone, 7: AcOEt (ethyl acetate), 8: THF (tetrahydrofuran), 9: $CHCl_3$ (chloroform), 10: CH_2Cl_2 (dichloromethane), 11: Toluene, 12: Et_2O (diethyl ether), 13: Hex (hexane), 14: MCH (methylcyclohexane).

Transient Absorption Spectra (TAS): the measurements were performed on a setup based on a regenerative amplifier Ti:sapphire laser (Legend, Coherent), pumped by a Ti:sapphire oscillator (Micra, Coherent), emitting at 800 nm (1 kHz repetition rate, 40 fs time duration). Excitation pulses at 350 nm were obtained as the third harmonic generation of the signal output produced by a commercial optical parametric amplifier (TOPAS, light conversion), pumped by the fundamental Ti:sapphire 800 nm laser radiation. The probe beam was obtained by focusing another small portion of the fundamental laser output on a 3 mm thick calcium fluoride window, generating a white light continuum covering the 370–760 nm spectral interval. The white light was then split into a probe and reference beam using a 50% beam splitter. Pump-probe delays were introduced by sending the fraction of the pulse used to generate the white light to a motorized translation stage. Both pump and probe beams were spectrally overlapped at the sample position, and after crossing into the sample, the probe and reference beams were sent through a spectrograph coupled to a home-made detector. The sample solution was contained in a 2 mm quartz cuvette, mounted on a movable stage to avoid photodegradation and multiple excitations. Transient absorption spectra were recorded over a time interval extending up to 3.5 ns, with the detection spectral range spanning from 370 to 760 nm. The time resolution of this experiment was about 150 fs.

3.2. MICROSCOPY

Atomic Force Microscopy (AFM): high resolution AFM was performed with a CYPHER-ES apparatus. The tapping mode was performed in air with the CYPHER (Asylum Research, USA) atomic force microscope. AC 160AC-NA silicon cantilevers (OPUS by MikroMasch) with resonance frequencies of 300 kHz and spring constants of 26 N/m were used. Images were processed using the IgorPro 6.3.8.1. (WaveMetrics, USA) software and Gwyddion 2.61. Nanoparticles were deposited via drop-casting on fresh cleaved mica discs (Highest Grade V1 AFM Mica Discs, 15mm, Ted Pella, INC). To obtain the punctured vesicles, they were subjected to several cycles of force application, acquiring images before and after the process. In fact, one of the vesicles eventually became completely deformed. In the other hand, low resolution AFM was performed with a Alpha300R – Alpha300A AFM Witec apparatus.

Scannning electron microscopy: Low resolution SEM was performed with a JEOL JSM-6460LV apparatus, gold metallization with an Emitech 500 apparatus. High resolution FESEM was performed with a ZEISS, FE-SEM Gemmini SEM560 apparatus, with a Schottky type field emission cathode. Nanoparticles were deposited via drop-casting on Silicon Wafer type P100 4", cut into 5x5mm chips (Micro-Tec). Although the samples measured by FESEM were of an organic nature, it was not necessary to subject them to a gold metallisation process, but the application of a voltage of 1.2 kV was enough.

Confocal microscopy:

- Chapter 1: it was performed with a Leica TCS SP8 STED 3X apparatus.
- Chapter 3: it was performed with a Leica TCS SP8 lighting apparatus.

High Resolution TEM (HR-TEM):

- Chapters 1 and 4: the equipment was a JEM-2200F working at 200kV of accelerating voltage. Samples were stained with uranyl acetate.
- Chapters 2B and 5: the equipment was a JEOL JEM GRAND ARM300FC working at 200kV of accelerating voltage.

Medium Resolution transmission electron microscopy (TEM): the equipment was a JEOL JEM 2100 working at 200kV of accelerating voltage. (chapters 2B and 5)

Widefield Single Molecule Microscopy: cells were imaged with a custom microscope with single-objective light sheet for fluorescence excitation. It reaches single molecule sensitivity up to 90 microns in depth. Several laser lines are available for excitation of fluorescent probes in the visible range combined with multiple fluorescence filters to select the fluorescence emission.